STIFFNESS AND FRICTION CHARACTERIZATION OF BRUSH SEALS

by

ERTUĞRUL TOLGA DURAN

Submitted to the Graduate School of Engineering and Natural Sciences
in partial fulfillment of
the requirements for the degree of
Doctor of Philosophy

SABANCI UNIVERSITY

August 2013

STIFFNESS AND FRICTION CHARACTERIZATION OF BRUSH SEALS

APPROVED BY:

Assoc. Prof. Mahmut F. AKŞİT *(Thesis Advisor)* .....

Assoc. Prof. Kemalettin ERBATUR .....

Assoc. Prof. Ali KOŞAR .....

Prof. Dr. Yahya DOĞU .....

Assoc. Prof. Hüseyin KIZIL .....

DATE OF APPROVAL: .....

STIFFNESS AND FRICTION CHARACTERIZATION OF BRUSH SEALS

Ertuğrul Tolga DURAN

Mechatronics, PhD. Dissertation, 2013

Thesis Advisor: Assoc. Prof. Mahmut F. AKŞİT

Keywords: Brush Seal, Brush Seal Stiffness, Brush Seal Structural Analysis, Brush Seal Finite Element Analysis, Brush Seal Hysteresis, Bristle Stress, Brush Seal Friction Characterization, Pressure Stiffening

ABSTRACT

Improvements in steam and gas turbine technologies constantly drive harsher conditions, which result in thermodynamic cycles having higher pressure ratios and inlet temperature levels as well as increased leakage flows. Necessity of reducing the internal leakage flows and thermodynamic cycle losses while increasing the turbine overall efficiency puts greater importance on improvements in sealing technologies. Labyrinth seals have been used almost since the invention of gas turbines and their technology is very well developed over the years. However, leakage rates are still not satisfactory and cannot meet the performance requirements of new generation turbines. Brush seals are fulfilling the leakage performance requirements and they can successfully compensate rotor interference at turbine transient conditions. Due to their superior and stable leakage performance and compact size, brush seals are replacing traditional labyrinth seals at critical sections of turbines. A brush seal consists of a series of bristles which rub on the shaft surface. Since the bristles slide against the high-speed rotating shaft, friction and wear at the bristle tip contact becomes a major concern as it determines the life and efficiency of the seal and also rotor stability. Evaluating bristle tip contact forces and resulting stress levels at operating conditions is critical to optimize the seal performance and safety. A brief literature survey reveals the lack of

test data and analysis methods for evaluating seal stiffness and stress levels at operating conditions. In an attempt to meet this need, custom test rig design and methodology has been developed to perform stiffness tests at turbine operating conditions. Analytical studies and finite element simulations have been performed for test seals and results have been correlated with the test data of this study. Furthermore, stiffness and friction characterization of brush seals has been conducted through correlated FE models, and MATLAB based code has been developed for automatic brush seal FE model generation for ABAQUS simulations.

FIRÇA KEÇELERİN KATILIK VE SÜRTÜNME KARAKTERİZASYONU

Ertuğrul Tolga DURAN

ME, Doktora Tezi, 2013

Tez Danışmanı: Doç. Dr. Mahmut F. AKŞİT

Anahtar kelimeler: Fırça Keçe, Fırça Keçe Katılığı, Fırça Keçe Yapısal Analizi, Fırça Keçe Sonlu Eleman Analizi, Fırça Keçe Histerisisi, Fiber Gerilmeleri, Fırça Keçe Sürtünme Karakterizasyonu, Basınç Altında Katılık Artışı

ÖZET

Buhar ve gaz turbin teknolojilerindeki gelişmeler sürekli olarak daha yüksek basınç oranlarına ve giriş sıcaklıklarına sahip termodinamik döngülere neden olan zorlu çalışma koşullarını da beraberinde getirmektedir. Türbin toplam verimini arttırmak için kaçak akışları ve termodinamik kayıpları indirgeme gereksinimi göz önünde bulundurulduğunda, sızdırmazlık teknolojilerindeki gelişmeler turbomakina endüstrisi için büyük önem arz etmektedir. Labirent tipi sızdırmazlık elemanları neredeyse gaz türbinlerinin icadından bu yana kullanılan bir teknoloji olup yıllar boyu doygunluk derecesine ulaşacak şekilde geliştirilmesine rağmen, kaçak akış oranları halen tatmin edici seviyede değildir ve yeni nesil türbin gereksinimlerini karşılayamamaktadır. Fırça tipi sızdırmazlık elemanları akış performans gereksinimlerini karşılamakta olup, türbin geçici rejim koşullarında da rotor temasını başarılı bir şekilde kompanze edebilmektedirler. Üstün performansları, kararlı sızdırmazlık karakteristikleri ve kompakt boyutları sebebiyle fırça tipi keçeler kritik türbin segmentlerinde geleneksel labirent keçelerin yerini almaktadırlar. Fırça keçeler bir araya getirilmiş fiberlerden ibaret olup, çalışma koşullarında bu fiberler yüksek hızda dönen şaft yüzeyine sürtmektedirler. Yüksek hızda dönen şaft yüzeyi üzerinde kayan fiber uçlarında gerçekleşen rotor teması ve bunun sonucunda oluşan sürtünme ve aşınma, fırça keçe

ömrünü ve verimini belirlemenin yanında rotor kararlılığı açısından da büyük önem arz etmektedir. Türbin çalışma koşullarında fiber ucu temas kuvvetlerini ve bunun sebep olduğu gerilme seviyelerini belirlemek, performans optimizasyonu ve keçe dayanımını açısından oldukça önemlidir. Gerçekleştirilen literatür taraması sonucunda çalışma koşullarında oluşan keçe katılığı ve fiber gerilmelerini hesaplayacak analiz metodlarının eksikliği belirlenmiştir. Bu eksikliği gidermek adına, türbin koşullarında katılık testleri yapmaya imkan verecek test düzeneği tasarımı gerçekleştirilmiş ve test metodolojisi geliştirilmiştir. Test keçeleri için analitik çalışmalar ve sonlu eleman analizleri gerçekleştirilerek elde edilen sonuçlar test verileri ile karşılşatırılmış ve korelasyon sağlanmıştır. Fırça keçe katılık ve sürtünme karakterizasyonu korele edilmiş sonlu eleman modelleri ile gerçekleştirilmiş, fırça keçe sonlu eleman analizleri için model dosyasınını otomatik olarak oluşturulmasına yarayan MATLAB tabanlı kod yazılmıştır.

TABLE OF CONTENTS

LIST OF FIGURES

LIST OF TABLES

NOMENCLATURE

A	=	Bristle cross section area
A_b	=	Projected bristle cross section area
$A_{eff\text{-}pad}$	=	Effective bristle area
a_1	=	Approximated bristle length for the linear pressure load high gradient
a_2	=	Approximated bristle length for the linear pressure load low gradient
a_3	=	Total bristle length for the linear pressure load
b	=	Loaded bristle length
b_{mod}	=	Modified loaded length with pressure load at combined loading
BH	=	Free bristle height
BH_{cor}	=	Corrected free bristle height
C_{RTR}	=	Effective bristle coefficient for rotary test rig
d	=	Bristle diameter
D	=	Corrected Bristle diameter
e	=	Geometric center of the distributed load
E	=	Elastic modulus of the bristle
E_c	=	Energy required to plastically strain the material in compression
E_s	=	Shear strain energy for a ductile material
FH	=	Fence height
F_b	=	Bristle tip contact force
$F_{b\text{-}y}$	=	y-component of the bristle tip contact force
$F_{b\text{-}z}$	=	z-component of the bristle tip contact force
$F_z(z)$	=	Internal axial force in the bristle
$F_{\Delta P}$	=	Normal force per bristle row acting on backing plate portion
I	=	Second moment of inertia for bristle section
$K_{seal\text{-}BTF}$	=	Seal stiffness – BTF
$K_{beam\text{-}BTF}$	=	Seal stiffness – beam theory
L	=	Free bristle length
L_{cor}	=	Corrected free bristle length
$L_{metallic\text{-}pad}$	=	Metallic pad arc length
$N_{bristle\text{-}effective}$	=	Number of bristle rows contacting the half rotor
$N_{briste\text{-}pad}$	=	Number of bristles contacting metallic pad
$l_{c\text{-}c}$	=	Center-to-center distance for end bristles
$l_{t\text{-}CAE}$	=	Effective tangential distance between end bristles in the CAE model
ΔL	=	The apparent shortening of the beam due to bending
M_1	=	Mass of the rotor fragment
M_2	=	Effective mass of the shell
$M_x(z)$	=	Internal bending moment in the bristle in local x-direction
$M_y(z)$	=	Internal bending moment in the bristle in local y-direction
NR	=	Number of bristle rows
NR_{ave}	=	Average number of bristle rows
NR_{calc}	=	Calculated number of bristle rows
P_b	=	Contact pressure
P_{bc}	=	Pressure at backing plate
P_B^*	=	Non-dimensional backing plate pressure
P_B	=	Pressure at backing plate upstream surface

P_{max}	=	Maximum indenter pressure
P_u	=	Upstream pressure
P_d	=	Downstream pressure
ΔP	=	Pressure load
ΔP_B	=	Pressure difference across the bristle pack above the fence height
RF_{total}	=	Total contact force on rotor for the CAE analysis
$RF_{measured}$	=	Measured force from load cell
RF_{circ}	=	Contact force per rotor unit circumferential length
r	=	Bristle radius
r_1	=	Approximated radial height for the linear pressure load high gradient
r_2	=	Approximated radial height for the linear pressure load low gradient
R	=	Brush seal inner radius
R_{bp}	=	Backing plate end radius
RF_{test}	=	Measured reaction force on metallic pad
RF_{RTR}	=	Measured reaction force in full rotor stiffness tests
ΔR	=	Radial interference
S_A	=	Axial spacing between bristles
$S_{A\text{-}min}$	=	Minimum axial spacing between bristles
S_T	=	Tangential spacing between bristles
$S_{T\text{-}min}$	=	Minimum tangential spacing between bristles
S_y	=	Yield strength
$V_x(z)$	=	Internal shear force in the bristle in local x-direction
$V_y(z)$	=	Internal shear force in the bristle in local y-direction
w	=	Load per unit length
w_1	=	Uniformly distributed load at fence height region
w_2	=	Height for the linear load w_{b2}
w_3	=	Difference between w_1 and w_2
w_{b1}	=	Slope of the linearly loaded region with high pressure gradient
w_{b2}	=	Slope of the linearly loaded region with low pressure gradient
x	=	x-coordinate
y	=	y-coordinate
y^*	=	Translated y-coordinate above the fence height region
y_d	=	Bristle tip deflection in y-direction
z	=	z-coordinate

Greek Symbols

θ	=	Cant angle
$\sigma_{bend\text{-}Mx}$	=	Bristle bending stress due to M_x
$\sigma_{bend\text{-}My}$	=	Bristle bending stress due to M_y
σ_{axial}	=	Bristle axial stress
τ_{xy}	=	Transverse shear stress - xy
τ_{zx}	=	Transverse shear stress - zx
τ_{zy}	=	Transverse shear stress – zy
τ_d	=	Dynamic shear strength of the material for impact analyses
σ_x	=	Normal stress in x-direction
σ_y	=	Normal stress in y-direction
σ_z	=	Normal stress in z-direction
σ_{VM}	=	Von Mises stress

ε_b	=	Bristle surface roughness
ε_r	=	Rotor surface roughness
ε_{bp}	=	Backing plate surface roughness
ϵ	=	Size of bristle asperity peaks
ρ	=	Density
μ_{bp}	=	Backing plate-bristle friction coefficient
μ_{ib}	=	Inter-bristle friction coefficient
μ_{rb}	=	Rotor-bristle friction coefficient
$\upsilon_{fragment}$	=	Velocity of the fragment
η	=	Bristle density *(Number of bristles per circumferential rotor length)*

Abbreviations

BTF	=	Bristle Tip Force
BTP	=	Bristle Tip Pressure
CAD	=	Computer Aided Design
CAE	=	Computer Aided Engineering
DOF	=	Degree Of Freedom
FE	=	Finite Element
FSS-TR	=	Free-State-Stiffness Test Rig
RTR	=	Rotary Test Rig
VM	=	Von Mises
RF	=	Reaction Force

1 INTRODUCTION

Improvements in steam and gas turbine technologies constantly drive harsher conditions, which result in thermodynamic cycles having higher pressure ratios and inlet temperature levels as well as increased leakage flows. Necessity of reducing the internal leakage flows and thermodynamic cycle losses while increasing the turbine overall efficiency puts greater importance on improvements in sealing technologies. Sealing technology plays an important role in controlling turbo machinery leakages and coolant flows in turbines and compressors. They also help to control overall rotor dynamic stability during transient conditions. Improvements in sealing lead to 0.2 to 0.6% reduction in heat rate and 0.3 to 1% increase in power output in compressor applications.

Seal clearance is the most important parameter in determining leakage performance, where excessive clearances cause efficiency losses and flow instabilities. Brush seals has emerged a seal technology in order to avoid clearance related problems and to achieve higher efficiencies. Labyrinth seals and carbon seals are other sealing elements that are commonly used in turbo-machinery sealing.

Labyrinth seals have been used almost since the invention of gas turbines and their technology is very well developed over the years. However, leakage rates are still not satisfactory and cannot meet the performance requirements of new generation turbines. Brush seals are fulfilling the leakage performance requirements and they can successfully compensate rotor interference at turbine transient conditions. Due to their superior and stable leakage characteristics and compact size, brush seals are replacing traditional labyrinth seals at critical sections of turbines. Studies in the literature have shown that improvements in reducing leakage flows can result in increases in thrust as much as 17% [1].

1.1 Overview of Sealing Technology

Controlling the turbo-machinery leakage flows and interface clearances is known to be the most effective method of improving total output efficiency. Seals are required to achieve critical needs in meeting the system performance requirements of modern turbo-machinery. In a steam turbine, the inter-stage shaft packing, bucket tips and end packing locations are known to be the critical locations for seals on an industrial steam turbine *(Figure 1.1)*. Leakage in a steam turbine at the gaps between stationary and rotating parts can account for as much as 29% of the total stage efficiency, which means that sealing accounts for nearly 1/3rd of total stage efficiency loss in steam turbines [2, 3].

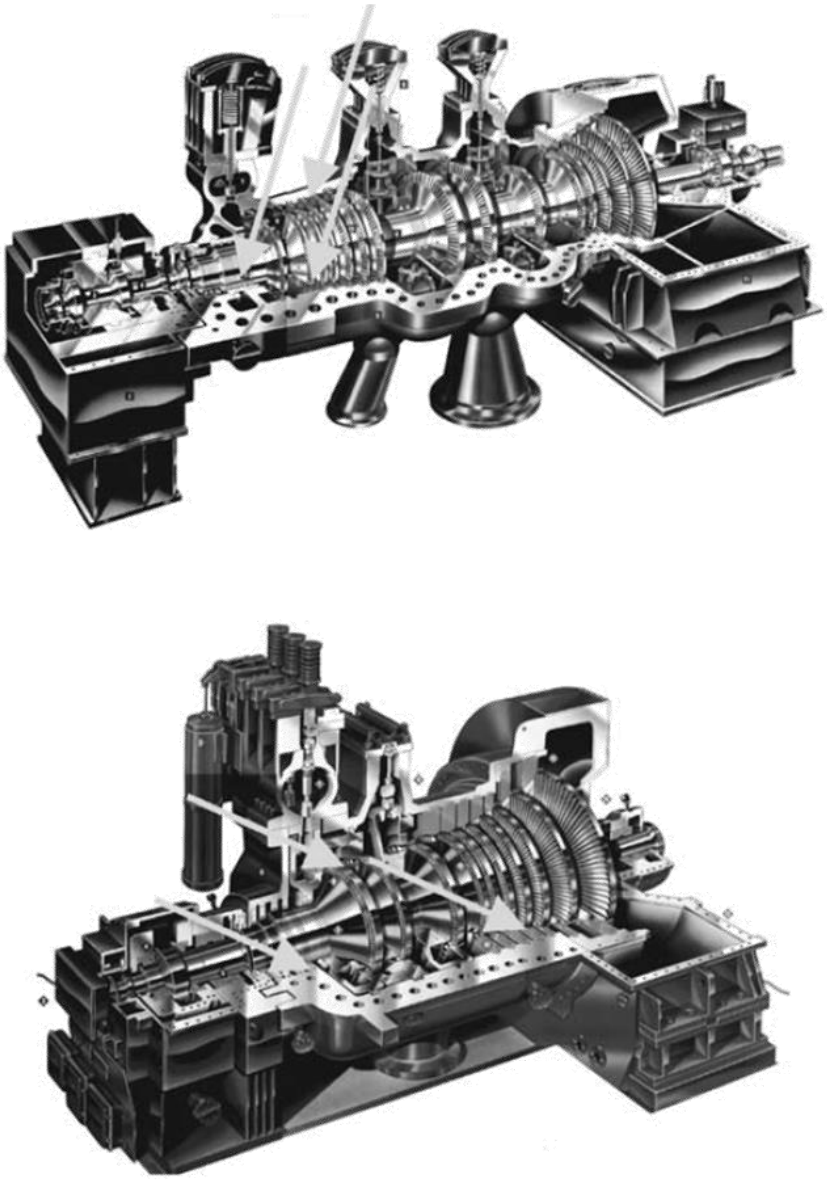

Figure 1.1: Typical sealing locations for industrial steam turbines [2]

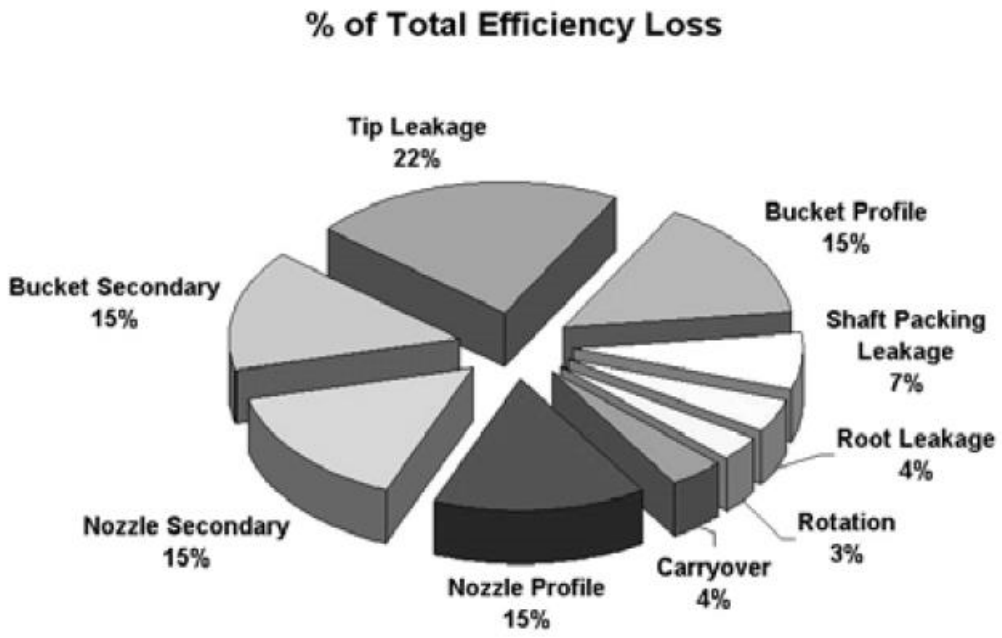

Figure 1.2: Typical sources of steam turbine stage efficiency loss [3]

Turbo-machinery sealing applications can be divided into three main groups as following; *"Static seals"*, *"Dynamic seals"* and *"Advanced seals"*. Static seals are used between static or slow interface relative movement locations in turbo-machinery such as junctions of combustors, nozzles, shrouds etc. [4]. Dynamic and advanced seals are used for clearance control between static and rotating components in various compressor and turbine stages. Considering the operation principle of turbo-machinery, dynamic seals have crucial importance in controlling leakages and improving total efficiency of turbines. Seal groups and typical types of seals are visualized in Figure 1.3.

TYPES OF SEALS		
STATIC SEALS	**DYNAMIC SEALS**	**ADVANCED SEALS**
1. Metallic seals	1. Tip sealing	1. Finger seal
2. Metallic cloth seals	2. Abradables	2. Non-contacting finger seal
3. Cloth and rope seals	3. Labyrinth seals	3. Leaf and wafer seals
	4. Brush seals	4. Hybrid brush seals
	5. Face seals	5. Aspirating brush seals
	6. Oil seals	6. Micro-dimple
	7. Buffer sealing	7. Wave interfaces
	8. Honeycomb seals	8. Seal bearing
	9. Rim sealing	

Figure 1.3: Sealing technology – Seal groups and typical seal types in turbo-machinery industry

Labyrinth seals have been used widely from the early days of gas turbines, and it is known as the most commonly used dynamic type of seal over turbine history. Labyrinth seals consist of multiple knife edges that can be configured in many ways [5] as visualized in Figure 1.4 [6]. Principal design parameters of labyrinth seals include clearance and throttle, tooth number and cavity geometry. Generalized schematics of labyrinth seal is detailed in Figure 1.5 [7].

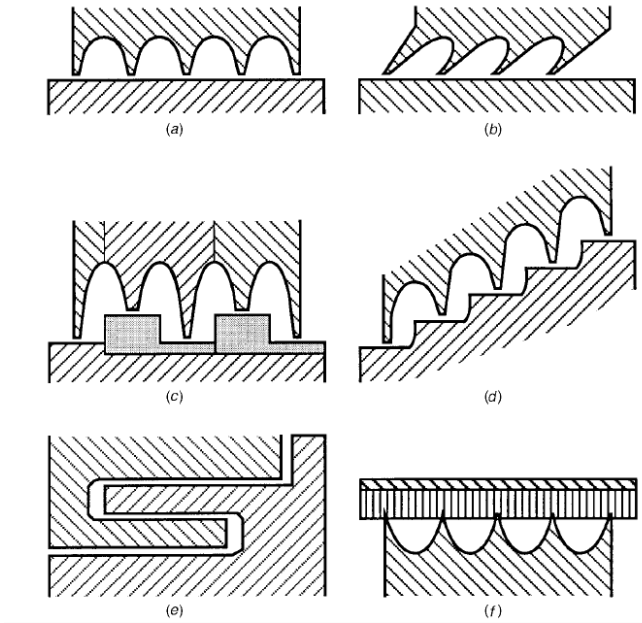

Figure 1.4: Labyrinth seal configurations: a) Straight labyrinth, b) Inclined/angled teeth straight labyrinth, c) Staggered labyrinth, d) Stepped labyrinth, e) Inter-locking labyrinth, f) Wear-in labyrinth [6]

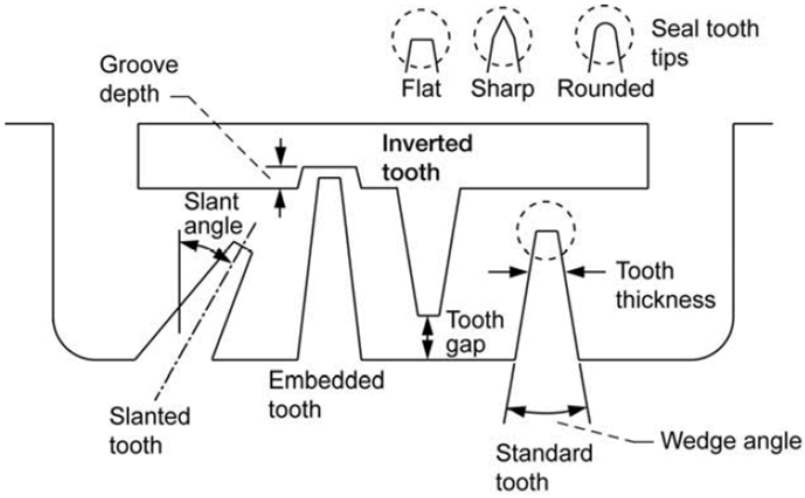

Figure 1.5: General schematics of labyrinth seal and typical design parameters [7]

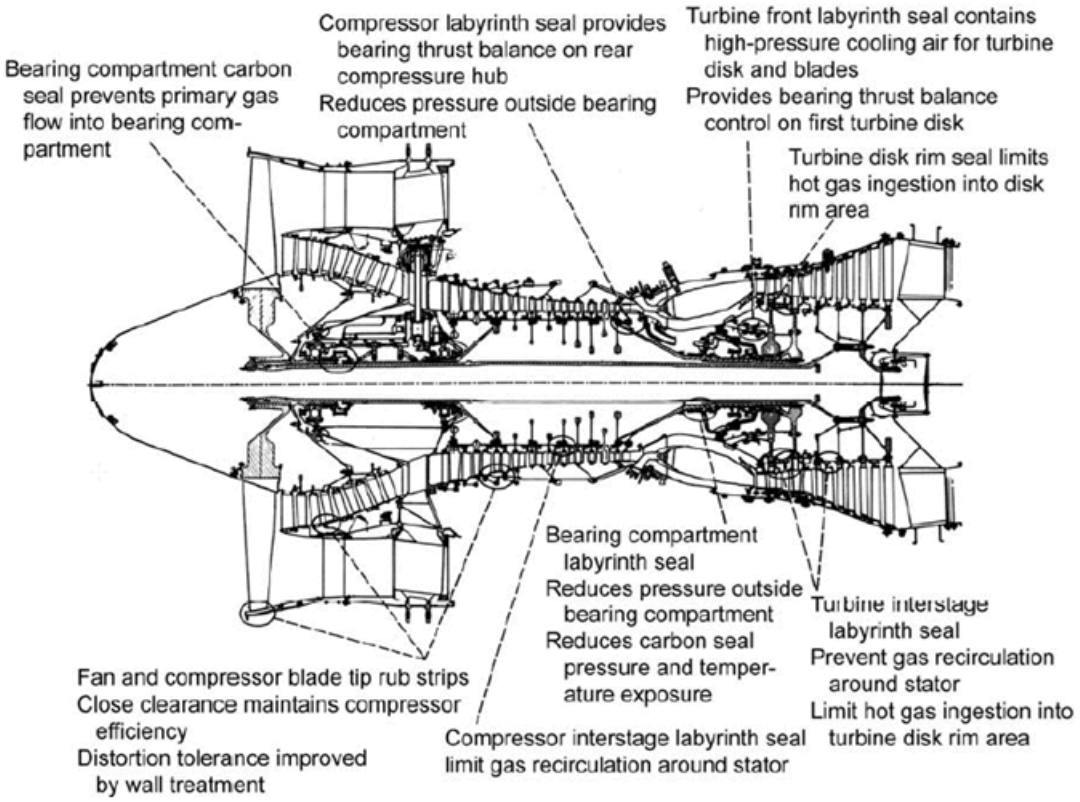

Figure 1.6: Key aero-engine sealing locations [8]

Labyrinth seals are utilized at several turbine locations *(Figure 1.6 [8])* and they are clearance seals which can rub against their shroud interface, such as abradables and honeycomb [4]. Since those labyrinth seals cannot accommodate excessive rotor interference at turbine transients, they are initially installed with certain level of clearance values. The requirement of initial clearance result in leakage performance degradation since rotor operates with that clearance at steady state conditions. Initial installation clearances can be tighter, but friction and wear induced by rotor rub and thermal growth yields parasitic leakages, performance loss, excessive heat generation and rotor instability issues. It is stated by Ludwig and Bill [9] that clearance increment of labyrinth seals can result in 17% loss in power and 7.5% increase in specific fuel consumption.

Brush seals has emerged a seal technology in order to avoid clearance related problems and to achieve higher efficiencies. They can successfully accommodate rotor transients and can be installed without clearance. The leakage performance comparison of single stage brush seal with various five-finned labyrinth seals at a pressure ratio of 2 is visualized in Figure 1.7, where the data has been collected by Chew et al. [10] at

Rolls-Royce PLC Laboratories. As it can be seen from the visualized data, the brush seal leakage performance is much better in comparison with labyrinth seals, which shows enormous sealing potential of brush seals. Significant leakage performance improvements of brush seals have also been stated by Carlile et al. [11], who reported leakage reduction up to 9.5 times in comparison with labyrinth seal.

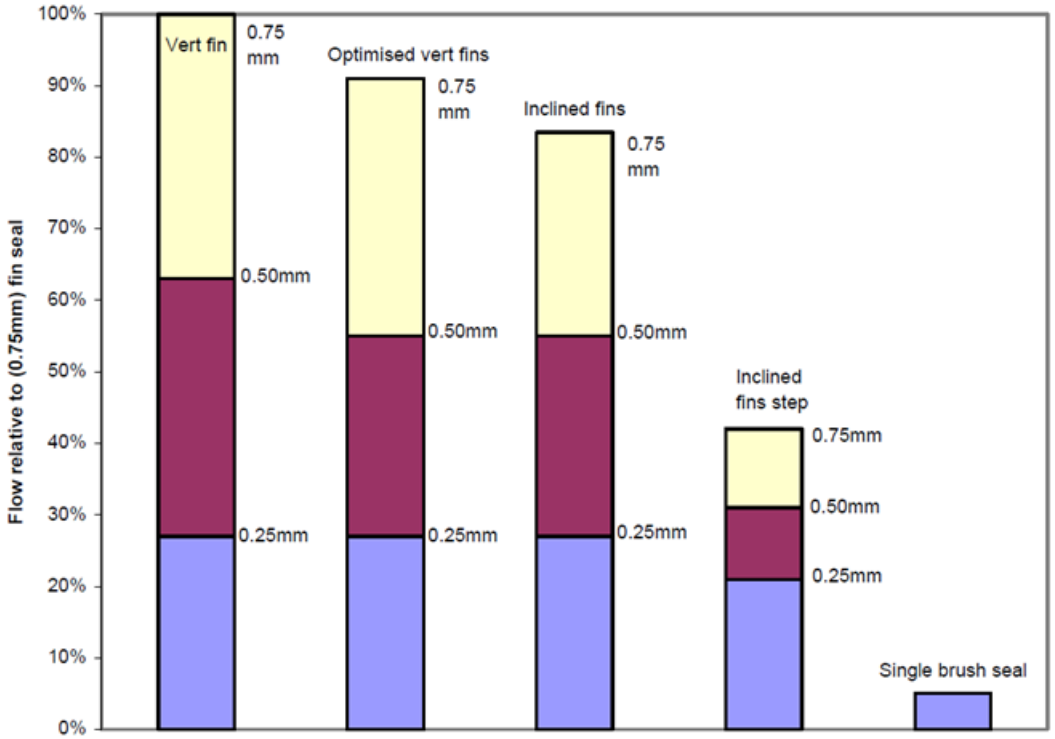

Figure 1.7: Sealing performance of brush seal compared with various five-finned labyrinth seals at a pressure ratio of 2.0 [10]

Carbon seals are also offering low leakage flow rates and can be stated as another alternative to labyrinth seals. However, those types of seals require highly polished surfaces and their axial shaft translation capability is low [12]. Assembly damage potential due to their brittle structure, high levels of heat generation at rotor rub and short operating lives are also other disadvantages of carbon seals when compared with brush seals.

1.2 Brush Seal

Brush seal is a dense pack of fine diameter *(0,05 to 0,15mm)* wire bristles which is sandwiched and welded between backing plate and the retaining plate *(front plate)*. Fiber density is around 785fiber/cm *(2000 fibers/in)*. The weld on the seal outer diameter is machined to obtain tight tolerances at the outer sealing surface which is fitted into a suitable housing. The wire bristles are extended radially inward after the backing plate, and they are machined to form a bore fit with the mating rotor. Brush seals are mounted around a rotor with a slight interference. Selection of interference must be properly done to avoid catastrophic rotor overheating and excessive rotor thermal growths. *"Fence height"* is the radial distance between backing plate inner radius and bristle tips, and *"Free bristle height"* is defined as the radial distance between pinch point and seal inner radius. Brush seal cross-section with typical dimensions is visualized in Figure 1.8 [13], and high quality photos for brush seals are given in Figures 1.9 and 1.10.

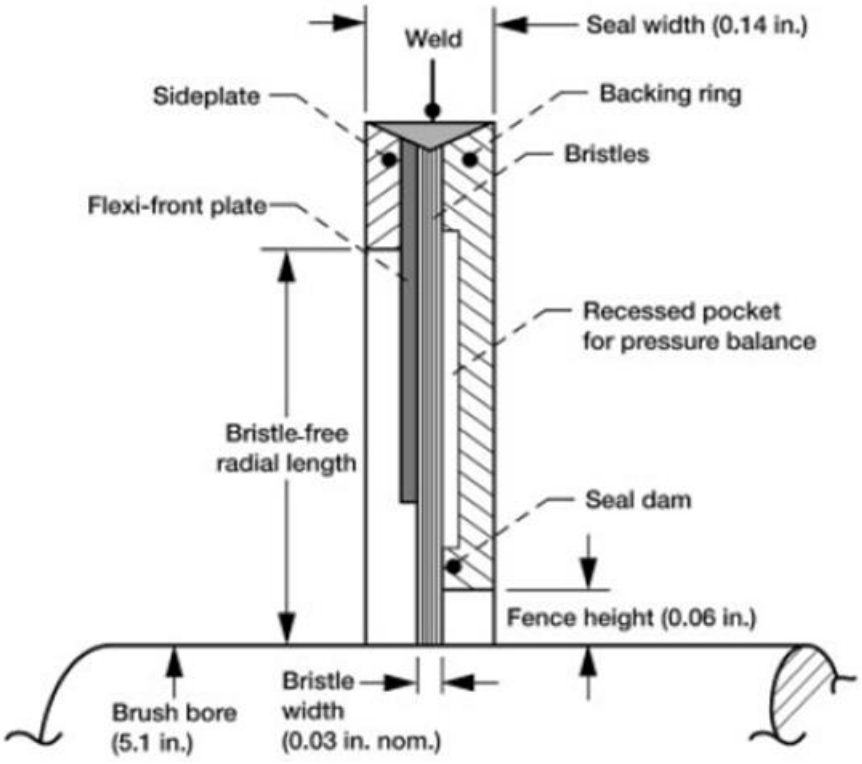

Figure 1.8: Brush seal cross-section with typical dimensions [13]

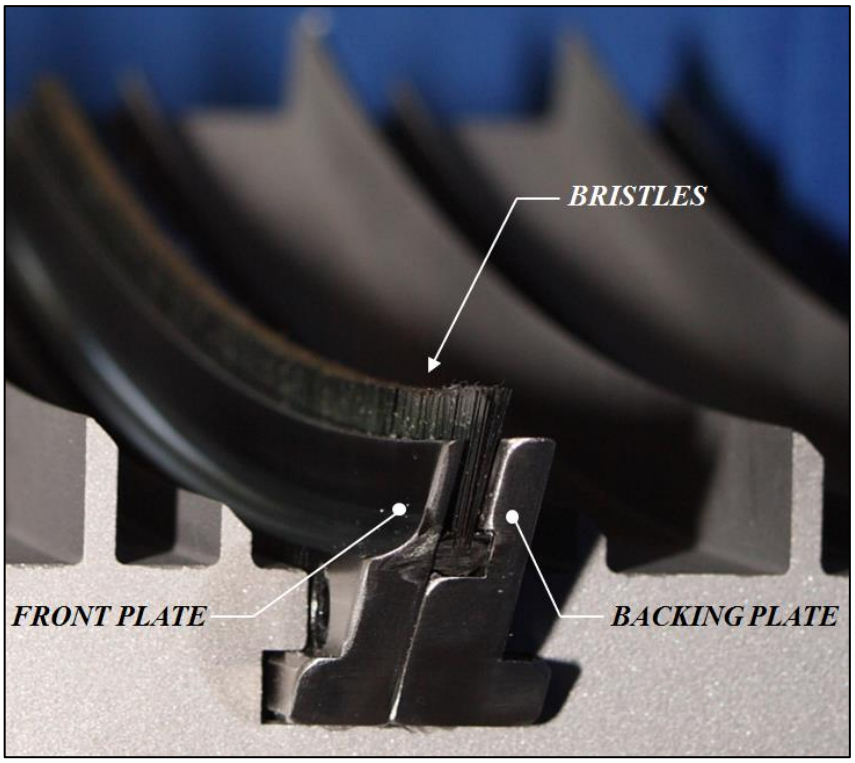

Figure 1.9: Typical brush seal cross-section

Figure 1.10: Brush seal application in vane and diaphragm assembly [77]

The brush seal is installed as front plate is positioned at upstream side with high pressure, and low pressure exist at the downstream side *(backing plate)*. The main leakage flow takes place in the rotor axial direction from upstream side to downstream side, and backing plate supports deformed bristles at operating conditions.

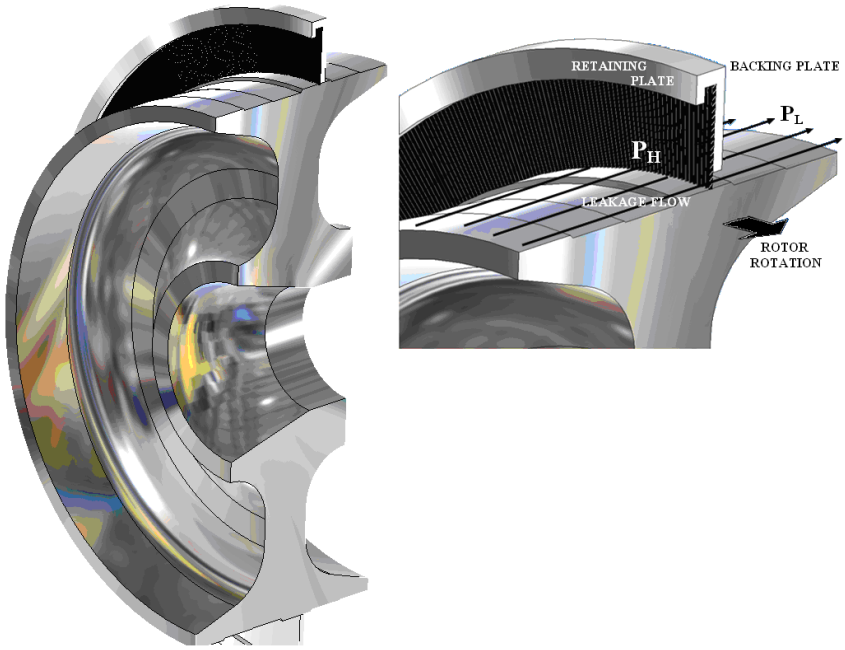

Figure 1.11: Brush seal installation and axial leakage flow

The circular seal is installed in a static member with bristles touching the rotor at an acute angle in the direction of the rotor rotation. This bristle angle is called as *"cant angle"*, which allows bristles to bend rather than buckle. This flexibility of bristles enables seal to survive large rotor excursions without any permanent damage. Since bristles slide against the rotor surface at elevated rpms, wear at the contact becomes a major concern as it determines the life and efficiency of the seal as well as rotor stability and fatigue failure. Brush seals go through an initial wear-in period, and eventually wear line-to-line at the maximum radial excursion point. Brush seal design parameters are more detailed in Chapter 2 of this study.

1.3 Main Phenomenon in Brush Seals

In brush seal applications, pressure difference between upstream and downstream sides results in fluid flow in rotor axial direction. In addition to that, small amount of radial flow can also be observed in brush seals since there is a slight pressure difference

between the upper and bottom sides of the brush pack. In brush seals, leakage performance of the seal is mostly related to axial flow as it is dominant.

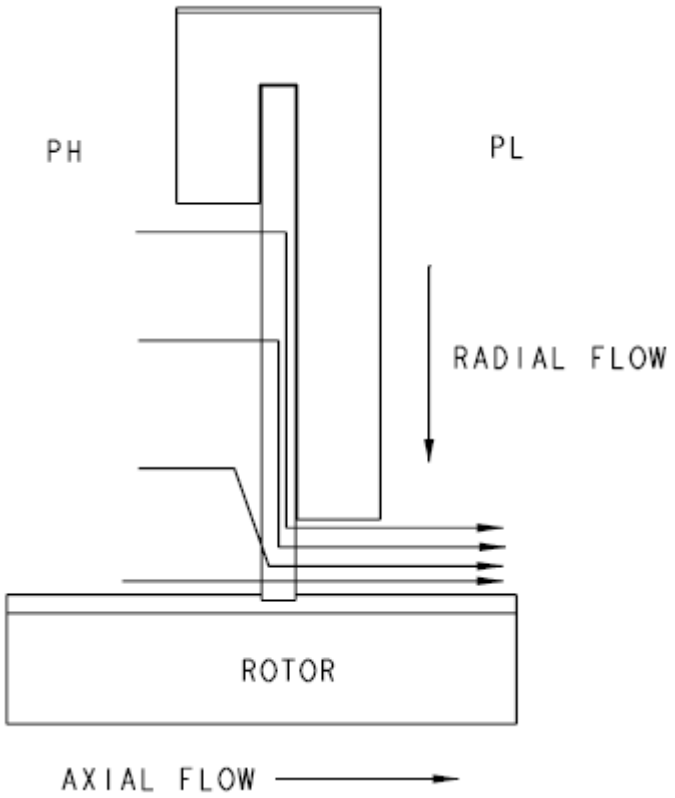

Figure 1.12: Leakage flow in a brush seal [15]

Together with frictional forces, loads generated by leakage flows and pressure gradients in radial and axial directions cause mainly four phenomenon in brush seal applications,

- Seal stiffness
- Hysteresis
- Blow-down *(Pressure closure)*
- Bristle fluttering

1.3.1 Seal Stiffness

Seal stiffness can be defined as the reaction force of the bristle on rotor surface per unit radial interference. Brush seals installed almost at line-to-line contact position with rotor, where bristles are touching the shaft surface with small preload. As rotor interference is introduced due to transients and/or thermal growth, bristles are pushed

outwards in radial direction, while seal pack shows resistance and induces contact forces on rotor surface. As a consequence of pressure load in axial direction and friction mechanism, frictional forces are generated in between the bristles and between the bristle pack and the backing plate. As a result of complicated inter-bristle and bristle-backing plate interactions under pressure, loaded seal behaves much stiffer at rotor excursion, which is also known as *"pressure stiffening"*. Bristle stiffening leads to increase in contact loads at the rotor surface *(Figure 1.16)*.

Designing brush seal with appropriate stiffness has crucial importance since insufficient stiffness yield bristle flutter and leakage performance loss, while excessive stiffness may result in high wear rates, overheating problems, rotor instability and fatigue issues as well as shorter brush seal operating lives. Pastrana et al. [2] presented brush seal and rotor surface inspection results for properly designed brush seal, which are given in Figures 1.13 and 1.14. It was reported by Pastrana et al. [2] that brush seal and rotor wear were at low levels as expected after a year and a half of service life.

A photographic evidence of rubbing damage from excessively stiff brush seals is given in Figure 1.15 [14]. It was stated by Little et al. [14] that improper brush seal design with excessive stiffness result in heavily worn rotor area where thermal bow high spot rubbed against seals.

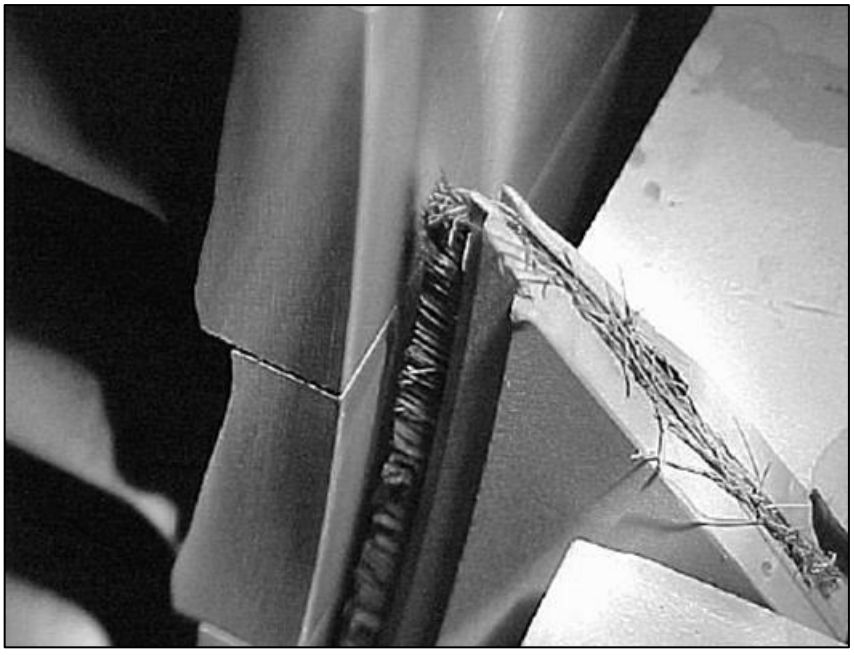

Figure 1.13: Properly design brush seal – Horizontal joint view of brush seal at bucket tips, inspection after a year and a half of service life [2]

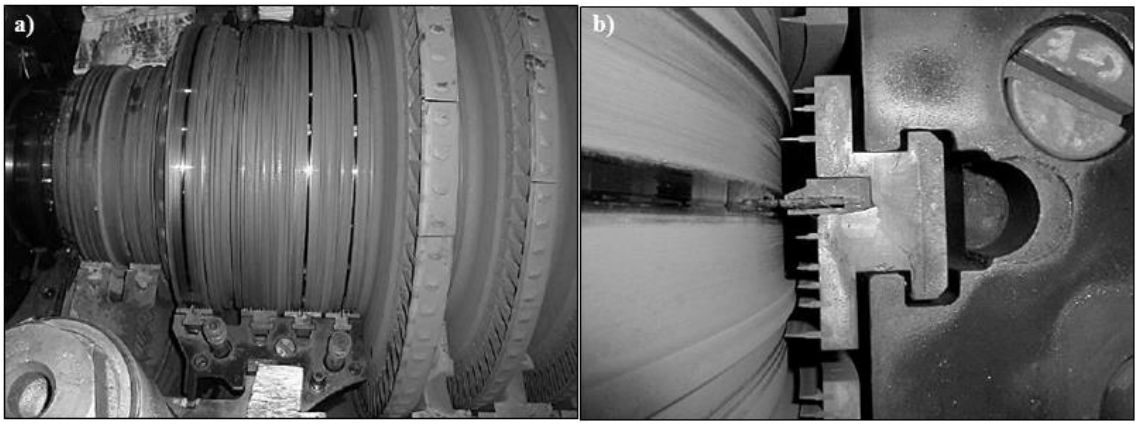

Figure 1.14: Properly designed brush seal - Wear on rotor surface due to brush seal contact, a) View of brush seals at HP end-packing, b) Typical rotor surface finish under a brush seal [2]

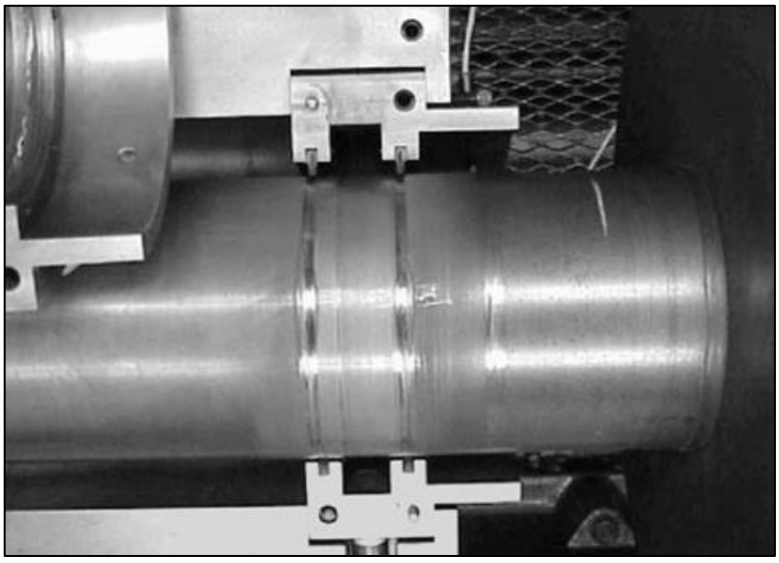

Figure 1.15: Photographic evidence of rubbing damage from excessively stiff brush seals [14]

1.3.2 Hysteresis

There are two types of hysteresis accounting leakage performance, one of which occurs in a time interval thereinafter rotor excursion and called dynamic hysteresis. During rotor excursion, bristles are pushed radially out in order to compensate eccentric and thermally expanded rotor. After steady conditions are reached, rotor returns to its steady state position and dimension whereas radially displaced bristles cannot follow the rotor, and remain hung-up due to pressure load and friction mechanism. Dynamic hysteresis creates a leakage problem since it causes leakage rate to increase by increasing seal clearance.

Other type of hysteresis is static hysteresis, which is observed without any rotor excursion. If a simple pressurization-depressurization cycle is applied to a brush seal, leakage rate for each leg of the cycle differs from each other. During pressurization leg, bristles are pushed radially out and locked in a certain position, again as a result of pressure load and friction mechanism. Therefore, same seal clearance cannot be obtained during depressurization leg which results in different leakage rate. Change of leakage rate with pressure load for a pressurization-depressurization cycle is called hysteresis curve.

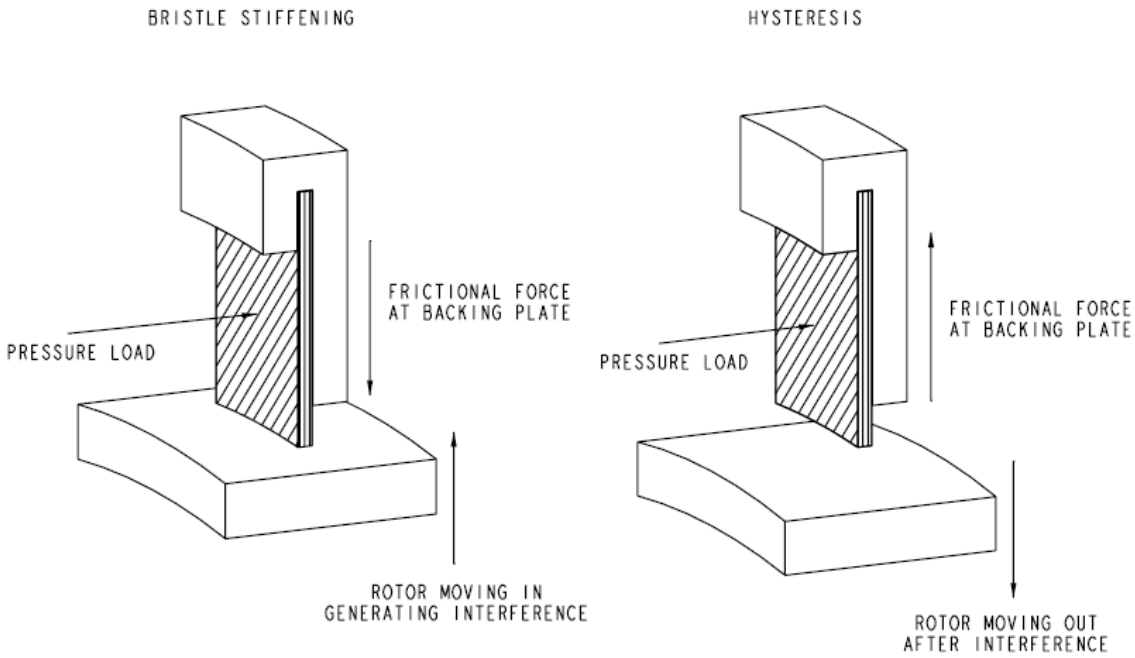

Figure 1.16: Bristle stiffening and dynamic hysteresis [15]

Frictional effects due to bristle-rotor-backing plate interactions also result in different bristle tip forces in loading and unloading steps *(rotor interference and resetting rotor position)*, which is named as *"Bristle tip force hysteresis"*. In ideal test conditions with unpressurized rotor interference, the BTF hysteresis is named as *"free-state hysteresis"*, while the term *"pressurized stiffness hysteresis"* is used for pressurized-rotor interference conditions.

1.3.3 Blow-down

As it was mentioned in the previous pages, a limited amount of radial flow within the bristle pack occurs due to slight pressure difference in the radial direction. Therefore, when a pressure load is applied to a brush seal, bristles at high pressure side are prone to move towards the rotor since they are lack of restriction compared with bristles at downstream side. This is called *"blow-down"* or *"pressure closure"*. This uneven bristle deformation towards rotor may result in wear at front plate side bristles as visualized in Figure 1.17.

In order to avoid pressure closure, extended retaining plates can be used. Although usage of extended retaining plates almost eliminates radial flow, pressure closure can still be observed. The reason for this pressure closure is the tendency of bristles to bend towards the rotor. Increasing pressure load and cant angle increases pressure closure.

In steady state conditions, blow down force driven by radial pressure gradients takes an important role in determining seal clearance.

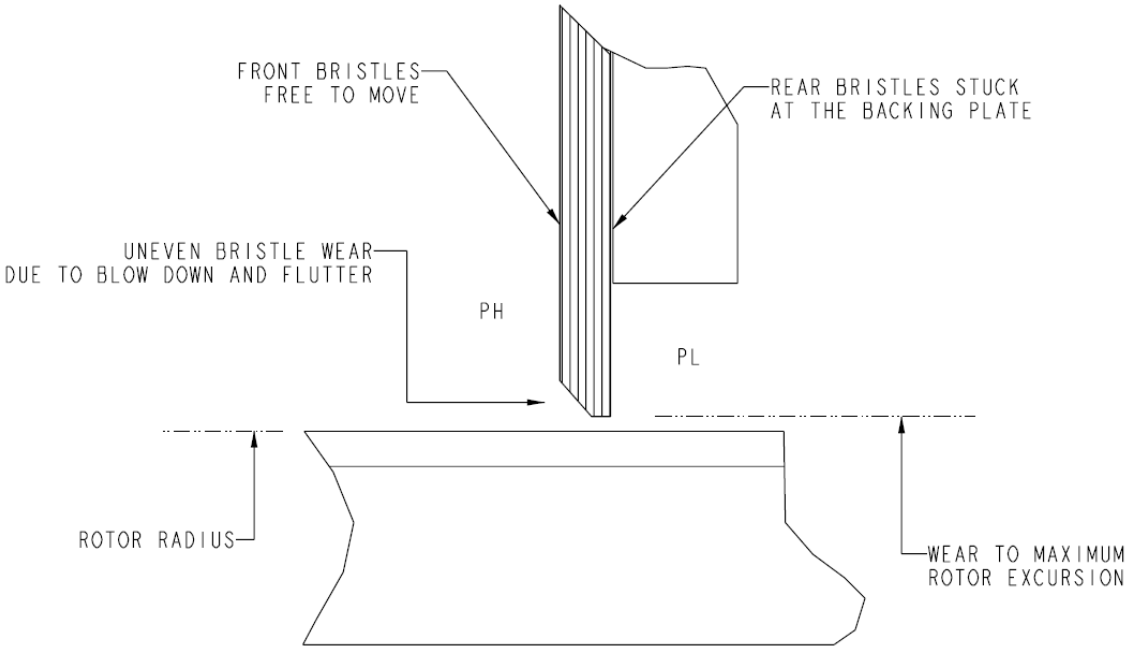

Figure 1.17: Uneven wear of bristle tips caused by blow-down and flutter [15]

1.3.4 Bristle Fluttering

As a result of lack of restriction, upstream side bristles tend to flutter under the aerodynamic disturbances at inlet region such as turbulence or jet flow coming from upstream brush seal in a cascaded setup. Fluttering problem is generally observed in air brush seal applications, and causes sudden loose or uneven wear of high pressure side bristles. Damping shims and extended retaining plates can be used in order to avoid bristle fluttering problem.

1.4 Historical Review for Brush Seals

The idea of using a brush for fluid sealing was first suggested in a patent in 1908, but it did not find any use at that time [16]. After half century, using a metal brush seal in turbines was first investigated in 1955 during GE J-47 engine tests, and proved to be successful [2].

The first usage of brush seals in aircraft engines initiates in early 1980s in Europe [17, 18]. Brush seals were tested in demonstration engines by Rolls Royce, and started to be used in their IAE V2500 engine in 1987. First publications in the literature for brush seal usage in gas turbines were published by Gorelov et al. [19] and Ferguson [20]. In their experimental studies, Gorelov et al. [19] and Ferguson et al. [20] reported superior leakage performance improvements of brush seals in comparison with labyrinth seal applications in gas turbines.

In United States, brush seals have been used in static sealing applications in earth propulsion systems in 1992 [21]. Holle et al. [22] reported successful tests of brush seals on two gas turbines in the joint project of U.S. army with Teledyne CAE [23]. Brush seals were introduced first into gas turbines and then steam turbines in the mid-1990s [24, 25].

Effect of brush seals on rotor dynamics and stability was first investigated by Conner et al. [26]. In their studies, four stage brush seals were tested to post-process contact forces on rotor. Conner et al. [26] mentioned that a four stage brush seal was stated to be more stable than a labyrinth seals. Due to their superior leakage

performance, industrial brush seal applications in gas turbines rapidly increase at late 1990s [33, 34, 35, 36]. Wolfe et al. [25] reported 1.9% power output increase from a single brush seal application.

First observations of brush seal capability to compensate rotor interferences at transients were reported by Holle et al. [22]. Leakage reductions of brush seals up to an order of magnitude over labyrinth seals as well as successful tolerance of brush seals at rotor excursions were demonstrated with the tests at Allison Gas Turbine Division in 1990 [22]. Schlumberger et al. [27] performed wear tests with excessive rotor eccentricities, and no brush seal damage was reported. Hendricks et al. [28] also performed tests at 0.13mm peak-to-peak rotor run-out and reported that bristles followed the rotor at 400rpm.

Studies on improving hysteresis and pressure closure characteristics of brush seals were started with Basu et al. [29], where they proposed a modified brush seal design and reported decrease in stiffness magnitudes of conventional brush seals. Short et al. [30] stated in their studies that the reduced pressure over-closure was obtained by using a tuned flexible flow deflector attached to the upstream side of bristle pack. Bidirectional brush seals proposed by Hendricks et al. [31] in order to sustain pressure differential in both directions. Although remarkable effort was put on overcoming hysteresis and pressure over-closure issues, tests performed by Aora et al. [32] illustrated that even these advanced designs exhibit considerable hysteresis, pressure closure and resulting performance degradation issues.

Literature on thermal aspects of brush seal remain limited, despite their increasing use in secondary flow sealing applications during the last few decades. In one of the early works, Gorelov et al. [19] showed that with the decrease of airflow rate, there is a marked heating of the brush. At the same time, very little airflow is sufficient for cooling at low-pressure differentials. Owen et al. [37] developed a formula to calculate the heat generation; however, their analysis requires the rotor surface temperature as an input. It was assumed that heat was conducted towards bristles and dissipated to the airflow. Chew and Guardino [38] developed a computational model for flow between the bristle tips and the rotor to calculate tip force, wear, and temperature. Their model includes heat conduction and heat generation due to contact friction. Demiroglu [39] developed a closed form equation to calculate heat generation. He measured the

temperature field over the rotor rim and fence height region using an infrared thermograph technique. In a more recent work, Dogu et al. [40] provided analytical and numerical investigations of brush seal temperature distribution after providing an outline for the seal heat transfer mechanism. The full flow and temperature field solution has been obtained using a two-dimensional axisymmetric CFD model.

1.5 Problem Statement

The efficiency of a brush seal is measured by its leakage rate. However, the overall performance of the seal is mostly affected by wear rate and durability. Seal stiffness, hysteresis and pressure closure behaviors play important roles in determining the leakage performance and rotor stability due to the fact that they directly affect wear rates and pressure load capacity of a seal. Complicated nature of bristle-rotor-backing plate interactions at operating conditions makes it difficult to inspect stiffness and durability of brush seals.

There are few available studies in the literature for measurements of seal stiffness levels and contact forces under pressure loads, none of which simulate the effect of rotor rotation and introduced bristle dynamics in turbine conditions. Basu et al. [29], Short et al. [30] and Wood et al. [41] present stiffness data at different pressure loads with static rotor. However, they do not provide sufficient description of tested seals and their test methodology. Although Long et al. [42] provides adequate description of testing procedure, their studies does not include the rotor rotation and induced dynamic effects. Bidkar et al. [43] give details of a special rig design to measure brush seal stiffness under pressure loads. However, the test rig design suggested in this study again cannot take the rotor rotation into account, which has direct effect on bristle tip force magnitudes due to frictional and inertial effects.

The analytical studies for stiffness and stress calculations in the literature are limited due to complex behavior of fine diameter bristles and frictional affects in the brush seal pack. Flower [17] considers a single bristle as a cantilever beam deforming under rotor interference. More complex formulation based on contact mechanics is provided by Stango et al. [44] to calculate bristle tip force and displacement under rotor rub conditions without pressure load. The only analytical formulation for bristle

deformation under pressure load is given by Zhao et al. [45]. However, they assume uniform pressure load that does not change with rotor interference and they do not evaluate bristle tip forces under pressurized conditions.

The bristle tip forces and stress levels strongly depends on frictional effects, which includes inter-bristle, bristle pack-backing plate and rotor-bristle interactions. The complicated nature of bristle deflection, pressure load and inter-bristle effects, which not only includes frictional forces but also includes inter bristle-locking phenomenon, does not lend itself to full analytical formulation. Therefore, comprehensive FEA is needed to include the complicated inter-bristle and transient effects into account. Brush seal CAE and correlation studies in the literature are very limited due to difficulties in modeling and converging nonlinear frictional contacts of brush seal pack. Crudgington et al. [46, 47] conducted brush seal FE analyses using Hexa and space beam elements at static-unpressurized rotor interference conditions and under pressure load without rotor incursion, while they mentioned that pressurized-rotor interference simulations were not performed due to convergence problems. Aksit [15] performed seal analyses by using space beam elements at unpressurized/pressurized-static rotor interference conditions *(non-rotating rotor),* and presented correlation only for free-state stiffness measurements. Guardino [48] and Lelli [49] were used home-based developed software, which was based on mathematical formulae, for simulating bristle deflection at non-rotating rotor interference.

Brush seals are complex structures having variety of design parameters, all of which affect seal behavior at operating conditions. The complicated nature of seal pack and frictional interactions of rotor, backing plate and bristles result in nonlinear response of brush seal to design parameter variances. Industrial applications for brush seal selection are mainly based on experience and simple analytical methodologies like simple beam theory of Flower [17], while CAE-based brush seal characterization does not exist in the literature.

As it was mentioned previously, evaluating bristle tip contact forces and resulting stress levels at operating conditions is critical to optimize the seal performance and safety. Literature survey reveals the lack of test data and analysis methods for evaluating seal stiffness and stress levels at operating conditions. In an attempt to meet this need, custom test rig design and methodology has been developed to perform

stiffness tests at turbine operating conditions. Analytical studies and finite element simulations have been performed for test seals and results have been correlated with the test data of this study. Furthermore, stiffness and friction characterization of brush seals has been conducted through correlated FE models, and MATLAB based code has been developed for automatic brush seal FE model generation for ABAQUS simulations.

Custom test rig designs, analyses and test procedures to measure seal stiffness are presented in this study. Unlike previous tests in the literature, dynamic stiffness tests have been performed in addition to static tests with non-rotating rotor. Tests have been conducted at free-state and pressurized conditions, which helps to give better understanding of main brush seal phenomena in determining seal performance. Analytical studies, which are new to open literature, have also been developed in order to simulate the seal stiffness and bristle stress levels at operating conditions.

Considering the critical importance of contact loads on seal overall performance and system health, and due to complicated structure of brush seals, where bristles are contacting with each other as well as with backing plate and rotor, CAE analyses with high fidelity is required to simulate the test and turbine operating conditions. For this purpose, FE methodology has been developed for structural analyses of brush seals. 3D finite element models of test seals have been constructed and simulations have been performed for free-state and pressurized rotor-rub conditions. CAE model of brush seals includes rotor-bristle, bristle pack-backing plate and inter-bristle contacts with friction. Steady state simulations with non-rotating rotor and transient analyses with rotating rotor have been conducted, and extracted bristle tip force levels are correlated with the test results, all of which have been evaluated in this study. Analyses have been repeated by using Hexahedral and Space beam elements to determine optimum solution methodology. Seal stiffness hysteresis and pressure stiffening affects have been simulated and correlated with the tests. Inertial effects during dynamic tests have also been simulated through transient analyses and results show good agreement with the dynamic test data. Displacement and stress profiles obtained from correlated FE models give better understanding of brush seal behavior at turbine operating conditions.

Brush seal stiffness and friction characterization have been performed by using the correlated FE models. A series of seal structural analyses have been performed with different brush seal parameters and various friction coefficients. Brush seal

characterization study has been conducted at steady-state conditions as well as at unpressurized and pressurized rotor-rub conditions. Bristle tip force and bristle stress levels have also been evaluated during characterization study.

A MATLAB code, which automatically generates the brush seal input file for ABAQUS simulations, has also developed within the content of this study. The input file generator shortens the pre-processing time for brush seal FE model generation to less than a minute from 2-3 days.

2 BRUSH SEAL DESIGN PARAMETERS AND GEOMETRIC INSPECTION

As mentioned before, the main purpose of this study is to develop analytical and computational methods as well as test procedures for stiffness and friction characterization of brush seals. Therefore, brush seals must be selected and inspected carefully to obtain high fidelity in simulations. In this chapter, test seal main design parameters are calculated and inspected. Main dimensions and material properties for bristles are also detailed in the following sections.

2.1 Brush Seal Design Parameters

The brush seal consists of a set of fine diameter metallic fibers densely packed between front and backing plates. As illustrated in Figures 2.1 and 2.2, the backing plate is positioned at the downstream side of the bristles to provide mechanical support for differential pressure loads. *"L"* denotes the free bristle length and *"BH"* shows the free bristle height, which is the distance between pinch-point and bristle inner radius. The fence height is denoted by *"FH"*, which is the distance between backing plate inner radius and seal inner radius. *"R"* is used for rotor radius, which also refers to the brush seal inner radius for line-to-line case. A retaining plate, which is also named as front plate, tightly clamps and holds the bristles in place. The extended section of the front plate from pinch point does not give any mechanical support, but blocks any possible turbulent flow at upstream side to avoid bristle loss issues due to fluttering.

The circular seal is installed in a static member with bristles touching the rotor at an acute angle in the direction of rotation. This bristle angle is called *"cant angle"* or *"lay angle"*. Typically, the cant angle, *"θ"*, changes between 35^{o} and 55^{o}. In the case of rotor excursions, cant angle helps to reduce the contact loads allowing bristles to bend rather than buckle. This inherent flexibility enables the seal to survive large rotor

excursions without sustaining any appreciable permanent damage. The list of brush seal design parameters and their typical range is given in Table 1.2.

Low pressure occurs at the downstream side while high pressure is obtained at the upstream side of the brush seal. Pressure difference between upstream and downstream sides is called *"pressure load"*. The pressure load leakage flow in rotor axial direction, which is constrained by the porous media composed by fine diameter bristles.

List of Brush Seal Main Design Parameters		
Definition	**Parameter**	**Typical Range**
Bristle diameter	d *[mm]*	0.07 - 0.15
Free bristle height	BH *[mm]*	10 - 20
Fence height	FH *[mm]*	1 - 2.5
Cant angle	θ *[deg]*	35 - 55

Table 2.1: Brush seal design parameters

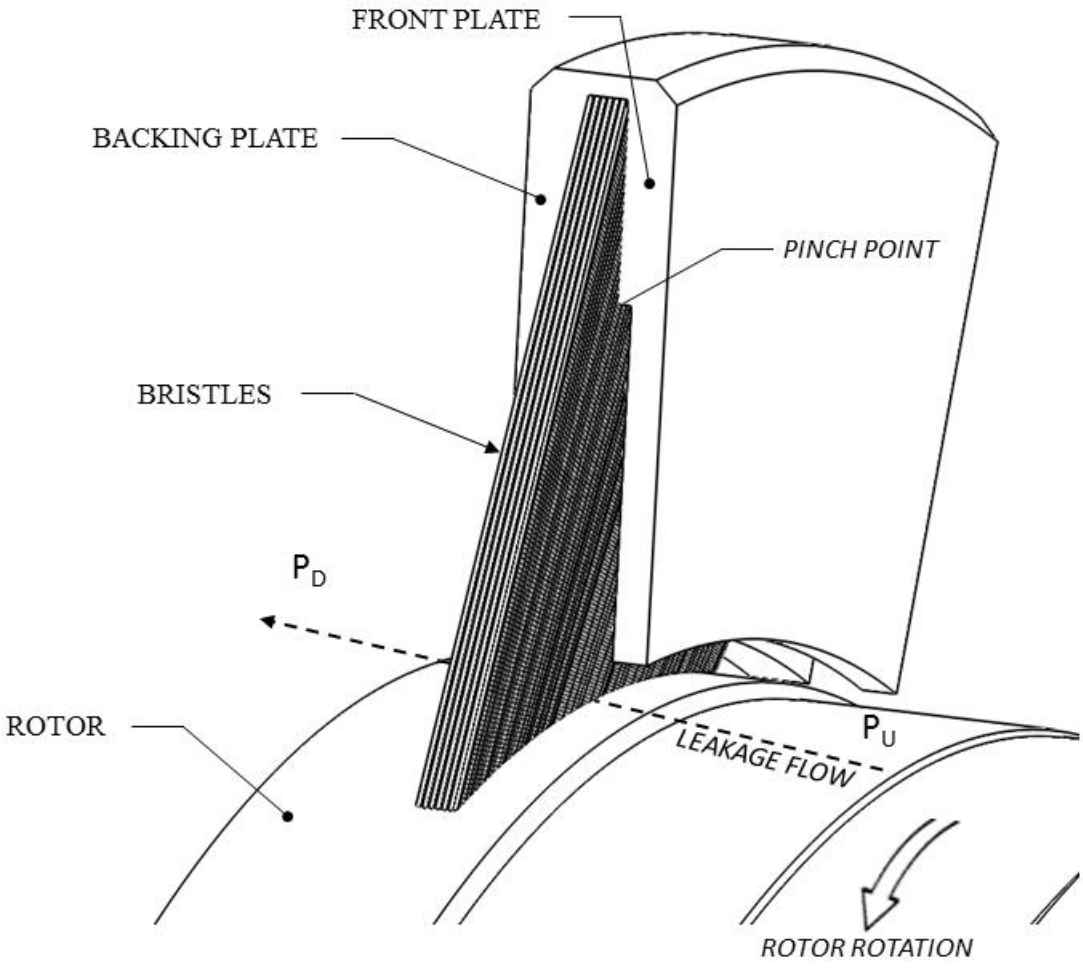

Figure 2.1: Brush seal schematic and main components

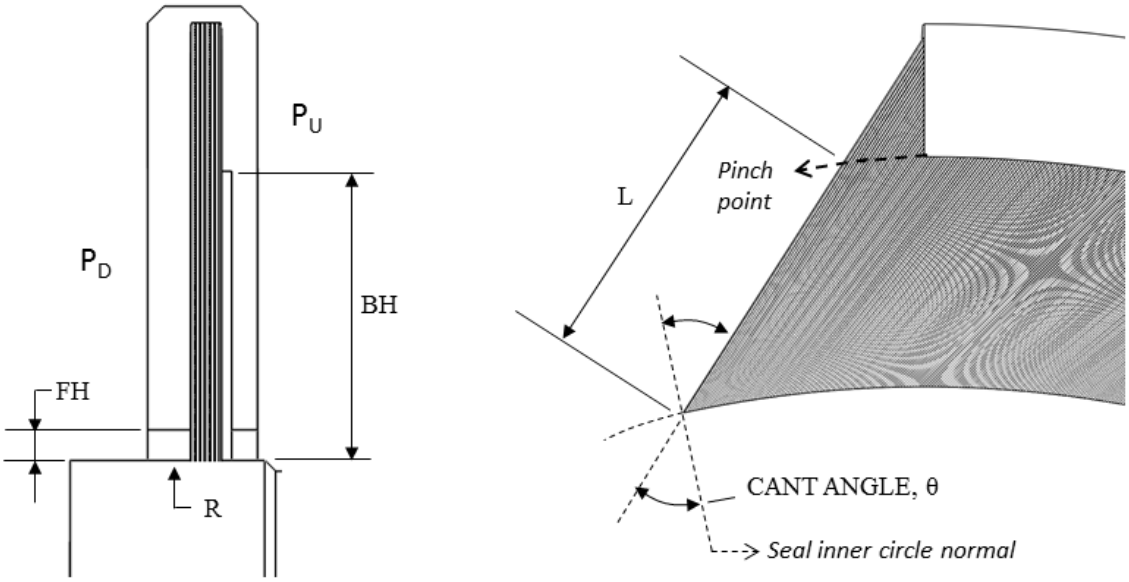

Figure 2.2: Brush seal main design parameters

2.2 Bristle Pack Properties

As described before, brush seal mainly consists of a backing plate, front plate and a dense pack of fine diameter bristles, which are preloaded with front and backing plate and welded together at the upper surface. In the literature [15, 46], brush seal design parameters are calculated by using the ideal unwrapped geometry, which does not take the effect of circular seal inner and outer diameters on seal parameters into account. In real life applications, the circular cross-section of the seal inner and outer diameter intersects the in-plane bristles having a specific cant angle, which results in differences in design parameters from the ideal case of unwrapped geometry calculations. Considering that the curvature will be more pronounced for the subscale test seals, which have smaller radii than seals for turbine applications, design parameters should be carefully calculated and *"corrected design parameters"* should be used for analyses and correlation study.

In this section, bristle pack properties and calculation methodologies for corrected design parameters is detailed.

2.2.1 Bristle Density and Cant Angle Definitions

Bristle density and cant angle are important design parameters in determining the leakage performance and stiffness of the brush seal. By definition, bristle density, *"η"*, is the number of bristles per circumferential length at seal inner radius, and cant angle, *"θ"*, is the angle between bristle axis and normal of seal inner circle. As it can be seen from definitions, those parameters strictly defined at seal inner radius, and they change from inner radius to pinch point circle radius.

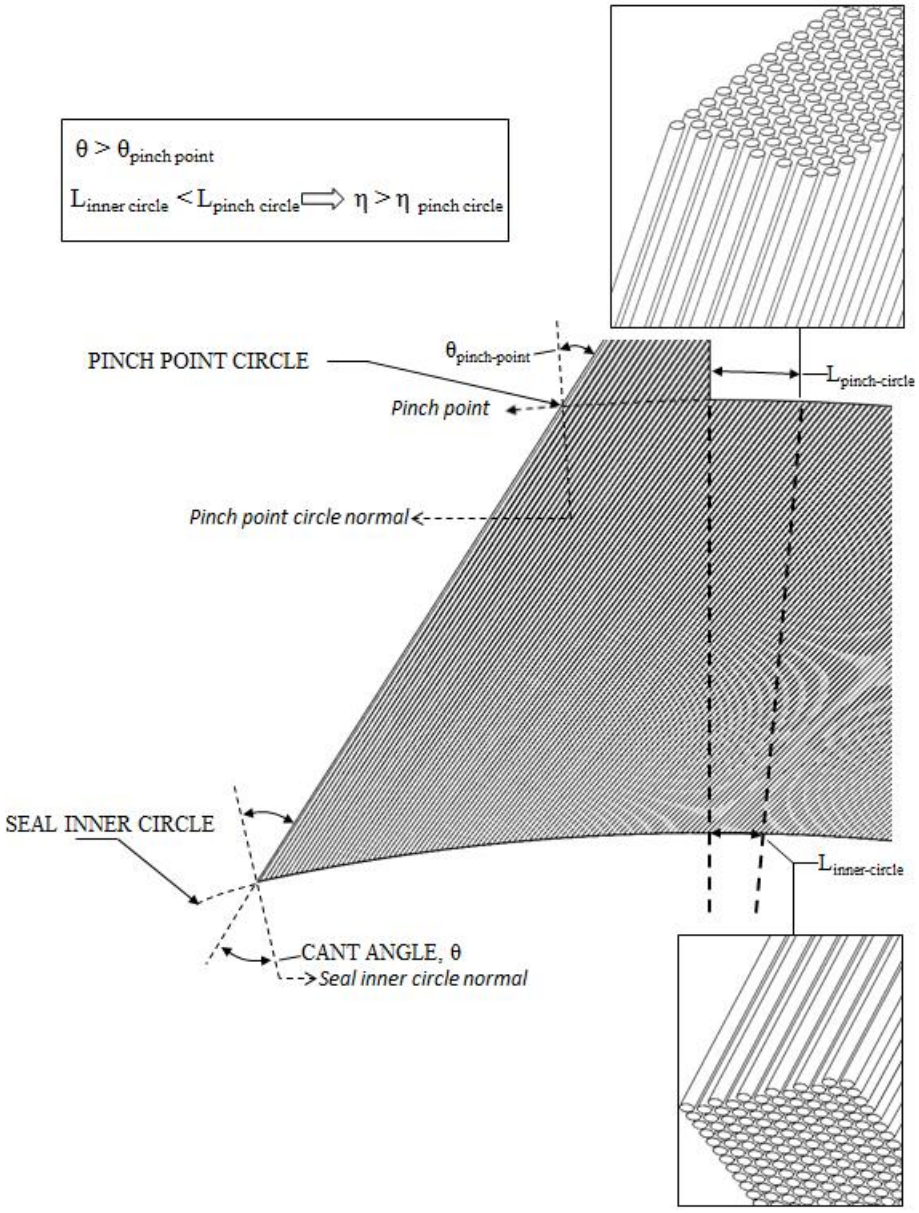

Figure 2.3: Cant angle and bristle density inspection on a brush seal

The bristle pack detailed view is shown in Figure 2.3. As it can be seen from the figure, both bristle pack density and cant angle decreases at the pinch point circle diameter.

The pinch point circle and seal inner circle have common normal at the same circumferential location. However, bristles with cant angle intersects pinch point circle and seal inner radius at different locations and results in smaller angle between bristle axis and pinch point circle.

2.2.2 Bristle Cross Section and Projected Bristle Area

Bristles in a brush pack are fine diameter fibers, where typical range for the diameter is 0.07-0.15mm. Brush seal manufacturing process is based on aligning bristle bundles together and machining the bristle tips to inner radius with wire EDM process [50,51]*(Figure 2.4)*. Due to specific cant angle of bristles, the circular cross-sections of the fibers are projected as ellipse at seal inner radius, and therefore on rotor surface. As illustrated in Figure 2.5, the projected bristle tip area can be found by dividing the circular fiber area to cosine of cant angle. In Equation 2.1, *"A_b"* is projected bristle tip area, *"d"* is bristle diameter and *"θ"* is cant angle.

$$A_b = \frac{\pi d^2}{4\cos\theta} \tag{2.1}$$

In Figure 2.6, microscopic image of a brush seal is given. The image is taken at seal inner radius with a Digital Microscope. As it can be seen from the figure, the projected bristle tip area in real life application is very close to the area suggested by Equation 2.1.

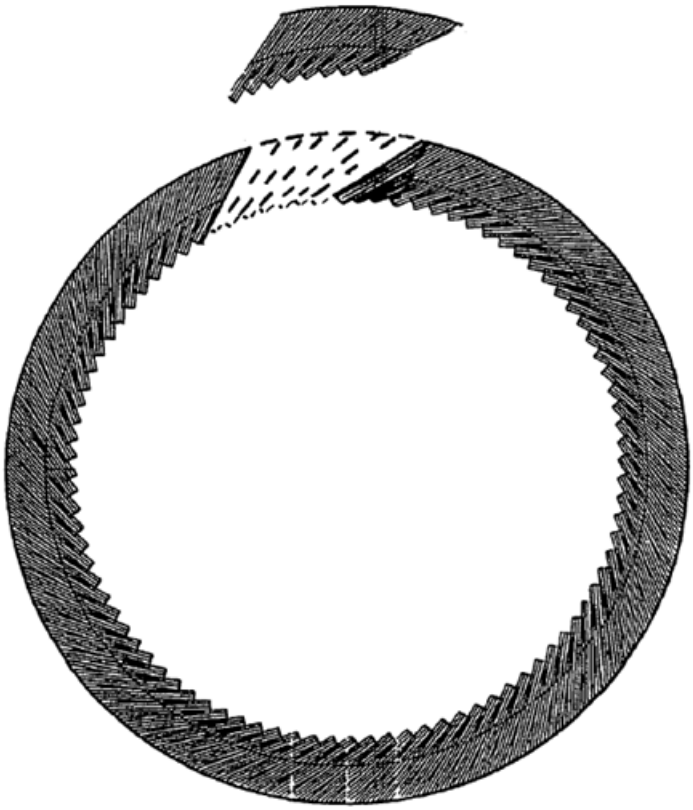

Figure 2.4: Brush seal manufacturing process - Bundle alignment and machining process for seal inner radius [51]

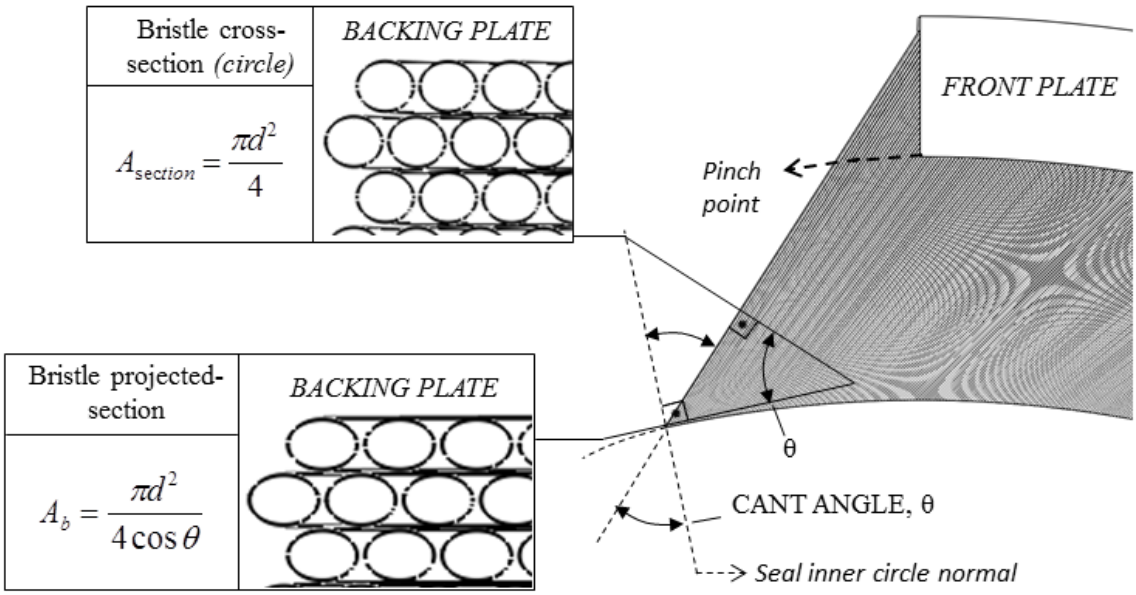

Figure 2.5: Projected bristle area at seal inner radius

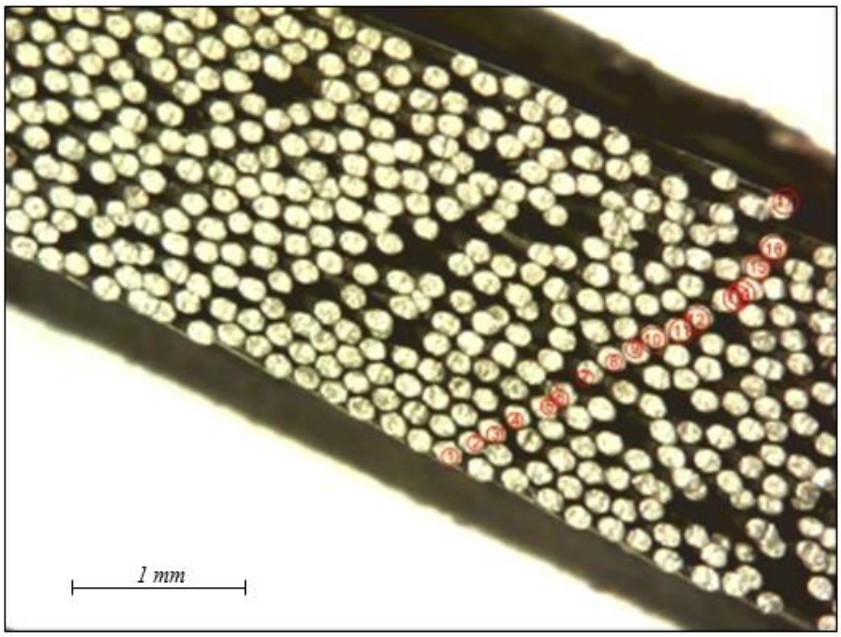

Figure 2.6: Microscopic image of a brush seal at its inner radius

2.2.3 Bristle Layout and Number of Bristle Rows

Bristle spacing is an important parameter since it affects the magnitude of leakage flow and seal stiffness. Modeling of bristle spacing is difficult since uniform spacing between bristles is unlikely to occur in a real brush seal pack. However, as it can be seen in Figure 2.7, the bristle layout is very close to staggered configuration.

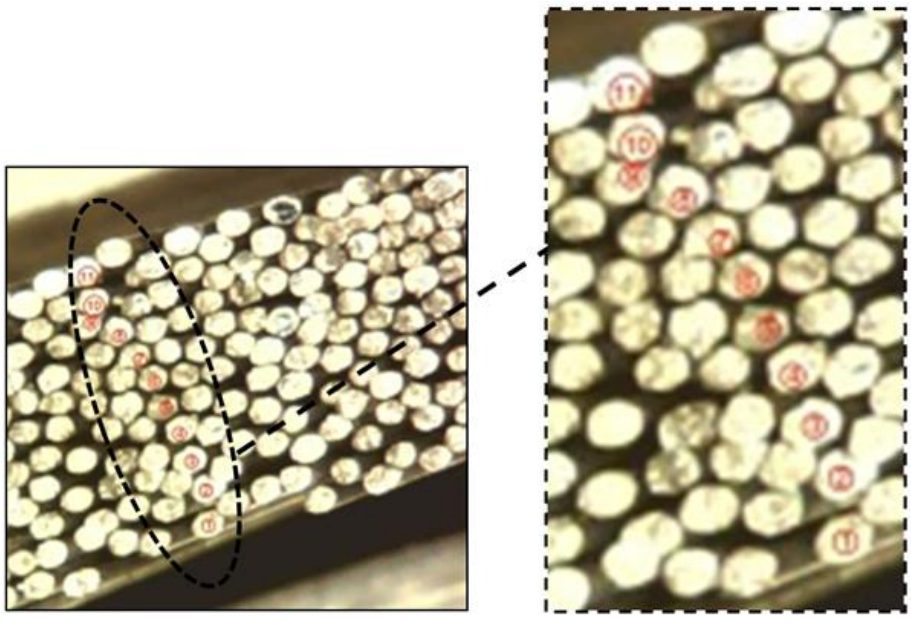

Figure 2.7: Microscopic image of a brush seal – detailed for bristle layout

The analytical studies are performed to estimate bristle spacing in a staggered configuration. Before initiating the bristle proximity characterization, it should be noted that corrected bristle diameter, which takes the surface roughness into account, could be used to estimate bristle layout.

$$D = d + 2\varepsilon \tag{2.2}$$

where *"d"* is the bristle diameter and *"ε"* is the size of asperity peaks.

In a staggered configuration, the bristle proximity is characterized by axial spacing, *"S_A"*, and tangential *(circumferential)* spacing, *"S_T"*, both of which depend on bristle density and surface roughness. Axial spacing and tangential spacing values refer to distance between bristles in unpressurized conditions. Considering the real operating conditions for a loaded seal, bristles are in contact with each other as given in Figure 2.8, and the minimum axial spacing, *"$S_{A\text{-}min}$"*, can be calculated by using the formula given in Eq. 2.3.

$$S_{A-min} = Dcos(30^o) \tag{2.3}$$

In the absence of pressure load, bristles bloom and relax in axial direction. Typical axial bloom is 20-25% [15], which results in axial spacing around 1.20-1.25 of minimum bristle spacing under pressure load. Considering 25% axial bloom, the axial spacing for an unloaded brush seal can be found by,

$$S_A = 1.25 S_{A-\min} \tag{2.4}$$

Tangential spacing, *"S_T"*, is the average bristle spacing in circumferential direction, where the minimum tangential spacing, *"$S_{T\text{-}min}$"*, is the projection of the corrected bristle diameter to the tangential plane.

$$S_{T-\min} = \frac{D}{\cos(\theta)} \tag{2.5}$$

In real life applications, it is not possible to achieve tangential spacing of $S_{T\text{-}min}$. Depending on the cant angle, the average tangential spacing values of 1.03-1.05x$S_{T\text{-}min}$ satisfies the measured seal density values. Considering 5% tangential bloom, the average tangential spacing for an unloaded seal can be found by,

$$S_T = 1.05 S_{T-\min} \tag{2.6}$$

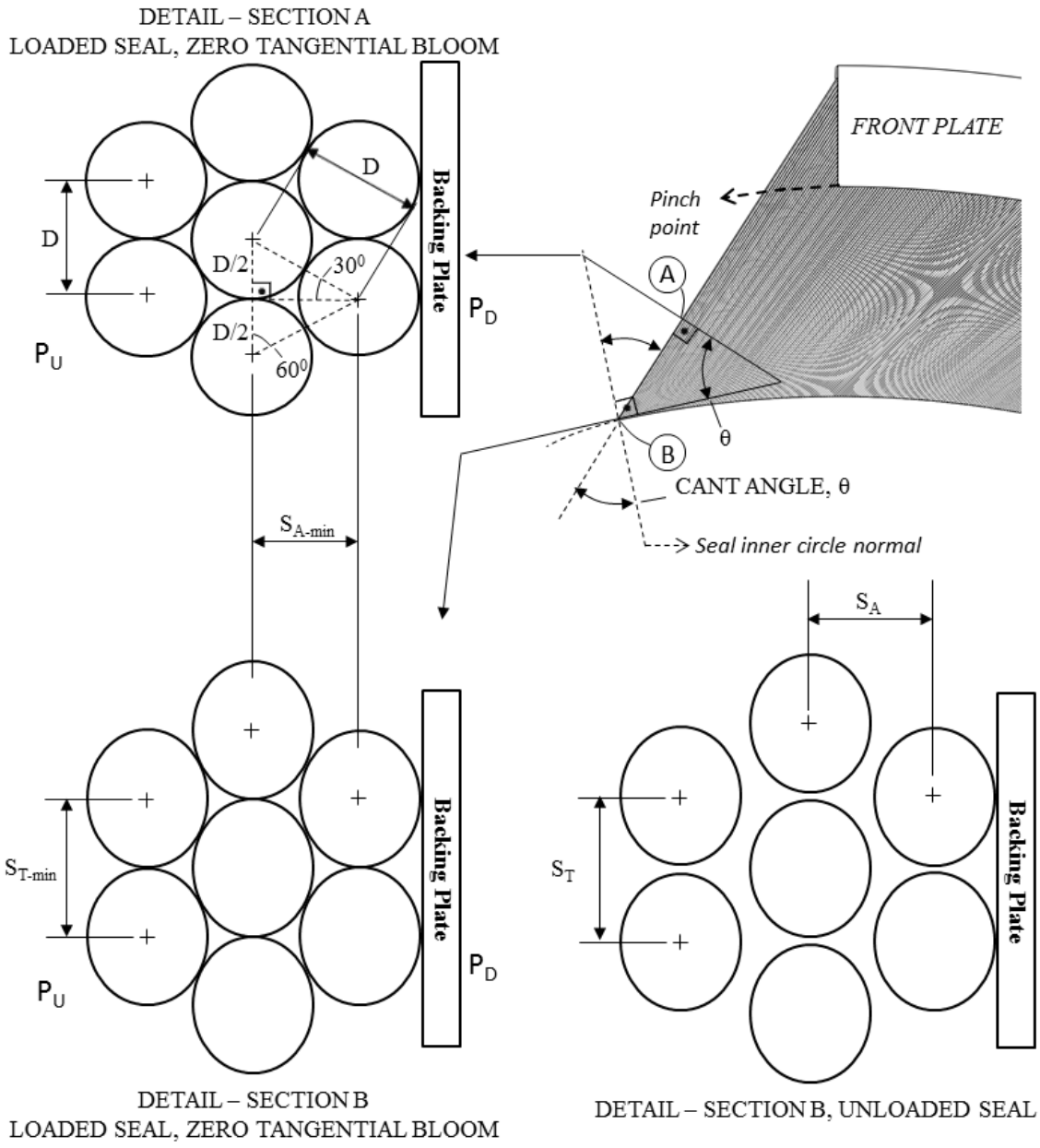

Figure 2.8: Microscopic image of a brush seal – detailed for bristle layout

Bristle density, *"η"*, is the number of bristles per circumferential seal length at inner diameter. Achieving exact bristle density is not possible due to production precision, and typically ± 200 bristle density range is provided by seal manufacturers.

The average number of bristle rows strongly affects seal stiffness levels, especially for a loaded seal. In order to obtain FE models with high fidelity, number of bristle rows should be carefully calculated and used in CAE analyses. The average number of bristle rows can be calculated by using Equation 2.7.

$$NR = \eta \cdot S_T \tag{2.7}$$

In Equation 2.7, *"NR"* is the calculated average number of bristle rows in rotor axial direction, *"η"* is the average bristle density, and *"S_T"* is the tangential spacing in an unloaded seal. Rule for counting number of bristles in a staggered configuration is given in Figure 2.9.

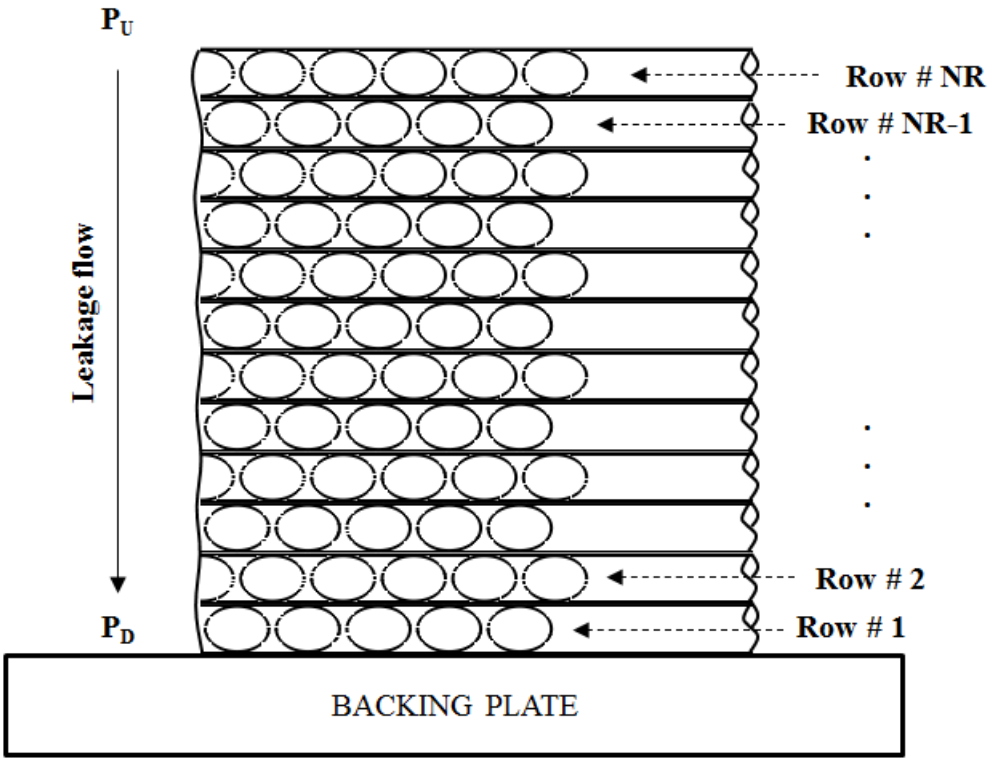

Figure 2.9: Number of bristle rows in seal axial direction for staggered configuration

2.2.4 Brush Seal Parameters - Dependence on Seal Inner Diameter

In the literature [15, 46, 47], brush seal free bristle height calculations are based on unwrapped geometry. The traditional method calculates the free bristle length by simply dividing the free bristle height to the cosine of the cant angle, where the free bristle height is calculated as the difference between brush seal inner radius and outer radius from pinch point *(Figure 2.10).*

$$BH = R_{pinch} - R \tag{2.8}$$

$$L = \frac{BH}{\cos\theta} \tag{2.9}$$

In Equation 2.8, *"R_{pinch}"* is the seal radius at pinch point, and *"R"* is the seal inner radius, which refers to rotor radius at line-to-line conditions.

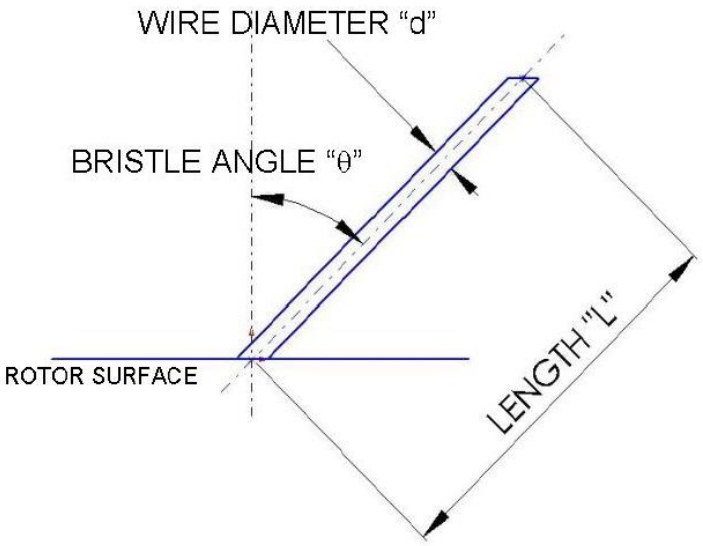

Figure 2.10: Bristle parameters for ideal unwrapped geometry [45]

Since the circular section of the seal inner and outer diameter intersects the in-plane bristles, which have a specific lay angle, the real bristle height differs from the length calculated by using the traditional method in the literature. The difference between the actual bristle height and calculated height through conventional method increases as the seal diameter gets smaller, as in the case of subscale test seals. Since the stiffness is the cubical function of the free bristle length, the corrected free bristle length must be calculated to obtain better correlation with tests. Therefore, a methodology has been developed and used in this study. Details of the methodology are given in Figure 2.11. The difference between traditional BH and corrected free bristle height is denoted by *"t"*, and the corrected free bristle height and length can be found by using the formulas below:

$$BH_{cor} = BH - t = (R_{pinch} - t) - R \tag{2.10}$$

$$L_{cor} = L - t/\cos(\theta) \tag{2.11}$$

$$L_{cor} = \frac{BH_{cor}}{\cos\theta} \tag{2.12}$$

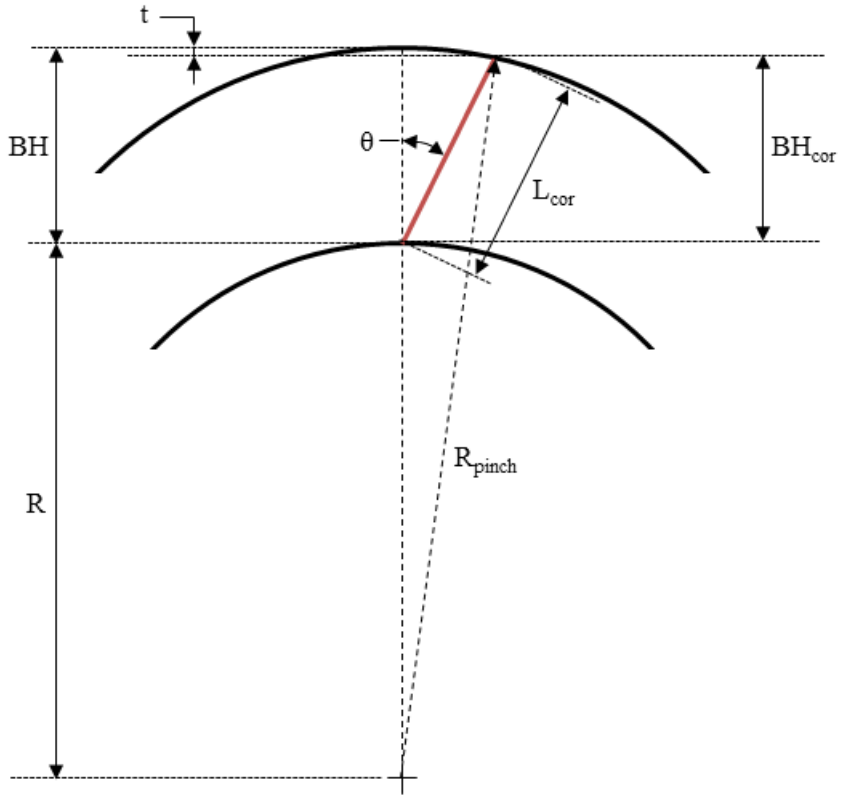

Figure 2.11: Corrected bristle height and length calculations

REPRESENTATIVE SEAL, θ=50°, R_{pinch}-R=14mm **Comparison for R=64.77mm *(Dynamic Stiffness and Leakage Test Rig Inner Radius)***		
Bristle height	Corrected free bristle height	12.29 mm
	Free bristle height, traditional method	14.00 mm
	Difference %	14%
Bristle length	Corrected free bristle length	19.12 mm
	Free bristle length, traditional method	21.78 mm
	Difference %	14%

Table 2.2: Brush seal design parameters

The difference between traditional and corrected calculations for free bristle height and length is shown in Figures 2.12, 2.13 and in Table 2.2 for a representative seal, whose cant angle is 50° and the traditional BH is 14 mm. As it can be seen from Figures, the difference between corrected and traditional parameters is more pronounced for smaller seal inner radii. The difference in free bristle height is 14% at 64.77mm seal inner radius, which corresponds to dynamic test rig rotor and test seal inner radius of this study. Considering that the stiffness of the seal is the cubical

function of free bristle height, using corrected parameters has crucial importance in obtaining correlation between analyses and tests.

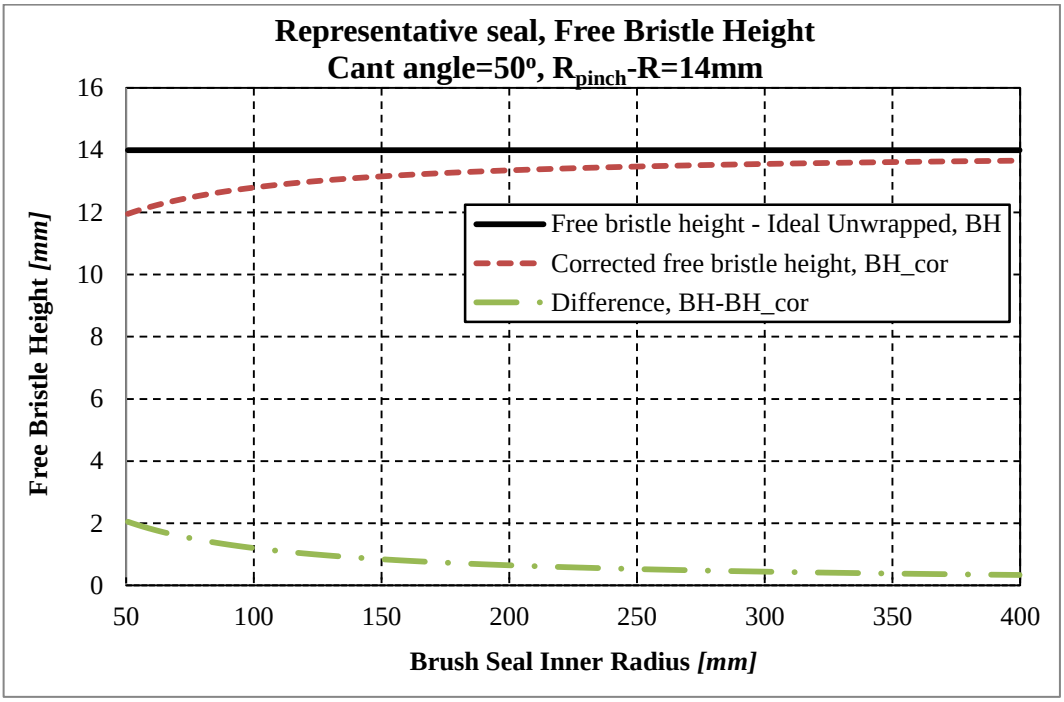

Figure 2.12: Corrected free bristle height change with seal inner radius for a representative seal

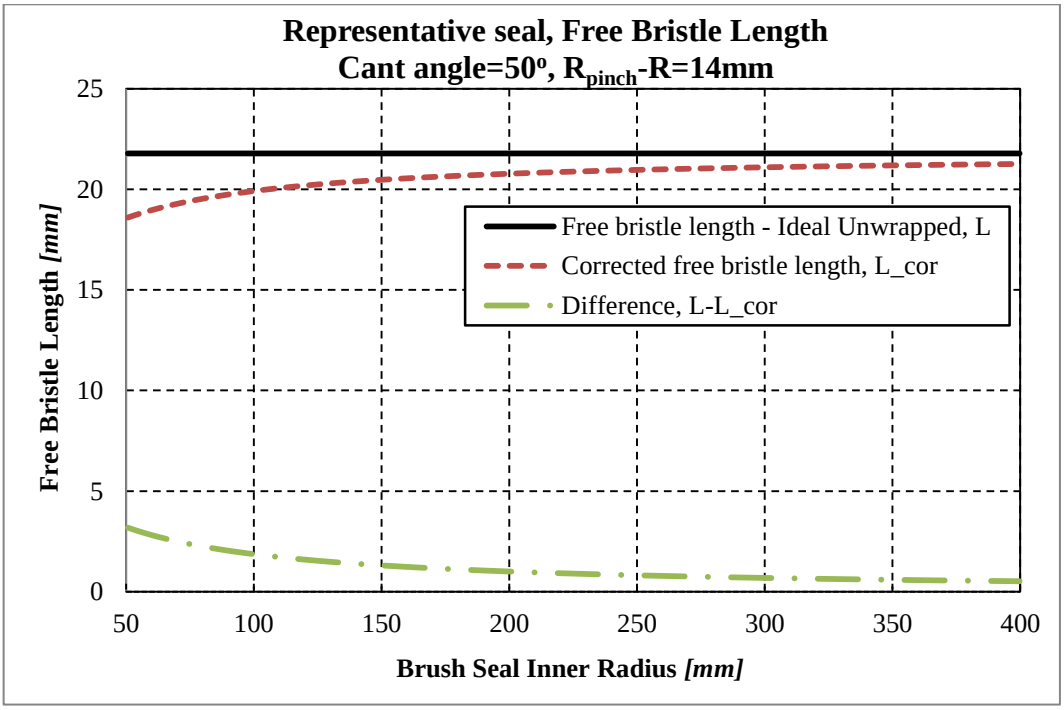

Figure 2.13: Corrected free bristle length change with seal inner radius for a representative seal

2.3 Selected Test Seals

The selected test seal parameters are detailed in Table 2.3. Test seals have been ordered as two pairs for dynamic stiffness measurements. The selected cant angle is 45^o, which is the commonly used value in real life applications. The brush seal has the bristle density value of 94 bristles per circumferential mm, and the bristle diameter is 0.1016 mm. The seal inner radius is 64.77mm, which is equal to dynamic stiffness and leakage test rig's rotor segment radius. Selected FH for the test seal is 1.3 mm. Bristles are made of Haynes 25, which is typically preferred in most of turbine sealing applications due to their superior strength and satisfactory ductility. Cold worked Haynes 25 sheet material with 10% cold reduction has 725MPa tensile yield strength and 1070MPa ultimate tensile strength limits at room temperature [52]. Seal photo is given in Figure 2.14, and brush seal dimensions are detailed in Figure 2.15.

Test Seal Design Parameters	
Seal inner radius, R *[mm]*	64.770
Seal backing plate end radius, R_{bp} *[mm]*	66.070
Brush seal fence height, FH *[mm]*	1.300
Brush seal packing width *[mm]*	6.300
Backing plate thickness *[mm]*	1.400
Brush seal cant angle, θ	45^o
Bristle density, η *[per mm]*	94
Bristle diameter, d *[mm]*	0.1016
Bristle material	Haynes 25

Table 2.3: Selected design parameters for test seals

Figure 2.14: Test seal photo

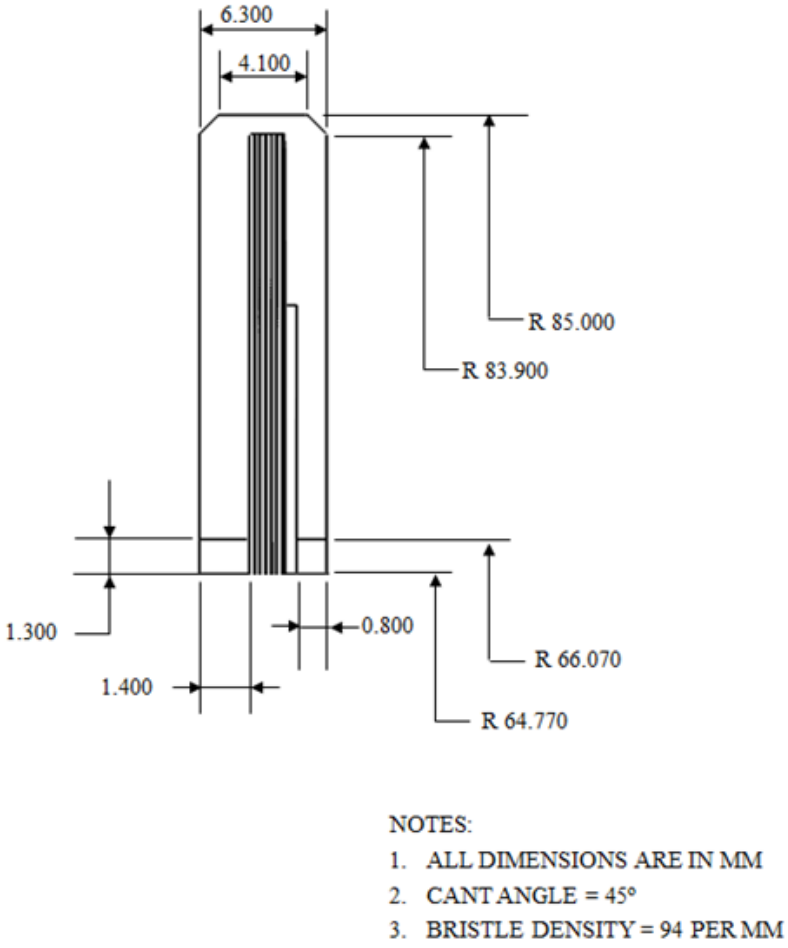

Figure 2.15: Dimensions for test seals

2.3.1 Calculated Test Seal Parameters

Brush seal main design parameters are calculated as the dimensions given in Figure 2.13 are determined. The methodology developed in this study has been utilized for the corrected free bristle height and length calculations. Minimum axial spacing and minimum tangential spacing values are calculated based on Equations 2.3 and 2.5, where typical surface roughness value of 1.27μm from literature [15] is used for size of asperity peaks. Axial spacing calculations for the unloaded seal assume 25% axial bloom, tangential spacing and number of bristle rows calculations assumes 5% tangential bloom. Calculated brush seal parameters are detailed in Table 2.4.

Calculated Design Parameters for Test Seals	
Bristle surface roughness, ε *[μm]*	1.27
Corrected bristle diameter, D *[μm]*	104.14
Minimum axial spacing, $S_{A\text{-}min}$ *[μm]*	90.18
Axial spacing – 25% bloom, S_A *[μm]*	112.73
Minimum tangential spacing, $S_{T\text{-}min}$ *[μm]*	147.27
Tangential spacing – 5% bloom, S_T *[μm]*	154.64
Calculated number of bristle rows, NR	14.5

Table 2.4: Calculated brush seal design parameters

2.3.2 Brush Seal Inspection for Number of Bristle Rows Correlation

As mentioned previously, determining bristle layout is difficult since uniform spacing between bristles is unlikely to occur in a real brush seal pack. Estimated average number of bristle rows is critical for CAE-test correlation since seal stiffness and induced tip force in pressurized conditions directly depend on NR value. Therefore, tangential spacing with 5% bloom and calculated NR values are needed to be confirmed for test seals. For this purpose, test seal cross-sections have been inspected by digital microscope.

Microscopic images of test seals are taken at 8 different sections as shown in Figure 2.16, by using the BW400X-digital microscope which has 5MP image sensor and 25-400X magnification ratio. Specifications of digital microscope are given in Table 2.5.

Digital Microscope – BW400X Specifications	
Image sensor	Up to 2M Pixel
Lens	Microscope glass lens, Resolution: 2M Pixel
Focus range	0mm ~ 40mm
Still image capture resolution	5M, 3M, 2M, 1.3M, VGA
Digital zoom	4X Sequence mode
Magnification ratio	25X ~ 400X

Table 2.5: Digital microscope specifications

Microscopic images of test seals are inspected carefully to determine number of bristle rows in staggered configuration. Bristles that intersect the drawn line in rotor axial direction is counted and included to NR calculations. If two parallel or nearly parallel bristles contact the drawn line at the same time, one of them is taken into account. Number of bristle rows for test seals are estimating by averaging the counted number of rows at 8 different sections. Microscopic images and counted number of

rows for *"Test seal # 1"* and *"Test seal # 2"* are detailed in Figures 2.17 and 2.18. Comparison for counted and calculated number of bristle rows is given in Table 2.6. As it can be seen from the table, NR calculations with 5% tangential bloom assumption successfully estimates the counted NR for test seals. In analytical studies and FE analyses, using 15 bristles in rotor axial direction will be a good approximation to simulate test seals.

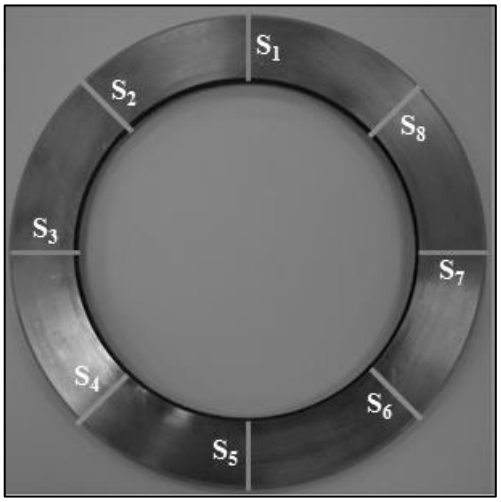

Figure 2.16: Sections for microscopic inspection of number of bristle rows

TEST SEAL # 1, AVERAGE NR=14.8			
SECTION 1	SECTION 2	SECTION 3	SECTION 4
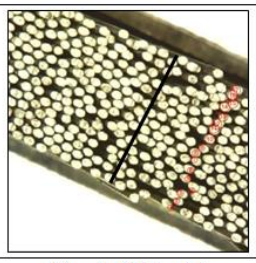	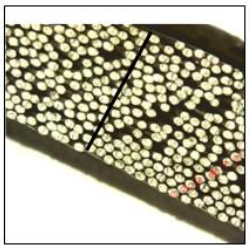	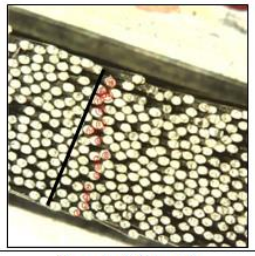	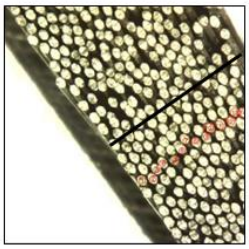
Counted NR = 14	*Counted NR=15*	*Counted NR=14*	*Counted NR=15*
SECTION 5	SECTION 6	SECTION 7	SECTION 8
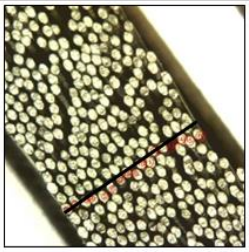	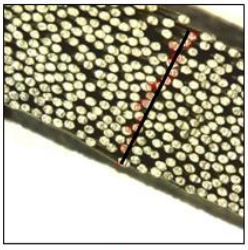	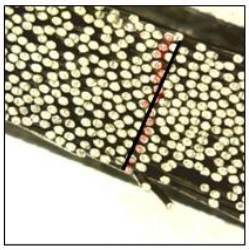	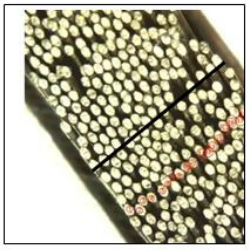
Counted NR = 15	*Counted NR=16*	*Counted NR=15*	*Counted NR=14*

Figure 2.17: Microscopic inspection of Test Seal #1

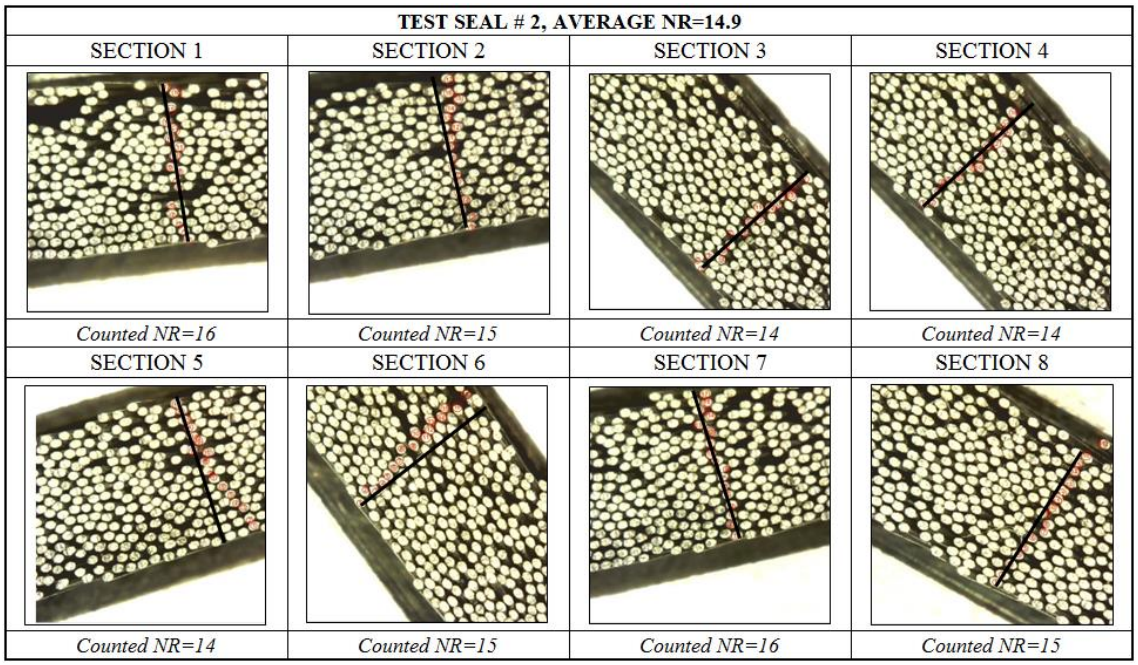

Figure 2.18: Microscopic inspection of Test Seal #2

Test Seals – Number of Bristle Rows			
Seal #	$NR_{counted}$	$NR_{calculated}$	NR_{CAE}
Test seal # 1	14.8	14.5	15
Test seal # 2	14.9	14.5	15

Table 2.6: Calculated and counted number of bristle rows comparison

2.3.3 Bristle Material Properties

Haynes 25 is a cobalt based alloy, which can be fabricated and formed by conventional techniques. Its excellent high-temperature strength, good oxidation resistance and forming characteristics make that material attractive for brush seals in turbine applications. Therefore, bristle materials for test seals are selected as Haynes 25 alloy. Considering the cold work process introduced during bristle manufacturing, material properties of cold worked Haynes 25 with 10% cold reduction is used in this study. Material properties are detailed in Table 2.7 [52]. Elastic modulus, yield strength and ultimate tensile strength change with temperature are detailed in Figures 2.19 thru 2.21.

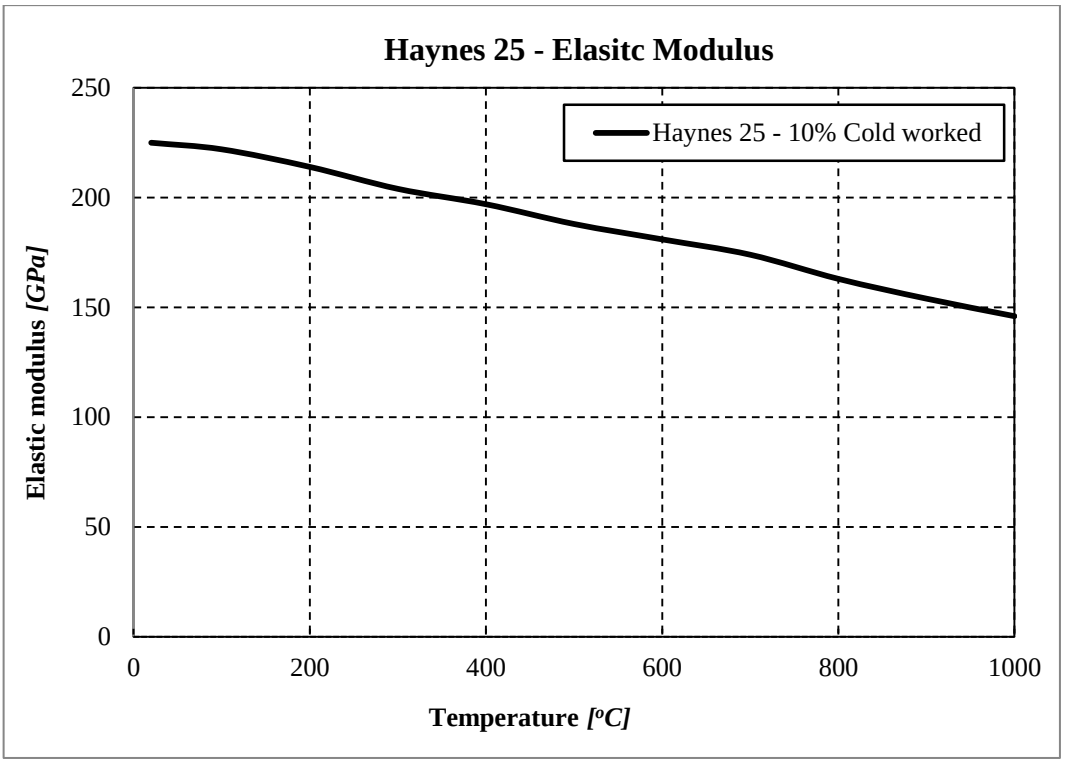

Figure 2.19: Haynes 25 – 10% cold worked, Elastic modulus change with temperature [52]

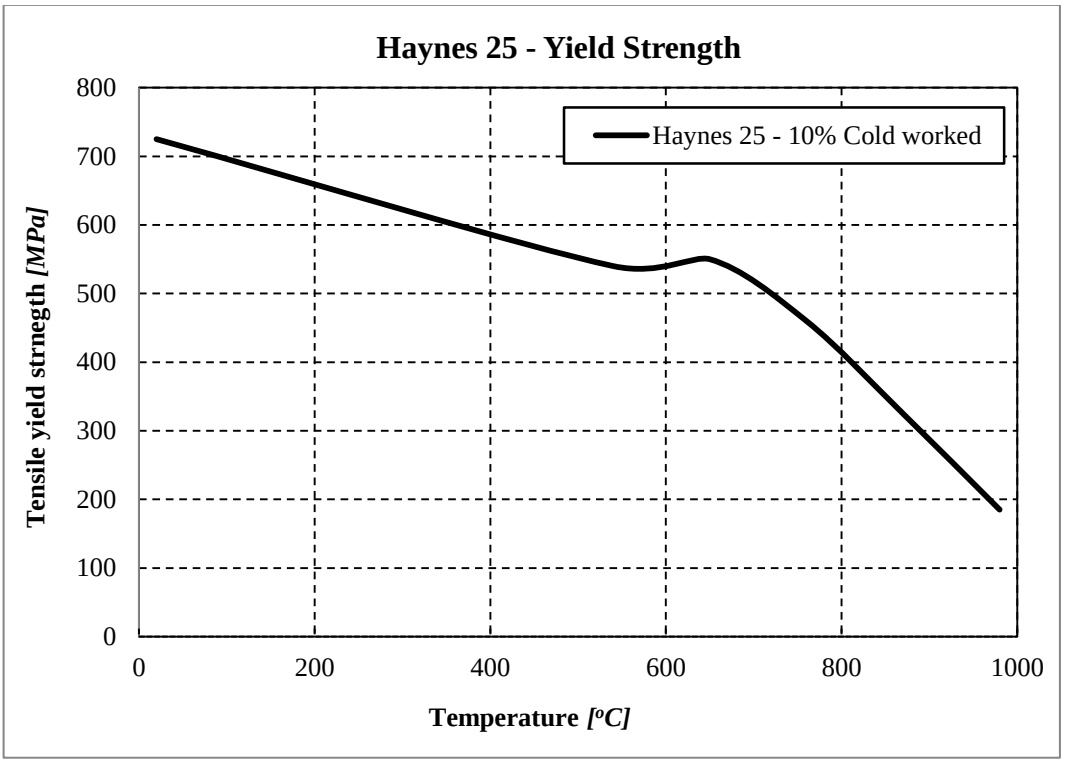

Figure 2.20: Haynes 25 – 10% cold worked, Yield strength change with temperature [52]

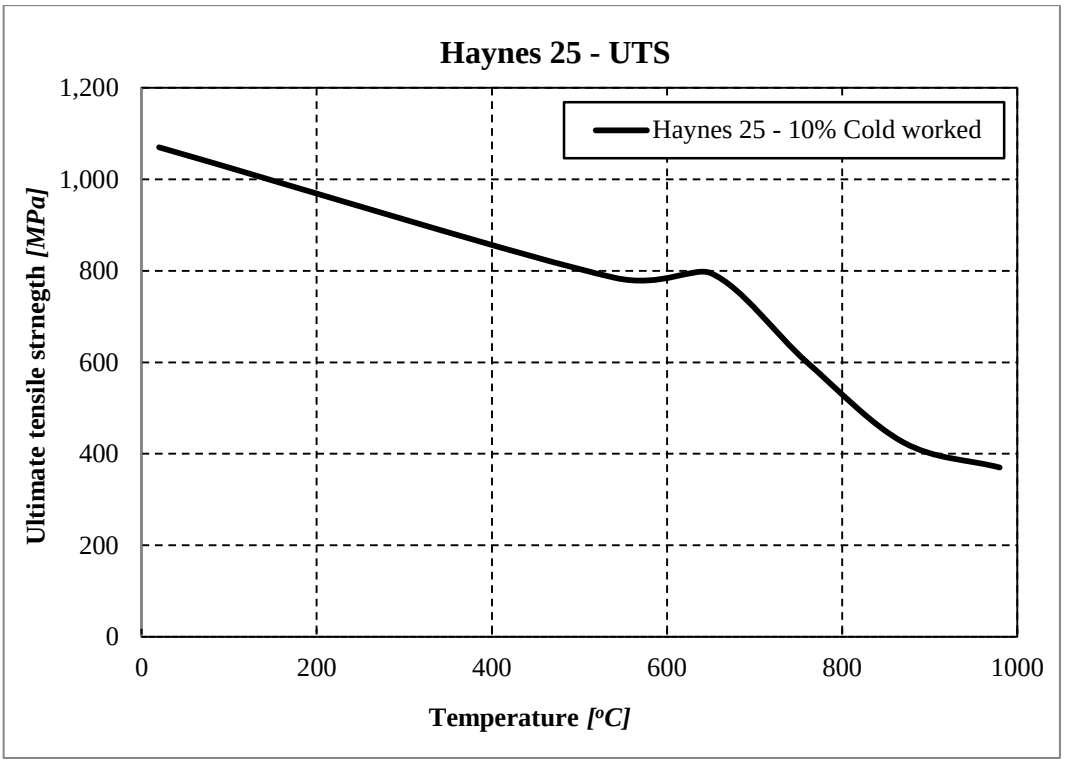

Figure 2.21: Haynes 25 – 10% cold worked, Ultimate tensile strength change with temperature [52]

Haynes 25 – 10% cold worked, Material Properties [52]	
Nominal chemical composition, weight percent	Co(51%)–Ni(10%)–Cr(20%)-W(15%)-Fe(3%)-Mn(1.5%)-Si(0.4%)-C(0.1%)
Tensile yield strength at room temperature	725MPa
Ultimate tensile strength at room temperature	1070MPa
Modulus of elasticity at room temperature	225,000MPa
Density at room temperature	9.13g/cm^3
Poisson's ratio	0.3

Table 2.7: Haynes 25 – 10% cold worked, material properties at room temperature [52]

3 FREE STATE STIFFNESS TEST RIG DESIGN FOR UNPRESSURIZED STIFFNESS MEASUREMENTS

Unpressurized stiffness measurements for brush seals provide useful data for CAE correlation, especially for bending characteristics of bristles and rotor-bristle friction coefficient verification. For this purpose, free-state stiffness test rig is designed and produced, where the rotor interference is simulated by pushing unloaded bristles with the aid of a metallic pad. In this section, test rig details and test procedure is detailed. Unpressurized stiffness measurements have been performed with FSSTR *(Free State Stiffness Test Rig)* for test seals, and results are also detailed in the related sections.

3.1 Main Rig Design and Details

Free-state stiffness measurement system has been designed to characterize the seal stiffness under unpressurized and static rotor conditions. The measurement relies on pressing a metallic pad, which has an arc surface having the diameter of seal inner circle, against unloaded bristles. As detailed in Figure 3.1, the free-state stiffness measurement system has six main components:

- Seal holder
- Seal fixers
- Legs
- Metallic pad
- Linear slide
- Base table

The seal holder is fixed on the base table with the aid of three legs. As shown in Figure 3.2, the linear slide, which holds the load cell and metallic pad, is attached to base plate. Seal fixers are bolted on seal holder, which constraints the circular brush seal located on seal holder during tests.

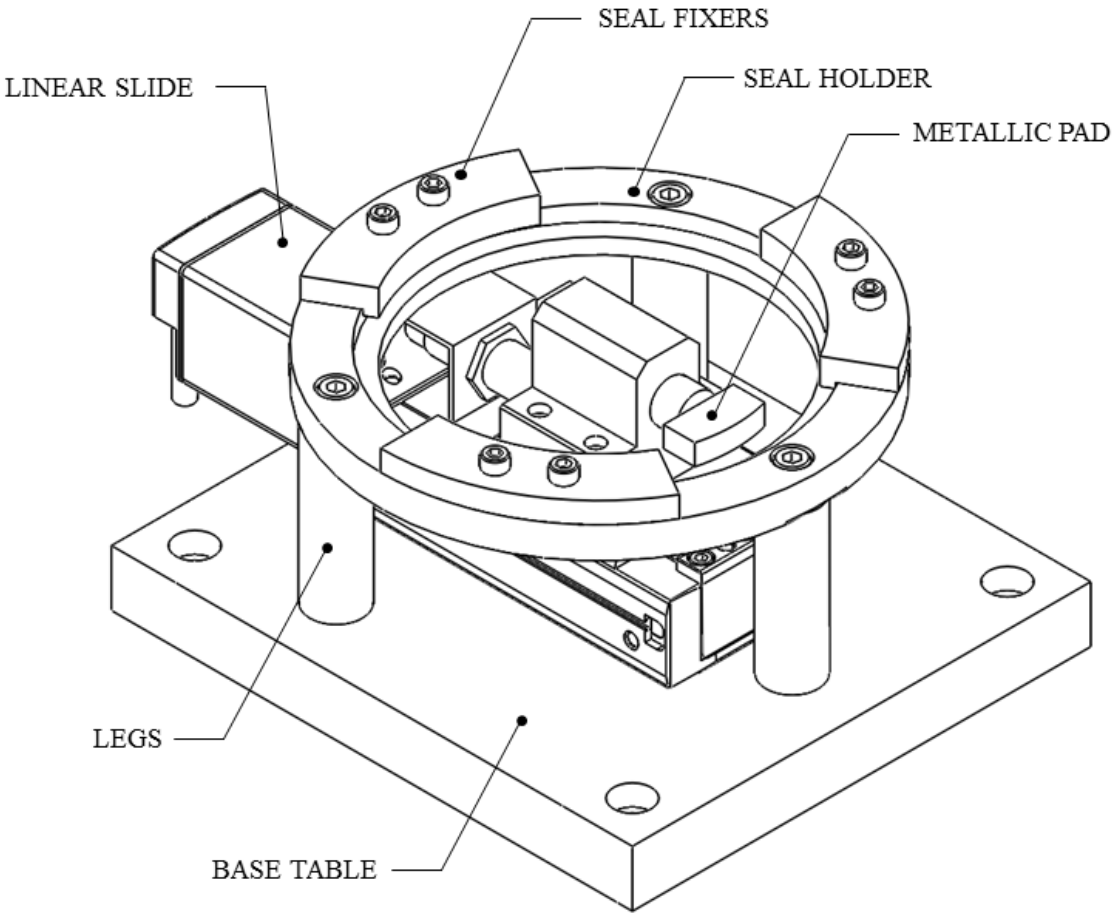

Figure 3.1: Free-state stiffness measurement system, main components

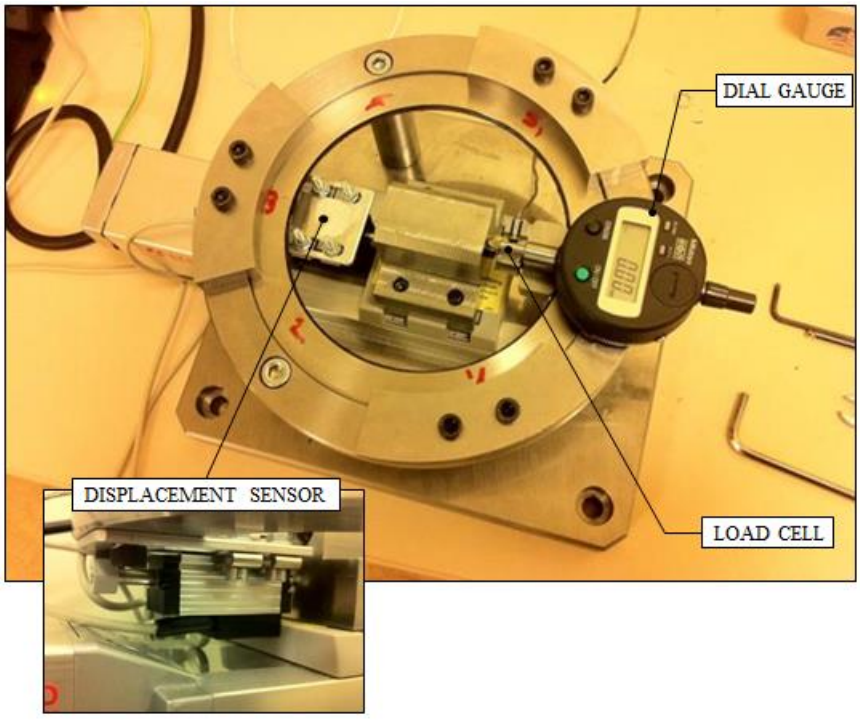

Figure 3.2: Free-state stiffness measurement system, assembled rig photo

As detailed in Figure 3.2, the metallic pad movement is excited by the linear slide. A controlled input is given to the slide by using the controller and PC. As the linear slide is moved, the load cell measures the force exerted to the metallic pad by the bristles. At the same time, the displacement sensor measures the magnitude of metallic pad – seal interference. The load cell and displacement sensor is connected to a data acquisition system to collect and store the data with a computer. An amplifier is used to increase the quality of the recorded test data and the accuracy of measurements.

3.2 Free-State Stiffness Measurement Procedure

Free-state stiffness tests are conducted with the aid of metallic pad, which represents approximately the 30^{o} slice of the rotor. The surface of the metallic pad has an arc form, whose diameter is equal to test seal inner circle diameter. The metallic pad is excited with the linear slide and pressed towards the bristles, and the reaction force applied by bristles is measured with the aid of load cell *(Figure 3.3)*.

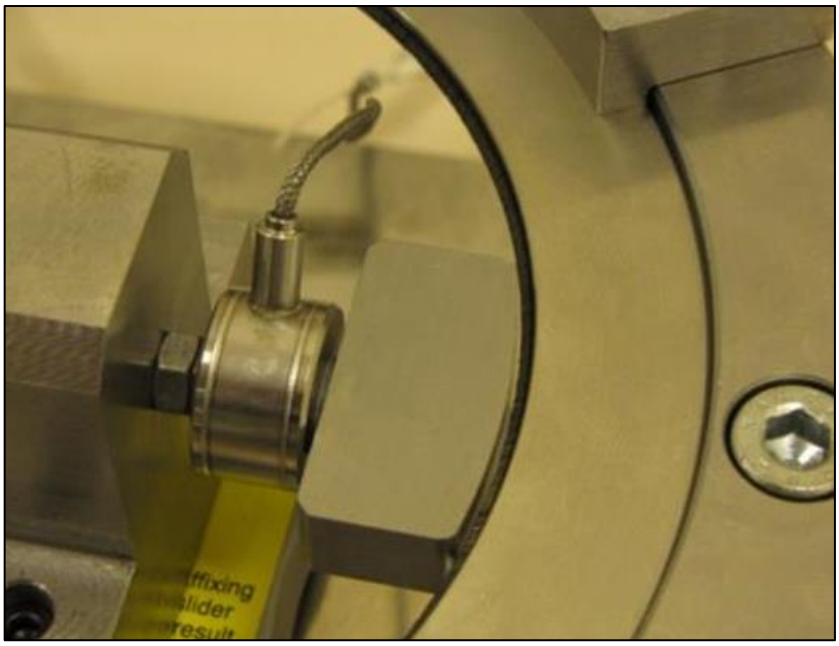

Figure 3.3: Metallic pad – brush seal contact during free-state stiffness measurements

The seal tests have been initiated with a clearance between metallic pad and bristles, and the interference level was set to zero as the reaction force was observed. Tests have been performed up to 0.6mm radial interference, and the reaction force was measured at interference step as well as while the pad is pulled back to its original

reference position. The measurement in loading and unloading steps enables to capture seal hysteresis due to friction. The travelled distance measured by displacement sensor and the reaction force measured by load cell were collected and stored in a PC with the aid of DAQ. The travelled distance was also measured with a dial gauge to assist calibration while setting the reference point for zero interference level. Tests have been conducted at four different seal sections, each of which are located at 90^o slice of the seal, and repeated continuously for two times to improve data accuracy and reduce measurement errors. Performing tests at four different sections also enables observing stiffness variability due to manufacturing tolerances.

3.3 FSS-TR - Stiffness Calculation Method

The free-state stiffness measurement with metallic pad stores the total reaction force applied by the bristles. To be able to perform brush seal stiffness characterization independent of metallic pad arc length, the measured force must be reduced to bristle level. In the literature [15, 46] is to calculate the bristle tip pressure – BTP – values from measured test data. The main idea for BTP calculation procedure is to divide the total measured force to effective shoe area, as given in Equation 3.1.

$$BTP = \frac{RF_{test}}{A_{eff-pad}} \tag{3.1}$$

"RF_{test}" is the measured reaction force on metallic pad *"$A_{eff\text{-}pad}$"* is the effective bristle area which is in contact with the metallic pad during tests. The effective seal area can be calculated by using the formula given below.

$$A_{eff-pad} = A_b \cdot N_{bristle-pad} \tag{3.2}$$

"A_b" is the projected bristle tip area given in Equation 2.1, and *"$N_{bristle\text{-}pad}$"* is the number of bristles contacting with the metallic pad surface. Number of bristles can be calculated by using the metallic pad arc length, *"$L_{metallic\text{-}pad}$"*, and the bristle density, *"η"*.

$$N_{bristle-pad} = \eta \cdot L_{metallic-pad} \tag{3.3}$$

Although using BTP values is the common practice in the literature, it has some drawbacks like rigorous post-processing and difficulties in comparing different seals having different bristle diameters. In BTP calculations, the projected bristle tip area requires the measured cant angle value, which requires detailed CNC inspection of bristles before tests. In addition to that, *"A_b"* is a function of bristle diameter, which makes it difficult to compare different seals in terms of generated heat due to friction and resulting rotor instability issues. In order to eliminate difficulties introduced with BTP, *"Bristle Tip Force, BTF"* is used for stiffness characterization of seals of this study. The BTF value corresponds to reaction force per bristle, and it can be calculated by dividing the measured reaction force to number of bristles contacting the metallic pad.

$$BTF = \frac{RF_{test}}{N_{bristle-pad}} \tag{3.4}$$

The seal stiffness is an important parameter for brush seal characterization in unpressurized condition. It can be calculated by dividing the bristle tip force, BTF, to corresponding interference level, ΔR.

$$K_{seal-BTF} = \frac{BTF}{\Delta R} \tag{3.5}$$

The metallic pad for the free-state stiffness test rig has the arc length of 31 mm, which corresponds to arc length at 27.4^o slice of the circle having 64.77mm radius *(Figure 3.4)*. Parameters for the free-state stiffness tests are detailed in Table 3.1.

Free State Stiffness Test Rig Parameters	
Definition	**Value**
Metallic pad – arc angle	27.4^o
Metallic pad radius	64.77mm
Metallic pad – arc length, $L_{metallic-pad}$	31mm
Test seals – bristle density, η	94 per mm
Number of bristles in contact, $N_{brislte-pad}$	2914.5

Table 3.1: Free state stiffness test rig - Parameters

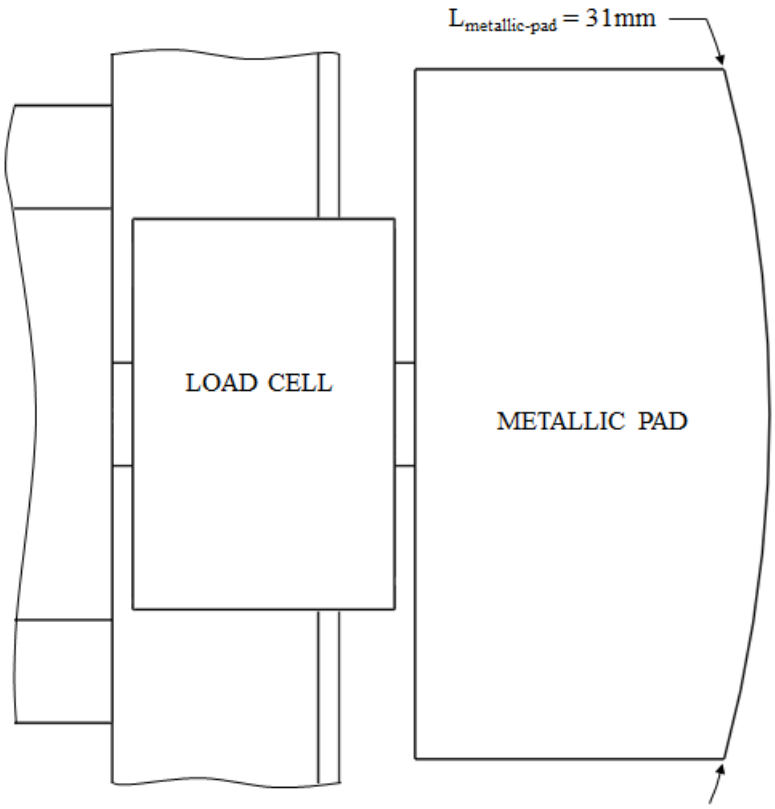

Figure 3.4: Metallic pad – effective arc length

3.4 Shoe Tests – Unpressurized Bristle Tip Pressure and Stiffness Measurements

Free-state stiffness tests have been performed for Test Seal # 1 and Test Seal # 2 at four different sections of seals and for two repetitions at each section. The maximum metallic pad-seal interference is 0.6mm, and the reaction force was collected both in loading and unloading steps.

3.4.1 Test Seal # 1, Free State Stiffness Test Rig – Measurements

The measured force data for two repetitions at four test points of Test Seal # 1 and the averaged force data are detailed in Table 3.2 and in Figures 3.5 thru 3.8. In Figure 3.9 and Table 3.3, the bristle tip force at each test point and their average, which represents the BTF of the seal # 1, are given. The bristle tip force at each test point is calculated by dividing the average measured force data to number of bristles in contact, which is equal to 2914.5.

Test Seal # 1, FSS-TR, Measured force at different test points													
	ΔR	Test point 1, RF *[N]*			Test point 2, RF *[N]*			Test point 3, RF *[N]*			Test point 4, RF *[N]*		
	[mm]	$RF_{1\text{-}1}$	$RF_{1\text{-}2}$	$RF_{1\text{-}ave}$	$RF_{2\text{-}1}$	$RF_{2\text{-}2}$	$RF_{2\text{-}ave}$	$RF_{3\text{-}1}$	$RF_{3\text{-}2}$	$RF_{3\text{-}ave}$	$RF_{4\text{-}1}$	$RF_{4\text{-}2}$	$RF_{4\text{-}ave}$
LOADING	0.0	0.000	0.000	**0.000**	0.000	0.000	**0.000**	0.000	0.000	**0.000**	0.000	0.000	**0.000**
	0.1	1.140	0.739	**0.940**	0.556	0.668	**0.612**	0.845	0.913	**0.879**	0.779	0.914	**0.846**
	0.2	2.032	1.658	**1.845**	1.474	1.671	**1.572**	2.260	1.965	**2.112**	1.467	1.831	**1.649**
	0.3	3.043	2.566	**2.805**	2.456	2.623	**2.539**	3.612	2.860	**3.236**	2.370	2.824	**2.597**
	0.4	4.439	3.432	**3.393**	3.745	3.890	**3.817**	5.408	3.926	**4.667**	3.348	4.008	**3.678**
	0.5	6.053	4.928	**5.490**	5.124	5.533	**5.328**	7.058	5.355	**6.206**	4.494	5.338	**4.916**
	0.6	8.094	6.968	**7.531**	7.232	7.624	**7.428**	8.424	7.334	**7.879**	6.049	7.092	**6.570**
UNLOADING	0.5	1.450	1.723	**1.586**	1.426	1.468	**1.447**	1.900	2.017	**1.958**	1.727	1.638	**1.683**
	0.4	0.938	1.139	**1.039**	0.912	0.963	**0.937**	1.426	1.442	**1.434**	1.223	1.190	**1.207**
	0.3	0.570	0.777	**0.673**	0.382	0.568	**0.475**	0.828	0.901	**0.865**	0.735	0.745	**0.740**
	0.2	0.192	0.318	**0.255**	0.098	0.064	**0.081**	0.275	0.514	**0.395**	0.459	0.294	**0.377**
	0.1	0.115	0.065	**0.090**	0.006	0.116	**0.061**	0.026	0.095	**0.060**	0.050	0.035	**0.042**
	0.0	0.000	0.000	**0.000**	0.000	0.000	**0.000**	0.000	0.000	**0.000**	0.000	0.000	**0.000**

Table 3.2: Test seal # 1, FSS-TR, measured force at different test points, $RF_{metallic\text{-}pad}$

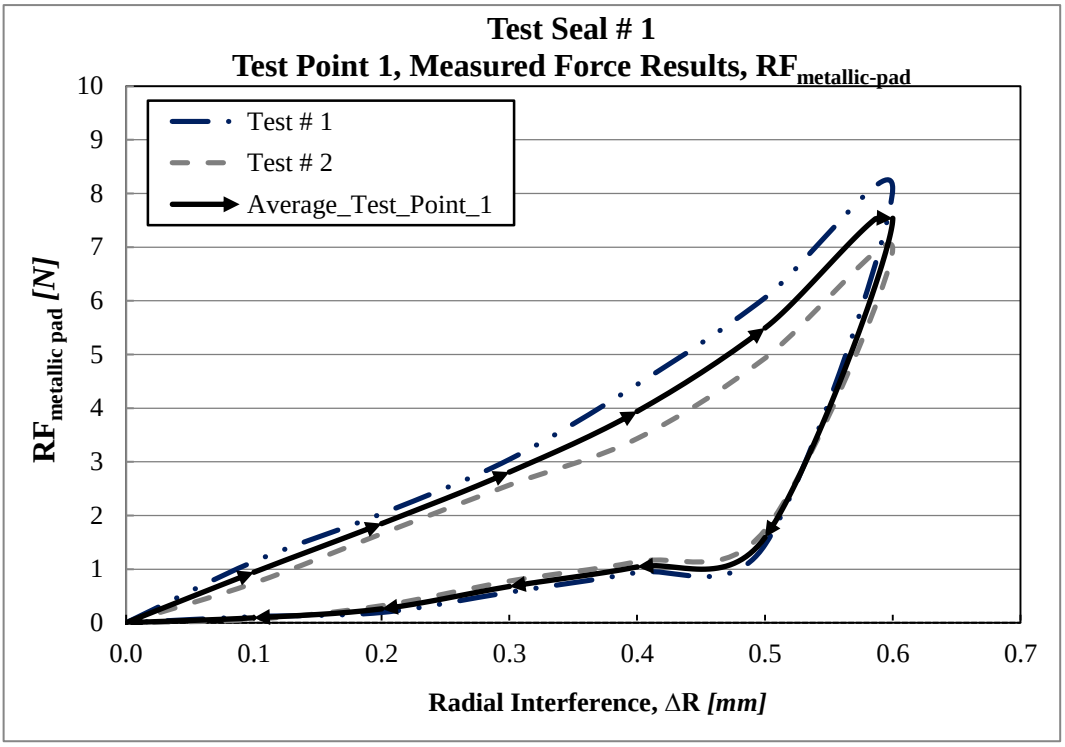

Figure 3.5: Test seal # 1, measured force data at test point 1

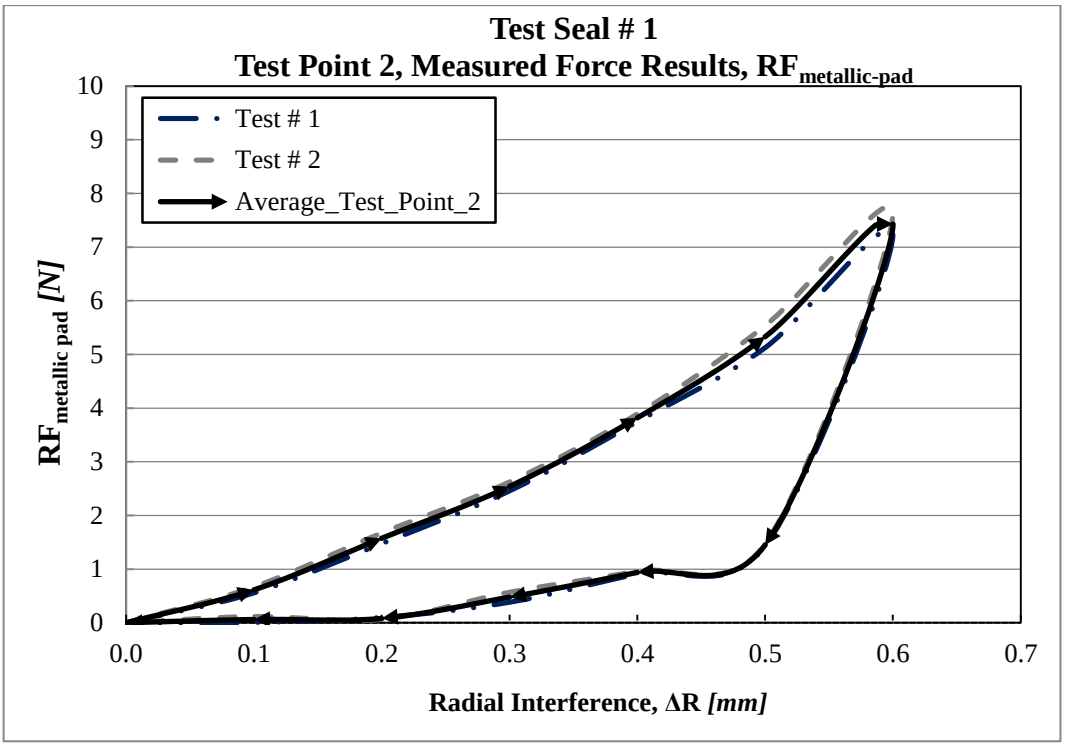

Figure 3.6: Test seal # 1, measured force data at test point 2

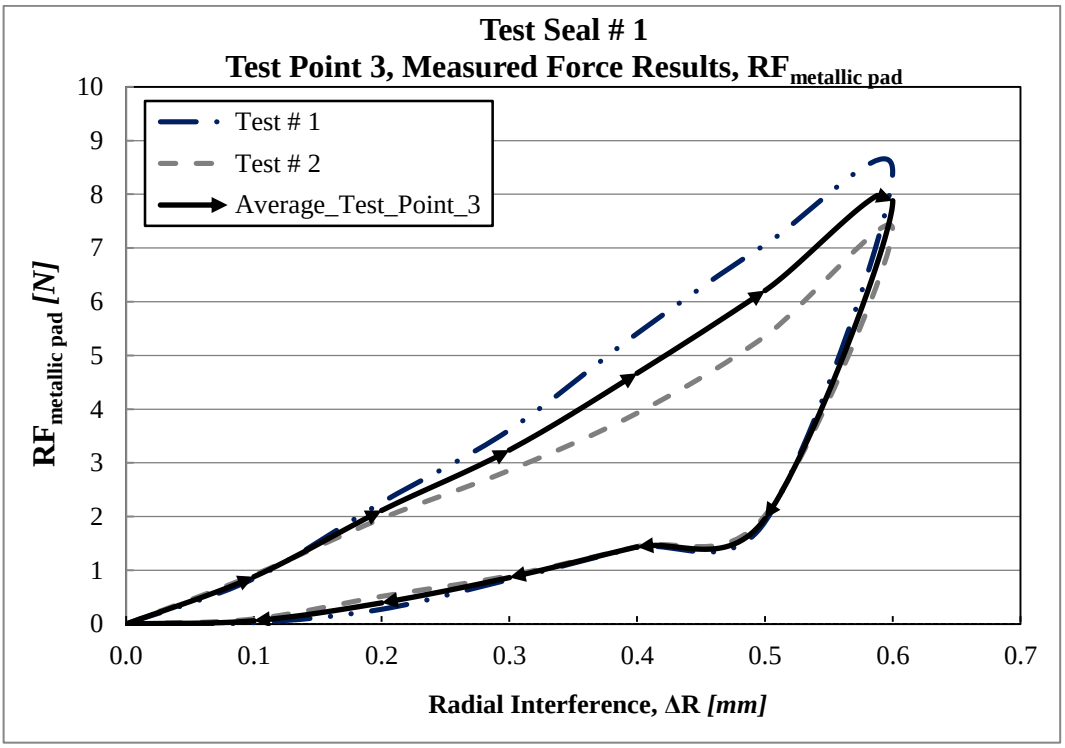

Figure 3.7: Test seal # 1, measured force data at test point 3

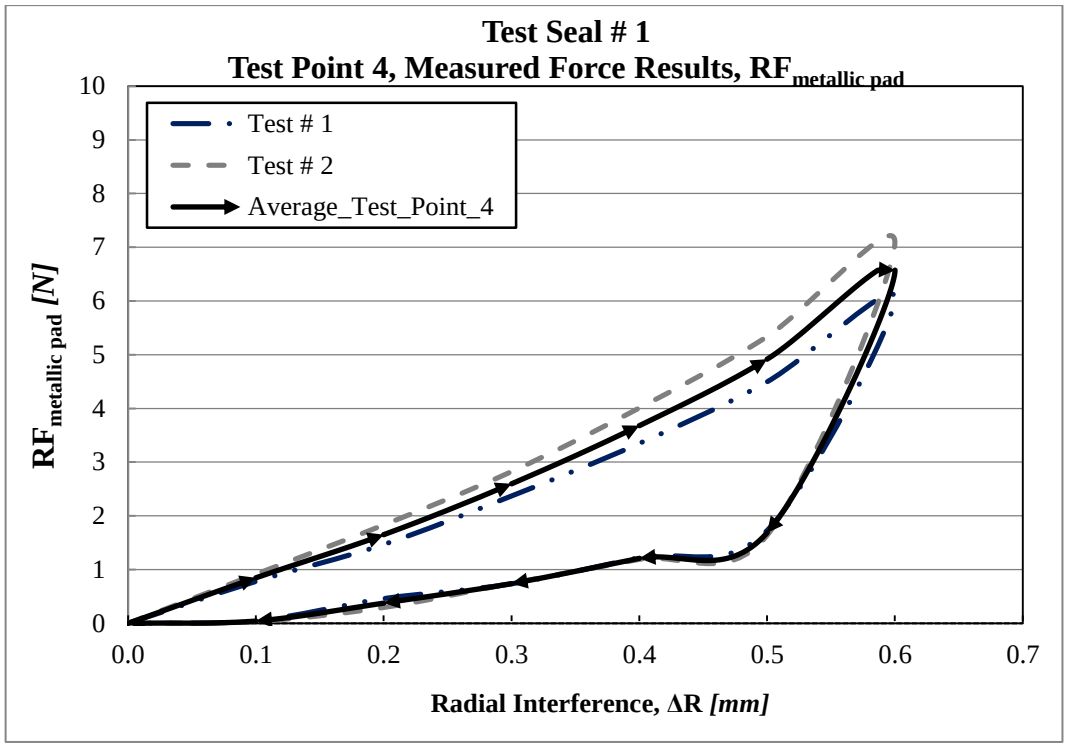

Figure 3.8: Test seal # 1, measured force data at test point 4

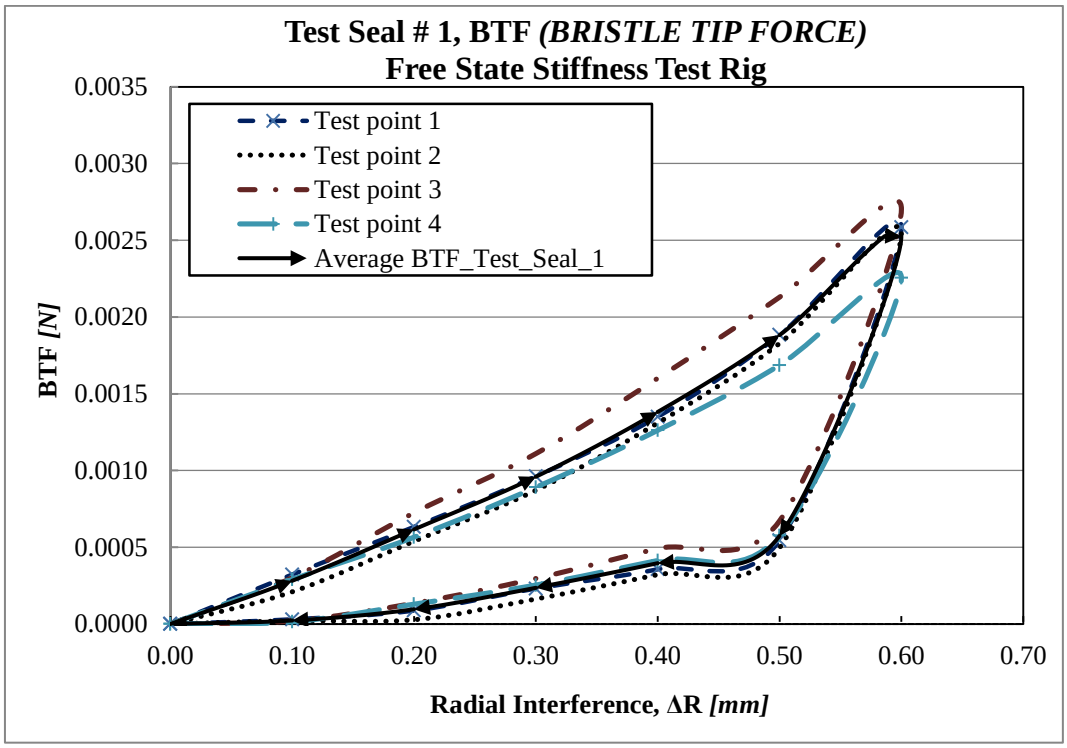

Figure 3.9: Test seal # 1, Bristle tip force at different test points and averaged BTF for FSS-TR measurements

Test Seal # 1, FSS-TR, BTF at different test points						
	ΔR *[mm]*	**$BTF_{ave\text{-}TP1}$ *[N]***	**$BTF_{ave\text{-}TP2}$ *[N]***	**$BTF_{ave\text{-}TP3}$ *[N]***	**$BTF_{ave\text{-}TP4}$ *[N]***	**$BTF_{ave\text{-}seal\ 1}$ *[N]***
LOADING	0.0	0.000000	0.000000	0.000000	0.000000	**0.000000**
	0.1	0.000323	0.000210	0.000302	0.000291	**0.000281**
	0.2	0.000633	0.000540	0.000725	0.000566	**0.000616**
	0.3	0.000963	0.000871	0.001111	0.000891	**0.000959**
	0.4	0.001350	0.001310	0.001601	0.001262	**0.001381**
	0.5	0.001884	0.001828	0.002130	0.001687	**0.001882**
	0.6	0.002584	0.002549	0.002703	0.002255	**0.002523**
UNLOADING	0.5	0.000544	0.000497	0.000672	0.000577	**0.000573**
	0.4	0.000357	0.000322	0.000492	0.000414	**0.000396**
	0.3	0.000231	0.000163	0.000297	0.000254	**0.000236**
	0.2	0.000088	0.000028	0.000136	0.000129	**0.000095**
	0.1	0.000031	0.000021	0.000021	0.000015	**0.000022**
	0.0	0.000000	0.000000	0.000000	0.000000	**0.000000**

Table 3.3: Test seal # 1, FSS-TR, averaged bristle tip force at different test points and averaged BTF for seal # 1

3.4.2 Test Seal # 2, Free State Stiffness Test Rig – Measurements

The measured force data for two repetitions at four test points of Test Seal # 2 and the averaged force data are detailed in Table 3.2 and in Figures 3.5 thru 3.8. In Figure 3.9 and Table 3.3, the bristle tip force at each test point and their average, which represents BTF of the seal # 2, are given. The bristle tip force at each test point is calculated by dividing the average measured force data to number of bristles in contact, which is equal to 2914.5.

Test Seal # 2, FSS-TR, Measured force at different test points													
	ΔR	**Test point 1, RF *[N]***			**Test point 2, RF *[N]***			**Test point 3, RF *[N]***			**Test point 4, RF *[N]***		
	[mm]	**$RF_{1\text{-}1}$**	**$RF_{1\text{-}2}$**	**$RF_{1\text{-}ave}$**	**$RF_{2\text{-}1}$**	**$RF_{2\text{-}2}$**	**$RF_{2\text{-}ave}$**	**$RF_{3\text{-}1}$**	**$RF_{3\text{-}2}$**	**$RF_{3\text{-}ave}$**	**$RF_{4\text{-}1}$**	**$RF_{4\text{-}2}$**	**$RF_{4\text{-}ave}$**
LOADING	0.0	0.000	0.000	**0.000**	0.000	0.000	**0.000**	0.000	0.000	**0.000**	0.000	0.000	**0.000**
	0.1	1.262	0.807	**1.035**	1.258	0.083	**0.671**	0.860	0.627	**0.743**	0.665	0.886	**0.775**
	0.2	2.505	1.827	**2.166**	2.443	1.654	**2.048**	2.073	1.874	**1.974**	1.718	1.683	**1.701**
	0.3	3.732	2.936	**3.334**	3.696	2.840	**3.404**	3.296	2.991	**3.144**	2.856	2.662	**2.759**
	0.4	4.900	4.614	**4.757**	5.526	4.493	**5.009**	4.729	4.860	**4.795**	4.089	4.025	**4.057**
	0.5	7.153	6.733	**6.943**	7.776	6.243	**7.010**	6.410	6.486	**6.448**	6.112	5.473	**5.792**
	0.6	9.112	8.621	**8.867**	9.218	8.234	**8.725**	8.289	8.489	**8.389**	7.955	7.554	**7.754**
UNLOADING	0.5	2.006	1.952	**1.979**	1.982	1.611	**1.797**	2.138	2.091	**2.115**	1.701	1.828	**1.765**
	0.4	1.408	1.213	**1.310**	1.437	0.951	**1.194**	1.261	1.396	**1.328**	1.136	1.199	**1.167**
	0.3	0.877	0.747	**0.812**	0.879	0.536	**0.708**	0.716	0.738	**0.727**	0.636	0.706	**0.671**
	0.2	0.511	0.221	**0.366**	0.422	0.140	**0.281**	0.300	0.194	**0.247**	0.358	0.428	**0.393**
	0.1	0.190	0.089	**0.140**	0.069	0.063	**0.066**	0.012	0.054	**0.033**	0.040	0.016	**0.028**
	0.0	0.000	0.000	**0.000**	0.000	0.000	**0.000**	0.000	0.000	**0.000**	0.000	0.000	**0.000**

Table 3.4: Test seal # 2, FSS-TR, measured force at different test points, $RF_{metallic\text{-}pad}$

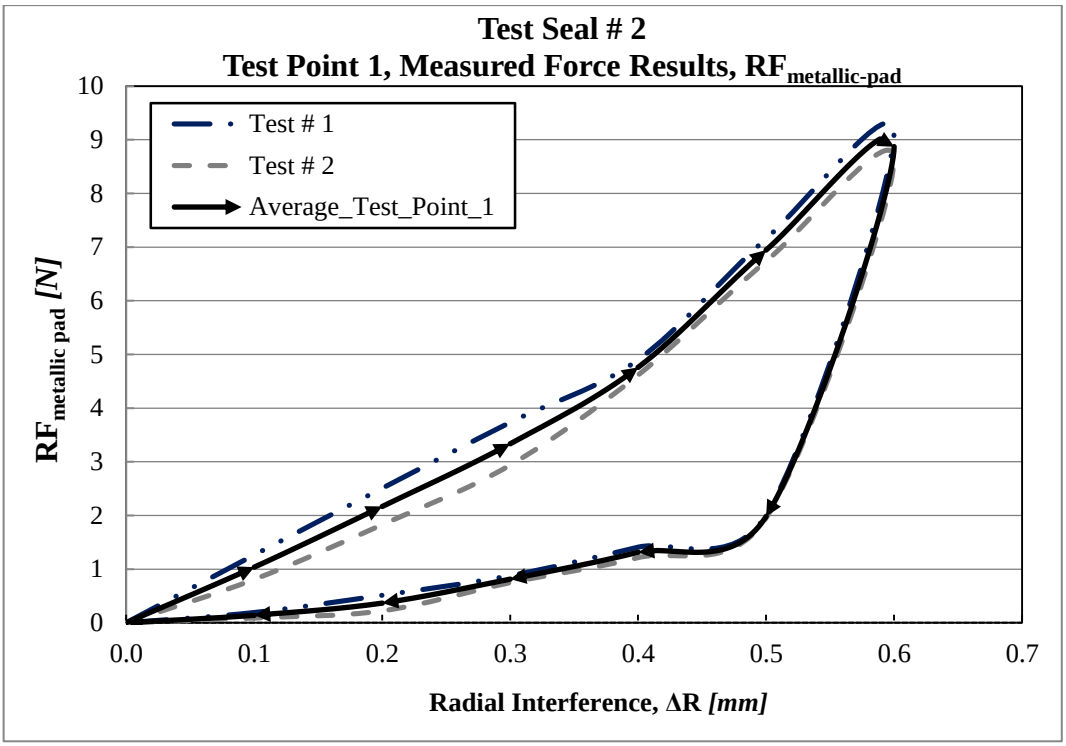

Figure 3.10: Test seal # 2, measured force data at test point 1

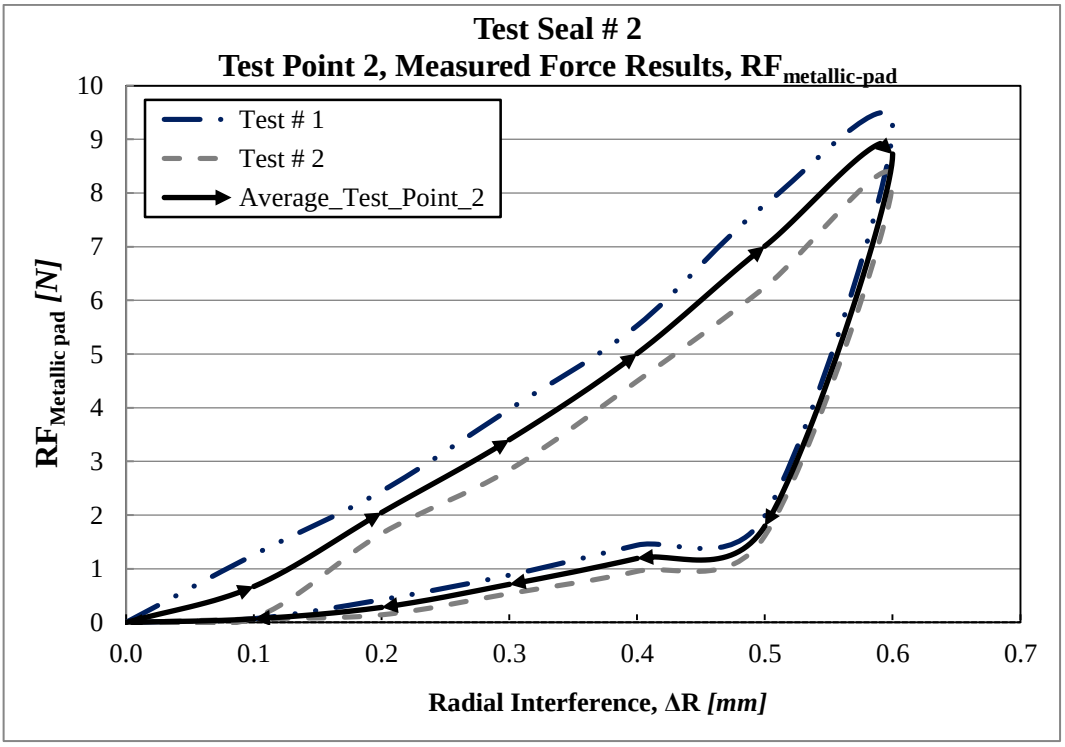

Figure 3.11: Test seal # 2, measured force data at test point 2

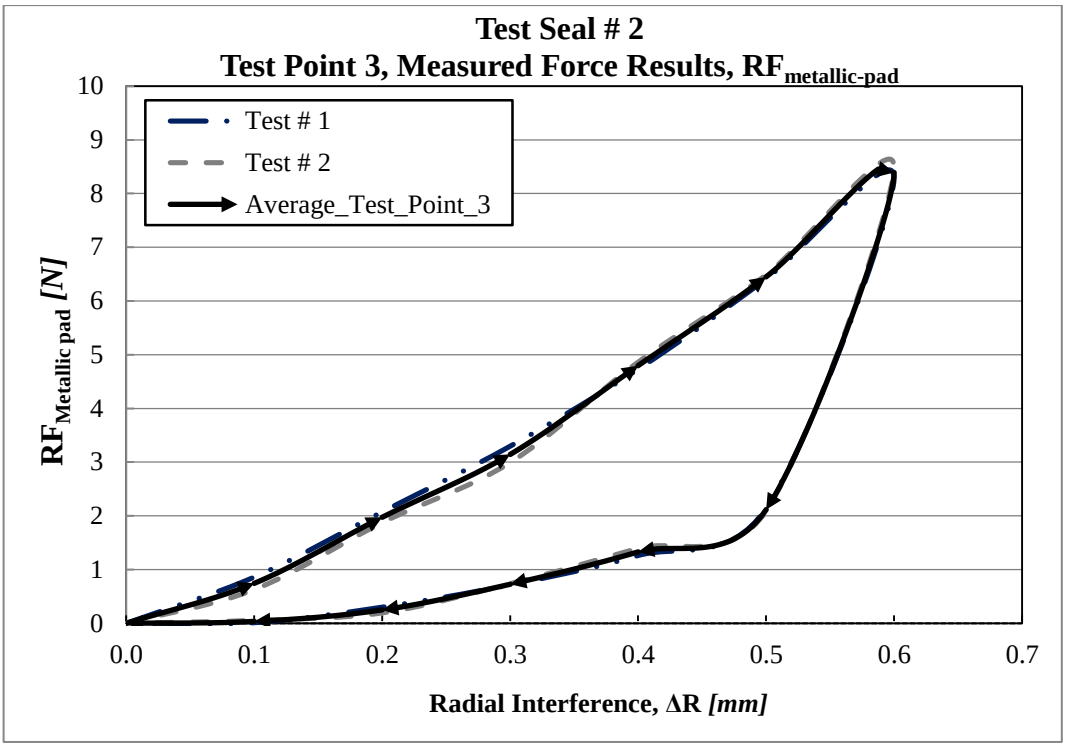

Figure 3.12: Test seal # 2, measured force data at test point 3

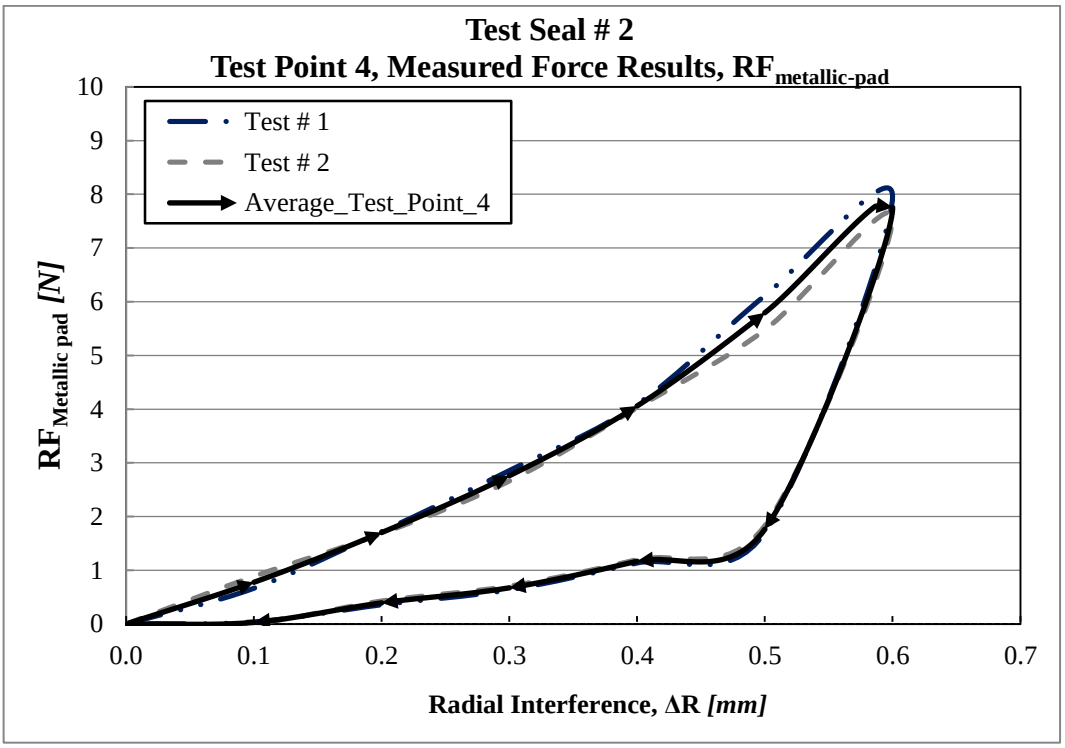

Figure 3.13: Test seal # 2, measured force data at test point 4

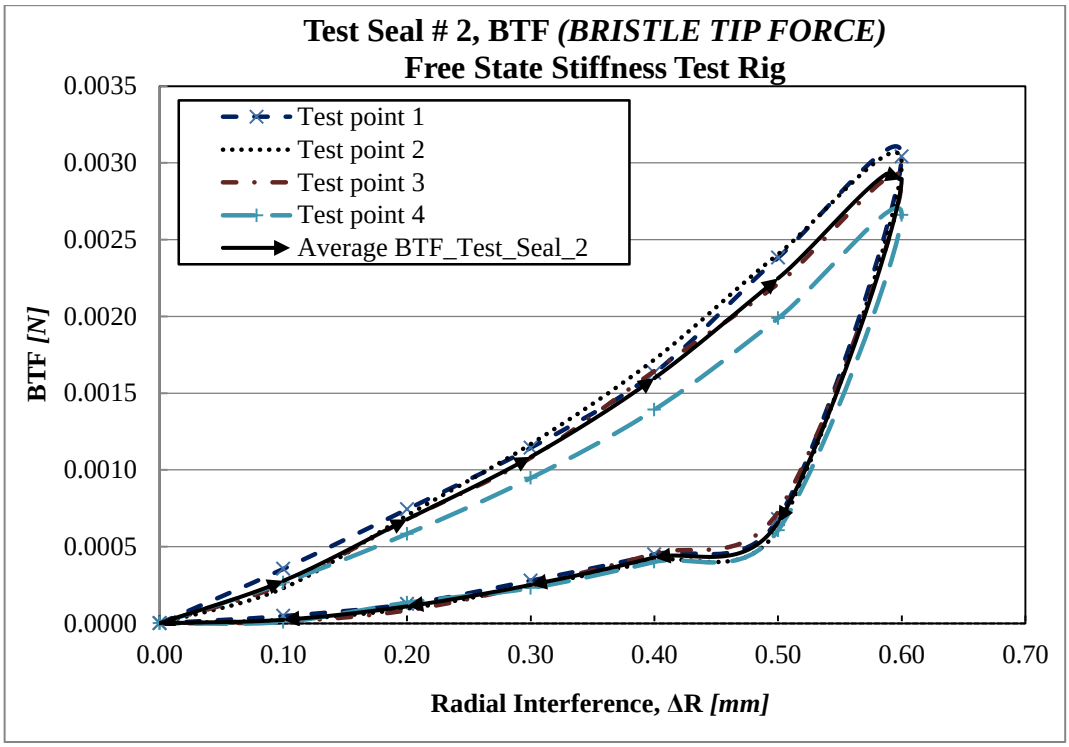

Figure 3.14: Test seal # 2, Bristle tip force at different test points and averaged BTF for FSS-TR measurements

Test Seal # 2, FSS-TR, BTF at different test points						
	ΔR *[mm]*	**$BTF_{ave\text{-}TP1}$ *[N]***	**$BTF_{ave\text{-}TP2}$ *[N]***	**$BTF_{ave\text{-}TP3}$ *[N]***	**$BTF_{ave\text{-}TP4}$ *[N]***	**$BTF_{ave\text{-}seal\ 2}$ *[N]***
LOADING	0.0	0.000000	0.000000	0.000000	0.000000	**0.000000**
	0.1	0.000355	0.000230	0.000255	0.000266	**0.000277**
	0.2	0.000743	0.000703	0.000677	0.000584	**0.000677**
	0.3	0.001144	0.001168	0.001079	0.000947	**0.001084**
	0.4	0.001632	0.001719	0.001645	0.001392	**0.001597**
	0.5	0.002382	0.002405	0.002213	0.001988	**0.002247**
	0.6	0.003042	0.002994	0.002879	0.002661	**0.002894**
UNLOADING	0.5	0.000679	0.000617	0.000726	0.000606	**0.000657**
	0.4	0.000450	0.000410	0.000456	0.000401	**0.000429**
	0.3	0.000279	0.000243	0.000250	0.000230	**0.000250**
	0.2	0.000126	0.000097	0.000085	0..000135	**0.000111**
	0.1	0.000048	0.000023	0.000011	0.000010	**0.000023**
	0.0	0.000000	0.000000	0.000000	0.000000	**0.000000**

Table 3.5: Test seal # 2, FSS-TR, averaged bristle tip force at different test points and averaged BTF for seal # 2

3.5 Shoe Tests – Conclusion

In Figure 3.15, the average BTF results for test seals are detailed. In Table 3.6, the free-state stiffness values, which are calculated by using Equation 3.5, are also provided.

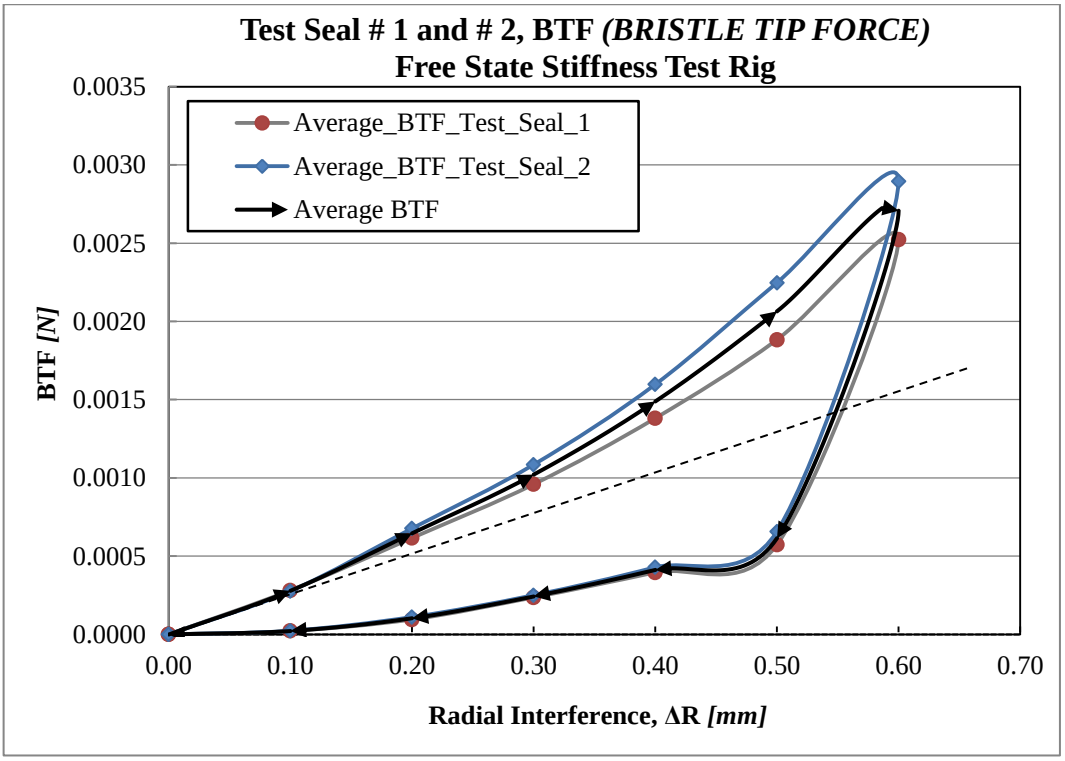

Figure 3.15: Test seal # 1 and #2, Averaged BTF comparison, FSS-TR measurements

Test Seal # 1 and #2, Averaged BTF and Seal Stiffness							
	ΔR *[mm]*	Test seal #1		Test seal #2		$BTF_{average}$ *[N]*	$K_{seal-BTF-ave}$ *[N/mm]*
		$BTF_{ave-seal\ 1}$ *[N]*	$K_{seal-BTF-1}$ *[N/mm]*	$BTF_{ave-seal\ 2}$ *[N]*	$K_{seal-BTF-2}$ *[N/mm]*		
LOADING	0.0	0.000000	N/A	0.000000	N/A	0.000000	N/A
	0.1	0.000281	0.002813	0.000277	0.002767	0.000279	0.002790
	0.2	0.000616	0.003080	0.000677	0.003384	0.000646	0.003232
	0.3	0.000959	0.003196	0.001084	0.003615	0.001022	0.003406
	0.4	0.001381	0.003453	0.001597	0.003993	0.001489	0.003723
	0.5	0.001882	0.003765	0.002247	0.004494	0.002065	0.004129
	0.6	0.002523	0.004205	0.002894	0.004823	0.002708	0.004514
UNLOADING	0.5	0.000573	0.001145	0.000657	0.001314	0.000615	0.001229
	0.4	0.000396	0.000990	0.000429	0.001073	0.000413	0.001032
	0.3	0.000236	0.000788	0.000250	0.000835	0.000243	0.000811
	0.2	0.000095	0.000476	0.000111	0.000553	0.000103	0.000515
	0.1	0.000022	0.000219	0.000023	0.000230	0.000022	0.000224
	0.0	0.000000	N/A	0.000000	N/A	0.000000	N/A

Table 3.6: Test seal #1 and #2, FSS-TR, averaged BTF and seal stiffness

As it can be seen form the figure, although some difference due to manufacturing variability is observed in BTF values of two tested seals, the results are comparable with each other.

In an ideal case for an unpressurized seal, the slope of the BTF-ΔR curve, which equals to free-state seal stiffness, should remain constant. However, as it can be seen from Figure 3.15, the seal stiffness continuously increases as radial interference increases, and the measured BTF deviates from the representative linear line.

The main reason for nonlinear increase in BTF during free-state stiffness test rig measurements is the non-uniform deflection of bristles, which is visualized in Figure 3.16. As the metallic pad interference is introduced during FSS-TR tests, the end bristle gets in contact with the neighbor bristle and deforms it. As a result of cascaded contact with side bristles, additional contribution to measured force is observed due to bending and friction from neighbor bristles, which in turn causes BTF results to increase in FSS-TR measurements. Since the contribution of side bristles increases with increasing ΔR, the slope of the BTF-ΔR curve increases continuously. In conclusion, it can be stated that the BTF results of FSS-TR measurements give higher BTF values than turbine applications, where side effects are minimal due to large interference surfaces.

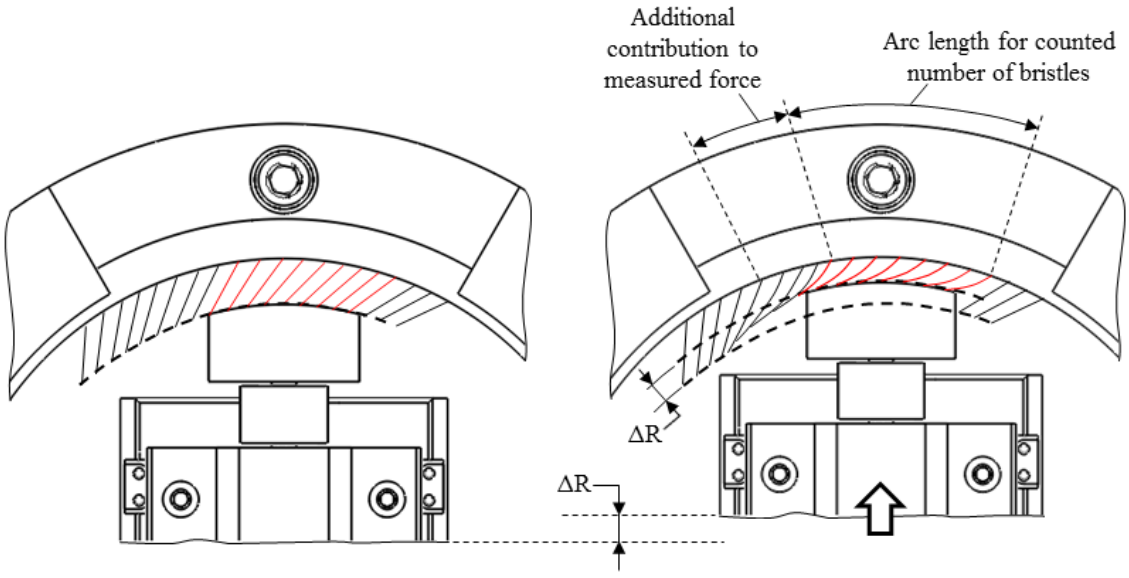

Figure 3.16: Non-uniform deformation during free-state stiffness test rig-force measurements

4 ROTARY TEST RIG DESIGN AND TIP FORCE MEASUREMENTS

Brush seals operate under different pressure loads and rotor interference levels in turbine conditions, where seal stiffness, hysteresis and pressure closure behaviors play important roles in determining the leakage performance and rotor stability. Unpressurized stiffness measurements with free-state stiffness test rig provide valuable results for back to back comparison of different seal designs, but FSS-TR has the disadvantage of increased BTF measurements due to non-uniform bristle deformation. In addition to that, seal stiffness under pressure load is needed to be tested to simulate the bristle tip force levels in turbine conditions.

There are few available studies in the literature for measurements of seal stiffness and contact forces under pressure loads, none of which simulate the effect of rotor rotation and introduced bristle dynamics in turbine conditions. Basu et al. [29], Short et al. [30] and Wood et al. [41] present stiffness data at different pressure loads with static rotor. However, they do not provide sufficient description of tested seals and their test methodology. Although Long et al. [42] provides adequate description of testing procedure, their studies does not include the rotor rotation and induced dynamic effects. Bidkar et al. [43] give details of a special rig design to measure brush seal stiffness under pressure loads. However, the test rig design suggested in this study again cannot take the rotor rotation into account, which has direct effect on bristle tip force magnitudes due to frictional and inertial effects.

In this study, custom test rig has been designed to better understand the seal stiffness behavior and leakage performance in turbine operating conditions. The high speed rotary test rig has two main functions, one of which is leakage measurements in different environments *(air, oil etc.)*, and the other one is to perform static and dynamic seal stiffness tests at different pressure levels and rotor speeds. Dynamic stiffness measurement capability enables simulating the turbine operating conditions.

Seal stiffness tests have been performed for static-unpressurized/pressurized conditions as well as for dynamic-unpressurized/pressurized test conditions. Dynamic stiffness measurements, which do not exist in the literature, help better understanding

the effect of dynamics on seal stiffness and hysteresis behavior in turbine operating conditions. Dynamic tests have been performed at 3000rpm, and pressurized stiffness characterization has been done at variable pressure loads.

The base structure of the rotary rig has been designed to test two seals at the same time and 45,000rpm rotor speed enables to obtain same surface speeds of turbine operating conditions in a subscale rig. Experimental setup has been designed to perform unpressurized static, unpressurized dynamic *(rotating rotor)*, pressurized static and pressurized dynamic stiffness tests. Pressurized dynamic stiffness test capability of the rig does not exist in the open literature, and it enables to simulate bristle tip force values in turbine conditions. Rotary test rig details and capabilities are summarized in Table 4.1.

High Speed Rotary Test Rig Seal and Roller Bearing Leakage Performance and Stiffness Characterization	
Test Conditions	
Test environment	Air, Oil
Test temperature	Room temperature
Maximum pressure load	5 bar
Turbine conditions	Steady state *(clearance)*, Line-to-Line *(new seal)*, Interference *(rotor rub conditions)*
Tested components	Dynamic seals *(Brush, Labyrinth, Honeycomb etc.)*, Roller Bearings
Spindle Details – GMN, HV-X 150-45000/25	
Maximum speed	45,000 rpm
Maximum torque	11.4 Nm
Maximum power	25kW
Controller	Bosch Rexroth RD500 RD52 Field Oriented Vector Controller
Test Capabilities	
Leakage tests	Static, Dynamic, Different Pressure Loads
Unpressurized stiffness tests	Static, Dynamic
Pressurized stiffness tests	Static, Dynamic, Different Pressure Loads
Other	Blow down, Fluttering, Hung-up, Full prototype seal wear tests, One-per-rev seal stability tests

Table 4.1: High speed rotary test rig capabilities

4.1 Main Rig Design and Details

Main rig design is detailed in Figures 4.1 thru 4.3. As shown in those figures, the rig mainly consists of seal housing assembly, spindle holder assembly and a solid base plate, which also can be named as *"platform"*. The spindle holder and the seal housing

are fixed onto the base plate, which is designed as thick steel component to damp vibration magnitudes induced at high test speeds.

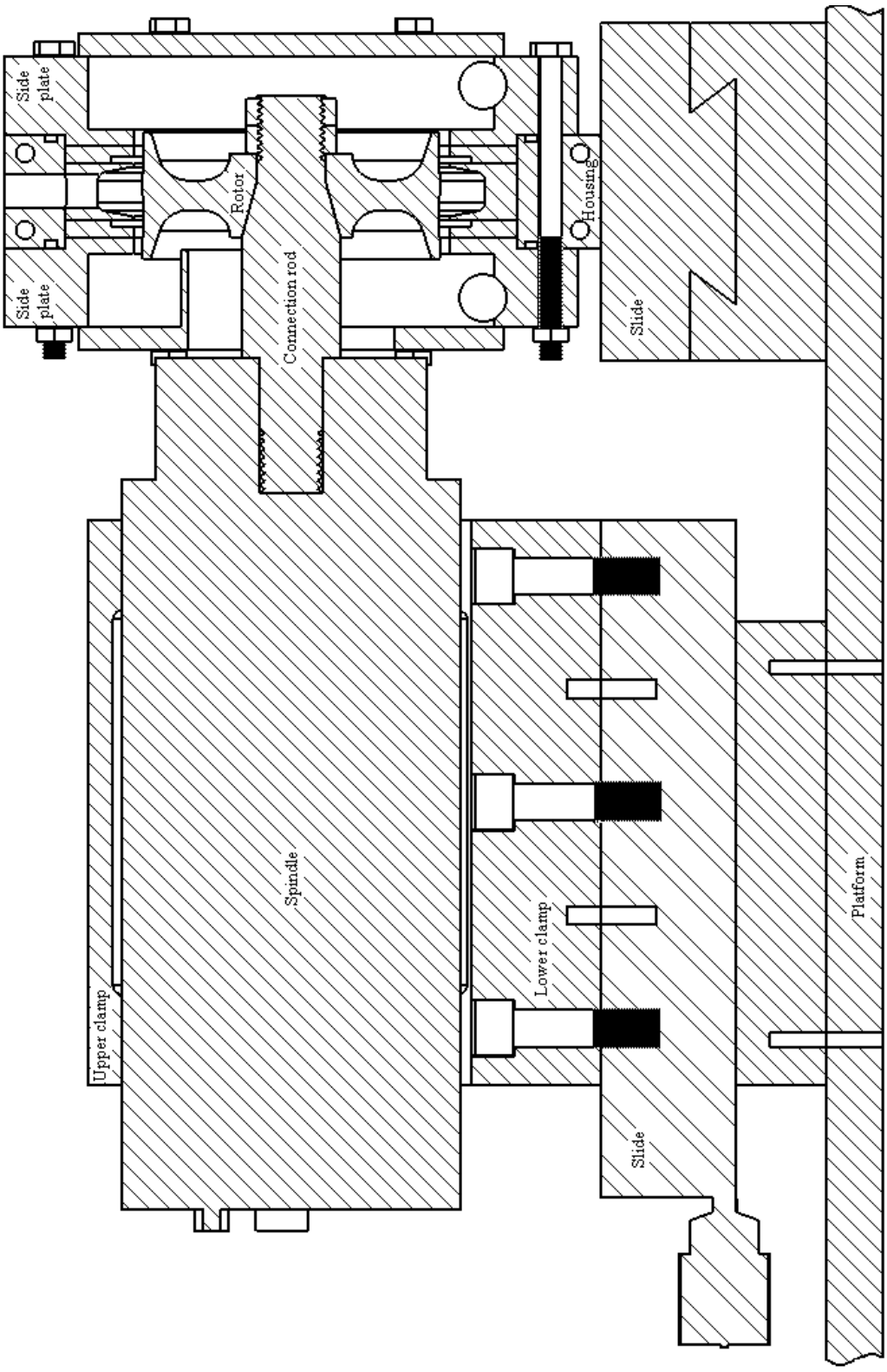

Figure 4.1: Cross-sectional view of the high speed rotary test rig

The spindle is tightly held with upper and lower clamps, which are machined at their inner surfaces to obtain sufficient spindle concentricity. The manual slider, on which the lower clamp is assembled, allows the spindle to move axially in the seal holder. This provides ease of assembly in pre-test phase and enables experimenter to change rotor axial location to obtain different rotor-seal clearance/interference levels during tests.

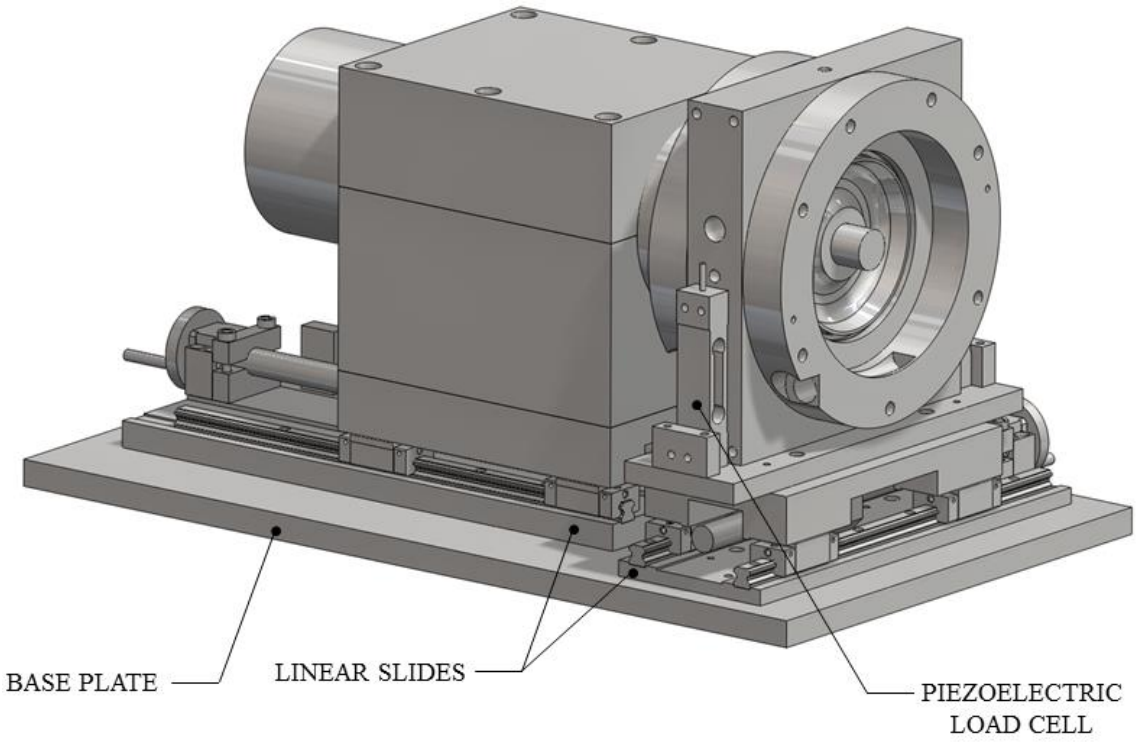

Figure 4.2: Isometric view of the high speed rotary test rig

The rig is powered by a GMN-high frequency spindle with 45,000rpm maximum speed and 25kW output rating. The torque is transmitted to the rotor with a connecting rod. Balancing of the rotor has an extreme importance as small imbalance together with high rotor speeds may cause serious durability problems. Therefore, the connecting rod component is produced from the run out test rod supplied with the spindle. The original test rod gives 8μm run out at 10cm from spindle end when the spindle is rotated with full speed. Exclusive use of stainless steel for all components of test rig allows testing up to 500^{o}C with some modifications.

Figure 4.3: High speed rotary test rig assembly photo

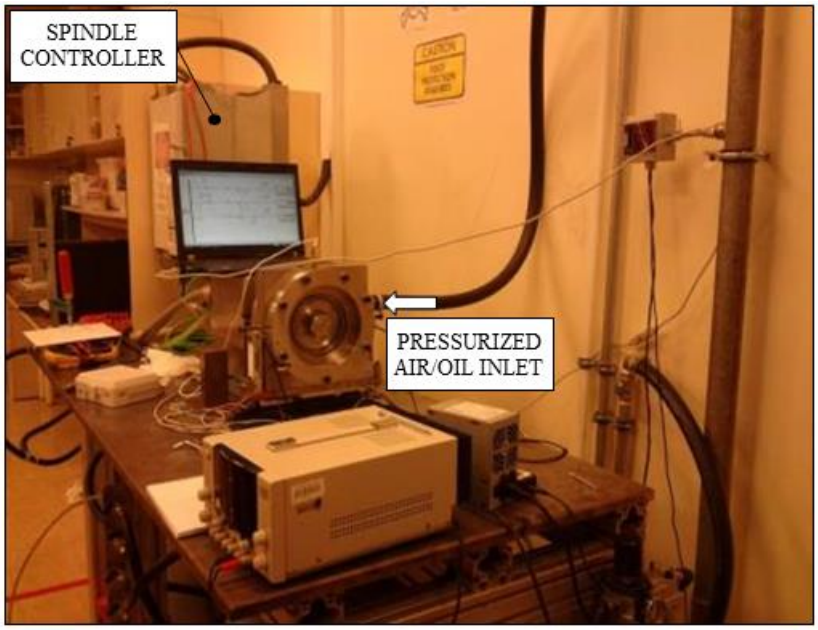

Figure 4.4: High speed rotary test rig photo

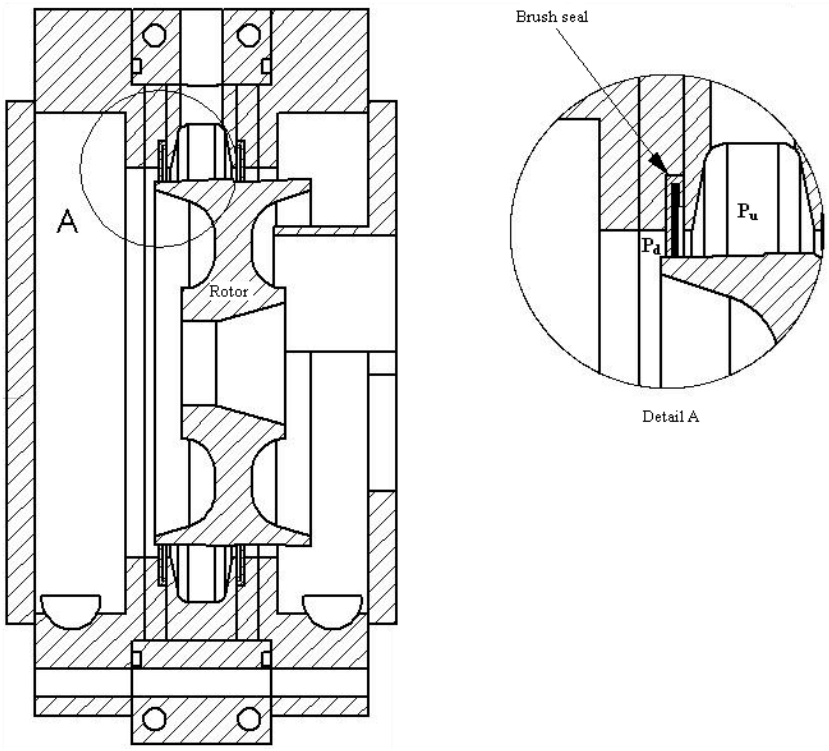

Figure 4.5: Section view of the seal housing assembly

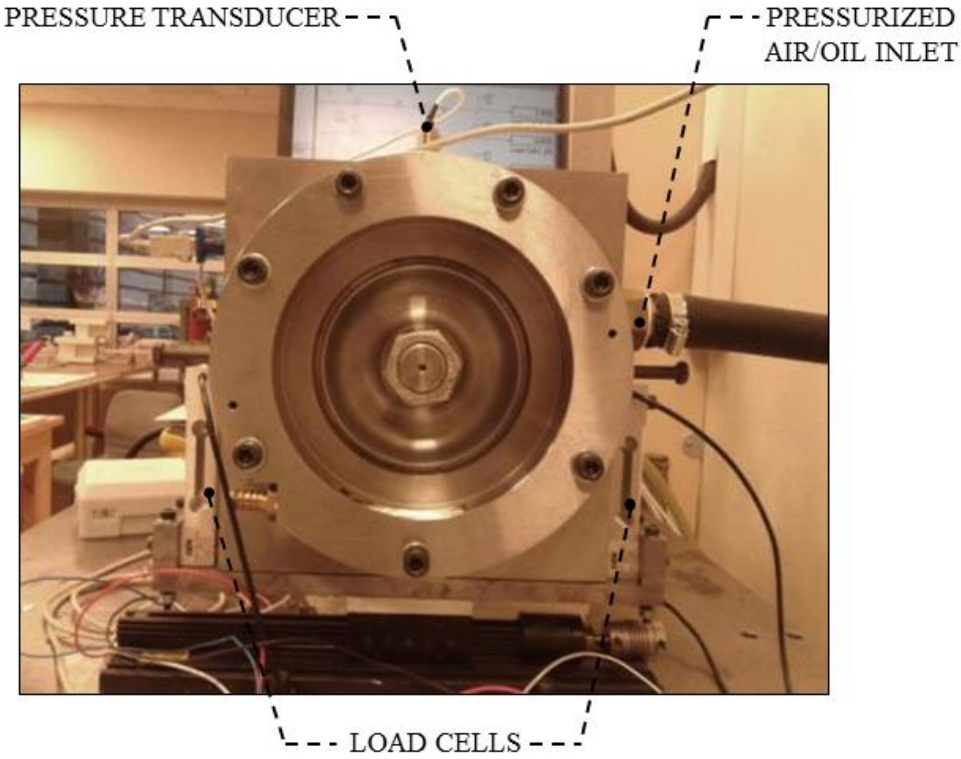

Figure 4.6: Seal housing assembly details

The seal housing assembly is designed to test two seals at the same time *(Figures 4.5-4.6).* Symmetric location of two brush seals eliminates any axial loading on the

rotor. This brings the advantage of high speed testing at elevated pressure levels, which are typically experienced in gas turbine brush seal applications. Removable seal rings allow testing of different brush seal geometries and facilitate testing of other rotary seals. The housing assembly is positioned on the piezoelectric load cells such that lateral loadings due to stiffness of brush seal can be measured during tests. Since the assembly is pended, frictional effects are eliminated and the results are expected to be more accurate. The housing is fixed onto a motorized-high precision linear slide, which enables accurate concentricity as well as simulation of extreme rotor rub conditions.

4.1.1 Spindle Holder Assembly: Design Details and Structural Analyses

Exploded view for the spindle holder assembly is given in Figure 4.7. Main components of the spindle assembly are:

- Spindle
- Lower and upper clamps
- Connecting rod
- Rotor

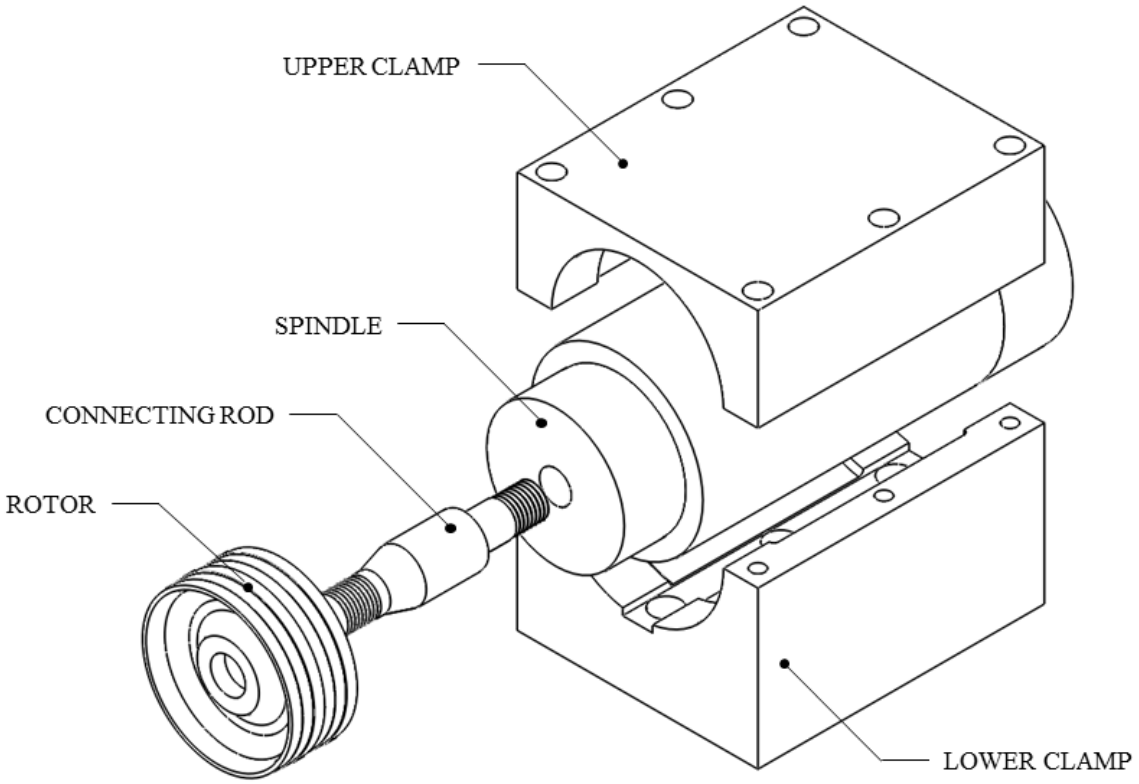

Figure 4.7: Exploded view of the spindle holder assembly

Connecting rod – Rotor assembly is the most critical component in terms of durability and vibration. Therefore, structural, modal and FRF analyses have been conducted and detailed in this section.

4.1.1.1 Clamps

Spindle is mounted between clamps and preloaded with the aid of six M12 imbus bolts. Both clamps have stepped inner surfaces, one of which has 75mm radius and the other one has the radius of 79mm.The spindle has direct contact with clamp surfaces having 75mm radii, and the preload obtained by bolts will be transmitted through these surfaces. The reason for having stepped design for clamps' inner surfaces is to avoid any possible decrease in preload that may be introduced by inappropriate manufacturing process. In addition to that, the design avoids direct contact of upper and lower clamps' mating surfaces and therefore assures sufficient preload for holding the spindle while operating at 45,000rpm. Drawings of lower and upper clamps are given in Figures 4.8 and 4.9.

Since the concentricity and the stabilization of the spindle are critical, the inner surfaces of the clamps are manufactured with tight tolerances and small surface roughness values. Lower clamp is placed onto a linear slide, and fixed with three M16 imbus bolts. The channel machined on the inner surface of the lower clamp enables easy assembly and provides enough space for bolt heads.

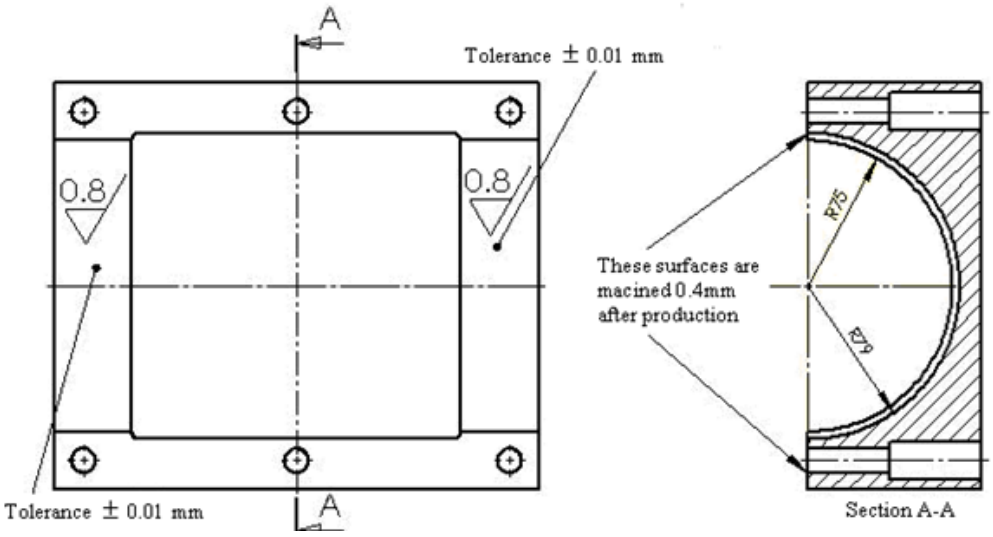

Figure 4.8: Section view of the upper clamp

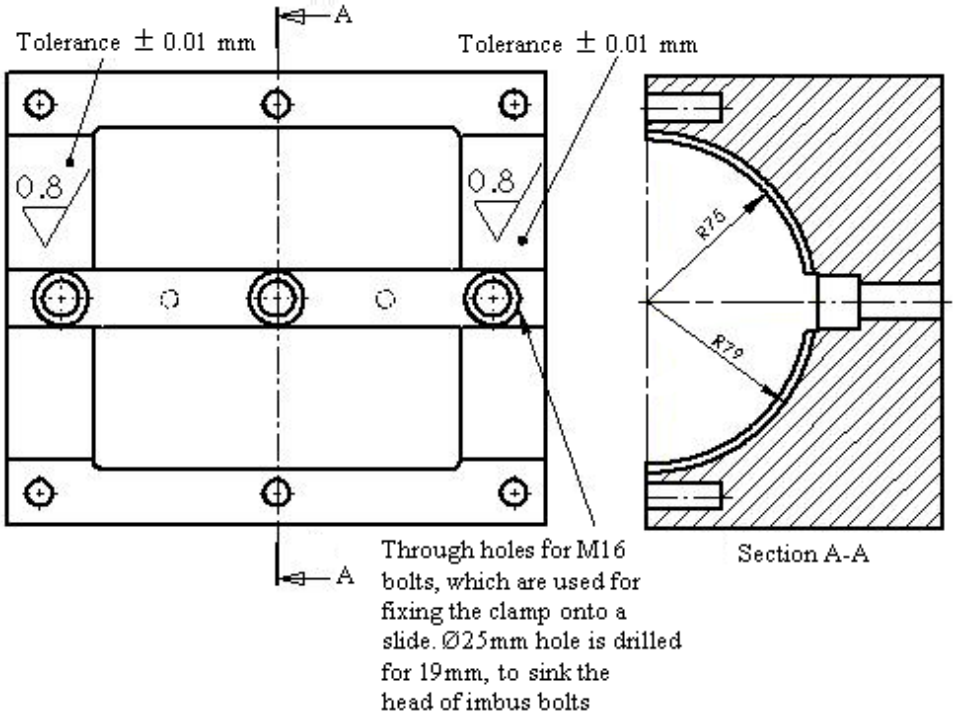

Figure 4.9: Section view of the lower clamp

4.1.1.2 Spindle, Connection Rod and Rotor

The rig is powered with GMN-HV-X 150-45000/25 spindle, which has 150mm diameter, 45,000rpm maximum rotational speed and 25kW output rating.

Power of the spindle is transmitted to the rotor with a connecting rod, which is produced from the rod provided by spindle vendor. 8μm test-rod run-out at 10cm from spindle end is assured by GMN at 45,000rpm. Detailed drawings for original test rod and manufactured connecting rod are given in Figure 4.10.

Screw-type connection is used for rod-spindle assembly, where thread major diameter is equal to 28mm. The rod section with 28mm diameter is completely sunk into the spindle head when installed for operation. The original section with 48.2mm is machined with 15^{o} cone angle, and the diameter is reduced to 30mm. The reduced part is threaded to tighten rotor with M30 nuts. Rotor is also bored with same cone angle so that the inner surface of the rotor becomes coincident with the conical surface of the connecting rod.

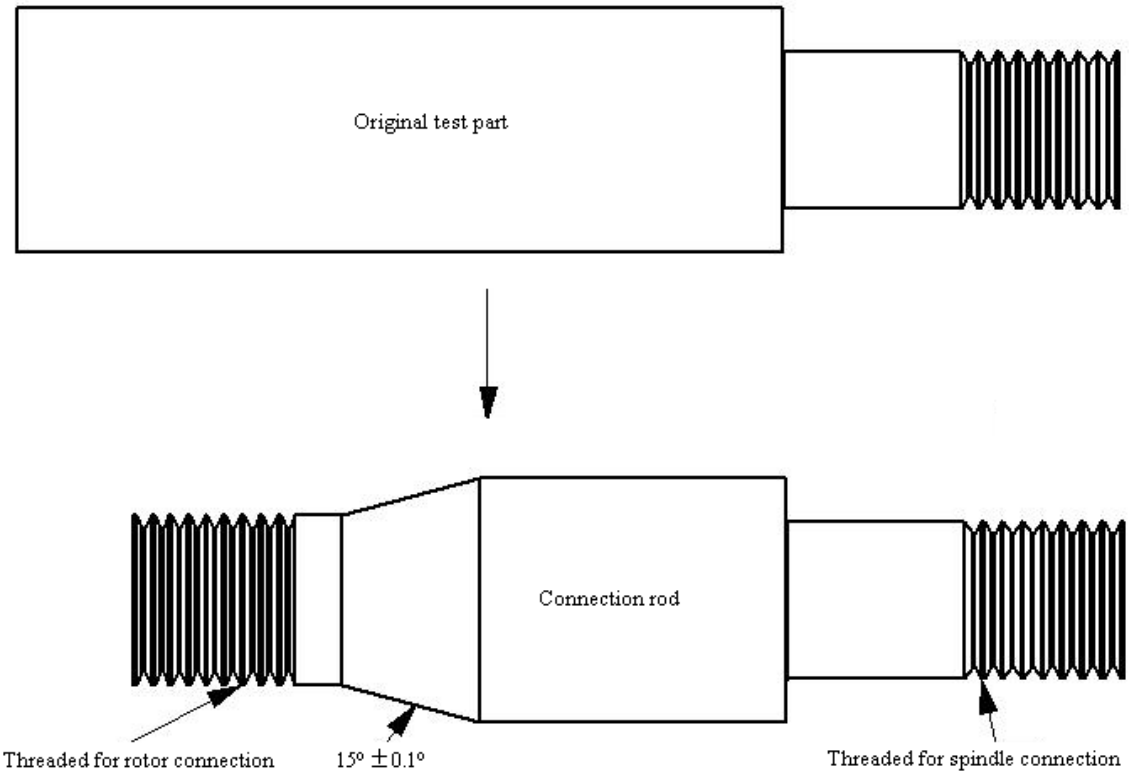

Figure 4.10: Technical drawings of the test rod and connecting rod

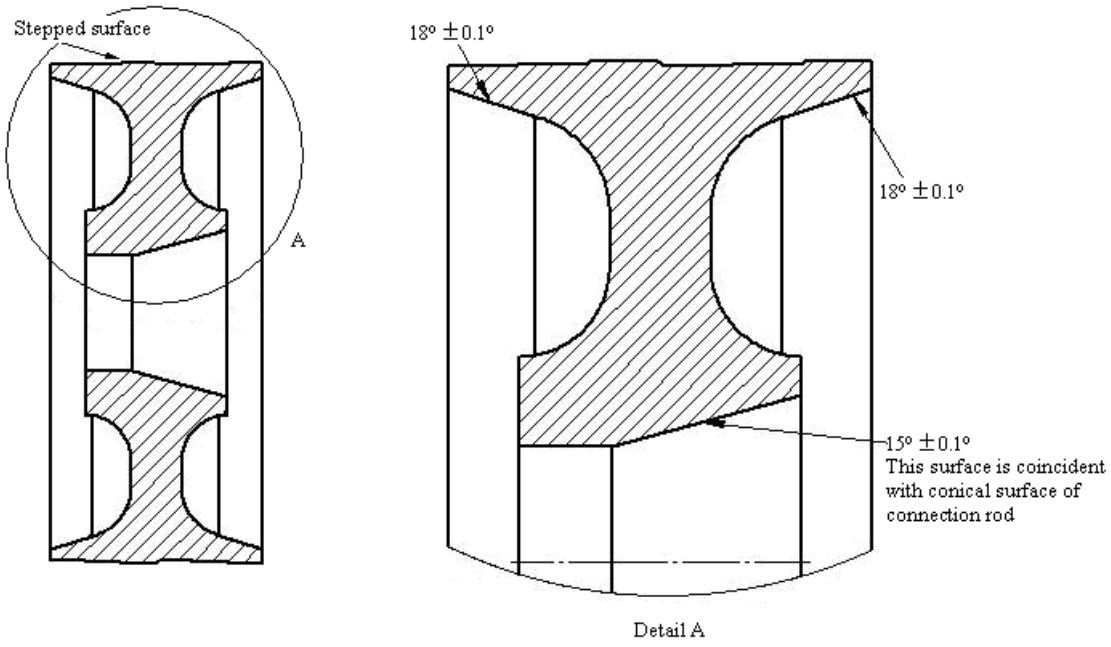

Figure 4.11: Cross-sectional view of the rotor

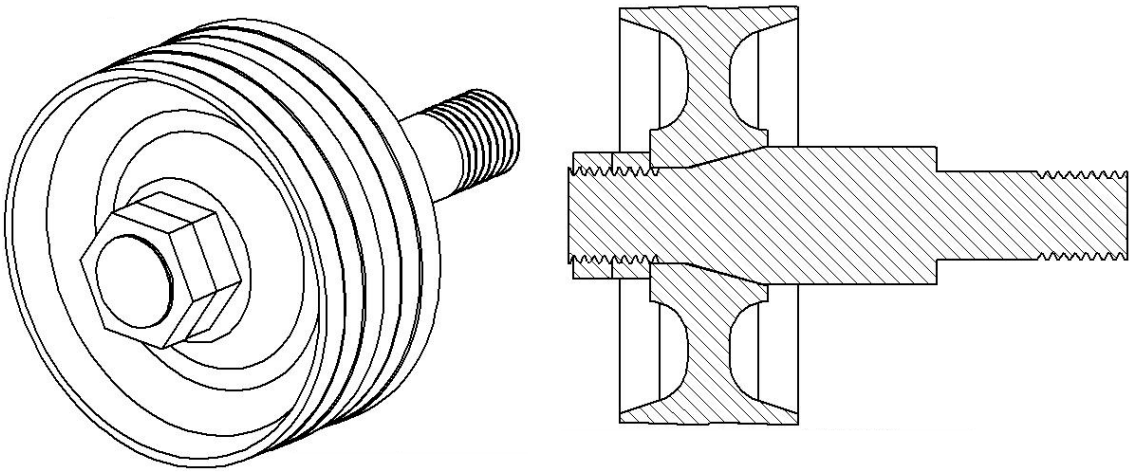

Figure 4.12: Detailed drawing of the connecting rod-rotor assembly

Experimental medium for brush seals is generated by the rotor. As it was mentioned before, rotor is placed and rotated in the seal housing. Varying diameter of the rotor surface allows testing of brush seals under different seal interferences. Center of the rotor is drilled with 15^{o} cone angle until the diameter of 30.5mm obtained. Cross-sectional view of the rotor and detailed view of connecting rod-rotor assembly is given in Figures 4.11 and 4.12, respectively.

4.1.1.3 CAE Analyses for Connecting Rod-Rotor Assembly

The most critical component for durability and vibration is the connecting rod-rotor assembly. Therefore, simulations given below have been performed:

- Structural analysis by including bolt preload, gravity and inertial forces
- Modal analysis for connecting rod-rotor assembly
- FRF analysis for connecting rod-rotor assembly

4.1.1.3.1 Structural Analyses for Connecting Rod-Rotor Assembly

The rotor-connecting rod assembly is rather critical as the balancing of the rotor is determinative on both the safety of the overall system and the accuracy of the measurements. Therefore, analyses have been carried out in order to assure system safety in terms of durability. Hypermesh software was used for pre-processing, and nonlinear CAE analyses were performed by using Abaqus solver.

The CAE model details, boundary conditions and analyses steps are detailed in Table 4.2 and in Figures 4.13 thru 4.15. In order to simulate real operating conditions, M30 nut, rotor and connecting rod are modeled as separate bodies, and contact with friction is defined between those components. Hard contact formulation, which is known to be the most accurate contact algorithm in the literature, is used with friction coefficient of 0.3 *(Figure 3.14)*. The rotor and connecting rod are made of stainless steel and mechanical properties are detailed in Table 4.2 [53]. C3D10M –Modified second order tetrahedral elements are used for increased stress and contact pressure simulation accuracy.

CAE Model Details for Rotor-Connecting Rod Structural Analysis	
Mesh details	
Element type	C3D10M – Modified formulation
Total number of elements	260397
Total number of nodes	393971
Pre-processor	Hypermesh
Solver	Abaqus/Standard
Post-processor	Abaqus Viewer
Material Properties – Stainless Steel, SS304 - Cold rolled	
Elastic modulus	189600 MPa
Density	7890 kg/m^3
Poisson's ratio	0.28
Yield strength	1103 MPa
Endurance limit	607 MPa *[54]*
Mass Properties	
Rotor mass	3.25 kg
Connecting rod mass	1.66 kg
M30 nut mass	0.21 kg
Total mass	5.12 kg
COG (x, y, z)	(0, 0, -64) *[mm]*

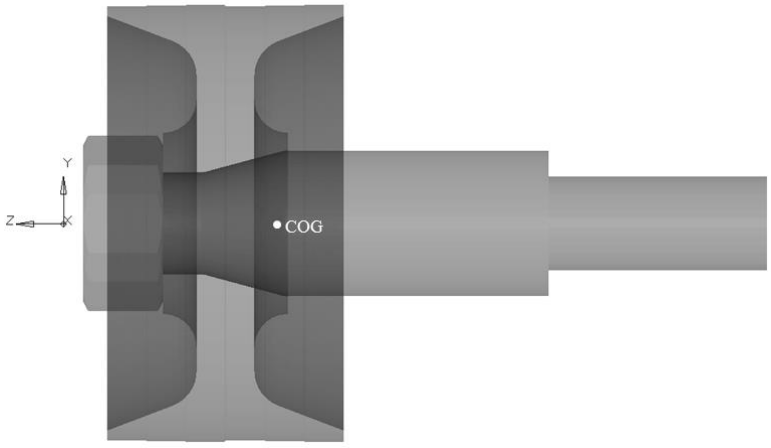

Table 4.2: RTR, Rotor-Connecting rod assembly, CAE model details for structural analysis

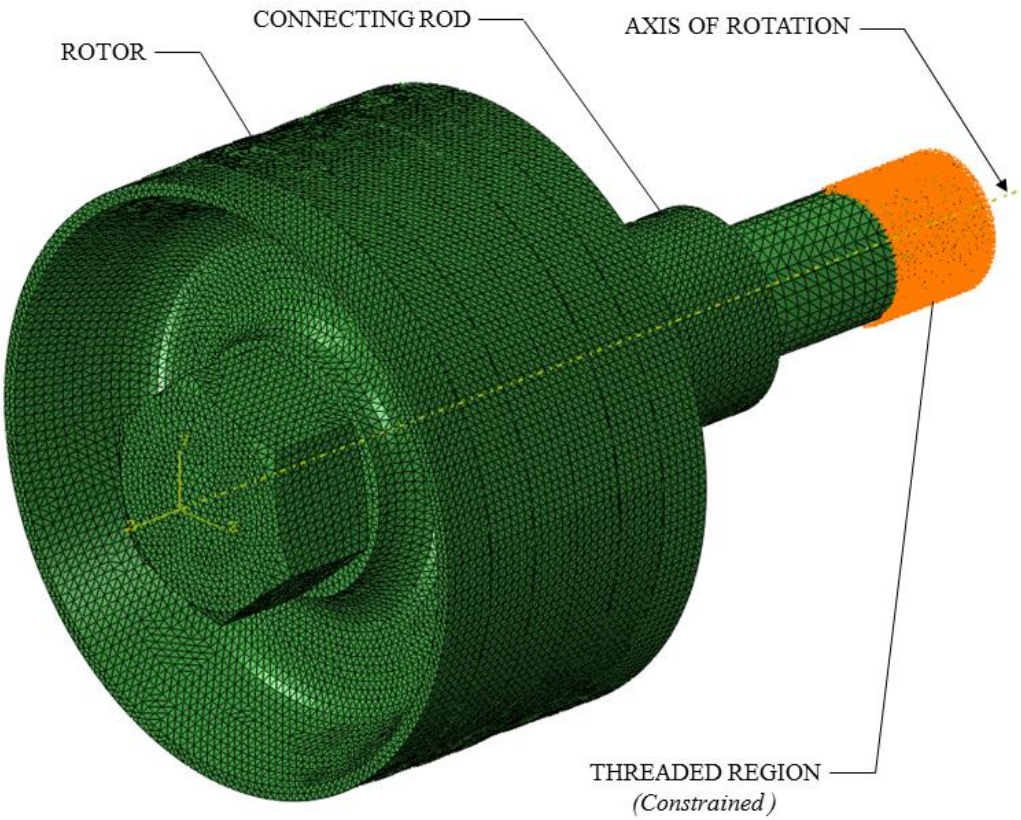

Figure 4.13: Rotor-Connecting rod structural analyses – Isometric view for the FE model

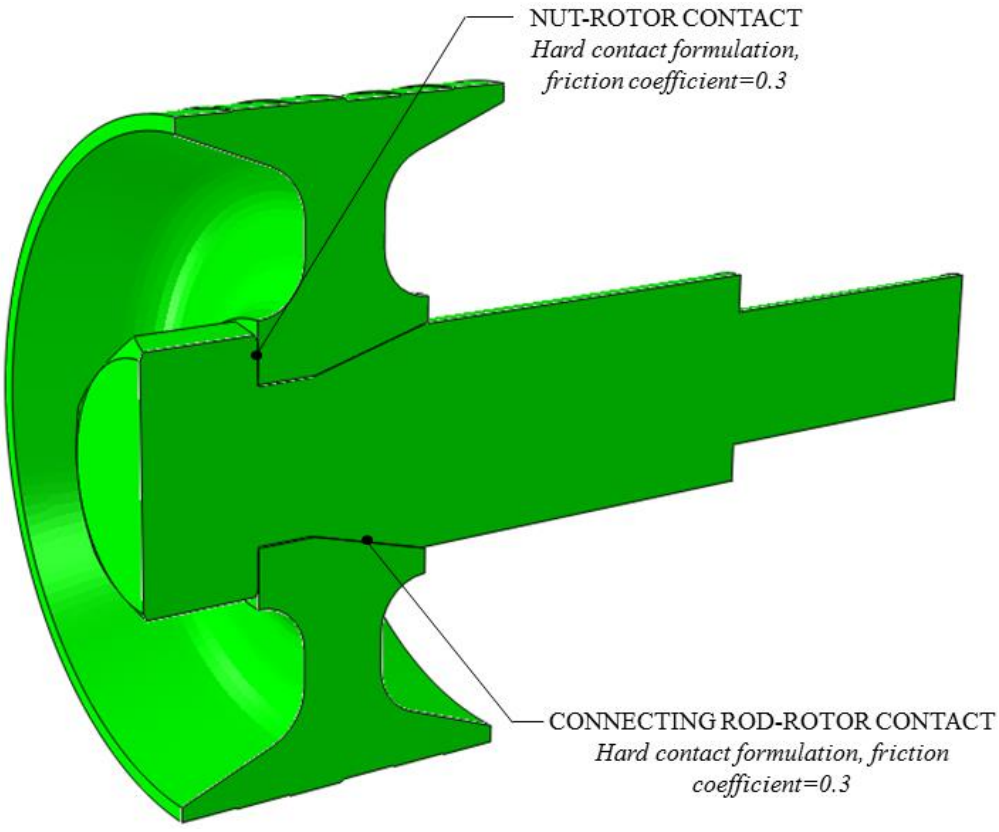

Figure 4.14: Rotor-Connecting rod structural analyses – Contact details

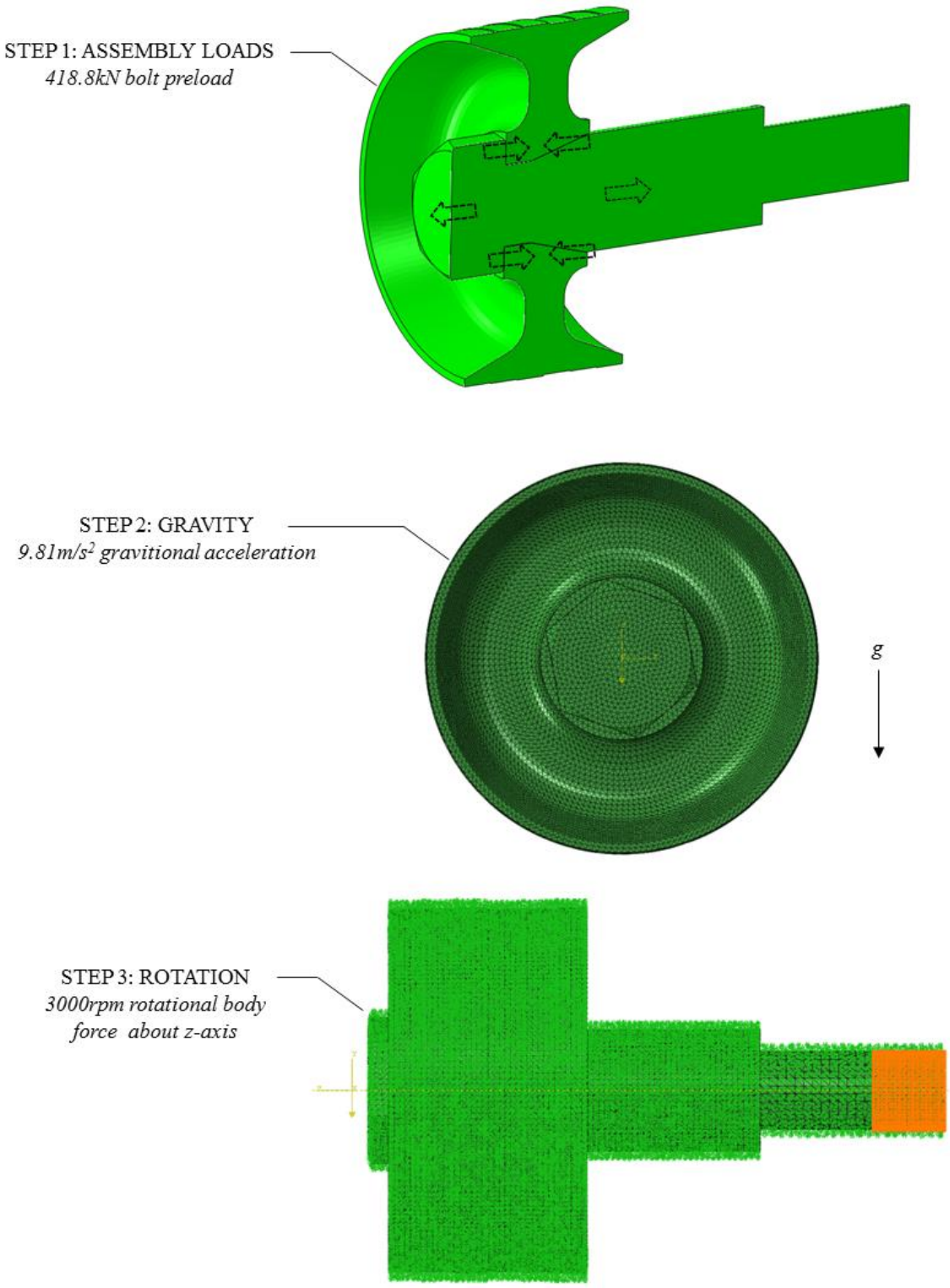

Figure 4.15: Rotor-Connecting rod structural analyses – Analysis steps

Spindle and clamps are assumed to be rigid, and the connecting rod is constrained in tangential and axial directions from the threaded region on spindle side. The analyses steps are:

- Bolt preload: Assembly simulation, Applied preload: 418.8kN
- Gravity: Gravity is applied to all components: 9.81m/s^2
- Rotation: Rotational body forces at different magnitudes

Bolt preload value of 418.8kN is calculated as 90% of proof strength for M30x3.5/Class 10.9 nut [53]. Since dynamic stiffness tests have been performed at maximum 3,000rpm, structural simulations start with 3,000rpm rotational body force.

4.1.1.3.1.1 Structural Analyses for Connecting Rod-Rotor Assembly – 3000rpm Results

Three critical items are needed to be checked for rotor-connecting rod assembly:

- Contact conditions, Target: No opening
- Rotor stress levels
  - Target 1: Safe against yielding
  - Target 2: Safe against HCF
- Rotor displacement levels at the surface
  - Target: Maintain clearance case during leakage tests

Contact conditions are detailed in Figure 4.16 for 3,000rpm analyses. As it can be seen from the figure, the contact pressure between rotor-nut surfaces is above 350MPa, and the rotor-connecting rod contact has average contact pressure value of 200MPa at 3000rpm operating conditions. The system is safe to operate at 3,000rpm since separation is not observed for rotor-nut and rotor-connecting rod contacts. The sticking contact condition is observed rotor-nut contact, and the rotor-connecting rod contact has slipping conditions, which is an expected result of conical surfaces and preload. The slip magnitudes are detailed in Figure 4.17. As it can be seen from the figure, most of the slip is introduced in the assembly step, where the slip magnitude is 0.2433mm. Additional slip introduced in rotation step is around 0.3µm, which is not at critical level.

VM and maximum principal stress contours for 3,000rpm are detailed in Figures 4.18 and 4.19. In Figure 4.20, change of maximum VM and principal stress levels with simulation step is given. Excluding FE discontinuities due to 90^o corner and localized contact, the maximum VM stress level is observed as ~450MPa, which is below the

yield strength value of 1103MPa. As detailed in Figure 4.20, majority of VM stress levels on rotor are due to bolt preload and in compressive mode.

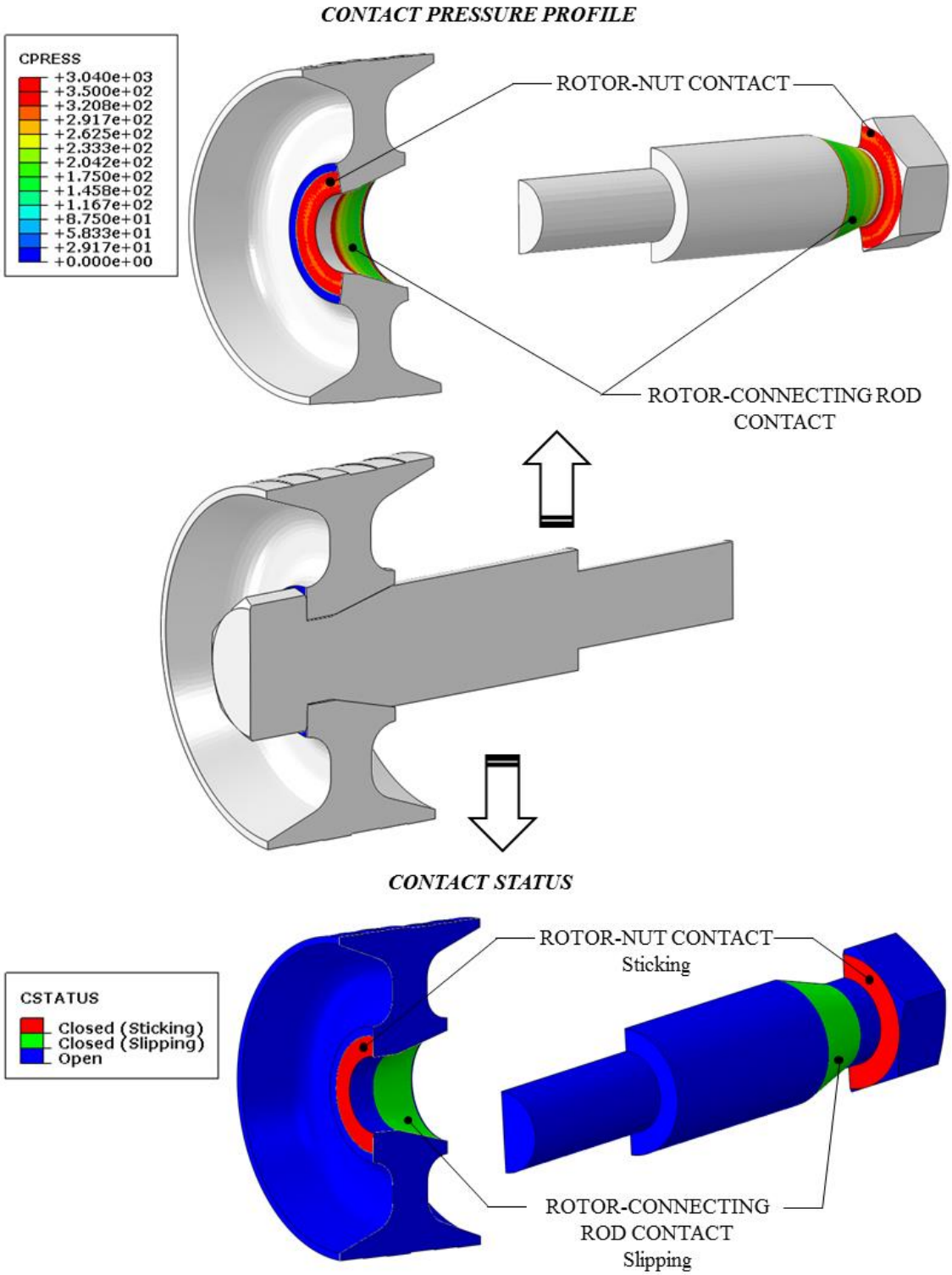

Figure 4.16: Rotor-Connecting rod structural analyses – Contact pressure and contact status at 3,000rpm

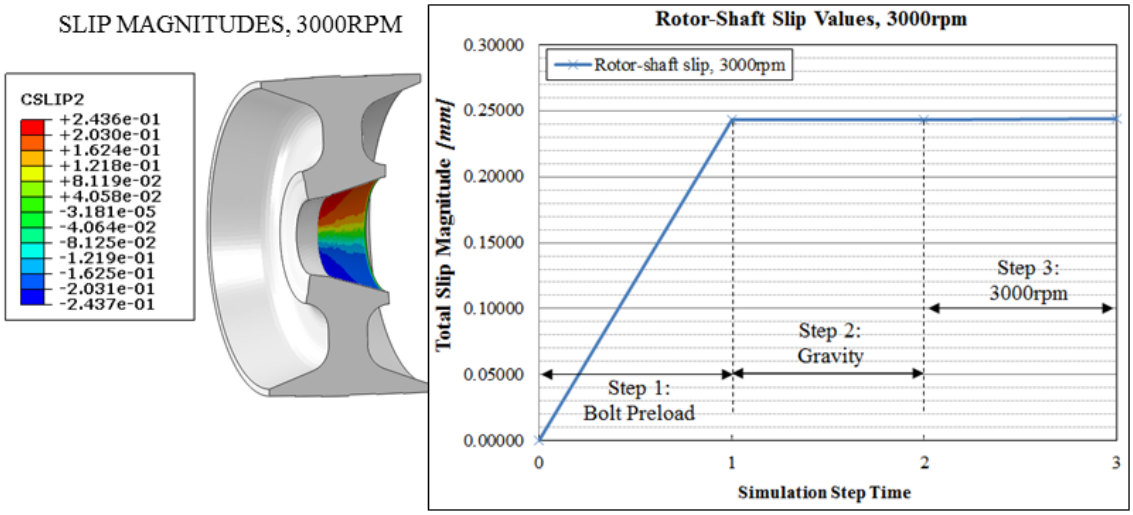

Figure 4.17: Rotor-Connecting rod structural analyses – Slip magnitudes for rotor-connecting rod *(shaft)* contact at 3,000rpm

Maximum principal stress level is around 252MPa for the rotor at 3000rpm. The bolt preload generates maximum principal stress level of 250MPa, and 3000 rotor rpm with gravity induces 2MPa stress in tension mode. Therefore, the dynamic loading on rotor generates a stress cycle which has 251MPa mean stress with ±1MPa alternating stress. Considering the 607MPa endurance limit of the rotor material, the system is safe against HCF failure.

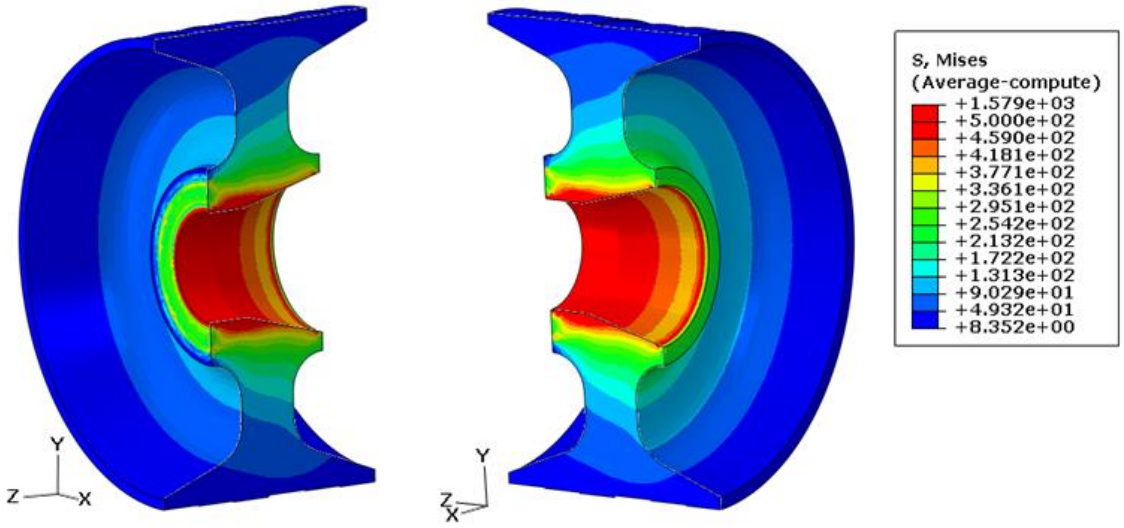

Figure 4.18: Rotor-Connecting rod structural analyses – Rotor VM stress contour at 3,000rpm

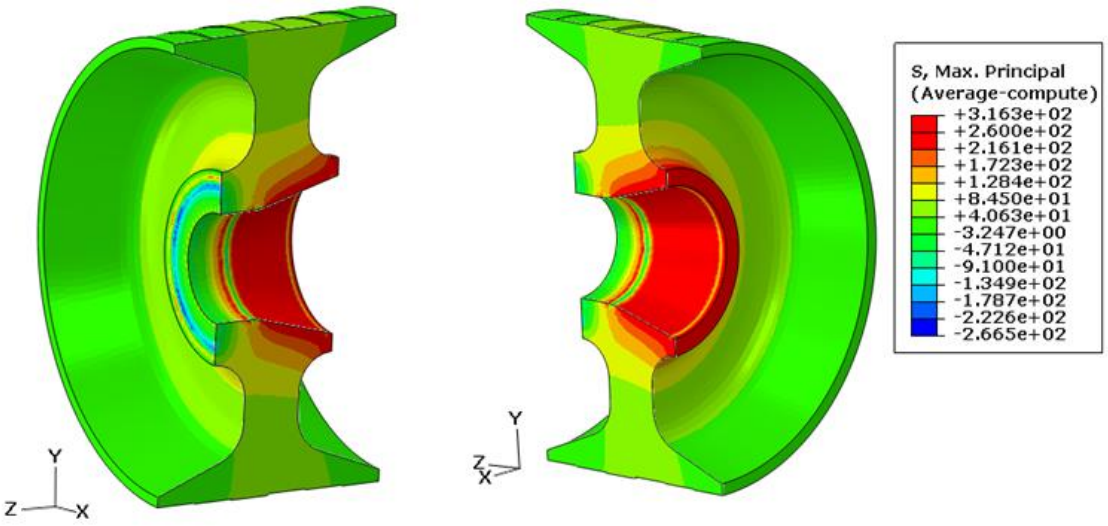

Figure 4.19: Rotor-Connecting rod structural analyses – Rotor Max. principal stress contour at 3,000rpm

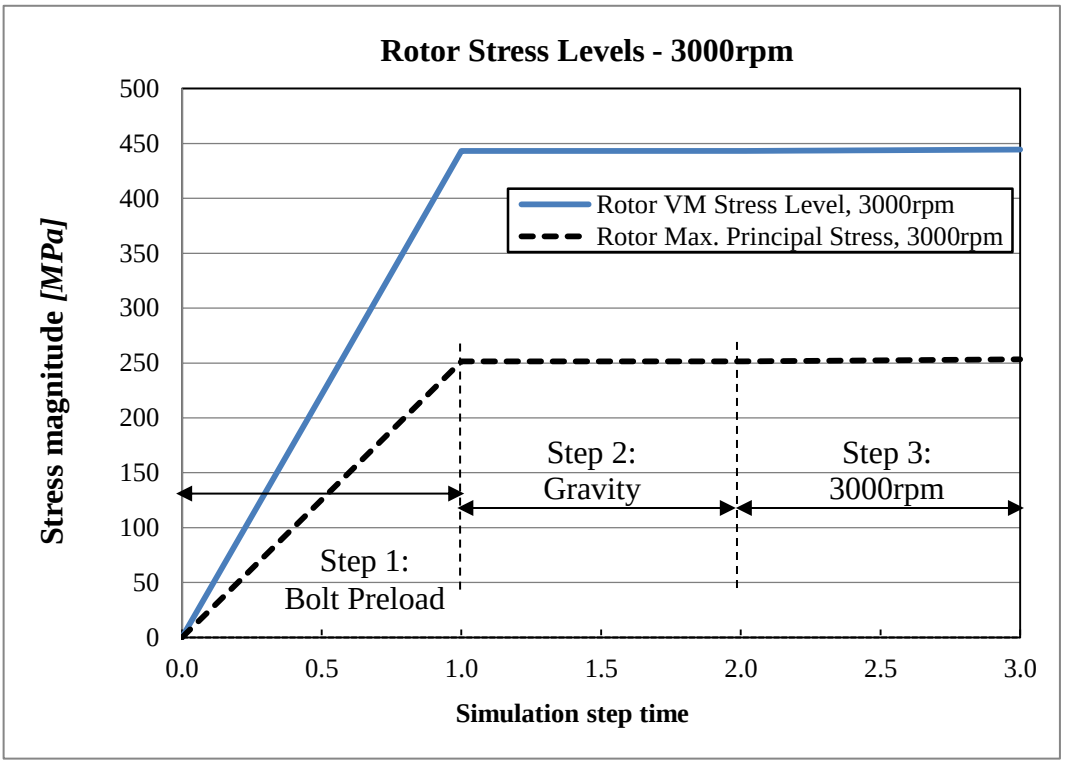

Figure 4.20: Rotor-Connecting rod structural analyses – 3,000rpm – Change of VM and Max. principal stress magnitude at critical rotor node *(element centroid)*

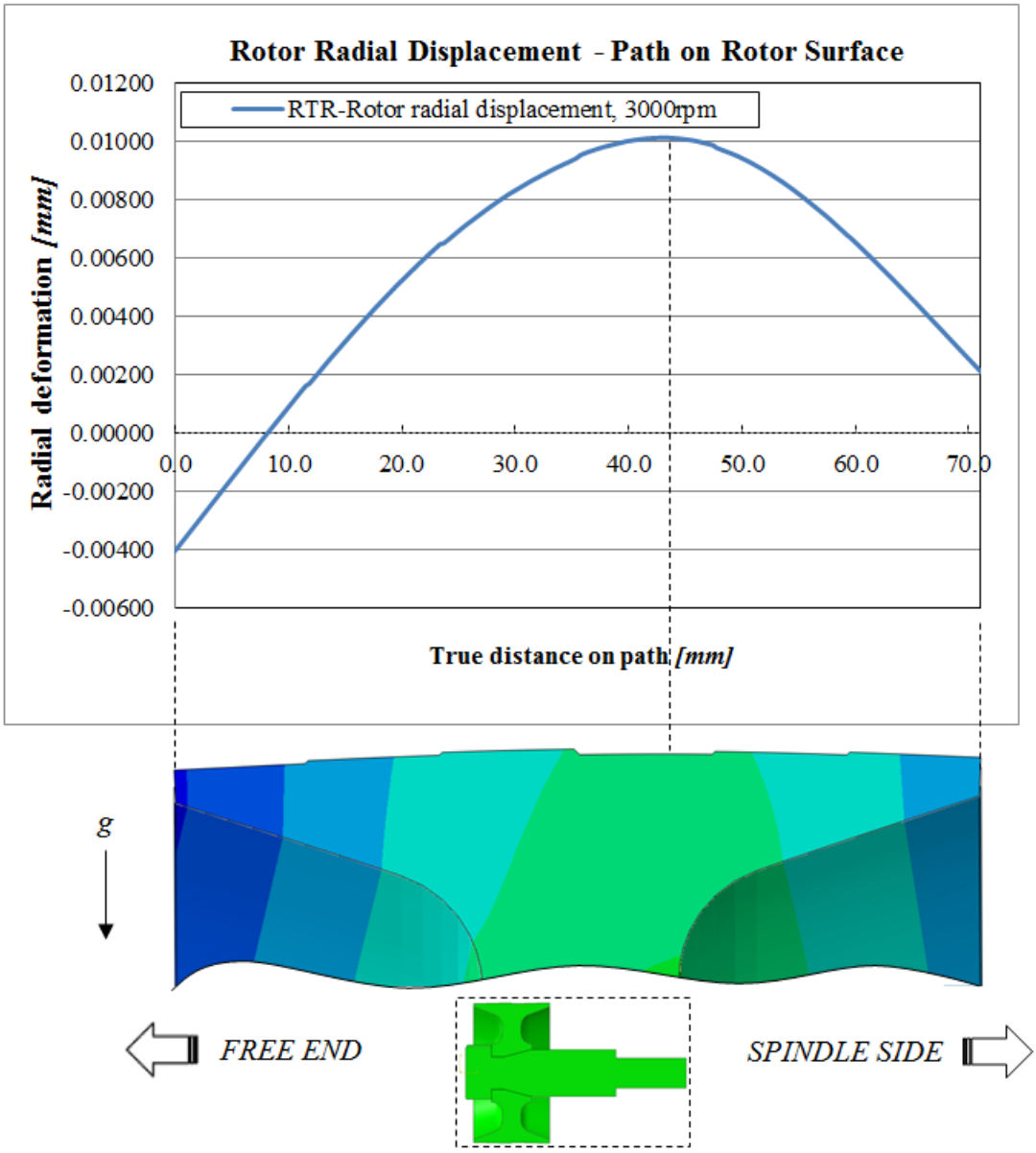

Figure 4.21: Rotor-Connecting rod structural analyses – 3,000rpm – Radial displacement profile at rotor surface

Radial displacement profile on rotor surface is given in Figure 4.21. The rotor-connecting rod assembly deforms like cantilever beam due to gravity, and it expands as 3,000rpm rotor speed is introduced. As it can be seen from the figure, the free end of the rotor surface has -4µm radial displacement, and the maximum 10µm radial expansion is observed at distance of 44mm from rotor free end. The equivalent clearance will be reduced by 6µm *(10µm-4µm=6µm)* while testing two seals at the same time for clearance leakage tests, which is less than 5% of 127µm target clearance.

4.1.1.3.1.2 Structural Analyses Results for Connecting Rod-Rotor Assembly, Different Rotor Speeds

Although dynamic stiffness tests of this study will be performed at maximum 3,000rpm, safety and functionality controls for the rotary test rig have been done by simulating 15,000-30,000-45,000rpms by including assembly loads and gravity. The risk assessment table has been detailed in Table 4.3. According to analyses results, the risk assessment of RTR: Rotor-Connecting rod assembly can be summarized as below:

- Safety against yield: No risk up to 45000rpm
- Safety against HCF: No risk up to 45000rpm
- Safety against rotor-nut separation: No risk up to 45000rpm
- Safety against rotor-connecting rod separation: No risk up to 45000rpm
- Leakage tests at clearance conditions: Can be performed up to 15000rpm
- Dynamic stiffness tests: Can be performed up to 30000rpm

RISK ASSESSMENT TABLE RTR: ROTOR-CONNECTING ROD ASSEMBLY				
SAFETY CONTROL				
Rotor Safety Against Yielding, Yield strength-S_y = 1103MPa				
	3000rpm	**15000rpm**	**30000rpm**	**45000rpm**
VM stress level	450MPa	476MPa	584MPa	783MPa
Risk assessment	Safe	Safe	Safe	Safe
Rotor Safety Against HCF, Endurance limit-S_e = 607MPa				
	3000rpm	**15000rpm**	**30000rpm**	**45000rpm**
Mean stress-tension	251MPa	277MPa	348MPa	468MPa
Alternating stress	1MPa	27MPa	98MPa	218MPa
Risk-assessment	Safe	Safe	Safe	Safe
FUNCTIONALITY CONTROL				
Rotor-Nut Contact Status, Target: No separation				
	3000rpm	**15000rpm**	**30000rpm**	**45000rpm**
Contact status	Sticking	Sticking	Sticking	Slipping
Risk-assessment	Safe	Safe	Safe	Safe
Rotor-Connecting Rod *(Shaft)* Contact Status, Target: No separation				
	3000rpm	**15000rpm**	**30000rpm**	**45000rpm**
Contact status	Slipping	Slipping	Slipping	Slipping-Partial opening initiates
Risk-assessment	Safe	Safe	Safe	Safe
Rotor Surface Radial Displacement				
	3000rpm	**15000rpm**	**30000rpm**	**45000rpm**
Radial displacement at rotor free end	-4µm	13µm	67µm	157µm
Radial disp. at mid-distance from free end	10µm	17µm	41µm	77µm
Leakage test at clearance conditions-127µm	Y	Y	N	N
Dynamic stiffness tests	Y	Y	Y	N

Table 4.3: RTR, Rotor-Connecting rod assembly, risk assessment table

Contact status is visualized in Figure 4.22 at different rotor speeds. The rotor-nut contact status is sticking for 3,000-15,000-3,0000rpms. The slipping contact condition is observed between rotor and nut at 45,000rpm, which is still safe since there is negligible separation between rotor and nut at that rotor speed.

Separation is not observed for rotor-connecting rod contact at 3,000-15,000-30,000rpms. As it can be seen from Figure 4.22, rotor-connecting rod separation just initiates at 45,000rpm, where the majority of contact has slipping conditions. Therefore, it can be stated that the rig is safe against separation up to 45,000rpm.

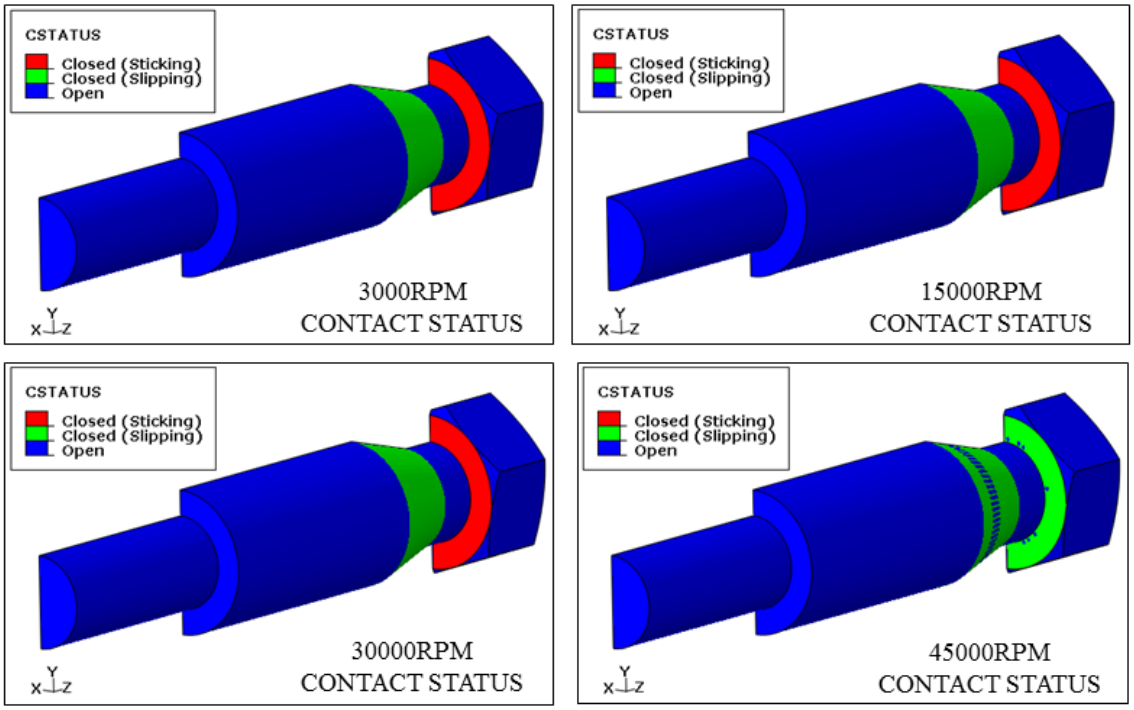

Figure 4.22: Rotor-Connecting rod structural analyses, Contact status at different rotor speeds

Analyses results and safety controls show that the rotor-connecting rod assembly does not have any durability issues up to 45,000rpm. However, it is not possible to perform leakage tests and dynamic stiffness tests at full speed. As it can be seen from the radial displacement profile given in Figure 4.23 and values provided in Table 4.3, it is not possible to perform leakage tests above 15,000rpm since the radial rotor expansion due to centrifugal forces does not allow obtaining sufficient clearance between rotor surface and brush seal. Similarly, performing dynamic stiffness tests above 30,000rpm is not suggested because excessive rotor radial deformation will cause bristle damage for brush seals.

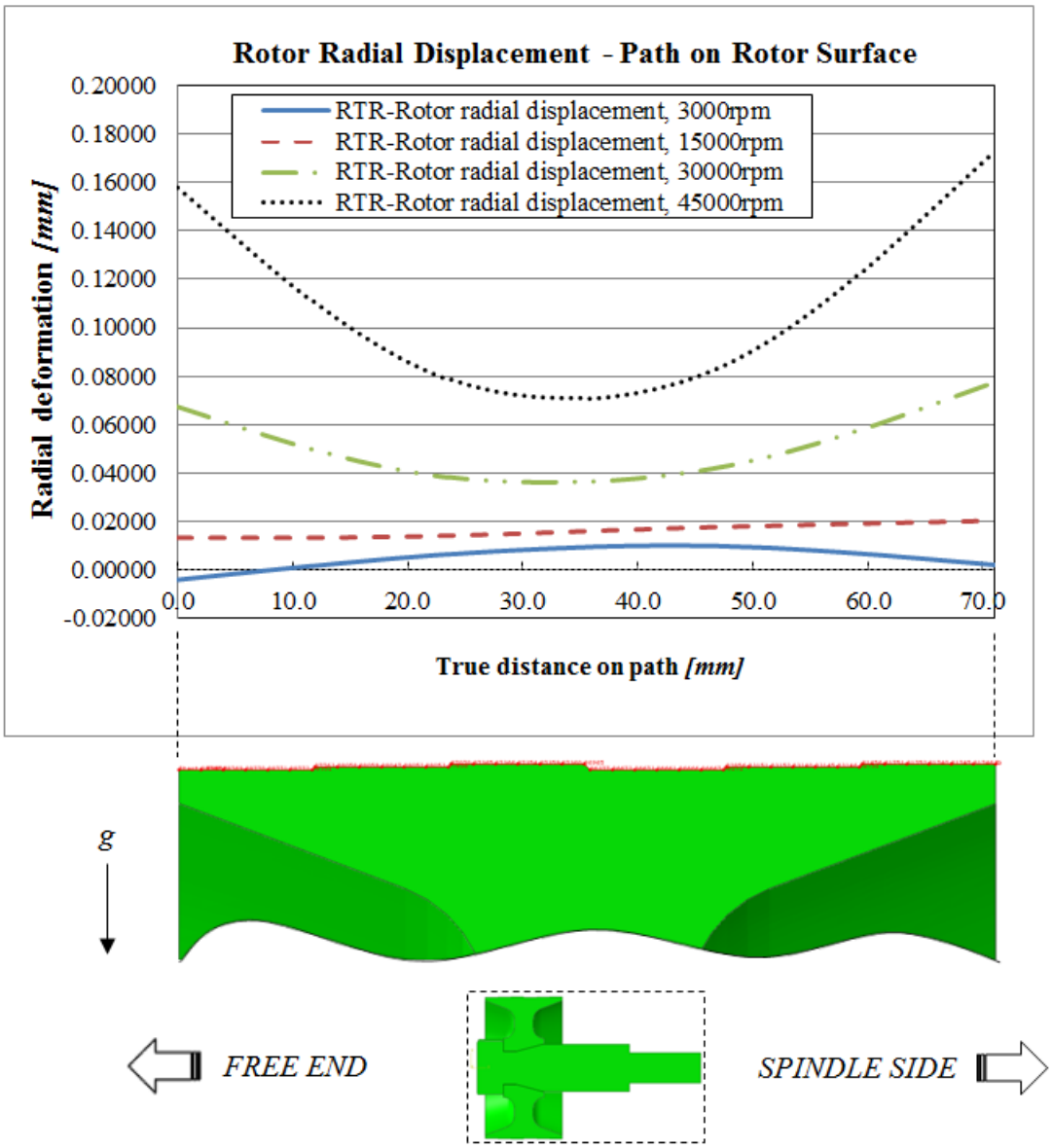

Figure 4.23: Rotor-Connecting rod structural analyses, Radial displacement profile on rotor surface at different rotor speeds

4.1.1.3.2 Rotor Dynamics

Modal characteristics of the rotary components are important to avoid system failure as well as functional operation of RTR. Therefore, modal analyses and frequency response analyses have been carried out to determine rotor critical speeds. The FE model and analyses details are given in the following sections.

4.1.1.3.2.1 Modal Analyses

Modal response is a system behavior rather than the response of individual components, and it is represented by the assembly. Therefore, the FE model for vibration analyses includes Rotor-Connecting Rod-Spindle assembly and bearings of that rotary system. Spindle main dimensions and bearing locations for GMN-HV-X 150-45000/25 are given in Figure 4.24 [55, 56]. The spindle has two roller bearings at the head, where the connecting rod is assembled, and two roller bearings and one axial bearing at the spindle end.

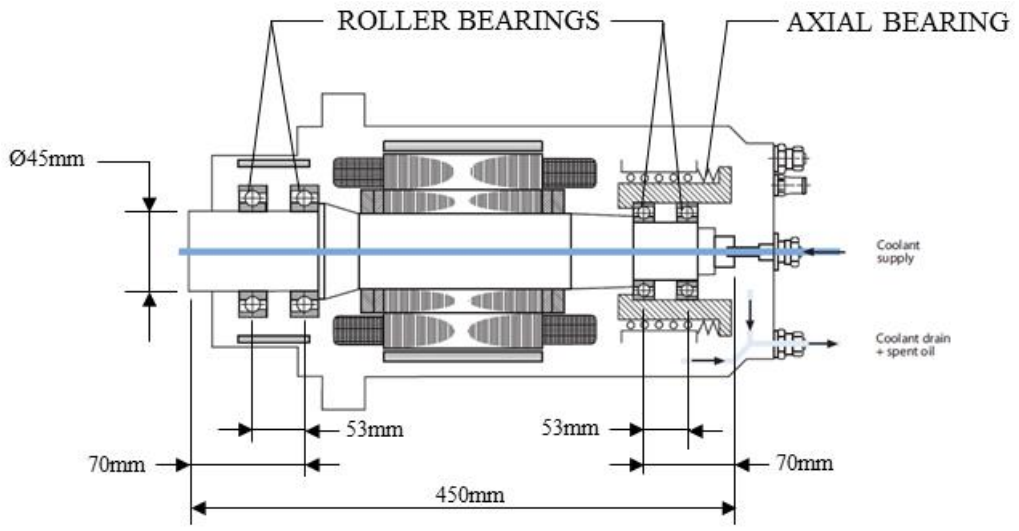

Figure 4.24: RTR – Bearing locations for GMN-HV-X 150-45000/25 [55, 56]

The finite element model details for RTR vibration analyses are given in Table 4.4 and in Figures 4.25-4.26. The spindle is modeled at equivalent 45mm diameter, and bearings are modeled with spring elements – CELAS1 [57]. The roller bearings have stiffness value of 150N/µm and the axial bearing stiffness is 91N/µm. Bearings' total stiffness values are extracted on the bearing surfaces by using the RBE3-Interpolation constraint elements [57]. The spindle housing and clamps are assumed to be rigid. Therefore, spring elements, which represent bearings, are connected to the dependent node of RBE3 elements at one end and constrained in all DOFs at the other end. The connecting rod and spindle have been equivalence at the threaded region. Rotor-nut and connecting rod-rotor surfaces have also been tied for linear modal analyses.

CAE Model Details for RTR Vibration Analyses	
Mesh details	
Element types	Tetra10, RBE3, CELAS1
Total number of elements	337285
Total number of nodes	517629
Pre-processor	Hypermesh
Solver	Radioss Linear/Optistruct
Post-processor	Hyperview
Material Properties – Stainless Steel, SS304 – Cold rolled	
Elastic modulus	189600 MPa
Density	7890 kg/m^3
Poisson's ratio	0.28
Global damping ratio	0.03
Bearing Properties	
Roller bearings stiffness	150N/µm *[56]*
Axial bearings stiffness	91N/µm *[56]*
Mass Properties	
Rotor mass	3.25 kg
Connecting rod mass	1.66 kg
M30 nut mass	0.21 kg
Spindle mass	5.36 kg
Total mass	10.48 kg

Table 4.4: RTR Vibration analyses, FE model details

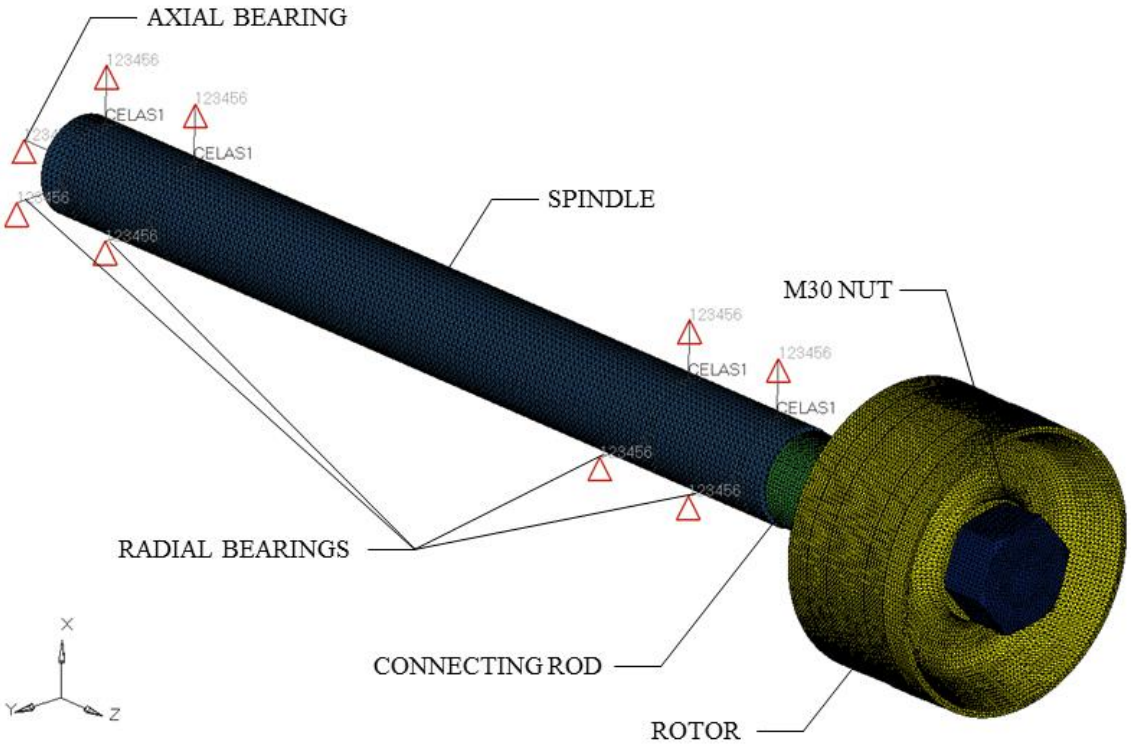

Figure 4.25: RTR – FE model details for modal analysis

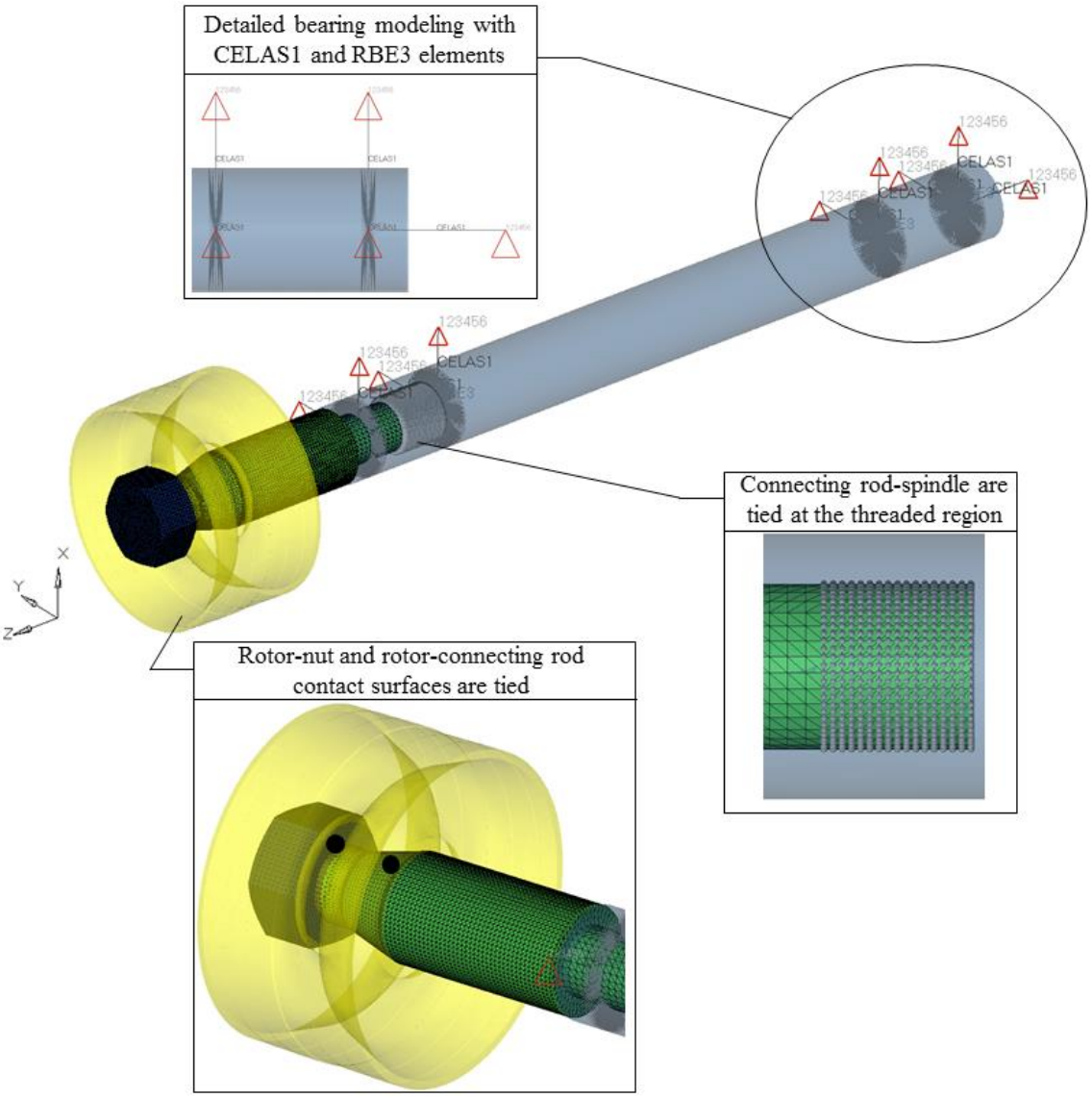

Figure 4.26: RTR – Assembly and bearing modeling details

The FE model has 337285 elements and 517629 nodes in total. The global damping ratio of 3% is applied to the model during vibration analyses. The FE model for modal analyses has been constructed in Hypermesh, analysis has been run in Radioss-Linear/Optistruct and results have been post-processed by using Hyperview. The modal analyses have been run up to 750Hz, which corresponds to 1st rotor order at 45,000rpm.

Modes of the system are detailed in Table 4.5. The RTR-Rotary component assembly has one rigid boy mode, two elastic modes and one mechanism mode at the rotor speed range of 0-45,000rpm.

The rigid body mode of the RTR-Rotary component assembly is due to rotational freedom of the system. The rigid body mode frequency is 0Hz as expected, and the assembly rotates about z-axis with almost zero strain energy. Mode shape, eigen-mode contour and strain energy contour for the rigid body mode are given in Figure 4.27.

Elastic modes of the system are observed at 172.9Hz, which corresponds to 10,374rpm for rotor 1st order, and mode shapes of those elastic modes are 1st order bending about y-axis and z-axis. Two modes at same frequency are due to rotational symmetry of rotor-connecting rod-spindle assembly. Since the roller bearings of spindle have high stiffness values, the mode shape of elastic modes are mainly the bending of connecting rod-rotor, and anti-nodes are observed at the bearing locations *(Figure 4.28-4.29)*.

The system has one mechanism mode at 462.5Hz, which corresponds to 27,750rpm, due to axial bearing. As shown in Figure 4.30, The system translates in axial direction as rigid body by inducing high strain energy only at the axial bearing.

The modal analyses results show that the system has critical speed at 10,374rpm, and dynamic tests should not be performed at that rotor speed since excessed vibration magnitudes will yield degradation of test accuracy and may result in safety and NVH problems. Rigid body and mechanism modes are not critical for system since in they will not yield any safety problems. However, again 27,750rpm can be stated as the rotor speed having minimal risk for test accuracy.

Frequency response analyses have also been performed for RTR-Rotary component assembly to support modal analyses results as well as to better determine testing rpms. Details of FRF analyses are given in the following section.

RTR – Rotary System Modes up to 45,000rpm				
Mode no	**Mode freq. *[Hz]***	**Corresponding rotor rpm**	**Mode type**	**Mode shape**
1	0	0	Rigid body	Rotation about z-axis
2	172.9	10374	Elastic	1st order bending about y-axis
3	172.9	10374	Elastic	1st order bending about y-axis
4	462.5	27750	Mechanism	Axial translation due to axial bearing

Table 4.5: RTR – Modal analyses results

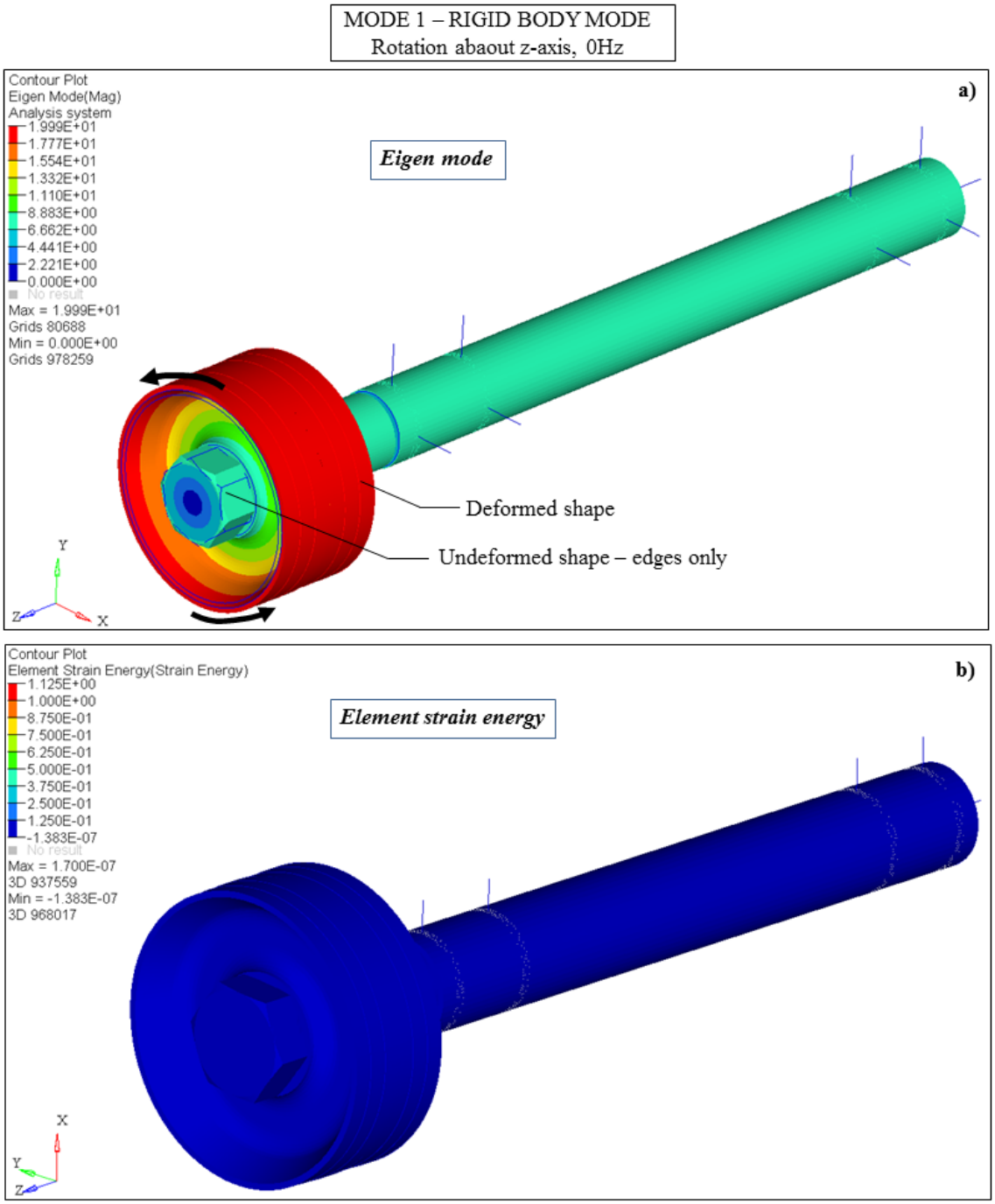

Figure 4.27: Mode 1 - Rigid body mode, rotation about z-axis, a) Eigen mode contour, b) Element strain energy contour

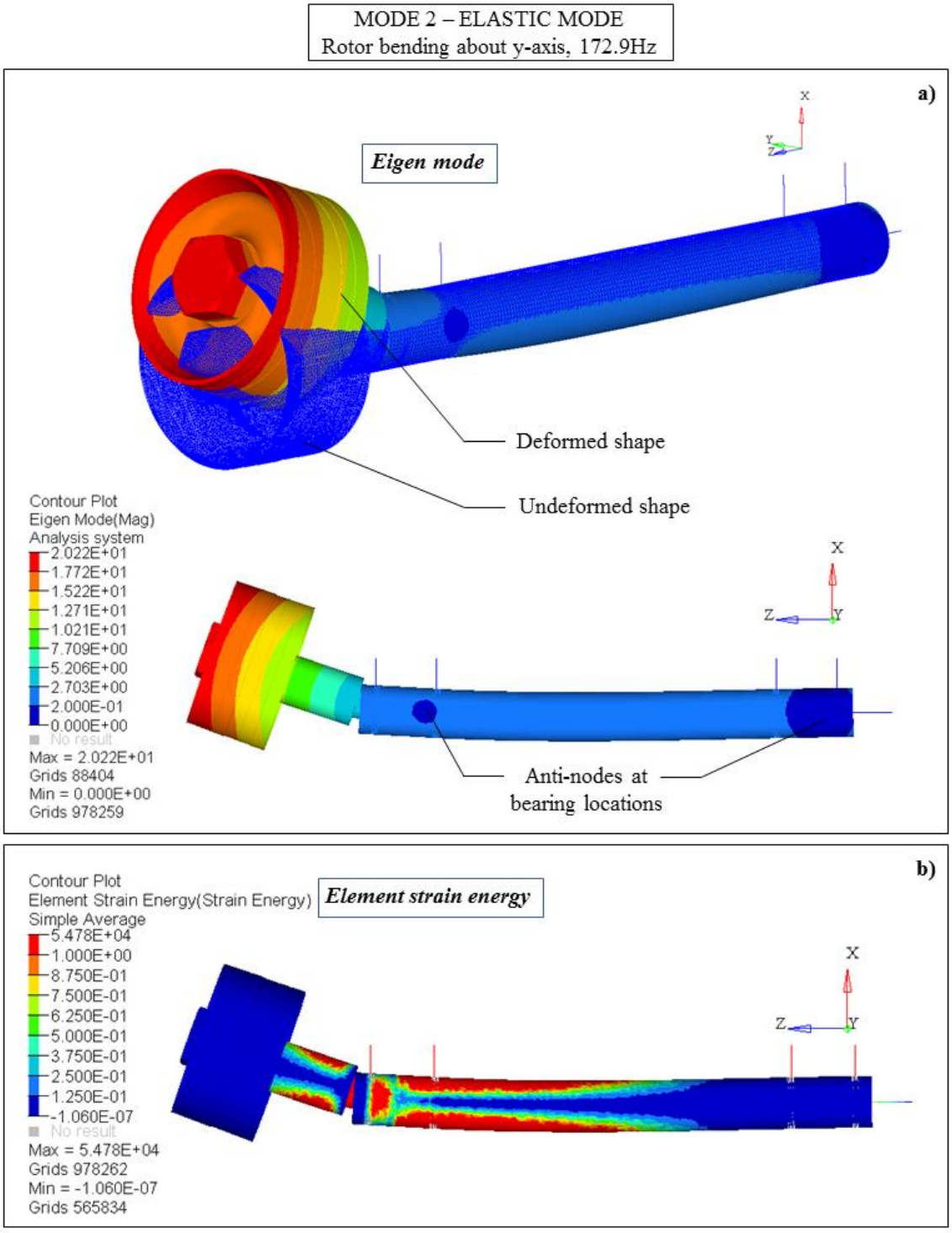

Figure 4.28: Mode 2 – Elastic mode, 1st order bending about y-axis, a) Eigen mode contour, b) Element strain energy contour

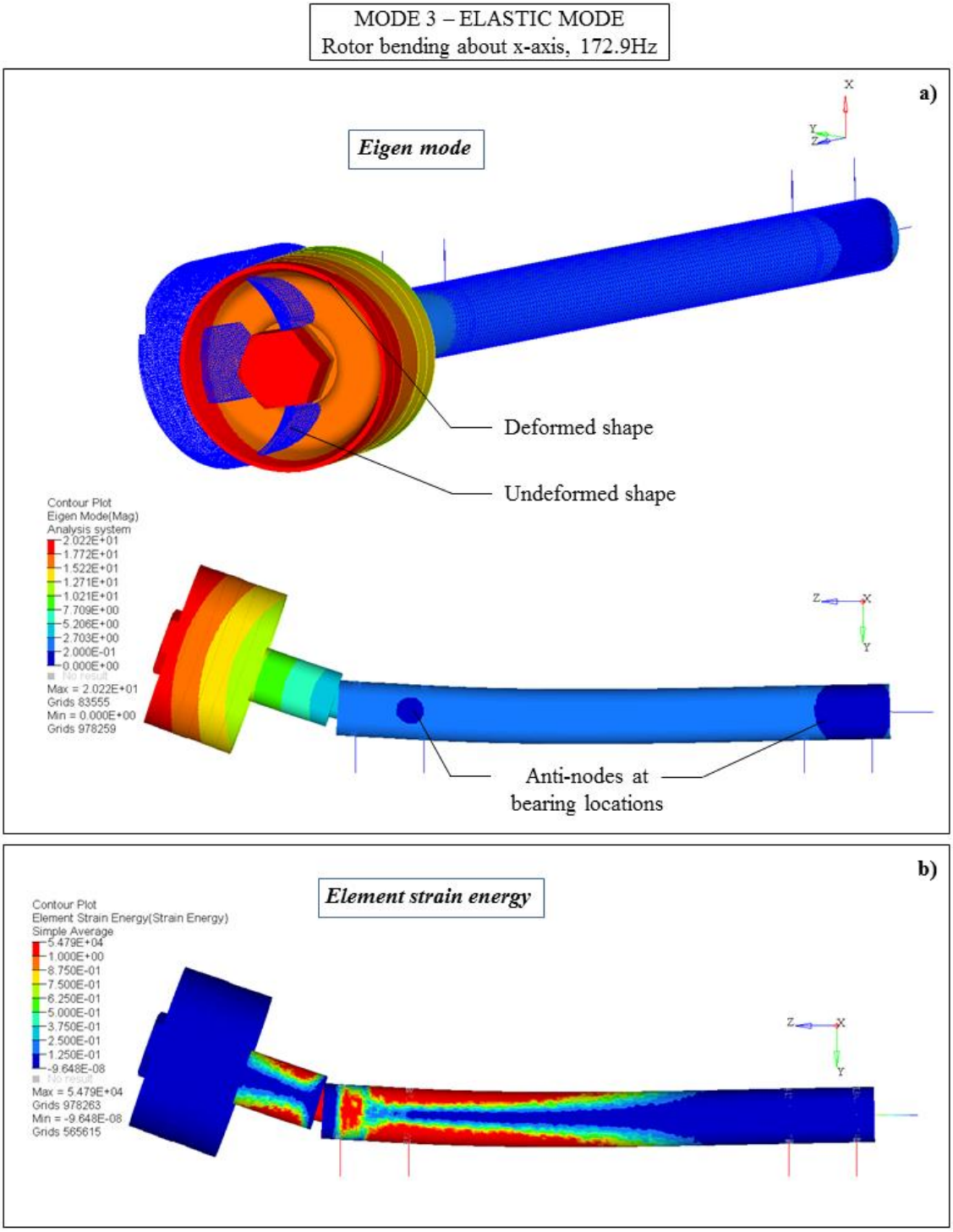

Figure 4.29: Mode 3 – Elastic mode, 1st order bending about x-axis, a) Eigen mode contour, b) Element strain energy contour

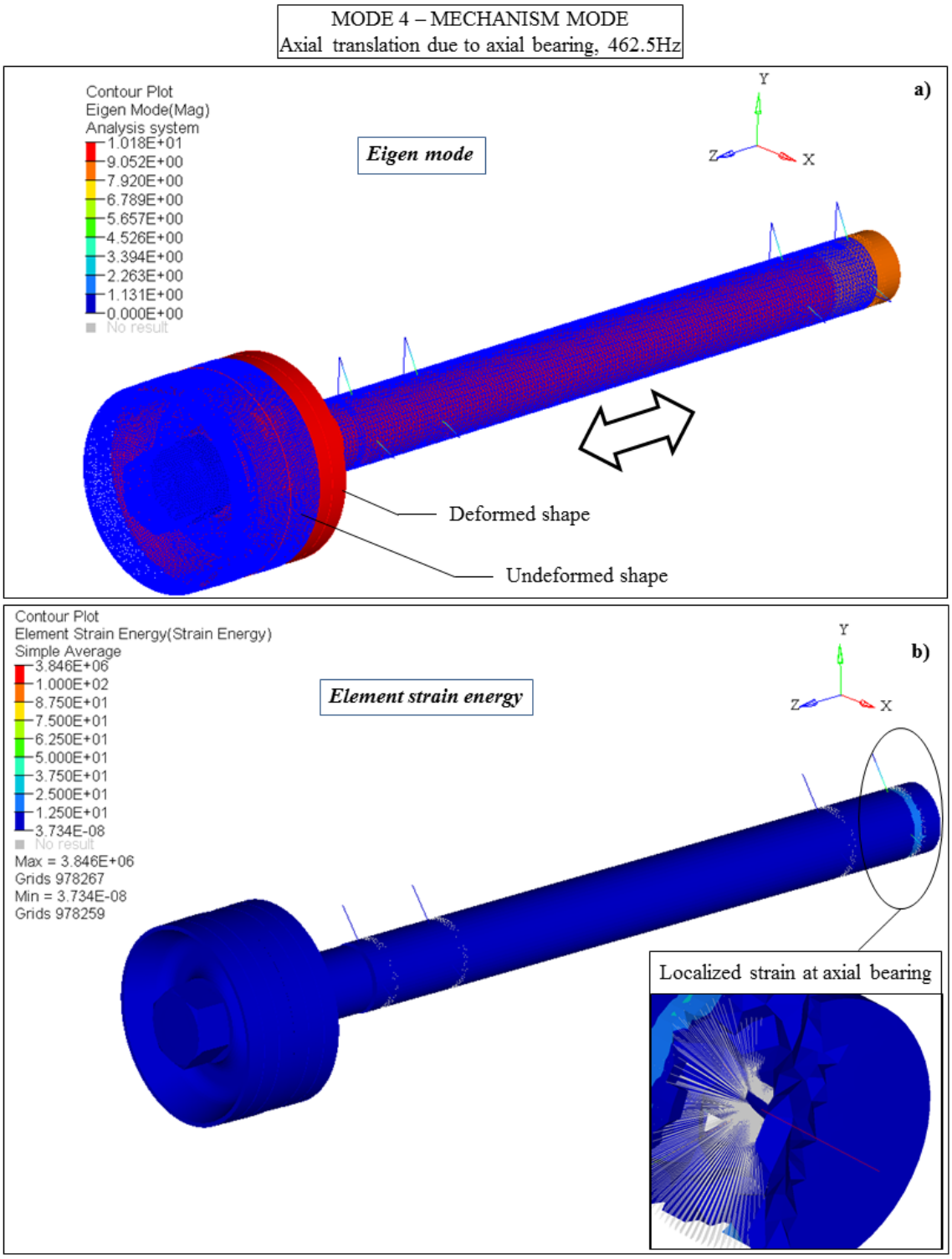

Figure 4.30: Mode 4 – Mechanism mode, axial translation due to axial bearing, a) Eigen mode contour, b) Element strain energy contour

4.1.1.3.2.2 Frequency Response Analyses

Frequency response analyses have been carried out for RTR-Rotary component assembly in order to determine the suggested testing frequency range where the vibrational affects due to critical speed excitation are not dominant. As shown in Figure 4.31, the system is excited at the center of the assembly, and the displacement response is extracted at the rotor surface. The excitation force is applied in all directions and at each frequency as white noise to be able to excite all modes and mode shapes.

The displacement frequency response on rotor surface to white noise excitation is detailed in Figure 4.32. As it can be seen from the graph, the displacement peak is observed at critical speed of 10,374rpm as expected, where x- and y- displacement magnitudes are equal to each other and they are larger than z-displacement. The response characteristic at 10,374rpm is a direct result of excited elastic mode shapes at that frequency. Modal and FRF analyses show that dynamic leakage and stiffness tests should not be performed between 9,000-11,4000rpm for the sake of avoiding degradation in test accuracy and possible NVH issues.

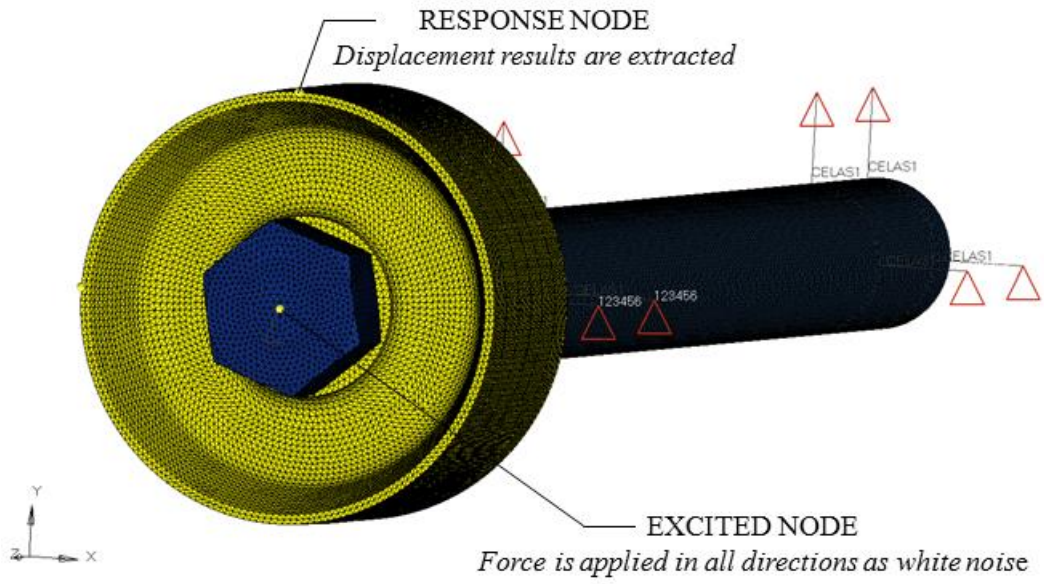

Figure 4.31: RTR-Rotary component assembly, FRF analyses details

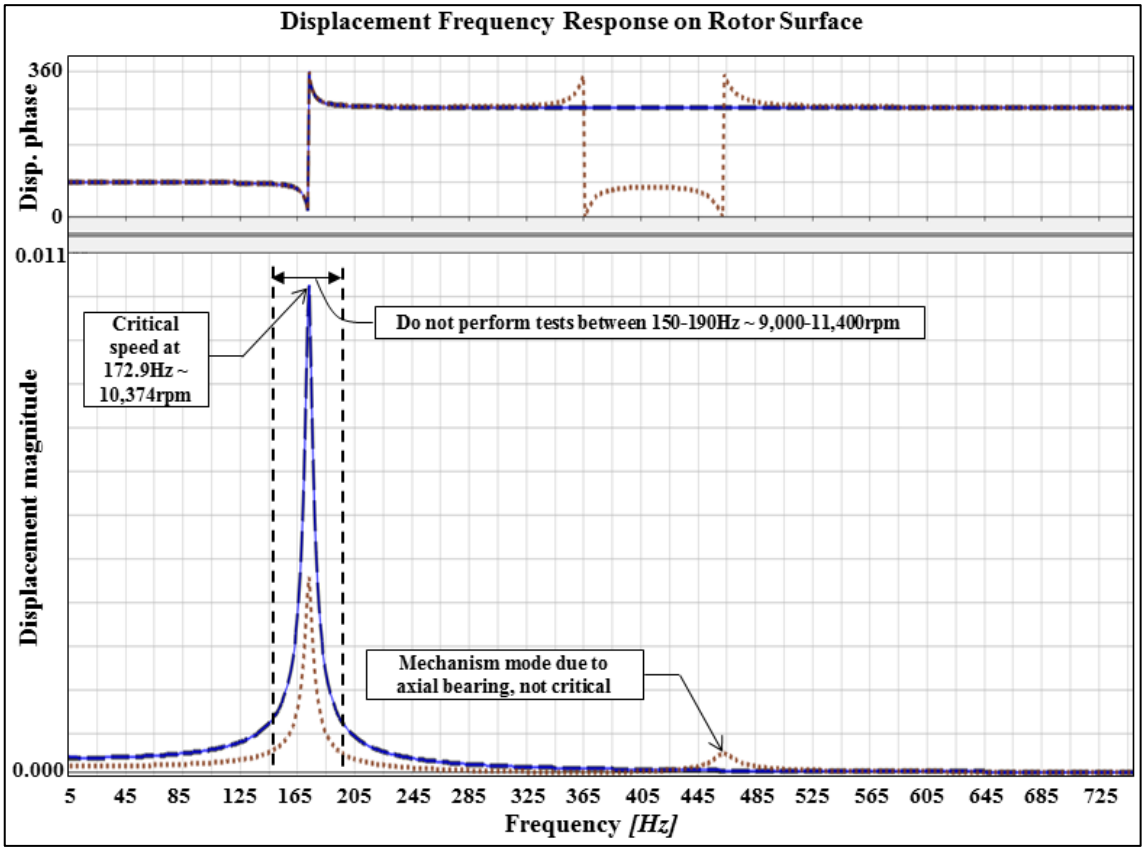

Figure 4.32: RTR-Rotary component assembly, FRF analyses results

Displacement peak is also observed in z-direction at 462.5Hz, which corresponds to 27,750rpm at operating conditions. The peak at that frequency is due to mechanism mode caused by the axial bearing, and it is not critical since it does not induce any excessive vibration, which may affect test accuracy.

The roller bearings used in spindle have very high stiffness values, and therefore mechanism mode due to roller bearings is not observed up to 45,000rpm. The critical speed of 10,374rpm is mainly due to large and heavy rotor used during tests, and it is not related to spindle design that is tightly constrained in radial direction with four roller bearings. Modal and FRF analyses should be repeated to determine critical speeds whenever rotor design is changed for performing different types of test.

4.1.2 Seal Housing Assembly: Design Details and Impact Analyses

Exploded view for the seal housing assembly is given in Figure 4.33. Main components of the seal housing assembly are:

- Housing
- Adaptor
- Side plates
- Seal rings
- Cover sheets

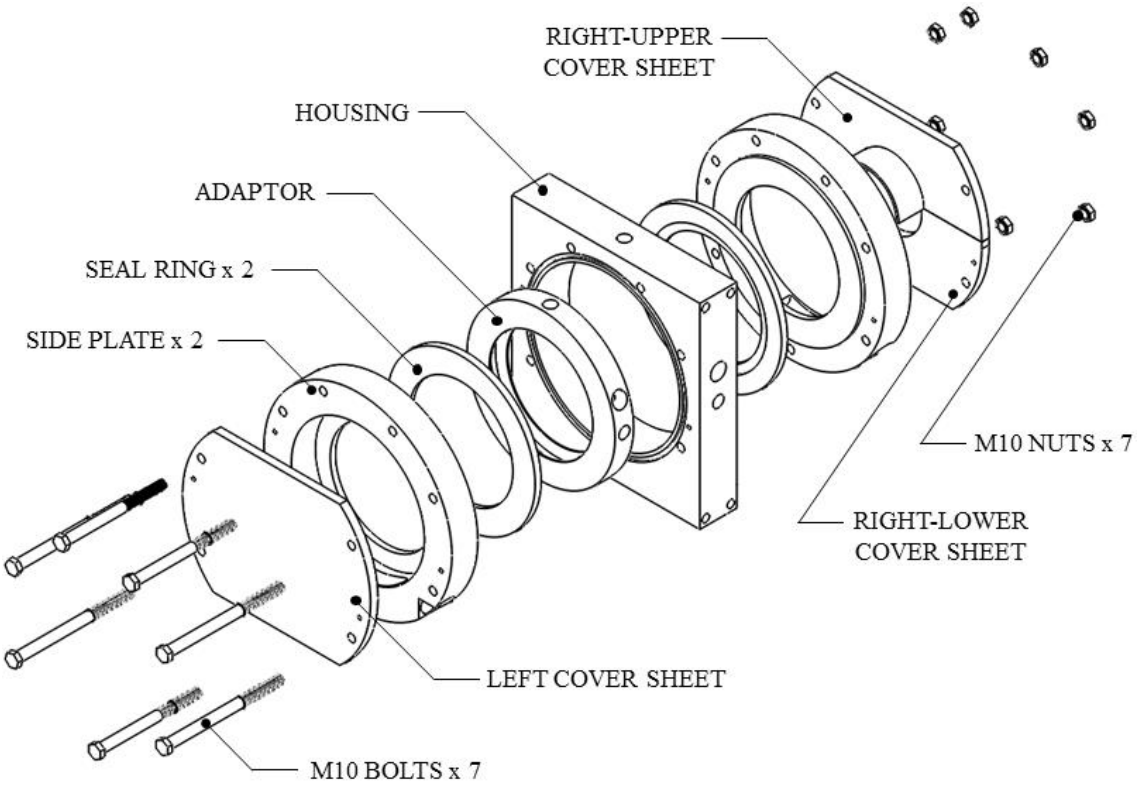

Figure 4.33: Exploded view of the seal housing assembly

4.1.2.1 Housing

The housing details are given in Figure 4.34. The housing is the base part for the seal housing assembly. Test air/oil is supplied through an air/oil inlet hole to the cavity between rotor and brush pack surfaces, and in between bristles. Three probe holes are threaded in accordance with 3/8-24UNJF-3B standard, two of which are for pressure gauges, and the third one is for the thermocouple. ETM-275-7BAR-A types of GE

pressure transducers are used, which has 707.927mV/BAR sensitivity and -18^{o}C to 100^{o}C compensated temperature range. Thermocouples are K-type with 1000^{o}C full scale range. Measured pressure and temperature values are transferred to the computer by means of 20-channel data acquisition system, and monitored via computer in Excel software. Since the testing medium is pressurized fluid, O-rings are used between mating parts of the housing assembly in order to avoid biased leakages. For this purpose, O-ring channels are opened on housing side surfaces. Seal housing assembly components are assembled with the aid of M10 bolts, and appropriate bolt holes are drilled in the housing component.

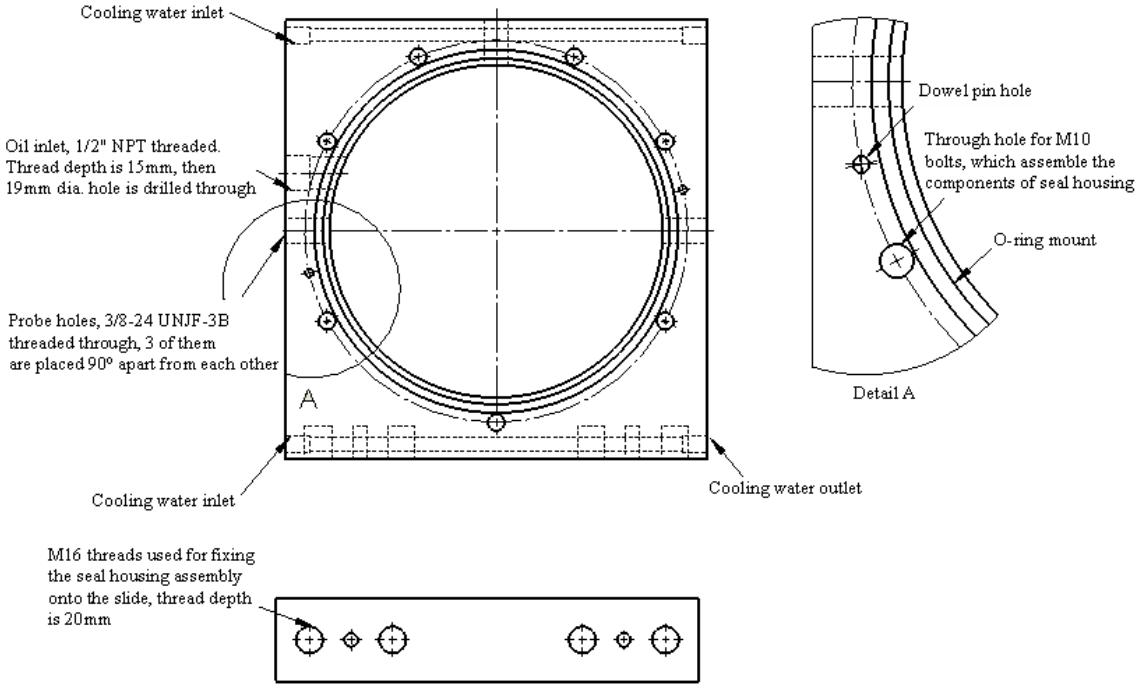

Figure 4.34: Technical drawing of the housing

Overheating of the housing should be avoided when the test environment is fluid at elevated temperatures. In order to overcome heating problem, water is used as a cooling fluid, which is pumped into the housing through the water inlet holes. Cooling water at the outlet is send to the water tank with the aid of circulation pump.

4.1.2.2 Adaptor and Seal Rings

Adaptor is designed to support brush seals and to form a sump for the fluid. Inlet region of the adaptor is manufactured with an angle in order to provide sufficient space

for the oil/air. Outer surface of the adaptor is mated to the inner surface of the housing, and brush seals are mounted at both sides of the adaptor with the aid of seal rings. Brush seals with different dimensions can be tested by only modifying the seal rings, whose simple geometry brings the advantage of low manufacturing cost and time. Details for the adaptor and seal rings are given in Figure 4.35.

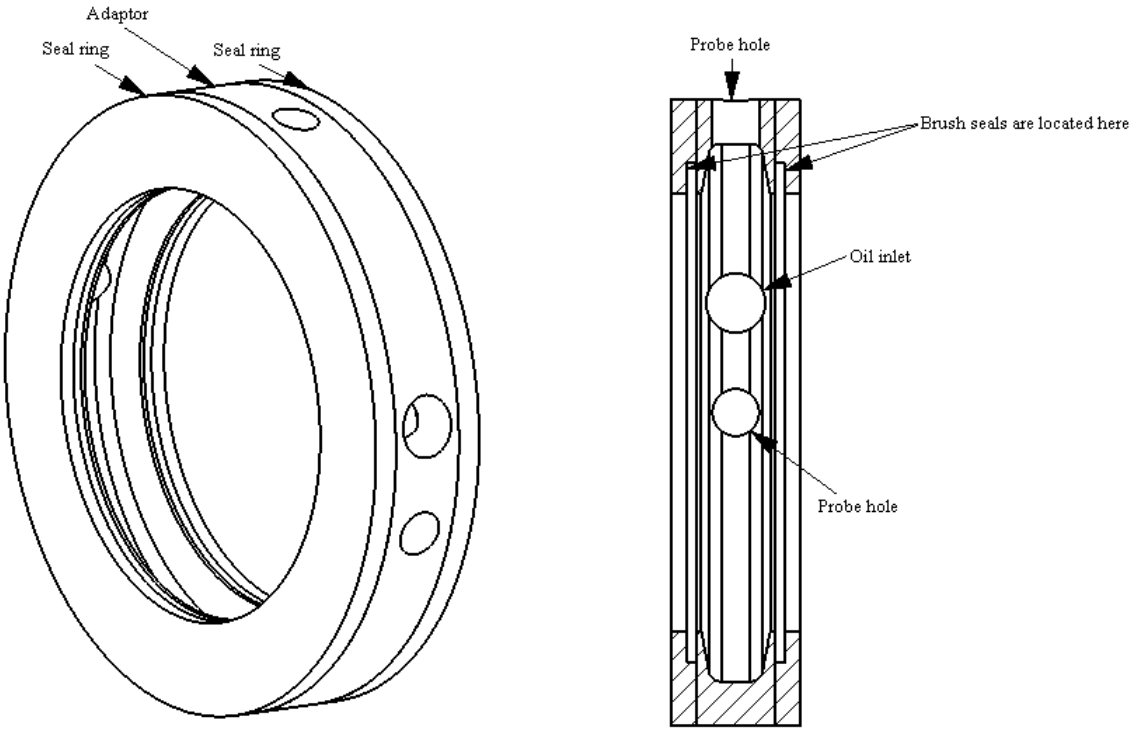

Figure 4.35: Technical drawing of the adaptor and seal rings

4.1.2.3 Side Plates

Side plates are mounted at both sides of the housing with through bolts. Direct contact of side plates with seal rings provides appropriate preload to hold the brush seals. During leakage tests, high pressure is obtained at the inlet region of the adaptor. Therefore, fluid flows from this inlet region to side plates. When the testing medium is oil, it leaks to the sump region, which is formed between side plates and cover sheets. Excessive oil is pumped to the oil tank from oil outlet, so that continuous circulation of oil is maintained. Detailed view of side plates is given in Figure 4.36.

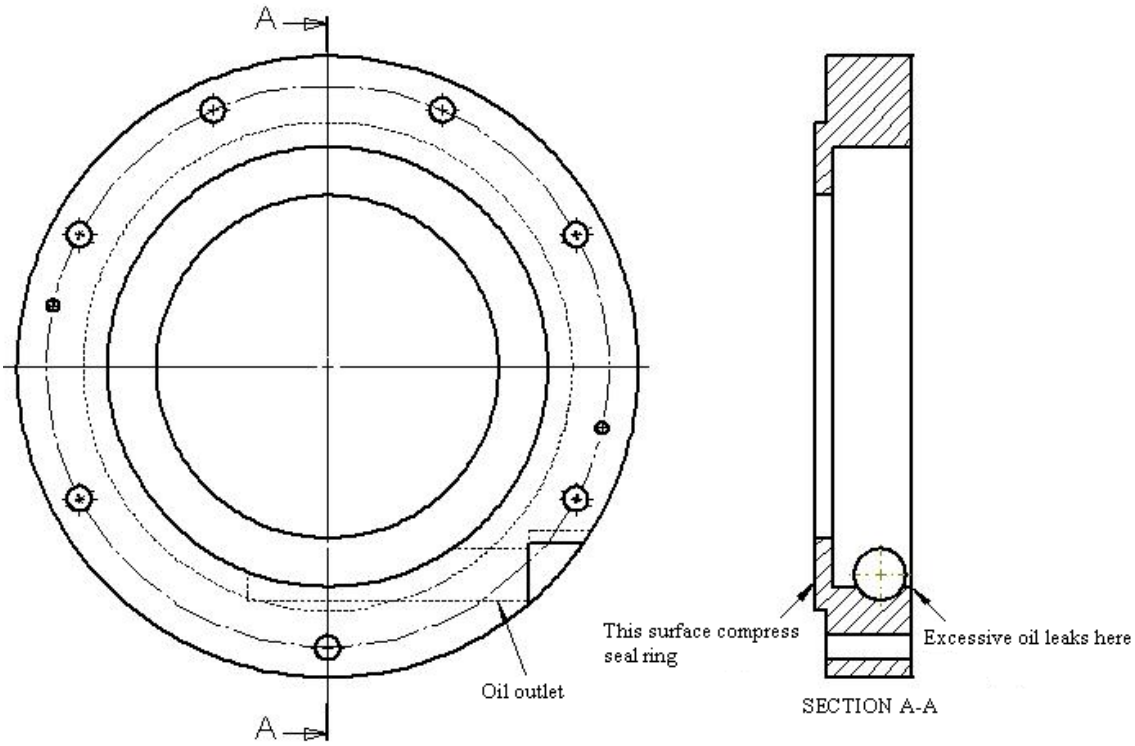

Figure 4.36: Technical drawing of the side plate

4.1.2.4 Cover Sheets

When the test medium is oil, contamination problem may arise from leakages. Together with side plates, cover sheets avoid contamination by forming a sump region for the downstream oil. Left cover sheet is produced as a single part whereas right cover sheet consists of two distinct components, which provides gap for rotor assembly. Upper component of right cover sheet has an extended region to prevent rotor-connecting rod from oil leakages.

Cover sheets are assembled onto side plates with M10 bolts, and they can be removed without disassembling seal housing. Therefore, intervention to the system at the time of any problem can be achieved by simply removing one of the cover sheets. Detailed view of left and right cover sheets are shown in Figure 4.37 and 4.38 respectively.

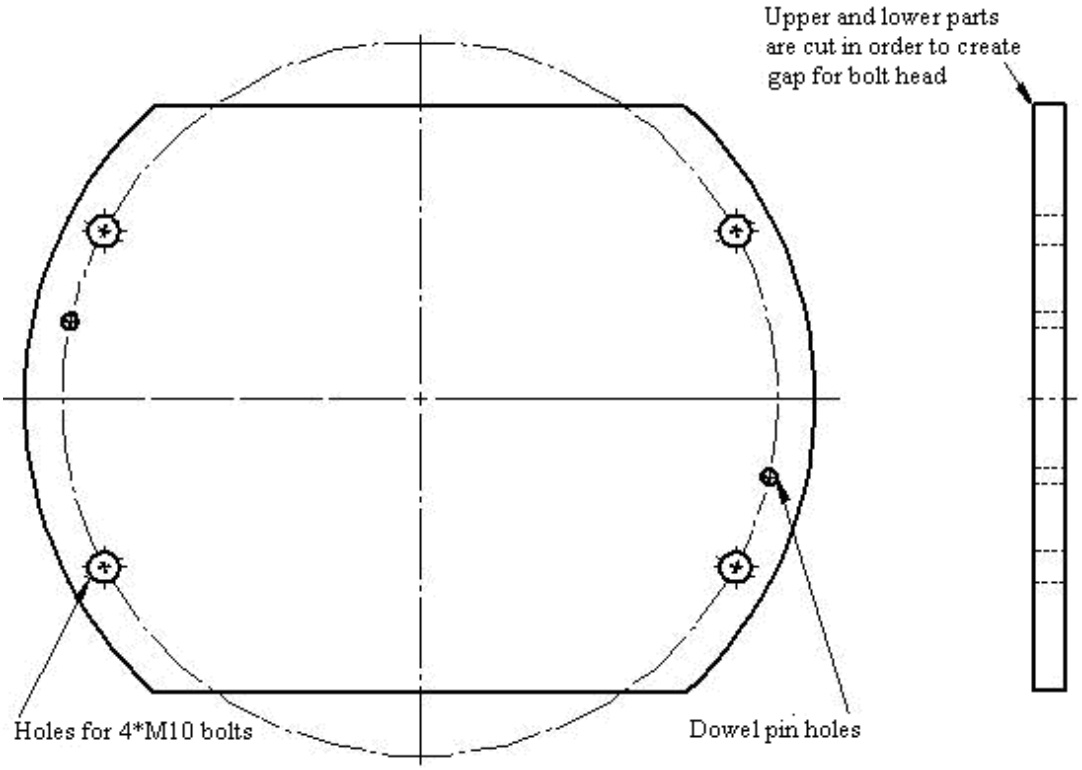

Figure 4.37: Technical drawing of the left cover sheet

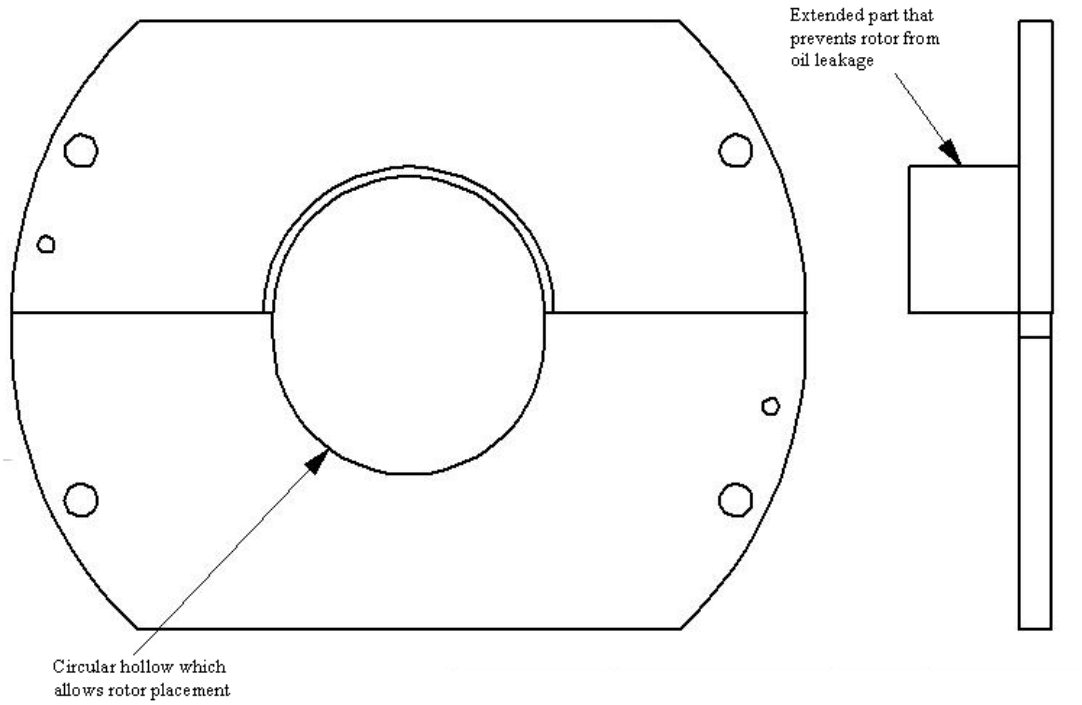

Figure 4.38: Technical drawing of the right cover sheet

4.1.2.5 Impact Analyses for the Seal Housing Assembly

Although structural and vibration analyses state that the rotor is safe against yielding and fatigue up to 45,000rpm, the impact failure of the housing should be considered as one of the possible failure states for the high speed rotary test rig. Any possible failure in rotor will result in sudden crash of high velocity rotor pieces to housing assembly components. In the case of any possible rotor failure, the housing assembly must be tough enough to compensate the impact energy, which is introduced by rotor fragments having high velocities.

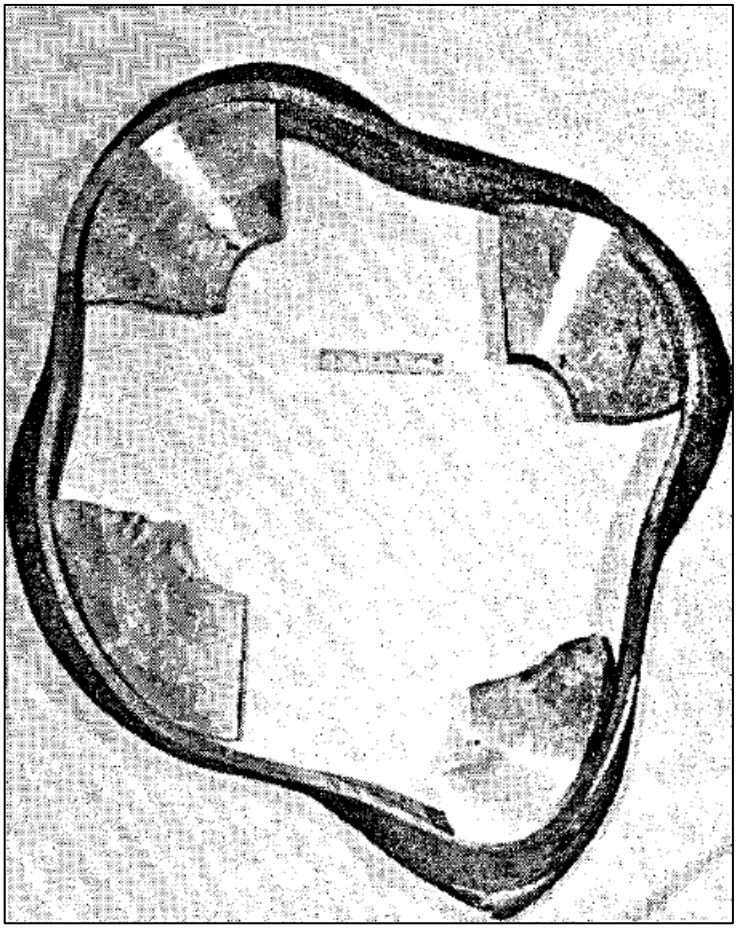

Figure 4.39: Rotor pieces and threshold containment after test, Hagg and Sankey [58]

The test indications [58] identify the possible failure of the system as a two stage process. The first stage of the containment process is a result of compression of material over the impact area, and shearing of material over the perimeter of the impact area due to the initial contact of the fragment. If this stage is successfully cleared, the containment process enters the second stage in which the possible failure is determined

by the dissipated energy in tension strain throughout an extended volume of cover material.

In Figure 4.39, high speed rotor failure after test and threshold containment picture is detailed [58]. Test indications show that the rotor is separated into quarter fragments and each fragment suddenly hits the cover. The fracture of the disc is explained by Hagg and Sankey in three steps, which are detailed in Figure 4.40. Disc fracture steps are:

- Step 1: Failure initiation at one notch and crack propagation in a radial plane to outside of the disc
- Step 2: The centrifugal forces cause the disc split into two halves
- Step 3: The rotating disk halves cause new cracks to initiate
- Step 4: Disc halves separate into two pieces. Eventually, four quarter fragments hit the covers assuming conserving the same rotor rpm

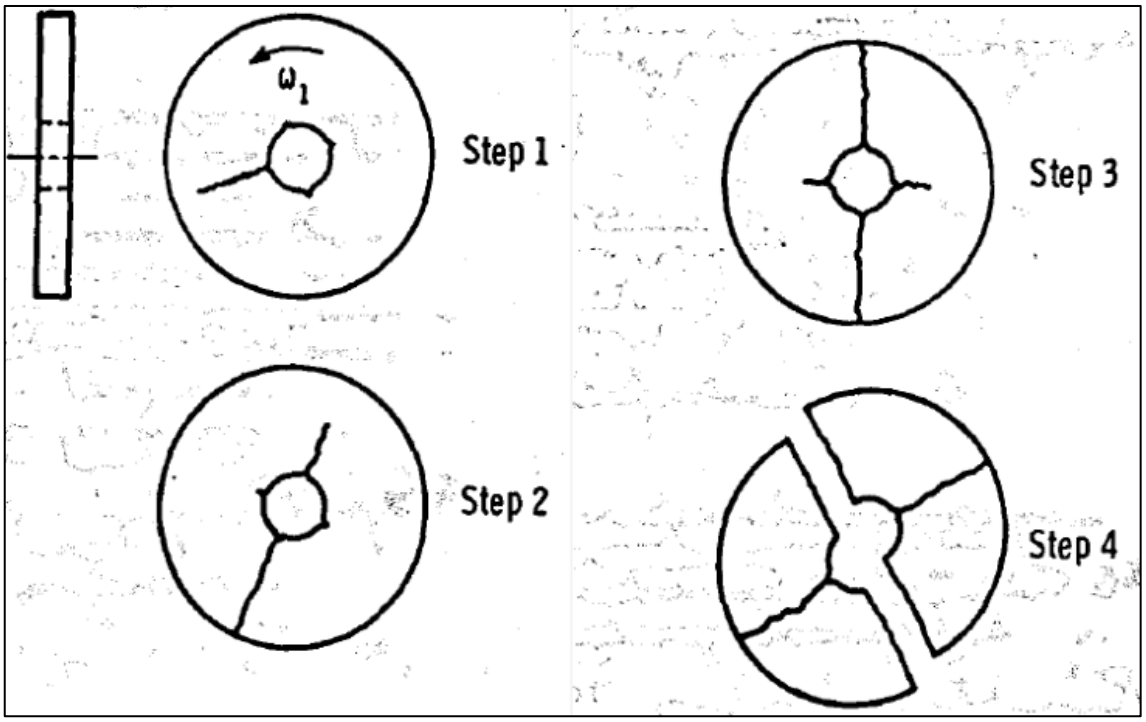

Figure 4.40: Steps for high speed rotating disc fracture, Hagg and Sankey [58]

The calculations also assume the rotor is separated into quarter fragments at the burst speed and retain the angular velocity ω_1 of the rotor at burst, and acquire the average translational velocity $v_{fragment} = r_{cog}.\omega_1$ where r_{cog} is the radius of the center-of-gravity of the quarter fragment.

4.1.2.5.1 General Design and Operating Conditions Data

Main dimensions for impact analyses suggested by Hagg and Sankey [58] are visualized in Figure 4.41.

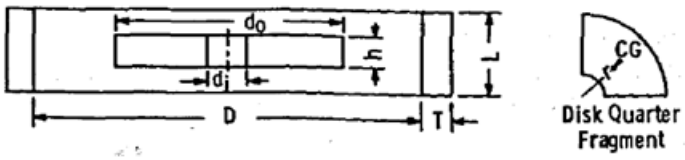

Figure 4.41: The disc *(rotor)* and cover dimensions suggested by Hagg and Sankey [58]

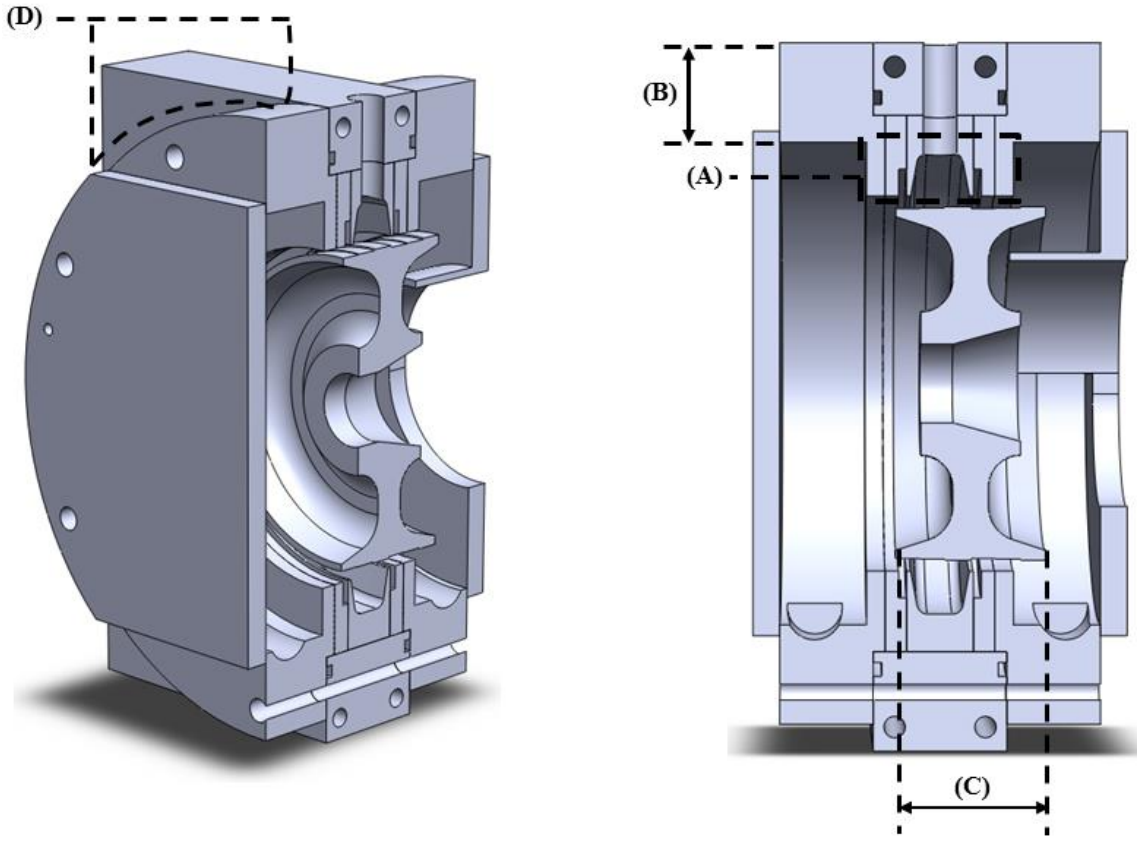

Figure 4.42: Rotary Test Rig – Main dimensional assumption for impact analysis of seal housing assembly

Main dimensional assumptions for RTR-Seal housing assembly impact analysis are detailed in Figure 4.42 and explained below:

- In order to be conservative, the minimum wall thickness of the seal covers and housing is taken into account. Sections shown in Figure 4.40-(A) are

excluded. The thickness shown in Figure 4.40-(B) is considered as the wall thickness for impact analyses.

- For conservative calculation process, all cover components are assumed to be circular, and the housing section shown in Figure 4.40-(D) is excluded.
- The rotor section having the maximum width – shown in Figure 4.40-(C)- is used in impact analysis to simulate the worst case scenario.

Using the assumptions above and dimensions given in Figure 4.43, RTR dimensions for impact analyses are as following:

- D = 184mm
- T = 35mm
- L = 120mm
- $d_{o\text{-}rotor}$ = 130.1mm
- $d_{i\text{-}rotor}$ = 30.5mm
- h_{rotor} = 70.5mm

Further information on the rotor and covers *(including housing)* is as following:

- Rotor:
  - Material: SS304-Cold rolled
  - Density of the rotor, ρ_{rotor}=7890 kg/m^3
  - Mass of the rotor, M_{rotor} = 3.25 kg
  - Maximum rotor rotational speed, n_{max} = 45,000rpm
  - Radius of the COG of the quarter fragment, r_{cog} = 32.01mm *(calculated from the FE model)*
  - Average translational velocity of the fragment, $\upsilon_{fragment}$ = 150.8m/s
- Housing and covers:
  - Material: SS304-Cold rolled
  - Density of the covers, ρ_{covers}=7890 kg/m^3 *[2]*
  - Yield strength, $S_{y\text{-}covers}$ = 1103MPa *[2]*
  - Ultimate tensile strength, $S_{ut\text{-}covers}$ = 1276MPa *[2]*
- Bolts:
  - Number of bolts, N_{bolts} = 4
  - Class and size of bolts: Class 10.9, M16-Fine thread
  - Effective area for each bolt, $A_{eff\text{-}M16}$ = 167.25mm^2 *[2]*

- Yield strength, $S_{y\text{-}M16}$ = 940MPa *[2]*
- Ultimate tensile strength, $S_{ut\text{-}M16}$ = 1040MPa *[2]*

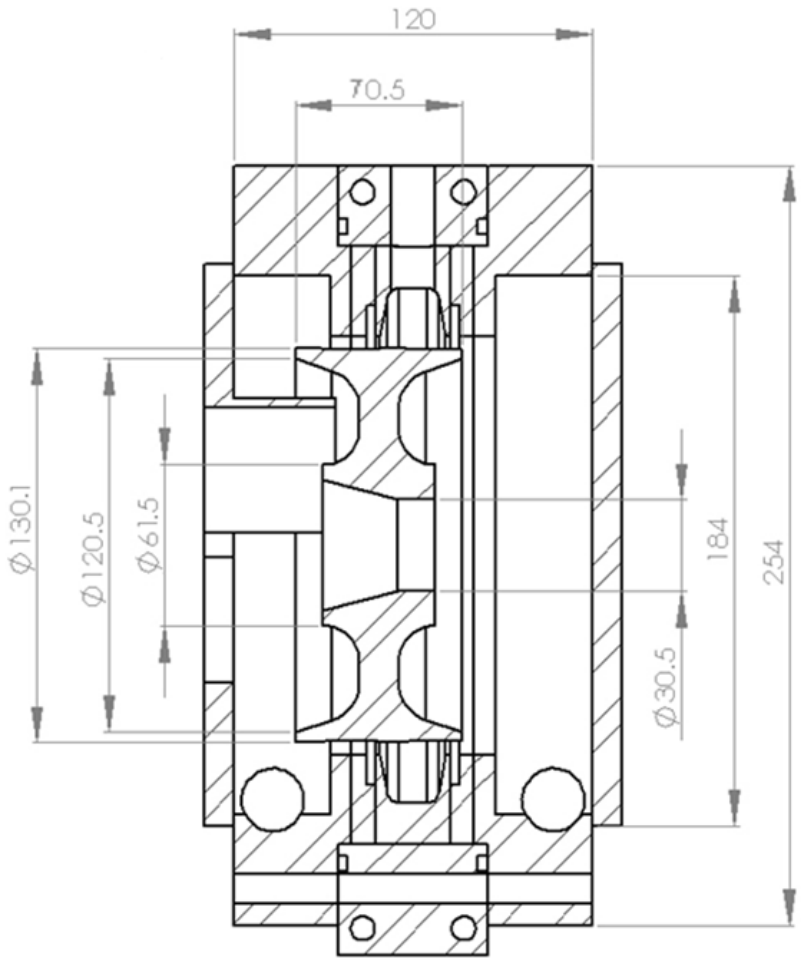

Figure 4.43: The disc *(rotor)* and cover dimensions for Rotary Test Rig

4.1.2.5.2 Impact Analysis Procedure

<u>Kinetic Energy Loss in Stage 1:</u>

The energy for Stage 1 is calculated via the energy dissipated in the momentum transfer under the assumption that the impact of the fragment is elastic and the momentum is conserved. On an energy basis, the minimum relative perforation energy occurs with the normal force imposed by the translational motion of the impacting fragment [58]. Thus, the energy for Stage 1 is;

$$\Delta E_1 = \frac{1}{2} \cdot M_1 \cdot \upsilon^2_{fragment} \cdot \left(1 - \frac{M_1}{M_1 + M_2}\right) \quad (4.1)$$

In Equation 4.1, M_1 is the mass for the fragment, $\upsilon_{fragment}$ is the velocity of the fragment and M_2 is the effective mass of the shell, which can be also named as effective target mass. The calculation of the ΔE_1 requires proper evaluation of the effective mass, M_2. The effective target mass, M_2 , is defined as the part of the target that can respond *(accelerate)* during the initial contact and momentum transfer. Referring to Figure 4.44, the mass m_{21} is expectedly a part of M_2. A limited volume of material that is adjacent to m_{21} can respond as well because of the shear forces. The factor of the m_{21} is determined from the tests [58] and are as following for different cases;

For long cylindrical shells - $M_2 = m_{21} + 0.34 m_{22}$

For short cylindrical shells with $a = 3T$ - $M_2 = m_{21} + 0.27 m_{22}$

For short cylindrical shells with $a = 2T$ - $M_2 = m_{21} + 0.29 m_{22}$

The last case has been assumed and used for the impact analyses of the RTR.

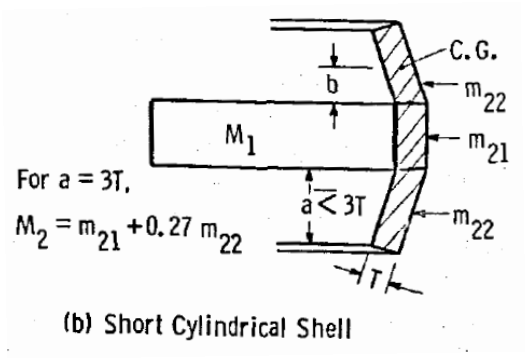

Figure 4.44: The effective mass calculation of a short cylindrical shell [58]

Strain Energy, Stage 1:

The shell material is compressed over the area in contact with the rotor fragment, and sheared along the perimeter of the area in contact. The energy required to plastically strain the material in compression is;

$$E_c = A \cdot T \cdot \varepsilon \cdot \sigma_d \quad (4.2)$$

where A is the contact area, T is the thickness of the shell wall, ε is the per unit plastic strain, and σ_d is the average dynamic plastic flow stress of the material in compression.

The shear energy E_s for a ductile material is,

$$E_s = 2 \cdot K \cdot \tau_d \cdot P \cdot \int_0^T (T - x)dx = K \cdot \tau_d \cdot P \cdot T^2 \tag{4.3}$$

where τ_d is the dynamic shear strength of the material, P is the perimeter of the sheared area, and K is an experimental constant with a value in the range of 0.3 to 0.5 [58].

Criterion for Nonperforation:

The energy ΔE_1 must be dissipated in strain energy at the contact region of the shell with the fragment. The criterion for nonperforation then becomes,

$$E_s + E_c > \Delta E_1 \quad \text{or,}$$

$$K \cdot \tau_d \cdot P \cdot T^2 + A \cdot T \cdot \varepsilon \cdot \sigma_d > \frac{1}{2} M_1 \cdot \upsilon_{fragment}^{\ 2} \cdot \left(1 - \frac{M_1}{M_1 + M_2}\right) \tag{4.4}$$

Criterion for Containment, Stage 2:

The residual fraction, ΔE_2, of the initial kinetic energy of the fragment, which is coming from the Stage 1 with nonperforation, is dealt with in Stage 2 of the process. In Stage 2, energy is dissipated by uni-axial tension strain *(stretching)* for the case of short cylindrical shells. The criterion for containment in stage 2 is,

$$E_t > \Delta E_2 \quad \text{or,}$$

$$Q \cdot \varepsilon \cdot \sigma_d > \frac{1}{2} M_1 \cdot \upsilon_{fragment}^{\ 2} \cdot \left(1 - \frac{M_1}{M_1 + M_2}\right) \tag{4.5}$$

where Q is the volume of the shell material that is strained an allowable amount ε at an average plastic flow stress σ_d. For a short cylindrical shell, the entire volume of a material is strained. With four fragments, the volume of material Q per fragment is equal to *"(πD/4).L.T"*, where D is the diameter of the shell, L is the length of the shell, and T is wall thickness.

Finally the reliability of the bolts which are used in assembling the housing to the slide will be investigated for the case of disk fragment-housing impact at maximum speed in vertical direction. For that investigation, the criterion for safety will be as following,

$$F < F_{BOLTS} \quad \text{where,}$$

$$F = M_1 \cdot \left(\frac{\upsilon_i - \upsilon_f}{\Delta t} \right) \quad \text{and} \quad F_{BOLTS} = \left(S_{UT-M16} \cdot A_{eff} \right) \cdot N_{bolts} \tag{4.6}$$

In Equation 4.6, υ_i refers to initial velocity of the quarter rotor fragment, and υ_f is the final velocity of the fragment after impact. In impact analyses of RTR, the initial fragment velocity is 150.8m/s and the final velocity is assumed to be zero to simulate the worst case scenario.

4.1.2.5.3 Impact Analysis for Rotary Test Rig

Impact analyses of Rotary Test Rig design has been performed by using the design parameters given *"General Design and Operating Conditions Data"* section. The impact analysis starts with the determination of the effective mass values for the rotor fragment and covers. The effective mass for the quarter rotor fragment can be calculated as:

$$M_1 = \frac{M_{rotor}}{4} = \frac{3.25}{4} = 0.8125kg \tag{4.7}$$

Calculation of effective target mass, M_2, requires m_{21} and m_{22} values as shown in Figure 4.44. The width of related sections in RTR can be extracted by using the dimensions provided in Figure 4.43. The widths of these two regions are, $w_{21}=70.50mm$ and $w_{22}=25.25mm$. The length of these regions can be calculated by using the equations below.

$$\phi_{AVG} = \frac{184 + 254}{2} = 219mm \tag{4.8}$$

$$l_{21} = l_{22} = \frac{1}{4} \cdot \pi \cdot 219 \approx 172mm \tag{4.9}$$

Combining the values calculated above, the m_{21} and m_{22} are as following,

$$m_{21} = l_{21} \cdot w_{21} \cdot T \cdot \rho_{covers} = 172 \cdot 70.5 \cdot 35 \cdot 7890 \cdot 10^{-9} = 3.348kg \quad (4.10)$$

$$m_{22} = l_{22} \cdot w_{22} \cdot T \cdot \rho_{covers} = 172 \cdot 25.25 \cdot 35 \cdot 7890 \cdot 10^{-9} = 1.199kg \quad (4.11)$$

As the m_{21} and m_{22} values are determined, the effective target mass, M_2, can be calculated by using the Equation 4.12.

$$M_2 = m_{21} + 0.29 \cdot m_{22} = 3.695kg \quad (4.12)$$

The kinetic energy loss in Stage 1 can be calculated by using the Equation 4.1. The kinetic energy loss for the rotary test rig at full speed is,

$$\Delta E_{1-RTR@45000rpm} = \frac{1}{2} \cdot M_1 \cdot \upsilon_{fragment}^2 \cdot \left(1 - \frac{M_1}{M_1 + M_2}\right) = 7.578 \cdot 10^3 J \quad (4.13)$$

The energy required to plastically strain the material in compression needs to be calculated as well. The contact area, A, should be calculated as first step.

$$A = \frac{\pi}{4} \cdot d_{o-rotor} \cdot h_{rotor} = 7.103 \cdot 10^3 mm^2 = 7.103 \cdot 10^{-2} m^2 \quad (4.14)$$

The σ_d and ϵ are defined in [58] as following,

$$\sigma_d = 1.5 \cdot S_{ut-covers} = 1914MPa = 1.914 \cdot 10^9 Pa$$

$$\varepsilon = 0.07 \quad (4.15)$$

The energy required to plastically strain the material in compression can be calculated for the RTR as following,

$$E_{c-RTR} = A \cdot T \cdot \varepsilon \cdot \sigma_d = 3.378 \cdot 10^4 J \quad (4.16)$$

The shear energy, E_s, for the cover should be calculated, but the first the perimeter of the sheared area, P, and the "$K.\tau_d$" should be determined. "$K.\tau_d$" is defined as the following in [58];

$$K \cdot \tau_d = 0.27 \cdot \sigma_d = 516.78MPa \approx 5.17 \cdot 10^8 Pa \quad (4.17)$$

$$P = 2 \cdot \left(\frac{\pi \cdot d_{o-rotor}}{4} + h_{rotor} \right) = 345.36mm \tag{4.18}$$

$$E_{s-RTR} = K \cdot \tau_d \cdot P \cdot T^2 = 2.186 \cdot 10^5 J \tag{4.19}$$

As the required parameters have been calculated, the criterion for nonperforation can now be checked,

$$Nonperforation \Rightarrow E_s + E_c > \Delta E_1$$

$$E_{s-RTR} + E_{c-RTR} = 2.524 \cdot 10^5 J > \Delta E_{1-RTR@45000rpm} = 7.578 \cdot 10^3 J \tag{4.20}$$

The criterion for nonperforation holds and the factor of safety at 45,000rpm is equal to the following,

$$N_{Stage1@45000rpm} = 33.31 \tag{4.21}$$

As the nonperforation is ensured, one should check the containment. The containment analyses starts with the calculation of *Q*, which is the volume of the material per fragment.

$$Q = \frac{\pi \cdot D}{4} \cdot L \cdot T = 6.06 \cdot 10^5 mm^3 = 6.06 \cdot 10^{-4} m^3 \tag{4.22}$$

$$E_{t-RTR} = Q \cdot \varepsilon \cdot S_d = 8.132 \cdot 10^4 J \tag{4.23}$$

The residual fraction ΔE_2, of the initial kinetic energy of the fragment is calculated as below.

$$\Delta E_{2-RTR@45000rpm} = \frac{1}{2} \cdot M_1 \cdot \upsilon_{fragment}^2 \cdot \left(\frac{M_1}{M_1 + M_2} \right) = 1.665 \cdot 10^3 J \tag{4.24}$$

As the required parameters have been calculated, the criterion for containment can now be checked,

$$E_{t-RTR} > \Delta E_{2-RTR@45000rpm} \Rightarrow 8.132 \cdot 10^4 J > 1.665 \cdot 10^3 J \tag{4.25}$$

The criterion for containment safety holds and the factor of safety at 45,000rpm is equal to the following,

$$N_{Stage2@45000rpm} = 48.82 \tag{4.26}$$

Another parameter to be checked for the safety of the system is the safety of the bolts that are used in assembling the housing to the slide below, in case of the disc hitting the housing in vertical direction. This approach assumes that the bolts need to counter the force exhibited by the rotor fragment on the housing while the speed of the rotor reaches to zero in a short span of time from its maximum value.

The amount of time for this impact analyses is assumed to be $1ms$. The basic equation of force equilibrium is applied in order to extract the force required to stop the rotor in this time. The parameters for the RTR are summarized below.

$$\upsilon_i = \upsilon_{fragment} = 150.8 m/s$$

$$\upsilon_f = 0$$

$$M_1 = 0.8125 kg$$

$$\Delta t = 0.001 s$$

The deceleration of the rotor fragment is,

$$a_{RTR} = \frac{\upsilon_i - \upsilon_f}{\Delta t} = 150.84 \cdot 10^3 m/s^2 \tag{4.27}$$

The force required to absorb the above deceleration is,

$$F = M_1 \cdot a_{RTR} = 122.56 \cdot 10^3 N \tag{4.28}$$

The maximum bolt force that M16 bolts can withstand is,

$$F_{BOLTS} = A_{eff} \cdot S_{ut-M16} \cdot N_{bolts} = 695.76 \cdot 10^3 N \tag{4.29}$$

For the bolts to withstand the crash of the fragment to the housing in vertical direction, the following criterion should hold,

$$F < F_{BOLTS} \Rightarrow 122.56 \cdot 10^3 N < 695.76 \cdot 10^3 N \tag{4.30}$$

The criterion for bolt safety holds and the factor of safety at 45,000rpm is equal to the following,

$$N_{bolts} = 5.67 \tag{4.31}$$

Summing up, the values acquired for the critical parameters, their limits and the safety factors for RTR calculated at 45,000rpm are detailed in Table

IMPACT ANALYSES SUMMARY FOR RTR AT 45,000RPM					
	Parameter to be checked	**Parameter Value**	**Lower limit to be checked**	**Lower limit value**	**Factor of safety**
Stage 1 - Nonperforation	$\mathbf{E_{s\text{-}RTR}+E_{c\text{-}RTR}}$	2.524×10^5J	$\mathbf{\Delta E_{1\text{-}RTR@45000rpm}}$	7.578×10^3J	33.31
Stage 2 - Containment	$\mathbf{E_{t\text{-}RTR}}$	8.132×10^4J	$\mathbf{\Delta E_{2\text{-}RTR@45000rpm}}$	1.665×10^3J	48.82
Bolt Safety	$\mathbf{F_{BOLTS}}$	695.76×10^3N	**F**	122.56×10^3N	5.67

Table 4.6: RTR – Impact analyses summary at 45,000rpm

4.2 Rotary Test Rig – Tip Force Measurement Procedure

The full rotor static and dynamic stiffness tests can be conducted in pressurized and unpressurized conditions. Two mirror seals are tested at the same time, which eliminates any possible axial loading on rotor during pressurized tests. Pressurized tests have been performed in air environment, where the air is fed into the inlet region of the adaptor in seal housing assembly. The upstream pressure is obtained at the cavity formed by the adaptor, rotor and seals, and the downstream pressure is ambient air at room temperature. The pressure load causes leakage flow from upstream side to downstream side. The controlled atmosphere at upstream side is assured by monitoring the pressure with the aid of a transducer. Two beam type load cells are used for measuring the reaction force during seal-rotor contact force measurements as shown in Figure 4.45.

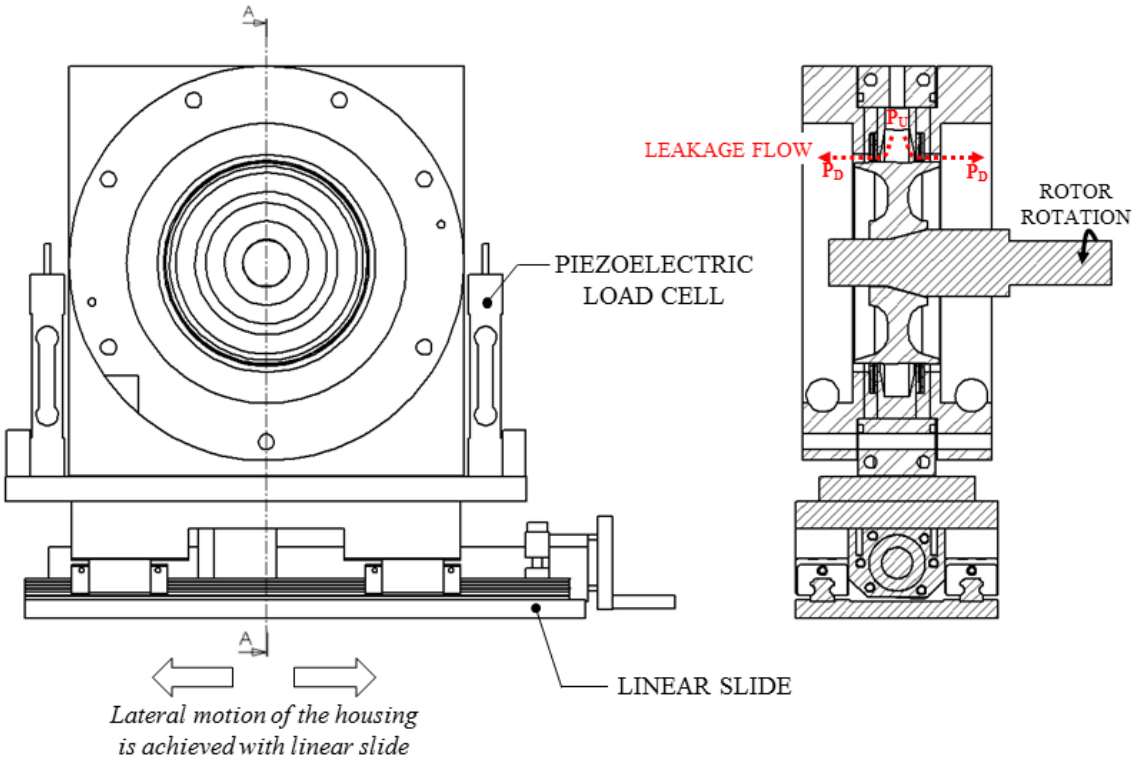

Figure 4.45: RTR-Seal housing assembly details for pressurized-dynamic stiffness tests

Full rotor unpressurized-static stiffness tests start with adjusting the rotor initial position to obtain concentric and line-to-line conditions with brush seals. The spindle holder assembly is moved in vertical direction via linear slide until the appropriate surface of the stepped rotor get in contact with seals. The rotor-seal concentricity is assured by moving the housing in lateral direction and by using the gauge pins. As the initial position of the rotor is adjusted, the radial interference is obtained by laterally moving the housing assembly to the rotor. The housing assembly is moved incrementally with the aid of precise linear slide. The radial interference is applied with 0.1mm increments, and the force output from both load cells is recorded. The rotor interference is applied up to a certain point to complete force measurements in loading cycle, and then the housing is slid back to its original position while keep measuring force values to characterize stiffness in unloading cycle.

In order to perform unpressurized-dynamic stiffness tests, the rotor is rotated at its adjusted reference position for concentricity and line-to-line seal contact. Radial interference is introduced as the desired rotor speed is reached. The remaining measurement procedure is same with the unpressurized-static stiffness tests.

The pressurized air is fed into inlet of the adaptor before introducing radial interference in pressurized stiffness tests. Remaining procedure is same with the unpressurized tests.

4.3 Rotary Test Rig – Bristle Tip Force Calculation Method

Similar to free-state stiffness measurement, total force is recorded in full rotor stiffness tests and the data is needed to be post-processed for stiffness characterization independent of rotor contact area. Therefore, bristle tip force should be calculated by using the formula given in Equation 4.32. "BTF_{RTR}" is the calculated bristle tip force, *"*RF_{RTR}*"* is the measured reaction force in full rotor stiffness tests, and *"*$N_{bristle\text{-}effective}$*"* is the total number of bristles which are effectively in contact with rotor during tests.

$$BTF_{RTR} = \frac{RF_{RTR}}{N_{bristle-effective}} \tag{4.32}$$

"$N_{bristle\text{-}effective}$*"* can be found by multiplying *"*$N_{bristle\text{-}rotor}$*"*, which refers to the total number of bristles in contact with half rotor, with the effective bristle coefficient for rotary test rig, *"*C_{RTR}*"*.

$$N_{bristle-effective} = C_{RTR} \cdot N_{bristle-rotor} \tag{4.33}$$

In Equation 4.33, *"*$N_{bristle\text{-}rotor}$*"* can be calculated by using the bristle density and the total rotor circumferential length which is in contact with seals, *"*L_{rotor}*"*. Since two mirror seals are tested at the same time in rotary test rig, the *"*$N_{bristle\text{-}rotor}$*"* calculation must include the contribution from both test seals #1 and #2.

$$N_{bristle-rotor\#1} = \eta_{\#1} \cdot L_{rotor} \tag{4.34}$$

$$N_{bristle-rotor\#2} = \eta_{\#2} \cdot L_{rotor} \tag{4.35}$$

$$N_{bristle-rotor} = N_{bristle-rotor\#1} + N_{bristle-rotor\#2} \tag{4.36}$$

In Equation 4.33, *"*$N_{bristle\text{-}rotor}$*"* can be calculated by using the bristle density and the total rotor circumferential length which is in contact with seals, *"*L_{rotor}*"*. Since two

mirror seals are tested at the same time in rotary test rig, the *"$N_{bristle\text{-}rotor}$"* calculation must include the contribution from both test seals #1 and #2.

Although the half of the rotor contacts with bristles, the effective force exerted on the rotor is smaller than the force that bends the bristles at half rotor surface. The case for effective force is visualized in Figure 4.46. In the figure, the force exerted to the bristle *"B_0"* equals to *"F_b"*. When the bristle *"B_R"*, which is located at angle *"α"* in CW direction from *"B_0"* is considered, although the same force of *"F_b"* bends the bristle, the force in y-direction-*"$F_b cos(\alpha)$"*- is felt by the rotor while the portion *"$F_b sin(\alpha)$"* is balanced with the mirror bristle on left hand side, *"B_L"*.

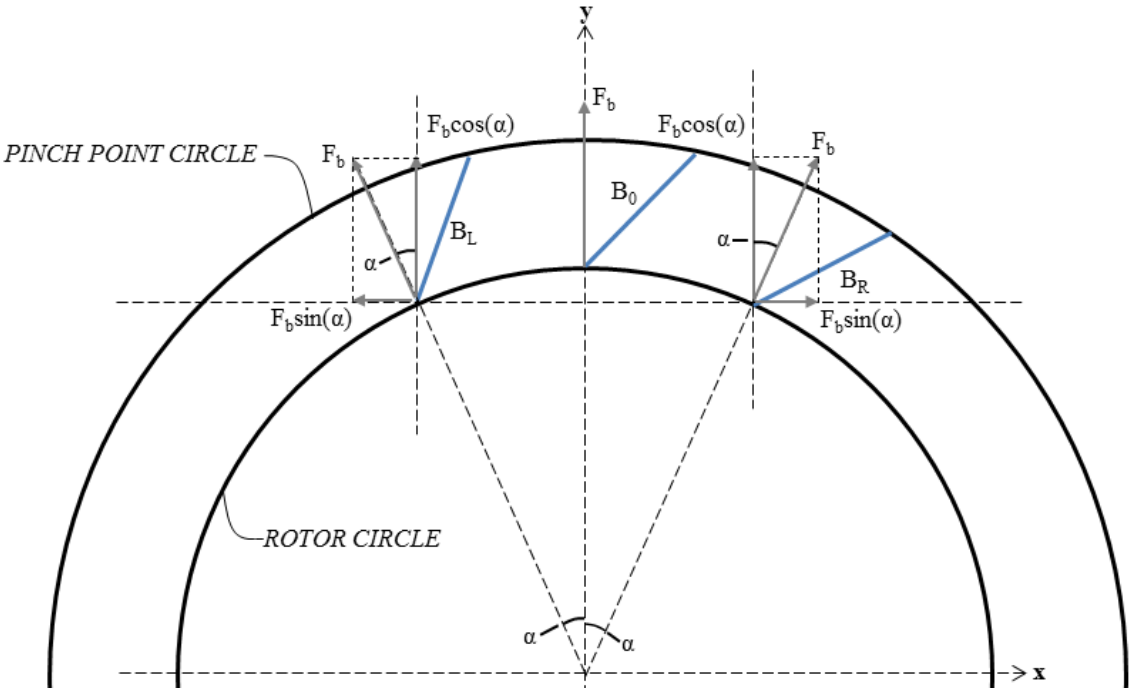

Figure 4.46: Visualization of force exerted on rotor during RTR stiffness tests

The force profile on half rotor surface during RTR stiffness tests is given in Figure 4.47. As it can be seen from the figure, the force profile on quarter rotor *(right hand side)* for one seal is named as *"$f(RF_{right})$"*, and it equals to,

$$f(RF_{right}) = BTF_{RTR} \cdot \cos\left(\frac{\pi}{2} \cdot \frac{(n-1)}{N}\right), \text{ n=1,2,…,N+1} \qquad (4.37)$$

In Equation 4.37, *"N"* is the number of bristles at the quarter rotor for one seal. Considering the half rotor surface and testing two mirror seals at the same time, *"N"* is approximately equal to *"$N_{bristle\text{-}rotor}/4$"*.

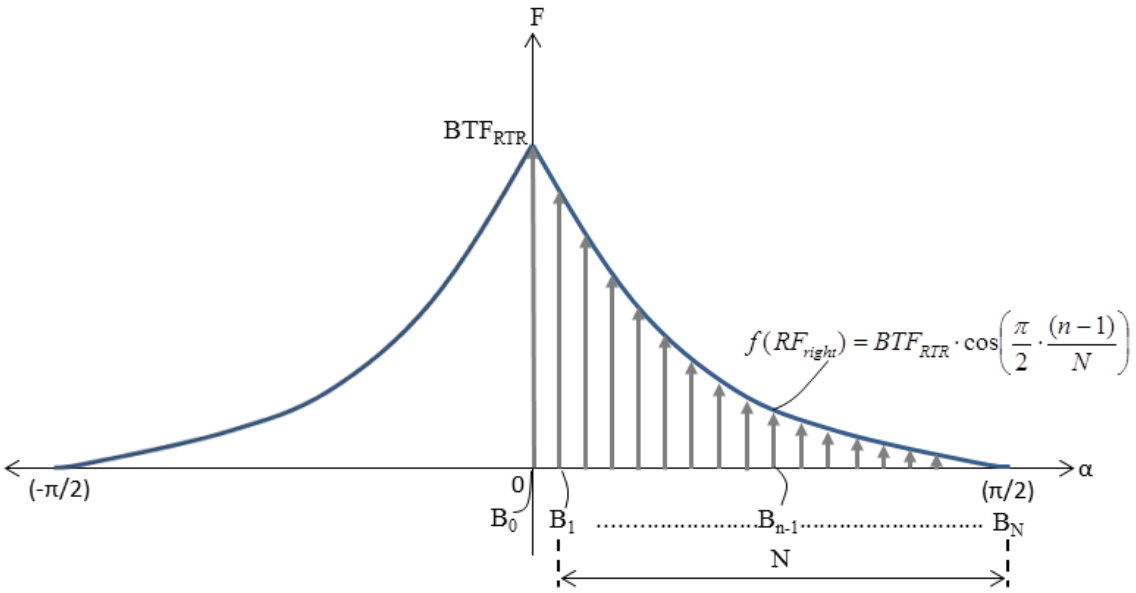

n=1, B_0, α_0=0°,	$F_{R0}=BTF_{RTR}\cos[0]=BTF_{RTR}$
n=2, B_1, $\alpha_1=(\pi/2)(1/N)$,	$F_{R2}=BTF_{RTR}\cos[\alpha_1]$
n=3, B_2, $\alpha_2=(\pi/2)(2/N)$,	$F_{R3}=BTF_{RTR}\cos[\alpha_2]$
. . .	.
. . .	.
. . .	.
n, B_{n-1}, $\alpha_{n-1}=(\pi/2)[(n-1)/N]$,	$F_{R(n-1)}=BTF_{RTR}\cos[\alpha_{n-1}]$
. . .	.
. . .	.
. . .	.
n=N+1, B_N, $\alpha_N=(\pi/2)$,	$F_{RN}=BTF_{RTR}\cos[0]=0$

Figure 4.47: Visualization of force profile on half rotor surface during RTR stiffness tests

The total reaction force on rotor during RTR-stiffness tests can be calculated by integrating the Equation 4.37 and multiplying it with four *(half rotor surface, testing two seals at the same time in RTR).*

$$RF_{right} = \int \left\{ BTF_{RTR} \cdot \cos\left(\frac{\pi}{2} \cdot \frac{(n-1)}{N} \right) \cdot dn \right\} \tag{4.38}$$

$$RF_{RTR} = 4 \cdot RF_{right} \tag{4.39}$$

Using the Equation 4.39, the *"BTF_{RTR}"* can be found as given in Equation 4.40. As it is given in Equation 4.40, the effective bristle number can be found by multiplying the *"$N_{bristle\text{-}rotor}$"* to coefficient *"C_{RTR}"*.

$$BTF_{RTR} = \frac{RF_{RTR}}{N_{bristle-effective}} \tag{4.40}$$

$$BTF_{RTR} = \frac{RF_{RTR}}{\left(C_{RTR} \cdot N_{bristle-rotor}\right)} \tag{4.41}$$

The RTR-rotor properties and calculated effective number of bristles during RTR stiffness measurements are detailed in Table 4.7. Bristle tip force calculations of full rotor stiffness tests, which have been performed with rotary test rig, use the effective number of bristles given in Table 4.7.

RTR – Effective Number of Bristles for BTF_{RTR} Calculations	
Rotor radius	64.77mm
Rotor half length	203.48mm
Bristle density, Test seal #1&2	94 bristles per mm

Table 4.7: Efective number of bristles for BTF_{RTR} calculations at full rotor-stiffness tests

4.4 Rotary Test Rig: Unpressurized – Static BTF Measurements

The RTR – Unpressurized static stiffness case refers to stiffness measurements with non-rotating rotor and zero pressure-load. Since test seal#1 and #2 are tested at the same time, the post-processed BTF values correspond to average values for test seals.

RTR-Unpressurized static stiffness tests have been performed up to 0.6mm rotor interference, and BTF results as well as their comparison with FSS-TR free-state BTF values are given in Figure 4.48 and tabulated in Table 4.8. As it can be seen from the figure, the RTR-unpressurized static and FSS-TR free-state measurements give almost same BTF result in loading step up to 0.1mm interference. However, due to side effects introduced in FSS-TR free state stiffness tests, the slope of the FSS-TR measurements increases continuously above 0.1mm, while the slope of the BTF curve is almost constant in RTR-unpressurized static stiffness tests. The RTR-unpressurized tests better

simulates the turbine operating conditions since the subscale rotor is pressed against bristles.

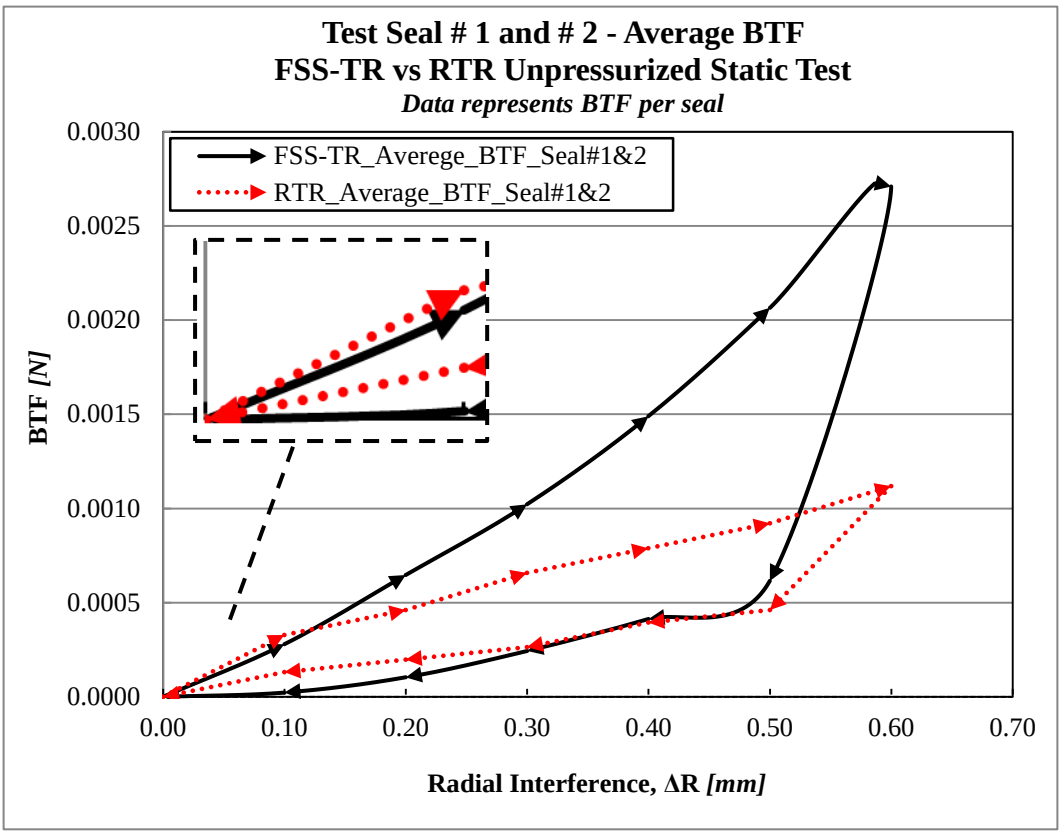

Figure 4.48: Bristle tip force change with rotor interference, comparison of RTR and FSS-TR measurements

Test Seal # 1 and #2, Averaged BTF RTR-Unpressurized static test vs. FSS-TR Free state stiffness test			
	ΔR *[mm]*	RTR – Unpressurized static	FSS-TR, Free state stiffness
		BTF *[N]*	BTF *[N]*
LOADING	0.0	0.000000	0.000000
	0.1	0.000329	0.000279
	0.2	0.000460	0.000646
	0.3	0.000658	0.001022
	0.4	0.000789	0.001489
	0.5	0.000921	0.002065
	0.6	0.001118	0.002708
UNLOADING	0.5	0.000460	0.000615
	0.4	0.000395	0.000413
	0.3	0.000263	0.000243
	0.2	0.000197	0.000103
	0.1	0.000132	0.000022
	0.0	0.000000	0.000000

Table 4.8: Bristle tip force comparison of RTR-Unpressurized static stiffness tests and FSS-TR free state stiffness tests

4.5 Rotary Test Rig: Unpressurized – Dynamic BTF Measurements

The RTR – Unpressurized dynamic stiffness case refers to stiffness measurements with rotating rotor and zero-pressure load. Since test seal#1 and #2 are tested at the same time, the post-processed BTF values correspond to average values for test seals.

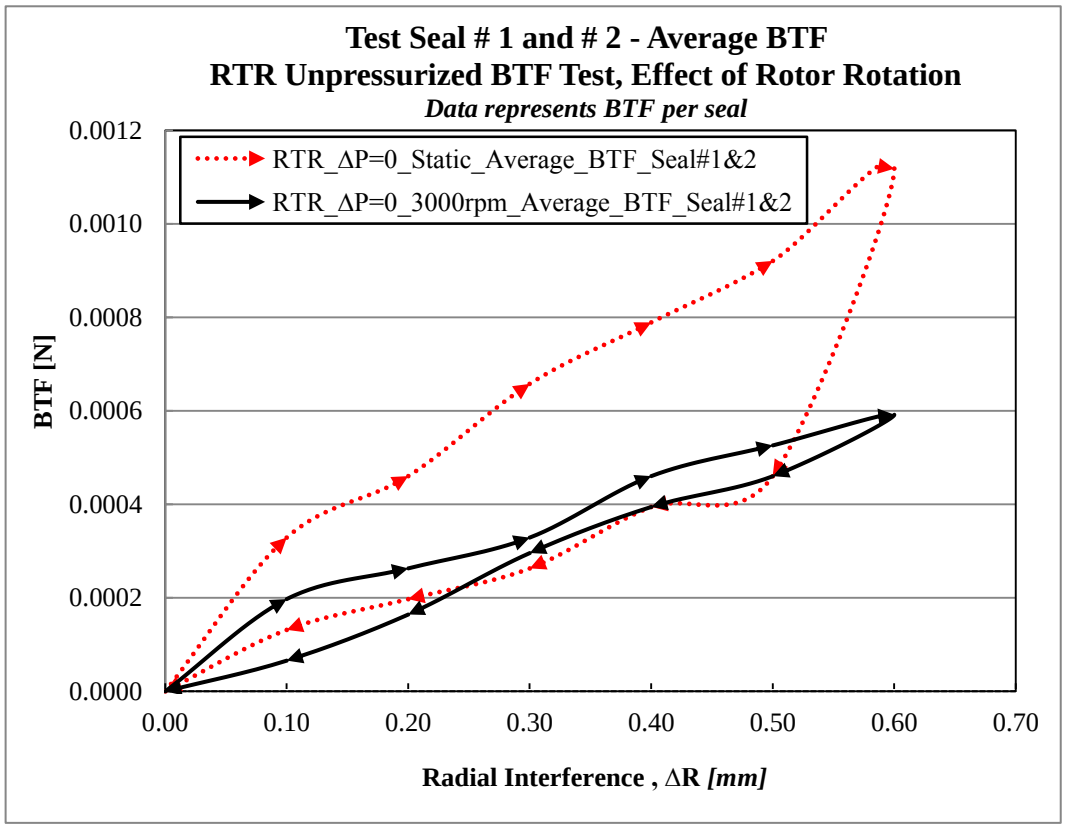

Figure 4.49: Bristle tip force change with rotor interference, effect of rotor rotation on RTR-Unpressurized stiffness measurements

Unpressurized dynamic tests have been performed up to 0.6mm rotor interference and at 3000rpm. BTF results for RTR-Unpressurized dynamic stiffness tests and their comparison with RTR-Unpressurized static BTF measurements are given in Figure 4.49 and tabulated in Table 4.9. As detailed in the figure, the BTF values decrease when the rotor rotation is introduced, which is an expected behavior of brush seal since the rotor-bristle friction decreases with increased surface speed, and rotor rotation causes dynamic effects, which result in some bristles to flutter and loose contact with rotor.

Test Seal # 1 and #2, Averaged BTF RTR-Unpressurized dynamic test vs. RTR-Unpressurized static test			
	ΔR *[mm]*	**RTR – Unpressurized dynamic tests at 3000rpm**	**RTR – Unpressurized static tests**
		BTF *[N]*	**BTF *[N]***
LOADING	0.0	0.000000	0.000000
	0.1	0.000197	0.000329
	0.2	0.000263	0.000460
	0.3	0.000329	0.000658
	0.4	0.000460	0.000789
	0.5	0.000526	0.000921
	0.6	0.000592	0.001118
UNLOADING	0.5	0.000460	0.000460
	0.4	0.000395	0.000395
	0.3	0.000296	0.000263
	0.2	0.000164	0.000197
	0.1	0.000066	0.000132
	0.0	0.000000	0.000000

Table 4.9: Bristle tip force comparison of RTR-Unpressurized dynamic stiffness tests and RTR - Unpressurized static stiffness tests

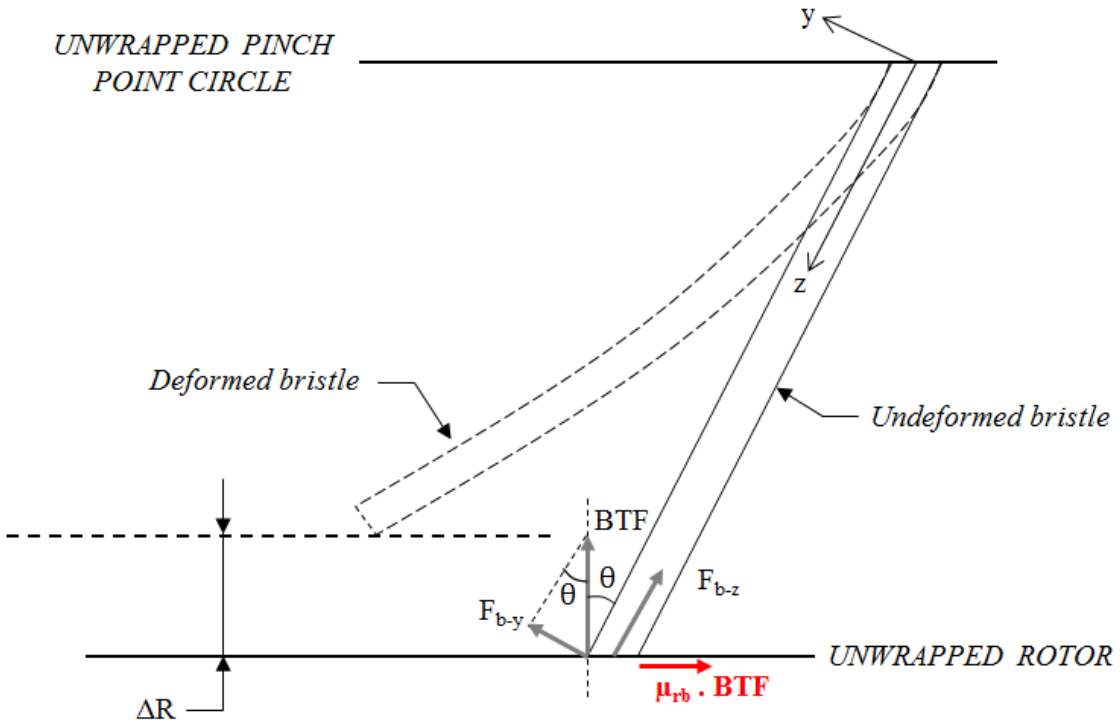

Figure 4.50: Force balance illustration on a bristle in unpressurized BTF measurements – loading step

The effect of rotation can also be observed as reduction in free-state hysteresis, which is mainly due to rotor-bristle friction as explained in Figure 4.50. In the loading step, bristles slide over the rotor surface while the friction force between bristle tip and rotor acts in the reverse direction to motion. As it can be seen from the figure, to be able to obtain same transverse load -$F_{b\text{-}y}$- to bend bristles, higher BTF is required when the friction is introduced. In conclusion, the effect of rotor rotation, which causes rotor-bristle friction to decrease and introduces bristle chattering, can be observed as reduction in measured BTF values in loading step and in free-state hysteresis *(measured BTF values in loading step are close to unloading step BTF measurements)*.

4.6 Rotary Test Rig: Pressurized – Static BTF Measurements

The RTR – Pressurized static stiffness case refers to stiffness measurements for a pressurized seal with non-rotating rotor. Since test seal#1 and #2 are tested at the same time, the post-processed BTF values correspond to average values for test seals.

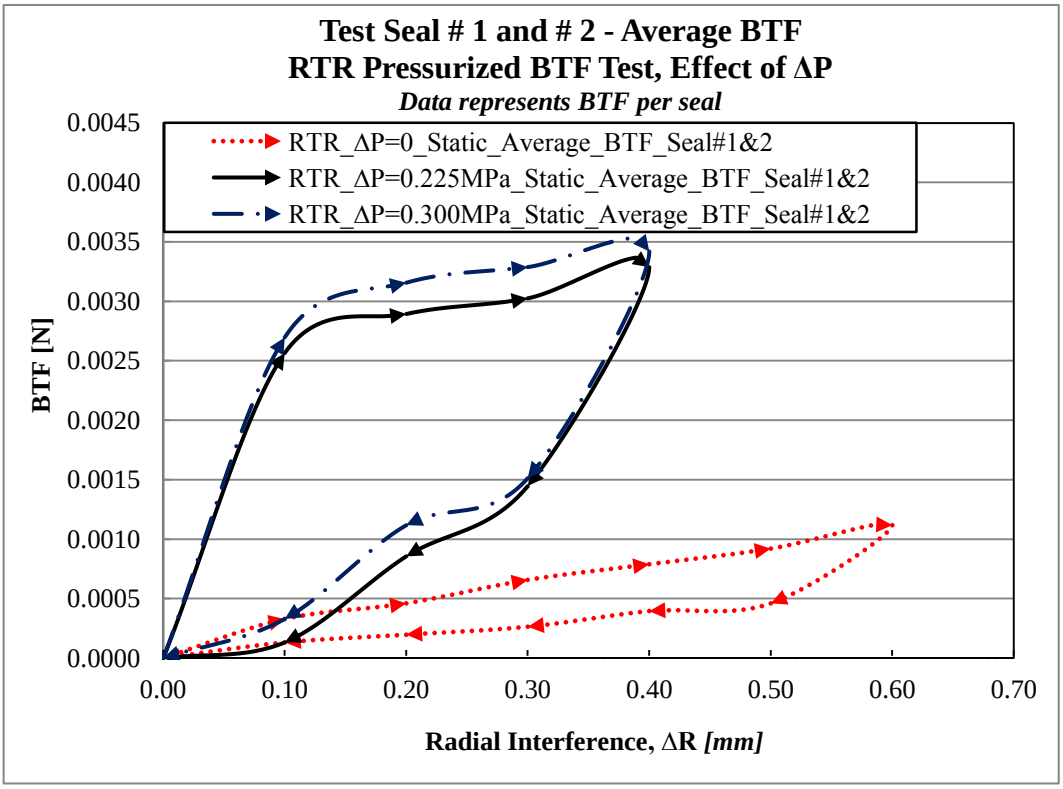

Figure 4.51: Bristle tip force change with rotor interference, effect of pressure load on RTR - Static stiffness measurements

Pressurized static tests have been performed up to 0.4mm rotor interference and at pressure loads of 2.25bar and 3bar. BTF results for RTR-Pressurized static stiffness tests and their comparison with RTR-Unpressurized static BTF measurements are given in Figure 4.51 and tabulated in Table 4.10. As detailed in the figure, the BTF values increase as the pressure load is introduced, which is also named as *"pressure-stiffening"* effect. The pressure load compresses the bristles and introduces inter-bristle and bristle pack-backing plate contact with friction. Therefore, bristles behave much stiffer to rotor interference when the pressure load is applied since the rotor interference not only overcomes the bristle bending, but also it overcomes the inter-bristle and backing plate frictional resistance.

Test Seal # 1 and #2, Averaged BTF RTR-Unpressurized static test vs. Pressurized static tests				
	ΔR *[mm]*	**Unpressurized, Static**	**ΔP=2.25 bar, Static**	**ΔP=3.00 bar, Static**
		BTF *[N]*	**BTF *[N]***	**BTF *[N]***
LOADING	0.0	0.000000	0.000000	0.000000
	0.1	0.000329	0.002565	0.002697
	0.2	0.000460	0.002894	0.003157
	0.3	0.000658	0.003025	0.003288
	0.4	0.000789	0.003288	0.003420
	0.5	0.000921	N/A	N/A
	0.6	0.001118	N/A	N/A
UNLOADING	0.5	0.000460	N/A	N/A
	0.4	0.000395	N/A	N/A
	0.3	0.000263	0.001447	0.001513
	0.2	0.000197	0.000855	0.001118
	0.1	0.000132	0.000132	0.000329
	0.0	0.000000	0.000000	0.000000

Table 4.10: Bristle tip force comparison of RTR-Unpressurized static stiffness tests and RTR - Pressurized static stiffness tests at different pressure load levels

As it can be seen from Figure 4.51, the bristle tip force suddenly increases up to 0.1mm rotor interference and then slightly increases above that point. This pressurized-nonrotating rotor BTF response is an expected behavior and can be named as *"BTF stabilization"*. Due to pressure load, inter-bristle and bristle pack-backing plate contacts with friction are introduced, and bristles bent under the backing plate while FH point acts as support. As the rotor is moved towards the pressurized seal to apply interference, inter-bristle and bristle pack-backing plate contact surfaces already have frictional stick-slip conditions, which is the main reason for pressure stiffening and high BTF values in pressurized-nonrotating rotor conditions. Therefore, bristle tip force for a loaded seal

suddenly increases up to 0.1mm rotor interference, and slightly changes above that point. The loading mechanism and deformation profile for bristles in a loaded seal will be further detailed with CAE analyses of this study and presented in next chapters.

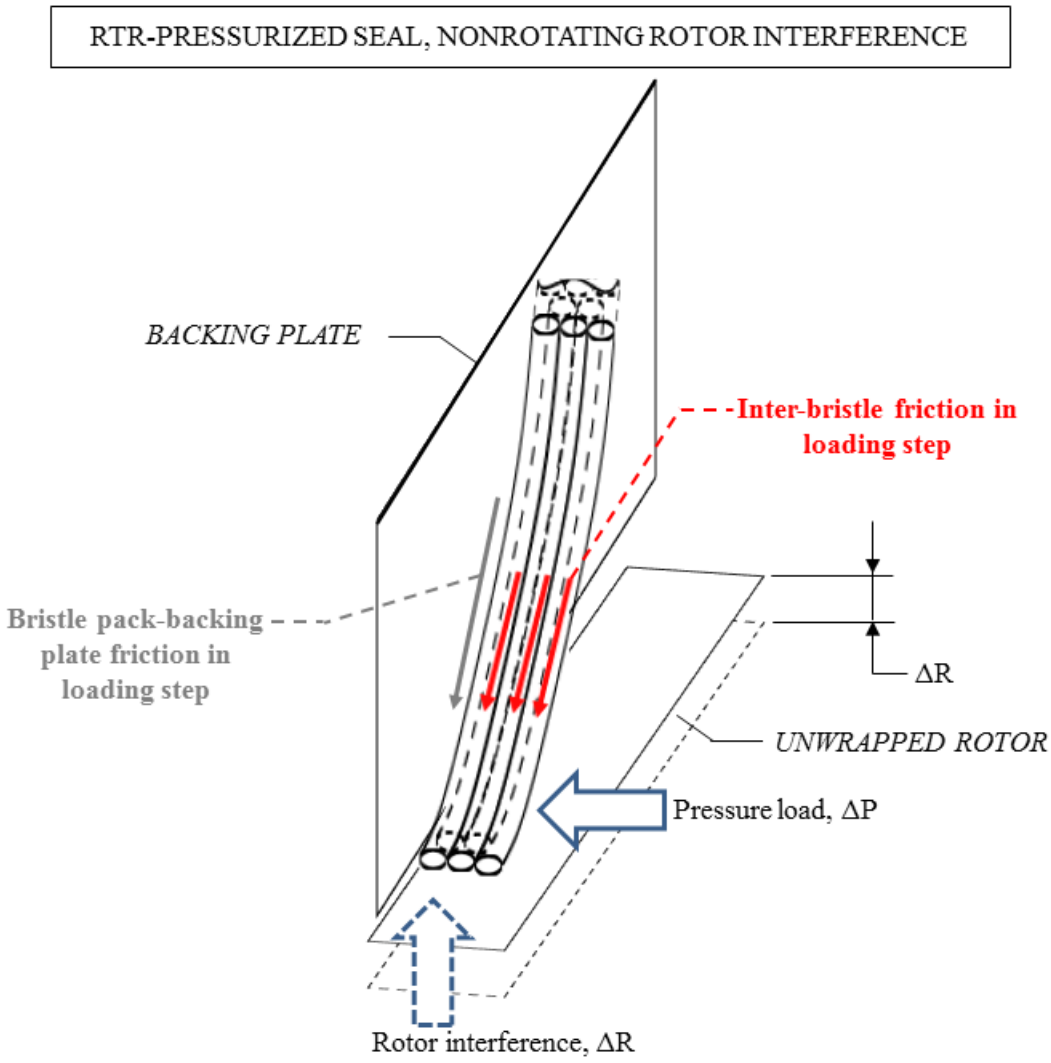

Figure 4.52: RTR-Pressurized seal, non-rotating rotor interference, illustration of inter-bristle friction and bristle-backing plate friction in loading step

The difference in BTF values in loading and unloading steps is larger for pressurized seals, which is named as *"pressurized hysteresis"*. As mentioned before, the reason for *"free-state hysteresis"* in an unpressurized seal is the friction between rotor and bristles. However, in a pressurized seal, the inter-bristle and bristle pack-backing plate friction cause seal stiffening and increase in BTF values in loading step, while frictional forces act in the reverse direction and cause much lower BTF values in unloading step, which in turn results in higher hysteresis in pressurized conditions. The

direction of frictional forces in loading step of a pressurized seal is illustrated in Figure 4.52. The direction of illustrated frictional forces is reversed while rotor is pulled back to its original position – in unloading step. In the case of very high pressure loads, bristle locking and hung-up phenomenon can be observed, where bristles cannot trace the rotor surface in unloading step due to frictional effects. This is very important phenomenon in turbine applications since hung-up issues yield effective clearance values to increase, which means degradation in seal leakage performance.

4.7 Rotary Test Rig: Pressurized – Dynamic BTF Measurements

The RTR – Pressurized dynamic stiffness case refers to stiffness measurements for a pressurized seal with rotating rotor. Since test seal#1 and #2 are tested at the same time, the post-processed BTF values correspond to average values for test seals.

Pressurized dynamic tests have been performed up to 0.4mm rotor interference and at pressure loads of 2.25bar and 3bar. BTF results for RTR-Pressurized dynamic stiffness tests and their comparison with RTR-Pressurized static BTF measurements are given in Figures 4.53 and 4.54 and tabulated in Table 4.11. As it can be seen from figures, the BTF values for a pressurized seal decrease in loading step when rotor rotation is applied. On the contrary, rotor rotation causes higher BTF values in the unloading step for pressurized seal, and pressurized hysteresis is much lower for pressurized-dynamic cases. The main reason for this is the dynamic effects introduced by rotor rotation, which results in bristle flutter and inter-bristle contact loose. Dynamic effects on bristles cause inter-bristle and bristle-backing plate friction to decrease both in loading and unloading cases, which results in less resistance in loading step and BTF-loading values to decrease, while loose of frictional forces yields BTF-unloading values to increase during the rotor is being moved back to its original position.

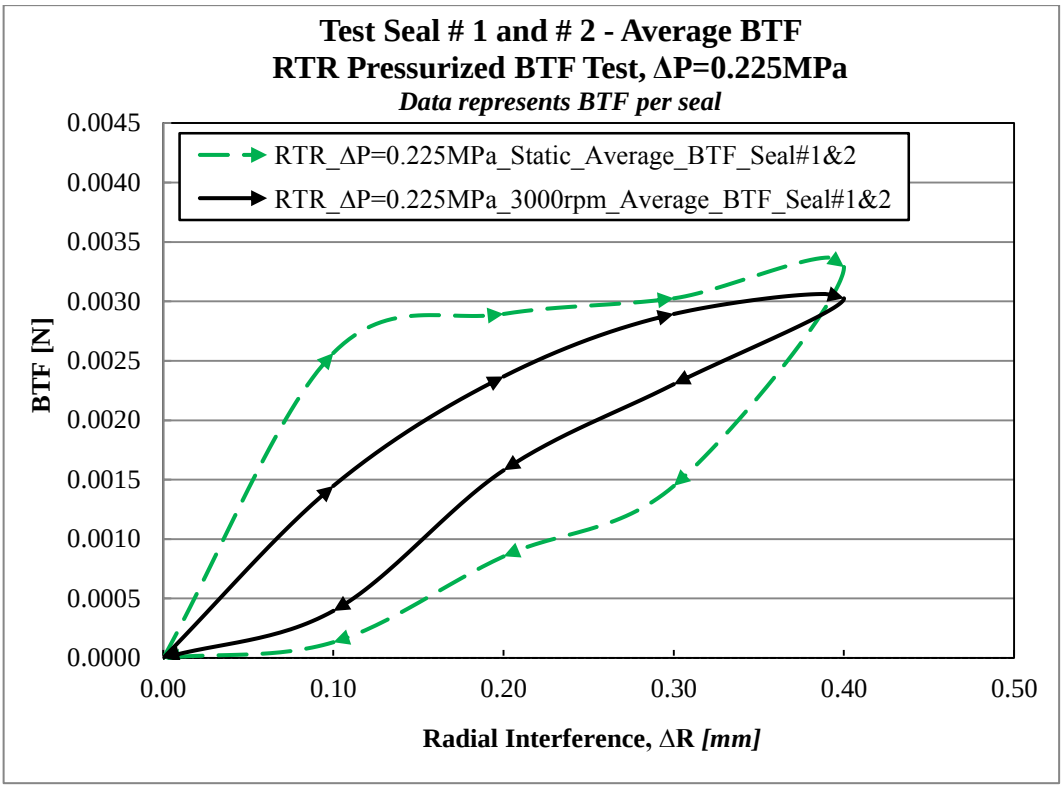

Figure 4.53: BTF comparison for pressurized – static and pressurized – dynamic measurements, ΔP=2.25 bar

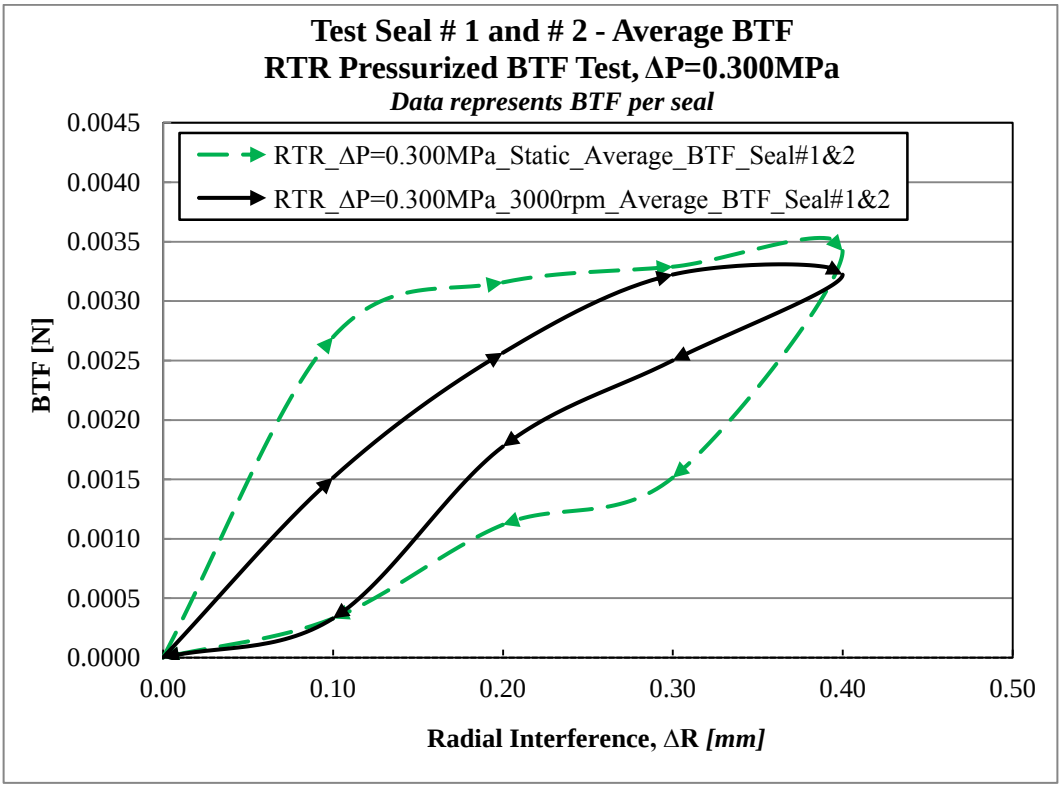

Figure 4.54: BTF comparison for pressurized – static and pressurized – dynamic measurements, ΔP=3 bar

Test Seal # 1 and #2, Averaged BTF RTR-Pressurized static test vs. Pressurized dynamic tests					
	ΔR *[mm]*	ΔP=2.25 bar		ΔP=3.00 bar	
		Static	3000rpm	Static	3000rpm
		BTF *[N]*	BTF *[N]*	BTF *[N]*	BTF *[N]*
LOADING	0.0	0.000000	0.000000	0.000000	0.000000
	0.1	0.002565	0.001447	0.002697	0.001513
	0.2	0.002894	0.002368	0.003157	0.002565
	0.3	0.003025	0.002894	0.003288	0.003223
	0.4	0.003288	0.003025	0.003420	0.003223
UNLOAD	0.3	0.001447	0.002302	0.001513	0.002499
	0.2	0.000855	0.001578	0.001118	0.001776
	0.1	0.000132	0.000395	0.000329	0.000329
	0.0	0.000000	0.000000	0.000000	0.000000

Table 4.11: Bristle tip force comparison for pressurized – static and pressurized – dynamic measurements at different pressure loads

5 BRUSH SEAL STRUCTURAL ANALYSIS – ANALYTICAL STUDIES AND CORRELATION WITH TESTS

Brush seal stiffness tests provide bristle tip force data, which is very important in determining wear ratios of bristles and identifying rotor stability issues. However, bristle stress levels and deformation profile of the bristle pack, both of which play important role in determining the stable leakage performance of the seal, cannot be measured with stiffness tests. Therefore, correlated structural analyses are required to obtain bristle stress levels and to avoid bristle loss issues due to LCF and HCF. Structural analyses for brush seals have been performed and detailed in this study. Analyses start with analytical studies and their correlation with stiffness tests, which are detailed in this section.

The analytical studies in the literature are limited due to complex behavior of fine diameter bristles and frictional affects in the brush seal pack. Flower [17] considers a single bristle as a cantilever beam deforming under rotor interference. More complex formulation based on contact mechanics is provided by Stango et al. [44] to calculate bristle tip force and displacement under rotor rub conditions without pressure load. The only analytical formulation for bristle deformation under pressure load is given by Zhao et al. [45]. However, they assume uniform pressure load that does not change with rotor interference and they do not evaluate bristle tip forces under pressurized conditions.

In this study, beam theory suggested by Flower [17] is applied to tested seals and results are compared with the RTR-unpressurized static BTF measurements. Modified beam theory, which includes the effect of rotor-bristle friction on unpressurized-static stiffness, has been developed and presented in this study. Analytical formulations for steady-state turbine conditions have been derived by using both uniform pressure load at FH region and 7^{th} order polynomial fit to experimental pressure profile provided by Bayley et al. [59] and Turner et al. [60]. Analytical studies have also been performed by including the effect of rotor interference on uniformly loaded length and pressure profile change. Furthermore, a closed-form formulation, where backing-plate-bristle and rotor-bristle frictional effects have been included, has been developed to evaluate

pressurized stiffness of brush seals, and results are compared with RTR-Unpressurized stiffness test data.

5.1 Analytical Studies for Unpressurized-Static Rotor Interference Conditions

Unpressurized static rotor interference case refers to conditions of RTR-unpressurized static stiffness tests, where the pressure load is zero and the rotor does not rotate. In addition to simple beam theory suggested by Flower [17], modified beam theory is developed and presented in the following sections. Analyses results are also compared with the RTR-Unpressurized static stiffness test data.

5.1.1 Simple Beam Theory – No Friction

The simple beam theory suggested by Flower [17] does not take any frictional effects into account, and it is the basic analyses to simulate bristle stresses and BTF at unpressurized rotor interference conditions. As visualized in Figure 5.1, the enforced motion introduced by the rotor results in bristle to deflect in local-y direction of the bristle. The bristle deflection formula using the simple beam theory is given in Equation 5.1. In the equation, *"y_d"* is the bristle tip deflection in y-direction, *"$F_{b\text{-}y}$"* is the y-component of the bristle tip force, *"F_b"*, *"E"* is the elastic modulus for the bristle material, *"I_x"* is the bristle's second moment of area about x-axis, and *"L"* is the free bristle length.

$$y_d = \frac{F_{b-y} \cdot L^3}{3EI_x} \tag{5.1}$$

$$I_x = \frac{\pi d^4}{64} \tag{5.2}$$

$$y_d = \frac{\Delta R}{\sin(\theta)} \tag{5.3}$$

Using Equations 5.1 thru 5.3, the bristle tip contact force using simple beam theory can be written as,

$$F_b = \frac{Ed^4 \Delta R}{6.7906 L^3 \sin^2(\theta)} \tag{5.4}$$

In Equation 5.4, *"d"* is the bristle diameter, *"θ"* is the cant angle and *"ΔR"* is the radial rotor interference. As the bristle tip force, *"F_b"*, is obtained, the seal stiffness can be found by simply dividing the force to radial rotor interference.

$$K_{beam-BTF} = \frac{F_b}{\Delta R} \tag{5.5}$$

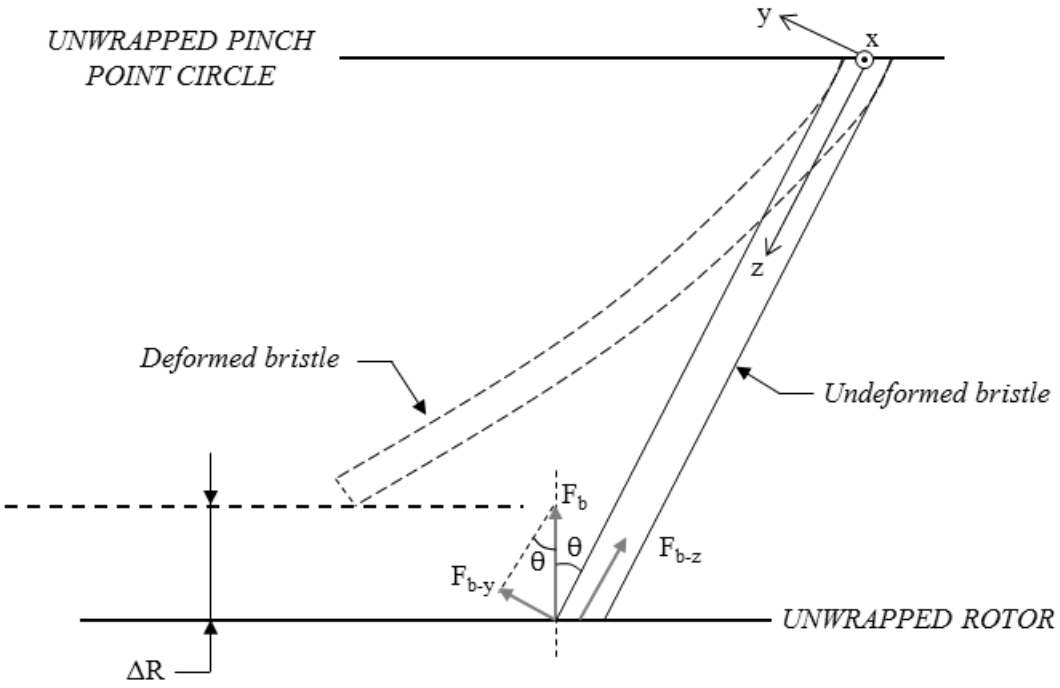

Figure 5.1: Simple beam theory – Loads acting on a bristle in unpressurized-static rotor interference conditions

The simple beam analysis can be utilized to calculate bristle stresses, which are induced by rotor interference in unpressurized conditions. The free body diagram and internal loads of a bristle in unpressurized rotor rub conditions are shown in Figure 5.2.

The bristle tip contact force causes axial and shear loads, and also generates a bending moment. The change of internal shear force in y-direction, $V_y(z)$, internal bending moment in x-direction, $M_x(z)$, and internal axial load, $F_z(z)$, are also given in Figure 5.2.

The most critical cross section in terms of stress is located at z=0, where $V_x(z)$, $F_z(z)$ and $M_x(z)$ take their maximum values. Three types of stresses are generated due rotor interference in unpressurized bristle as given in Equations 5.6 thru 5.8. In those equations, *"A"* is the bristle cross-sectional area, *"r"* is the bristle radius and *"y"* is the y-distance from the geometric center of the bristle cross-section.

- Normal stress due to bending moment $M_x(z)$,

$$\sigma_{bend-M_x} = \frac{M_x}{I_x} \cdot y \tag{5.6}$$

- Normal stress due to axial load $F_z(z)$,

$$\sigma_{axial} = \frac{F_z}{A} \tag{5.7}$$

- Transverse shear stress due to $V_y(z)$,

$$\tau_{zy} = \frac{4}{3} \cdot \frac{V_y}{\pi r^2} \cdot \left(1 - \frac{y^2}{r^2}\right) \tag{5.8}$$

As it can be seen from the Figure 5.2, the most critical cross-section for the bristle is located at z=0, which refers to pinch point. Three critical points exist at the pinch-point cross-section,

- Stress state for the critical point 1, (x,y) = (0,-d/2)
  - Maximum normal stress due to bending, tensile, $\sigma_{bend\text{-}Mx\text{-}max}$
  - Maximum normal stress due to axial load, compressive, $\sigma_{axial\text{-}max}$
- Stress state for the critical point 2, (x,y) = (0,0)
  - Maximum normal stress due to axial load, compressive, $\sigma_{axial\text{-}max}$
  - Maximum transverse shear stress, $\tau_{zy\text{-}max}$
- Stress state for the critical point 3, (x,y) = (0,d/2)
  - Maximum normal stress due to bending, compressive, $\sigma_{bend\text{-}Mx\text{-}max}$
  - Maximum normal stress due to axial load, compressive, $\sigma_{axial\text{-}max}$

Equivalent Von-Mises stress should be calculated for the 3D stress-states at critical points.

$$\sigma_{VM} = \sqrt{\frac{(\sigma_x - \sigma_y)^2 + (\sigma_y - \sigma_z)^2 + (\sigma_z - \sigma_x)^2 + 6 \cdot (\tau_{xy}^2 + \tau_{yz}^2 + \tau_{zx}^2)}{2}} \tag{5.9}$$

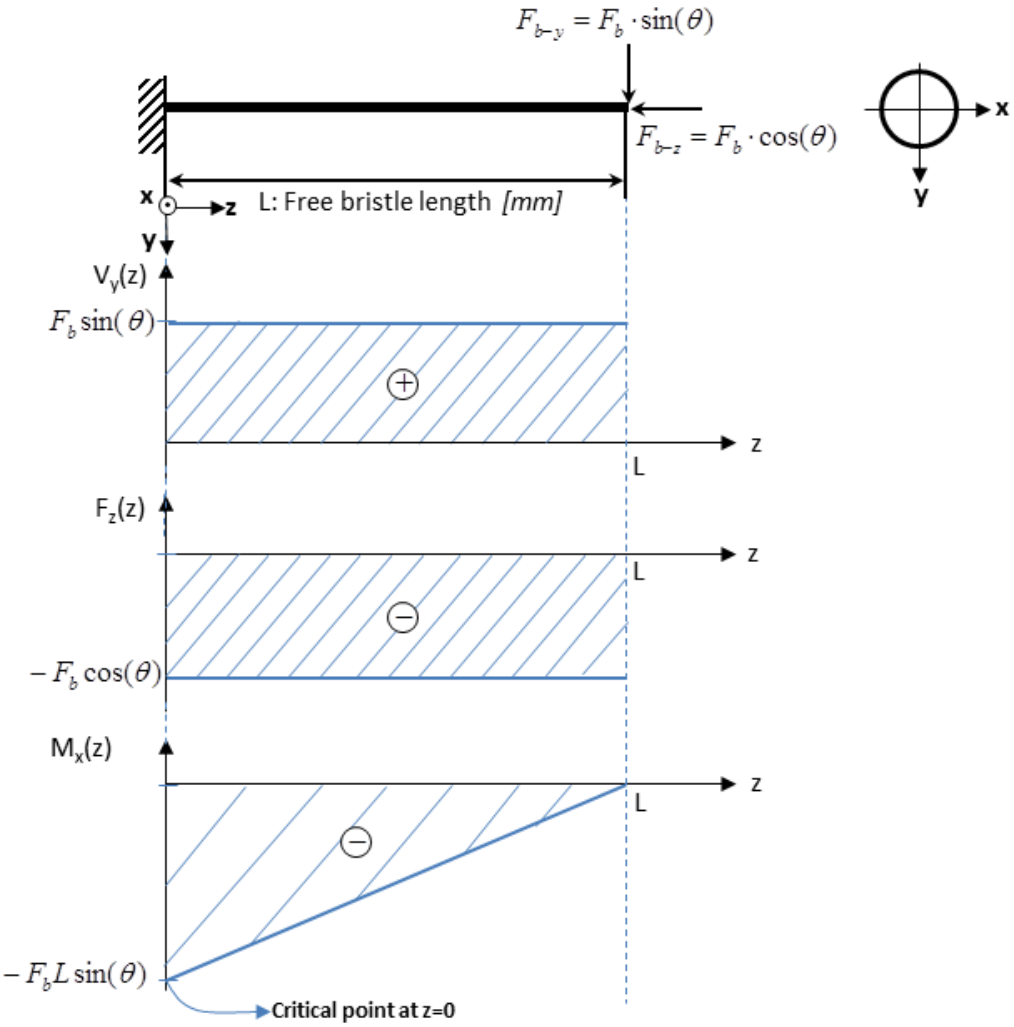

Figure 5.2: Bristle internal forces and moments under unpressurized-rotor interference conditions

The simple beam theory has been run for test seal parameters given in Tables 2.3 and 2.4 with the Haynes 25 material properties at room temperature provided in Table 2.7. Comparison of BTF and stiffness values obtained from the simple beam theory with the RTR-Unpressurized static stiffness test results is given in Figure 5.3 and Table 5.1. As it can be seen from the figure and table, the simple beam theory cannot simulate the hysteresis since it does not take the frictional affects into account, and it gives exactly same BTF values at same interference levels of loading and unloading steps. However, in reality, the frictional affects causes much lower BTF values in the unloading step than the values obtained in the loading step, which is so called free-state hysteresis. As a result of excluded frictional effects, the simple beam theory BTF values are lower than the loading step BTF values of RTR-Unpressurized static stiffness tests. In contrary, simple beam theory gives higher BTF magnitudes than the RTR test results in the unloading step, where frictional affects takes place in the reverse direction.

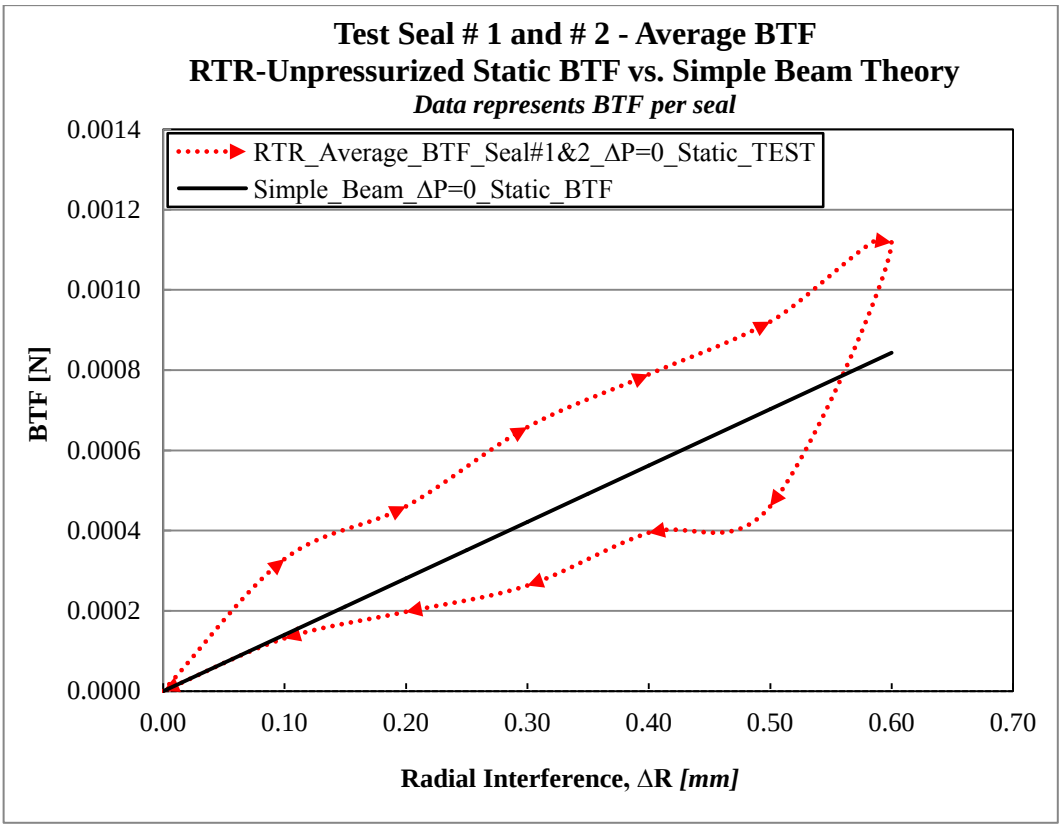

Figure 5.3: Unpressurized static rotor conditions – BTF comparison for test seals, RTR test results vs. Simple beam theory

RTR – Unpressurized static test vs. Simple Beam Theory *RTR results are averaged data for Test Seal #1&2*					
	ΔR *[mm]*	**RTR – Unpressurized static**		**Simple beam theory**	
		BTF *[N]*	**$K_{seal-RTR}$ *[N/mm]***	**BTF *[N]***	**$K_{simple-beam}$ *[N/mm]***
LOADING	0.0	0.000000		0.000000	
	0.1	0.000329	0.00329	0.000141	0.00141
	0.2	0.000460	0.00230	0.000282	0.00141
	0.3	0.000658	0.00219	0.000423	0.00141
	0.4	0.000789	0.00197	0.000564	0.00141
	0.5	0.000921	0.00184	0.000705	0.00141
	0.6	0.001118	0.00186	0.000846	0.00141
UNLOADING	0.5	0.000460	0.00092	0.000705	0.00141
	0.4	0.000395	0.00099	0.000564	0.00141
	0.3	0.000263	0.00088	0.000423	0.00141
	0.2	0.000197	0.00099	0.000282	0.00141
	0.1	0.000132	0.00132	0.000141	0.00141
	0.0	0.000000		0.000000	

Table 5.1: Unpressurized static rotor conditions – BTF and stiffness comparison for test seals, RTR test results vs. Simple beam theory

Unpressurized Static Rotor Interference for Test Seals Stress Levels on a Bristle – Simple Beam Theory			
Critical point 1, (x,y,z) = (0, -d/2, 0)			
ΔR *[mm]*	Max. bending stress $\sigma_{bend\text{-}Mx\text{-}max}$ *[N/mm²]*	Max. axial stress $\sigma_{axial\text{-}Mx\text{-}max}$ *[N/mm²]*	VM stress *[N/mm²]*
0.0	0.000	0.000	0.000
0.1	-16.534	-0.012	16.546
0.2	-33.067	-0.025	33.092
0.3	-49.601	-0.037	49.637
0.4	-66.134	-0.049	66.183
0.5	-82.668	-0.061	82.729
0.6	**-99.201**	**-0.074**	**99.275**
Critical point 2, (x,y,z) = (0, 0, 0)			
ΔR *[mm]*	Max. transverse shear stress, $\tau_{zy\text{-}max}$ *[N/mm²]*	Max. axial stress $\sigma_{axial\text{-}Mx\text{-}max}$ *[N/mm²]*	VM stress *[N/mm²]*
0.0	0.000	0.000	0.000
0.1	0.016	-0.012	0.031
0.2	0.033	-0.025	0.062
0.3	0.049	-0.037	0.093
0.4	0.065	-0.049	0.123
0.5	0.082	-0.061	0.154
0.6	0.098	-0.074	0.185
Critical point 3, (x,y,z) = (0, d/2, 0)			
ΔR *[mm]*	Max. bending stress $\sigma_{bend\text{-}Mx\text{-}max}$ *[N/mm²]*	Max. axial stress $\sigma_{axial\text{-}Mx\text{-}max}$ *[N/mm²]*	VM stress *[N/mm²]*
0.0	0.000	0.000	0.000
0.1	16.534	-0.012	16.521
0.2	33.067	-0.025	33.042
0.3	49.601	-0.037	49.564
0.4	66.134	-0.049	66.085
0.5	82.668	-0.061	82.606
0.6	**99.201**	**-0.074**	**99.127**

Table 5.2: Unpressurized static rotor conditions – Stress levels at critical points of bristle critical section, simple beam theory

Stress levels at critical points of bristle critical cross-section have been calculated for selected test seals by using the simple beam theory, and the results are summarized in Table 5.2. The VM stress level at the bristle increases with rotor interference as expected for unpressurized static rotor interference conditions. As a result of large L/d ratio of the bristle, the stress state is bending dominant, where axial and transverse shear stress levels are almost equal to zero. Although VM stress levels are almost equal to each other for critical points 1 and 3, the point 3 is the most critical one since the dominant bending stress is in tension mode.

5.1.2 Modified Beam Theory

Stiffness and bristle tip force results of simple beam theory and their comparison with RTR-Unpressurized static stiffness measurements emphasized the effect of friction and the lack of friction included analytical formulation in the literature. Therefore, modified beam theory has been developed in this study.

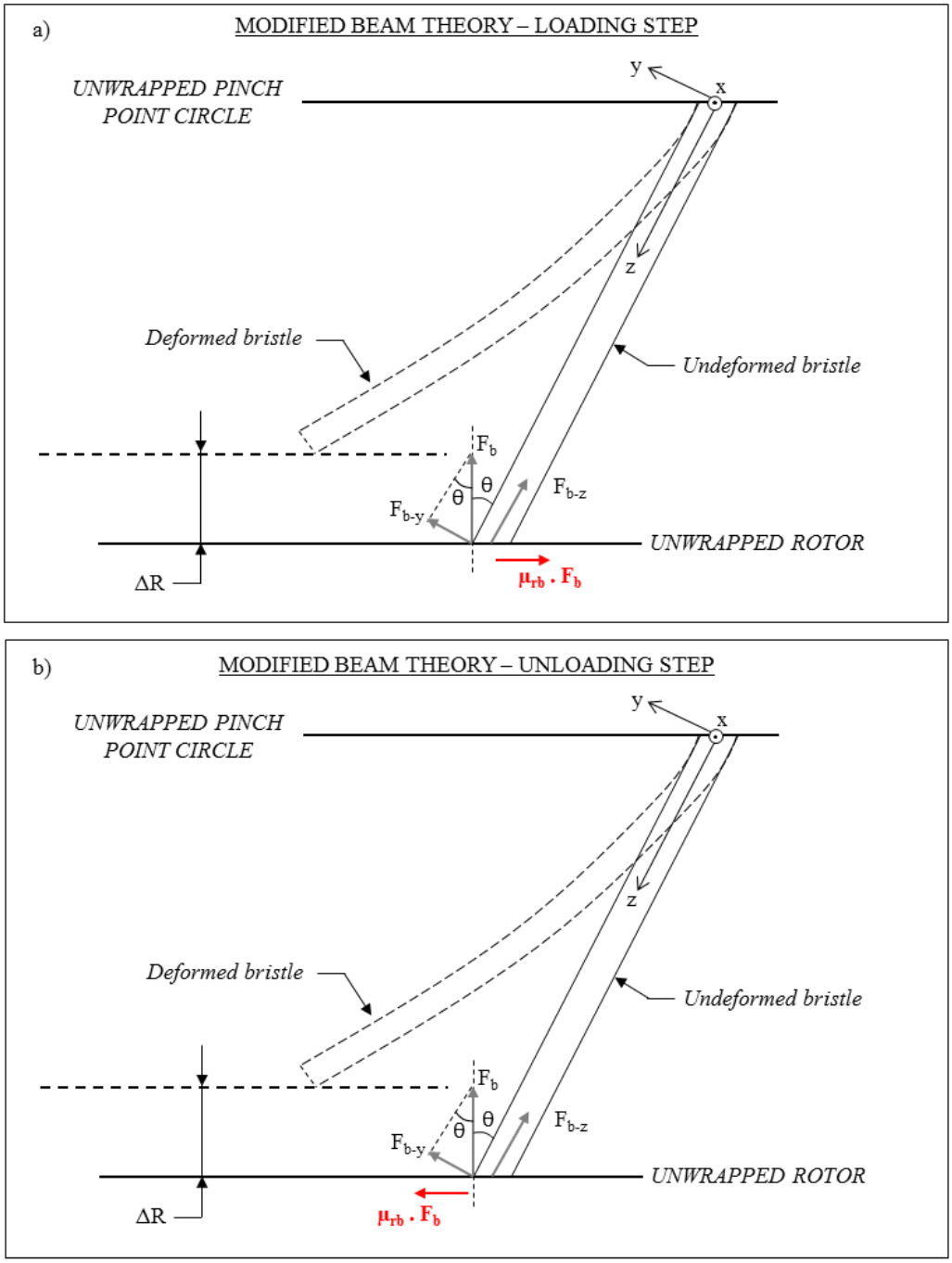

Figure 5.4: Modified beam theory – Loads acting on a bristle in unpressurized-static rotor interference conditions, a) Loading step, b) Unloading step

In the modified beam theory, the effect of frictional forces between bristles and rotor is included to analytical formulations. The frictional forces in the loading and unloading steps are applied in the opposite direction. Loads acting on a bristle in modified beam theory are detailed in Figure 5.4, and formulas for modified beam theory and their comparison with the simple beam theory are given in Table 5.3.

Simple Beam Theory	**Modified Beam Theory – Loading step**	**Modified Beam Theory – Unloading step**
$y_d = \frac{F_{b-y} \cdot L^3}{3EI_x} = \frac{\Delta R}{\cos(\theta)}$	$y_d = \frac{F_{b-y} \cdot L^3}{3EI_x} = \frac{\Delta R}{\cos(\theta)}$	$y_d = \frac{F_{b-y} \cdot L^3}{3EI_x} = \frac{\Delta R}{\cos(\theta)}$
$F_{b-y} = \frac{Ed^4 \Delta R}{6.7906 L^3 \sin(\theta)}$	$F_{b-y} = \frac{Ed^4 \Delta R}{6.7906 L^3 \sin(\theta)}$	$F_{b-y} = \frac{Ed^4 \Delta R}{6.7906 L^3 \sin(\theta)}$
$F_b = \frac{F_{b-y}}{\sin(\theta)}$	$F_b = \frac{F_{b-y}}{\left[\sin(\theta) - \mu_{rb} \cdot \cos(\theta)\right]}$	$F_b = \frac{F_{b-y}}{\left[\sin(\theta) + \mu_{rb} \cdot \cos(\theta)\right]}$
$F_{b-z} = F_b \cdot \cos(\theta)$	$F_{b-z} = F_b \cdot \cos(\theta) + \mu_{rb} \cdot F_b \cdot \sin(\theta)$	$F_{b-z} = F_b \cdot \cos(\theta) - \mu_{rb} \cdot \sin(\theta)$
$\sigma_{bend-\max} = \frac{F_{b-y} L}{I} \cdot \left(\frac{d}{2}\right)$	$\sigma_{bend-\max} = \frac{F_{b-y} L}{I} \cdot \left(\frac{d}{2}\right)$	$\sigma_{bend-\max} = \frac{F_{b-y} L}{I} \cdot \left(\frac{d}{2}\right)$
$\tau_{transv-\max} = \frac{4F_{b-y}}{3A}$	$\tau_{transv-\max} = \frac{4F_{b-y}}{3A}$	$\tau_{transv-\max} = \frac{4F_{b-y}}{3A}$
$\sigma_{axial} = \frac{F_{b-z}}{A}$	$\sigma_{axial} = \frac{F_{b-z}}{A}$	$\sigma_{axial} = \frac{F_{b-z}}{A}$
**** Please see the nomenclature for the definitions of variables used in formulas.***		

Table 5.3: Analytical formulations for unpressurized static rotor conditions – Simple beam theory vs. Modified beam theory

The effect of rotor-bristle friction coefficient on seal stiffness is included to analysis in modified beam theory through bristle tip force, F_b. There are several studies exist in the literature for Haynes 25 – rotor pair friction characterization based on friction and wear tests of H25 bristles [61, 62, 63, 64]. Fellenstein et al. [61] performed friction and wear tests for Haynes 25 bristles vs. nickel based super-alloy – I718 – journal, and reported friction coefficients ranged from 0.25 to 0.47 for different temperature levels and surface speeds. Those results are also tabulated in Table 5.4. In their other studies [62, 63, 64], Fellenstein et al. conducted friction-wear tests by

rubbing H25 bristles against surfaces having different types of coating, and found friction coefficients ranging from 0.32 to 0.42. They also mentioned that the effect of processing method on friction coefficient is minimal while the material content has the major effect in determining the friction and wear characteristics of the tribo-pair. Crudgington et al. [46] used the coefficient of 0.4 as the highest value for the friction coefficient between H25 bristles and rotor in their analyses.

Haynes 25 vs. I718, Friction Coefficient at Different Test Conditions Environment: Air			
Test Conditions			Average friction coefficient
Temperature	Surface speed	Contact force	
20 ^{o}C	1.99 m/s	0.49 N	0.34 ± 0.05
20 ^{o}C	1.99 m/s	0.98 N	0.42 ± 0.05
20 ^{o}C	23.94 m/s	0.49 N	0.41 ± 0.05
20 ^{o}C	23.94 m/s	0.98 N	0.47 ± 0.05
650 ^{o}C	1.99 m/s	0.49 N	0.25 ± 0.05
650 ^{o}C	1.99 m/s	0.98 N	0.27 ± 0.05
650 ^{o}C	23.94 m/s	0.49 N	0.33 ± 0.05
650 ^{o}C	23.94 m/s	0.98 N	0.40 ± 0.05

Table 5.4: Haynes 25 vs. I718, friction coefficient at different test conditions at air environment, Fellenstein et al. [61]

RTR - Unpressurized static tests of this study have been performed with stainless steel rotor. Therefore, friction coefficients ranging from 0.20 to 0.35 have been used for analytical studies of selected test seals with modified beam theory. Test seal parameters tabulated in Tables 2.3 and 2.4, and H25 material properties at room temperature provided in Table 2.7 have been used for modified beam calculations.

Comparison of BTF and stiffness values obtained from the modified beam theory with the RTR-Unpressurized static stiffness measurements is given in Figures 5.5-5.6 and tabulated in Table 5.4. As it can be seen from the figures, the modified beam theory successfully simulates the effect of friction on BTF values, and results show good agreement with the test data for rotor-bristle friction coefficient of 0.35. The correlated friction coefficient value of 0.35 is also consistent with the friction data in the literature [61, 62, 63, 64]. Unlike simple beam theory, the free-state hysteresis is successfully simulated with developed modified beam theory. The difference between loading and unloading step BTF magnitudes increases with increasing rotor-bristle friction coefficient as expected. The modified beam theory provides a quick and valuable data for stiffness comparison of different seal designs.

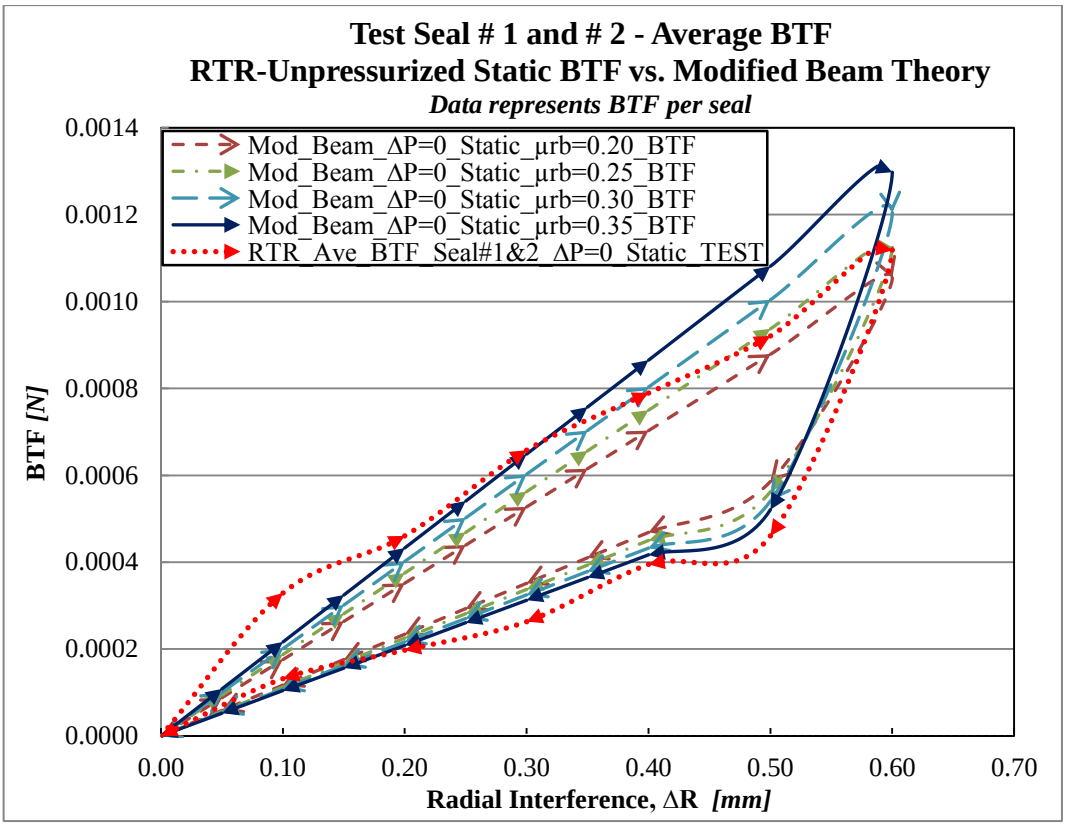

Figure 5.5: Unpressurized static rotor conditions – BTF comparison for test seals, RTR test results vs. modified beam theory at different rotor-bristle friction coefficients

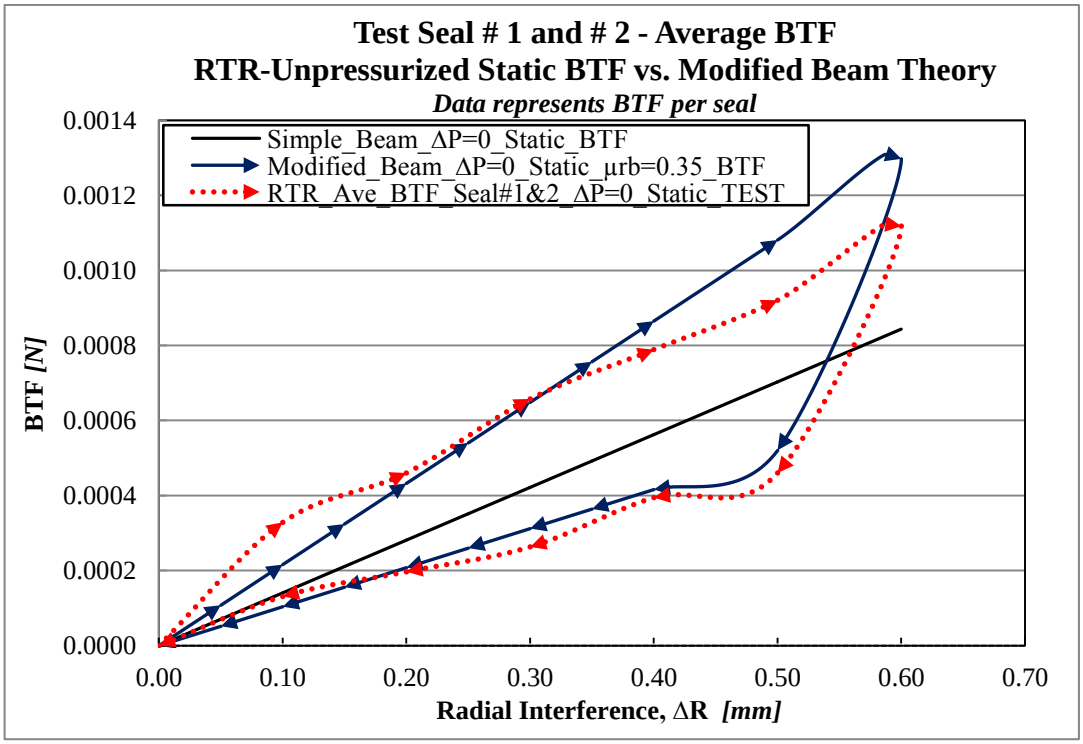

Figure 5.6: Unpressurized static rotor conditions – BTF comparison for test seals, RTR test results comparison with simple beam theory and modified beam theory with μ_{rb}=0.35

TR – Unpressurized static test vs. Modified Beam Theory *RTR results are averaged data for Test Seal #1&2*											
	ΔR	**RTR–Unpress. Static Tests**		**Modified Beam Theory**							
				μ_{rb} = 0.20		**μ_{rb} = 0.25**		**μ_{rb} = 0.30**		**μ_{rb} = 0.35**	
	[mm]	**BTF *[N]***	**$K_{seal-RTR}$ *[N/mm]***	**BTF *[N]***	**K_{mod-b} *[N/mm]***	**BTF *[N]***	**K_{mod-b} *[N/mm]***	**BTF *[N]***	**K_{mod-b} *[N/mm]***	**BTF *[N]***	**K_{mod-b} *[N/mm]***
LOADING	0.0	0.000000		0.000000		0.000000		0.000000		0.000000	
	0.1	0.000329	0.00329	0.000176	0.00176	0.000187	0.00187	0.000201	0.00201	0.000216	0.00216
	0.2	0.000460	0.00230	0.000352	0.00176	0.000374	0.00187	0.000402	0.00201	0.000432	0.00216
	0.3	0.000658	0.00219	0.000528	0.00176	0.000561	0.00187	0.000603	0.00201	0.000648	0.00216
	0.4	0.000789	0.00197	0.000704	0.00176	0.000748	0.00187	0.000804	0.00201	0.000864	0.00216
	0.5	0.000921	0.00184	0.000880	0.00176	0.000935	0.00187	0.001005	0.00201	0.001080	0.00216
	0.6	0.001118	0.00186	0.001056	0.00176	0.001122	0.00187	0.001206	0.00201	0.001296	0.00216
UNLOAD	0.5	0.000460	0.00092	0.000585	0.00117	0.000560	0.00112	0.000540	0.00108	0.000520	0.00104
	0.4	0.000395	0.00099	0.000468	0.00117	0.000448	0.00112	0.000432	0.00108	0.000416	0.00104
	0.3	0.000263	0.00088	0.000351	0.00117	0.000336	0.00112	0.000324	0.00108	0.000312	0.00104
	0.2	0.000197	0.00099	0.000234	0.00117	0.000224	0.00112	0.000216	0.00108	0.000208	0.00104
	0.1	0.000132	0.00132	0.000117	0.00117	0.000112	0.00112	0.000108	0.00108	0.000104	0.00104
	0.0	0.000000		0.000000		0.000000		0.000000		0.000000	

Table 5.5: Unpressurized static rotor conditions – BTF and stiffness comparison for test seals, RTR test results vs. Modified beam theory at different rotor-bristle friction coefficients

Unpressurized Static Rotor Interference for Test Seals Stress Levels on a Bristle – Modified vs. Simple Beam Theory						
Critical point 1, (x,y,z) = (0, -d/2, 0)						
ΔR *[mm]*	Max. bending stress $\sigma_{bend-Mx-max}$ *[N/mm²]*		Max. axial stress $\sigma_{axial-Mx-max}$ *[N/mm²]*		VM stress *[N/mm²]*	
	Simple t.	Modified t.	Simple t.	Modified t.	Simple t.	Modified t.
0.0	0.000	0.000	0.000	0.000	0.000	0.000
0.1	-16.534	-16.534	-0.012	-0.025	16.546	16.599
0.2	-33.067	-33.067	-0.025	-0.051	33.092	33.118
0.3	-49.601	-49.601	-0.037	-0.076	49.637	49.677
0.4	-66.134	-66.134	-0.049	-0.102	66.183	66.236
0.5	-82.668	-82.668	-0.061	-0.127	82.729	82.795
0.6	**-99.201**	**-99.201**	**-0.074**	**-0.153**	**99.275**	**99.354**
Critical point 2, (x,y,z) = (0, 0, 0)						
ΔR *[mm]*	Max. transverse shear stress, τ_{zy-max} *[N/mm²]*		Max. axial stress $\sigma_{axial-Mx-max}$ *[N/mm²]*		VM stress *[N/mm²]*	
	Simple t.	Modified t.	Simple t.	Modified t.	Simple t.	Modified t.
0.0	0.000	0.000	0.000	0.000	0.000	0.000
0.1	0.016	0.016	-0.012	-0.025	0.031	0.038
0.2	0.033	0.033	-0.025	-0.051	0.062	0.076
0.3	0.049	0.049	-0.037	-0.076	0.093	0.114
0.4	0.065	0.065	-0.049	-0.102	0.123	0.152
0.5	0.082	0.082	-0.061	-0.127	0.154	0.190
0.6	0.098	0.098	-0.074	**-0.153**	0.185	0.228
Critical point 3, (x,y,z) = (0, d/2, 0)						
ΔR *[mm]*	Max. bending stress $\sigma_{bend-Mx-max}$ *[N/mm²]*		Max. axial stress $\sigma_{axial-Mx-max}$ *[N/mm²]*		VM stress *[N/mm²]*	
	Simple t.	Modified t.	Simple t.	Modified t.	Simple t.	Modified t.
0.0	0.000	0.000	0.000	0.000	0.000	0.000
0.1	16.534	16.534	-0.012	-0.025	16.521	16.508
0.2	33.067	33.067	-0.025	-0.051	33.042	33.016
0.3	49.601	49.601	-0.037	-0.076	49.564	49.524
0.4	66.134	66.134	-0.049	-0.102	66.085	66.032
0.5	82.668	82.668	-0.061	-0.127	82.606	82.540
0.6	**99.201**	**99.201**	**-0.074**	**-0.153**	**99.127**	**99.048**

Table 5.6: Unpressurized static rotor conditions – Stress levels at critical points of bristle critical section, simple beam theory vs. modified beam theory

Bristle stress levels at rotor interference conditions have been calculated using the modified beam theory. Comparison of results with simple beam theory is provided in Table 5.6. Analyses results show that the equivalent VM stress levels evaluated by using the modified beam theory are slightly different than the simple beam theory data since the dominant bending stress due to interference is same for both theories. The reason for the slight difference is due to increased axial loads in modified beam theory, which is a result of introduced rotor-bristle friction.

5.2 Analytical Studies for Steady State Conditions

Steady state case refers to turbine operating conditions without rotor interference, where seal operates under pressure load. Bristle stress levels at steady state are critical in determining seal life since brush seals operate mostly in steady state turbine conditions. Analytical studies for steady state pressure load conditions start with simple approach, which assumes uniform pressure load only at the fence height region. Advanced methodology is developed for steady state calculations and presented in this study, which approximates the pressure load of 7^{th} order polynomial fit to experimental pressure profile provided by Bayley et al. [59] and Turner et al. [60].

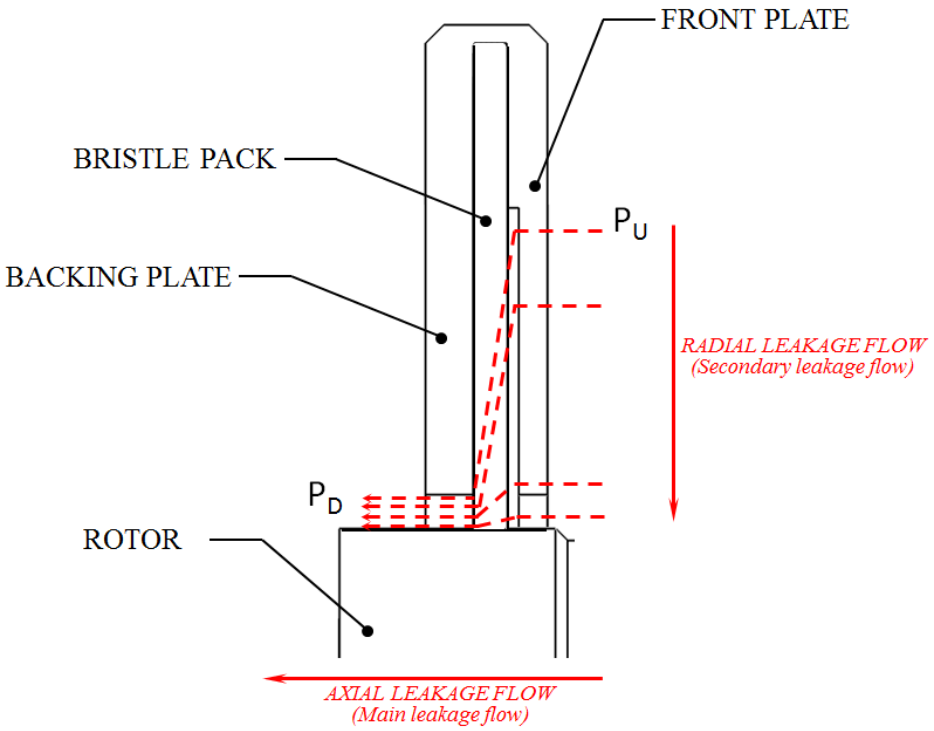

Figure 5.7: Leakage flow profile through the bristle pack

Studies performed by Duran [65] and Bhate et al. [66] indicate almost linear pressure drop in the axial direction as illustrated in Figure 5.7. Steady state analytical formulations of this study also assume linear pressure change amongst the bristle pack in the axial direction.

5.2.1 Simple Approach for Steady State Conditions

Pressure load in the axial direction is the main reason for the bending of bristles at steady state conditions. Assuming that the radial interference is zero, and neglecting the friction, the bristles can be simply assumed to be loaded uniformly with the distributed load of *"w"* at the fence height region as given in Figure 5.8. Last row of bristles are supported by the backing plate inner radius. Loads and constraints for the last row of bristles at steady state conditions *(with zero radial interference)* are illustrated in Figure 5.7. In the figure, *"L"* denotes the free bristle length and *"b"* is the loaded length. The loaded length is calculated by using the Equation 5.10.

$$b = \frac{FH}{\cos\theta} \tag{5.10}$$

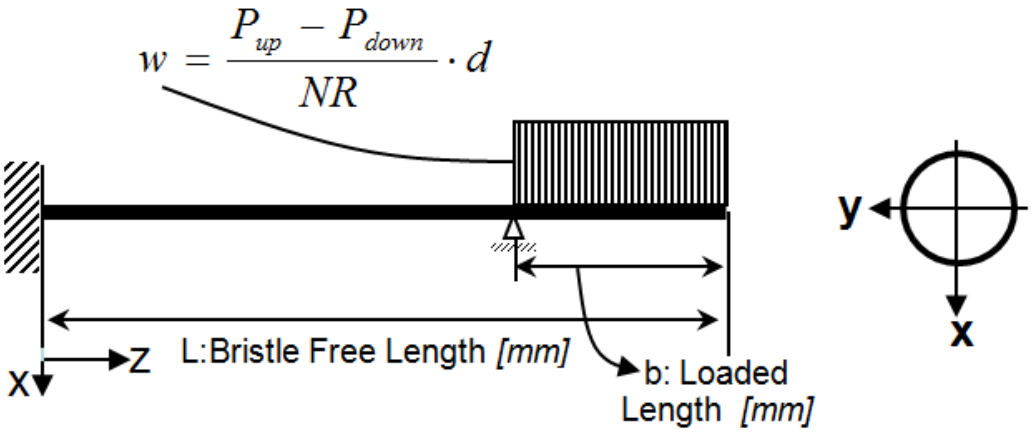

Figure 5.8: Steady state conditions – Simple approach, Loads and constraints for the last row of bristles *(backing plate side)*

The uniformly distributed load on a single bristle at steady state conditions is denoted by *"w"*, and defined by Equation 5.11.

$$w = \frac{P_u - P_d}{NR} \cdot d = \frac{\Delta P}{NR} \cdot d \tag{5.11}$$

In Equation 5.11, *"P_u"* is the upstream pressure, *"P_d"* is the downstream pressure, *"ΔP"* is the total pressure load in axial direction, *"NR"* is the number of bristle rows in axial direction and *"d"* is the bristle diameter.

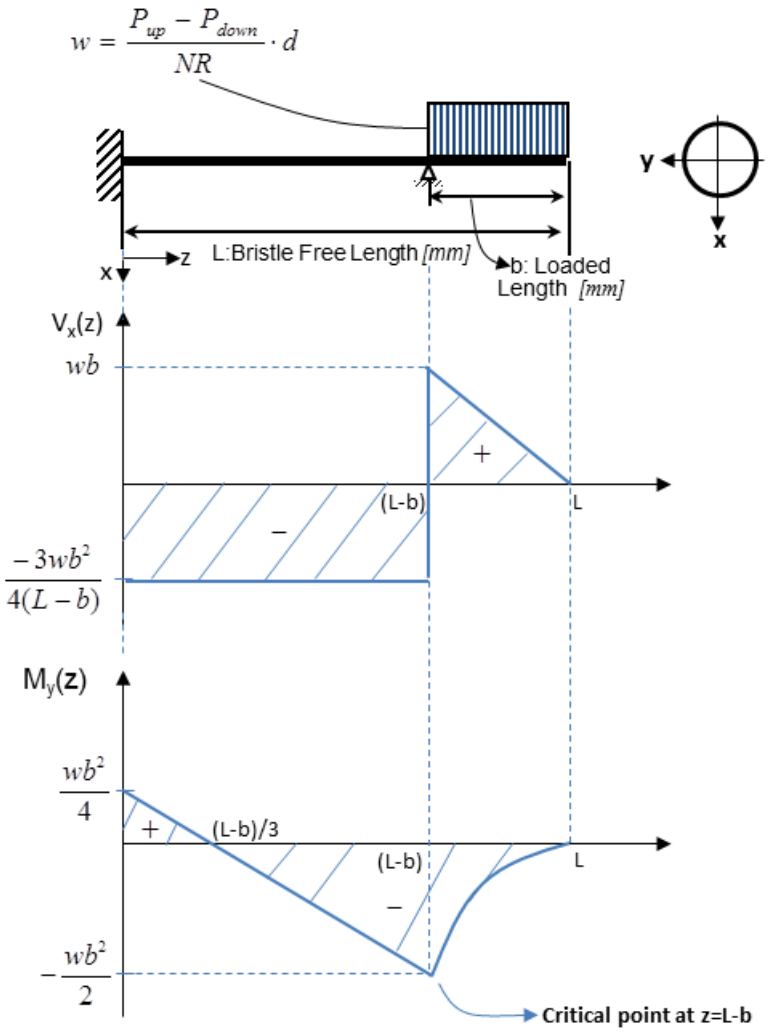

Figure 5.9: Steady state conditions – Simple approach, Bristle internal forces and moments under pressure load without rotor interference

Considering the above loadings and constraints on a bristle, internal shear force in x-direction, $V_x(z)$, and internal bending moment in y-direction, $M_y(z)$ are induced at steady state conditions with zero radial interference. The change of internal load is given in Figure 5.9. The critical cross section in terms of stresses is located at z=L-b *(fence height point, which corresponds to backing plate inner radius support)*, where the $M_y(z)$ takes its maximum absolute value. Singularity functions for $V_x(z)$ and $M_y(z)$ are given in Equations 5.12 and 5.13.

$$V_x(z) = \frac{wb^2}{4}\langle z-0\rangle^{-1} - \frac{3}{4}\frac{wb^2}{(L-b)}\langle z-0\rangle^{0} + wb\left\{1+\frac{3b}{4(L-b)}\right\}\langle z-(L-b)\rangle^{0} - w\langle z-(L-b)\rangle^{1} \quad (5.12)$$

$$M_y(z) = \frac{wb^2}{4}\langle z-0\rangle^{0} - \frac{3}{4}\frac{wb^2}{(L-b)}\langle z-0\rangle^{1} + wb\left\{1+\frac{3b}{4(L-b)}\right\}\langle z-(L-b)\rangle^{1} - \frac{w}{2}\langle z-(L-b)\rangle^{2} \quad (5.13)$$

Two types of stresses are generated due to pressure load at steady state conditions:

- Normal stress due to bending moment $M_y(z)$,

$$\sigma_{bend-M_y} = \frac{M_y}{I_y}\cdot x \quad (5.14)$$

- Transverse shear stress due to $V_x(z)$,

$$\tau_{zx} = \frac{4}{3}\cdot\frac{V_x}{\pi r^2}\cdot\left(1-\frac{x^2}{r^2}\right) \quad (5.15)$$

In Equations 5.14 and 5.15, *"I_y"* is the bristle's second moment of area about y-axis, and *"r"* is the bristle radius. Steady state analyses have been run at 0.3MPa pressure load with the test seal parameters and H25 material properties, which have already been detailed in Chapter 2.

Steady State Conditions – Simple Approach for Test Seals, ΔP = 0.3MPa, ΔR = 0			
Critical section: z = L-b *(Fence height)*			
ΔP *[MPa]*	Max. bending stress $\sigma_{bend\text{-}My\text{-}max}$ *[N/mm²]*	Max. transverse shear stress $\tau_{zx\text{-}max}$ *[N/mm²]*	Max. VM stress *[N/mm²]*
0.3	33.326	0.610	33.326
Critical section: z = 0 *(Pinch point)*			
ΔP *[MPa]*	Max. bending stress $\sigma_{bend\text{-}My\text{-}max}$ *[N/mm²]*	Max. transverse shear stress $\tau_{zx\text{-}max}$ *[N/mm²]*	Max. VM stress *[N/mm²]*
0.3	16.663	0.060	16.663

Table 5.7: Steady State Conditions – Simple beam theory, Stress levels at critical cross section of test seals at ΔP = 0.3MPa

As detailed in Table 5.7, the bending stresses are dominant at steady state conditions, and the transverse shear stress, τ_{zx}, is almost zero, which is a direct result

of high *"L/d"* ratios. The maximum VM stress level at steady state conditions is directly equal to maximum bending stress since the transverse shear stress is equal to zero when the bending stress takes its maximum value at the critical section.

5.2.2 Advanced Approach for Steady State Conditions

In real operating conditions, bristles are exposed to a varying pressure load at full bristle length. Therefore, assuming uniform pressure load only at the fence height region, as in the case of steady state – simple approach analyses, may not fully capture the stresses induced by the complex flow and pressure field. The advanced pressure profile analysis has been developed within the content of this study, and does not exist in the open literature.

In a brush seal, the section below the fence height is exposed to full pressure load of ΔP. However, along the backing plate region the pressure is higher than downstream cavity pressure *(P_d)* at the low pressure side of the brush pack. Therefore, the pressure load on bristles is lower than full ΔP. The experimental data, which was provided by Bayley et. al.[59] and Turner et.al.[60], indicated that pressure load quickly drops to one-tenth of ΔP at the backing plate region *(as moved radially outwards from backing plate inner diameter)*. The non-dimensional pressure at backing plate, P_B^*, can be calculated by fitting a seventh order polynomial to test data.

$$
\begin{aligned}
&P_B^* = 92.9848{Y_s}^{*7} - 378.6135{Y_s}^{*6} + 637.1967{Y_s}^{*5} - 572.4562{Y_s}^{*4} + 295.3330{Y_s}^{*3} \\
&- 87.1507{Y_s}^{*2} + 13.6926{Y_s}^{*} + 0.0034 \\
&\textit{where} \\
&Y_s = y_s / BH, \\
&{Y_s}^{*} = {y_s}^{*} / (BH - FH) \\
&{y_s}^{*} = y_s - FH
\end{aligned}
\qquad (5.16)
$$

"y_s" is the radial distance from brush seal inner diameter, and *"${y_s}^*$"* is the radial distance from fence height, as shown in Figure 5.10. *"Y_s"* and *"${Y_s}^*$"* are the non-dimensional coefficients. A comparison of the non-dimensional pressure equation with the experimental data is given in Figure 5.11, *(${Y_s}^* = 0$ at FH, and ${Y_s}^* = 1$ at BH)*, and the polynomial fit shows good agreement with measurements.

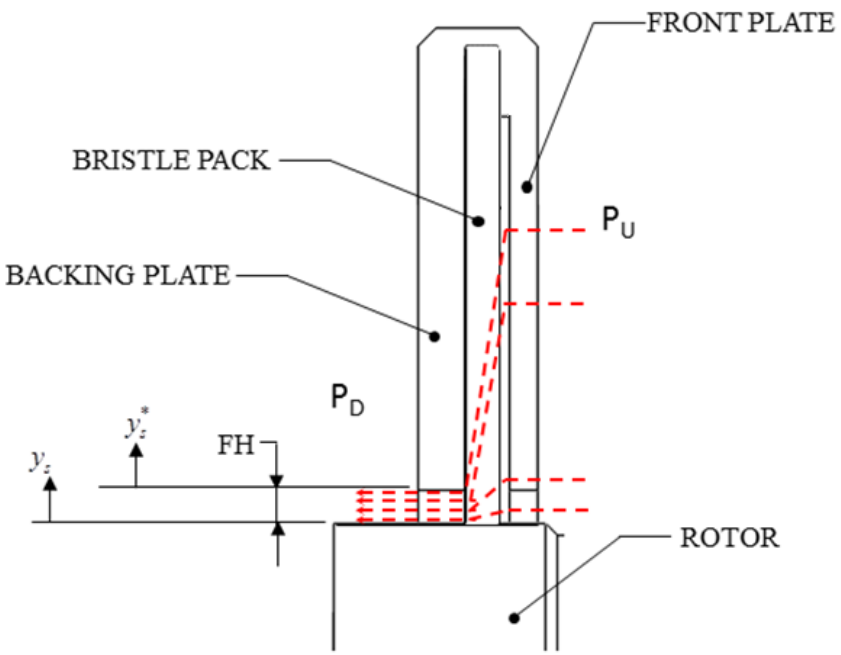

Figure 5.10: Radial distance "y_s" from seal inner diameter and "y_s^*" from fence height for backing plate pressure profile calculations

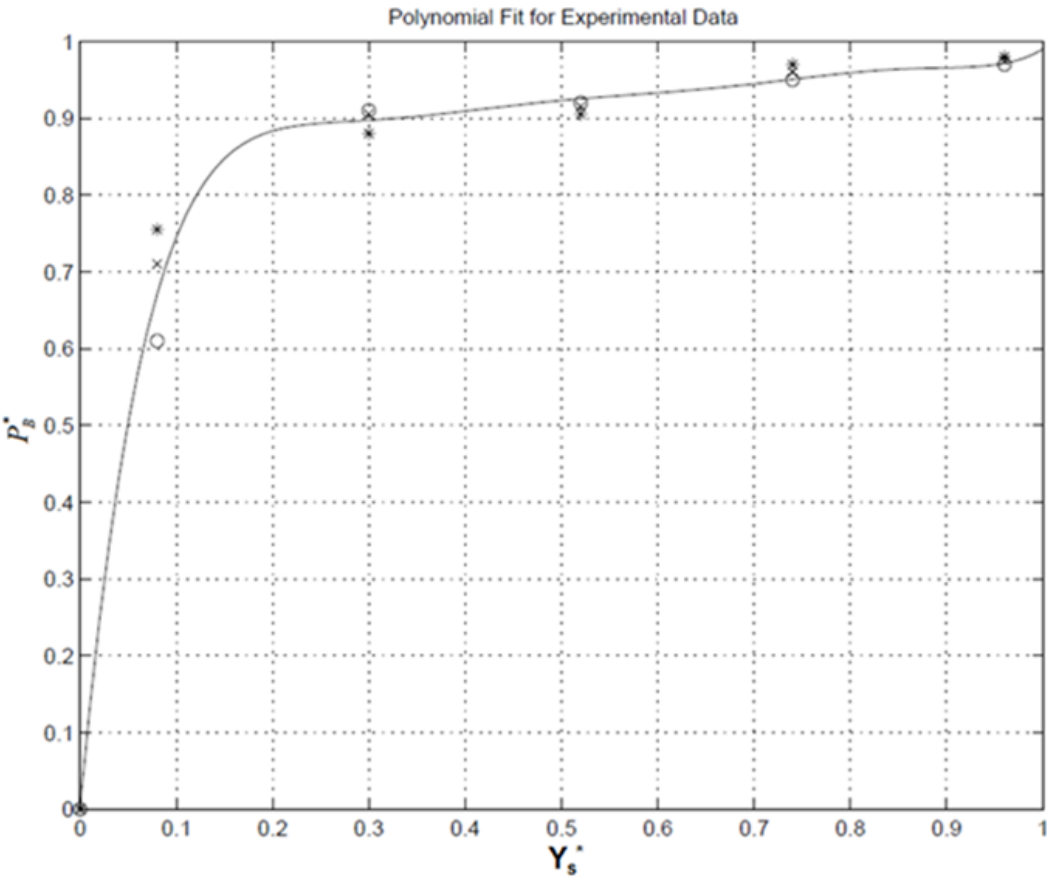

Figure 5.11: Non-dimensional backing plate pressure – 7th order polynomial fit to experimental data [59, 60]

The pressure profile at backing plate *(above the fence height)* can be calculated by using the formula below.

$$P_B = P_B^*(P_u - P_d) + P_d \tag{5.17}$$

Assuming linear pressure drop also at the upper region of the bristle pack, which is the region above the fence height, the pressure load exerted on bristles can be calculated by using the upstream pressure, *"P_u"* and the backing plate pressure, *"P_B"*. In that case, the pressure load at the fence height and backing plate region will be as follows.

- Fence height region:
  - Pressure load at fence height region,

$$\Delta P = (P_u - P_d) \tag{5.18}$$

  - Pressure load per bristle row at fence height region,

$$\Delta P / NR = (P_u - P_d) / NR \tag{5.19}$$

- Backing plate region:
  - Pressure load at backing plate region,

$$\Delta P_B(y_s) = (P_u - P_B(y_s)) \tag{5.20}$$

  - Pressure load per bristle row at backing plate region,

$$\Delta P_B(y_s) / NR = (P_u - P_B(y_s)) / NR \tag{5.21}$$

Equations 5.18 through 5.21 can be used to calculate the pressure load profile on a bristle as a function of *"y_s"*, which is aligned with seal radial direction *(Figure 5.10)*. In steady state conditions, where rotor interference is equal to zero, the uniformly loaded length is equal to *"FH"*, and the backing plate region corresponds to *"BH-FH"*.

The pressure load change with y_s-coordinate *(radial direction)* is given in Figure 5.12 for the test seals, where the full pressure load for the seal, $\Delta P = P_u - P_d$, is taken as 0.3MPa. The figure includes the pressure load profile on a single bristle at zero rotor interference.

As it can be seen from Figure 5.12, the pressure load profile can be divided into three main regions at steady state conditions *(zero rotor interference)*:

- Region 1: $0<y_s<FH$, Uniform full pressure load region,
- Region 2: $FH<y_s<FH+r_1$, Almost linearly loaded region with high pressure gradient of *"$(\Delta P_{1\text{-per row}}-\Delta P_{2\text{-per row}})/r_1$"*,
- Region 3: $FH+r_1<y_s<BH$, Almost linearly loaded region with low pressure gradient of *"$\Delta P_{2\text{-per row}}/r_2$"*.

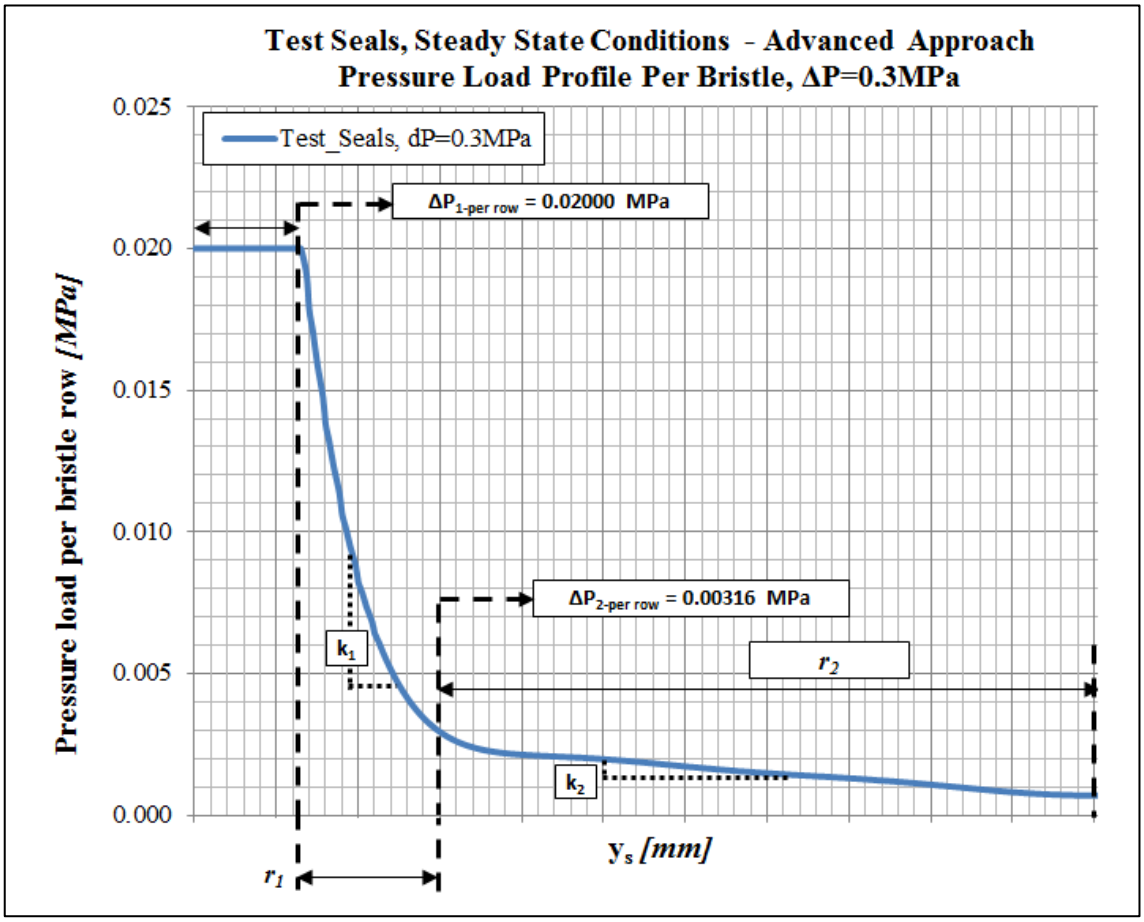

Figure 5.12: Steady state conditions – Advanced approach, Pressure load profile on a single bristle row at ΔP = 0.3MPa, test seals

In advanced approach calculations, the fitted pressure profile on a bristle, which is a 7th order function of y_s-coordinate, is approximated with two linearly and one uniformly distributed load as given in Figure 5.13. *"w_1"* is the uniformly distributed load at fence height region *(Region 1)*, *"w_{b1}"* is the slope of the linearly loaded region with high pressure gradient *(Region 2)*, and *"w_{b2}"* is the slope of the linearly loaded region with low pressure gradient *(Region 3)*.

$$w_1 = \Delta P_{1-per-row} \cdot d = \frac{\Delta P}{NR} \cdot d \tag{5.22}$$

$$w_2 = \Delta P_{2-per-row} \cdot d = \frac{\left[P_u - P_B(FH + r_1)\right]}{NR} \cdot d \tag{5.23}$$

$$w_3 = w_2 - w_1 \tag{5.24}$$

$$w_{b1} = w_3 / a_1 \tag{5.25}$$

$$w_{b2} = w_2 / a_1 \tag{5.26}$$

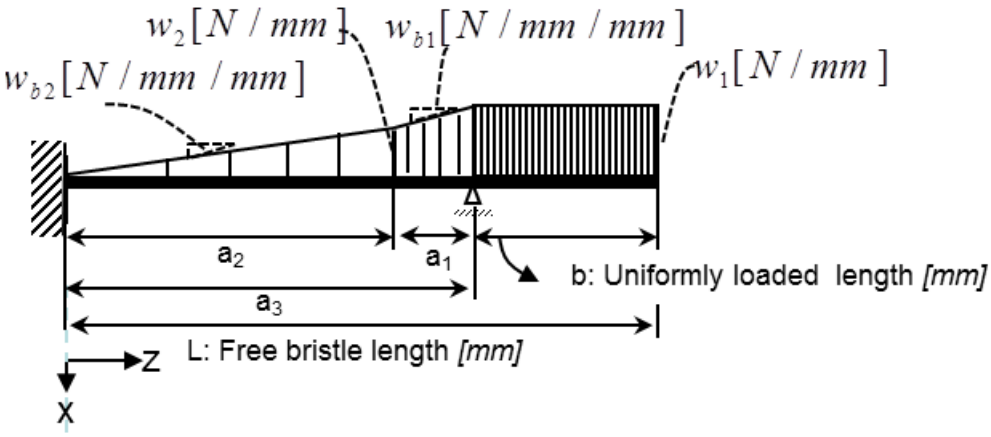

Figure 5.13: Steady state conditions – Advanced approach, Pressure load profile approximation on a single bristle row

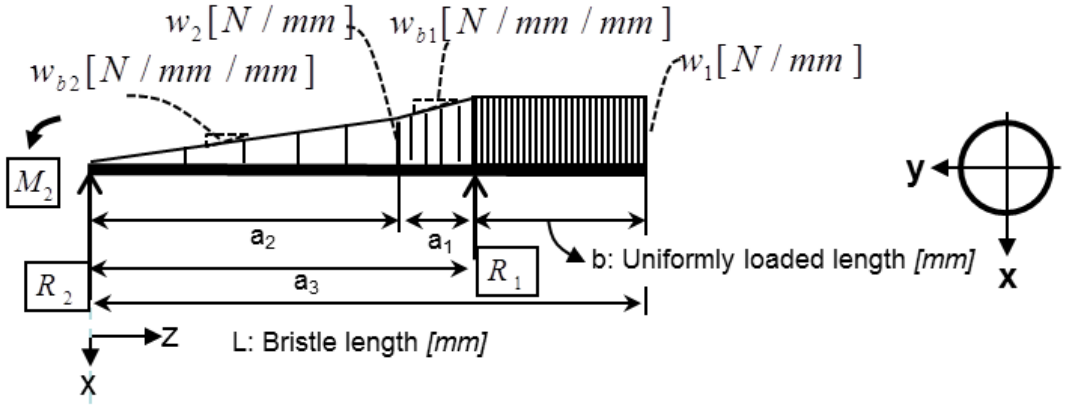

Figure 5.14: Steady state conditions – Advanced approach, Free body diagram for a single bristle under pressure load

At steady state conditions, the uniformly loaded length, *"b"*, is equal to *"FH/cos(θ)"*; the free bristle length, *"L"*, is equal to *"BH/cos(θ)"*; and the length for the linearly loaded region with high pressure gradient, *"a_1"*, is equal to *"r_1/cos(θ)"*.

"a_2*"* is the bristle length which is linearly loaded with low pressure gradient and it equals to *"L-b-*a_1*"*. *"*$a_3=a_1+a_2$*"* is the total length of linearly loaded bristle region.

The free body diagram for the bristle is given in Figure 5.14. *"*R_1*"* and *"*R_2*"* are reaction forces, and *"*M_2*"* is the reaction moment, and their formulae are as following.

$$R_2 = \left\{ (L-a_3)\cdot t_1 - t_2 + \frac{2t_3}{a_3^2} \right\} \cdot \frac{3}{2a_3} \tag{5.27}$$

$$R_1 = -t_1 - R_2 \tag{5.28}$$

$$M_2 = R_2 \cdot L + R_1 \cdot (L-a_3) + t_2 \tag{5.29}$$

where

$$\begin{aligned} t_1 = &-\frac{w_{b2}}{2}L^2 + \frac{w_{b2}}{2}(L-a_2)^2 - \frac{w_{b1}}{2}(L-a_2)^2 - w_1(L-a_3) + w_2(L-a_3) \\ &+ \frac{w_{b1}}{2}(L-a_3)^2 + w_3(L-a_3) \end{aligned} \tag{5.30}$$

$$\begin{aligned} t_2 = &-\frac{w_{b2}}{6}L^3 + \frac{w_{b2}}{6}(L-a_2)^3 - \frac{w_{b1}}{6}(L-a_2)^3 \\ &- \frac{w_1}{2}(L-a_3)^2 + \frac{w_2}{2}(L-a_3)^2 + \frac{w_{b1}}{6}(L-a_3)^3 + \frac{w_3}{2}(L-a_3)^2 \end{aligned} \tag{5.31}$$

$$t_3 = -\frac{w_{b2}}{120}a_3^5 + \frac{w_{b2}}{120}(a_3-a_2)^5 - \frac{w_{b1}}{120}(a_3-a_2)^5 \tag{5.32}$$

The internal shear force, *"*$V_x(z)$*"*, and internal bending moment, *"*$M_y(z)$*"* are given in Equations 5.33 and 5.34 in singular form:

$$\begin{aligned} V_x(z) = &-M_2\langle z-0\rangle^{-1} + R_2\langle z-0\rangle^0 - \frac{w_{b2}}{2}\langle z-0\rangle^2 + \frac{w_{b2}}{2}\langle z-a_2\rangle^2 - \frac{w_{b1}}{2}\langle z-a_2\rangle^2 \\ &+ R_1\langle z-a_3\rangle^0 - w_1\langle z-a_3\rangle^1 + w_2\langle z-a_3\rangle^1 + \frac{w_{b1}}{2}\langle z-a_3\rangle^2 + w_3\langle z-a_3\rangle^1 \end{aligned} \tag{5.33}$$

$$\begin{aligned} M_y(z) = &-M_2\langle z-0\rangle^0 + R_2\langle z-0\rangle^1 - \frac{w_{b2}}{6}\langle z-0\rangle^3 + \frac{w_{b2}}{6}\langle z-a_2\rangle^3 - \frac{w_{b1}}{6}\langle z-a_2\rangle^3 \\ &+ R_1\langle z-a_3\rangle^1 - \frac{w_1}{2}\langle z-a_3\rangle^2 + \frac{w_2}{2}\langle z-a_3\rangle^2 + \frac{w_{b1}}{6}\langle z-a_3\rangle^3 + \frac{w_3}{2}\langle z-a_3\rangle^2 \end{aligned} \tag{5.34}$$

As the internal shear force and bending moment values are evaluated at the fence height point, transverse shear and bending stress levels can be found by using Equations 5.14 and 5.15. MATLAB based code has been developed and steady state analyses using advanced approach have been conducted for 0.3MPa pressure load with the test seal parameters and H25 material properties, which have already been detailed in Chapter 2. Advanced analyses results and their comparison with simple approach-steady state conditions are detailed in Table 5.8. Due to extended loading profile of advanced approach, evaluated pinch point bristle stress levels are higher than simple approach as expected.

Steady State Conditions – ΔP = 0.3MPa, ΔR = 0 Advanced Approach vs. Simple Approach for Test Seals						
Test seal parameters for advanced approach						
FH *[mm]*		1.30	$\Delta P_{1\text{-per row}}$ *[MPa]*		0.02000	
θ *[deg]*		45	$\Delta P_{2\text{-per row}}$ *[MPa]*		0.00316	
Critical section: z = L-b *(Fence height)*						
ΔP *[MPa]*	Max. bending stress $\sigma_{bend\text{-}My\text{-}max}$ *[N/mm²]*		Max. transverse shear stress $\tau_{zx\text{-}max}$ *[N/mm²]*		Max. VM stress *[N/mm²]*	
	Simple a.	Advanced a.	Simple a.	Advanced a.	Simple a.	Advanced a.
0.3	33.326	**33.353**	0.610	**0.619**	33.326	**33.353**
Critical section: z = 0 *(Pinch point)*						
ΔP *[MPa]*	Max. bending stress $\sigma_{bend\text{-}My\text{-}max}$ *[N/mm²]*		Max. transverse shear stress $\tau_{zx\text{-}max}$ *[N/mm²]*		Max. VM stress *[N/mm²]*	
	Simple a.	Advanced a.	Simple a.	Advanced a.	Simple a.	Advanced a.
0.3	16.663	**41.434**	0.060	**0.186**	16.663	**41.434**

Table 5.8: Steady State Conditions – Advanced approach vs. Simple approach, Stress levels at critical cross section of test seals at ΔP = 0.3MPa

The analytical studies for steady state conditions do not include inter-bristle and bristle-backing plate contact into account, both of which is effective in determining bristle stress levels. Discussion will be detailed in Chapter 6, where frictional affects and contacts have been included through CAE analyses.

5.3 Analytical Studies for Combined Loading Conditions

The rotor interference condition without pressure load is the ideal case to simulate test conditions, which have been widely used to characterize brush seals in terms of stiffness. However, in turbine operating conditions, the rotor rub conditions occur under pressure load. In turbojet engines, the turbulence is the main reason for transients,

where rotor partially rubs the seal due to eccentricity. In steam and gas turbines, the rotor reaches to its steady state temperature before casing, and thermal expansion of the rotor yields full rotor-seal interference at turbine start-up. Therefore, simulating combined loading conditions is critical to determine contact forces and stress levels of bristles to optimize the seal stiffness, life and performance. For this purpose, analytical methodologies have been developed in this study to calculate the bristle stress levels at combined loading calculations. Two different approaches: Simple and Advanced approach have been used for simulating rotor interference of a loaded seal. Inter-bristle and bristle-pack-backing plate friction has not been included to analytical studies.

In the case of combined loading, the bristle is bent and loaded length decreases with the increasing rotor interference, and therefore internal loads induced by pressure load change. The modified loaded length, *"b_{mod}"*, is illustrated in Figure 4.16. In the case of combined loading, the bristle deflection due to rotor interfernce, *"y(z)"*, is a function of *"z"*, and can be found by using the formula given in Equation 5.35.

$$y(z) = \frac{F_b \sin(\theta)}{EI_x}\left\{\frac{Lz^2}{2} - \frac{z^3}{6}\right\} \tag{5.35}$$

The projection of the steady state case - uniformly loaded length, *"b"*, on a deflected bristle under rotor interference can be found by using the Equation 5.36. The function *"g(z)"* in the Equation refers to projected length of *"b"* on a deflected bristle due to rotor interference.

$$g(z) = b_{\text{mod}} + y(L-b)\cdot\tan(\theta) \tag{5.36}$$

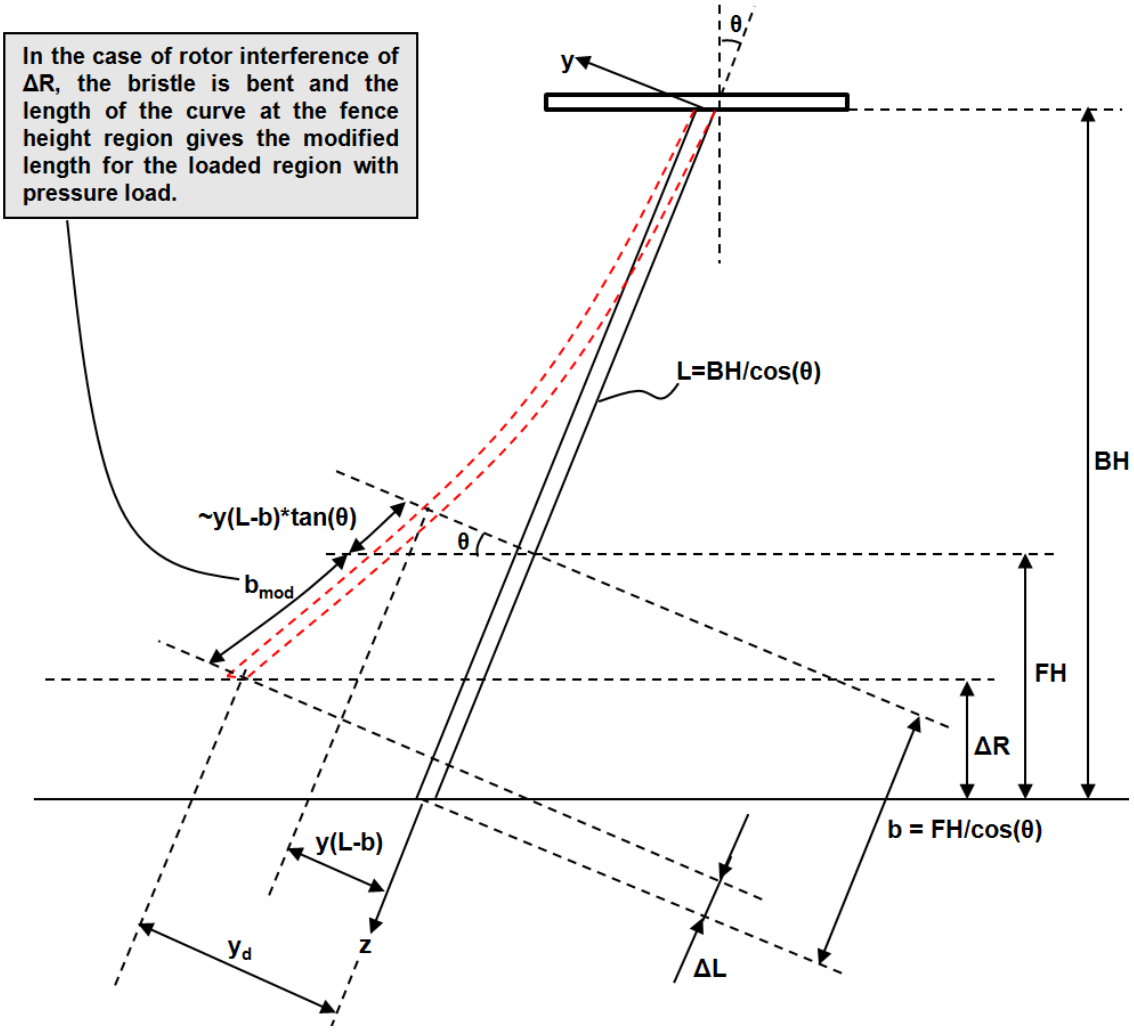

Figure 5.15: Bristle geometry and change of loaded length in the case of combined loading of rotor interference with pressure load

The differential projected length can be written as following,

$$d(g(z)) = \sqrt{dy^2 + dz^2} = \left[\sqrt{1+\left(\frac{dy}{dz}\right)^2}\right]dz \tag{5.37}$$

where *"z"* is the axial coordinate for the bristle and *"y"* is the deflection function of the bristle under rotor interference. Derivation of the function *"y(z)"* given in Equation 5.35 yields,

$$\frac{dy(z)}{dz} = \frac{F_b \sin(\theta)}{EI_x}\left\{Lz - \frac{z^2}{2}\right\} \tag{5.38}$$

The total length for projected length, *"g(z)"*, can be found by integrating the Equation 5.37, where the lower and upper limits of the integral is *"L-b"* and *"L-ΔL"* respectively.

$$g(z) = \int_{z=L-b}^{z=L-\Delta L} \sqrt{1+\left(\frac{dy}{dz}\right)^2} \cdot dz \tag{5.39}$$

In Equation 5.39, *"L"* is the free bristle length, and *"ΔL"* is the decrease in the projected length, which is illustrated in Figure 5.15. The projected length decreases for bent bristle can be found by using the formula given in Equation 5.40 *(Young et al. [67]).*

$$\Delta L = \frac{1}{2}\int\left(\frac{dy}{dz}\right)^2 \cdot dz \tag{5.40}$$

As the value of projected length, *"g(z)"*, is found, the modified loaded length, *"b_{mod}"* can be found by subtracting the length above FH point form the projected length, g(z).

$$b_{\text{mod}} = \int_{z=L-b}^{z=L-\Delta L} \sqrt{1+\left(\frac{dy}{dz}\right)^2} \cdot dz - y(L-b)\cdot\tan(\theta) \tag{5.41}$$

$$y(L-b) = \frac{F_b \sin(\theta)}{EI_x}\left\{\frac{L(L-b)^2}{2} - \frac{(L-b)^3}{6}\right\} \tag{5.42}$$

The loaded length change calculations for test seals have been performed by using MATLAB based code, and given in Figure 5.16 and Table 5.9 up to rotor interference level of 0.4mm. The test seal parameters have already been given in Chapter 2.

Test Seals, Uniformly Loaded Length Change									
ΔR *[mm]*	0.00	0.05	0.10	0.15	0.20	0.25	0.30	0.35	0.40
b_{mod} *[mm]*	1.84	1.78	1.72	1.66	1.60	1.54	1.48	1.42	1.35

Table 5.9: Test Seals – Uniformly loaded length change with rotor interference

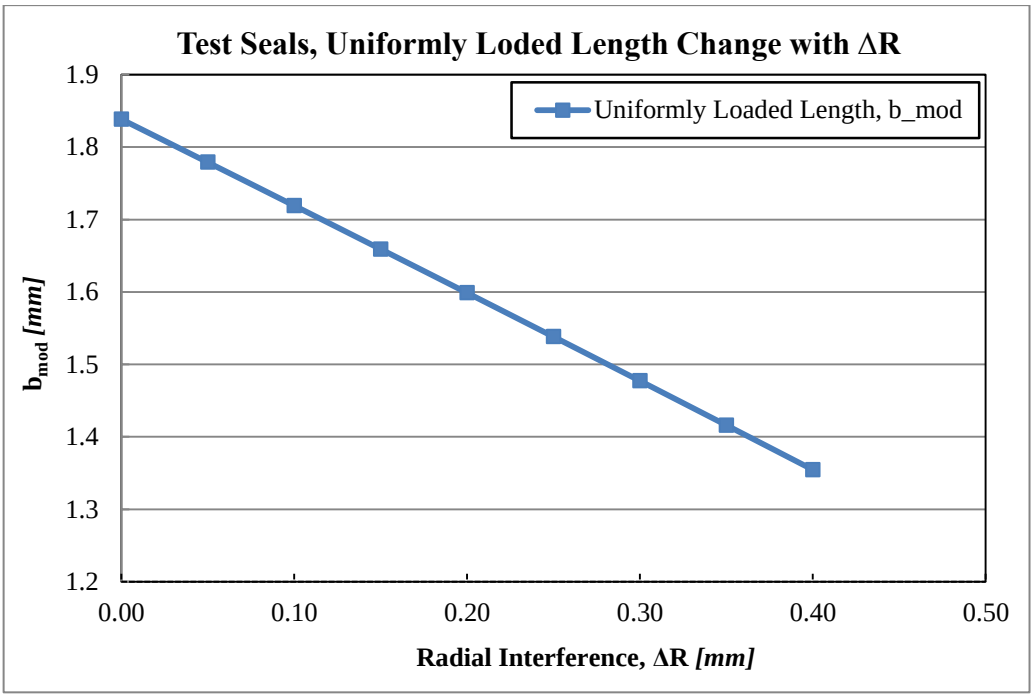

Figure 5.16: Test seals - Uniformly loaded length change with rotor interference

5.3.1 Simple Approach for Combined Loading Conditions

A formulation has been derived for bristle stress calculations, where the analyses include the combined loading effect of rotor interference and uniformly applied pressure load at the fence height region. The deflection due to rotor interference has effect on the loaded length of pressure load. The combined loading formulation for the bristle stress calculations takes this effect into account. Combined loading analyses simulate the case of rotor rub conditions when the bristle is already loaded with pressure load. Simple approach for combined loading conditions assume uniform load only at the FH region, which is induced due to axial pressure load ΔP. Assumptions for the combined rotor interference and simple approach pressure load analysis are:

- Friction between bristles and friction between bristle pack and backing plate is neglected
- No radial flow
- Uniform pressure load at the fence height region is applied to simulate the effect of axial flow

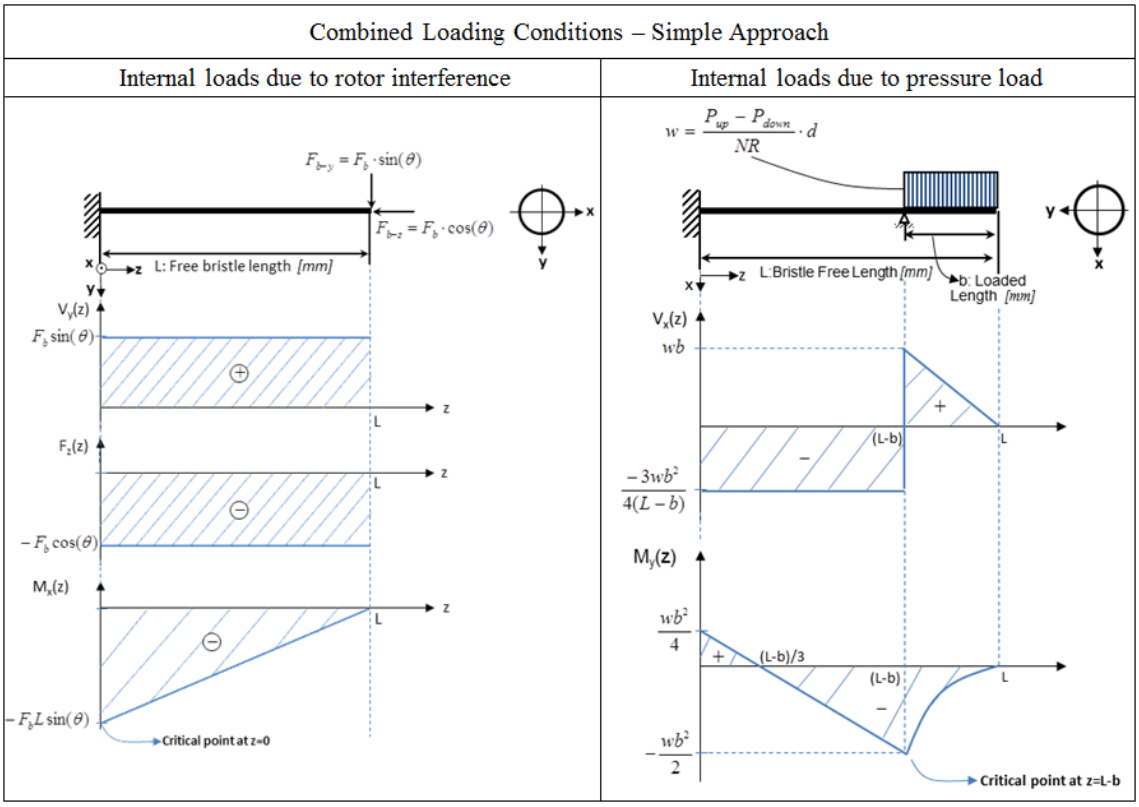

Figure 5.17: Test seals - Uniformly loaded length change with rotor interference

In the case of combined loading, rotor interference and pressure load act at the same time and cause bending moments and deflection of the beam at two principal axes. Bristle internal forces and moments for combined loading-simple approach are detailed in Figure 5.17. Bristle internal forces and moments induced due to combined loading are as following:

- The bristle tip contact force due to rotor interfernce causes:
  - Internal shear force in y-direction, $V_y(z)$,
  - Internal bending moment in x-direction, $M_x(z)$,
  - Internal axial load, $F_z(z)$.
- The pressure load causes:
  - Internal shear force in x-direction, $V_x(z)$,
  - Internal bending moment in y-direction, $M_y(z)$.

As it can be seen from Figure 5.16, two critical cross-sections exist for the bristle:

- Cross-section located at z = 0 *(pinch point)*, where the internal bending moment $M_x(z)$ is maximum,
- Cross-section located at z = L-b *(fence height point)*, where the internal bending moment $M_y(z)$ is maximum.

In the case of combined loading, the bristle is bent and loaded length decreases with the increasing rotor interference, and therefore internal loads induced by pressure load change. The modified loaded length, b_{mod}, is illustrated in Figure 5.15, and it is included in combined loading-simple approach studies by using the Equations 5.41 and 5.42.

Bristle internal loads in combined loading conditions causes stress state as following:

- $V_y(z)$: Internal shear force due to rotor interference → $\tau_{zy} = \frac{4}{3} \cdot \frac{V_y}{\pi r^2} \cdot \left(1 - \frac{y^2}{r^2}\right)$

- $M_x(z)$: Internal bending moment due to rotor interference → $\sigma_{bend-Mx} = \frac{M_x}{I_x} y$

- $F_z(z)$: Internal axial load due to rotor interference → $\sigma_{axial} = \frac{F_z}{A}$

- $V_x(z)$: Internal shear force due to pressure load → $\tau_{zx} = \frac{4}{3} \cdot \frac{V_x}{\pi r^2} \cdot \left(1 - \frac{x^2}{r^2}\right)$

- $M_y(z)$: Internal bending moment due to pressure load → $\sigma_{bend-My} = \frac{M_y}{I_y} x$

- Equivalent VM stress → $\sigma_{VM} = \sqrt{\frac{(\sigma_x - \sigma_y)^2 + (\sigma_y - \sigma_z)^2 + (\sigma_z - \sigma_x)^2 + 6(\tau_{xy}^2 + \tau_{yz}^2 + \tau_{zx}^2)}{2}}$

MATLAB based code has been developed for combined loading-simple approach calculations. Seal parameters, pressure load and interference level are input for the code, and the stress profiles at the critical cross-sections of the bristle are evaluated. Change of uniformly loaded length also included to MATLAB calculations, where the definite integral given in Equations 5.14 and 5.15 are solved at each interference level. Stress profiles at critical cross-sections of test seals are detailed in Figures 5.18 thru 5.21 for combined loading – simple approach at ΔP=0.3MPa and ΔR=0.1mm.

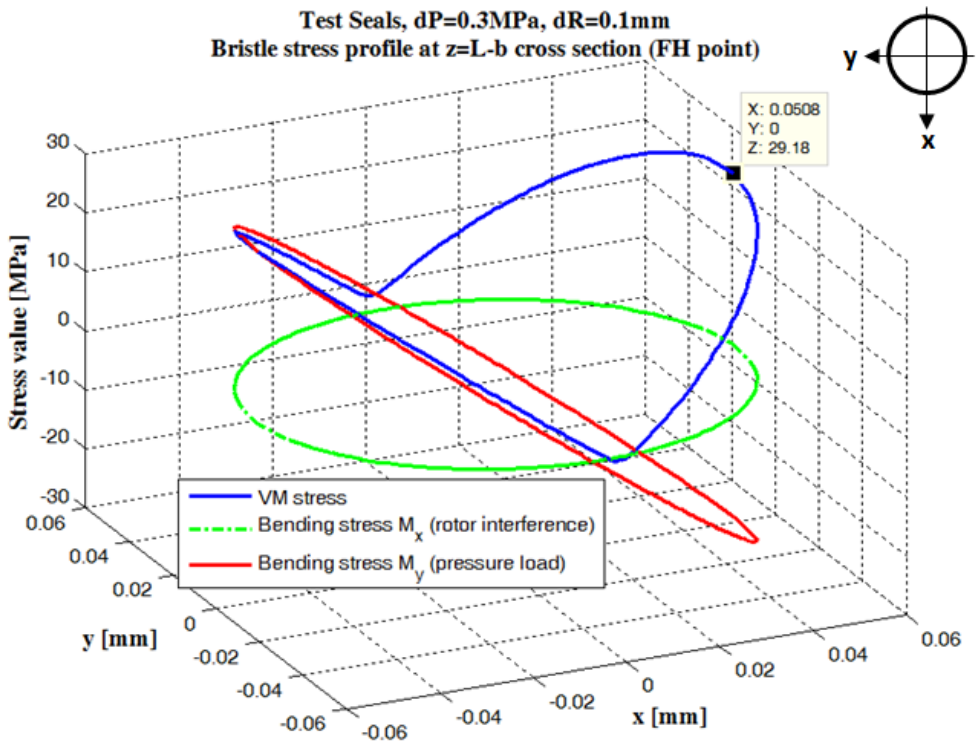

Figure 5.18: Combined loading-Simple Approach, Bending stresses and VM stress profile for test seal bristle at z=L-b cross-section *(FH point)*, ΔP=0.3MPa, ΔR=0.1mm

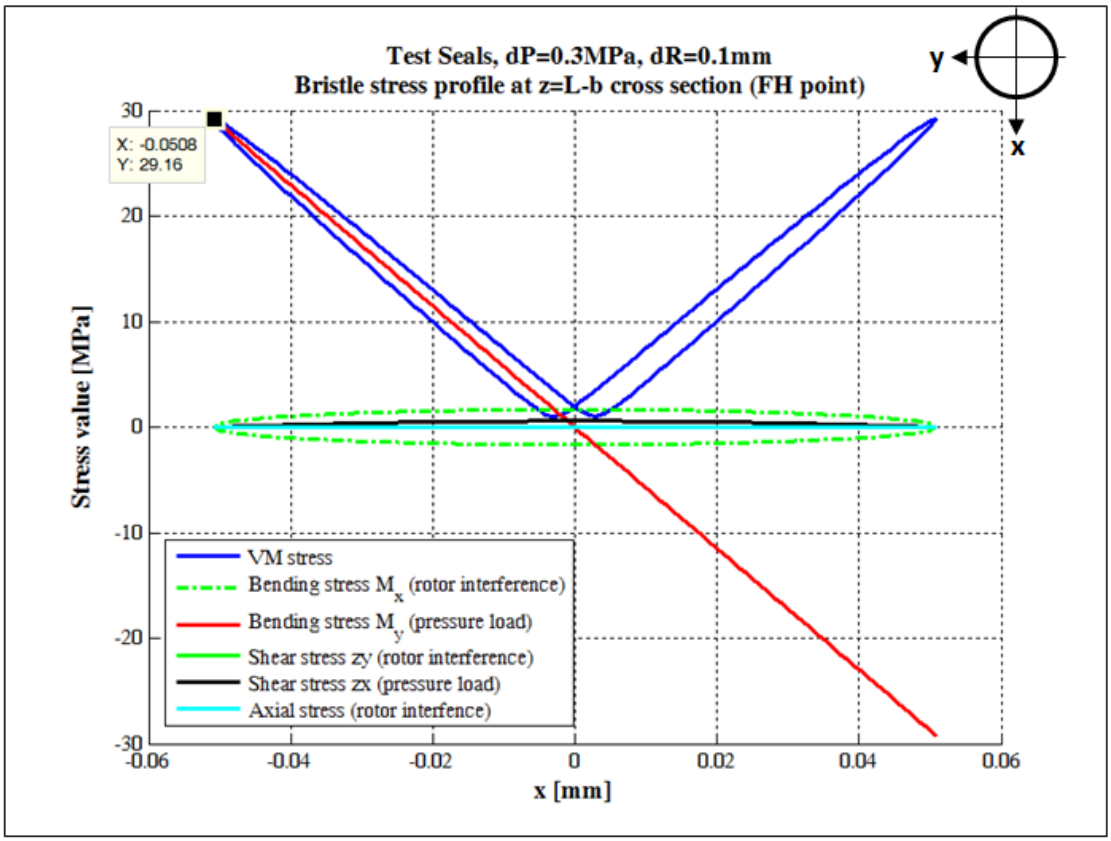

Figure 5.19: Combined loading-Simple Approach, Stress profile for test seal bristle at z=L-b cross-section *(FH point)*, ΔP=0.3MPa, ΔR=0.1mm

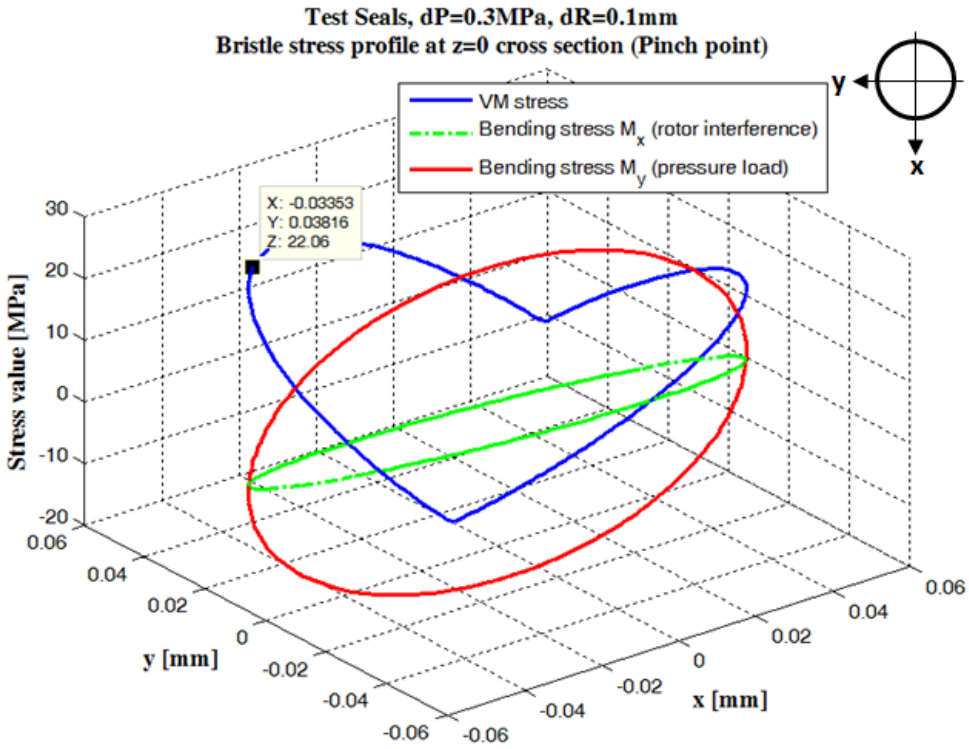

Figure 5.20: Combined loading-Simple Approach, Bending stresses and VM stress profile for test seal bristle at z=0 cross-section *(Pinch point)*, ΔP=0.3MPa, ΔR=0.1mm

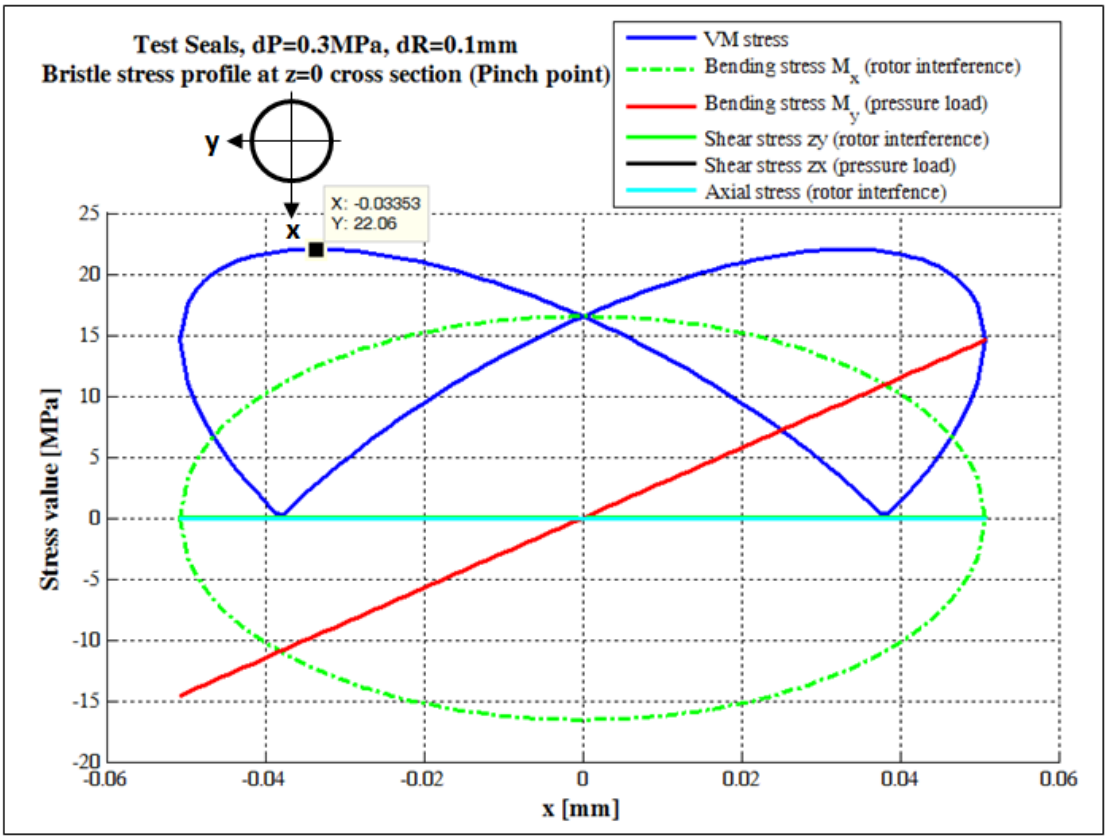

Figure 5.21: Combined loading-Simple Approach, Stress profile for test seal bristle at z=0 cross-section *(Pinch point)*, ΔP=0.3MPa, ΔR=0.1mm

In combined loading conditions, critical points at critical cross-section depend on seal parameters, pressure load and interference level. This is the direct consequence of interference and pressure load induced bending stress profiles, which take their maximum values at different points. The bending stress magnitude induced by pressure load is maximum at (x,y)=(d/2,0) and (x,y)=(-d/2,0) while rotor interference related bending stress magnitude is maximum at (x,y)=(0,d/2) and (x,y)=(0,-d/2). The maximum VM stress, which is the combination of all components of the 3D stress state at the bristle cross-section, can take its maximum value at an arbitrary point on the critical cross-section. This phenomenon is observed for the test seals at ΔP=0.3MPa and ΔR=0.1mm. At the critical cross-section located at z=L-b *(FH point),* the bending stress induced by the pressure load is dominant and therefore maximum 29.18MPa VM stress level is also observed at (x,y)=(d/2,0) and (x,y)=(-d/2,0) *(Figures 5.18 and 5.19).* The deviation of VM stress level from *"$\sigma_{bend\text{-}My}$"* is due to contribution of other stress components *($\sigma_{bend\text{-}Mx}$, τ_{zy}, τ_{zx} and σ_{axial}).* However, at the critical section located at z=0 *(Pinch point),* both pressure load and rotor interference induced bending stresses are effective, and the maximum 22.06MPa VM stress is observed at (x,y)=(0.033mm,0.038mm) and (x,y)=(-0.033mm,0.038mm) *(Figures 5.19 and5.20).* As it can be seen from the figures, bending stress components are dominant in combined loading conditions, which is a result of high L/d ratio of bristles.

The combined loading-simple approach has been run for maximum pressure load of test conditions and up to maximum rotor interference level, ΔP_{max}=0.3MPa and ΔR_{max}=0.4mm. Maximum VM stress level change with rotor interference is given in Figure 5.22 and Table 5.10.

As it can be seen from Figure 5.22, maximum VM stress at z=L-b cross section is mainly due to pressure load. Since the loaded length decreases with increasing rotor interference ΔR, the maximum VM stress at z=L-b also decreases with increasing ΔR.

The pinch point VM stress level has smaller value than the stress at z=L-b cross-section for ΔR=0, since the pressure load is the only contributor at that condition, which refers to steady state. Up to rotor interference value of 0.15mm, the VM stress at pinch point cross-section is smaller than the FH section stress *(z=L-b).* As ΔR takes values larger than 0.15mm, the rotor interference induced bending becomes more effective at z=0 cross-section and VM stress level at pinch point becomes larger than FH point

section. The pinch point VM stress change with ΔR is not linear. For the specific design parameters and loading conditions of test seals, the pinch point VM stress is almost constant up to 0.05mm interference, and it starts to increase above that point, where the contribution of radial interference becomes dominant and pressure load becomes less effective due to decrease in loaded length. Trends of VM stress curves will be similar for different seal parameters, but slopes, stress peaks and the ΔR value where VM at z=0 cross-section starts to increase may change.

Test Seals, Combined Loading – Simple Approach ΔP=0.3MPa, ΔR_{max}=0.4mm									
ΔR *[mm]*	0.00	0.05	0.10	0.15	0.20	0.25	0.30	0.35	0.40
VM, z=L-b *[MPa]*	33.35	31.23	29.18	27.18	25.36	23.65	21.99	20.39	18.89
VM, z=0 *[MPa]*	16.68	17.67	22.06	28.29	35.41	42.98	50.79	58.75	66.80

Table 5.10: Test Seals – Uniformly loaded length change with rotor interference

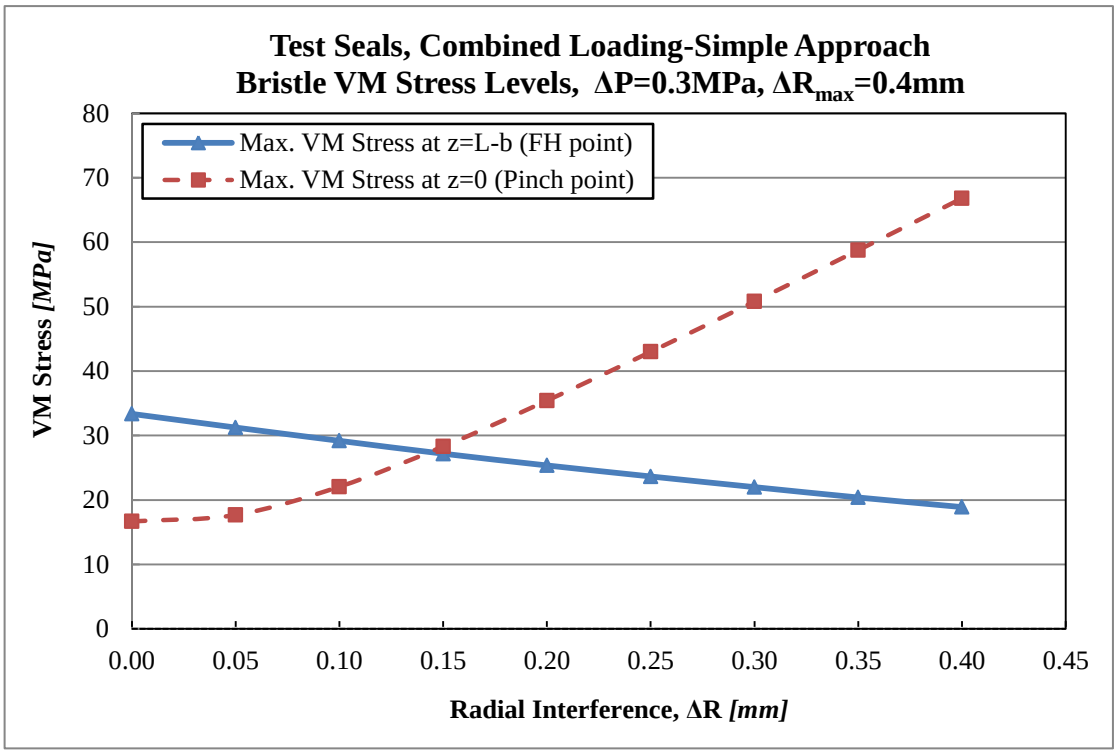

Figure 5.22: Combined loading - Simple Approach, Maximum VM stress level change for test seals' critical cross-sections, ΔP_{max}=0.3MPa, ΔR_{max}=0.4mm

5.3.2 Advanced Approach for Combined Loading Conditions

As mentioned before, bristles are exposed to a varying pressure load at full bristle length in real operating conditions, which can be approximated by 7th order polynomial

fit to experimental data of Bayley et. al.[59] and Turner et.al.[60]. The advanced pressure profile, which has already been detailed in Section 5.2.2, is applied in combined loading calculations. In combined loading-advanced approach the rotor interference cause uniformly loaded length to decrease as well as it changes the pressure profile at backing plate region. The pressure profile on a single bristle using the advanced method is given in Figure 5.23 at ΔP=0.3MPa and at different interference levels for test seals. As mentioned earlier and detailed in Figures 5.13 and 5.14, at steady state conditions, the uniformly loaded length, *"b"*, is equal to *"FH/cos(θ)"*; the free bristle length, *"L"*, is equal to *"BH/cos(θ)"*; and the length for the linearly loaded region with high pressure gradient, *"*a_1*"*, is equal to *"*$r_1/cos(\theta)$*"*. *"*a_2*"* is the bristle length which is linearly loaded with low pressure gradient and it is equal to *"L-b-*a_1*"*. *"*$a_3=a_1+a_2$*"* is the total length of linearly loaded bristle region. As it can be observed from Figure 5.23, when rotor interference is introduced:

- Region 1 becomes shorter, b_{mod} *(Uniformly loaded length change)*
- Region 2 remains almost constant, a_1
- Region 3 becomes longer, a_{2mod}
- Projected bent bristle length changes, L'

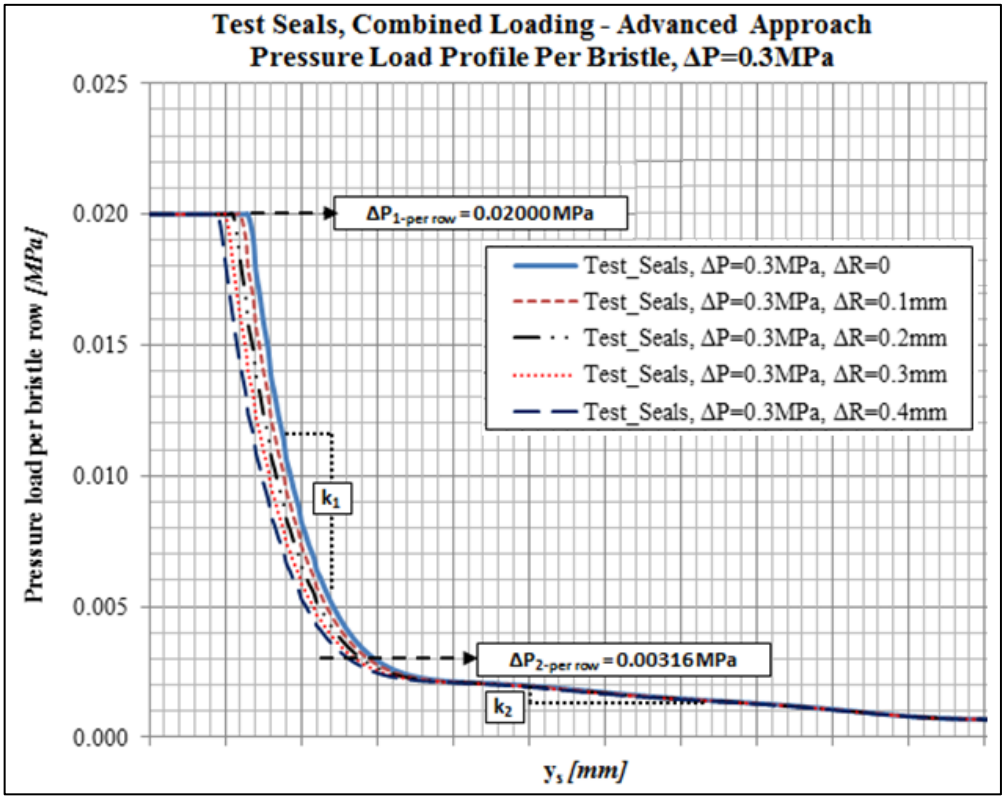

Figure 5.23: Combined loading-Advanced Approach-Test seals, Pressure load profile on a bristle row at different interference levels, ΔP=0.3MPa, ΔR_{max}=0.4mm

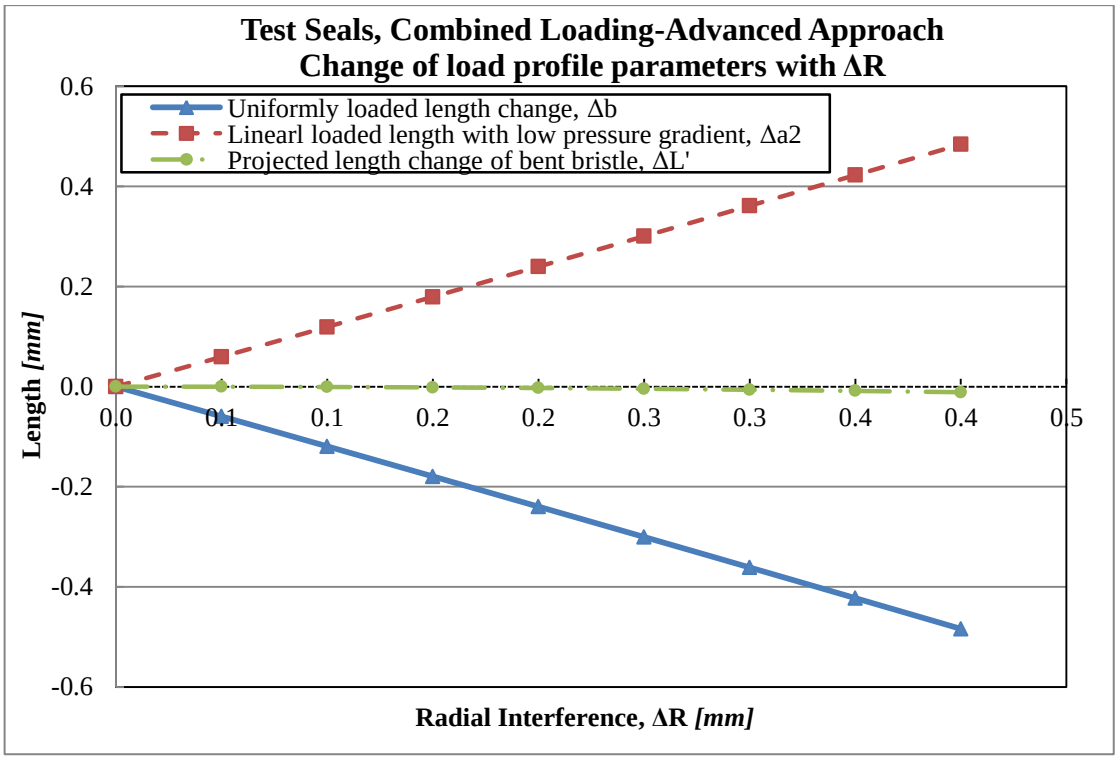

Figure 5.24: Combined loading-Advanced Approach-Test seals, Change of load profile parameters with radial interference

Combined Loading-Advanced Approach – ΔP = 0.3MPa, ΔR_{max} = 0.4mm Test Seal Parameters and Change of Load Profile Parameters									
Test seal parameters for advanced approach									
FH *[mm]*		1.30			$\Delta P_{1\text{-per row}}$ *[MPa]*		0.02000		
θ *[deg]*		45			$\Delta P_{2\text{-per row}}$ *[MPa]*		0.00316		
Change of load profile parameters									
ΔR *[mm]*	0.00	0.05	0.10	0.15	0.20	0.25	0.30	0.35	0.40
Δb *[mm]*	0.0000	-0.0595	-0.1193	-0.1794	-0.2397	-0.3003	-0.3613	-0.4225	-0.4839
Δa_2 *[mm]*	0.0000	0.0595	0.1193	0.1794	0.2397	0.3003	0.3613	0.4225	0.4839
ΔL' *[mm]*	0.0000	-0.0002	-0.0007	-0.0016	-0.0028	-0.0044	-0.0063	-0.0086	-0.0112

Table 5.11: Combined Loading Conditions – Advanced approach - Test seals, Change of load profile parameters with radial interference – tabulated data

Combined loading-advanced approach calculations have been performed for test seals by using a MATLAB based code. The MATLAB code automatically calculates the change of uniformly loaded length and length change of low gradient-linearly loaded region, and evaluates maximum VM stress levels at critical sections by sweeping 3D stress states at all points at the section. VM stress levels have been calculated at test conditions: ΔP=0.3MPa and ΔR_{max}=0.4mm. Change of uniformly loaded length, Δb, change of length of region 3 – linearly loaded region with low gradient, Δa_2 and decrease in the projected length of bent bristle, ΔL' are detailed in Figure 5.24 and

Table 5.11. As it can be seen from the data, the uniformly loaded length decreases with radial interference while increase is observed at the region of linear load with low gradient. The projected length of bent bristle also decreases in very small magnitudes.

Maximum VM stress level change with rotor interference is detailed in Figure 5.26 for test seals using combined loading-advanced approach methodology. Stress magnitudes for advanced approach and their comparison with simple approach are also detailed in Table 5.12. Due to extended loading profile of advanced approach, evaluated pinch point-bristle stress levels are higher than combined-loading as expected.

Combined Loading Conditions – ΔP = 0.3MPa, ΔR_{max} = 0.4mm Advanced Approach vs. Simple Approach for Test Seals		
Critical section: z = L-b *(Fence height)*, Max. VM Stress *[MPa]*		
ΔR *[mm]*	Simple approach	Advanced approach
0.00	33.35	33.35
0.05	31.23	31.23
0.10	29.18	29.18
0.15	27.18	27.18
0.20	25.36	25.36
0.25	23.65	23.65
0.30	21.99	21.99
0.35	20.39	20.39
0.40	18.89	18.89
Critical section: z = 0 *(Pinch point)*, Max. VM Stress *[MPa]*		
ΔR *[mm]*	Simple approach	Advanced approach
0.00	16.68	41.43
0.05	17.67	43.65
0.10	22.06	47.25
0.15	28.29	51.94
0.20	35.41	57.45
0.25	42.98	63.57
0.30	50.79	70.14
0.35	58.75	77.04
0.40	66.80	84.18

Table 5.12: Combined Loading Conditions – Advanced approach vs. Simple approach, Stress levels at critical cross section of test seals at ΔP = 0.3MPa

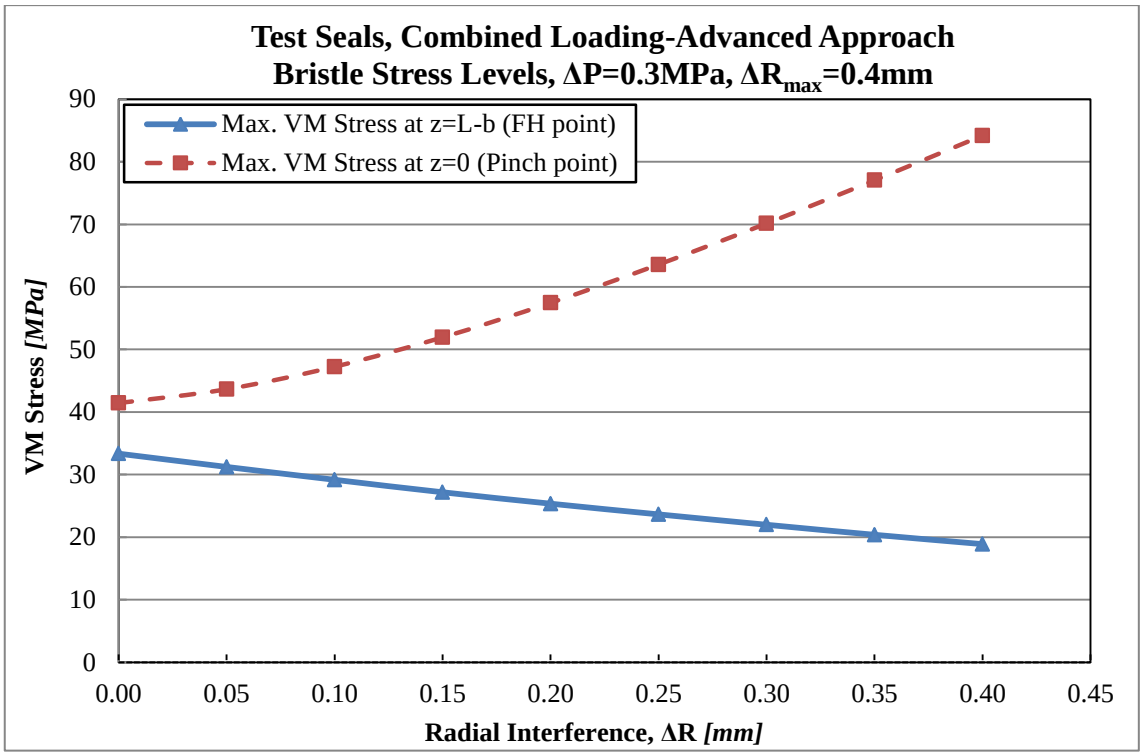

Figure 5.25: Combined loading - Advanced Approach, Maximum VM stress level change for test seals' critical cross-sections, ΔP_{max}=0.3MPa, ΔR_{max}=0.4mm

5.4 Analytical Studies for Pressurized – Static BTF Calculations

Bristle tip forces for a pressurized brush seal is an important parameter since the contact force transmitted to rotor and generated heat in turbine operating conditions directly depend on this parameter. Bristle tip force calculations in the literature [17, 44] consider only unpressurized-static *(non-rotating rotor)* case, which is an ideal case for test conditions. In this study, a closed-form formulation, where backing-plate-bristle and rotor-bristle frictional effects have been included, has been developed to evaluate pressurized stiffness of brush seals, and results are compared with RTR-Unpressurized stiffness test data.

Analytical studies for pressurized conditions take the backing plate-bristle and rotor-bristle friction into account as detailed in Figure 5.26. As the pressure load is applied to seal pack, the bristles deform in axial direction and touch each other. As a result of pressure load and backing plate-bristle friction, bristles behave much stiffer than free-state case, which is known as *"pressure stiffening"*. Loads acting on a bristle at rotor interference condition of pressurized seal are visualized in Figure 5.26. In

addition to rotor-bristle friction, the bristle-backing plate friction also acts at the reverse direction to motion. Pressurized-BTF analysis also use 7th order polynomial fit to backing plate pressure profile suggested by Bayley et. al.[59] and Turner et.al.[60].

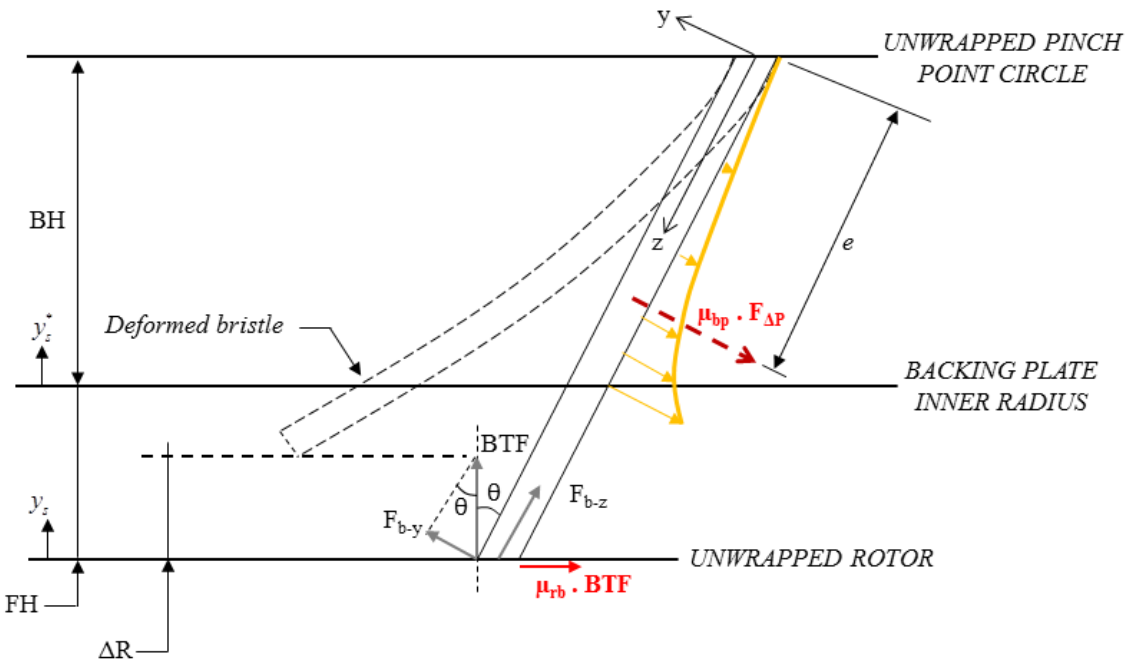

Figure 5.26: Analytical studies for pressurized-static BTF calculations – Loads acting on a bristle at rotor interference conditions of pressurized seal

As shown in Figure 5.26, the backing plate frictional force can be approximated by a concentrated force *"$\mu_{bp}F_{\Delta P}$"* which is acting at distance *"e"* from pinch point. In the figure, *"$F_{\Delta P}$"* is the normal force per bristle row acting on backing plate portion, and *"e"* is the geometric center of the distributed load.

$$F_{\Delta P} = \frac{1}{NR} \cdot \int \left(\Delta P_B\right) \tag{5.43}$$

$$NR = \eta \cdot S_T \tag{5.44}$$

In Equations 5.43 and 5.44, *"ΔP_B"* is the pressure load at backing plate region, which has already been detailed in Section 5.2.2 through Equations 5.16-5.21. In Equations 5.43 and 5.44, *"$F_{\Delta P}$"* and *"e"* are functions of seal parameters and loading conditions, all of which are known. Knowing the functions of *"$F_{\Delta P}$"* and *"e"*, the bristle loading conditions at pressurized conditions now can be reduced to a beam problem as visualized in Figure 5.27. In the figure, *"$F_{tip\text{-}y}$"* is the tip force in y-direction, *"R_1"* and

"M_1" are reaction forces and moments. Solving the force balance, the reaction force and moment is found as,

$$R_1 = F_{tip-y} - F_{\Delta P} \tag{5.45}$$

$$M_1 = F_{tip-y} \cdot L - F_{\Delta P} \cdot e \tag{5.46}$$

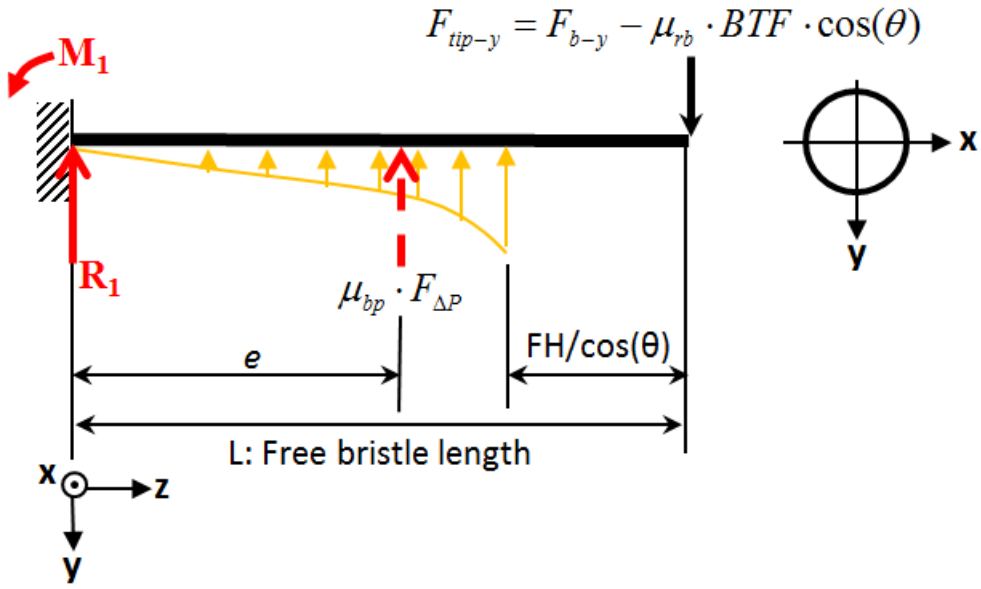

Figure 5.27: Analytical studies for pressurized-static BTF calculations – Free body diagram for a loaded bristle

The internal shear force, *"V(z)"*, internal bending moment, *"M(z)"*, slope, *"dy/dz"*, and deflection, *"y(z)"*, singularity functions for the beam given in Figure 5.26 are as following,

$$V(z) = R_1 \cdot \langle z-0 \rangle^0 - M_1 \cdot \langle z-0 \rangle^{-1} + \mu_{bp} F_{\Delta P} \cdot \langle z-e \rangle^0 - F_{tip-y} \cdot \langle z-L \rangle^0 \tag{5.47}$$

$$M(z) = R_1 \cdot \langle z-0 \rangle^1 - M_1 \cdot \langle z-0 \rangle^0 + \mu_{bp} F_{\Delta P} \cdot \langle z-e \rangle^1 - F_{tip-y} \cdot \langle z-L \rangle^1 \tag{5.48}$$

$$-E \cdot I_x \cdot \frac{dy(z)}{dz} = \frac{R_1}{2} \cdot \langle z-0 \rangle^2 - M_1 \cdot \langle z-0 \rangle^1 + \frac{\mu_{bp} F_{\Delta P}}{2} \cdot \langle z-e \rangle^2 - \frac{F_{tip-y}}{2} \cdot \langle z-L \rangle^2 \tag{5.49}$$

$$-E \cdot I_x \cdot y(z) = \frac{R_1}{6} \cdot \langle z-0 \rangle^3 - \frac{M_1}{2} \cdot \langle z-0 \rangle^2 + \frac{\mu_{bp} F_{\Delta P}}{6} \cdot \langle z-e \rangle^3 - \frac{F_{tip-y}}{6} \cdot \langle z-L \rangle^3 \tag{5.50}$$

where *"E"* is the elastic modulus for the bristle material and *"I_x"* is the second moment of area about x-axis for the bristle cross-section. When the rotor interference – ΔR – introduced, the deflection at bristle tip *(z=L)* is equal to radial interference. Other than that, boundary conditions are,

$$V(0)=M(0)=0 \tag{5.51}$$

$$V(L)=M(L)=0 \tag{5.52}$$

$$y(0)=dy(0)/dz=0 \tag{5.53}$$

Solving the equations by using boundary conditions given in Equations 5.51 thru 5.53 gives the BTF value, which has been solved in a MATLAB based code to obtain BTF values.

The pressurized-static BTF calculations have been conducted for test seals *(parameters and material properties have already been detailed in Chapter2)*, at ΔP=0.3MPa and for μ_{bp}=0.25 with different rotor-bristle friction coefficient. Pressurized-static BTF change with ΔR and its comparison with unpressurized-static BTF calculations of modified beam theory is given in Figure 5.28. As it can be seen from the figure, both methodologies, which are developed within the content of this study, give consistent results with real life applications. Pressure stiffening and BTF stabilization can successfully be simulated the developed methodology. BTF magnitudes of both pressurized-static and unpressurized-static conditions increase with increasing rotor-bristle friction coefficient as expected, but increase in BTF-pressurized-static case is more pronounced due to pressure stiffening affect.

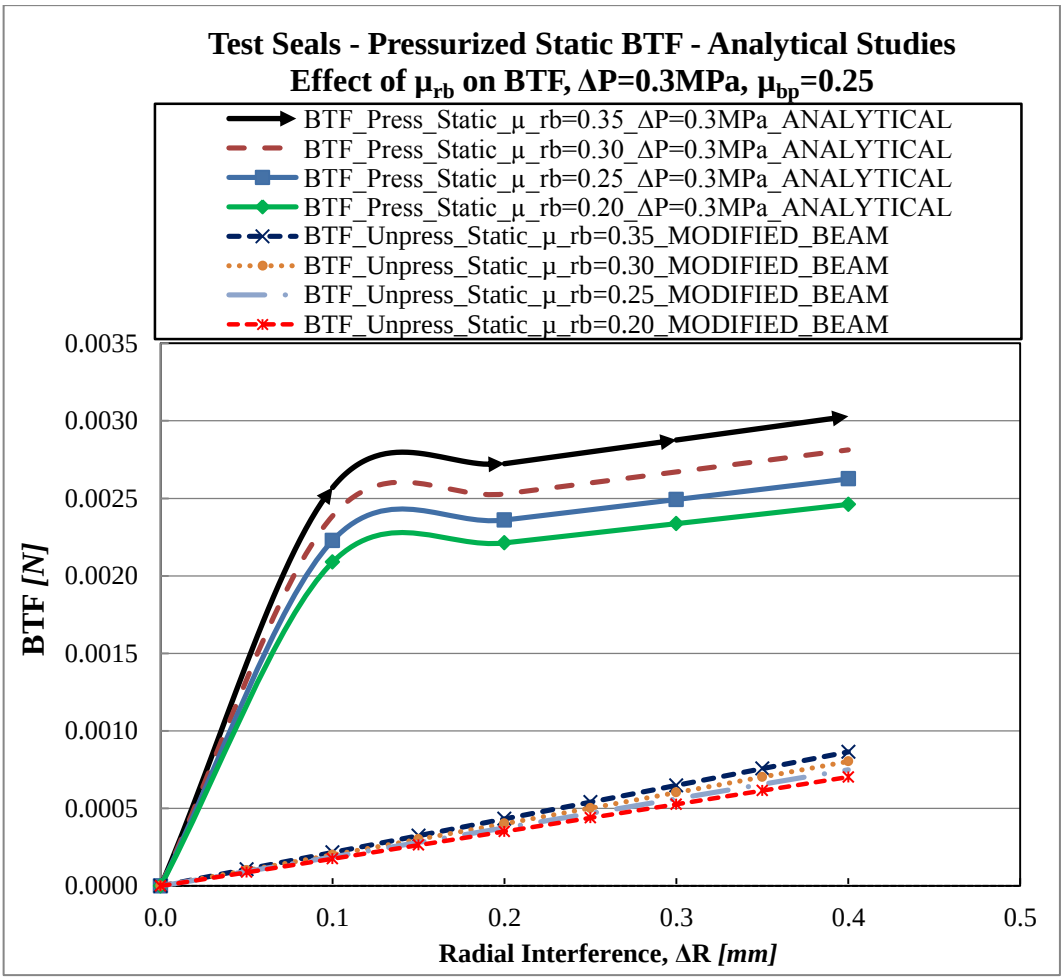

Figure 5.28: Analytical studies for pressurized-static BTF calculations – Test seals, pressurized BTF@ΔP=0.3MPa vs. free-state BTF *(Modified beam theory)* at different rotor-bristle friction coefficients

The pressurized-static BTF calculations have been performed for test seals *(parameters and material properties have already been detailed in Chapter2)* at RTR-Pressurized static test conditions *(ΔP=0.3MPa and ΔP=0.225MPa)*. The rotor-bristle friction coefficient, μ_{rb}, has been taken as 0.35, and different backing plate-bristle friction coefficients are used ranged from 0.25 to 0.35. Calculated pressurized-static BTF change with ΔR and its comparison with RTR-Pressurized static BTF measurements are given in Figures 5.29 and 5.30 for ΔP=0.3MPa and ΔP=0.225MPa respectively. As it can be seen from figures, the developed methodology gives consistent results with test measurements for the range of 0.25-0.35 for μ_{bp} values. Selecting the appropriate friction coefficient for backing plate-bristle contact will be done in Chapter 6, as full brush seal FE analyses will be performed and compared with test results and analytical studies.

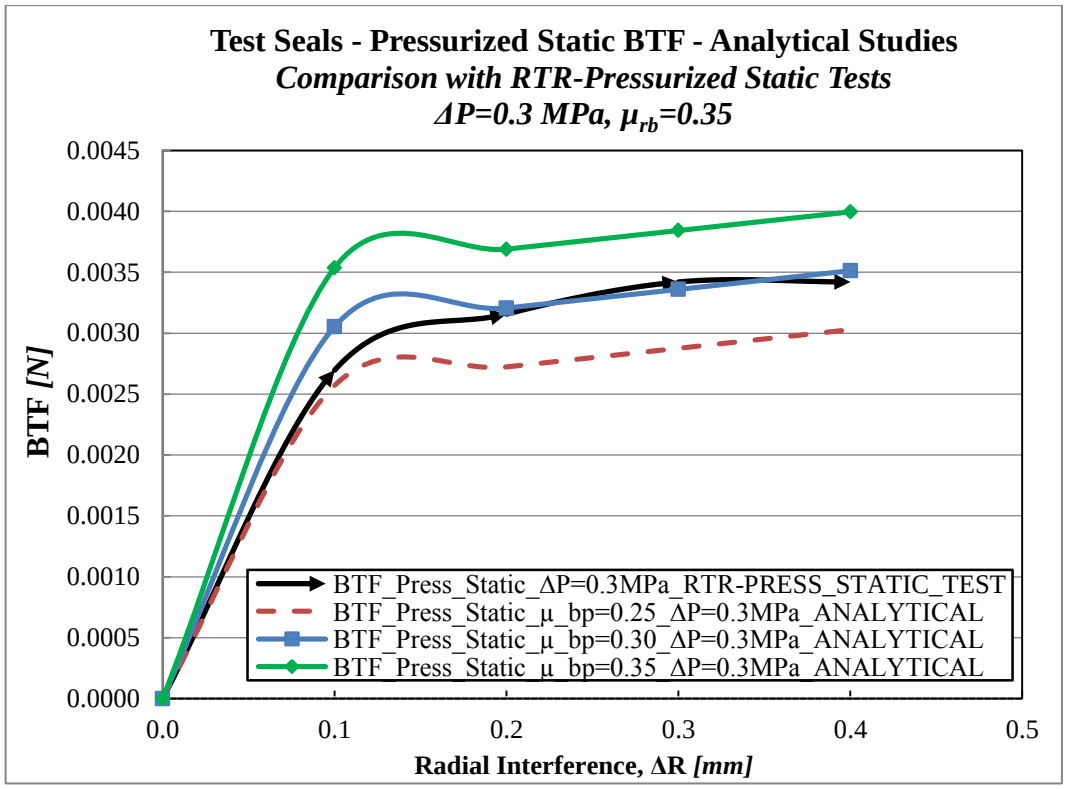

Figure 5.29: Analytical studies for pressurized-static BTF calculations – Test seals, pressurized BTF@ΔP=0.3MPa vs. RTR-Pressurized static BTF measurements

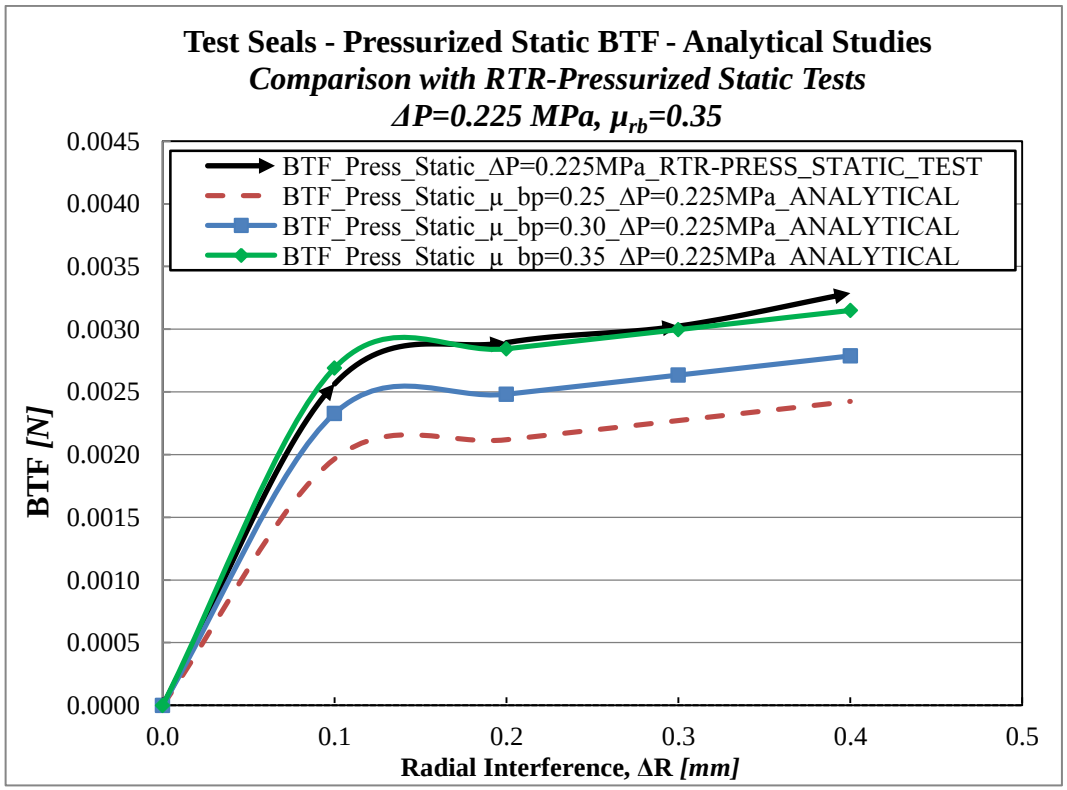

Figure 5.30: Analytical studies for pressurized-static BTF calculations – Test seals, pressurized BTF@ΔP=0.225MPa vs. RTR-Pressurized static BTF measurements

6 BRUSH SEAL FINITE ELEMENT ANALYSES AND CORRELATION WITH TESTS

The bristle tip forces and stress levels strongly depends on the frictional effects, which includes inter-bristle friction, bristle pack-backing plate friction and friction between rotor and bristles. The complicated nature of bristle deflection, pressure load and inter-bristle effects, which not only includes frictional forces but also includes inter bristle-locking phenomenon, does not lend itself to full analytical formulation. Although beam based analytical methodologies developed in this study shows good agreement with unpressurized and pressurized static BTF measurements as well as give an overall idea about bristle deformation and stress levels, comprehensive FEA is needed to include the complicated inter-bristle and transient effects into account.

Brush seal CAE and correlation studies in the literature are very limited due to difficulties in modeling and converging nonlinear friction and contacts of brush seal pack. Crudgington et al. [46,47] conducted brush seal FE analyses using Hexa and space beam elements at static-unpressurized rotor interference conditions and pressure load without rotor incursion, while they mentioned that pressurized-rotor interference simulations were not performed due to convergence problems. Aksit [15] performed seal analyses by using space beam elements at unpressurized-static rotor interference and pressurized-static rotor interference conditions *(non-rotating rotor)*, and presented correlation only for free-state stiffness measurements. Guardino [48] and Lelli [49] were used home-based developed software, which was based on mathematical formulae and not FE-based, to simulate bristle deflection at non-rotating rotor interference.

In this study, brush seal simulations have been performed at unpressurized-nonrotating rotor interference, pressure load, pressurized-nonrotating loading conditions as well as unpressurized-dynamic and pressurized-dynamic *(rotating rotor)* rotor rub conditions. FE analyses results have also been correlated with the RTR-BTF measurements, which also have been conducted within the content of this study. Two different FE models using 3D Hexa and space beam elements have been constructed for static simulations, and results are compared with the RTR-test data and analytical results. Dynamic rotor incursion analyses have been conducted through transient

analyses with rotating rotor, which simulate inertial effects and resulting bristle relaxing and flutter effects into account. FE models have been constructed in HYPERMESH, and analyses have been performed by using ABAQUS solver.

6.1 Selecting the Appropriate Element Type

Selected the correct element type has crucial importance in achieving the FE simulations with high fidelity. The element library of ABAQUS consists of variety of elements with hybrid and modified formulations. Commonly used element families are visualized in Figure 6.1.

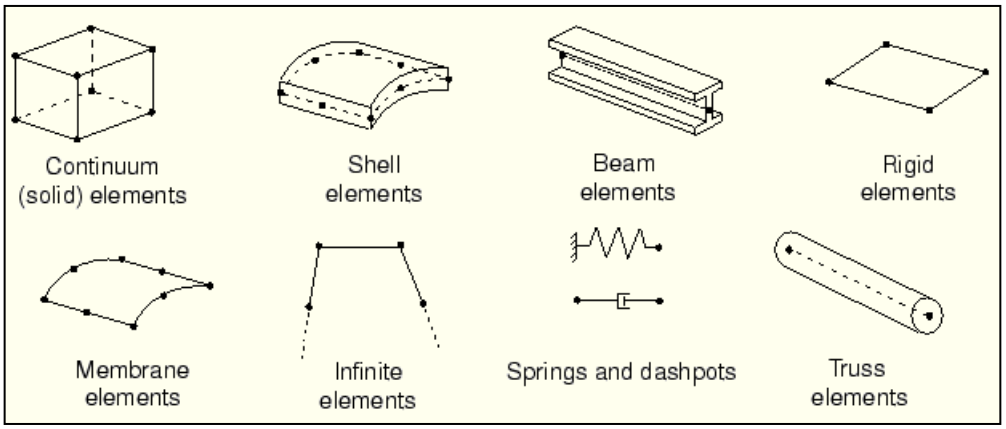

Figure 6.1: Commonly used element families in finite element methods [68]

In the FE analyses of brush seals, using shell, membrane, infinite and truss elements is not possible due to geometry and stress formulation of bristles. Amongst continuum elements, penta elements are not preferred due to their inaccuracy in stress calculations during structural analyses. Similarly, first order tetrahedral elements are not used since they act extremely rigid due to their formulations and have shear locking problems. Second order tetrahedral elements are known to be accurate in structural analyses, but increased number of nodes and possible warpage problems during bending of bristles avoids usage of these elements in brush seal simulations. Therefore, the most appropriate element types for brush seal analyses are reduced to Hexahedral and Beam type elements.

Second order hexahedral elements are not preferred due to the fact that contact formulation of second order elements may yield contact pressure discontinuities, which

in turn will cause accuracy problems in BTF correlation. C3D8R elements are 8-node brick elements with reduced integration, and they are not preferred in brush seal modeling since hour-glassing mode in bending will yield smaller stress levels than real life applications. Therefore, amongst hexahedral elements, *"C3D8I-8 node hexahedral elements with incompatible modes"* is selected, which is known to have good accuracy in bending problems and avoided shear locking problem. However, care must be taken in FE modeling since the accuracy of the simulation strongly depends on the element quality and Jacobian criteria.

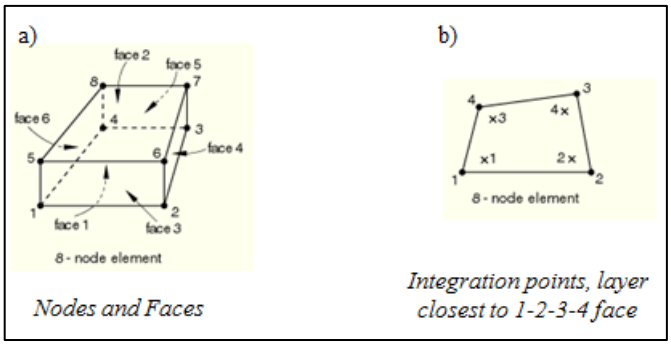

Figure 6.2: C3D8I element type, a) Node ordering and face numbering on elements, b) Numbering of integration points for output [68]

The circular cross-section and large L/d ratios of bristles enables usage of beam elements in simulations. The brush seal problem is a three dimensional problem, therefore B31 – space beam with circular cross-section is the most appropriate problem which can simulate three dimensional deformation as well as stress state. The B31 section integration point layout is given in Figure 6.3.

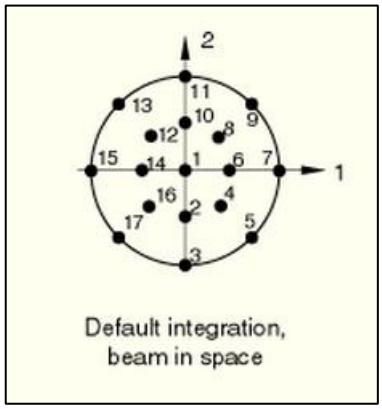

Figure 6.3: B31 space beam with circular cross-section, integration points *(3 points radially, 8 points circumferentially, 17 in total)* [68]

Prior to FE modeling and full brush seal simulations, CAE analyses have been performed for simple bending problem defined in Figure 6.4. The geometry of the problem has large L/d ratio as in the case of brush seal bristles. The applied force at the tip is 0.0058N, and isotropic material properties having elastic modulus value of 197197MPa and Poisson's ratio value of 0.3 have been used. Maximum VM stress level at pinch point and deflection at bristle tip calculated from beam theory are as following.

$$\sigma_{bend-\max} = \sigma_{VM-\max} = 1063MPa \tag{6.1}$$

$$y_{\max} = 11.65mm \tag{6.2}$$

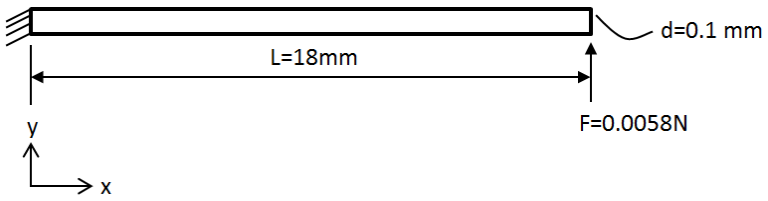

Figure 6.4: Simple bending problem, dimensions and boundary conditions

FE simulations for simple bending problems have been conducted by using four different element types: C3D8I, C3D8R, C3D8R-Enhance hour-glassing control and B31 elements. The cross-section using C3D8 elements have 16 nodes at section circumferential direction, as shown in Figure 6.5.

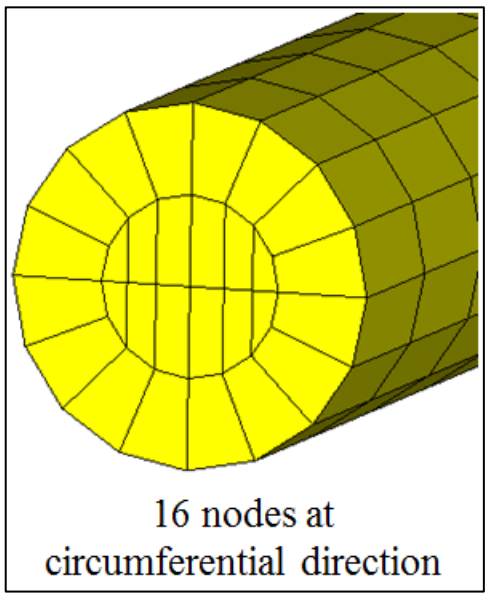

Figure 6.5: Simple bending problem, FE mesh details for models using C3D8 elements

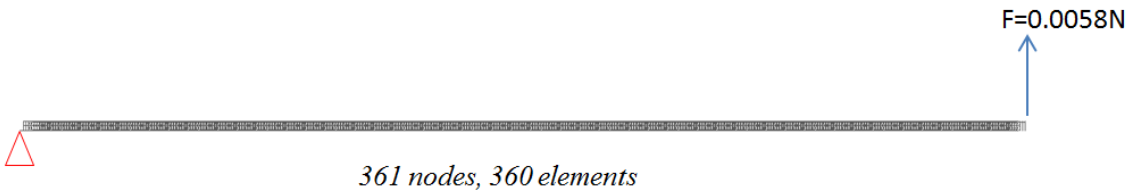

Figure 6.6: Simple bending problem, FE mesh details for model using B31 elements

FE simulations for simple bending problems have been conducted by using four different element types: C3D8I, C3D8R, C3D8R-Enhanced hour-glassing control and B31 elements. The cross-section using C3D8 elements have 16 nodes at section circumferential direction, as shown in Figure 6.5. The FE model using B31 elements have 361 nodes and 360 elements in total, as displayed in Figure 6.6.

Figure 6.7: Simple bending problem – Displacement profile for the FE simulation with C3D8I elements

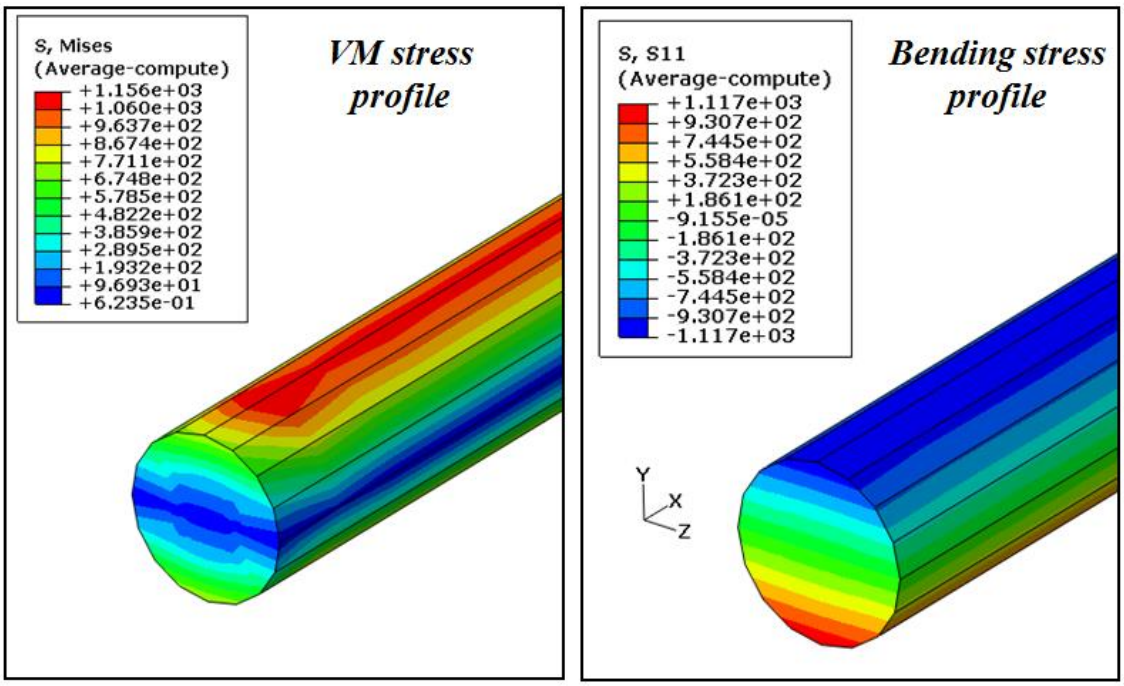

Figure 6.8: Simple bending problem – Stress profile for the FE simulation with C3D8I elements

Displacement and stress profile for simple bending simulation with C3D8I elements is visualized in Figures 6.7 and 6.8 as a representative example. The maximum deflection at tip for simulations with C3D8I elements is 12.11mm. Maximum bending stress at pinch point is 1117MPa and maximum VM stress is 1156MPa. As it can be seen from the results, the stress and displacement results of C3D8I elements, which are known to be most accurate element type for bending problems, are very close to beam theory calculations. The reason for slight difference is due to 3D effects, which cannot be taken into account in beam theory.

Maximum displacement and stress results for simple bending problem using different type of elements are tabulated in Table 6.1. As it can be seen from the table, FE simulations with B31 elements give almost same result with beam theory, and results are very close to analyses using C3D8I elements. Apparently, C3D8R elements are not appropriate for brush seal problem since the hour-glassing modes of reduced integration result in inaccurate stress results.

Simple Bending Problem – Comparison of Element Types					
	C3D8I	**C3D8R**	**C3D8R-Enh. Hour-glassing c.**	**B31**	**Beam theory**
y_{max}	**12.21mm**	13.00mm	12.25mm	**11.65mm**	11.65mm
$\sigma_{bend-max}$	**1117MPa**	887MPa	844MPa	**1062MPa**	1063MPa
σ_{VM-max}	**1156MPa**	893MPa	839MPa	**1062MPa**	1063MPa

Table 6.1: Combined Loading Conditions – Advanced approach - Test seals, Change of load profile parameters with radial interference – tabulated data

The FE experience, which is confirmed with simple bending case-study, indicates that C3D8I and B31 are the most appropriate element types for brush seal problem. Therefore, brush seal FE analyses will be performed by busing these two types of elements.

6.2 Unpressurized - Nonrotating Rotor Interference Conditions – Test Seals

Unpressurized nonrotating rotor interference conditions refer to free-state rotor rub conditions, where the seal is not loaded with pressure and rotor does not rotate. Although this condition is an idealized test condition, it is very useful to perform quick comparison between different seal designs and widely preferred in turbo-machinery industry. CAE analyses for this condition have been performed for test seals, where

geometric dimensions, bristle layout and material properties have already been detailed in Chapter 2 *(Tables 2.3, 2.4, 2.6 and 2.7).*

6.2.1 CAE Analyses with B31 Elements

6.2.1.1 FE Model Details and Analysis Steps

The unwrapped seal-rotor geometry is used for CAE modeling with B31 elements. Since the backing plate and the rotor have very large stiffness values in comparison to bristles, those components are modeled as analytical rigid bodies. Bristles are modeled as elastic bodies with B31 elements having circular cross-section. The modeled brush seal has 15 rows in the rotor axial direction. In the circumferential direction, three rows of bristles are modeled with cyclic boundary conditions. Test seals are modeled with staggered configuration having the axial spacing of 112.73µm and tangential spacing of 154.64µm. CAE model details are given in Figure 6.9 and Table 6.2.

<table>
<tr><th colspan="4">Test Seals, CAE Model Details – B31</th></tr>
<tr><td colspan="2">Element type for bristles</td><td colspan="2">B31</td></tr>
<tr><td colspan="2">Number of nodes per bristle</td><td colspan="2">19</td></tr>
<tr><td colspan="2">Total number of nodes</td><td colspan="2">760</td></tr>
<tr><td colspan="2">Total number of elements</td><td colspan="2">722</td></tr>
<tr><th colspan="4">Material properties</th></tr>
<tr><td></td><td colspan="2">Bristles (Haynes 25)</td><td>Rotor and backing plate</td></tr>
<tr><td>Elastic modulus</td><td colspan="2">225000 MPa</td><td rowspan="4">Rigid (Relatively high stiffness in comparison with bristles)</td></tr>
<tr><td>Density</td><td colspan="2">9.13×10^{-9} tonne/mm^3</td></tr>
<tr><td>Poisson’s ratio</td><td colspan="2">0.3</td></tr>
<tr><td>Yield strength</td><td colspan="2">725 MPa</td></tr>
<tr><th colspan="4">Brush seal properties</th></tr>
<tr><td colspan="3">Bristle surface roughness [µm]</td><td>1.27</td></tr>
<tr><td colspan="3">Rotor surface roughness [µm]</td><td>1.00</td></tr>
<tr><td colspan="3">Backing plate roughness [µm]</td><td>1.00</td></tr>
<tr><td colspan="3">Axial spacing, S_A [µm]</td><td>112.73</td></tr>
<tr><td colspan="3">Tangential spacing, S_T [µm]</td><td>154.64</td></tr>
</table>

Table 6.2: Test seal FE model details – B31 elements

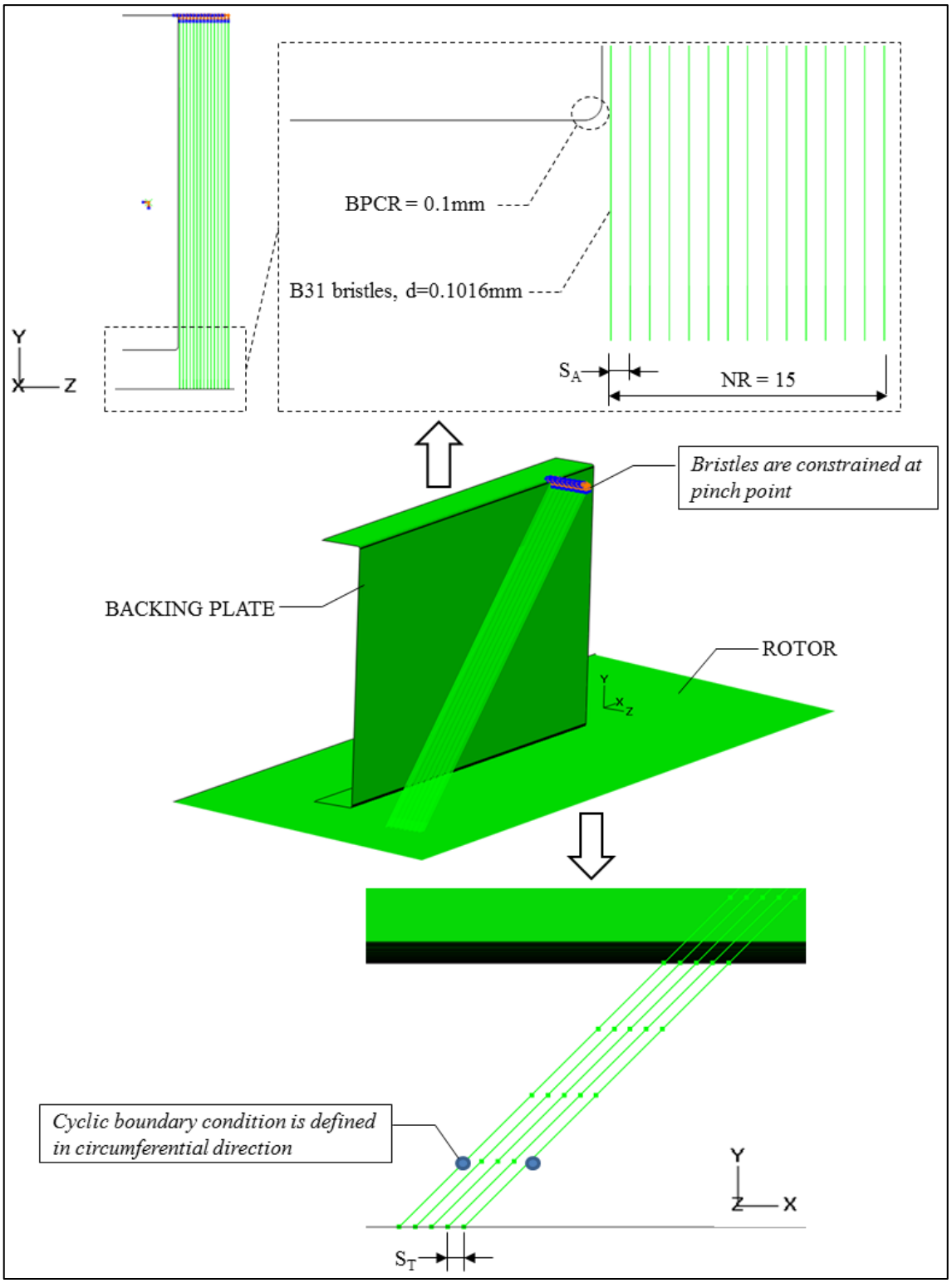

Figure 6.9: Brush seal CAE model with B31 elements – CAE model details

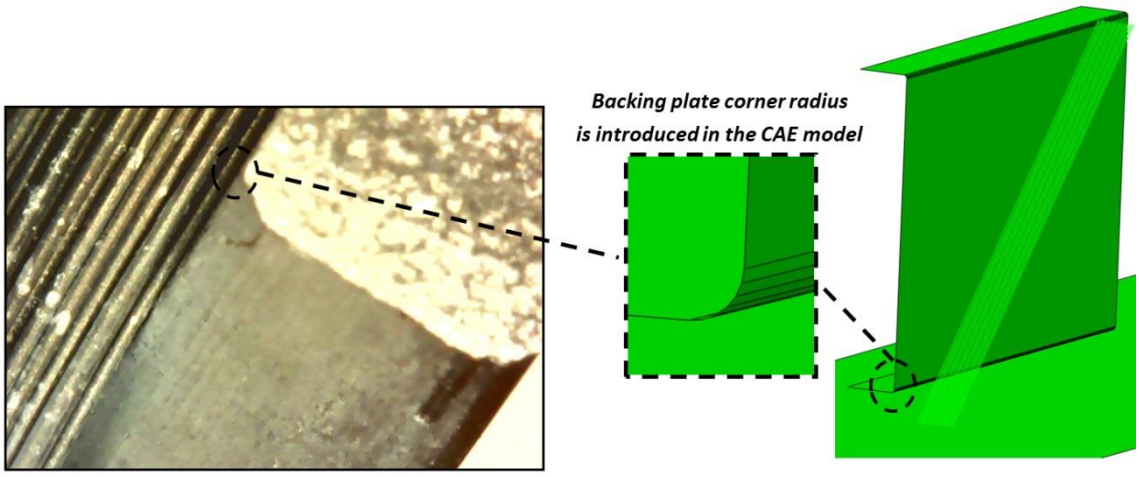

Figure 6.10: Brush seal CAE model with B31 elements – Modeling backing plate corner radius

Test seal photo given in Figure 6.10 shows that the backing plate corner has a small radius *(at the FH contact with bristles)*, which is introduced during manufacturing process. Therefore, the backing plate is modeled with 0.1mm corner radius for simulations.

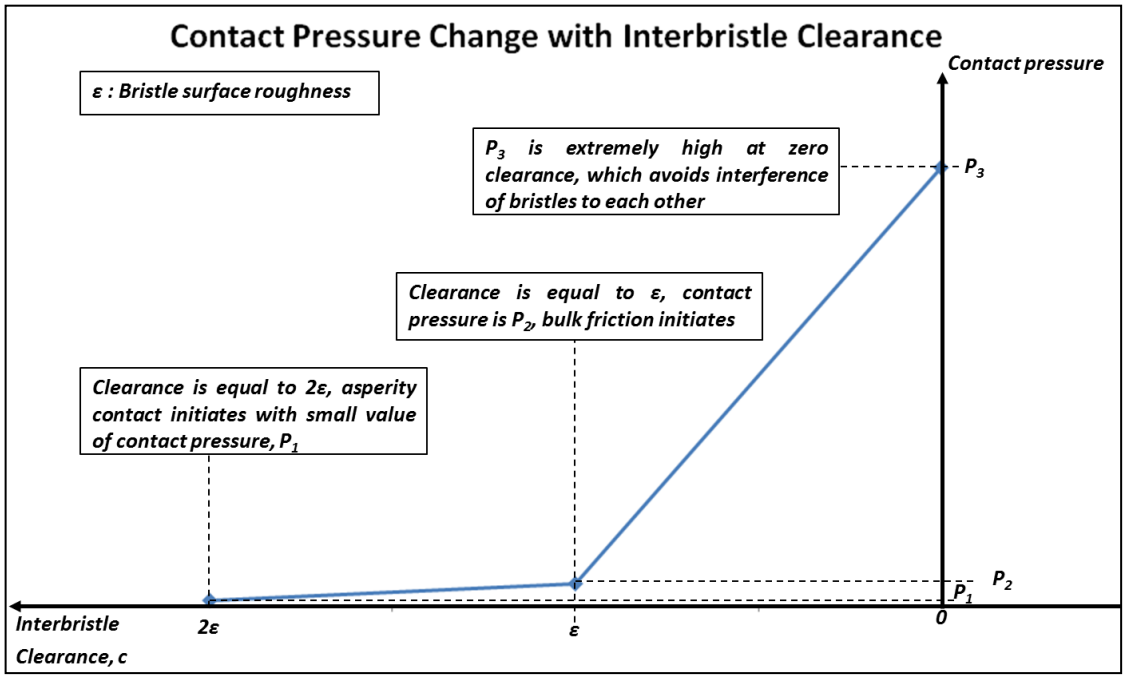

Figure 6.11: Inter-bristle contact formulation, transition from asperity contact to bulk friction

Each bristle has 19 nodes, where dense mesh is preferred at the local region of fence height. The inter-bristle, bristle-rotor and bristle-backing plate contacts and frictions are included in simulations. The soft contact formulations are used during simulations to define the physical contact accurately; where the contact pressure has

low values when asperity peaks get in contact, and it becomes extremely high when the clearance between bristles approaches to zero. Similar approach has also been used while defining the backing plate-bristle and rotor-bristle contacts. The clearance values for contact pressure definitions are functions of surface roughness values tabulated in Table 6.2. Asperity contact threshold is the sum of surface roughness values of contact pairs as given in Figure 6.11. The inter-bristle and bristle-backing plate friction coefficients of 0.3 have been used for analyses. Different values of rotor-bristle friction coefficients are simulated and correlated with free-state stiffness test data.

The unpressurized-nonrotating rotor simulations have been run up to 0.6mm radial interference with 0.1mm resolution. The rotor movement has been defined by applying enforced displacement to rotor reference point. Rotor rub has been followed by pull back of the rotor to its original position to simulate loading and unloading steps conditions *(Figure 6.12)*.

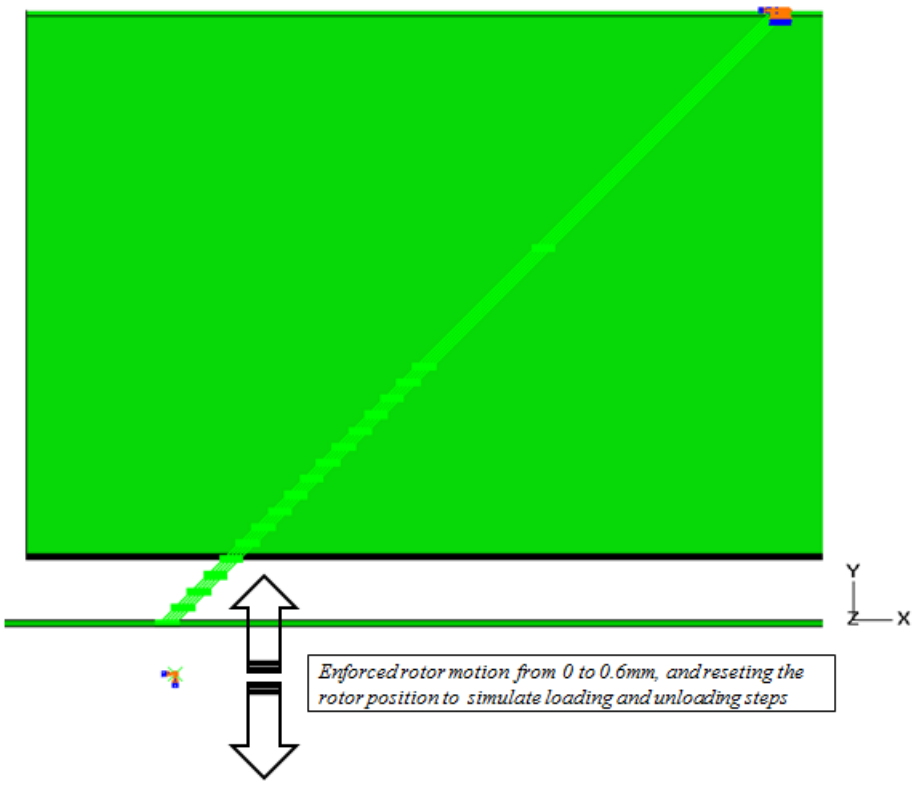

Figure 6.12: Analysis steps for unpressurized non-rotating rotor interference simulations – B31

6.2.1.2 Analysis Results and Correlation with Test Data

Displacement contour in unpressurized-nonrotating rotor interference simulation is detailed in Figure 6.13 for 0.6mm radial interference. Due to frictional effects and cant angle of 45^{o}, the rotor interference deflects the bristles both in radial and tangential directions. Magnitude of the maximum bristle tip displacement is around 0.825mm for rotor interference of 0.6mm.

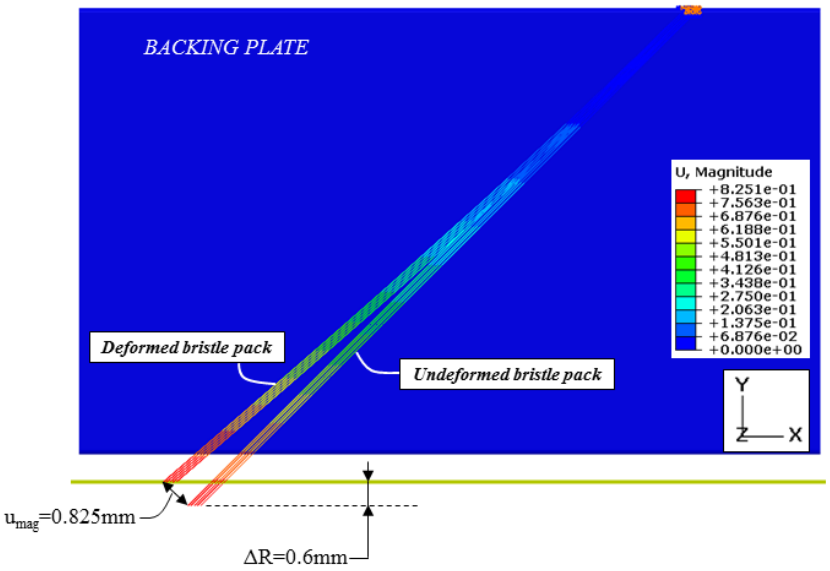

Figure 6.13: Unpressurized nonrotating rotor interference CAE analysis with B31 elements for test seals – Displacement profile at 0.6mm rotor interference

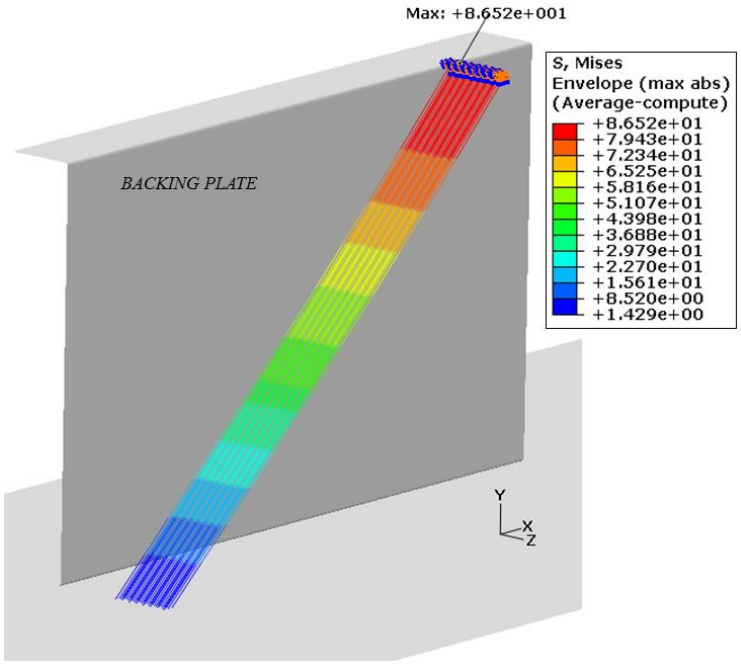

Figure 6.14: Unpressurized nonrotating rotor interference CAE analysis with B31 elements for test seals – VM stress profile at 0.6mm rotor interference

VM stress profile at 0.6mm rotor interference is given in Figure 6.14 for test seals. The maximum VM stress magnitude, which is equal to 86.5MPa, is observed at pinch point as expected. The VM stress levels at different interference levels are tabulated in Table 6.3 test seals.

Unpressurized-nonrotating rotor interference – ΔP = 0, ΔR_{max} = 0.6mm CAE Analysis with B31 elements for Test Seals	
Critical section: z = 0 *(Pinch point)*, Max. VM Stress *[MPa]*	
ΔR *[mm]*	CAE – B31
0.00	0.00
0.10	16.09
0.20	30.33
0.30	44.41
0.40	58.38
0.50	72.53
0.60	89.52

Table 6.3: Unpressurized nonrotating rotor interference CAE analysis with B31 elements for test seals – Maximum VM stress level at different interference levels

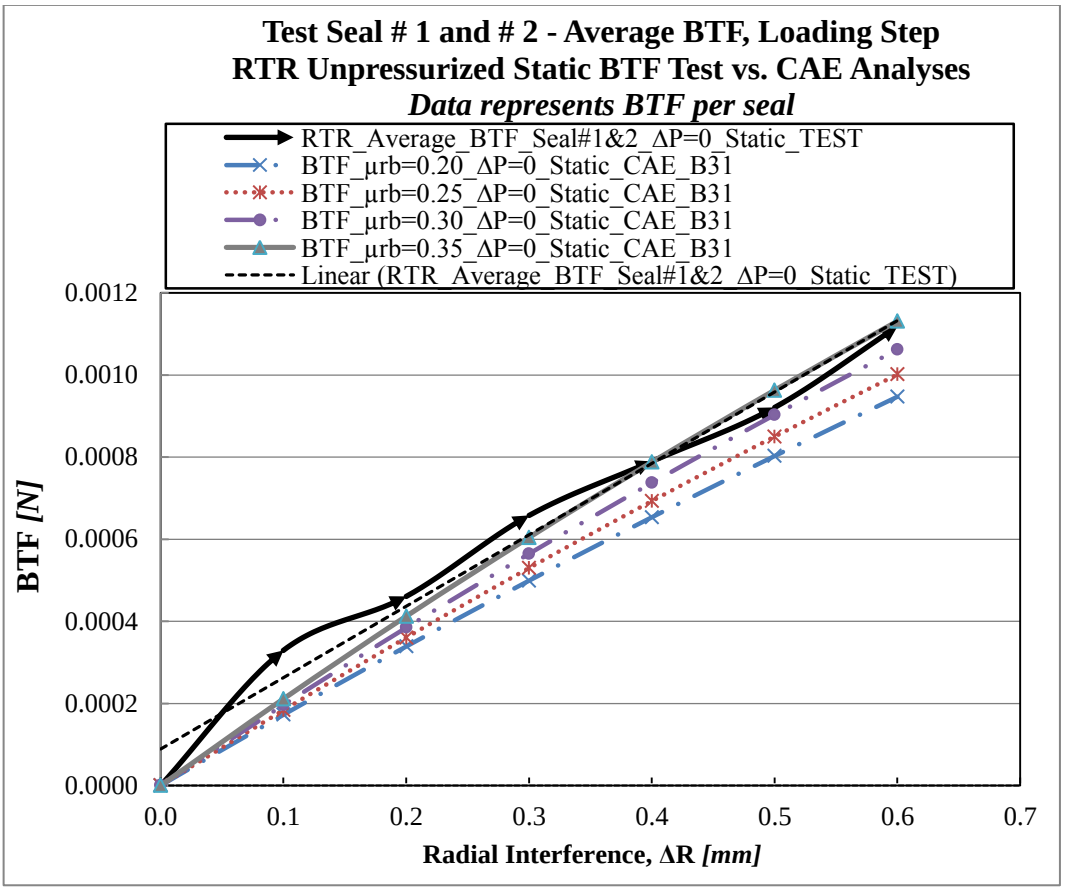

Figure 6.15: CAE analysis with B31 elements for test seals – BTF values and their comparison with RTR-Unpressurized static BTF measurements at loading step *(Rotor bristle friction, μ_{rb}=0.20-0.35)*

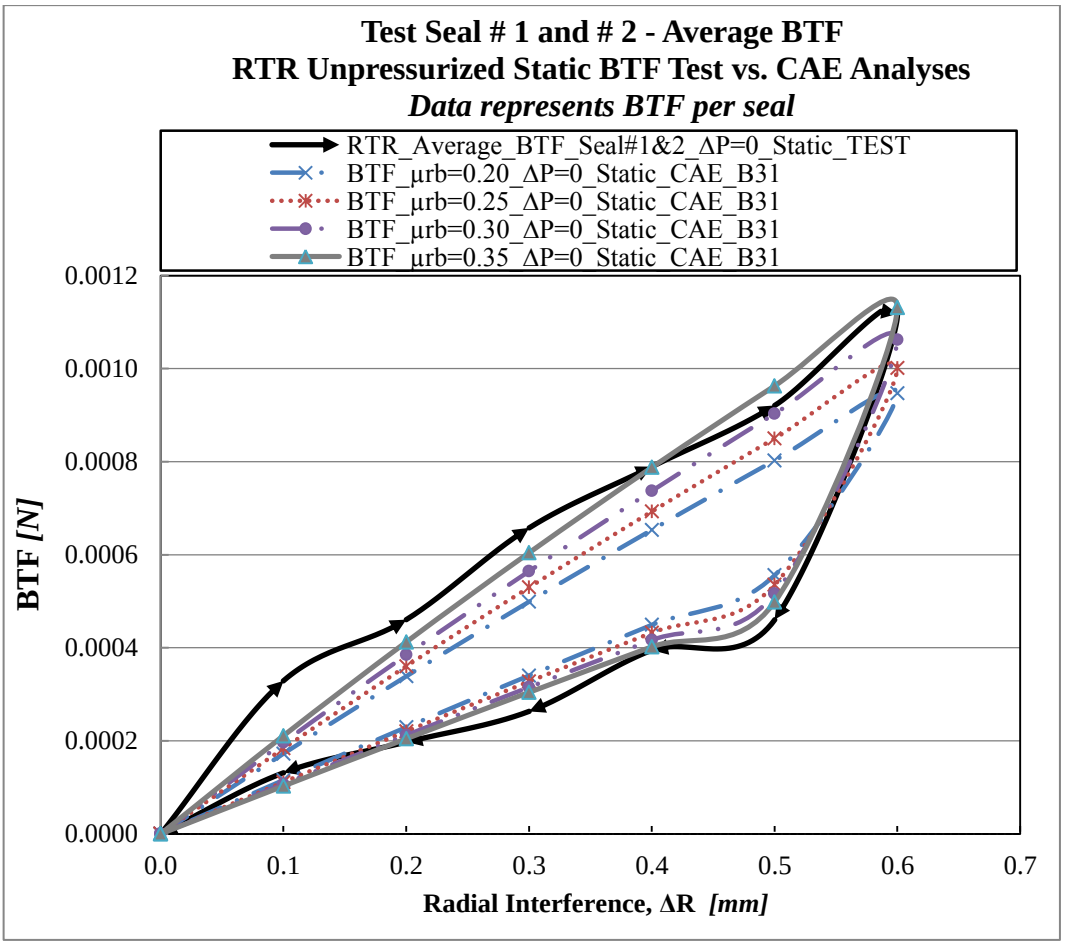

Figure 6.16: CAE analysis with B31 elements for test seals – BTF values and their comparison with RTR-Unpressurized static BTF measurements *(Rotor bristle friction, μ_{rb}=0.20-0.35)*

Free-state bristle tip contact force values are simulated for test seals by using rotor-bristle friction coefficients ranging from 0.20 to 0.35. Comparison of simulated BTF values with RTR-unpressurized static BTF measurements are given in Figure 6.15 for loading step. As it can be seen from the figure, the analyses results show good agreement with test data for rotor-bristle friction coefficient of 0.35. Therefore, further simulations will be performed by using the correlated friction coefficient of 0.35 for rotor-bristle contact.

The BTF results in loading and unloading steps of FE analyses and tests are given in Figure 6.16. The FE simulations with B31 elements successfully simulate the free-state hysteresis, and show good correlation with the test data both in loading and unloading steps. The free-state hysteresis increases with increasing rotor-bristle friction coefficient as expected, which is due to change in direction of frictional forces in loading and unloading steps.

6.2.2 CAE Analyses with C3D8I Elements

6.2.2.1 FE Model Details and Analysis Results

Full circular seal-rotor geometry is used for CAE modeling with C3D8I elements, which includes bristle density, cant angle and axial spacing change in radial direction. The backing plate is modeled as discrete rigid and the rotor is modeled as analytical rigid body, both of which have very large stiffness values in comparison to bristles having high L/d ratios. Bristles are modeled with C3D8I elements, where the mesh size is sufficiently small to capture bristle geometry accurately with high element quality. Bristles' sections have 16 nodes at their circumferences, and 435 nodes are used through the free bristle length of a single bristle. Each bristle has 23,055 nodes, and the FE model has 1,559,108 elements and 1,215,740 nodes in total. The FE model satisfies the element quality criteria checks as summarized in Table 6.4.

Test Seals, CAE Model Details – C3D8I		
Element type for bristles		C3D8I
Number of nodes through free bristle length of a single bristle		435
Number of nodes at bristle section circumference		16
Number of nodes per bristle		23,055
Total number of nodes		1,215,740
Total number of elements		1,559,108
Material properties		
	Bristles *(Haynes 25)*	Rotor and backing plate
Elastic modulus	225000 MPa	Rigid *(Relatively high stiffness in comparison with bristles)*
Density	9.13×10^{-9} tonne/mm^3	
Poisson's ratio	0.3	
Yield strength	725 MPa	
Brush seal properties		
Bristle surface roughness *[μm]*		1.27
Rotor surface roughness *[μm]*		1.00
Backing plate roughness *[μm]*		1.00
Axial spacing, S_A *[μm]*		112.73
Tangential spacing, S_T *[μm]*		154.64
Element Quality Check		
Criteria	Quality Check Results	
Jacobian < 0.50	0% Failed, The minimum Jacobian is 0.50	
Warpage > 5.00	0% Failed, The maximum Warpage is 14.00	
Aspect > 5.00	0% Failed, The maximum Aspect Ratio is 4.06	
Vol AR > 5.00	0% Failed, The maximum Volume Aspect Ratio is 4.06	

Table 6.4: Test seal FE model details – C3D8I elements

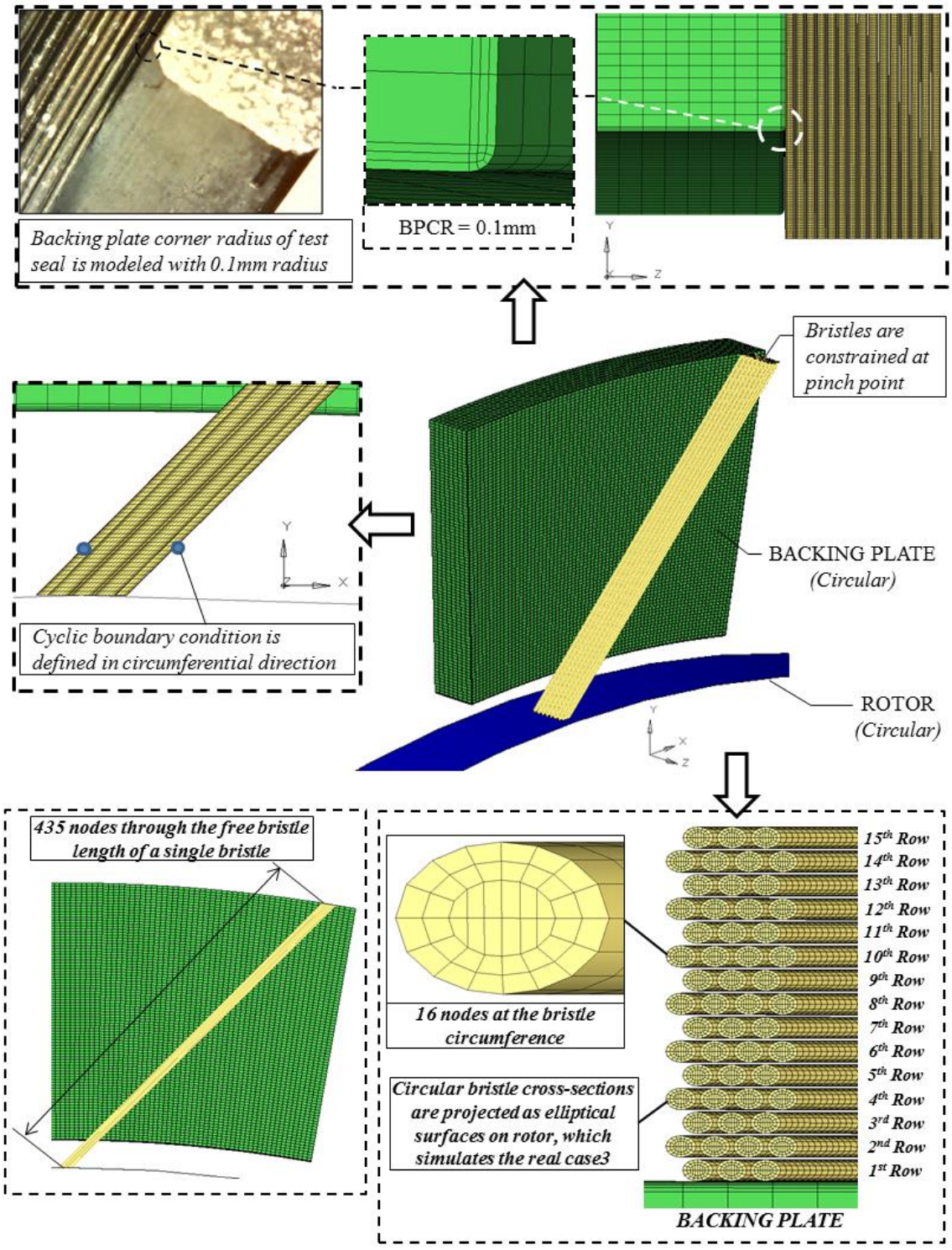

Figure 6.17: Brush seal CAE model with C3D8I elements – CAE model details

The modeled brush seal has 15 rows in the rotor axial direction. In the circumferential direction, four rows of bristles are modeled with cyclic boundary conditions. Test seals are modeled with staggered configuration having the axial spacing of 112.73µm and tangential spacing of 154.64µm. The backing plate corner

radius *(at the FH contact with bristles)*, which is introduced during manufacturing process, is included to FE model with 0.1mm radius. CAE model details are given in Figure 6.9 and Table 6.2.

The inter-bristle, bristle-rotor and bristle-backing plate contacts and frictions are included in simulations. Contact formulation, where contact pressure profile is detailed in Figure 6.11, is same with the CAE model having B31 elements. The inter-bristle and bristle-backing plate friction coefficients of 0.3 have been used for analyses. Correlated friction coefficient value of 0.35 has been used for rotor-bristle contact.

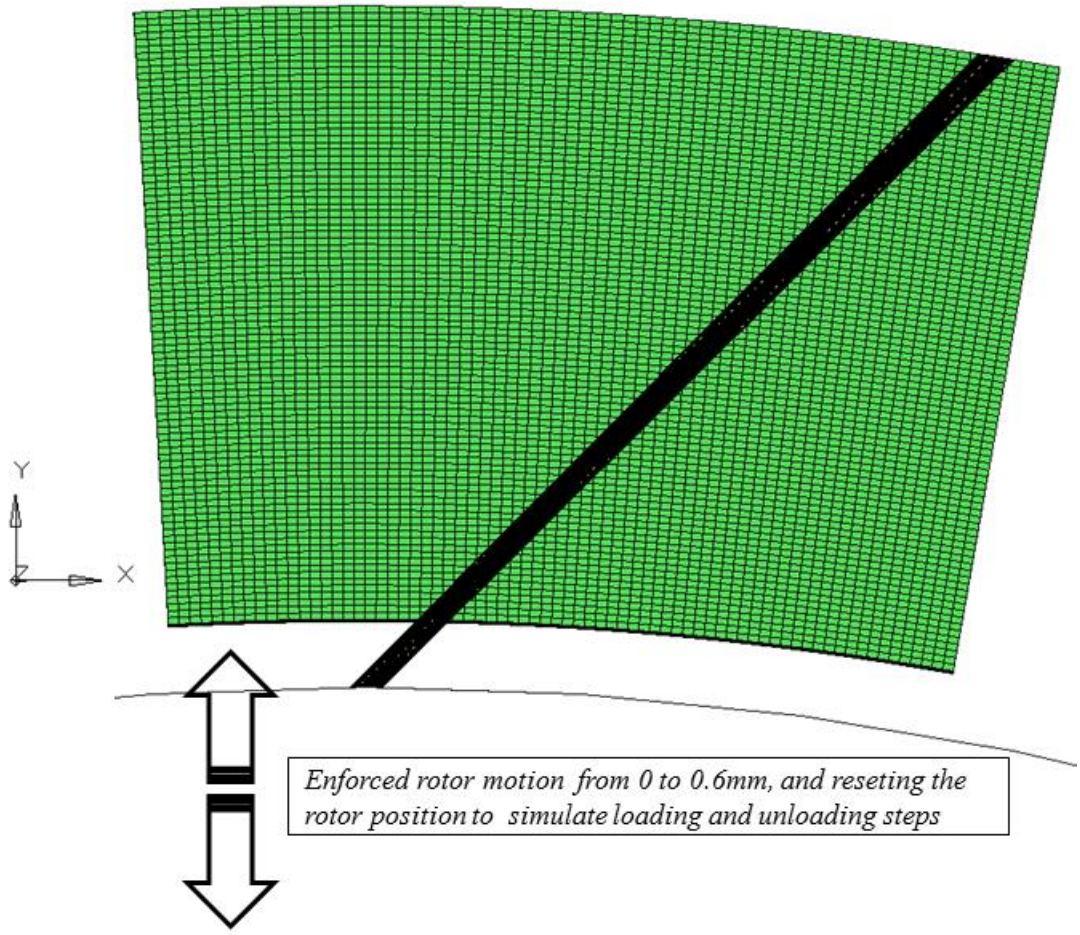

Figure 6.18: Analysis steps for unpressurized non-rotating rotor interference simulations – C3D8I

As in the case of CAE analysis with B31 elements, the unpressurized-nonrotating rotor simulations with C3D8I elements have also been run up to 0.6mm radial interference with 0.1mm resolution. The rotor movement has been defined by applying enforced displacement to circular rotor's reference point. Rotor rub has been followed

by pull back of the rotor to its original position to simulate loading and unloading steps conditions *(Figure 6.18)*.

6.2.2.2 Analysis Results and Correlation with Test Data

Displacement contour in unpressurized-nonrotating rotor interference simulation with C3D8I elements is detailed in Figure 6.19 for 0.6mm radial interference. Due to frictional effects and cant angle of 45^{o}, the rotor interference deflects the bristles both in radial and tangential directions. Magnitude of the maximum bristle tip displacement is around 0.832mm for rotor interference of 0.6mm. Usage of C3D8I elements instead of B31 elements enables better viewing of displacement profile with smoother contour.

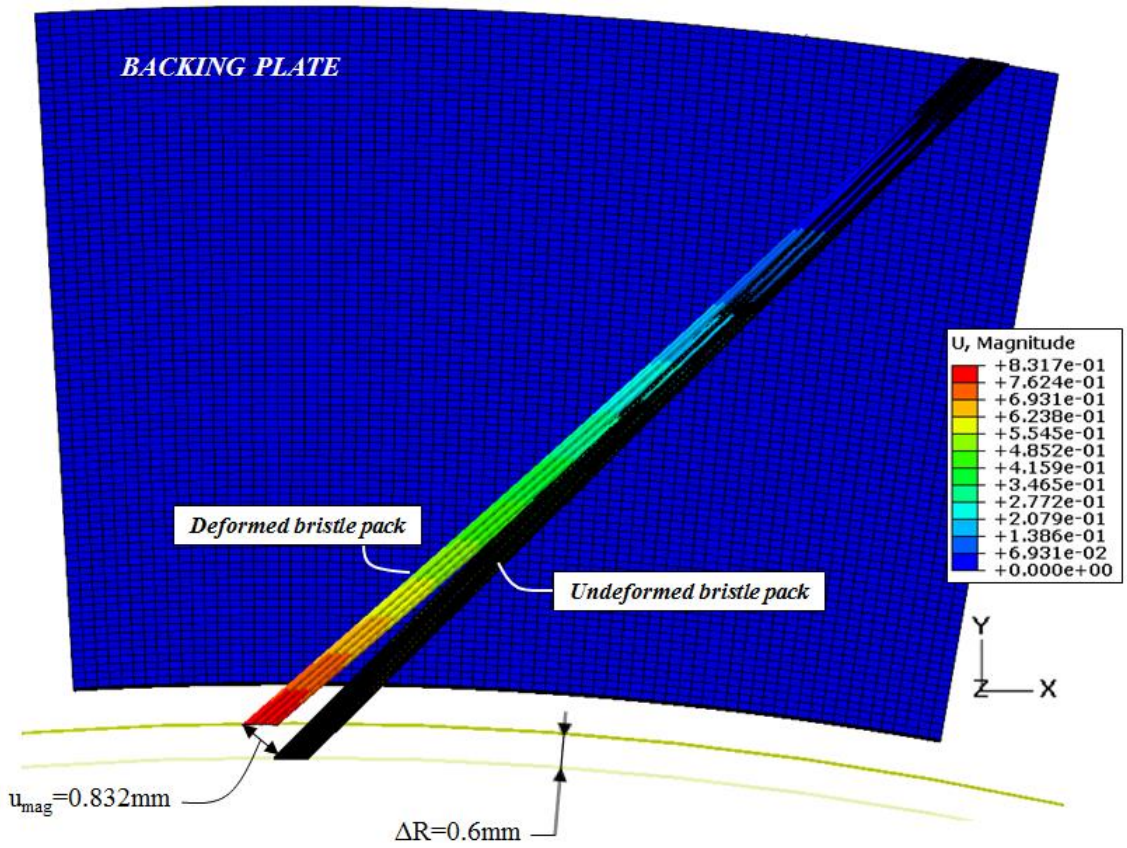

Figure 6.19: Unpressurized nonrotating rotor interference CAE analysis with C3D8I elements for test seals – Displacement profile at 0.6mm rotor interference

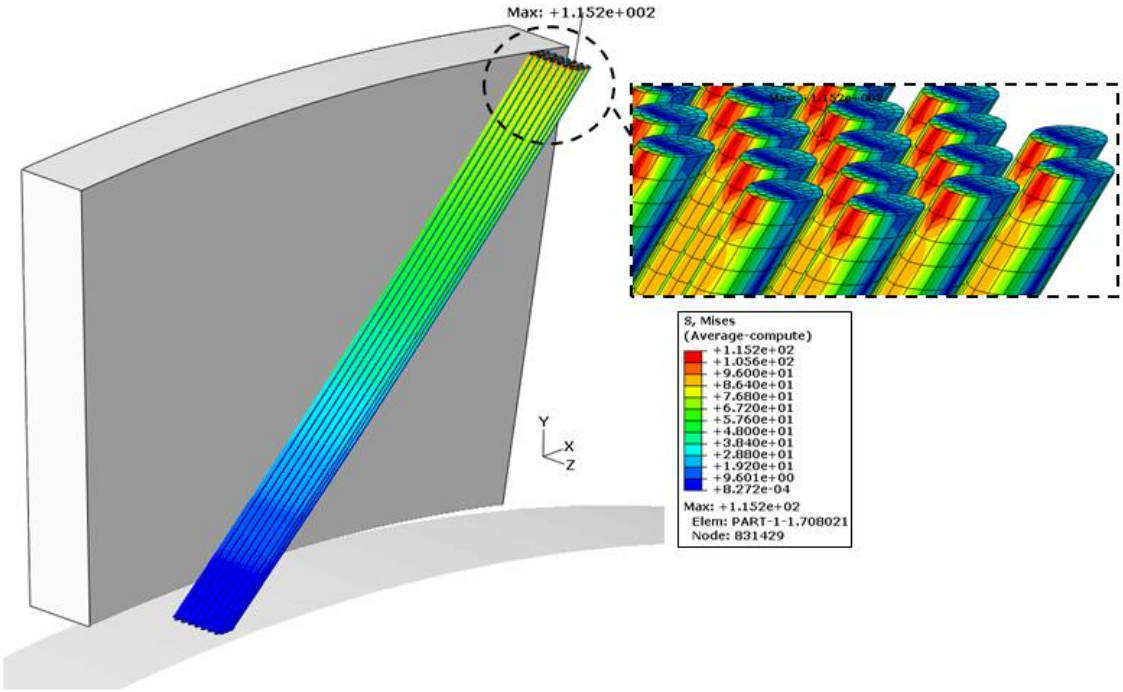

Figure 6.20: Unpressurized nonrotating rotor interference CAE analysis with C3D8I elements for test seals – VM stress profile at 0.6mm rotor interference

Unpressurized-nonrotating rotor interference – $\Delta P = 0$, $\Delta R_{max} = 0.6$mm CAE Analysis with B31 and C3D8I elements for Test Seals		
Critical section: z = 0 *(Pinch point)*, Max. VM Stress *[MPa]*		
ΔR *[mm]*	CAE – C3D8I	CAE – B31
0.00	0.00	0.00
0.10	20.09	16.09
0.20	39.92	30.33
0.30	59.51	44.41
0.40	78.86	58.38
0.50	96.83	72.53
0.60	115.20	89.52

Table 6.5: Unpressurized nonrotating rotor interference CAE analysis with B31 and C3D8I elements for test seals – Maximum VM stress level at different interference levels

VM stress profile at 0.6mm rotor interference is given in Figure 6.20 for FE model using C3D8I elements. The smooth stress contour of C3D8I elements gives better understanding of stress profile of bristles. The maximum VM stress is observed at pinch point, which is direct result of loading condition at unpressurized conditions. Bristles act like a cantilever beam constrained from top and transversely loaded from bristle tip. The maximum VM stress level at pinch point is equal to 115.2MPa for rotor interference level of 0.6mm. The VM stress levels for C3D8I bristles at different interference levels and their comparison with the results of B31 simulations are

tabulated in Table 6.5. Stress levels of CAE model-C3D8I are higher than the results obtained from FE simulations with B31 elements, which is mainly due to more accurate modeling of C3D8I elements for 3D stress state.

Contact pressure profile for CAE analyses-C3D8I is detailed in Figure 6.21 at 0.6mm radial interference. As it can be seen from the figure, the rotor-bristle contact is localized at small region of projected area, which is due to cant angle and bending deformation of bristles. As rotor get in contact with bristles, they start to bend while the cross-section of them remain almost perpendicular to neutral axis of bristle. The strain of the bristle mainly localize at pinch point, and the angle of bristle tips with rotor become larger than cant angle, which in turn avoids full contact of bristle tip area with rotor and results in localized rotor-bristle contact. As it can be seen from the figure, inter-bristle contact cannot initiate for unpressurized-rotor interference conditions with ideal initial bristle layout, where bristles are not touching each other initially and all bristles are perfectly touching the rotor with definite cant angle.

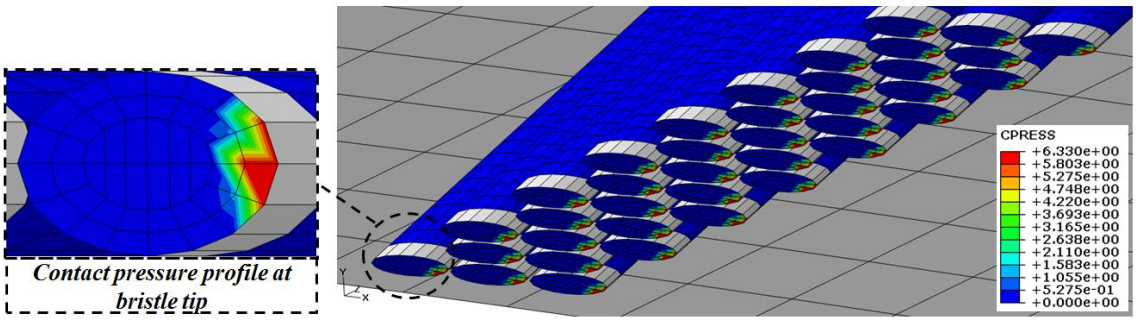

Figure 6.21: Unpressurized nonrotating rotor interference CAE analysis with C3D8I elements for test seals – Contact pressure profile at 0.6mm rotor interference

Free-state bristle tip contact force values are simulated with C3D8I elements, where correlated rotor-bristle friction coefficient of 0.35 is used. Comparison of simulated C3D8I-BTF values with RTR-unpressurized static BTF measurements and simulations with B31 elements are given in Figure 6.22 for loading step. As it can be seen from the figure, the CAE-C3D8I analyses results show good agreement with the test data and give similar results with CAE-B31 analyses. The BTF results in loading and unloading steps of FE analyses and tests are given in Figure 6.23. The FE simulations using both C3D8I and B31 elements successfully simulate the free-state hysteresis, and show good correlation with the test data both in loading and unloading steps.

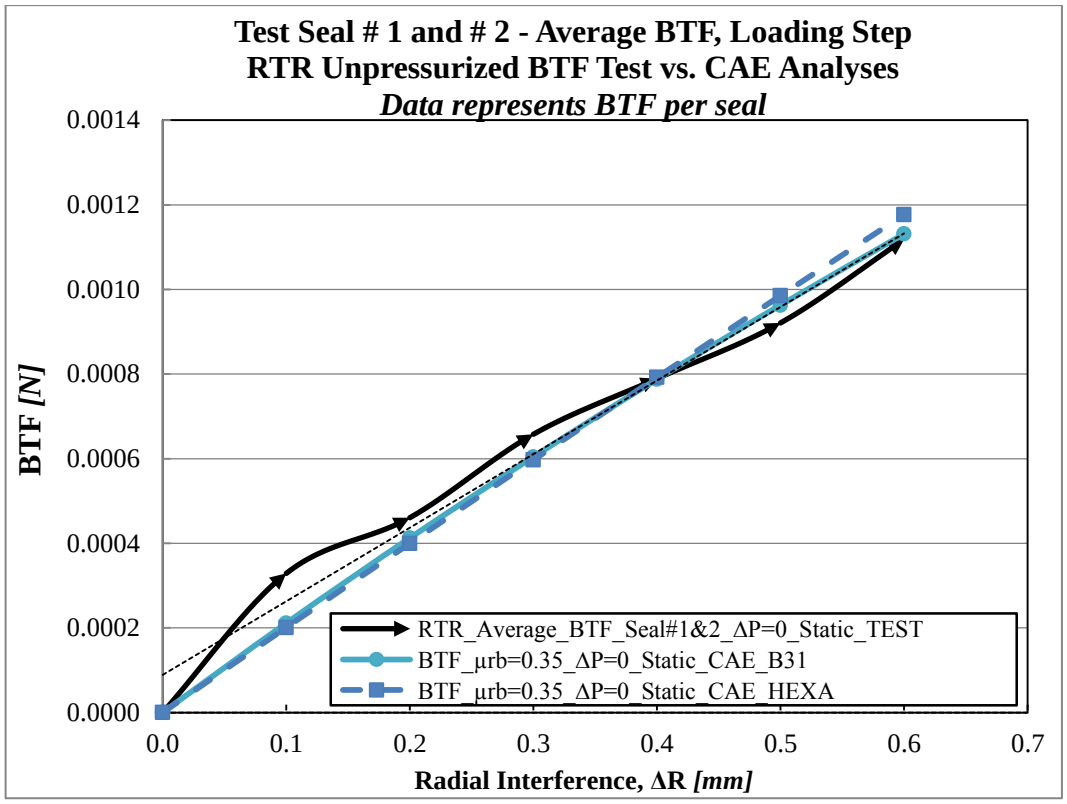

Figure 6.22: CAE analysis with B31 and C3D8I elements for test seals – BTF values and their comparison with RTR-Unpressurized static BTF measurements at loading step *(Rotor bristle friction, μ_{rb}=0.35)*

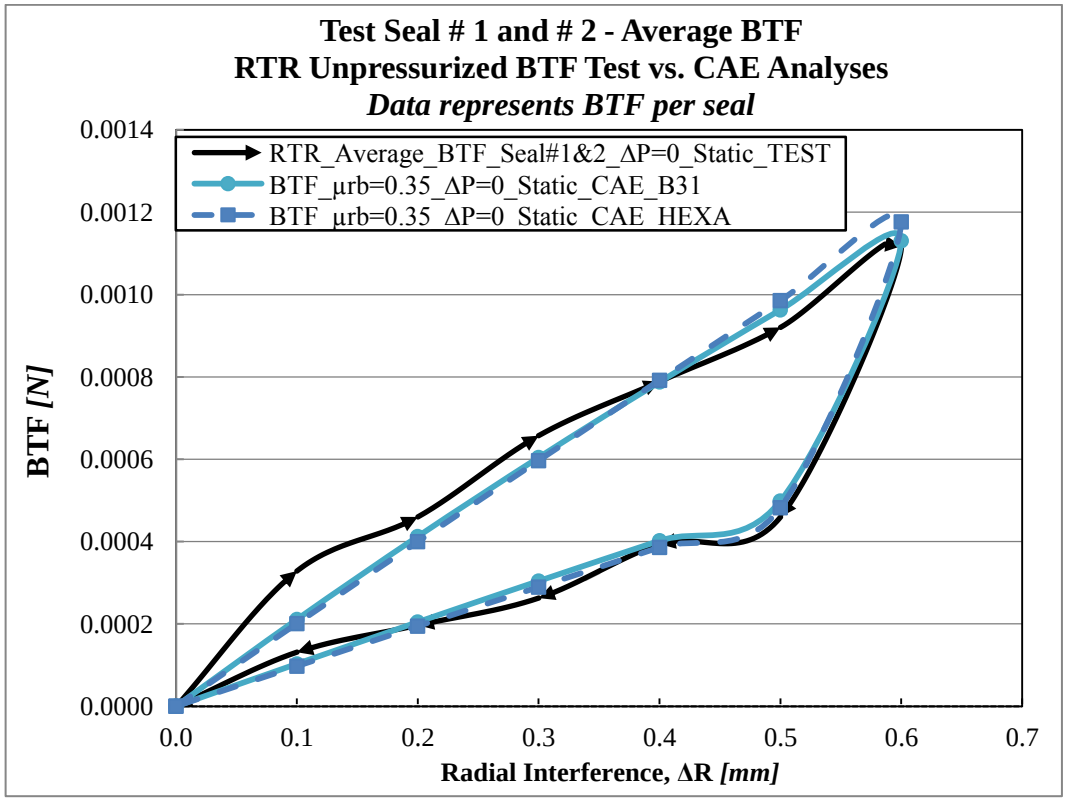

Figure 6.23: CAE analysis with B31 and C3D8I elements for test seals – BTF values and their comparison with RTR-Unpressurized static BTF measurements *(Rotor bristle friction, μ_{rb}=0.35)*

6.2.3 Comparison of CAE Simulations and Analytical Methodologies with Tests

Different analytical and CAE methodologies have been developed for unpressurized non-rotating rotor rub conditions within the content of this study, which are as listed below:

- Analytical methodologies
  - Simple beam theory *(Flower [17])*
  - Modified beam theory
- CAE methodologies
  - CAE model with B31 elements
  - CAE model with C3D8I elements

Analytical methodologies and FE analyses have been run for test seals, and BTF results are compared with each other as well as with the test data. To summarize, BTF comparison of all methodologies with test is also detailed in this section and given in Figures 6.24, 6.25 and Table 6.6. As it can be seen from the Figures, the simple beam theory in the literature *[17]* cannot be correlated with the test data since it does not include any frictional effects into account. CAE analyses using C3D8I and B31 elements give similar BTF results with each other, and CAE results of both also show good correlation with the test data. The modified beam theory, where rotor-bristle friction is included, also gives consistent results with CAE and test data. Considering the contact pressure profile of CAE analyses with C3D8I elements, this is an expected result since rotor-bristle friction is the main reason for free-state hysteresis and BTF magnitudes.

The BTF results of CAE analyses change almost perfectly linear with rotor interference, while BTF measurements slightly deviate from constant stiffness. The almost perfect linear increase in BTF results of analyses is due to idealized initial bristle layout, where all bristles are equally spaced from each other and rotor, and also have same cant angle with rotor. However, in real life applications, bristles are not equally spaced from each other and from rotor, indeed some of them are touching each other as shown section photos of test seals *(Figure 2.17)*. Therefore, it is expected to have slight deviation from constant BTF stiffness for RTR-Unpressurized static stiffness tests.

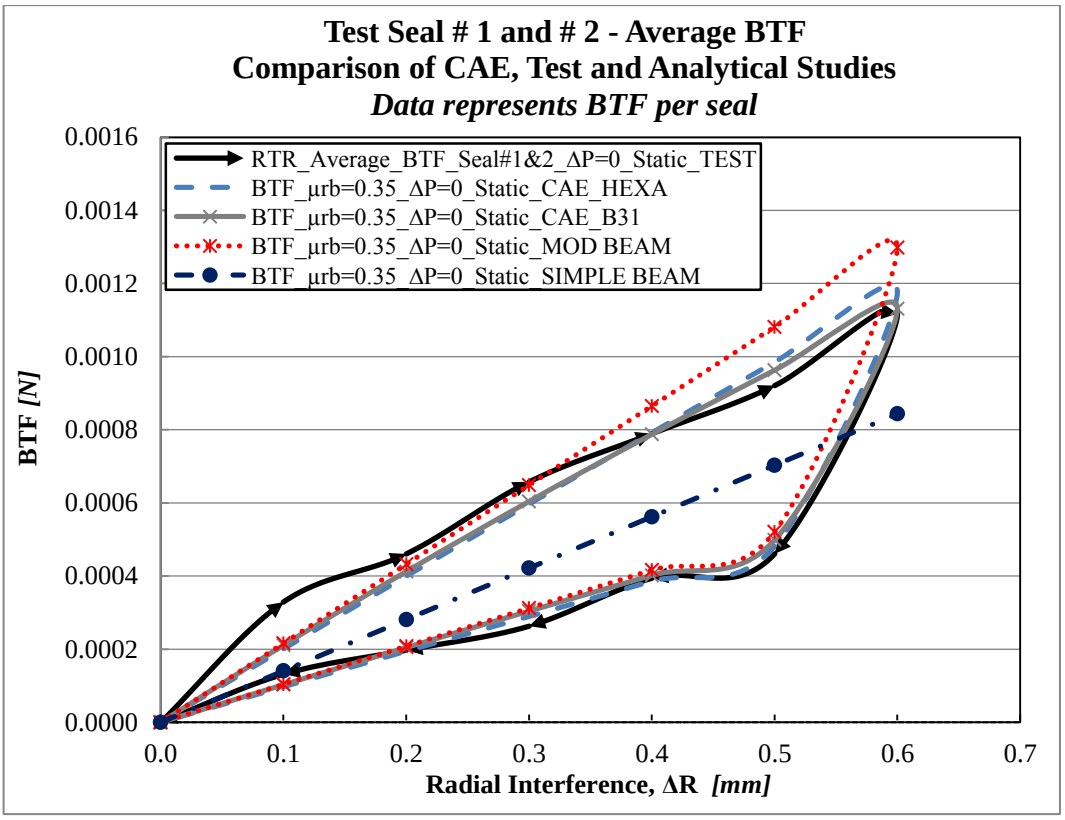

Figure 6.24: Unpressurized nonrotating rotor interference, Comparison of BTF results of CAE, analytical methods *(modified and simple beam)* and test data *(Rotor bristle friction, μ_{rb}=0.35)*

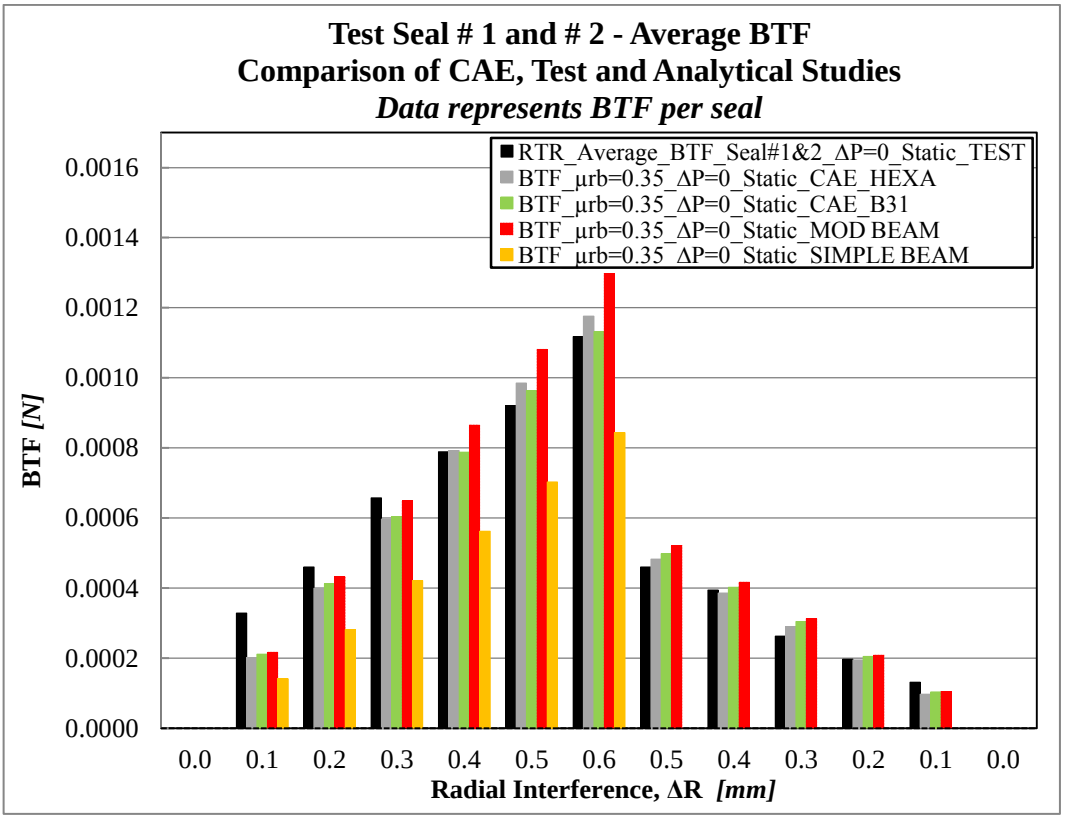

Figure 6.25: Unpressurized nonrotating rotor interference, Comparison of BTF results of CAE, analytical methods *(modified and simple beam)* and test data *(Rotor bristle fric, μ_{rb}=0.35)* – Bar chart

Unpressurized-nonrotating rotor interference – $\Delta P = 0$, $\Delta R_{max} = 0.6$mm Comparison of BTF values for CAE, Analytical Methods and Test					
ΔR *[mm]*	**BTF – Bristle Tip Force *[N]***				
	RTR-Test	CAE – C3D8I	CAE – B31	Modified beam	Simple beam
0.00	0.000000	0.000000	0.000000	0.000000	0.000000
0.10	0.000329	0.000211	0.000201	0.000216	0.000141
0.20	0.000460	0.000412	0.000400	0.000433	0.000281
0.30	0.000658	0.000604	0.000597	0.000649	0.000422
0.40	0.000789	0.000788	0.000792	0.000865	0.000562
0.50	0000921	0.000963	0.000985	0.001081	0.000703
0.60	0.001118	0.001131	0.001177	0.001298	0.000843
0.50	0.000460	0.000498	0.000482	0.000521	-
0.40	0.000395	0.000402	0.000386	0.000417	-
0.30	0.000263	0.000304	0.000290	0000312	-
0.20	0.000197	0.000205	0000195	0.000208	-
0.10	0.000132	0.000103	0.000097	0.000104	-
0.00	0.000000	0.000000	0.000000	0.000000	-

Table 6.6: Unpressurized nonrotating rotor interference, Comparison of BTF results of CAE, analytical methods *(mod. and simple beam)* and test data *(μ_{rb}=0.35)* – Tabulated data

The comparison of maximum VM stress levels is given in Table 6.7 for CAE analyses and analytical studies. As it can be seen from the tabulated data, the CAE-C3D8I analyses give higher stress levels than CAE-B31 analyses. Although displacement and BTF results are similar for two FE methodologies, the VM stress calculation of C3D8I elements is more accurate due to complex 3D stress state formulations at integration points. Modified beam theory and simple beam theory almost gives same VM stress results with each other, which is also smaller than the CAE-C3D8I analyses.

Unpressurized-nonrotating rotor interference – $\Delta P = 0$, $\Delta R_{max} = 0.6$mm Comparison of VM stress levels for CAE and Analytical Studies				
Critical section: z = 0 *(Pinch point)*, Max. VM Stress *[MPa]*				
ΔR *[mm]*	CAE – C3D8I	CAE – B31	Mod. beam	Simple beam
0.00	0.00	0.00	0.00	0.00
0.10	20.09	16.09	16.55	16.55
0.20	39.92	30.33	33.11	33.09
0.30	59.51	44.41	49.67	49.63
0.40	78.86	58.38	66.24	66.18
0.50	96.83	72.53	82.79	82.73
0.60	115.20	89.52	99.35	99.27

Table 6.7: Unpressurized nonrotating rotor interference, Comparison of VM stress results of CAE and analytical methods *(mod. and simple beam)* *(μ_{rb}=0.35)* – Tabulated data

6.3 Pressure Load without Rotor Interference *(Steady State)* – Test Seals

Pressure load without rotor interference case refers to steady state turbine/turbojet engine operating conditions. As the brush seals installed with slight interference or line-to-line contact with rotor, small gap is maintained at steady state operating conditions after fist start of the engine. Therefore, the turbine/turbojet shaft-brush seal have 1 to 2 mils clearance at their operating conditions without transients. Although pressure load without rotor interference condition does not alter rotor-bristle contact related frictional heat generation or wear, this case has crucial importance in determining the seal life and performance stability since most of the bristle failures in real life applications are caused from pressurizing-depressurizing cycles of the turbine/turbojet engine. Considering the strain measurement constraints on bristles at operating conditions simulating steady state conditions with correlated CAE model has crucial importance in determining any possible failure states for bristle loss issues.

Two different FE methodologies, which are using C3D8I and B31 elements, have been used in this study to simulate steady state turbine operating conditions. Both CAE models are correlated with test data, where Free-state stiffness correlation has already been detailed in the previous sections, and pressurized stiffness correlation will be given in the following sections of this study. Pressurized seal simulations without rotor interference helps better understanding of bristle deformation and stress-critical points for a brush seal at steady state turbine operating conditions.

6.3.1 CAE Analyses with B31 Elements

6.3.1.1 FE Model Details and Analysis Steps

The FE model for pressure load simulations is same with the one that has been used for unpressurized-rotor interference analyses, only the analysis steps are different. The analyses are run for 0.225MPa and 0.3MPa pressure loads, both of which simulate the pressurized test conditions of this study. 7^{th} order polynomial fit to experimental data of Bayley et al. [59] and Turner et al. [60] is used for pressure load, and applied as equivalent line loads on B31 elements in rotor axial direction as shown in Figure 6.26.

Linear pressure drop suggested by Duran [65] and Bhate et al. [66] is used through the bristle pack. The pressure load profile per bristle row in FE model is shown in Figure 6.27 for 0.225MPa and 0.3MPa pressure loads.

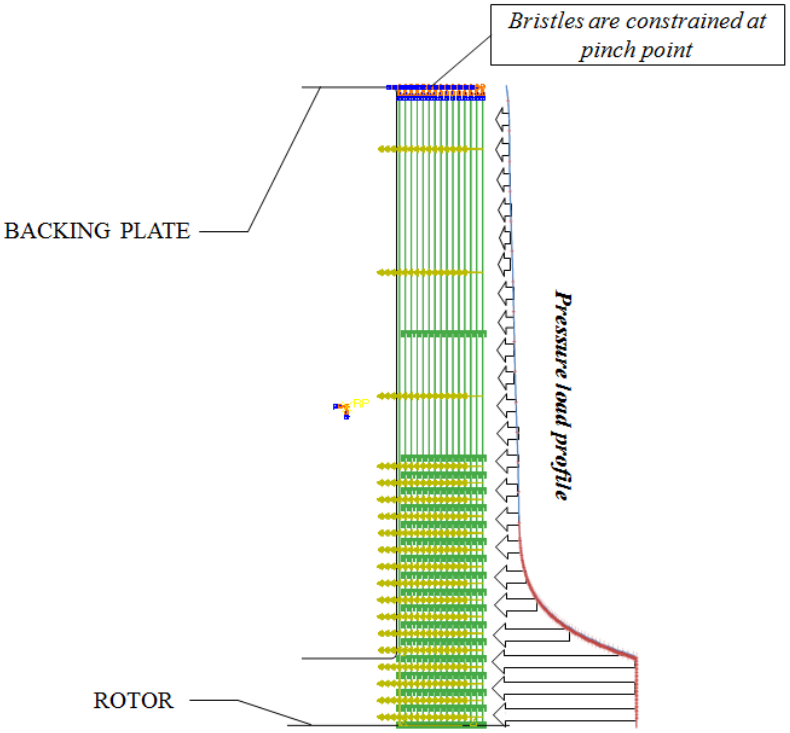

Figure 6.26: Pressure load without rotor interference – CAE-B31, Pressure load profile

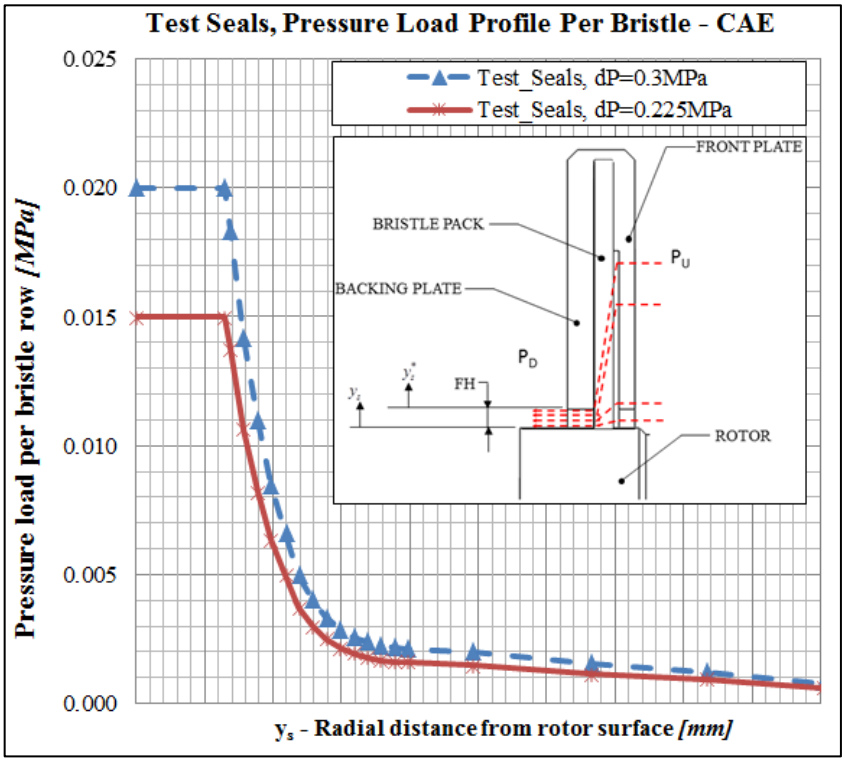

Figure 6.27: Pressure load without rotor interference – CAE-B31, Pressure load profile per bristle at ΔP=0.225MPa and ΔP=0.3MPa

Contact definitions are also same with the FE model that has already been detailed in Section 6.2.1, and correlated rotor-bristle friction coefficient of 0.35 is used for simulations. The inter-bristle and bristle-backing plate friction coefficients of 0.3 have been used for analyses.

6.3.1.2 Analysis Results

The displacement profile for test seal under 0.3MPa pressure load is given in Figure 6.28. As a result of pressure load, which is maximum at the fence height region, bristles bend axially while backing plate act as pivot point for the first bristle row *(backing plate side)*. As a result, the overhanging part of the bristles deform under the backing plate in the flow direction.

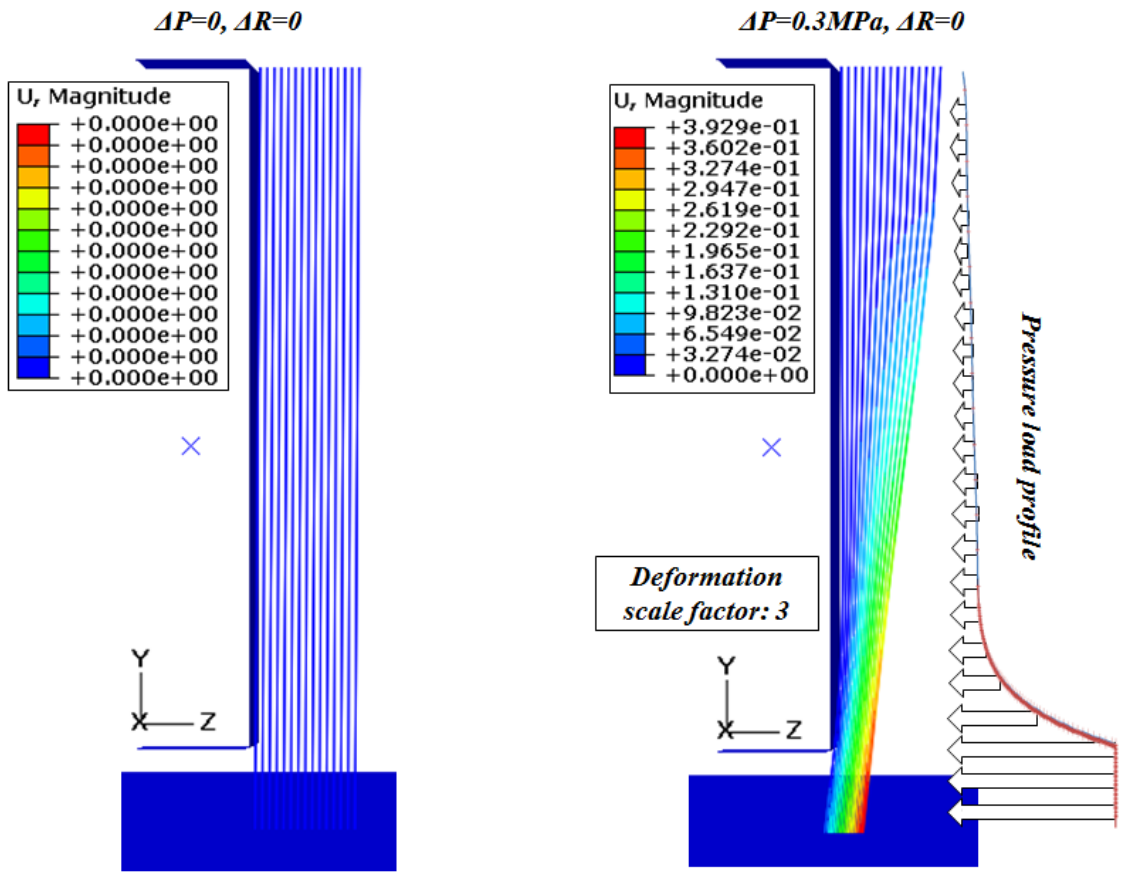

Figure 6.28: Pressure load without rotor interference – CAE-B31, Displacement magnitude contour at ΔP=0.3MPa

The space between bristles is closed and inter-bristle contact is observed when the pressure load is applied. Therefore, bristles at the front plate side *(last row (15th row))* have the highest displacement magnitude, which is equal to 0.39mm at 0.3MPa pressure load. The initial pack thickness, which is around 1.68mm, is reduced to 1.34mm at inner diameter of the seal. As it can be seen from the Figure 6.29, the initial pack thickness at the seal inner diameter decreases by 25% when 0.3MPa pressure load is applied. Decrease percent in pack thickness is equal to initially defined axial bloom value of 25%.

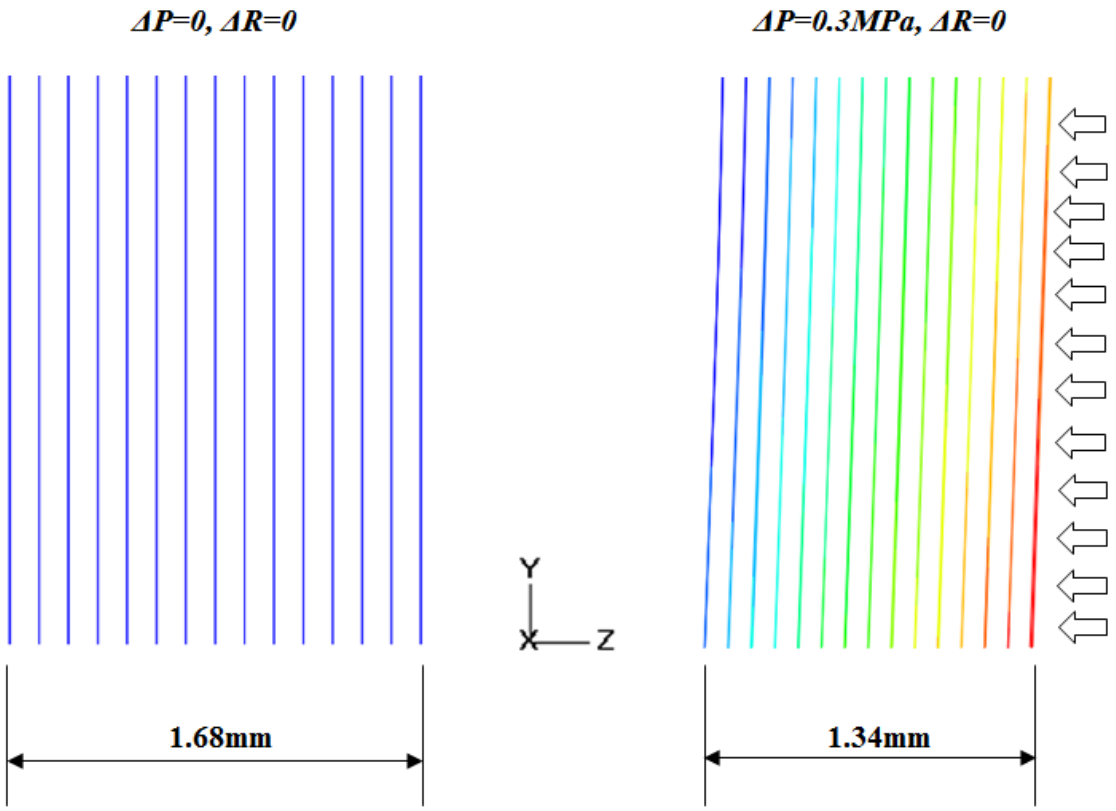

Figure 6.29: Pressure load without rotor interference – CAE-B31, Seal pack thickness decrease at ΔP=0.3MPa

Resultant displacement vectors and detailed deformation of 1st row *(downstream / backing plate side)* and 15th row *(upstream / front plate side)* of bristles under 0.3MPa are given in Figure 6.30, which gives better understanding of seal behavior under pressure load. As it can be seen from the figure, the overhung portion of the backing plate side bristles bend under the backing plate in the flow direction, while portion

above the FH point deforms in the reverse direction. The FH corner of backing plate acts as pivot point and the backing plate – bristle contact is localized at that region, which explains the bristle failure at FH point in real life applications. However, the bristles at the front plate side *(15th row)* deforms in the flow direction, where deformation is maximum at the FH region as bristles are free to move and not supported by backing plate. Above FH, the support from inter-bristle contact cause displacement magnitudes of front plate side bristles to decrease, and bristle deformation is equal to zero at pinch point.

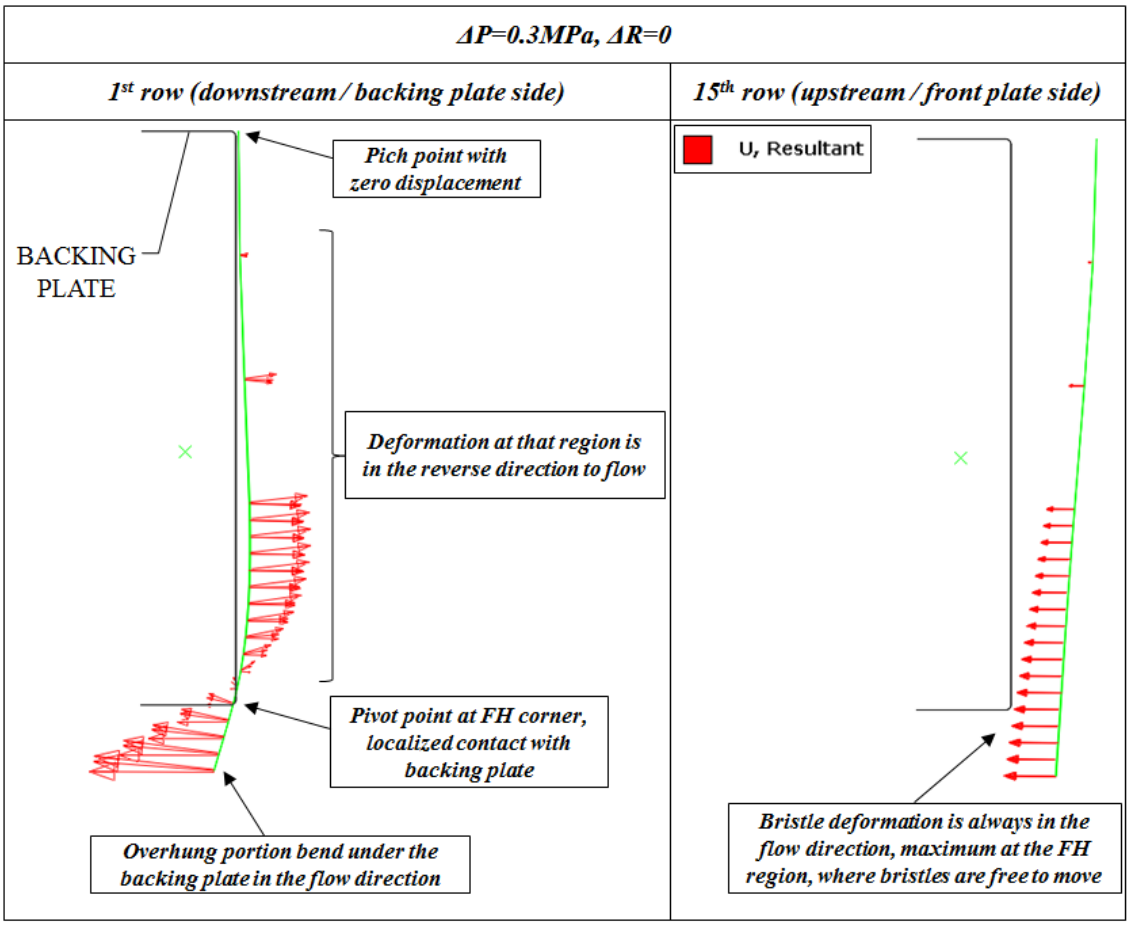

Figure 6.30: Pressure load without rotor interference – CAE-B31, Detailed bristle deformation and resultant vectors for 1st row *(backing plate side)* and 15th row *(front plate side)* bristles, ΔP=0.3MPa

Von Mises *(VM)* stress profile at 0.3MPa pressure load is presented in Figure 6.31 for the test seal. The effect of bristle deformation profile and localized contact at local region of FH point can be observed better in stress profile. As a result of localized backing plate and bristle contact, the maximum VM stress is observed around the backing plate corner *(corresponds to FH)* at the first row *(downstream / backing plate*

side). The maximum VM stress at FH point of downstream side bristles is around 99.2MPa for ΔP=0.3MPa. At the pinch point, the downstream side bristles have the VM stress value of 7MPa. However, the front plate side *(upstream side, 15th row)* bristles are supported by other bristles with inter-bristle contact, and therefore they do not suffer from localized contact pressure and have their maximum stress at pinch point. The VM stress at the pinch point of upstream / front plate side bristles equals to 69MPa, while FH point stress magnitude is around 10MPa for this bristle row.

Steady state stress profile obtained from FE analysis is consistent with real life applications. It is known from the industrial applications that the failure of downstream/backing plate side bristles usually occurs at the fence height point *(backing plate inner diameter)*, if seal gets over pressurized.

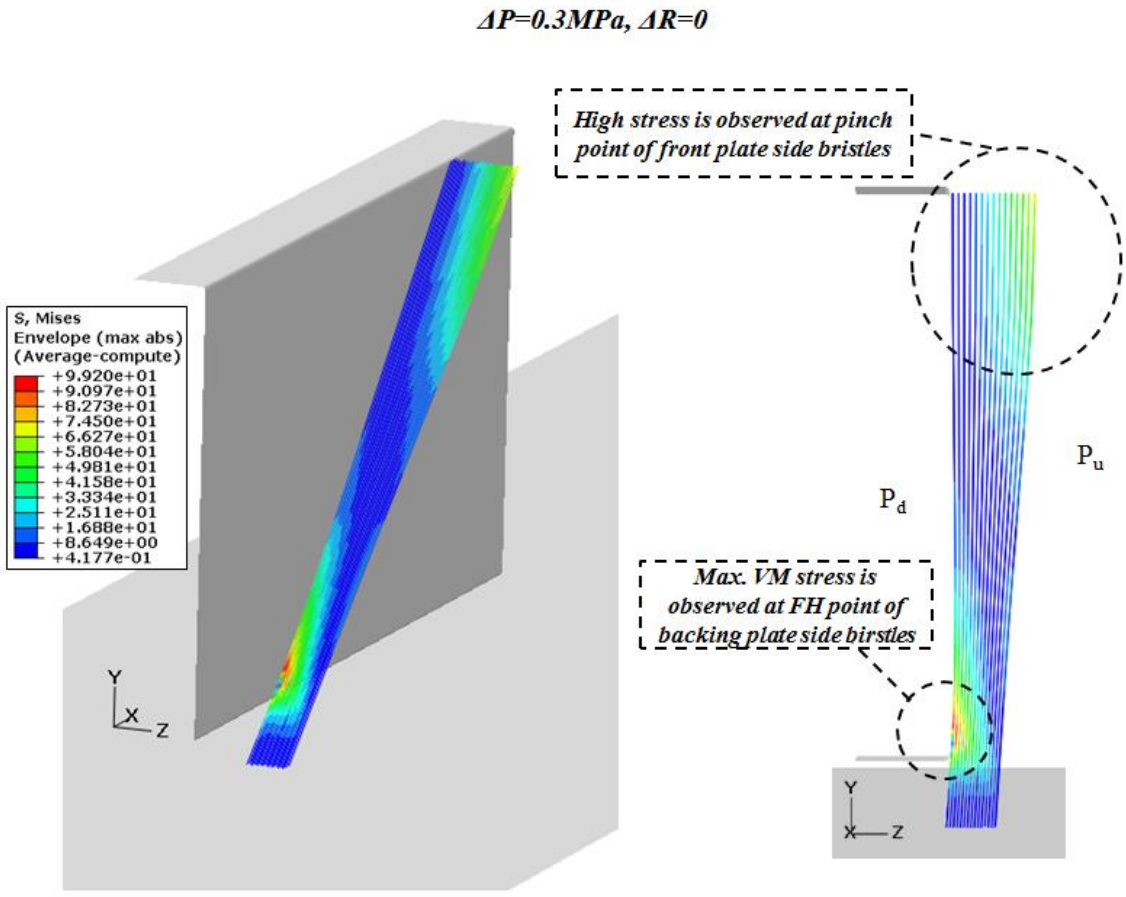

Figure 6.31: Pressure load without rotor interference – CAE-B31, VM stress profile, ΔP=0.3MPa

Stress and displacement results for test seal CAE-B31 analyses are summarized in Table 6.8 for ΔP=0.225MPa and 0.3MPa. The maximum displacement magnitude and decrease in pack thickness for ΔP=0.225MPa are almost same with 0.3MPa analyses,

which is expected since both pressure loads can deform front plate side until the first inter-bristle contact. Decrease percent in pack thickness is equal to initially selected axial bloom, which is 25%. The maximum VM stress at FH point of backing plate side bristles is equal to 85.8MPa for 0.225MPa pressure load, which is lower than the stress levels obtained under pressure load of 0.3MPa. Upstream side bristles have 66MPa VM stress magnitude at pinch point when 0.225MPa pressure load is applied.

Pressure load without rotor interference CAE Analysis with B31 elements for Test Seals			
Displacement results			
		ΔP=0.225MPa	ΔP=0.3MPa
Max. displacement magnitude		0.38mm	0.39mm
Initial pack thickness		1.68mm	1.68mm
Deformed pack thickness		1.34mm	1.34mm
Decrease in pack thickness		25%	25%
Stress results			
Backing plate side *(downstream, 1st row)*	FH point	85.8MPa	99.2MPa
	Pinch point	~8MPa	~7MPa
Front plate side *(upstream, 15th row)*	FH point	~9MPa	~10MPa
	Pinch point	66.0MPa	69.0MPa

Table 6.8: Pressure load without rotor interference – CAE-B31, Stress and displacement profile at ΔP=0.225MPa and ΔP=0.3MPa

6.3.2 CAE Analyses with C3D8I Elements

6.3.2.1 FE Model Details and Analysis Steps

CAE analyses for steady state turbine conditions have also been run with C3D8I elements, where FE model details have already been provided in Section 6.3.1.2. Considering the convergence difficulty of pressing circular rotor on 3D bristles, which causes chattering issues, and also bearing in mind that the circular rotor having large diameter contacting the bristles with cyclic BCs at small region in comparison with its radius, the rigid rotor is modeled as flat surface for the sake of overcoming convergence difficulties.

Pressure load profile given in Figure 6.27 is used for analyses, where pressure on 3D faces of C3D8I elements are used instead of line loads, as detailed in Figure 6.32. The pressure load is applied on usptream protion of the bristle surfaces.

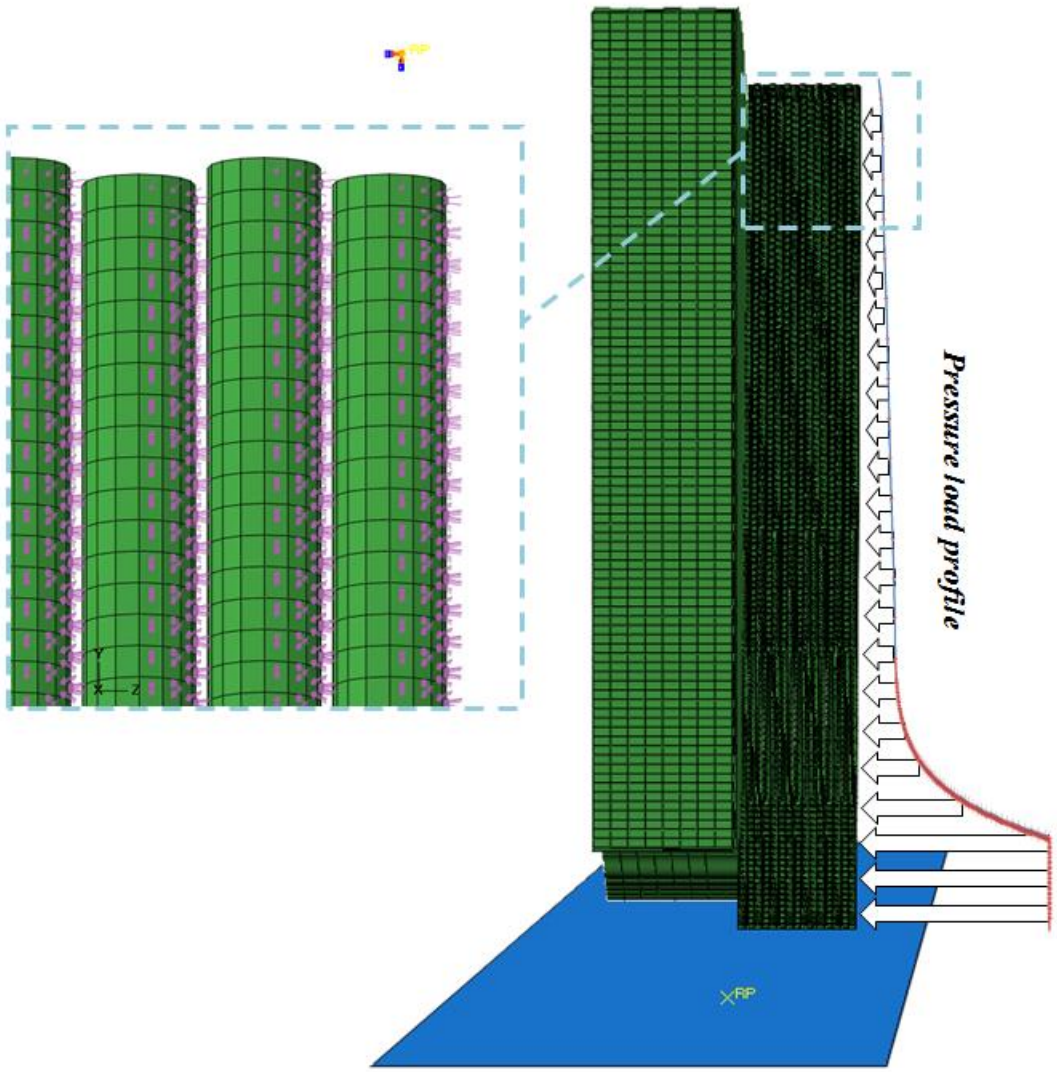

Figure 6.32: Pressure load without rotor interference – CAE-C3D8I, Pressure load profile

All contacts are defined in a same manner with the FE model detailed in Section 6.3.1.2. The correlated rotor-bristle friction coefficient value of 0.35 is used, while the inter-bristle and bristle pack-backing plate friction coefficient is taken as 0.3.

6.3.2.2 Analysis Results

The displacement profile for test seal under 0.3MPa pressure load is given in Figure 6.33, where results have been obtained from CAE analyses with C3D8I elements. The CAE-C3D8I results gives better viewing for deformation profile, where apparently bristles bend and deflects in the rotor axial direction while backing plate corner *(corresponds to FH)* act as pivot point. In the FH region, where bristles are free

to move, the overhanging portion of the bristles bends under the backing plate in the flow direction. The maximum displacement magnitude at bristle tip is 0.42mm.

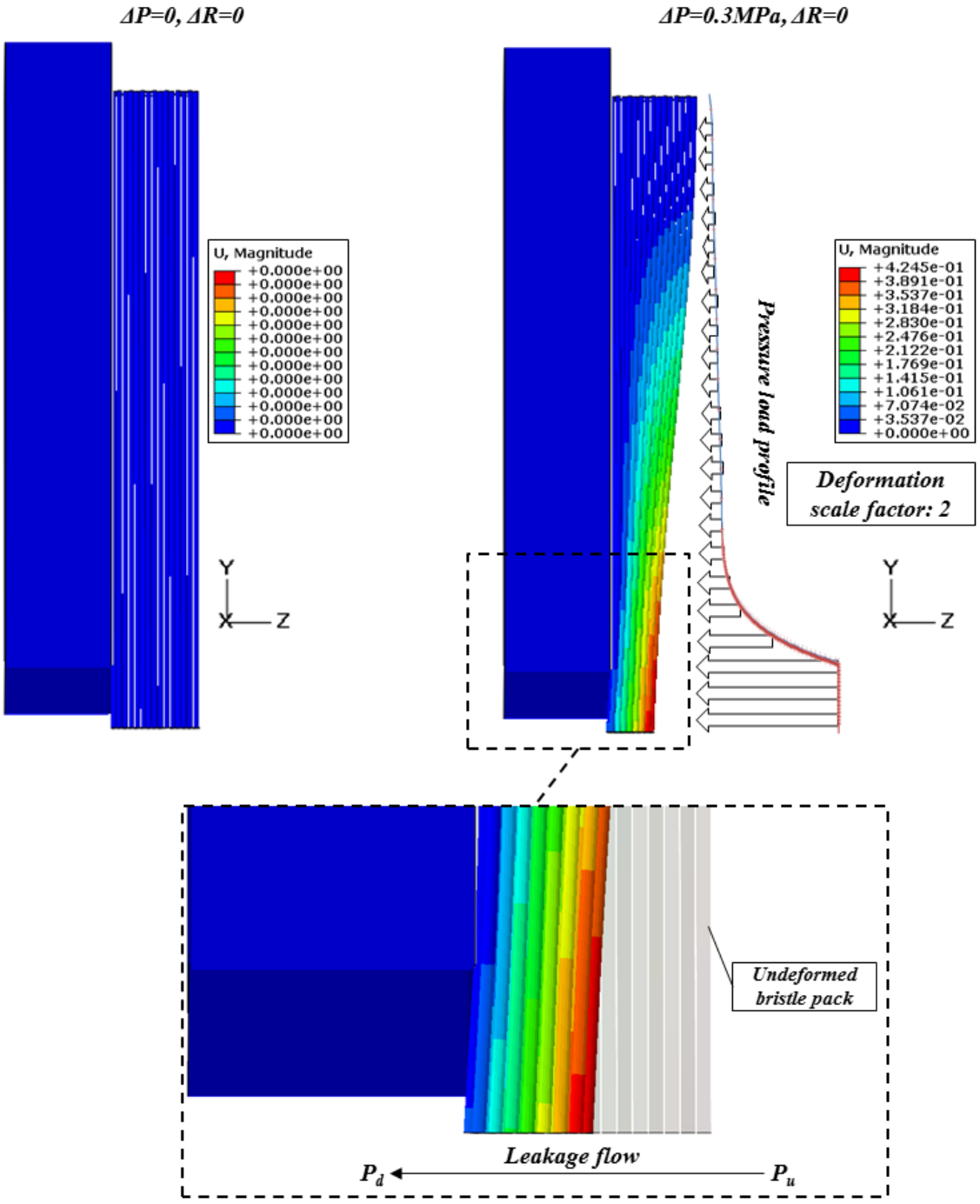

Figure 6.33: Pressure load without rotor interference – CAE-C3D8I, Displacement magnitude contour at ΔP=0.3MPa

The axial spacing between bristles is closed and inter-bristle contact initiates as the pressure load of 0.3MPa is introduced. As shown in Figure 6.34, the pack thickness

of the test seal is reduced to 1.34mm from 1.68mm, which means 25% decrease in pack thickness at seal inner diameter.

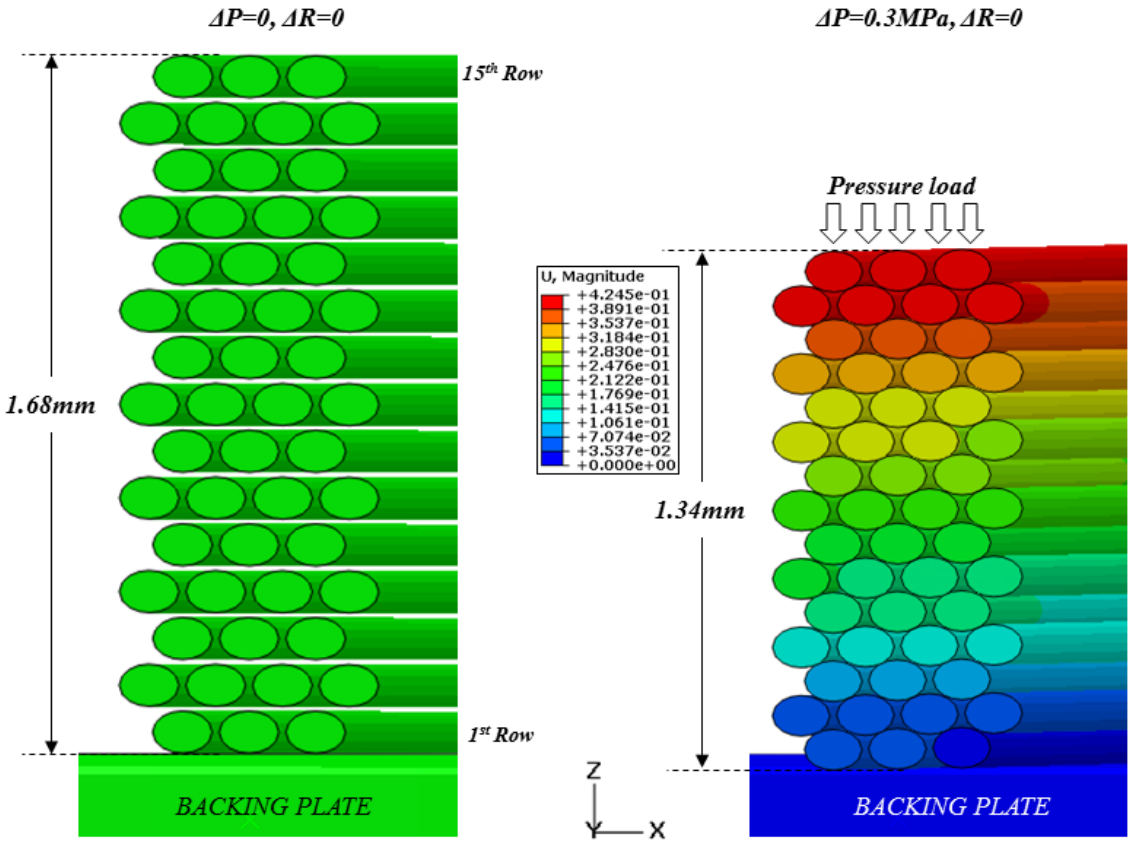

Figure 6.34: Pressure load without rotor interference – CAE-C3D8I, Seal pack thickness decrease at ΔP=0.3MPa

Resultant displacement vectors of CAE-C3D8I analyses and detailed deformation of 1st row *(downstream / backing plate side)* and 15th row *(upstream / front plate side)* of bristles under 0.3MPa are given in Figure 6.35, which gives better understanding of seal behavior under pressure load. As it can be seen from the figure, the overhung portion of the backing plate side bristles bend under the backing plate in the flow direction, while portion above the FH point deforms in the reverse direction. The FH corner of backing plate acts as pivot point and the backing plate – bristle contact is localized at that region, which explains the bristle failure at FH point in real life applications. However, the bristles at the front plate side *(15th row)* deforms in the flow direction, where deformation is maximum at the FH region as bristles are free to move and not supported by backing plate. Above FH, the support from inter-bristle contact cause displacement magnitudes of front plate side bristles to decrease, and bristle deformation is equal to zero at pinch point.

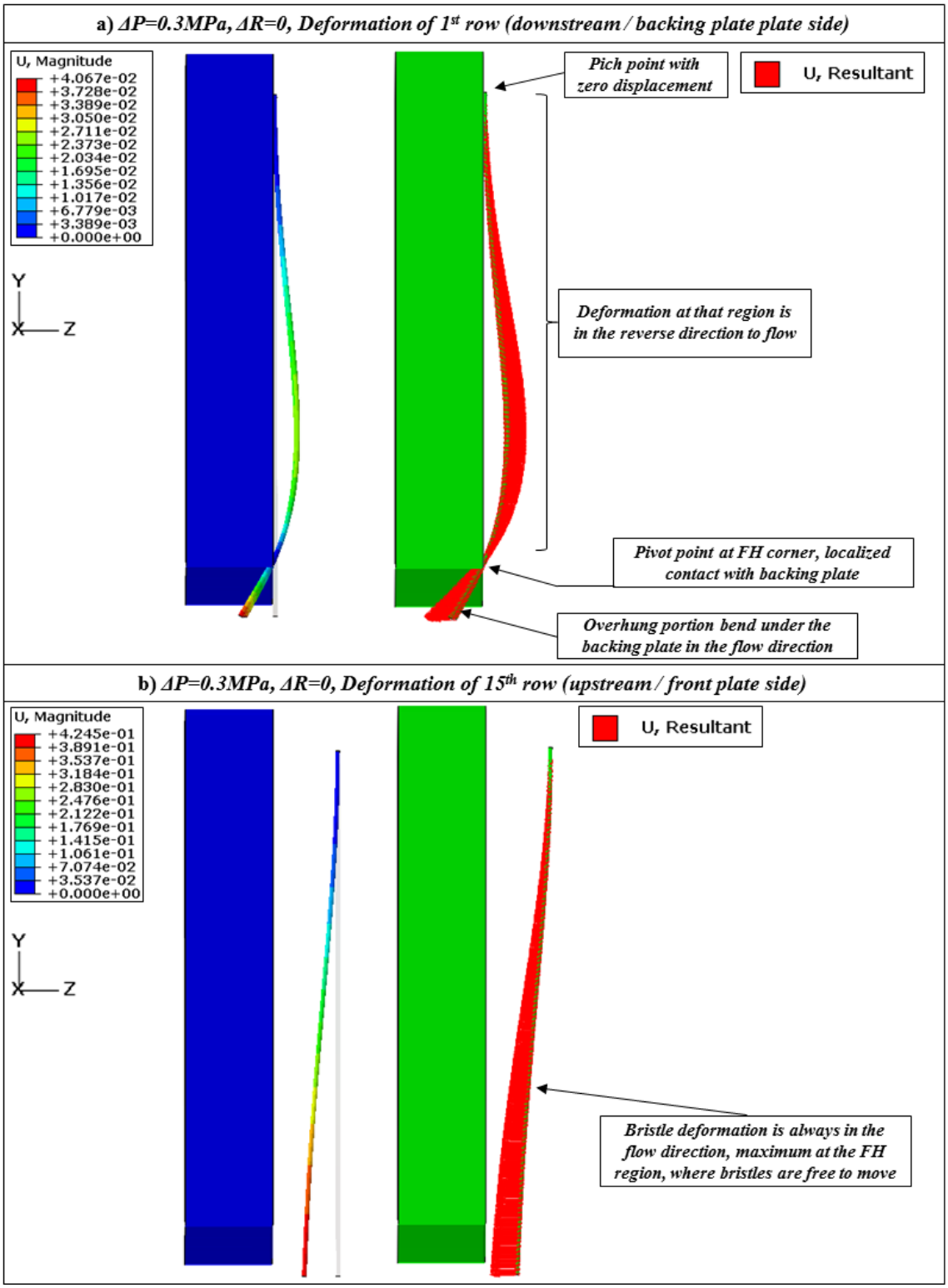

Figure 6.35: Pressure load without rotor interference – CAE-C3D8I, Deformation details under 0.3MPa pressure load, a) Downstream/backing plate side bristles *(1st row)*, b) Upstream/front plate side bristles *(15th row)*

VM stress profile for CAE-C3D8I analyses of test seal under 0.3MPa pressure load is presented in Figure 6.36. Taking the advantage of solid elements and small mesh size, the stress profile of the loaded seal can be visualized clearly. The localized contact at the backing plate corner causes increased contact pressure levels at that region, where the pressure load of the seal pack is carried by backing plate bristles at that small contact area. As a result of this, the maximum VM stress in the model is observed at the FH point of downstream / backing plate side bristles *(1st row)*. The maximum VM stress level is 125MPa when the FE related discontinuities are excluded. VM stress magnitude at pinch point of downstream side bristles is around 15MPa. On the other hand, the deformation profile and therefore the stress contour show different characteristics for front plate side *(upstream side, 15th row)* bristles, which are supported by other bristles with inter-bristle contact, and therefore they do not suffer from localized contact pressure and have their maximum stress at pinch point. The VM stress at the pinch point of upstream / front plate side bristles equals to 100MPa *(excluding FE discontinuities)*, while FH point stress magnitude is around 35MPa for this bristle row.

Steady state stress profile obtained from FE analysis – C3D8I is consistent with real life applications. It is known from the industrial applications that the failure of downstream/backing plate side bristles usually occurs at the fence height point *(backing plate inner diameter)*, if seal gets over pressurized.

Contact pressure profile obtained from CAE-C3D8I analyses of loaded test seal at 0.3MPa is given in Figure 6.37. The backing plate-bristle localized contact can be clearly observed with high contact pressure at the local region of FH. The backing plate and bristles have stick-slip contact status at that region.

The pressure load also causes axial spacing to be closed and initiates inter-bristle contact. The inter-bristle contact at upstream side *(last three rows)* is localized at the region just above the bristle tip, and extended up to FH point as moved in the axial direction towards to backing plate.

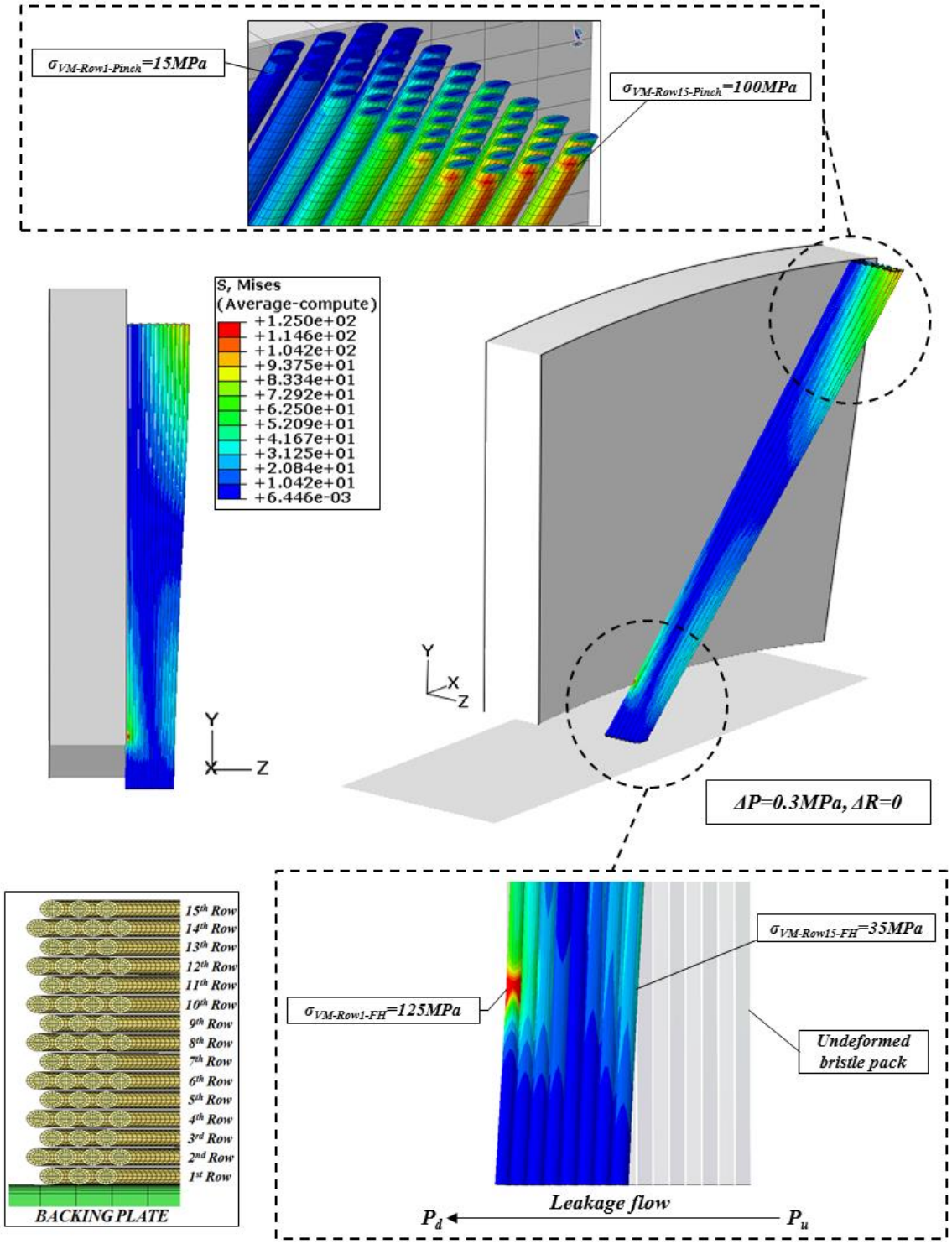

Figure 6.36: Pressure load without rotor interference – CAE-C3D8I, VM stress profile at ΔP=0.3MPa

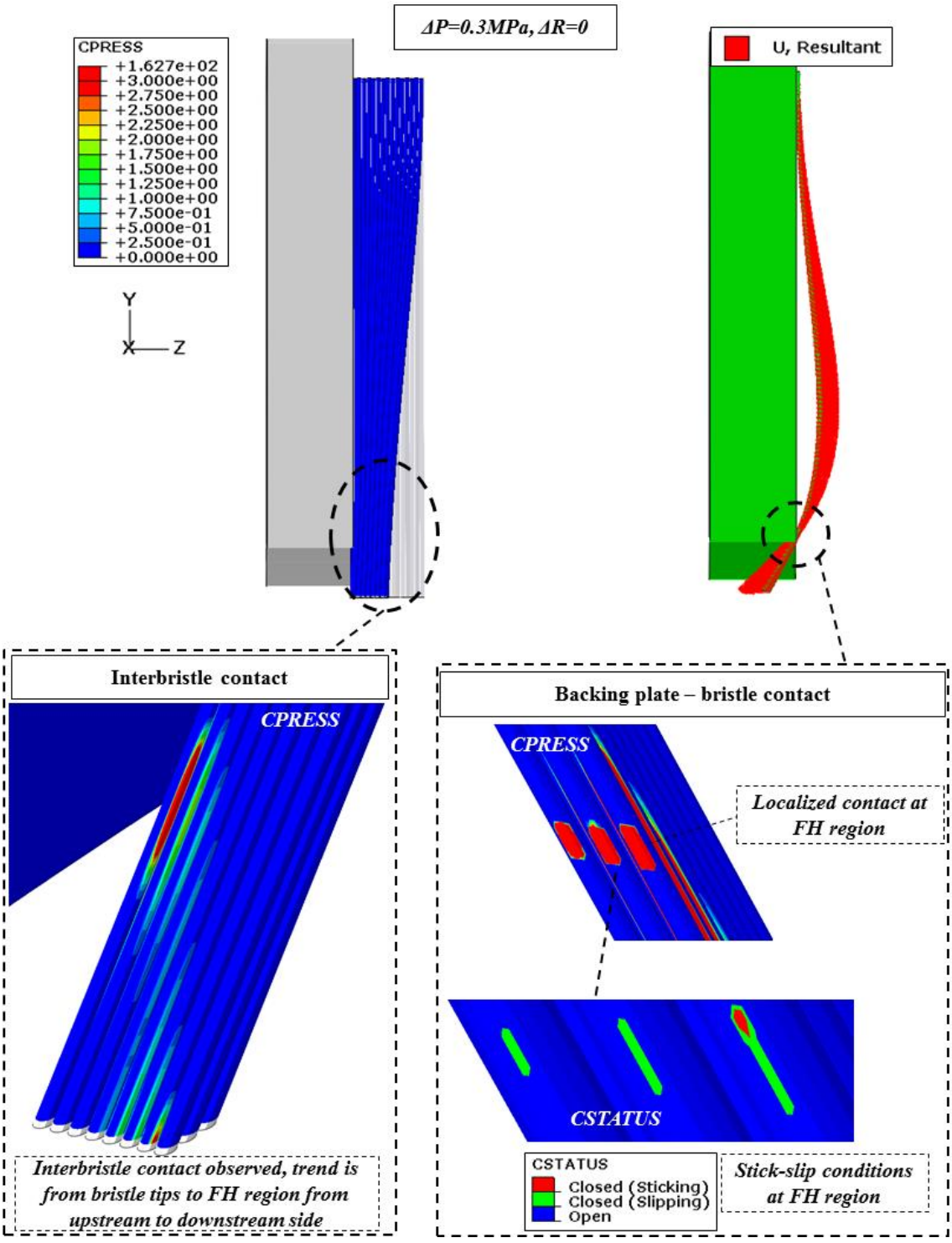

Figure 6.37: Pressure load without rotor interference – CAE-C3D8I, Contact pressure profile at ΔP=0.3MPa

Stress and displacement results for test seal CAE-C3D8I analyses are summarized in Table 6.9 for ΔP=0.225MPa and 0.3MPa. The maximum displacement magnitude and decrease in pack thickness for ΔP=0.225MPa are almost same with 0.3MPa analyses, which is expected since both pressure loads can deform front plate side

bristles until the first inter-bristle contact. The maximum VM stress at FH point of backing plate side bristles is equal to 105MPa for 0.225MPa pressure load, which is lower than the stress levels obtained under pressure load of 0.3MPa. Upstream side bristles have 94MPa VM stress magnitude at pinch point when the seal is pressurized with 0.225MPa pressure load.

Pressure load without rotor interference CAE Analysis with C3D8I elements for Test Seals			
Displacement results			
		ΔP=0.225MPa	ΔP=0.3MPa
Max. displacement magnitude		0.41mm	0.42mm
Initial pack thickness		1.68mm	1.68mm
Deformed pack thickness		1.34mm	1.34mm
Decrease in pack thickness		25%	25%
Stress results			
Backing plate side *(downstream, 1st row)*	FH point	105MPa	125MPa
	Pinch point	~14MPa	~15MPa
Front plate side *(upstream, 15th row)*	FH point	~26MPa	~35MPa
	Pinch point	94MPa	100MPa

Table 6.9: Pressure load without rotor interference – CAE-C3D8I, Stress and displacement profile at ΔP=0.225MPa and ΔP=0.3MPa

6.3.3 Comparison of CAE Simulations and Analytical Methodologies

Different analytical and CAE methodologies have been developed for steady state seal conditions, which refer to pressure load without rotor interference. Developed methodologies are as listed below:

- Analytical methodologies
  - Simple approach
  - Advanced approach
- CAE methodologies
  - CAE model with B31 elements
  - CAE model with C3D8I elements

Test seals have been analyzed at ΔP=0.225MPa and 0.3MPa by using the methodologies listed above. VM stress and displacement results are tabulated in Table 6.10. CAE analysis with C3D8I elements is the reference model due to high accuracy of this element type in stress and contact formulations.

As it can be seen from the tabulated data, although CAE-C3D8I and CAE-B31 analyses give similar results for displacement magnitude and pack thickness decrease, the VM stress results obtained from CAE-B31 analyses are lower than the values extracted from CAE-C3D8I analyses. The reason for this variation is the difference in contact and stress formulations of B31 and C3D8I elements. The contact formulation of C3D8I elements better simulate the contact pressure transmission at the localized contact region between bristles and backing plate, while the contact pressure is transmitted on B31 elements as line load has less precision.

Pressure load without rotor interference for Test Seals Comparison of CAE Analyses and Analytical Studies					
ΔP=0.3 MPa					
		CAE		**Analytical Studies**	
		CAE-C3D8I	CAE-B31	Simple Approach	Advanced Approach
Max. displacement magnitude		0.42mm	0.39mm	-	-
Initial pack thickness		1.68mm	1.68mm	-	-
Deformed pack thickness		1.34mm	1.34mm	-	-
Decrease in pack thickness		25%	25%	-	-
Backing plate side *(downstream, 1st row)*	FH point	125.00MPa	99.20MPa	33.32MPa	33.35MPa
	Pinch point	~15MPa	~7MPa	16.60MPa	41.4MPa
Front plate side *(upstream, 15th row)*	FH point	~35MPa	~10MPa	-	-
	Pinch point	100.00MPa	69.00MPa	-	-
ΔP=0.225 MPa					
		CAE-C3D8I	CAE-B31	Simple Approach	Advanced Approach
Max. displacement magnitude		0.41mm	0.38mm	-	-
Initial pack thickness		1.68mm	1.68mm	-	-
Deformed pack thickness		1.34mm	1.34mm	-	-
Decrease in pack thickness		25%	25%	-	-
Backing plate side *(downstream, 1st row)*	FH point	105.00MPa	85.80MPa	25.01MPa	25.01MPa
	Pinch point	~14MPa	~8MPa	12.51MPa	43.24MPa
Front plate side *(upstream, 15th row)*	FH point	~26MPa	~9MPa	-	-
	Pinch point	94.00MPa	66.00MPa	-	-

Table 6.10: Pressure load without rotor interference for Test Seals – Comparison of CAE analyses and analytical studies

The inter-bristle friction and localized backing plate-bristle contact has crucial importance in determining stress profile at steady state conditions. Therefore, it can be stated that determining stress levels of a loaded seal by analytical studies is extremely difficult since the complex bristle behavior and complicated nature of seal deformation under pressure load does not lend itself to full analytical formulation. This statement can also be observed from stress results given in Table 6.10. Although beam based

analytical studies – simple and advanced approach – give useful insight about bristle stress levels, the stress magnitudes obtained from those methodologies are lower than the CAE analyses at FH point. Since the localized contact effect at the backing plate corner radius cannot be included through analytical studies, stress levels are almost ¼th of CAE-C3D8I analyses. On the contrary, the backing plate side bristles' pinch point stress levels of analytical studies have larger values than CAE analyses, which is due to the fact that inter-bristle contact cannot be included to analytical studies.

6.4 Pressurized - Nonrotating Rotor Interference Conditions – Test Seals

Pressurized-nonrotating rotor interference conditions have been simulated for test seals, dimensions and material properties of which have already been detailed in Chapter 2 *(Tables 2.3, 2.4 and 2.7)*. CAE-B31 and CAE-C3D8I models have been run and results are compared with each other as well as with test data. This case is very close to turbine transients and seal response in real operating conditions.

6.4.1 CAE Analyses with B31 Elements

6.4.1.1 FE Model Details and Analysis Steps

The CAE-B31 model, which has been used in steady state simulations and detailed in Section 6.2.1.1, is utilized for simulating pressurized-nonrotating rotor interference conditions for test seals. Analyses start with pressure load, and radial interference is introduced to loaded seal. Pressurized rotor interference simulations are run up to 0.4mm rotor incursion and for pressure loads of 0.225MPa and 0.3MPa. Analyses steps are visualized in Figure 6.38.

The rotor-bristle contact is defined in the model with the correlated friction coefficient of 0.35. The inter-bristle and bristle-backing plate friction coefficients ranging from 0.25 to 0.30 are used for BTF correlation with tests.

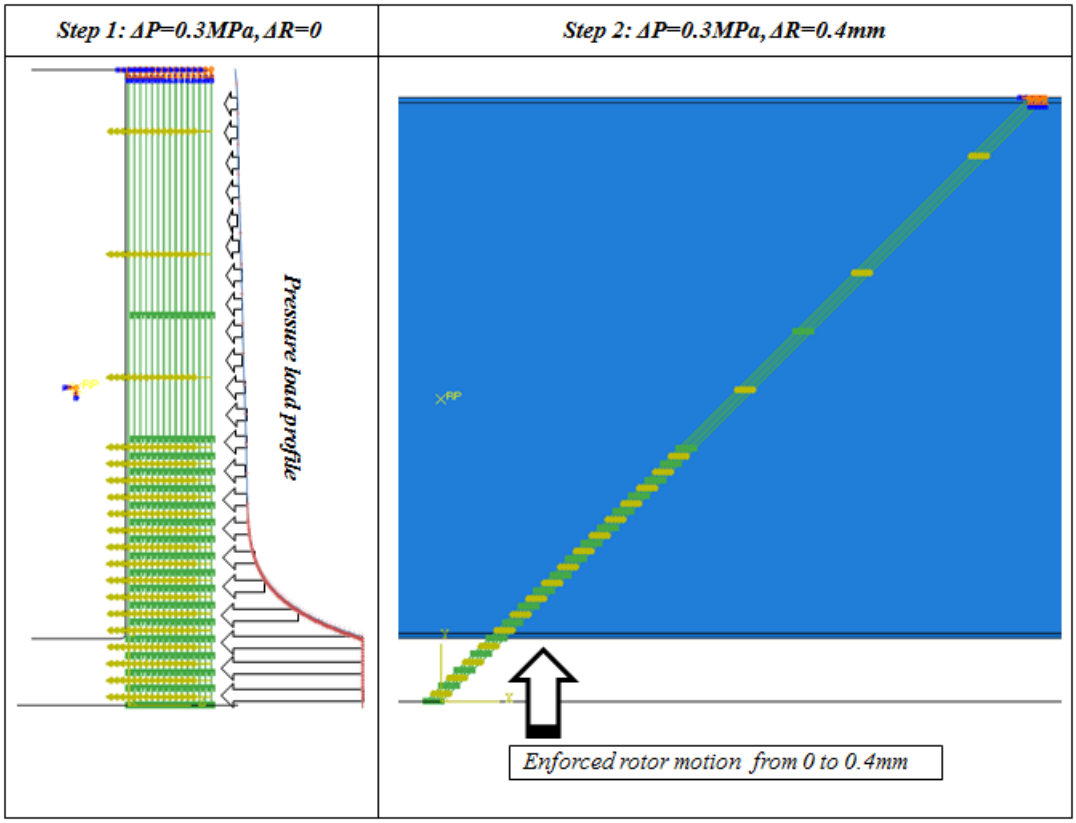

Figure 6.38: Pressurized, nonrotating rotor interference for test seals – CAE-B31, Analysis steps

6.4.1.2 Analysis Results and Correlation with Test Data

Displacement and VM stress profiles of CAE-B31 analyses at pressurized-nonrotating rotor interference conditions of test seals are given in Figures 6.39-6.40 and in Table 6.11. *(ΔP=0.3MPa, ΔR_{max}=0.4mm)*. Step by step examination of seal pack response in combined loading conditions will be very useful to give better understanding of brush seal behavior in turbine operating conditions. As detailed below, the downstream/backing plate side bristle deformation profile plays key role in determining bristle stress levels and tip force magnitudes.

- Test seal, ΔP=0.3MPa, ΔR=0
  - As the pressure load is applied, the axial spacing is closed and inter-bristle contact initiates. The initial pack thickness, which equals to 1.64mm, is reduced to 1.34mm.
  - Bristles bend axially while backing plate act as pivot point. The maximum bristle tip displacement magnitude is 0.39mm, which

directly equals to bristle tip deformation magnitude in rotor axial direction *(z-direction)*.

- Overhung portion of the backing plate side bristles bend under the backing plate in flow direction, while the portion above the FH deforms in the reverse direction. This yields localized bristle-backing plate contact at the FH point *(backing plate corner)*.
- As a result of localized contact at backing plate corner, downstream side bristles come up with high contact pressure and resulting high VM stress magnitudes at FH point. The maximum VM stress in the seal pack is observed as 99.2MPa at the local region of FH projection of backing plate side bristles. The stress levels at FH projection gradually decrease from downstream side to upstream side. However, the upstream/front plate side bristles have high stress levels at pinch point. The front plate side bristle VM stress magnitude at pinch point is 69MPa for steady state conditions with 0.3MPa pressure load.

- Test seal, ΔP=0.3MPa, ΔR=0.1mm
  - As 0.1mm radial interference is introduced to loaded seal pack, the rotor pushes the loaded bristles outwards in radial direction *(y-direction)*. The downstream/backing plate side bristles slide over the backing plate corner radius, and the effective FH is reduced to 1.2mm. The radial displacement of the bristle tip increases to 0.1mm, while the axial displacement is reduced to 0.38mm. The displacement magnitude at bristle tip increases and take the value of ~0.41mm.
  - 0.1mm radial interference cause downstream/backing plate side bristles to bend more in y-z plane, and bending in x-y plane is also introduced. As a result, contact pressure levels at localized contact region at backing plate corner become more severe, and maximum VM stress level at FH point of downstream side bristles increase to 108.3MPa. Upstream side bristle stress levels at pinch point also increase to 73.6MPa.
- Test seal, ΔP=0.3MPa, ΔR=0.4mm
  - As the radial interference takes its maximum value, the downstream side bristles become aligned with the backing plate, and contact

localization becomes less severe. The VM stress level at FH point of downstream side bristles reduces to 103.7MPa.

- The x-y plane bending, which is mainly induced by rotor interference, becomes dominant within the seal pack and more uniform stress contour is observed through the axial direction. The pinch point VM stress magnitude at upstream side bristles takes the value of 77.2MPa.
- Although the displacement magnitude increases to ~0.67mm, the axial displacement *(z-direction)* is reduced to 0.36mm while the bristles become more aligned with the backing plate. The main reason in displacement magnitude increase is the rise in radial displacement of bristle tips, which is introduced by 0.4mm rotor rub.

Pressurized non-rotating rotor interference CAE Analysis with B31 elements for Test Seals				
			ΔP=0.225MPa	ΔP=0.3MPa
ΔR=0	Backing plate side *(downstream, 1st row)*	FH point	**85.8MPa**	**99.2MPa**
		Pinch point	~8MPa	~7MPa
	Front plate side *(upstream, 15th row)*	FH point	~9MPa	~10MPa
		Pinch point	**66.0MPa**	**69.0MPa**
ΔR=0.1mm	Backing plate side *(downstream, 1st row)*	FH point	**90.8MPa**	**108.3MPa**
		Pinch point	~13MPa	~16MPa
	Front plate side *(upstream, 15th row)*	FH point	~16MPa	~13MPa
		Pinch point	**69.2MPa**	**73.6MPa**
ΔR=0.2mm	Backing plate side *(downstream, 1st row)*	FH point	**82.5MPa**	**96.8MPa**
		Pinch point	~11MPa	~8MPa
	Front plate side *(upstream, 15th row)*	FH point	~19MPa	~19MPa
		Pinch point	**70.4MPa**	**76.7MPa**
ΔR=0.3mm	Backing plate side *(downstream, 1st row)*	FH point	**86.5MPa**	**99.5MPa**
		Pinch point	~25MPa	~23MPa
	Front plate side *(upstream, 15th row)*	FH point	~20MPa	~20MPa
		Pinch point	**70.6MPa**	**77.0MPa**
ΔR=0.4mm	Backing plate side *(downstream, 1st row)*	FH point	**90.9MPa**	**103.8MPa**
		Pinch point	~40MPa	~37MPa
	Front plate side *(upstream, 15th row)*	FH point	~21MPa	~22MPa
		Pinch point	**70.7MPa**	**77.2MPa**

Table 6.11: Pressurized, nonrotating rotor interference for test seals – CAE-B31, VM stress change with rotor interference, ΔP=0.225MPa and ΔP=0.3MPa

VM stress magnitudes at critical points are tabulated in Table 6.11 at pressure loads of 0.225MPa and 0.3MPa. The maximum VM stress level increases as 0.1mm rotor interference is introduced to loaded seal. However, decrease is observed at 0.2mm radial interference, where bristles become aligned with backing plate, which reduces the effect of localized contact. Above that interference level, maximum VM stress level at FH point again starts to increase due to increasing interference magnitudes. This

specific interference level is seal and pressure dependent, and will be different for different seal parameters.

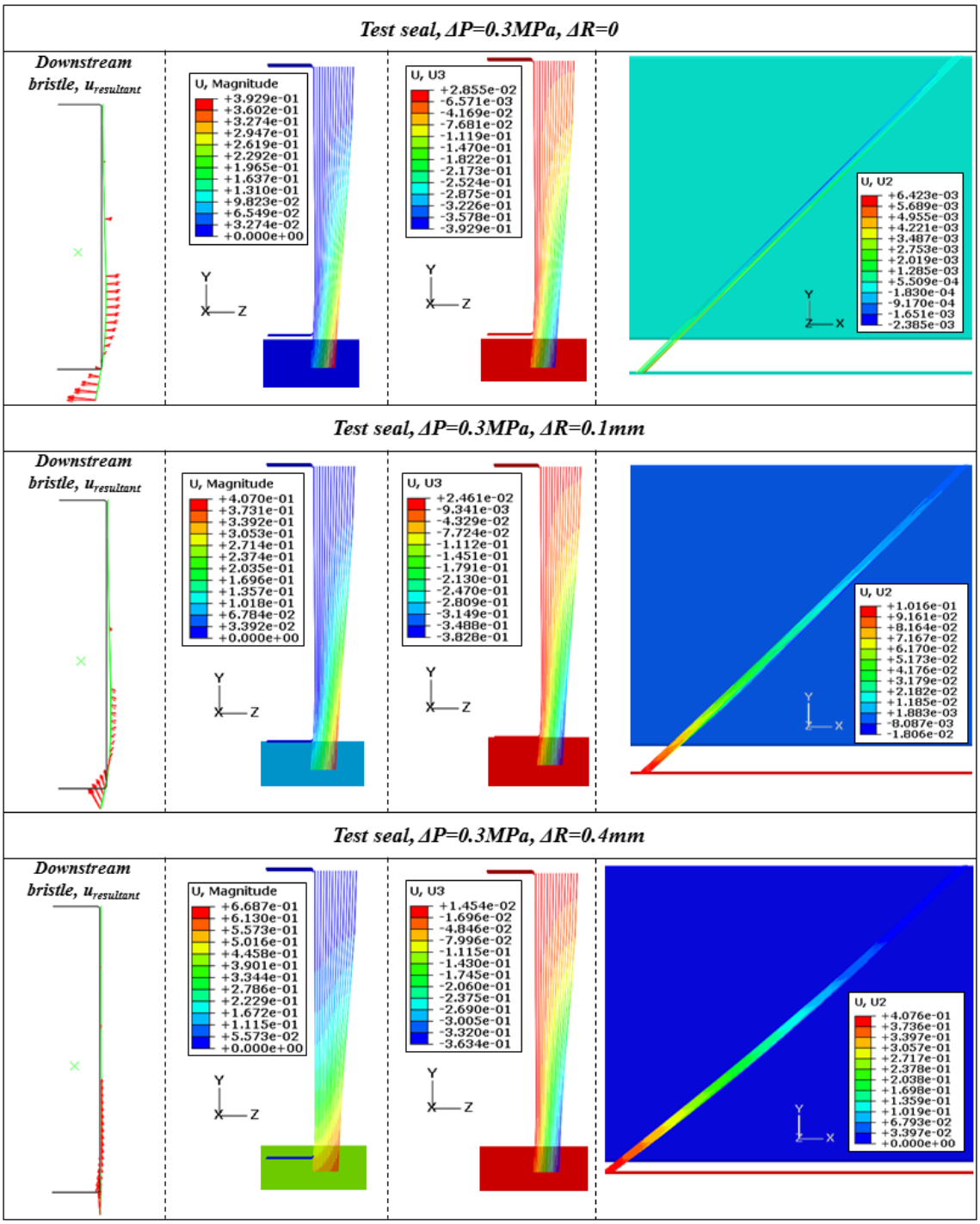

Figure 6.39: Pressurized, nonrotating rotor interference for test seals – CAE-B31, Displacement profile at ΔP=0.3MPa

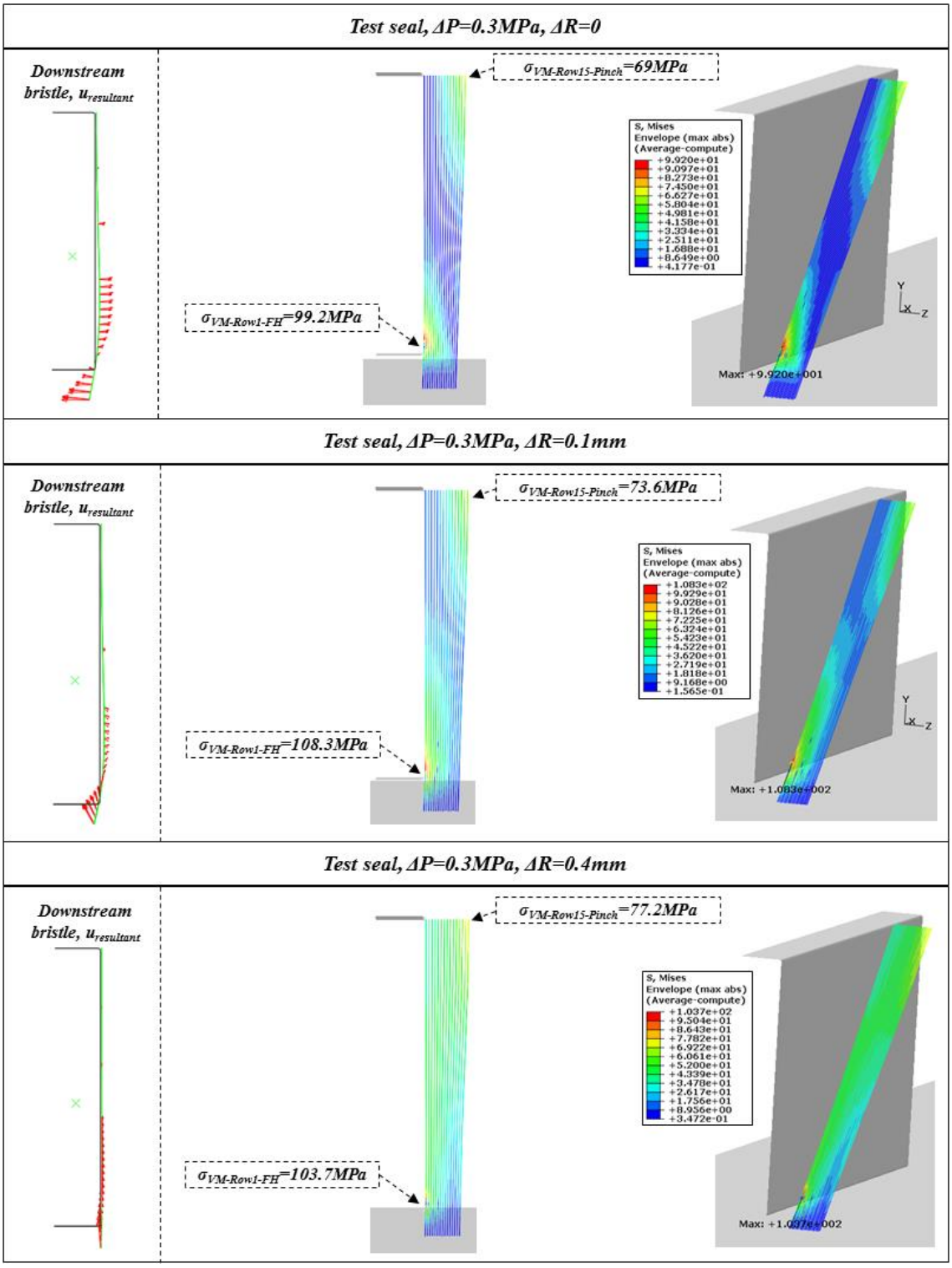

Figure 6.40: Pressurized, nonrotating rotor interference for test seals – CAE-B31, VM stress profile at ΔP=0.3MPa

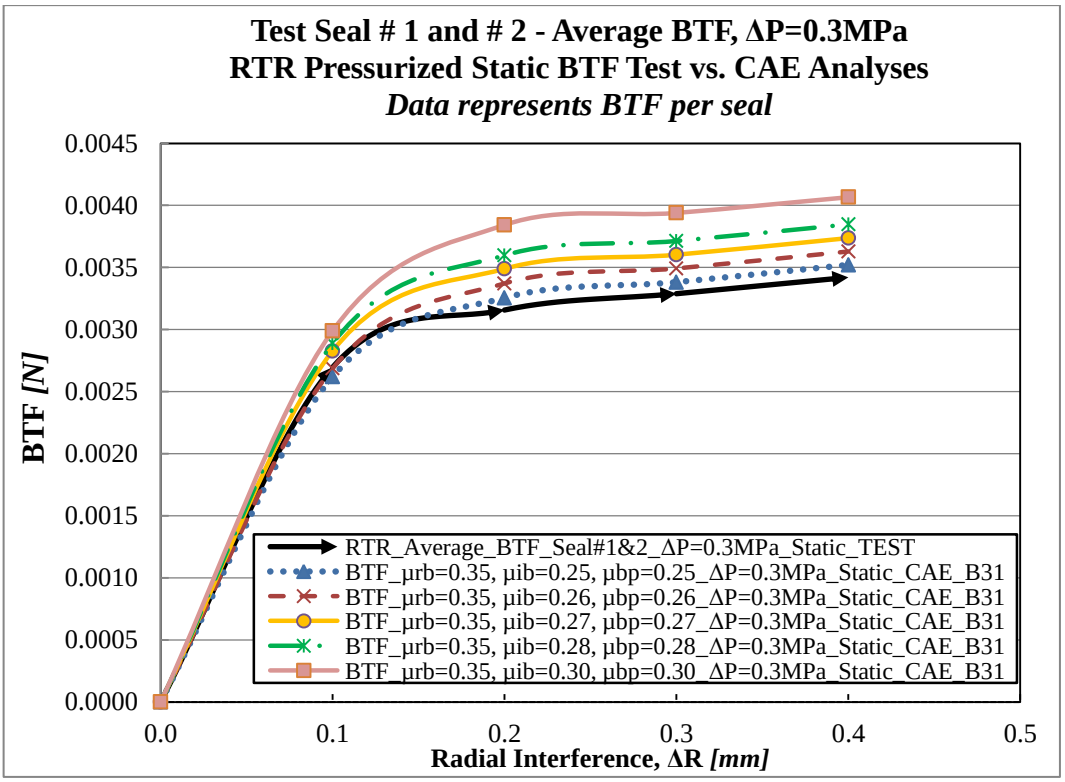

Figure 6.41: Pressurized, nonrotating rotor interference for test seals – CAE-B31, Bristle tip force results and comparison with test, ΔP=0.3MPa

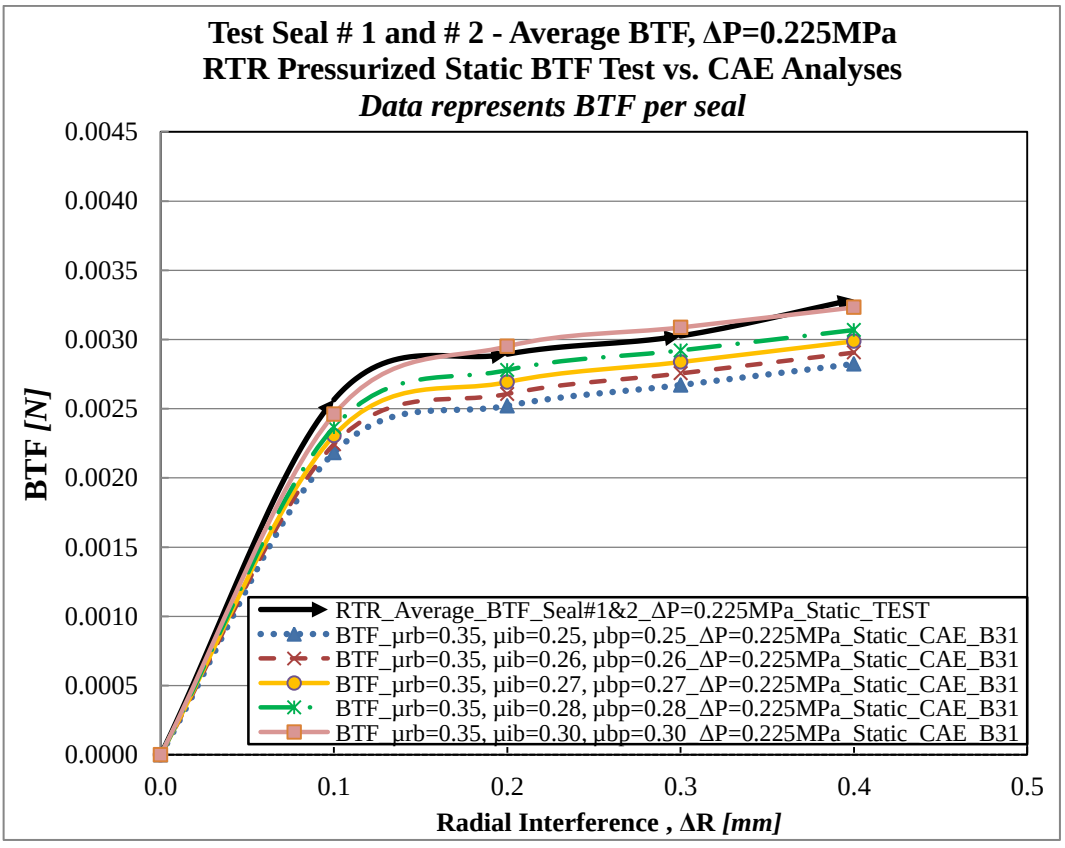

Figure 6.42: Pressurized, nonrotating rotor interference for test seals – CAE-B31, Bristle tip force results and comparison with test, ΔP=0.225MPa

BTF results of CAE-B31 analyses at pressurized-nonrotating rotor interference conditions of test seals and their comparison with RTR tests are given in Figures 6.39 and 6.40 for ΔP=0.3MPa and ΔP=0.225MPa respectively. As it can be seen from figures, the CAE-B31 analyses give consistent results with test measurements for the inter-bristle and bristle-backing plate friction coefficient range of 0.25-0.35. Increase in BTF values due to pressure stiffening and BTF stabilization of loaded seals at rotor interference levels of 0.1mm can be successfully simulated in CAE analyses. According to the BTF results and comparison with the test data, the inter-bristle and bristle-backing plate friction coefficient is selected as 0.25, which gives best overall correlation with BTF measurements.

The CAE analyses also give better insight to BTF stabilization of loaded seals, which is explained as following. When a seal is loaded with pressure load, all bristles get in contact with each other and with backing plate, and bent under backing plate at FH region. When the rotor interference is introduced, the loaded seal already have frictional stick-slip contact at inter-bristle and bristle-backing plate locations. Therefore, BTF values for a loaded seal-nonrotating rotor increases rapidly up to 0.1mm interference, where the main contributor is the pressure stiffening effect, and slightly changes above that point.

6.4.2 CAE Analyses with C3D8I Elements

6.4.2.1 FE Model Details and Analysis Steps

Test seal pressurized-nonrotating rotor interference simulations are performed by using C3D8I elements for bristles and results are compared with the test measurements. The CAE model, details of which has already been given in Section 6.2.2 and 6.3.2, is used with the boundary conditions detailed in Figure 6.43 and 6.44. Pressure loads of 0.3MPa and 0.225MPa are analyzed up to maximum rotor interference level of 0.4mm. The enforced motion is defined to rotor until the maximum rotor incursion, and then rotor is pulled back to its original position to simulate loading and unloading steps pressurized tests.

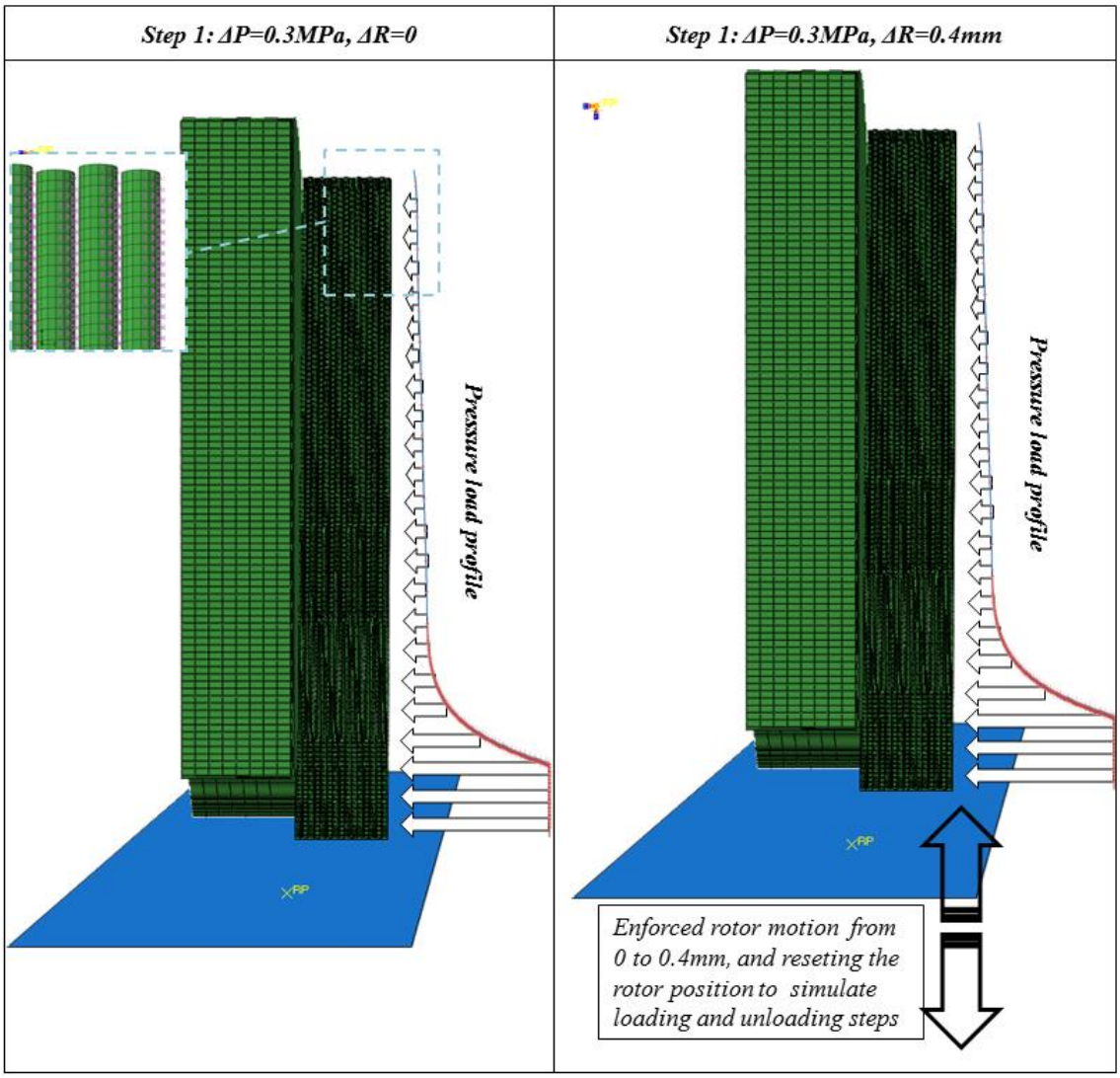

Figure 6.43: Pressurized, nonrotating rotor interference for test seals – CAE-C3D8I, Analysis steps

6.4.2.2 Analysis Results and Correlation with Test Data

Resultant displacement at different interference levels of CAE-C3D8I analyses of test seals under 0.3MPa are given in Figures 6.44 thru 6.46. Displacement and VM stress profiles of CAE-C3D8I analyses at pressurized-nonrotating rotor interference conditions of test seals are also given in Figures 6.47-6.48 *(ΔP=0.3MPa, ΔR_{max}=0.4mm)*. As it can be seen from the figures, the pressurized seal pack deformation and stress characteristics at rotor rub conditions can be examined clearly by taking the advantage of C3D8I elements and small mesh size.

Step by step examination of seal pack response in combined loading conditions will be very useful to give better understanding of brush seal behavior in turbine operating conditions. As detailed below, the downstream/backing plate side bristle deformation profile plays key role in determining bristle stress levels and tip force magnitudes.

- Test seal, ΔP=0.3MPa, ΔR=0
    - As the pressure load is applied, the axial spacing is closed and inter-bristle contact initiates. The initial pack thickness, which equals to 1.64mm, is reduced to 1.34mm.
    - Bristles bend axially while backing plate act as pivot point. The maximum bristle tip displacement magnitude is 0.42mm, which directly equals to bristle tip deformation magnitude in rotor axial direction *(z-direction)*.
    - Overhung portion of the backing plate side bristles bend under the backing plate in flow direction, while the portion above the FH deforms in the reverse direction. This yields localized bristle-backing plate contact at the FH point *(backing plate corner)*.
    - As a result of localized contact at backing plate corner, downstream side bristles come up with high contact pressure and resulting high VM stress magnitudes at FH point. The maximum VM stress in the seal pack is observed as 125MPa at the local region of FH projection of backing plate side bristles. The stress levels at FH projection gradually decrease from downstream side to upstream side. However, the upstream/front plate side bristles have high stress levels at pinch point. The front plate side bristle VM stress magnitude at pinch point, which is induced by pressure load related bending, is 100MPa for steady state conditions with 0.3MPa pressure load.
    - The inter-bristle contact at upstream side *(last three rows)* is localized at the region just above the bristle tip, and extended up to FH point as moved in the axial direction towards to backing plate.
- Test seal, ΔP=0.3MPa, ΔR=0.1mm
    - As 0.1mm radial interference is introduced to loaded seal pack, the rotor pushes the loaded bristles outwards in radial direction *(y-direction)*. The downstream/backing plate side bristles slide over the

backing plate corner radius, and the effective FH is reduced to 1.2mm. The radial displacement of the bristle tip increases to 0.1mm, while the displacement magnitude takes the value of 0.48mm.

- 0.1mm radial interference cause downstream/backing plate side bristles to bend more in y-z plane, and bending in x-y plane is also introduced. As a result, contact pressure levels at localized contact region at backing plate corner become more severe, and maximum VM stress level at FH point of downstream side bristles increase to 138MPa. Upstream side bristle stress levels at pinch point also increase to 108MPa, which is the combination of pressure load and rotor interference induce bending.
- The inter-bristle contact is mainly observed at the overhung portion of the bristles. The rotor-bristle contact is localized at small region of projected bristle tip area, which is due to cant angle and bending deformation of bristles.

- Test seal, ΔP=0.3MPa, ΔR=0.4mm
  - Although the maximum displacement magnitude increases to ~0.71mm, the axial displacement magnitude *(z-direction)* is reduced to 0.42mm for upstream side bristles, and downstream/backing plate side bristles' z-deformation is reduced to the levels of -0.05mm. As a result, the backing plate side bristles become more aligned with the backing plate. The main reason in displacement magnitude increase is the rise in radial displacement of bristle tips, which is introduced with 0.4mm rotor rub.
  - As the radial interference takes its maximum value, the downstream side bristles become more aligned with the backing plate, and contact localization becomes less severe. The VM stress level at FH point of downstream side bristles reduces to 134MPa.
  - The x-y plane bending, which is mainly induced by rotor interference, becomes dominant within the seal pack and more uniform stress contour is observed through the axial direction. VM stress magnitude at upstream side bristles takes the value of 128MPa.

- The inter-bristle contact is mainly observed at the overhung portion of the bristles. The rotor-bristle contact is extended, but still localized at small region of projected bristle tip area.

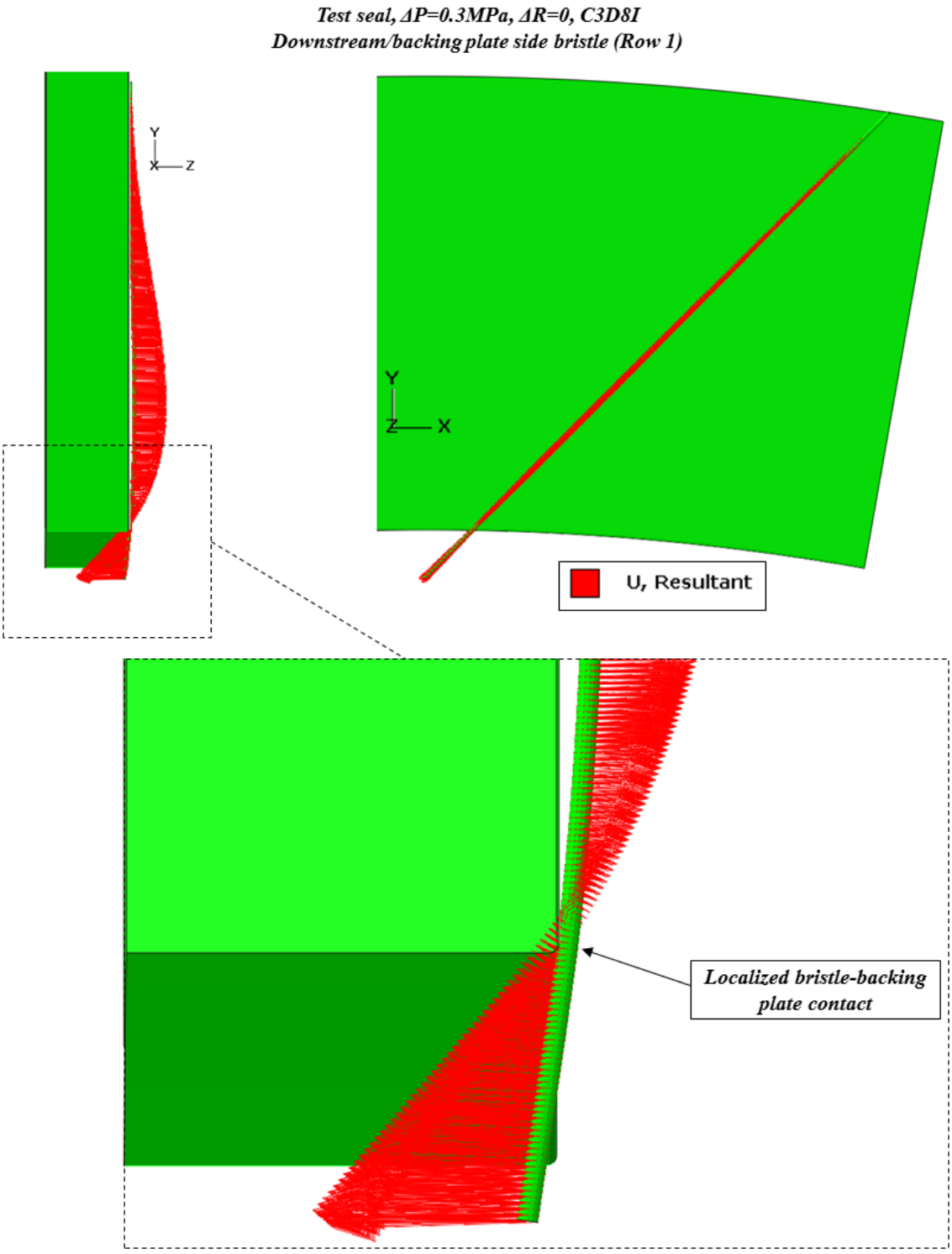

Figure 6.44: Pressurized, nonrotating rotor interference for test seals – CAE-C3D8I, Resultant deformation vector for downstream/backing plate side bristles at ΔP=0.3MPa, ΔR=0

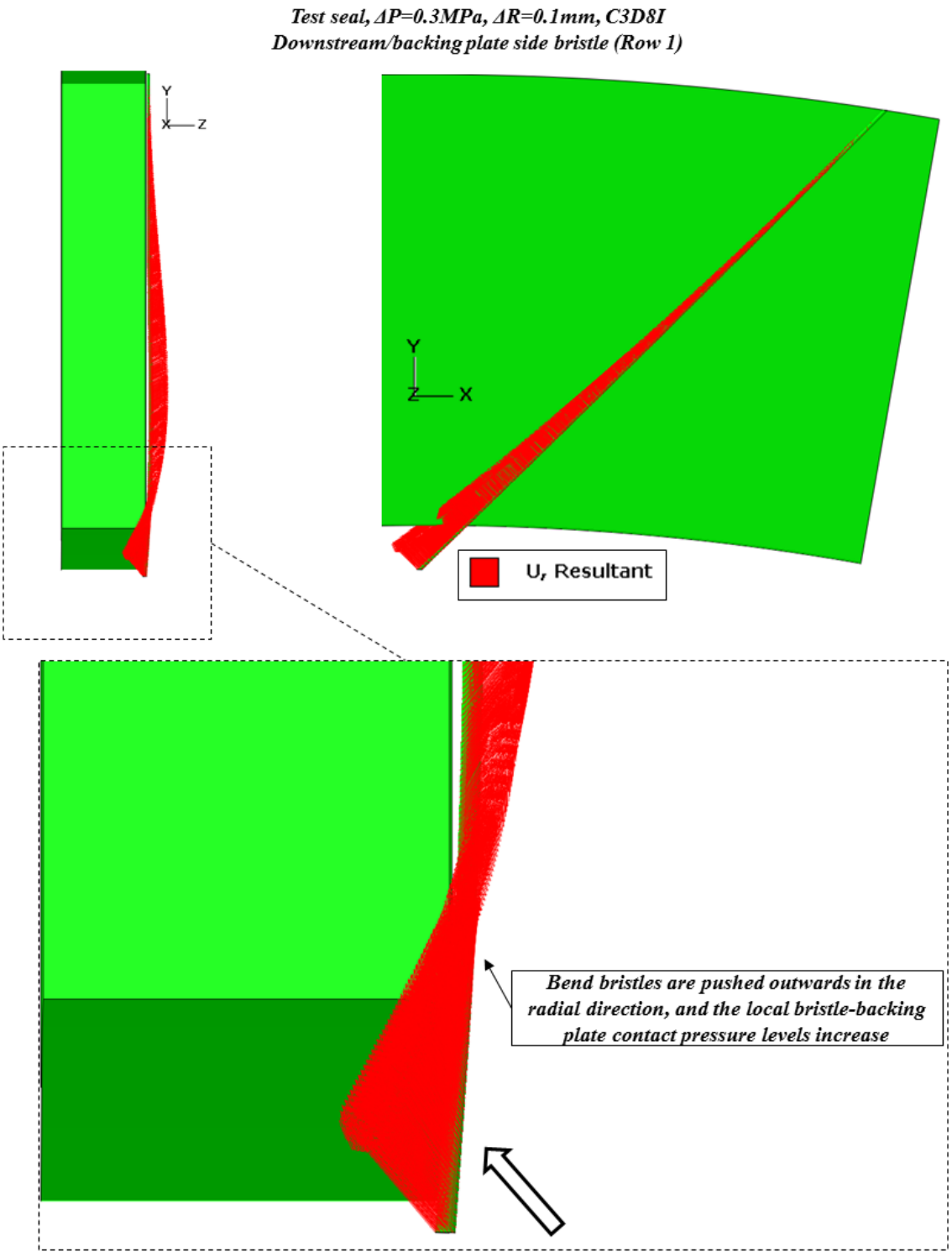

Figure 6.45: Pressurized, nonrotating rotor interference for test seals – CAE-C3D8I, Resultant deformation vector for downstream/backing plate side bristles at ΔP=0.3MPa, ΔR=0.1mm

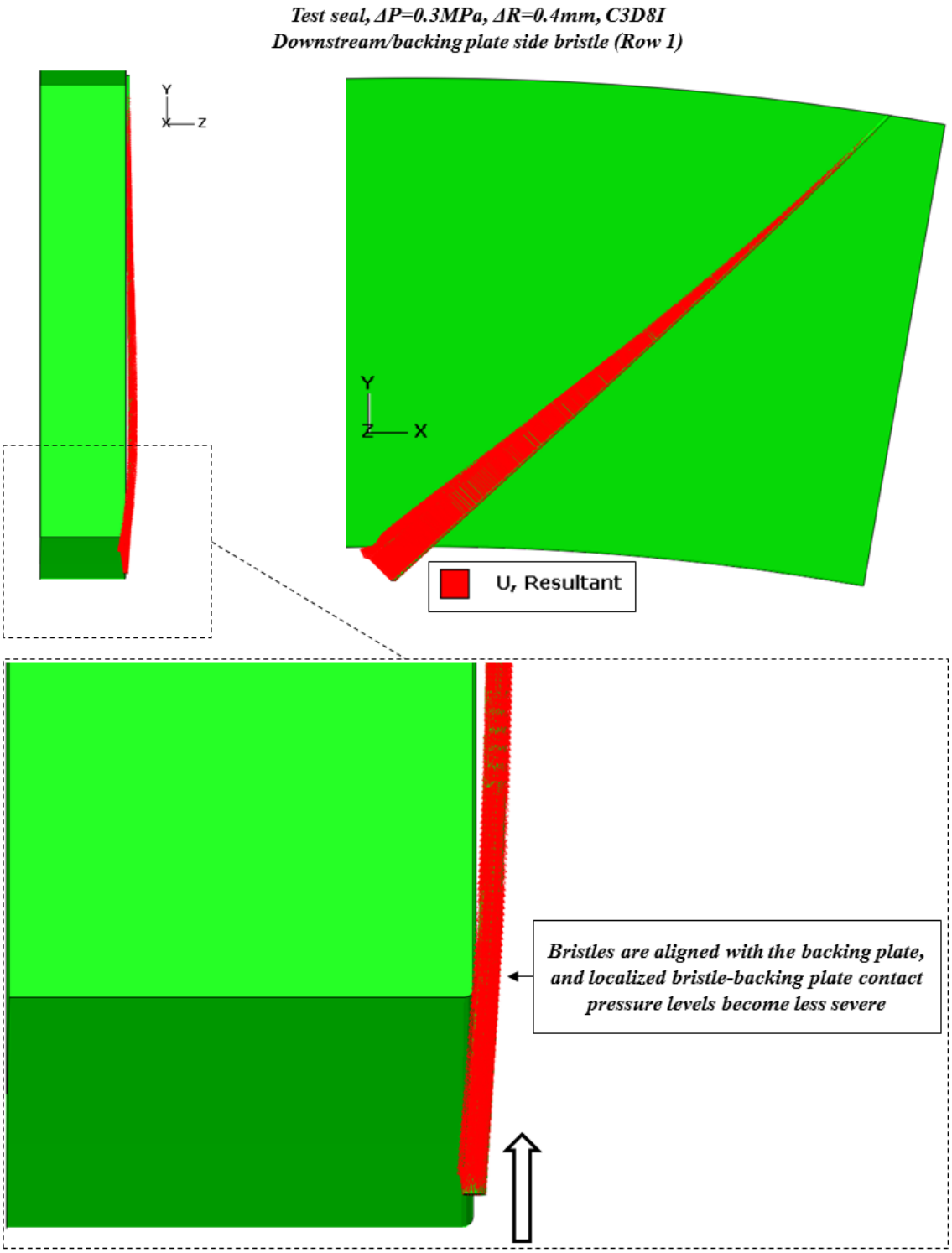

Figure 6.46: Pressurized, nonrotating rotor interference for test seals – CAE-C3D8I, Resultant deformation vector for downstream/backing plate side bristles at ΔP=0.3MPa, ΔR=0.4mm

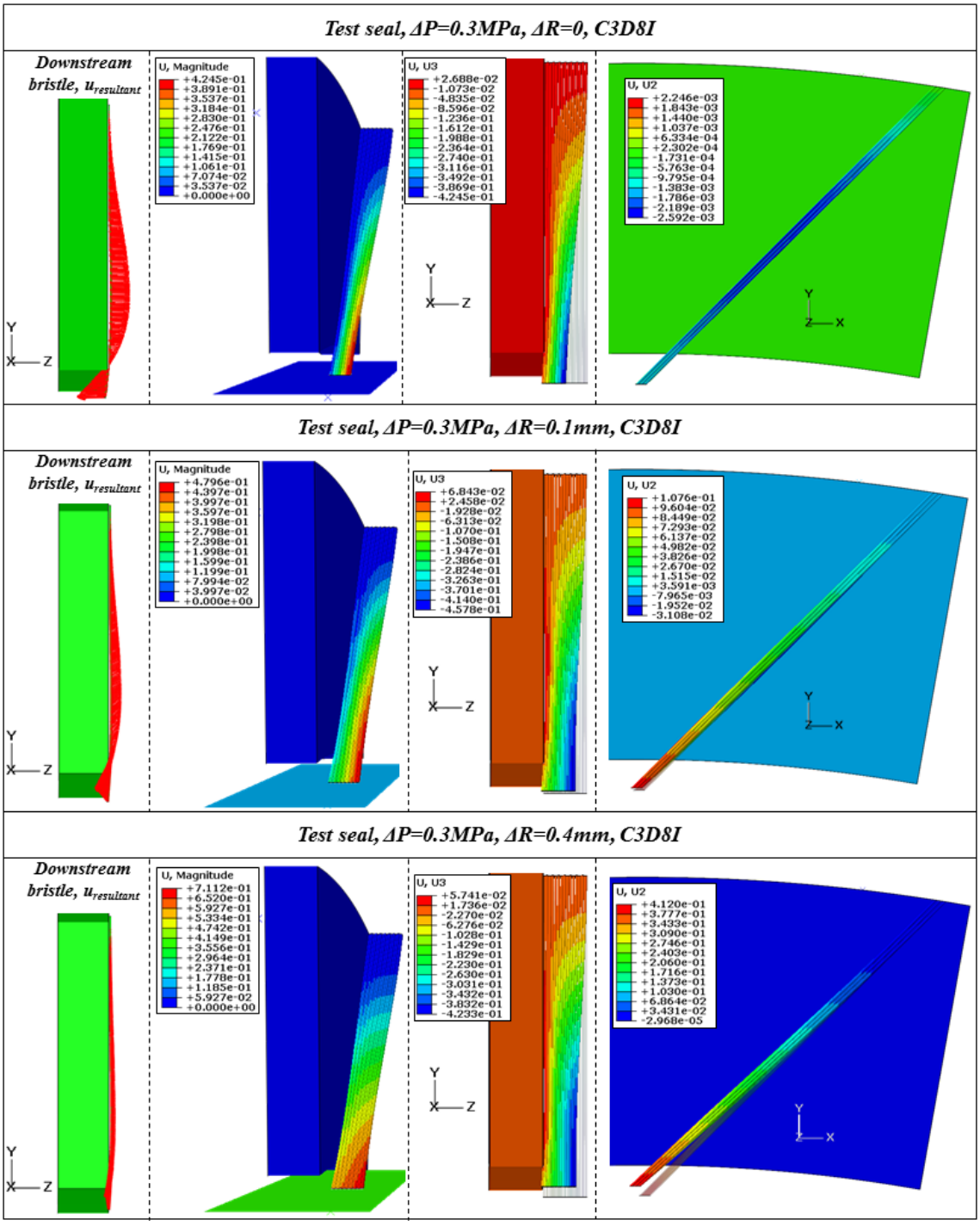

Figure 6.47: Pressurized, nonrotating rotor interference for test seals – CAE-C3D8I, Displacement profile at ΔP=0.3MPa

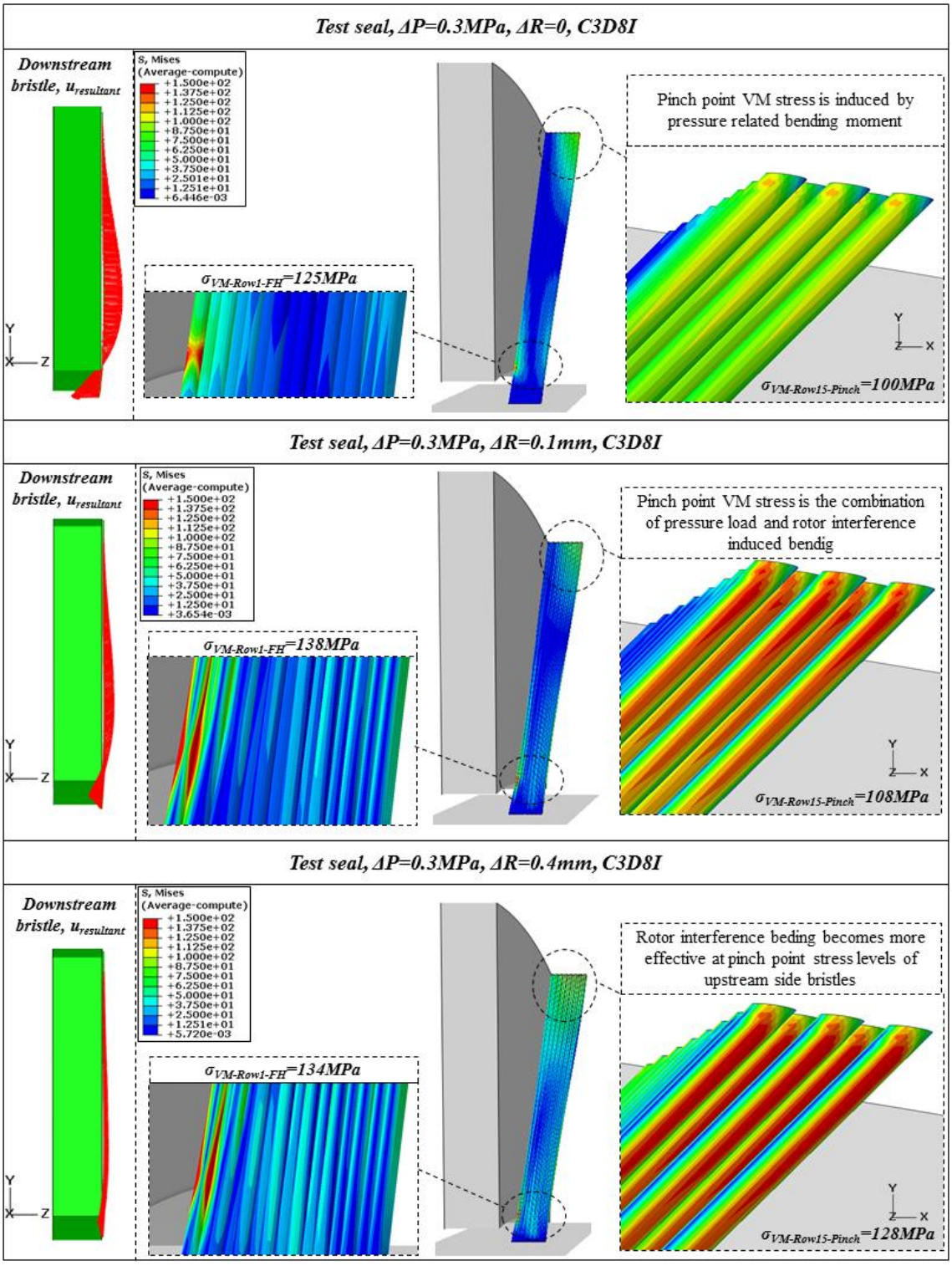

Figure 6.48: Pressurized, nonrotating rotor interference for test seals – CAE-C3D8I, VM stress profile at ΔP=0.3MPa

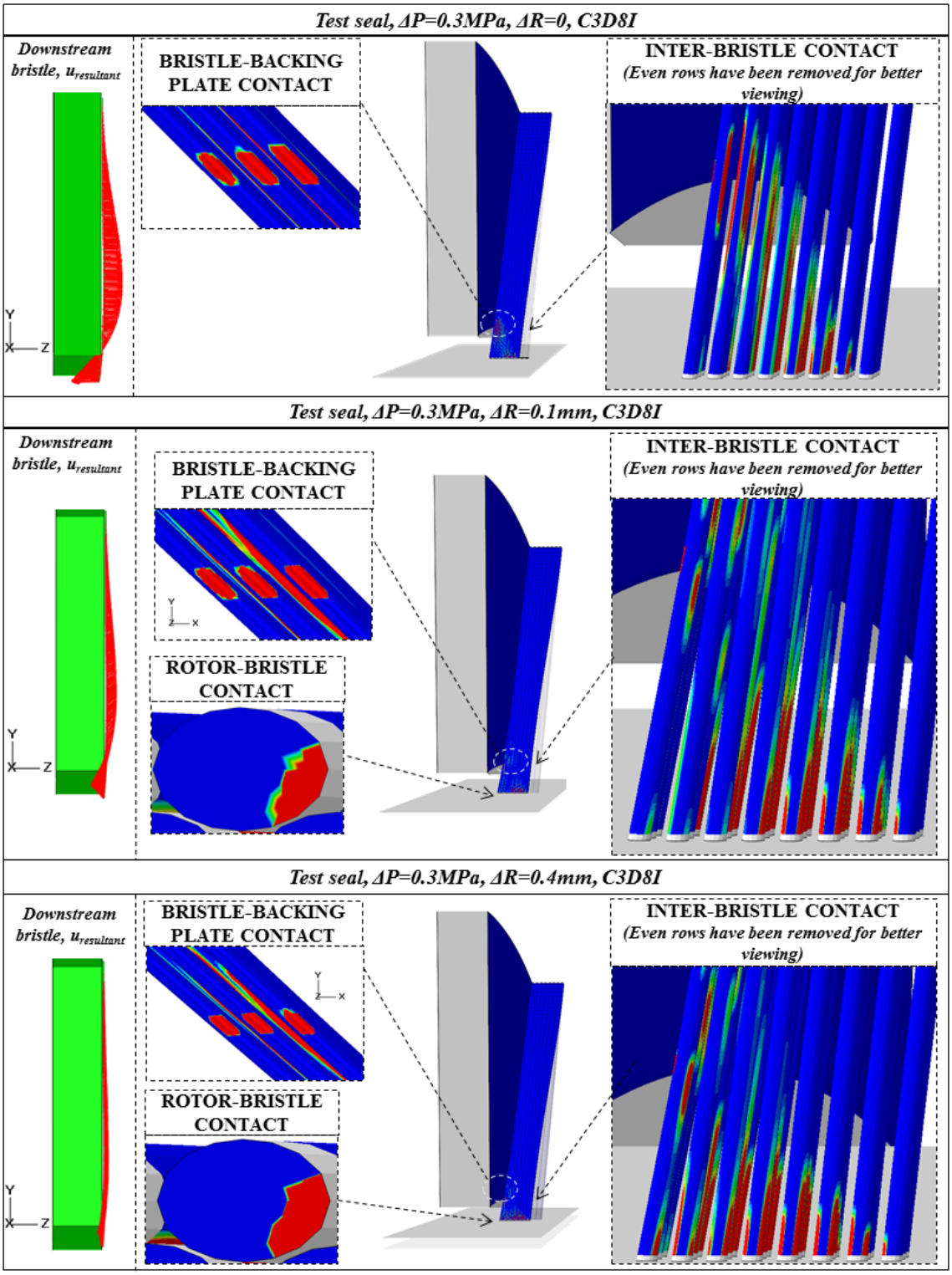

Figure 6.49: Pressurized, nonrotating rotor interference for test seals – CAE-C3D8I, Contact pressure profile at ΔP=0.3MPa

Pressurized non-rotating rotor interference CAE Analysis with C3D8I elements for Test Seals				
			ΔP=0.225MPa	ΔP=0.3MPa
ΔR=0	Backing plate side *(downstream, 1st row)*	FH point	**105MPa**	**125MPa**
		Pinch point	~14MPa	~15MPa
	Front plate side *(upstream, 15th row)*	FH point	~26MPa	~35MPa
		Pinch point	**94MPa**	**100MPa**
ΔR=0.1mm	Backing plate side *(downstream, 1st row)*	FH point	**118MPa**	**138MPa**
		Pinch point	~26MPa	~30MPa
	Front plate side *(upstream, 15th row)*	FH point	~40MPa	~45MPa
		Pinch point	**104MPa**	**108MPa**
ΔR=0.2mm	Backing plate side *(downstream, 1st row)*	FH point	**120MPa**	**140MPa**
		Pinch point	~35MPa	~37MPa
	Front plate side *(upstream, 15th row)*	FH point	~35MPa	~43MPa
		Pinch point	**110MPa**	**115MPa**
ΔR=0.3mm	Backing plate side *(downstream, 1st row)*	FH point	**119MPa**	**135MPa**
		Pinch point	~51MPa	~55MPa
	Front plate side *(upstream, 15th row)*	FH point	~35MPa	~42MPa
		Pinch point	**117MPa**	**123MPa**
ΔR=0.4mm	Backing plate side *(downstream, 1st row)*	FH point	**117MPa**	**134MPa**
		Pinch point	~63MPa	~65MPa
	Front plate side *(upstream, 15th row)*	FH point	~30MPa	~40MPa
		Pinch point	**121MPa**	**128MPa**

Table 6.12: Pressurized, nonrotating rotor interference for test seals – CAE-C3D8I, VM stress change with rotor interference, ΔP=0.225MPa and ΔP=0.3MPa

VM stress magnitudes at critical points are tabulated in Table 6.12 at ΔP=0.225MPa and ΔP=0.3MPa. As it can be seen from the table, maximum VM stress level is observed at 0.2mm rotor incursion. The reason for that is the complex localized contact condition at backing plate corner. As the first rotor interference is introduced, the overhung portion of the bristle, which already bent under the backing plate due to pressure load, is pushed outward and local bristle-backing plate contact becomes more severe. However, as more rotor rub is introduced, downstream side bristles are forced to become aligned with backing plate. During this period, the contact localization conditions change and maximum localization is observed at 0.2mm rotor interference for test seal design parameters and 0.3MPa pressure load. The radial interference level at which seal pack takes maximum VM stress level strongly depends on seal parameters and requires advanced CAE analyses with high fidelity.

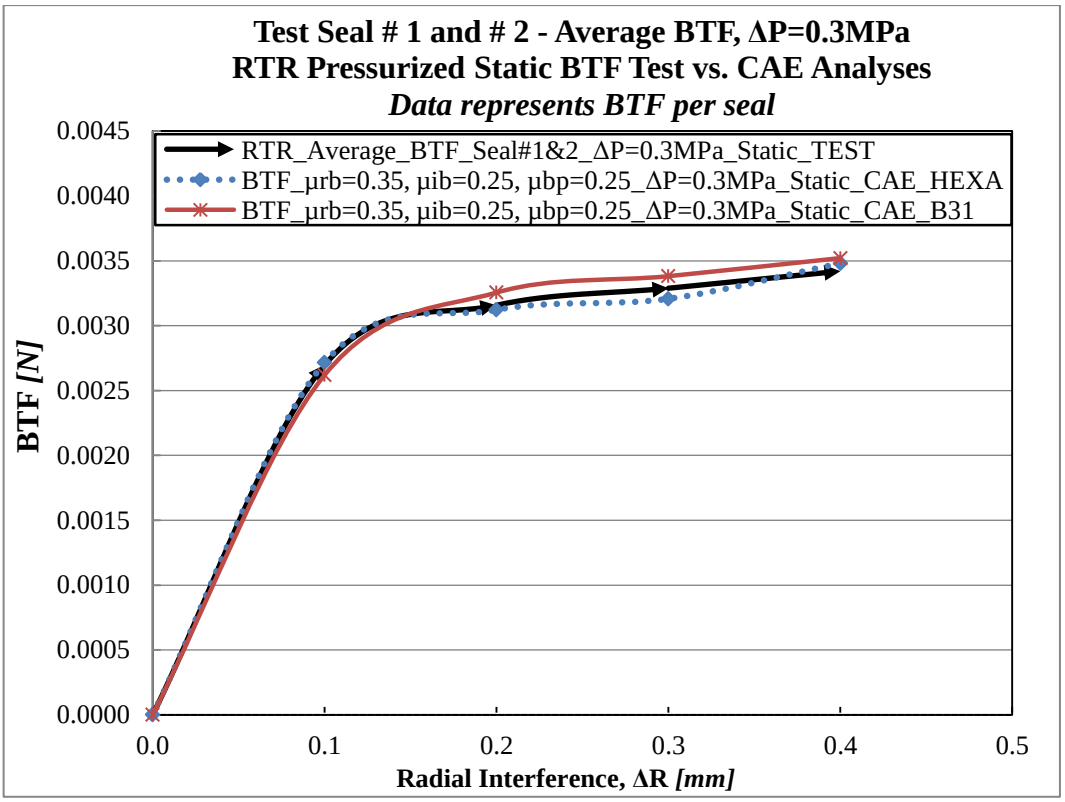

Figure 6.50: Pressurized, nonrotating rotor interference for test seals – CAE-C3D8I & CAE-B31-Loading step, BTF results and comparison with test, ΔP=0.3MPa *(μ_{rb}=0.35, μ_{ib}= μ_{bp}=0.25)*

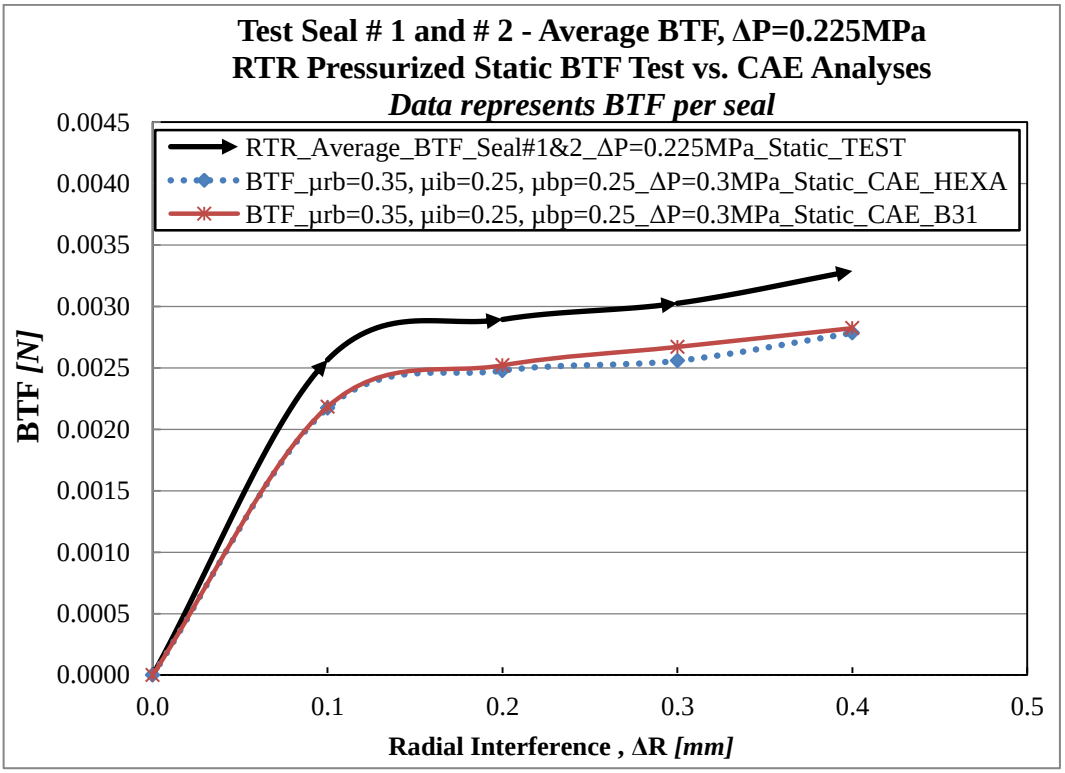

Figure 6.51: Pressurized, nonrotating rotor interference for test seals – CAE-C3D8I & CAE-B31-Loading step, BTF results and comparison with test, ΔP=0.225MPa *(μ_{rb}=0.35, μ_{ib}= μ_{bp}=0.25)*

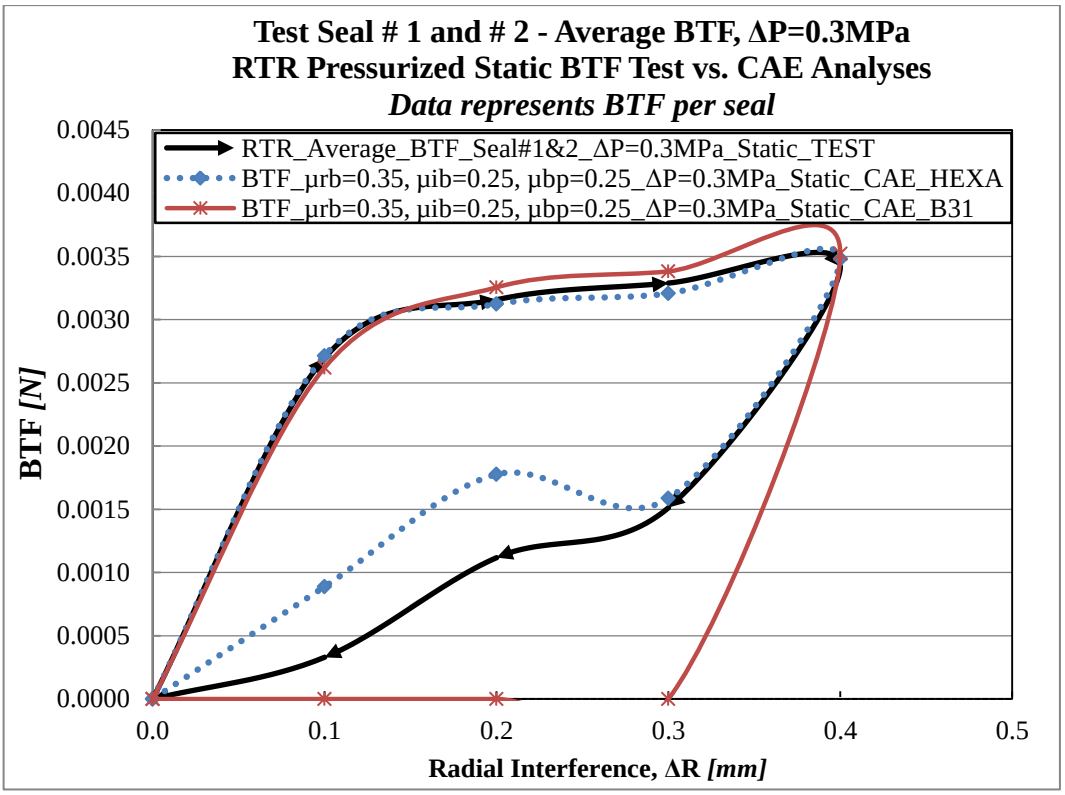

Figure 6.52: Pressurized, nonrotating rotor interference for test seals – CAE-C3D8I & CAE-B31, BTF results and comparison with test, ΔP=0.3MPa *(μ_{rb}=0.35, μ_{ib}= μ_{bp}=0.25)*

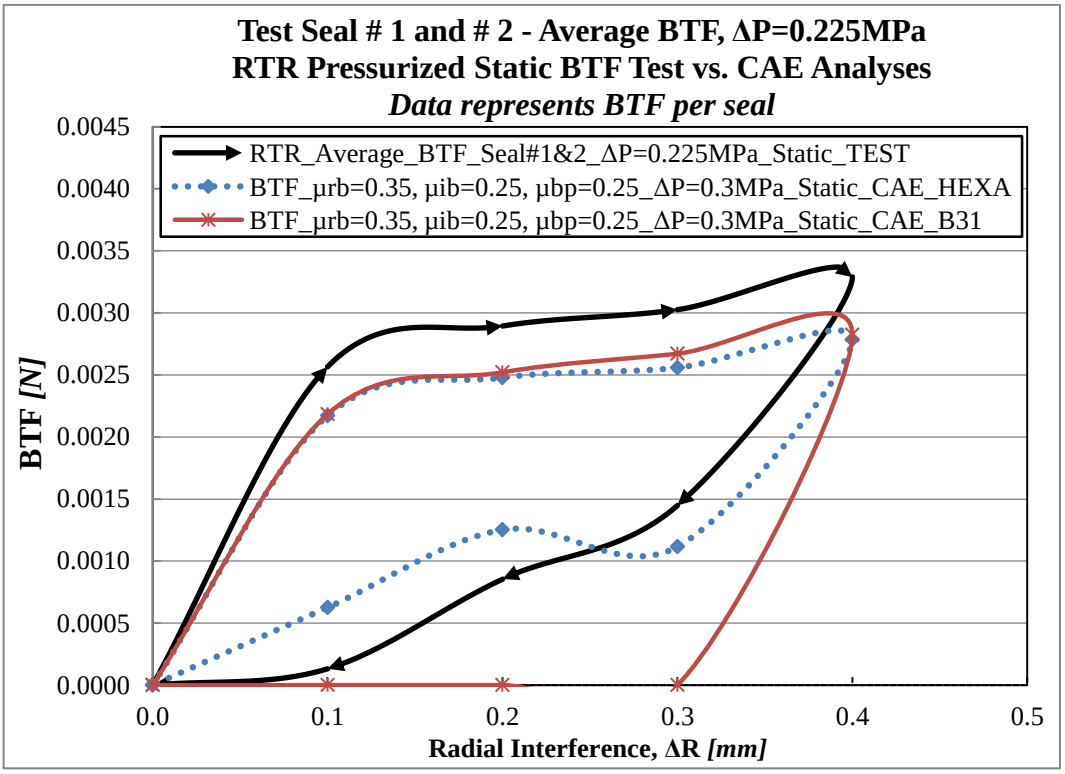

Figure 6.53: Pressurized, nonrotating rotor interference for test seals – CAE-C3D8I & CAE-B31, BTF results and comparison with test, ΔP=0.225MPa *(μ_{rb}=0.35, μ_{ib}= μ_{bp}=0.25)*

Bristle tip force results of CAE-C3D8I analyses at combined loading calculations are given in Figure 6.50 and 6.51 for loading steps. Analyses have been run with correlated friction coefficients for rotor-bristle, inter-bristle and bristle-backing plate, where μ_{rb}=0.35 and μ_{ib}= μ_{bp} =0.25. In Figures 6.52 and 6.53, the BTF results of CAE-C3D8I and CAE-B31 analyses and their comparison with test measurements is detailed in both loading and unloading steps of ΔP=0.3MPa& ΔP=0.225MPa simulations. As a result of detailed contact modeling of the CAE model with C3D8I elements as well as pressure load which creates additional bristle moment profile of real life application, the real testing conditions have been simulated successfully both in loading and unloading steps. Pressure stiffening, BTF stabilization and pressurized hysteresis can successfully be simulated with CAE analyses using C3D8I elements. CAE analyses with B31 elements also give consistent results with tests in the loading step. However, the CAE model with B31 elements cannot simulate the unloading step and pressurized hysteresis; therefore BTF values obtained from B31 analyses deviate from test results and CAE-C3D8I simulations while rotor is being pulled back. The reason for zero BTF values in unloading step of CAE-B31 elements is the applied equivalent line loads instead of pressure, which result in bristle hung-up at any magnitude of pressure load, even in very low magnitudes.

6.4.3 Comparison of CAE Simulations and Analytical Methodologies with Tests

Different analytical and CAE methodologies have been developed for pressurized non-rotating rotor interference conditions within the content of this study, which are as listed below:

- Analytical methodologies
  - Simple approach for stress calculations *(Section 5.3.1)*
  - Advanced approach for stress calculations *(Section 5.3.2)*
  - Pressurized-static BTF calculation methodology *(Section 5.4)*
- CAE methodologies
  - CAE model with B31 elements
  - CAE model with C3D8I elements

Analytical methodologies and FE analyses have been run for test seals, and BTF results are compared with each other as well as with the test data. To summarize, BTF comparison of all methodologies with test is also detailed in this section and given in Figures 6.54 thru 6.51 for 0.225MPa and 0.3MPa pressure loads. BTF results are also tabulated in 6.13.

Pressurized non-rotating rotor interference, Test seals Comparison of CAE Analyses and Analytical Studies				
ΔR *[mm]*	**BTF – Bristle Tip Force *[N]*, ΔP=0.3MPa**			
	RTR-Test	CAE – C3D8I	CAE – B31	Analytical method
0.00	0.000000	0.000000	0.000000	0.000000
0.10	0.002697	0.002715	0.002619	0.002570
0.20	0.003157	0.003122	0.003255	0.002723
0.30	0.003288	0.003207	0.003382	0.002876
0.40	0.003420	0.003481	0.003521	0.003029
0.30	0.001513	0.001587	0.000000	
0.20	0.001118	0.001776	0.000000	
0.10	0.000329	0.000888	0.000000	
0.00	0.000000	0.000000	0.000000	
ΔR *[mm]*	**BTF – Bristle Tip Force *[N]*, ΔP=0.225MPa**			
	RTR-Test	CAE – C3D8I	CAE – B31	Analytical method
0.00	0.000000	0.000000	0.000000	0.000000
0.10	0.002565	0.002172	0.002183	0.001966
0.20	0.002894	0.002478	0.002521	0.002119
0.30	0.003025	0.002558	0.002671	0.002272
0.40	0.003288	0.002785	0.002824	0.002425
0.30	0.001447	0.001115	0.000000	
0.20	0.000855	0.001253	0.000000	
0.10	0.000132	0.000626	0.000000	
0.00	0.000000	0.000000	0.000000	

Table 6.13: Pressurized-nonrotating rotor interference, Comparison of BTF results of CAE, analytical methods *(mod. and simple beam)* and test data *(μ_{rb}=0.35, μ_{ib}= μ_{bp}=0.25)* – Tabulated data

CAE-C3D8I methodology is the most advanced analysis, where contacts and pressure loads can be simulated with high precision. In addition to that, the stress formulation of C3D8I elements makes them the most suitable element for bending dominated problems as in the case of brush seals. As a result of this, BTF results of CAE-C3D8I analyses show good agreement with the RTR-Pressurized non-rotating tests both in loading and unloading steps. Pressure stiffening, BTF stabilization and pressurized hysteresis can successfully be simulated with CAE-C3D8I model.

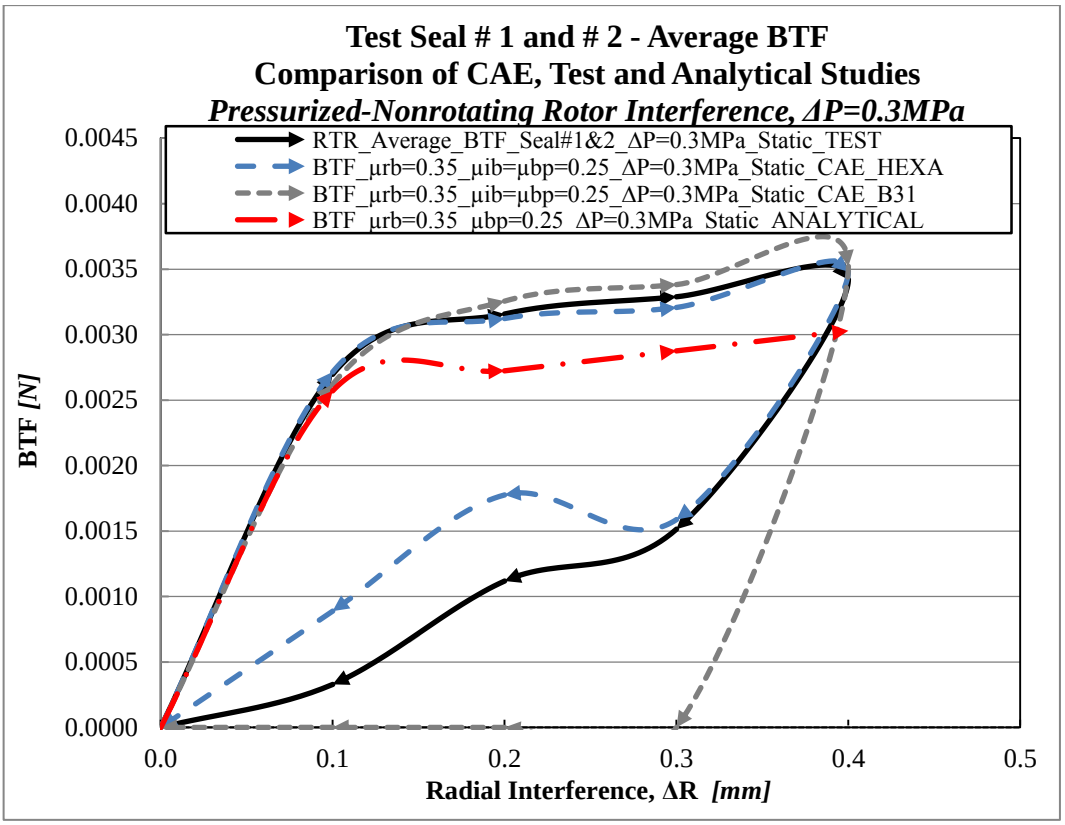

Figure 6.54: Pressurized, nonrotating rotor interference for test seals – CAE and analytical studies BTF results and comparison with test, ΔP=0.3MPa (μ_{rb}=0.35, μ_{ib}= μ_{bp}=0.25)

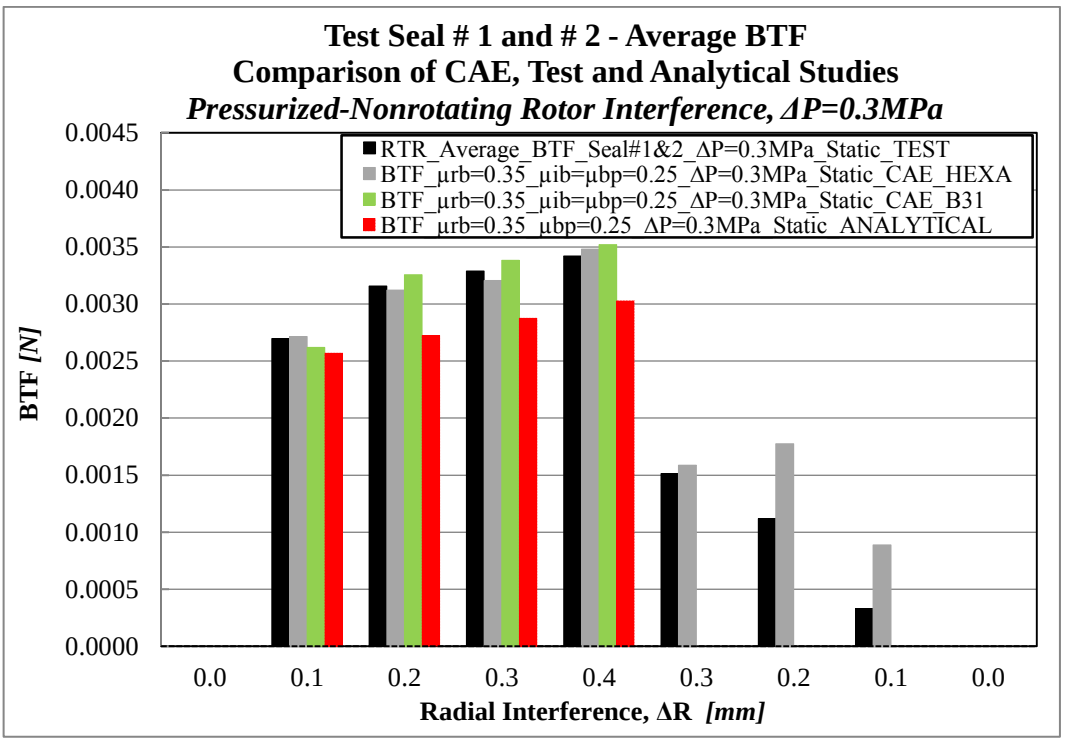

Figure 6.55: Pressurized, nonrotating rotor interference for test seals – CAE and analytical studies BTF results and comparison with test, ΔP=0.3MPa (μ_{rb}=0.35, μ_{ib}= μ_{bp}=0.25)-Bar chart

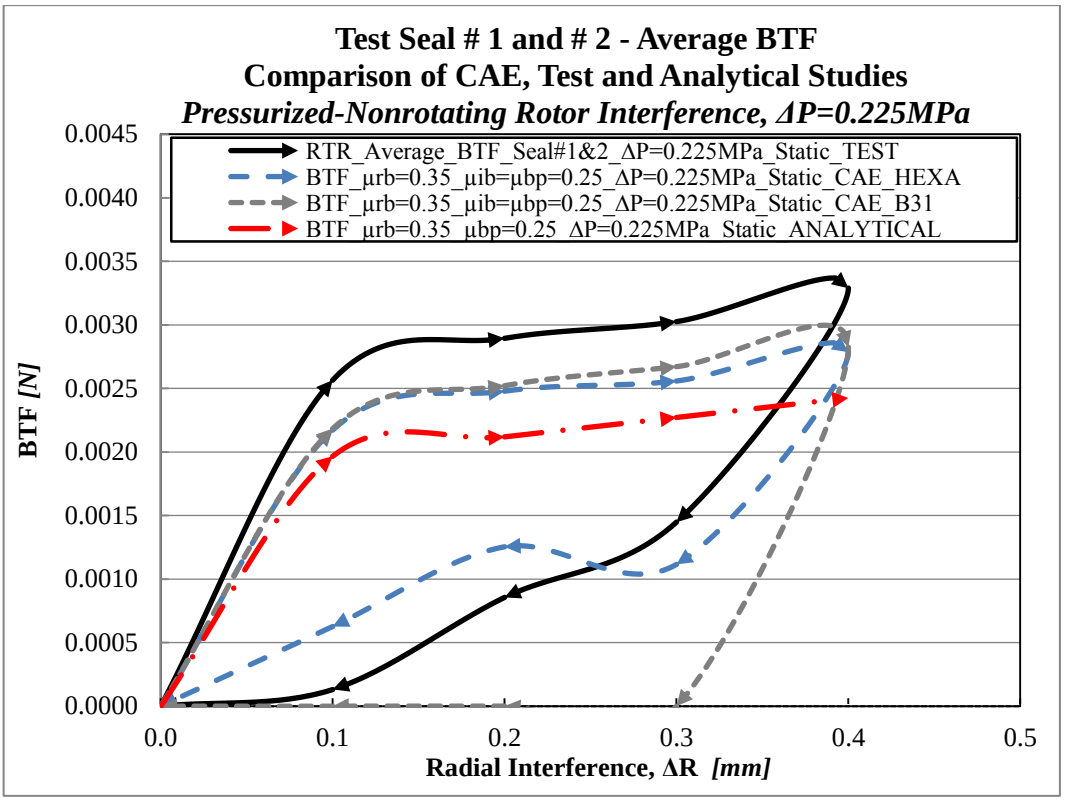

Figure 6.56: Pressurized, nonrotating rotor interference for test seals – CAE and analytical studies

BTF results and comparison with test, ΔP=0.225MPa *(μ_{rb}=0.35, μ_{ib}= μ_{bp}=0.25)*

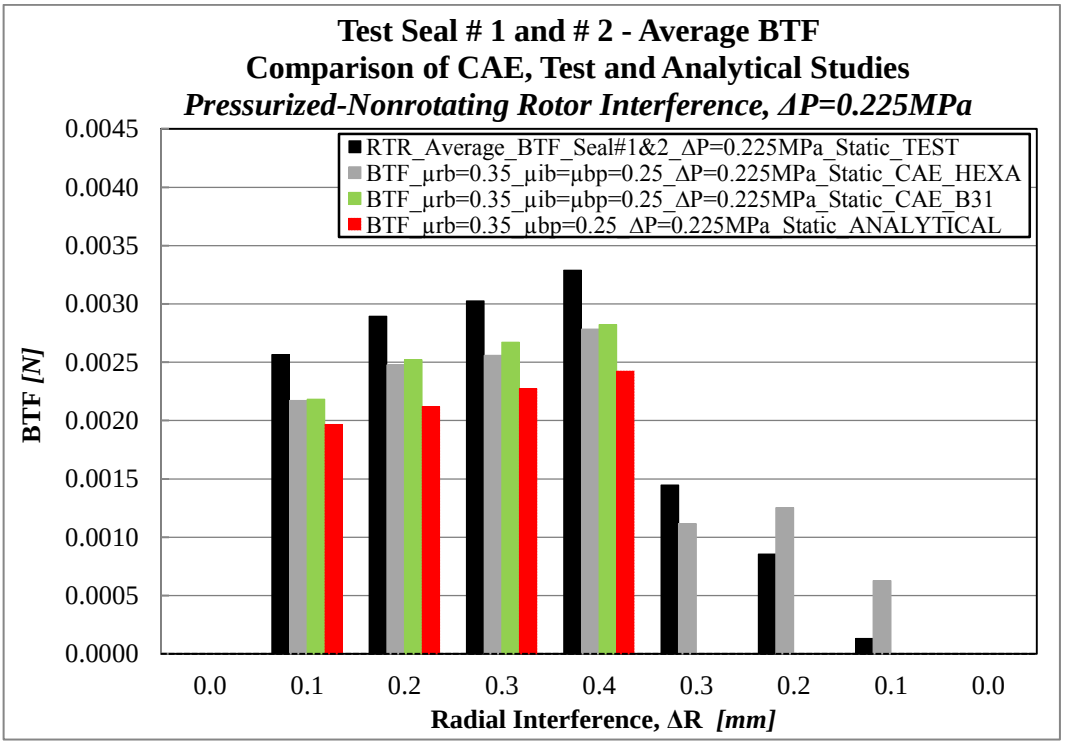

Figure 6.57: Pressurized, nonrotating rotor interference for test seals – CAE and analytical studies

BTF results and comparison with test, ΔP=0.225MPa *(μ_{rb}=0.35, μ_{ib}= μ_{bp}=0.25)* -Bar chart

In Figures 6.54 thru 6.57, BTF results of CAE-B31 elements are also given. In the loading step of pressurized-nonrotating rotor rub simulations, CAE-B31 analyses give similar results with CAE-C3D8I elements as well as show good agreement with the test data. The pressure stiffening and BTF stabilization can successfully be simulated with CAE-B31 analyses. However, the pressurized hysteresis cannot be simulated by using B31 elements since the pressure load is applied as equivalent line loads, which cannot generate moment profile that deflects bristles towards the rotor surface. Therefore, CAE-B31 simulations cause artificial hung-up even at very low magnitudes of ΔP, and BTF values directly reduce to zero while rotor is being pulled back to its initial position.

The analytical methodology for BTF calculations under pressurized-nonrotating rotor interference simulations also gives consistent results with tests and CAE analyses. Although BTF magnitudes obtained by using the analytical methodology have small deviation from test data, results have satisfactory agreement with BTF measurements. The analytical calculations can successfully simulate frictional effects, pressure stiffening and BTF stabilization. Considering that FE modeling and analysis requires advanced FE knowledge and long CPU time, the developed methodology for pressurized-nonrotating rotor interference presents invaluable closed form function for brush seal literature.

Bristle stress levels for pressurized-nonrotating rotor rub simulations and analyses are detailed in Table 6.14 for $\Delta P=0.3$MPa. The BTF correlated CAE-C3D8I model is the reference model for correlation.

Although CAE-B31 analyses give almost same BTF values with CAE-C3D8I simulations, stress levels of FE model using B31 elements have smaller VM stress magnitudes at steady state and combined loading conditions. The reason for this difference is the advanced and more precise contact pressure calculation of C3D8I elements, especially at the localized contact area at backing plate corner radius. Since the pressure load cause localized backing plate-bristle contact, 3D contact surface profile and small mesh size of C3D8I elements better simulates contact pressure peaks and resulting stress-critical points at that region. Slide line contact definition of B31 elements can successfully simulate contact forces, but CAE-B31 model cannot simulate local contact pressure peaks as precisely as CAE-C3D8I analyses do, and therefore stress levels have smaller magnitudes for B31 elements. The importance of localized

contact pressure modeling can be observed more clearly in stress calculations using analytical methods, where contact and friction is not included. Both simple and advanced approach underestimates the stress levels at FH point of downstream side bristle, while pinch point stress magnitudes are relatively close to CAE simulation results.

Pressurized non-rotating rotor interference, Test seals, ΔP=0.3MPa Comparison of CAE Analyses and Analytical Studies						
			CAE		**Analytical Studies**	
			CAE-C3D8I	CAE-B31	Simple app.	Advanced app.
ΔR=0	Backing plate side *(downstream, 1st row)*	FH point	125MPa	99.2MPa	33.35	33.35
		Pinch point	~15MPa	~7MPa	16.68	41.43
	Front plate side *(upstream, 15th row)*	FH point	~35MPa	~10MPa	-	-
		Pinch point	100MPa	69.0MPa	-	-
ΔR=0.1mm	Backing plate side *(downstream, 1st row)*	FH point	138MPa	108.3MPa	29.18	29.18
		Pinch point	~30MPa	~16MPa	22.06	47.25
	Front plate side *(upstream, 15th row)*	FH point	~45MPa	~13MPa	-	-
		Pinch point	108MPa	73.6MPa	-	-
ΔR=0.2mm	Backing plate side *(downstream, 1st row)*	FH point	140MPa	96.8MPa	25.36	25.36
		Pinch point	~37MPa	~8MPa	35.41	57.45
	Front plate side *(upstream, 15th row)*	FH point	~43MPa	~19MPa	-	-
		Pinch point	115MPa	76.7MPa	-	-
ΔR=0.3mm	Backing plate side *(downstream, 1st row)*	FH point	135MPa	99.5MPa	21.99	21.99
		Pinch point	~55MPa	~23MPa	50.79	70.14
	Front plate side *(upstream, 15th row)*	FH point	~42MPa	~20MPa	-	-
		Pinch point	123MPa	77.0MPa	-	-
ΔR=0.4mm	Backing plate side *(downstream, 1st row)*	FH point	134MPa	103.8MPa	18.89	18.89
		Pinch point	~65MPa	~37MPa	66.80	84.18
	Front plate side *(upstream, 15th row)*	FH point	~40MPa	~22MPa	-	-
		Pinch point	128MPa	77.2MPa	-	-

Table 6.14: Pressurized, nonrotating rotor interference for test seals – VM stress comparison of CAE analyses and analytical studies, ΔP=0.3MPa

6.5 Unpressurized - Dynamic Rotor Interference Conditions *(Rotating Rotor)*

Unpressurized dynamic rotor interference case refers to rotating rotor incursion and zero-pressure load. Transient analyses have been conducted with B31 elements for test seals, and results are compared with the test data.

6.5.1 FE Model Details and Analysis Steps

RTR-Unpressurized dynamic tests show that BTF values decrease when the rotor rotation is introduced, which is an expected behavior of brush seal since rotor rotation causes dynamic effects and result in some bristles to flutter and loose contact with rotor.

To be able to simulate this condition, a cylindrical rotor surface is modeled with large radius, which can be assumed to be flat at bristle tip contact region. Similar to non-rotating rotor simulations, backing plate and rotor surfaces are modeled as analytical rigid bodies. Cyclic boundary conditions are defined for B31 bristles in circumferential direction. Transient analyses are run for test seals in order to simulate inertial and dynamic effects of rotating rotor on bristles. Test seal parameters and material properties have already been given in Chapter 2 *(Tables 2.3, 2.4, 2.6 and 2.7)*. Inter-bristle, backing plate-bristle and rotor-bristle contacts are defined with correlated friction coefficients *(μ_{rb}=0.35, μ_{ib}=μ_{bp}=0.25)*. Rotation is defined as angular velocity at rotor's reference point, and enforced motion is given to rotor for radial interference up to 0.6mm. Both loading and unloading steps of dynamic test are simulated by moving rotor towards the bristles and then pulling it back to its initial position. Analysis steps are visualized in Figure 6.58.

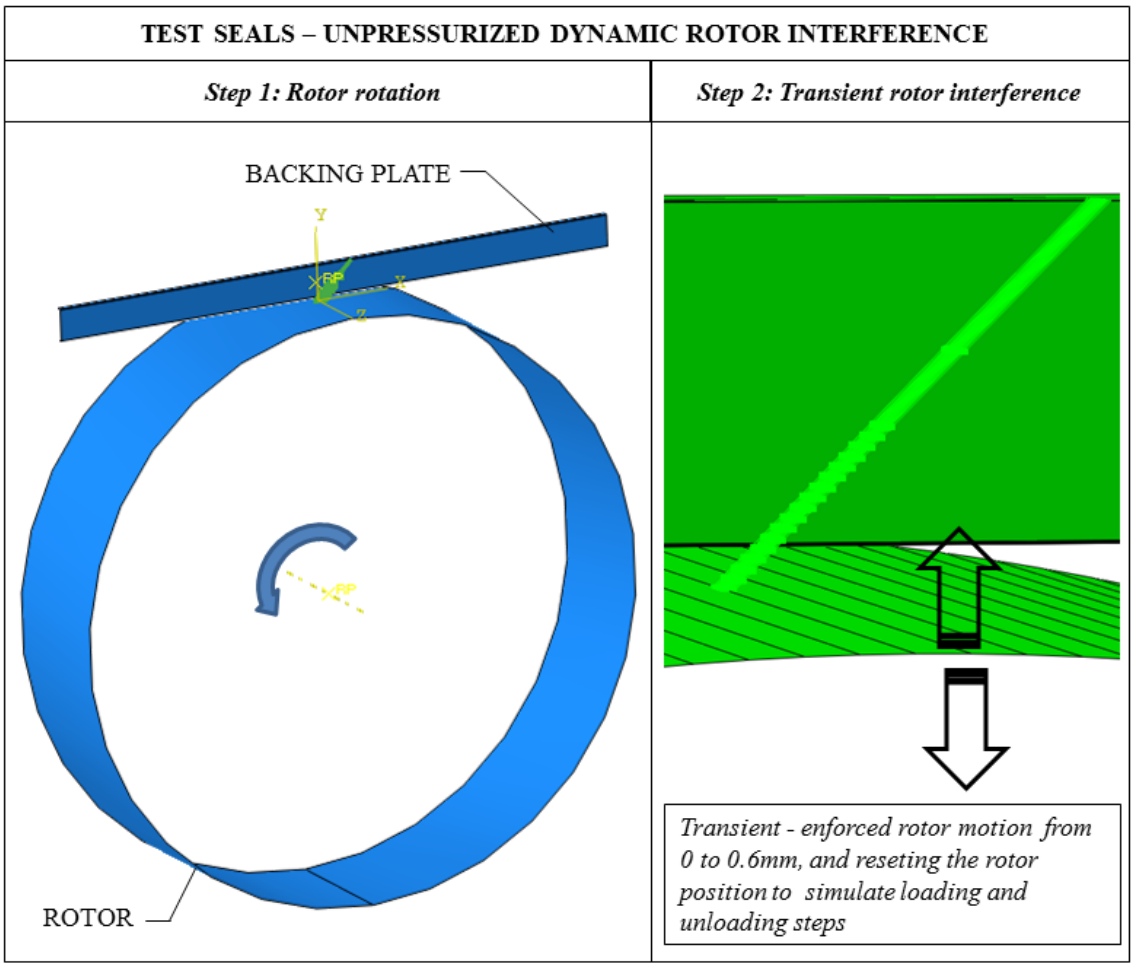

Figure 6.58: Transient CAE analysis steps - Unpressurized-rotating rotor interference for test seals

6.5.2 Analysis Results and Correlation with Test Data

Unpressurized static/dynamic rotor interference analyses results and their comparison with BTF measurements are given in Figure 6.59. In Figure 6.60, unpressurized-dynamic rotor rub simulation data in loading and unloading steps are compared with test results.

In transient analysis, the bristle tip force read from the rotor reference point varies within each displacement step due to chattering of bristles caused from inertial effects. Therefore, CAE results have been saved at each increment of the simulation and BTF values have been post-processed carefully at variable rotor interference intervals. The BTF values of unpressurized static analyses decreases when rotor rpm and inertial effects are introduced, and free-state hysteresis narrows as in the case of tests. As it can be seen from the figures, unpressurized transient analyses show good agreement with the test data.

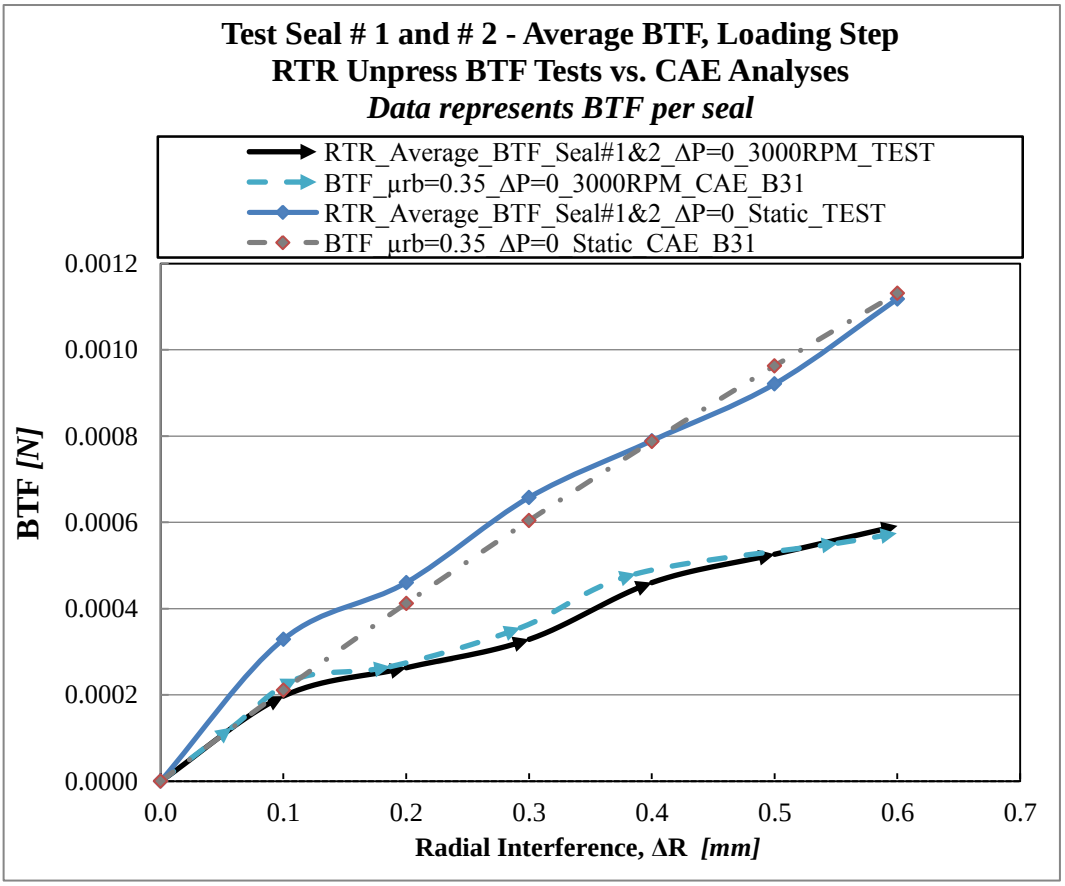

Figure 6.59: Unpressurized static/dynamic rotor interference - BTF results of CAE analyses and comparison with test, loading step only

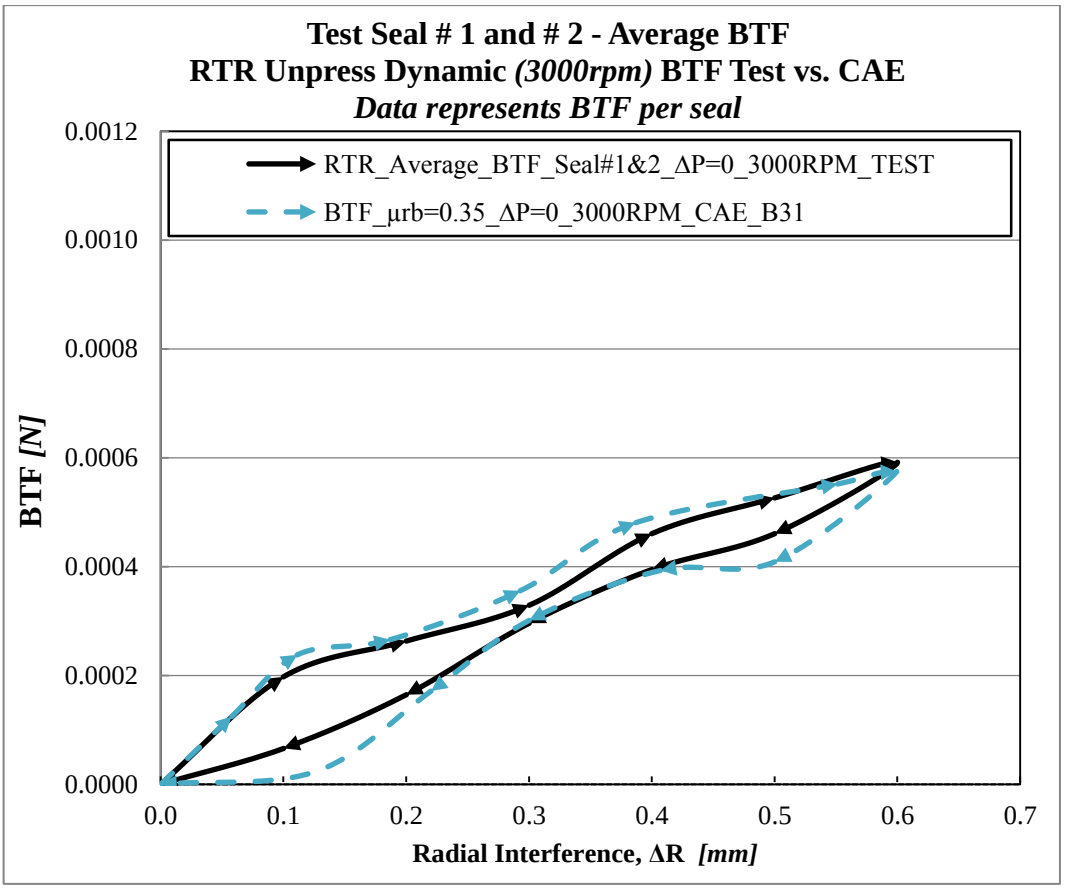

Figure 6.60: Unpressurized dynamic rotor interference - BTF results of CAE analyses and comparison with test

6.6 Pressurized - Dynamic Rotor Interference Conditions *(Rotating Rotor)*

Pressurized dynamic stiffness case refers to rotating rotor interference to loaded seal. This case directly simulates the rotor transients in turbine operating conditions. Transient analyses have been conducted with B31 elements for test seals, and results are compared with the test data.

6.6.1 FE Model Details and Analysis Steps

RTR-Pressurized dynamic tests show that BTF values decrease when the rotor rotation is introduced. In addition to that, BTF stabilization of pressurized-static rotor interference cannot be observed for rotating rotor case, which is due to dynamic effects introduced by rotor rpm. To be able to simulate this condition, the rotating rotor is

pressed onto loaded seal pack and transient analyses are performed for including inertial effects. Test seal parameters and material properties have already been given in Chapter 2 *(Tables 2.3, 2.4, 2.6 and 2.7)*. Inter-bristle, backing plate-bristle and rotor-bristle contacts are defined with correlated friction coefficients *(μ_{rb}=0.35, μ_{ib}=μ_{bp}=0.25)*. Rotation is defined as angular velocity at rotor's reference point, 7th order pressure profile is applied to bristles, and rotor interference is given to loaded seal pack by applying enforced motion to rotor. Analyses are performed up to 0.4mm radial interference and for ΔP=0.225MPa and ΔP=0.3MPa. Simulation steps are visualized in Figure 6.61.

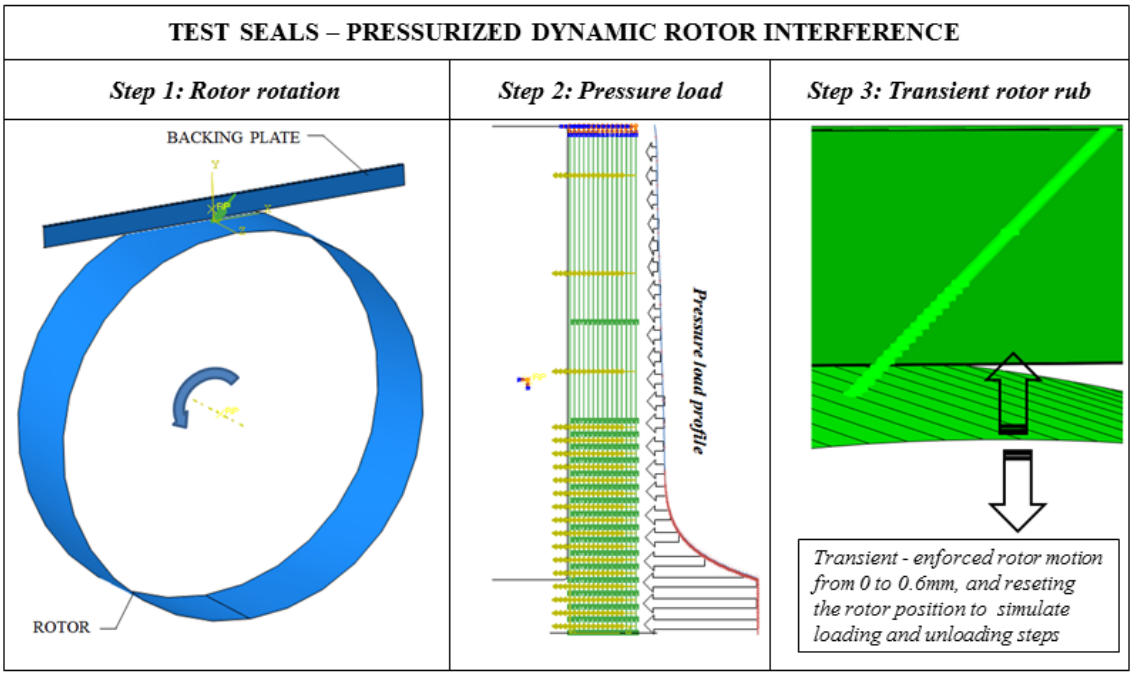

Figure 6.61: Transient CAE analysis steps - Pressurized-rotating rotor interference for test seals

6.6.2 Analysis Results and Correlation with Test Data

Pressurized - dynamic rotor interference analyses results and their comparison with BTF measurements are given in Figure 6.62 and Figure 6.63. The BTF values of pressurized static analyses decreases when rotor rpm and inertial effects are introduced. As it can be seen from figures, BTF stabilization cannot be observed in transient FE analysis of rotating rotor incursion, which means that dynamic effects are successfully simulated. Pressurized transient analyses show good agreement with the test data for both ΔP=0.3MPa and ΔP=0.225MPa.

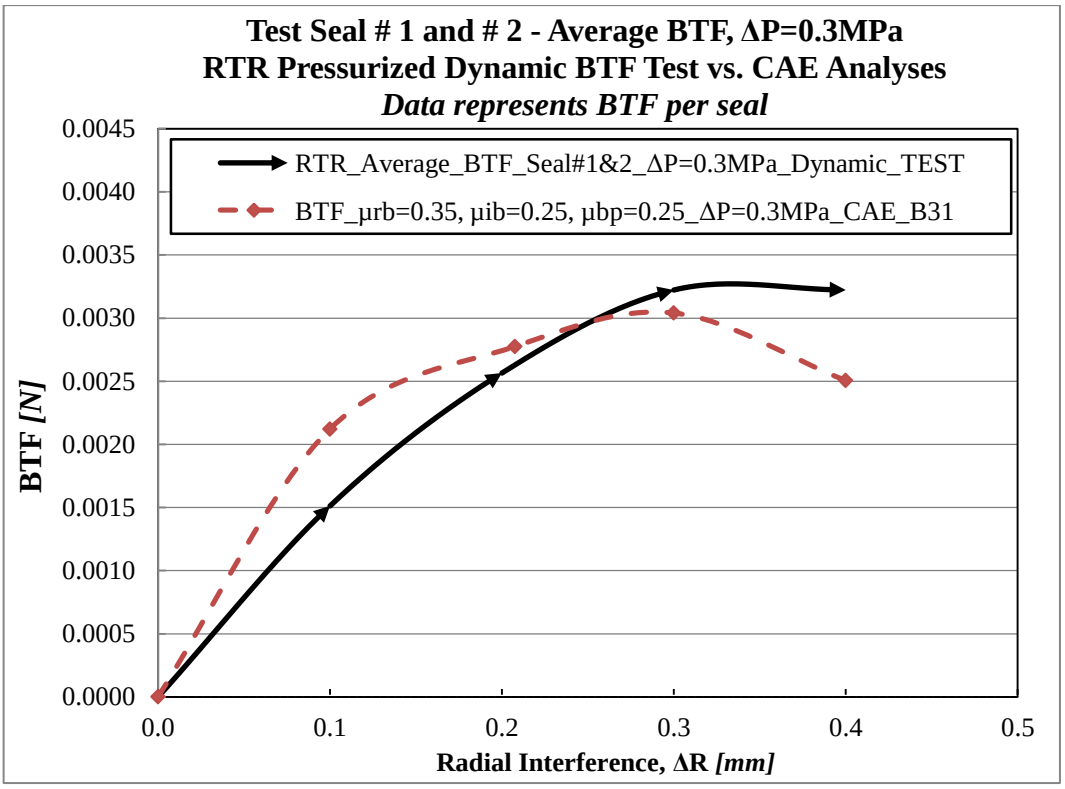

Figure 6.62: Pressurized dynamic rotor interference - BTF results of CAE analyses and comparison with test at ΔP=0.3MPa

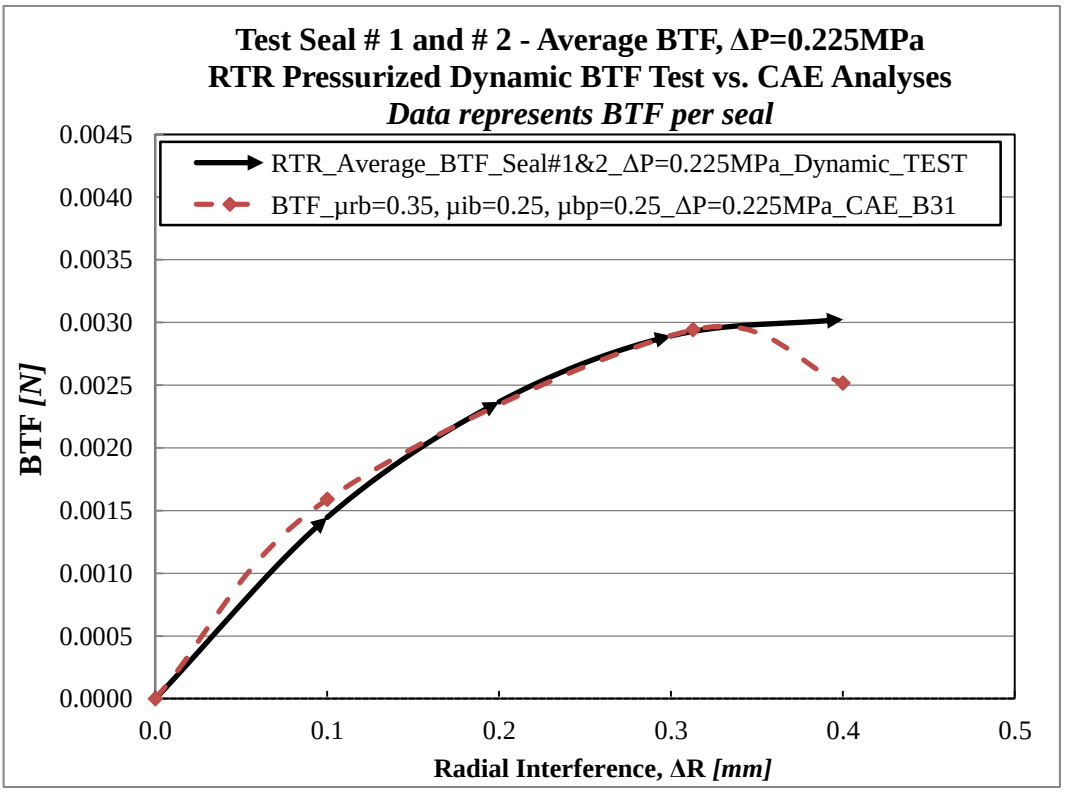

Figure 6.63: Pressurized dynamic rotor interference - BTF results of CAE analyses and comparison with test at ΔP=0.225MPa

7 CAE BASED BRUSH SEAL CHARACTERIZATION

Brush seals are complex structures having variety of design parameters, all of which affect seal behavior at operating conditions. The complicated nature of seal pack and frictional interactions of rotor, backing plate and bristles result in nonlinear response of brush seal to design parameter variances. Industrial applications for brush seal selection are mainly based on experience and simple analytical methodologies like simple beam theory of Flower [17], while CAE-based brush seal characterization does not exist in the literature.

This study presents CAE based characterization of brush seals, where correlated CAE models have been used to examine the effect of design parameters and frictional properties of the seal pack on brush seal stiffness and stress levels. Considering the absence of such data, results of this characterization work will be very beneficial for seal literature. Characterization study covers free-state rotor rub, steady state *(pressure load without rotor interference)* and pressurized-rotor interference conditions.

7.1 Selecting the CAE Methodology

Two different CAE methodologies have been developed within the content of this study, one of which uses C3D8I elements for bristles, and the second methodology runs the FE model having B31 elements. CAE analyses and correlation studies show that B31 elements show good agreement with BTF measurements, yet they have shorter simulation times when compared with CAE-C3D8I simulations. The hardware requirements and CPU requirements for two different models are summarized in Table 7.1.

As summarized in tabulated values, CAE-C3D8I simulations take 5-6 days while CAE-B31 analyses are completed less than an hour. In addition to that, the output file sizes on disk for CAE-C3D8I analyses are at the levels of 50-60GB. On the contrary CAE-B31 *".odb"* file sizes are as small as Kb's. Considering that characterization study requires variety of analyses, and bearing in mind that CAE-B31 simulations show good

agreement with tests, CAE-B31 FE model is used for brush seal stiffness and friction characterization.

Free State Rotor Interference Simulations						
	RAM	CPU	Pre-process	Simulation	Post-process	Output size
CAE-B31	100-150Mb	8 CPUs@2.7GHz	1-2 days	5-10 min	~0.1 day	~150Kb
CAE-C3D8I	40-45Gb	16 CPUs@3.1GHz	2-3 days	3-4 days	~0.2 day	~60Gb
Steady State Simulations *(Pressure load w/o rotor interference)*						
	RAM	CPU	Pre-process	Simulation	Post-process	Output size
CAE-B31	150-200Mb	8 CPUs@2.7GHz	2-3 days	5-10 min	~0.1 day	~200Kb
CAE-C3D8I	50-60Gb	16 CPUs@3.1GHz	3-4 days	3-4 days	~0.2 day	~80Gb
Pressurized Rotor Interference Simulations						
	RAM	CPU	Pre-process	Simulation	Post-process	Output size
CAE-B31	150-200Mb	8 CPUs@2.7GHz	2-3 days	15-20 min	~0.1 day	~300Kb
CAE-C3D8I	50-60Gb	16 CPUs@3.1GHz	3-4 days	5-6 days	~0.2day	~120Gb

Table 7.1: CAE methodologies for brush seal analyses – Hardware and CPU requirements

Brush seal characterization study will be performed by conducting approximately 60-70 analyses, which means pre-processing periods up to 200 days and unnecessary burden. In order to shorten pre-processing periods, a MATLAB based code has been generated, which construct the ABAQUS input file automatically from seal parameters.

The MATLAB code shortens the pre-processing time requirements to 1-2 minutes, which enables efficient FE modeling. Furthermore, a user without FE experience can run the MATLAB code to generate CAE model of the brush seal, where all contacts, mesh, loadings and boundary conditions are defined automatically. FE model parameters such as mesh size, biased mesh, region of dense mesh can be given as input to MATLAB code. The code also calculates 7^{th} order pressure profile at backing plate and generates equivalent line loads on bristles by using ΔP value and design parameters. Input files for free-state rotor rub, steady state and pressurized-rotor interference simulations can be generated by using the code, and radial interference increments at each simulation step are defined by the user. Friction coefficients of rotor, bristle and backing plate contact surfaces are also defined by user. Required parameters for MATLAB code – CAE model generator are detailed in Figure 7.1.

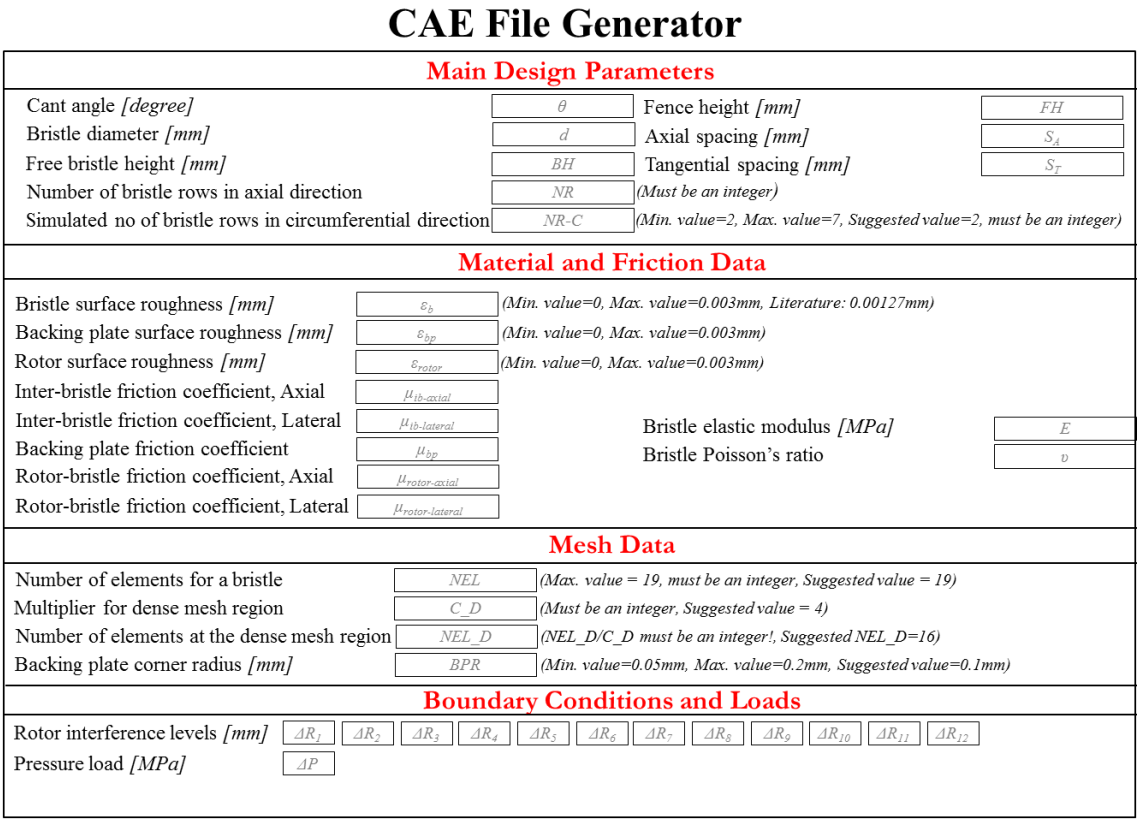

Figure 7.1: MATLAB Code – CAE Model Generator, Required inputs

7.2 Brush Seal Design Parameters

Brush seal characterization studies have been performed for seal design parameters and friction coefficients. Analyses include:

- Effect of bristle diameter, d
- Effect of free bristle height, BH
- Effect of fence height, FH
- Effect of cant angle, θ
- Effect of bristle density, η
- Effect of rotor-bristle friction, μ_{rb}
- Effect of inter-bristle and bristle-backing plate friction, μ_{ib} and μ_{bp}

Effect of listed parameters on BTF and stress levels have been examined in free-state rotor excursion, steady state and pressurized-rotor interference conditions. Nominal values for design parameters and friction coefficients are given in Table 7.2.

While the effect of specific parameter on brush seal behavior is being analyzed, nominal values are used for other parameters.

Brush Seal Design Parameters – Nominal Values	
Bristle diameter, d *[mm]*	0.10
Free bristle height, BH *[mm]*	12.50
Fence height, FH *[mm]*	1.35
Cant angle, θ *[deg]*	45
Bristle density, η *[per mm]*	80
Axial spacing with 25% bloom, S_A *[mm]*	0.111
Tangential spacing with 5% bloom, S_T *[mm]*	0.152
Number of bristle rows, NR	12
Rotor-bristle friction coefficient, μ_{rb}	0.30
Inter-bristle and bristle-backing plate friction coefficient, $\mu_{ib=}$ μ_{bp}	0.30
Other Parameters	
Bristle elastic modulus, E *[MPa]*	225000
Bristle poisson's ratio, υ	0.3
Bristle surface roughness, ε *[μm]*	1.27
Backing plate surface roughness, ε_{bp} *[μm]*	1.00
Rotor surface roughness, ε_r *[μm]*	1.00
Backing plate corner radius *[mm]*	0.10
Pressure load, ΔP *[MPa]*	0.30

Table 7.2: CAE based brush seal characterization – Nominal values for design parameters

Number of bristle rows is important parameter to characterize total heat generation on rotor surface. Considering two different seals having same design parameters except NR, total heat generation due to rotor-bristle friction will be different for those seals although they have same BTF values. Therefore, *"Contact force per rotor unit circumferential length, RF_{circ}"* should also be examined when seals having different number of bristle rows are compared. *"RF_{circ}"* can be calculated by using the Equation 7.1.

$$RF_{circ} = \frac{RF_{2-CAE}}{l_{t-CAE}} \tag{7.1}$$

$$l_{t-CAE} = l_{c-c} + 2d \tag{7.2}$$

In Equations 7.1 and 7.2, *"$RF_{2\text{-}CAE}$"* is the total reaction force on rotor in CAE analyses, *"$l_{t\text{-}CAE}$"* is the effective circumferential length of the simulated bristles, *"$l_{c\text{-}c}$"* is the center-to-center distance for end bristles in FE model, and *"d"* is the bristle diameter. Effective circumferential length, *"$l_{t\text{-}CAE}$"*, is visualized in Figure 7.2.

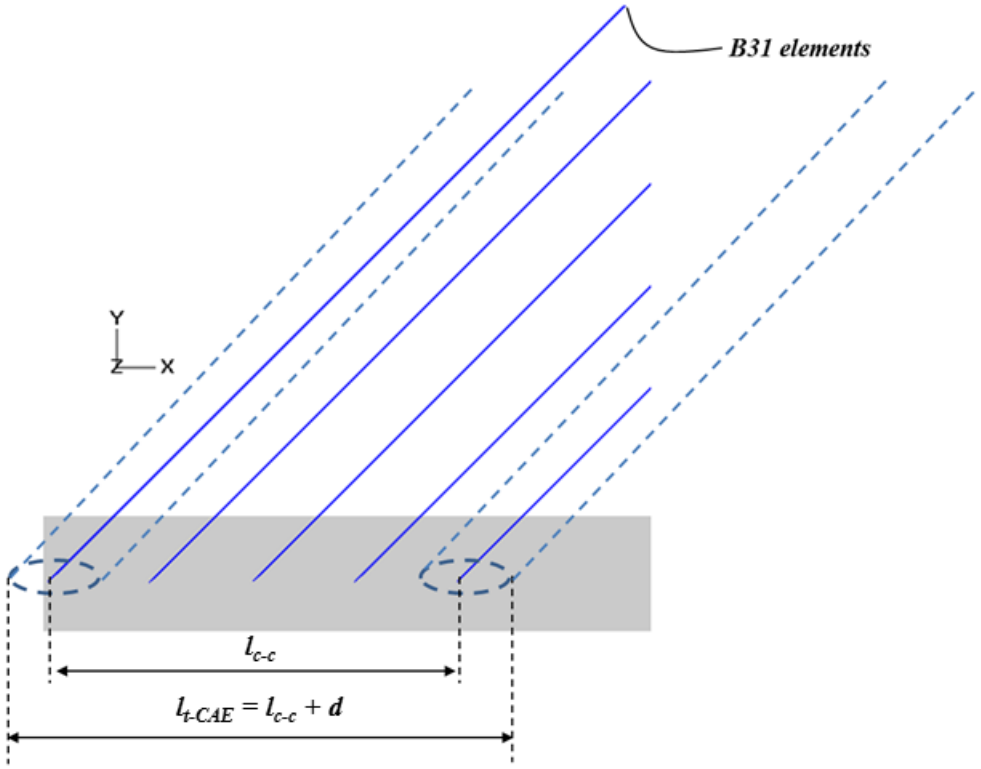

Figure 7.2: Brush seal – Effective circumferential length for CAE model, $l_{t\text{-}CAE}$

7.3 Effect of Bristle Diameter

Bristle diameter is one of the most important design parameters, which directly affects BTF and bristle stress levels at pressurized/unpressurized rotor interference conditions as well as steady state case. Typical industrial application in selecting the appropriate bristle diameter is know-how based, and larger diameters are selected for high pressure loads. However, industrial applications show that the pressure load capacity of a brush seal does not increase continuously with bristle diameter, and maximum ΔP capacity for single stage seal is limited to 20 bar [69]. In order to extend the pressure load capacity of the brush seal, multi-stage and multi-layer brush seals have been tried [70, 71, 72, 73, 74, 75]. However, due to nonlinear pressure drop between seal stages for multi-stage applications and introduced bristle locking phenomenon in multi-layer seal applications, the improvement in pressure load capacities are limited to 20%. Maximum pressure load capacity for a brush seal is reported as 27 bar *(Dinc et al. [76]).*

In this section, effect of bristle diameter on BTF and stress levels at pressurized/unpressurized rotor interference and steady state conditions will be analyzed through correlated CAE models. Since axial and tangential spacing parameters change with bristle diameter, number of bristle rows also changes with bristle diameter. Therefore, contact force per rotor unit circumferential length, *"RF_{circ}"*, will also be examined in addition to BTF. Considering that the nonlinear interactions in a loaded seal are main reasons which limit the pressure load capacity at large bristle diameters, this study presents valuable outputs for seal literature.

7.3.1 Effect of Bristle Diameter at Unpressurized-Nonrotating Rotor Interference Conditions

Effect of bristle diameter on seal response at unpressurized-nonrotating rotor interference conditions *(free-state rotor rub)* has been examined by running the cases detailed in Table 7.3.

Effect of Bristle Diameter					
	Case 1	Case 2	Case 3	Case 4	Case 5
Bristle diameter, *d [mm]*	0.09	0.10	0.11	0.12	0.13
Axial spacing, S_A *[mm]*	0.100	0.111	0.121	0.132	0.143
Tangential spacing, S_T *[mm]*	0.137	0.152	0.167	0.181	0.196
Number of bristle rows, NR	11	12	13	15	16
Max. rotor interference, ΔR_{max} *[mm]*	0.80	0.80	0.80	0.80	0.80
Effective circumferential length, $l_{t\text{-}CAE}$ *[mm]*	0.364	0.404	0.444	0.483	0.523
PS: Nominal values given in Table 7.2 has been used for remaining parameters.					

Table 7.3: Effect of bristle diameter – Cases for unpressurized nonrotating rotor interference conditions

Bristle tip force. Free-state BTF change with bristle diameter is given in Figure 7.3 at different rotor interference levels. Second moment of area for the bristle cross-section is 4^{th} order function of bristle diameter, therefore required tip force to bend the bristles up to certain interference level is higher for larger bristle diameters. Free-state BTF increases nonlinearly with bristle diameter, which is consistent with the BTF formula given in Equation 5.4. Increase in free-state BTF with bristle diameter is more pronounced at large interference levels. In Figure 7.4, free-state BTF change with rotor interference is detailed for different bristle diameter. As it can be seen from the figure,

free-state hysteresis also increases with bristle diameter since rotor-bristle friction is more effective at large projected areas of bristle tip.

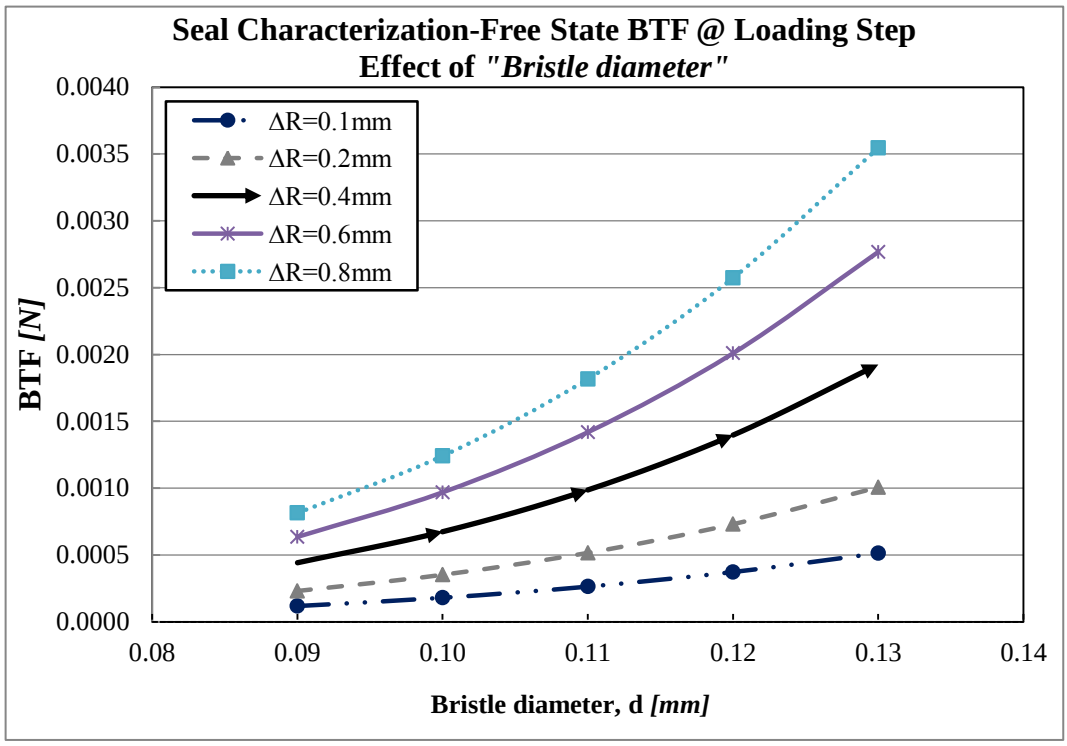

Figure 7.3: Change of BTF with bristle diameter, Unpressurized-nonrotating rotor interference-loading step

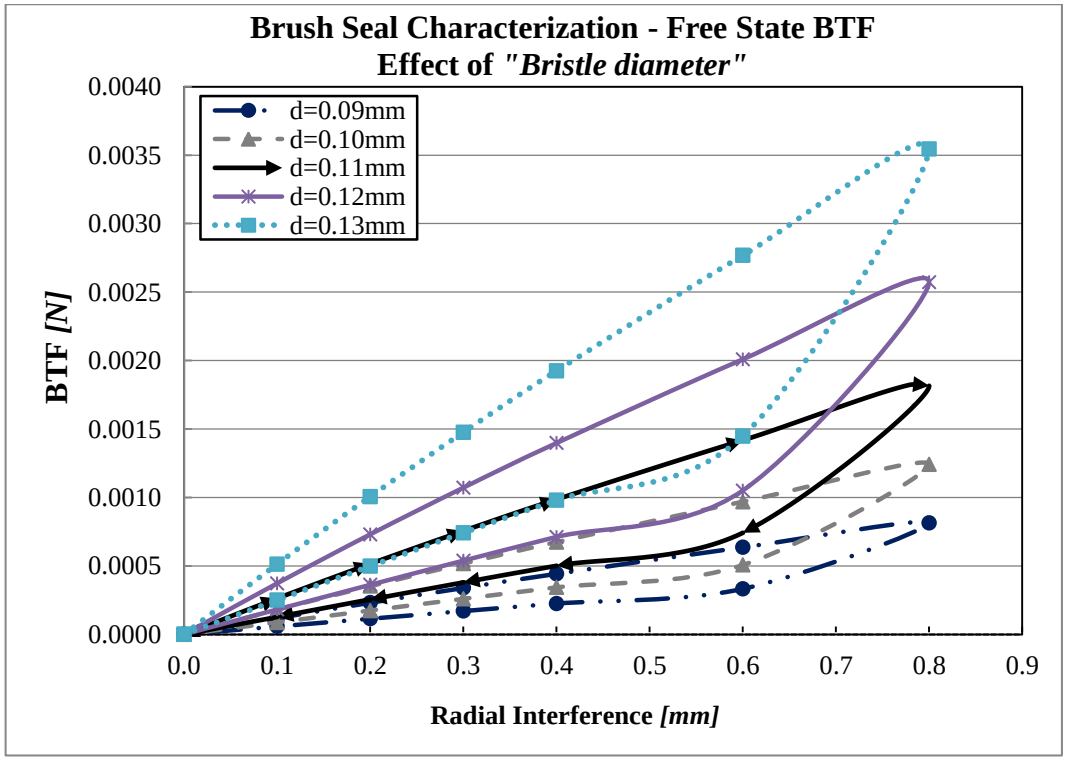

Figure 7.4: Effect of bristle diameter on BTF values at unpressurized-nonrotating rotor interference conditions

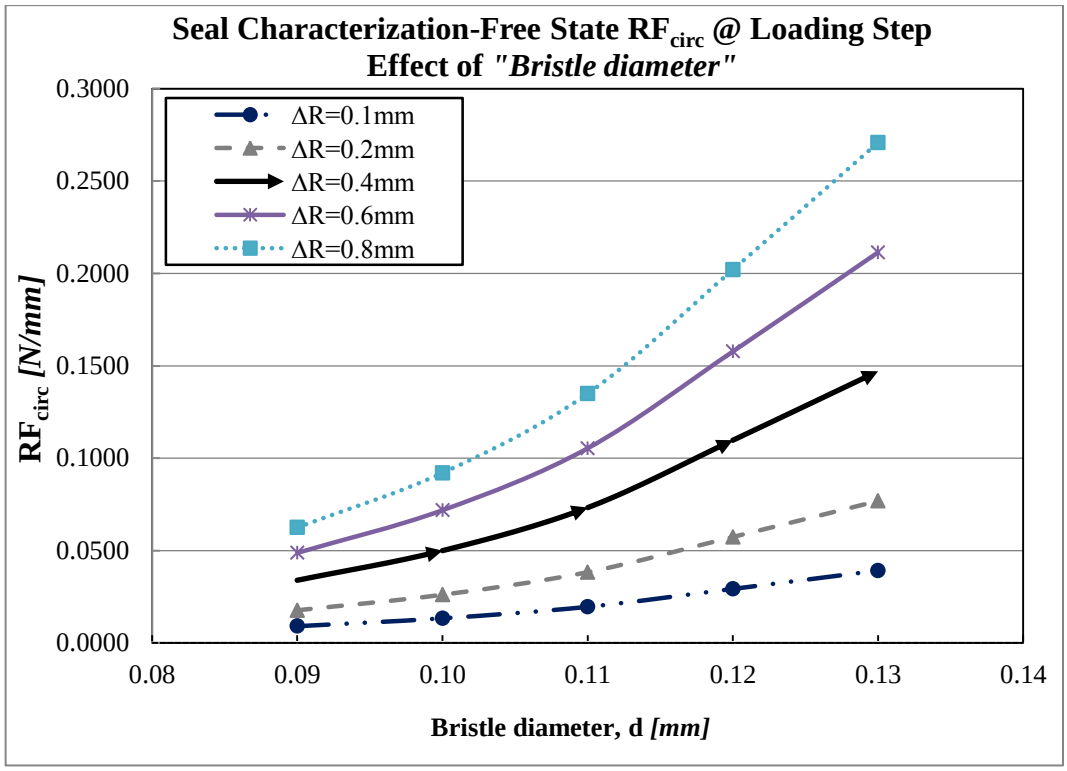

Figure 7.5: Change of RF$_{circ}$ *(Contact force per rotor unit circumferential length)* with bristle diameter, Unpressurized-nonrotating rotor interference-loading step

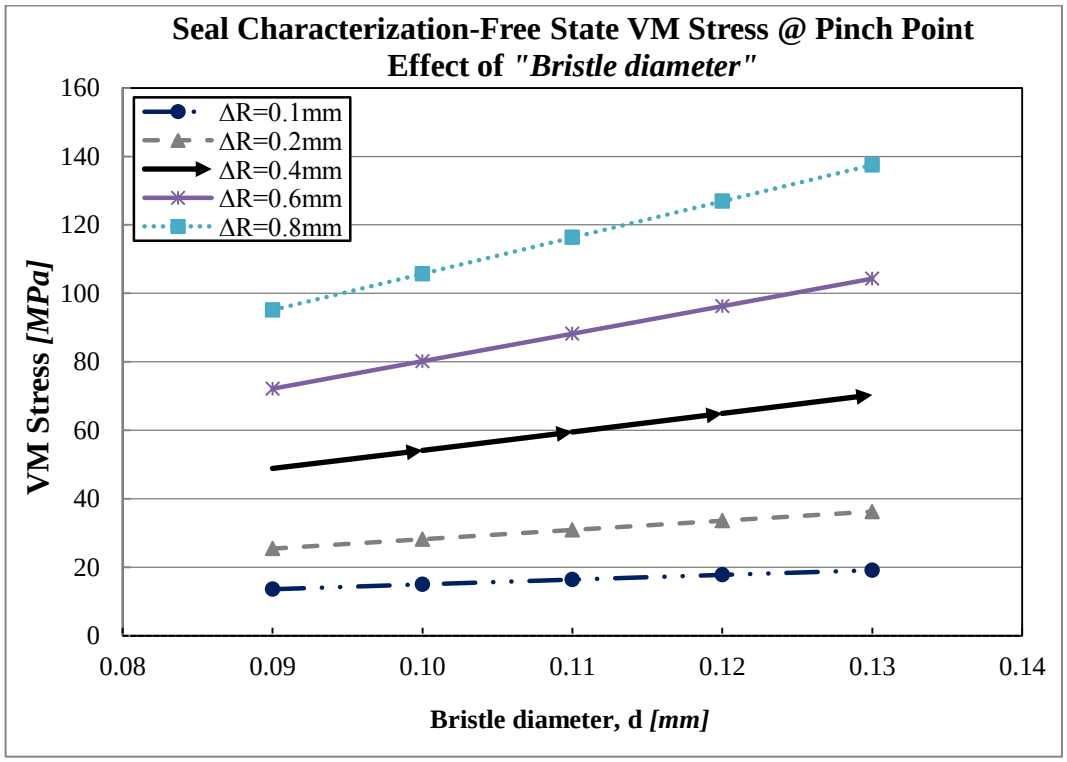

Figure 7.6: Change of pinch point VM stress levels with bristle diameter, unpressurized-nonrotating rotor interference conditions

Contact force per rotor unit circumferential length. Change of free-state RF_{circ} *(contact force per rotor unit circumferential length)* with bristle diameter is also detailed in Figure 7.5 at different rotor incursion levels. RF_{circ} also increases with bristle diameter, but increase is more pronounced than BTF since the NR – number of bristle rows in rotor axial direction – also contributes the total contact force.

Bristle stress. As detailed in the previous chapters, pinch point is critical for unpressurized rotor rub conditions since the BTF induces the maximum VM stress at that cross-section. Therefore, free-state characterization studies mainly focus on stress magnitudes at that critical bristle section. Pinch point VM stress change with *"d"* at different interference levels of unpressurized seal is given in Figure 7.6. Although bristle cross-section inertia increases with bristle diameter, the maximum VM stress magnitude at free-state conditions takes larger values with increasing bristle diameter. Considering that the VM stress at free-state rotor interference is almost equal to bending stress levels induced by BTF, and bearing in mind that increasing cross-section inertia requires higher BTF values to deform bristles to specified level of radial interference, the VM stress increase with ΔR is an expected seal behavior and consistent with analytical calculations of unpressurized conditions. The bending stress induced by rotor incursion is a function of BTF induced bending, second moment of area, *"I"*, and bristle diameter, where both BTF and second moment of area are 4^{th} order functions of bristle diameter and their change with *"d"* are cancelling each other at free-sate VM stress calculations.

$$\sigma_{free-state} = \frac{M_{BTF}(d^4)}{I(d^4)} \cdot (d/2) \tag{7.3}$$

7.3.2 Effect of Bristle Diameter at Steady State Conditions

Effect of bristle diameter on bristle stress levels at steady state conditions *(pressure load without rotor interference)* has been examined by running the cases detailed in Table 7.4.

Effect of Bristle Diameter at Steady State Conditions, ΔP=0.3MPa, ΔR=0					
	Case 1	Case 2	Case 3	Case 4	Case 5
Bristle diameter, *d [mm]*	0.09	0.10	0.11	0.13	0.14
Axial spacing, S_A *[mm]*	0.100	0.111	0.121	0.143	0.154
Tangential spacing, S_T *[mm]*	0.137	0.152	0.167	0.196	0.211
Number of bristle rows, NR	11	12	13	16	17
PS: Nominal values given in Table 7.2 has been used for remaining parameters.					

Table 7.4: Effect of bristle diameter – Cases for steady state conditions, ΔP=0.3MPa and ΔR=0

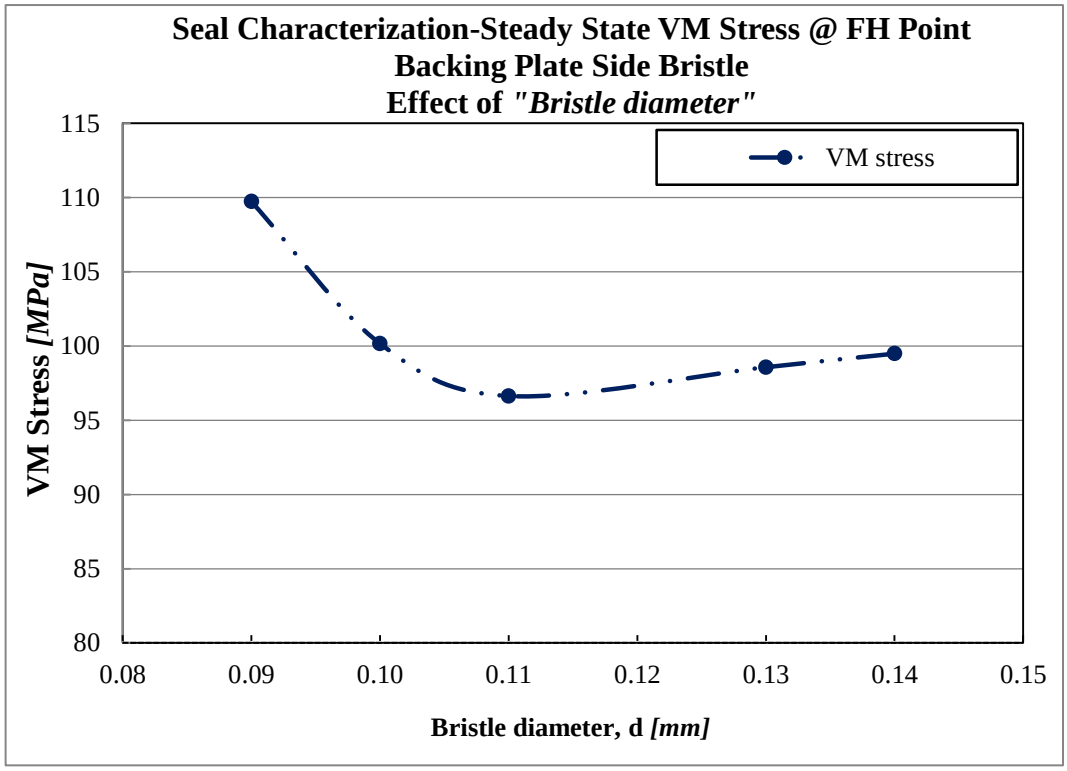

Figure 7.7: Change of backing plate side FH point-VM stress levels with bristle diameter, steady state conditions at ΔP=0.3MPa

Bristle stress. As detailed in the previous chapters, FH point is critical for steady state conditions since pressure load causes localized bristle contact at backing plate corner radius. Therefore, steady state characterization studies mainly focus on stress magnitudes at that critical section. VM stress levels at FH point of backing plate side bristles and their change with bristle diameter is detailed in Figure 7.7 for steady state conditions at ΔP=0.3MPa. Up to bristle diameter value of 0.11mm, the maximum VM stress decreases as expected since the cross-sectional inertia increases. However, steady state VM stress levels do not decrease continuously with increasing *"d"*, and stabilize at certain level of bristle diameter. The saturation point depends on seal parameters, and for the selected nominal values, this saturation point for steady state stress level is d=0.11mm. Steady state VM stress stabilization with bristle diameter is well known

phenomenon in the industry, but the root-cause does not exist in the literature due to the lack of CAE-based characterization in the literature. The reason for steady state VM stress stabilization with bristle diameter is the complex contact-frictional inter-bristle and bristle-backing plate interactions, which does not lend itself to full analytical formulation. Recall that when the pressure load is applied, the overhung portion of the downstream side bristles bend under the backing plate in the flow direction, while the portion above FH region deforms in the reverse direction. This deformation profile is mainly the reason for localized contact and high stress peaks at backing plate corner radius *(FH point)*. Therefore, it can be stated that stress magnitudes under differential pressure not only a function of bristle diameter, but also it is function of difference between aft bending of overhung portion and forward bending of bristle above FH region. Difference between aft bending and forward bending depends on initial layout and inter-bristle/bristle-backing plate interactions, and its identification requires advanced CAE analyses. Backing plate bristles' deformation profiles for Case1, 2 and 5 are detailed in Figure 7.8. Case 1 analyses, where the bristle diameter equals to 0.09mm, have maximum downstream side bristle displacement magnitude value of 0.038mm, and the difference between aft and forward bending is around 0.042mm. Case 2 simulation with 0.10mm bristle diameter gives 0.036mm displacement magnitude while the difference in aft and forward bending is around 0.039mm. Together with increase in bristle diameter, decrease in aft bending-forward bending difference in Case 2 simulations yields decrease in steady state VM stress levels. However, for Case 5 analyses, where the bristle diameter is increased to 0.14mm, the aft-forward bending difference increases up to 0.07mm and cause more localized backing plate contact, and therefore decrease in FH-point VM stress cannot be observed.

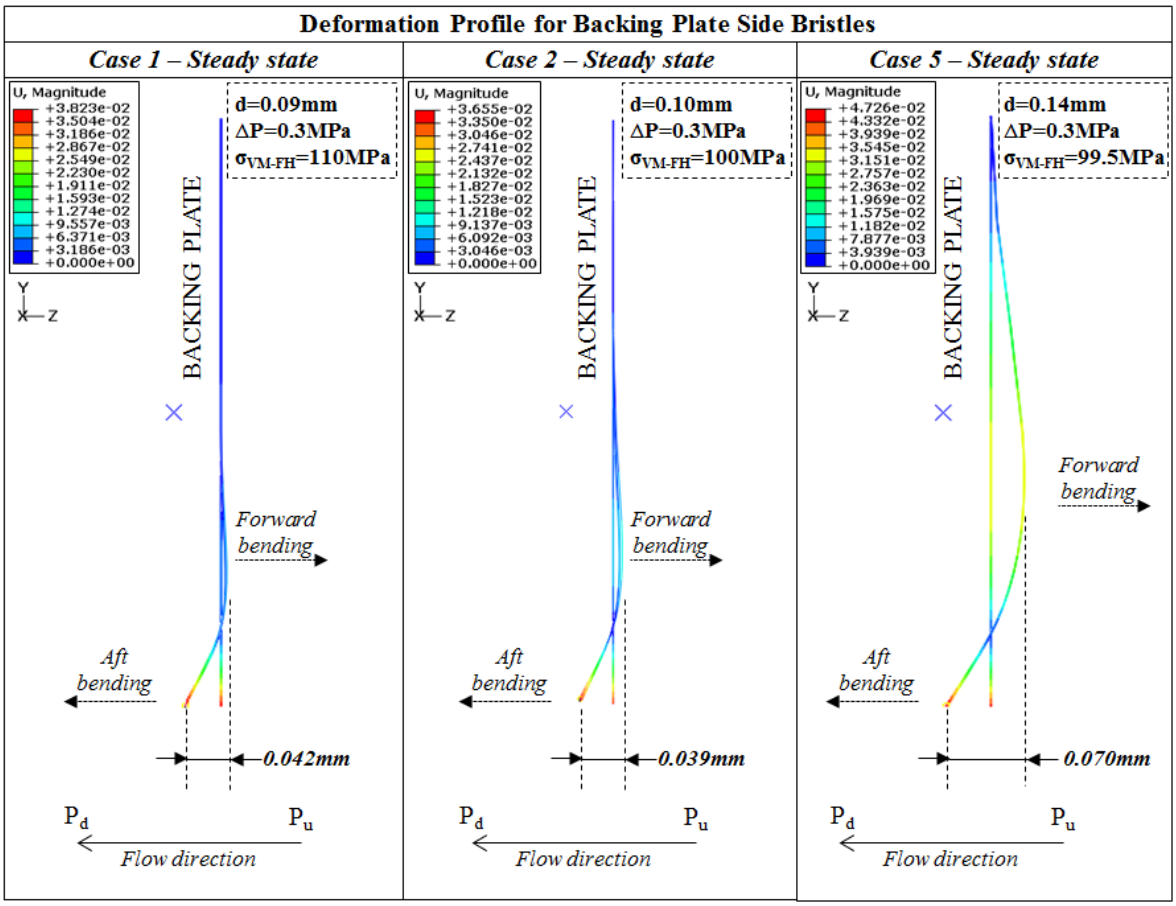

Figure 7.8: Change of backing plate side FH point-VM stress levels with bristle diameter, steady state conditions at ΔP=0.3MPa

7.3.3 Effect of Bristle Diameter at Pressurized-Nonrotating Rotor Interference Conditions

Effect of bristle diameter on BTF and bristle stress levels at pressurized-nonrotating rotor rub conditions *(combined loading)* has been examined by running the cases detailed in Table 7.5.

Effect of Bristle Diameter at Combined Loading Conditions, ΔP=0.3MPa, ΔR_{max}=0.35mm					
	Case 1	Case 2	Case 3	Case 4	Case 5
Bristle diameter, *d [mm]*	0.09	0.10	0.11	0.13	0.14
Axial spacing, S_A *[mm]*	0.100	0.111	0.121	0.143	0.154
Tangential spacing, S_T *[mm]*	0.137	0.152	0.167	0.196	0.211
Number of bristle rows, NR	11	12	13	16	17
Maximum rotor interference, ΔR_{max} *[mm]*	0.35	0.35	0.35	0.35	0.35
Effective circumferential length, $l_{t\text{-}CAE}$ *[mm]*	0.364	0.404	0.444	0.523	0.563
PS: Nominal values given in Table 7.2 has been used for remaining parameters.					

Table 7.5: Effect of bristle diameter–Cases for combined loading conditions, ΔP=0.3MPa

Bristle tip force. Combined loading BTF change with bristle diameter is detailed in Figure 7.9 for ΔP=0.3MPa and ΔR_{max}=0.35mm. Increase in bristle diameter does not alter pressurized-BTF at interference levels of 0.1mm. However, for higher rotor incursion levels, the inter-bristle interactions and pressure stiffening effect becomes more pronounced with larger values of *"d"*, and BTF magnitudes increase with bristle diameter. It should be noted that the increase in BTF is more severe for bristle diameter levels above 0.11mm. This observation is consistent with typical industrial applications, where seals with large bristle diameters cause excessive wear of rotor due to complicated inter-bristle interactions and bristle-locking phenomenon.

Contact force per rotor unit circumferential length. RF_{circ} at pressurized rotor interference conditions and its change with bristle diameter is given in Figure 7.10. As in the case of combined loading-BTF results, effect of bristle diameter on RF_{circ} is much more pronounced at high rotor interference levels.

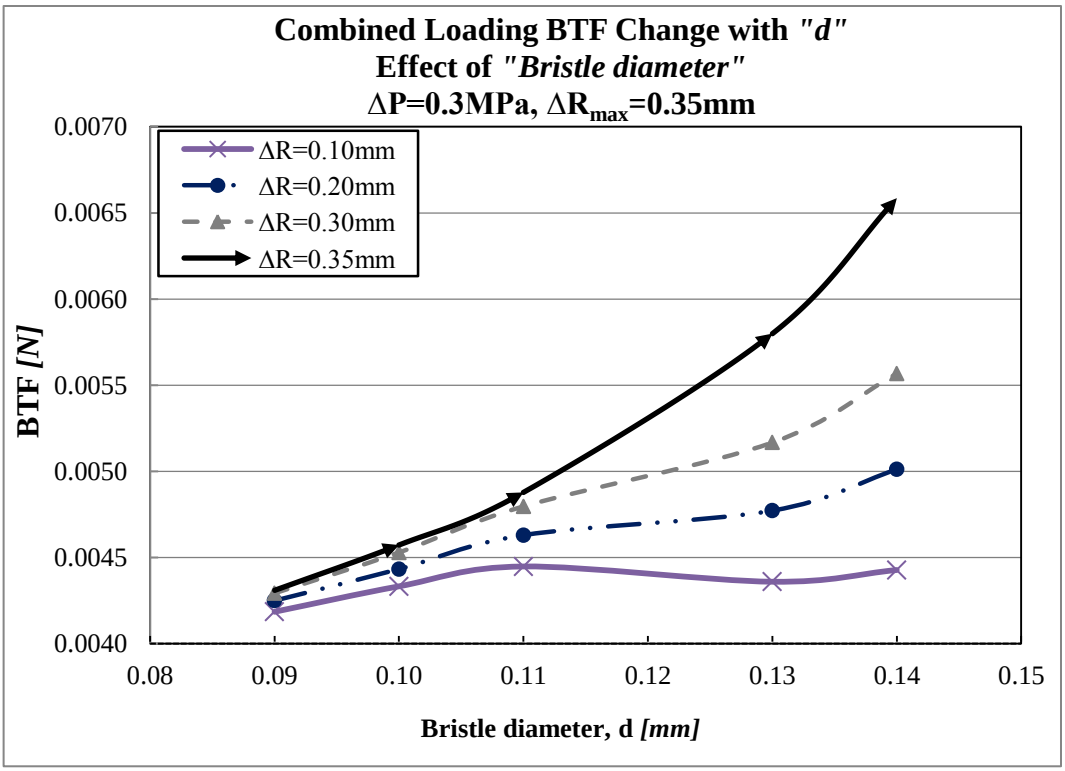

Figure 7.9: Change of BTF with bristle diameter, Pressurized-nonrotating rotor interference-loading step, ΔP=0.3MPa, ΔR_{max}=0.35mm

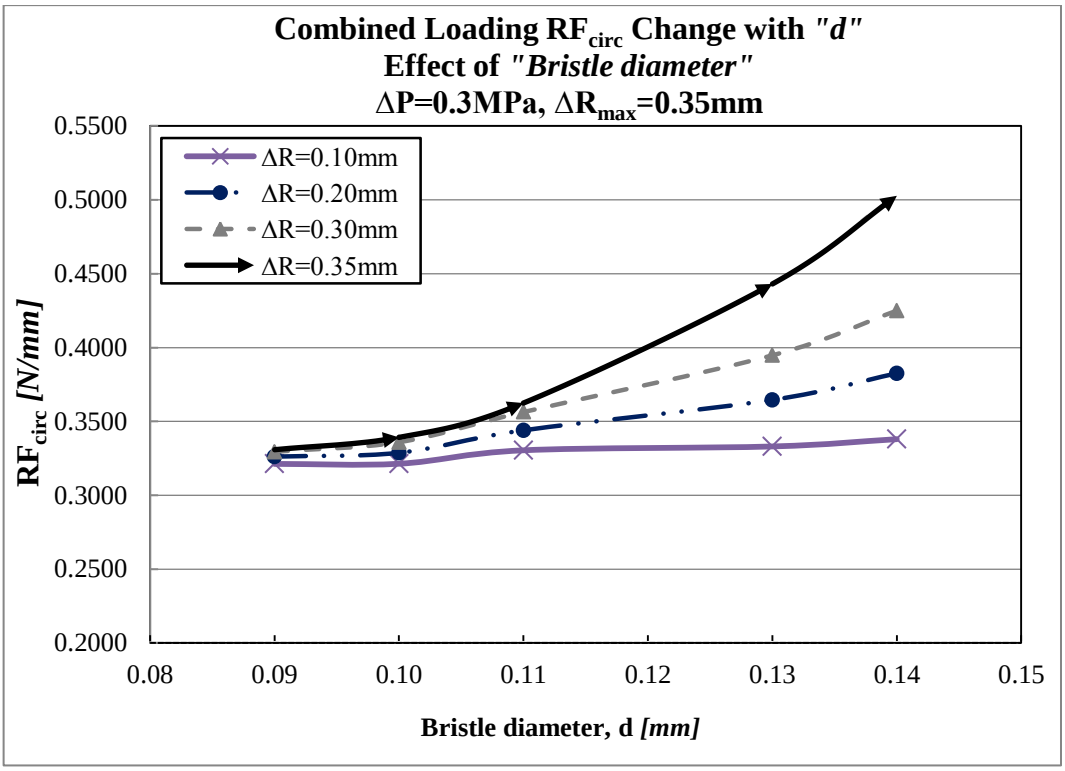

Figure 7.10: Change of RF_{circ} *(contact force per rotor unit circumferential length)* with bristle diameter, Pressurized-nonrotating rotor interference-loading step, ΔP=0.3MPa, ΔR_{max}=0.35mm

Bristle stress. As detailed in the previous chapters, FH point is critical for pressurized rotor-rub conditions since pressure load causes localized bristle contact at backing plate corner radius. Therefore, seal characterization studies at combined loading conditions mainly focus on stress magnitudes at that critical section. VM stress levels at FH point of backing plate side bristles and their change with bristle diameter is detailed in Figure 7.11 for combined loading of ΔP=0.3MPa and ΔR_{max}=0.35mm. As in the case of steady state simulations, VM stress magnitudes at combined loading conditions do not decrease continuously with increasing *"d"*, and stabilize at certain level of bristle diameter. Although each interference levels show different combined loading VM stress characteristics due to modified contact conditions, it can be stated that bristle diameter values larger than 0.11mm do not cause significant decrease in VM stress levels for pressurized rotor interference conditions of selected nominal seal parameters. Combined loading case-VM stress stabilization with bristle diameter is well known phenomenon in the industry, while the main root-cause is the complex contact-frictional inter-bristle and bristle-backing plate interactions as detailed previously.

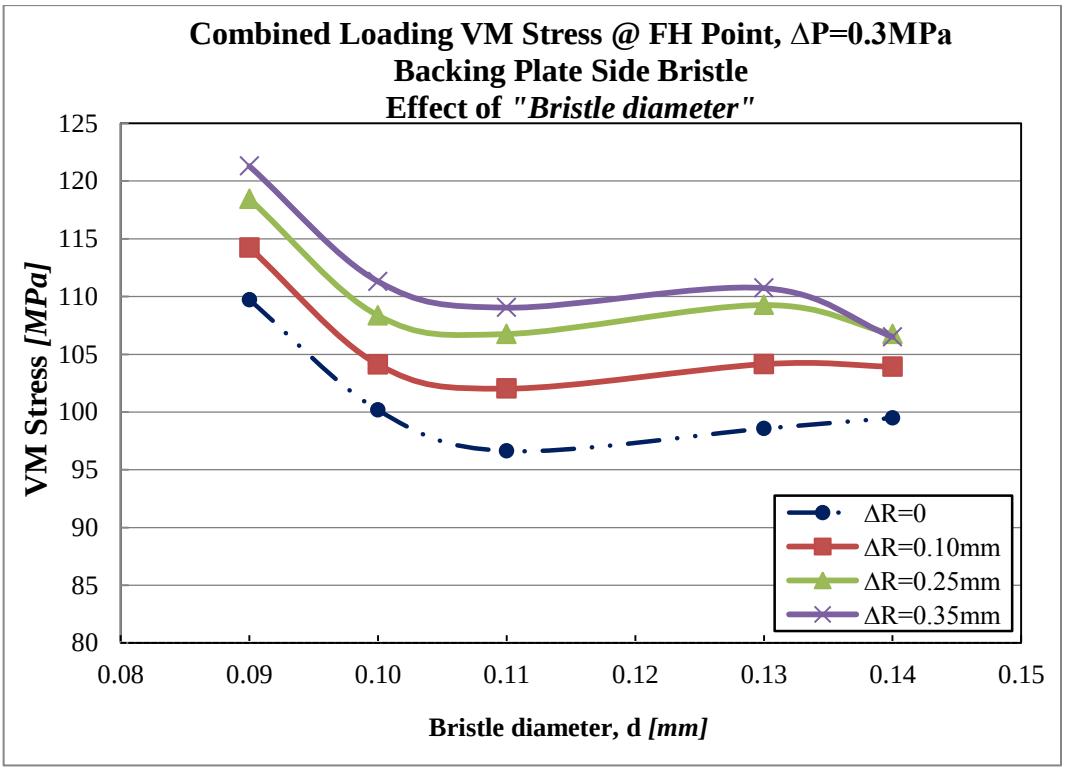

Figure 7.11: Change of backing plate side FH point-VM stress levels with bristle diameter, Pressurized-nonrotating rotor interference-loading step, ΔP=0.3MPa, ΔR_{max}=0.35mm

7.4 Effect of Free Bristle Height

Free bristle height, *"BH"*, is the radial distance between pinch point and bristle tip, and it affects both BTF and bristle stress levels at pressurized/unpressurized rotor interference conditions as well as at steady state. Selecting free bristle height is relevant to bristle diameter since obtaining appropriate L/d ratios is important in determining seal stiffness and wear at operating conditions. Although selecting appropriate L/d ratios is the common methodology used in the industry, which is based on experience on free-state stiffness calculations, CAE based characterization is required due to the fact that inter-bristle and bristle-backing plate interactions are very effective in determining stress levels and BTF magnitudes for a pressurized seal. Brief survey reveals the lack of such characterization, and it is believed that CAE analyses of this study will be very useful for seal literature. Several cases have been run to examine the effect of BH on seal stiffness and stress levels, and results are detailed in the following sections.

7.4.1 Effect of Free Bristle Height at Unpressurized-Nonrotating Rotor Interference Conditions

Effect of free bristle height on seal response at unpressurized-nonrotating rotor interference conditions *(free-state rotor rub)* has been examined by running the cases detailed in Table 7.6.

Effect of Free Bristle Height						
	Case 1	Case 2	Case 3	Case 4	Case 5	Case 6
Free bristle height, *BH [mm]*	10	11	12	13	14	15
PS: Nominal values given in Table 7.2 has been used for remaining parameters.						

Table 7.6: Effect of free bristle height – Cases for unpressurized nonrotating rotor interference conditions

Bristle tip force. Free-state BTF change with free bristle height is given in Figure 7.12 at different rotor incursion levels. Higher BH values results in longer bristles with high L/d ratios, and causes BTF magnitudes to decrease. Free-state BTF change with BH is nonlinear, which is consistent with the BTF formula provided in Equation 5.4. Decrease in free-state BTF with bristle free height is more pronounced at large interference levels. In Figure 7.13, BTF change with ΔR is detailed at different BH values. Reduction in BTF levels also results in free-state hysteresis to decrease with free bristle height since rotor-bristle friction becomes less effective.

Bristle stress. As detailed in the previous chapters, pinch point is critical for unpressurized rotor rub conditions since the BTF induces the maximum VM stress at that cross-section. Therefore, free-state characterization studies mainly focus on stress magnitudes at that critical bristle section. Pinch point VM stress change with BH at different interference levels of unpressurized seal is given in Figure 7.14. As it can be seen from the figure, although the length of *"moment-arm"* increases with BH, VM stress magnitudes decreases since BTF has inverse proportion with *"L^3"*.

$$\sigma_{free-state} = \frac{BTF(L^{-3}) \cdot L \cdot \sin(\theta)}{I} \cdot (d/2) \tag{7.4}$$

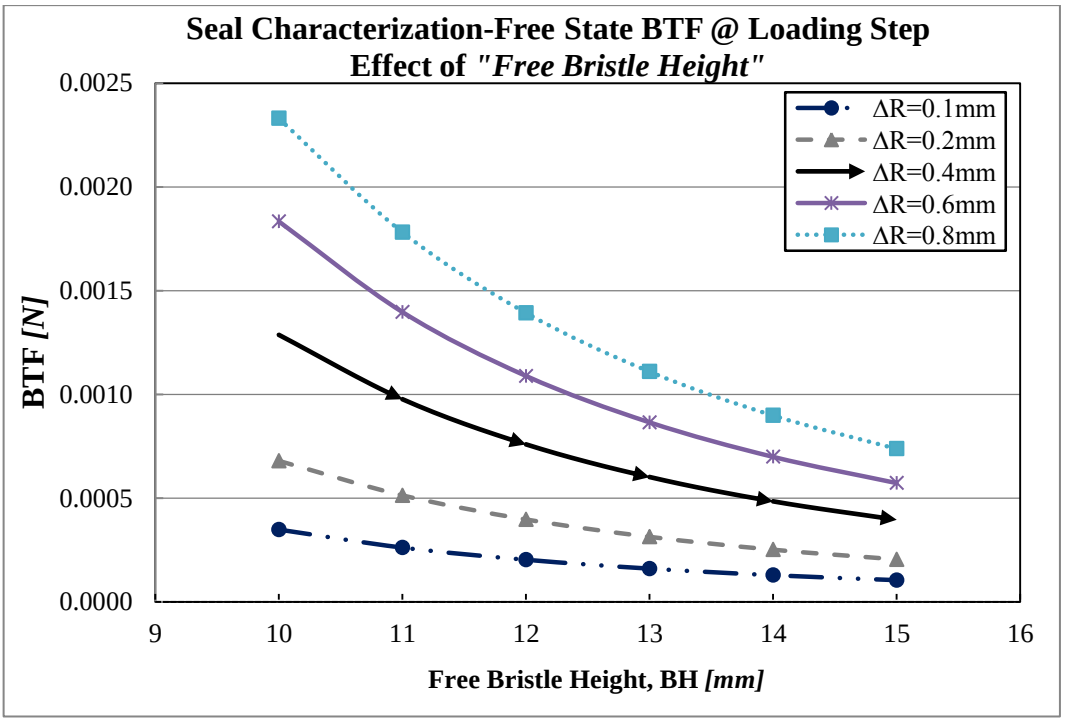

Figure 7.12: Change of BTF with free bristle height, Unpressurized-nonrotating rotor interference-loading step

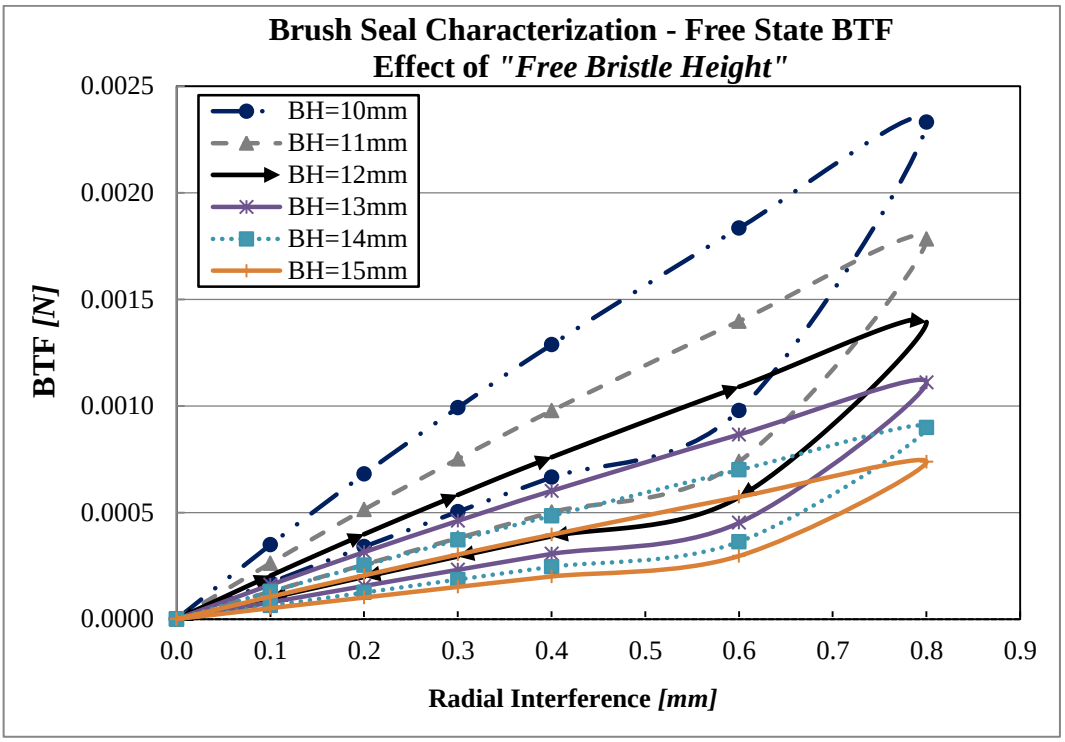

Figure 7.13: Effect of free bristle height on BTF values at unpressurized-nonrotating rotor interference conditions

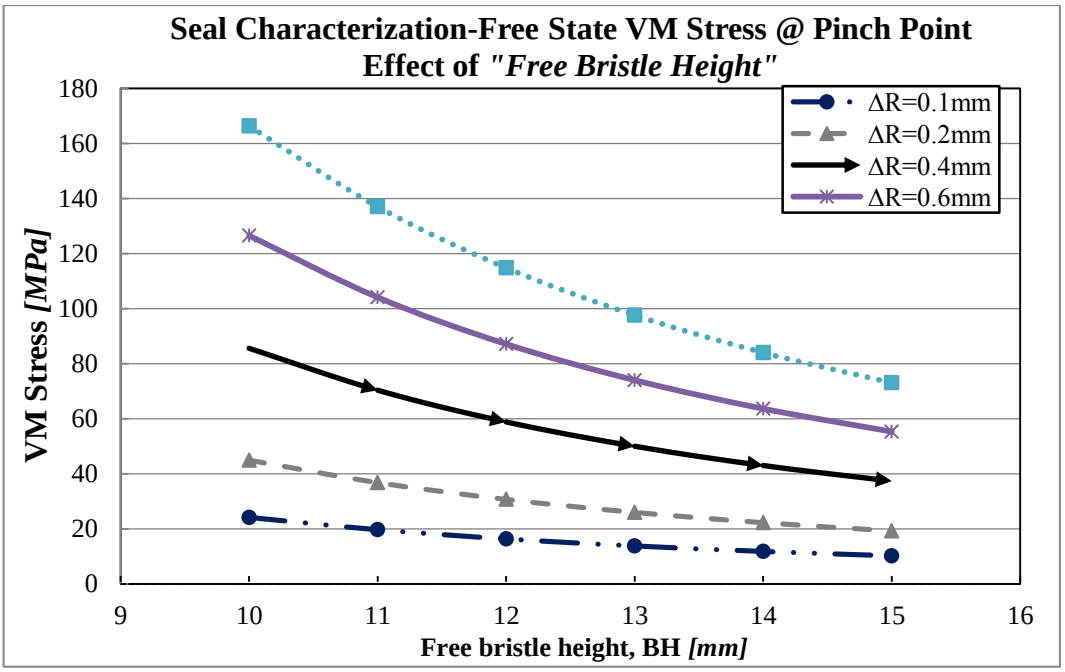

Figure 7.14: Change of pinch point VM stress levels with free bristle height, unpressurized-nonrotating rotor interference conditions

7.4.2 Effect of Free Bristle Height at Steady State Conditions

Effect of BH on bristle stress levels at steady state conditions *(pressure load without rotor interference)* has been examined by running the cases that have already been detailed in Table 7.4.

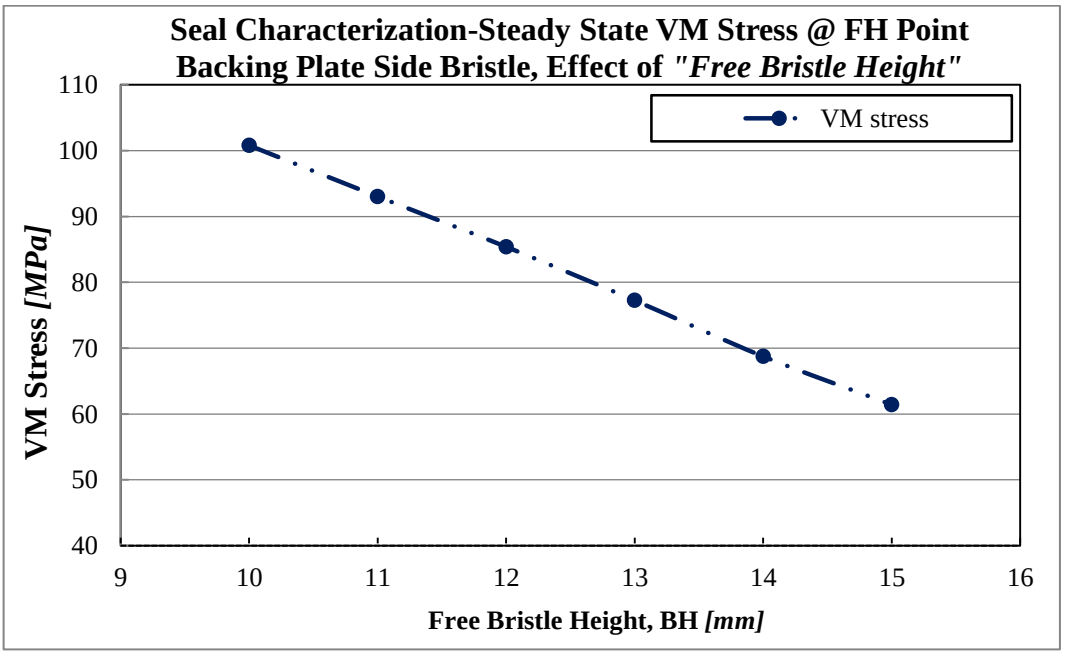

Figure 7.15: Change of backing plate side FH point-VM stress levels with free bristle height, steady state conditions at ΔP=0.3MPa

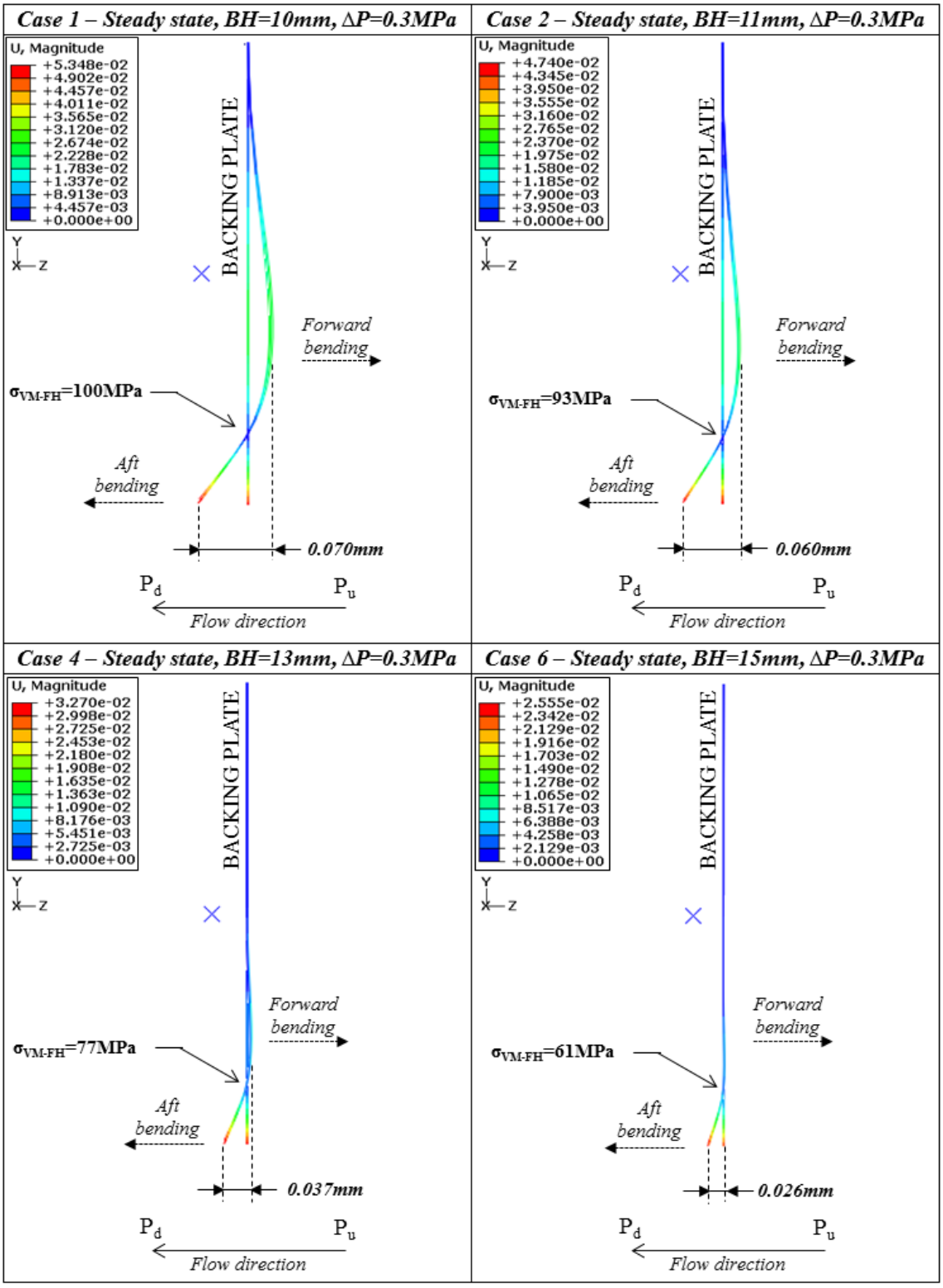

Figure 7.16: Backing plate side bristle deformation profiles at different BH cases, steady state conditions at ΔP=0.3MPa

Bristle stress. As detailed in the previous chapters, FH point is critical for steady state conditions since pressure load causes localized bristle contact at backing plate corner radius. Therefore, steady state characterization studies mainly focus on stress magnitudes at that critical section. VM stress levels at FH point of backing plate side bristles and their change with bristle free height is detailed in Figure 7.15 for steady state conditions at ΔP=0.3MPa. As it can be seen from the figure, VM stress level decreases as BH takes larger values, which can be better explained by examining the downstream side deformation profile *(Figure 7.16)*. As detailed in the previous chapters with advanced CAE analyses, FH point stress peaks under pressure load are mainly due to localized contact induced by different bending characteristics of overhung portion *(aft bending)* and bristle portion above FH *(forward bending)*. Keeping the FH same, the bristle length above the FH regions become longer with BH, and forward bending as well as the aft bending decreases, which in turn cause less severe localization of contact. As a result of this, difference between aft and forward bending decreases for larger BH values, which in turn result in reduction in contact localization and therefore VM stress levels under pressure load.

7.4.3 Effect of Free Bristle Height at Pressurized-Nonrotating Rotor Interference Conditions

Effect of bristle free height on BTF and bristle stress levels at pressurized-nonrotating rotor rub conditions *(combined loading)* has been examined by running the BH cases detailed in Table 7.6.

Bristle tip force. Combined loading BTF change with free bristle height is given in Figure 7.17 for ΔP=0.3MPa and ΔR_{max}=0.35mm. As it can be seen from the figure, BTF values for pressurized seal increases with free bristle height. Recall that the BTF response of pressurized seal is the combination of free-state BTF and resistance coming from inter-bristle and bristle-backing plate contacts with friction. The effect of BH on components of combined loading BTF is different: The free-state BTF decreases with BH, while pressure stiffening due to inter-bristle and bristle-backing plate interactions increases as BH gets larger values, which is due to extended loaded length at backing plate region. Considering the pressure stiffening effect is dominant at combined loading conditions, it is expected to obtain higher BTF values for pressurized seal when larger

BH values are used. The increase in BTF-combined loading conditions is more pronounced at low interference levels, where the contribution of free-state tip force to total BTF response is minimal.

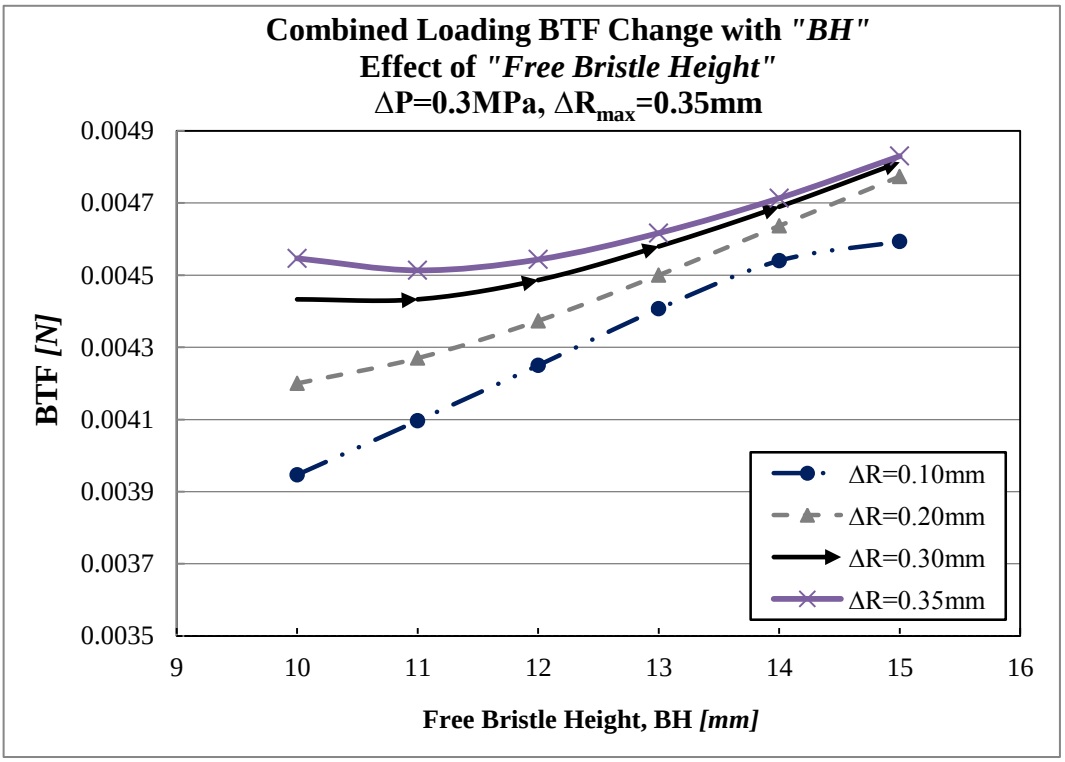

Figure 7.17: Change of BTF with free bristle height, Pressurized-nonrotating rotor interference-loading step, ΔP=0.3MPa, ΔR_{max}=0.35mm

Bristle stress. As detailed in the previous chapters, FH point is critical for pressurized rotor rub conditions since pressure load causes localized bristle contact at backing plate corner radius. Therefore, seal characterization studies at combined loading conditions mainly focus on stress magnitudes at that critical section. VM stress levels at FH point of backing plate side bristles and their change with free bristle height is detailed in Figure 7.18 for combined loading of ΔP=0.3MPa and ΔR_{max}=0.35mm. As in the case of steady state simulations, VM stress magnitudes at combined loading conditions decreases with increasing *"BH"*, which is due to decrease in aft bending-front bending difference and resulting more uniform *(less localized)* contact at backing plate corner. Although each interference levels show different combined loading VM stress characteristics due to modified contact conditions, it can be stated that FH point VM stress magnitudes decrease as BH takes larger values.

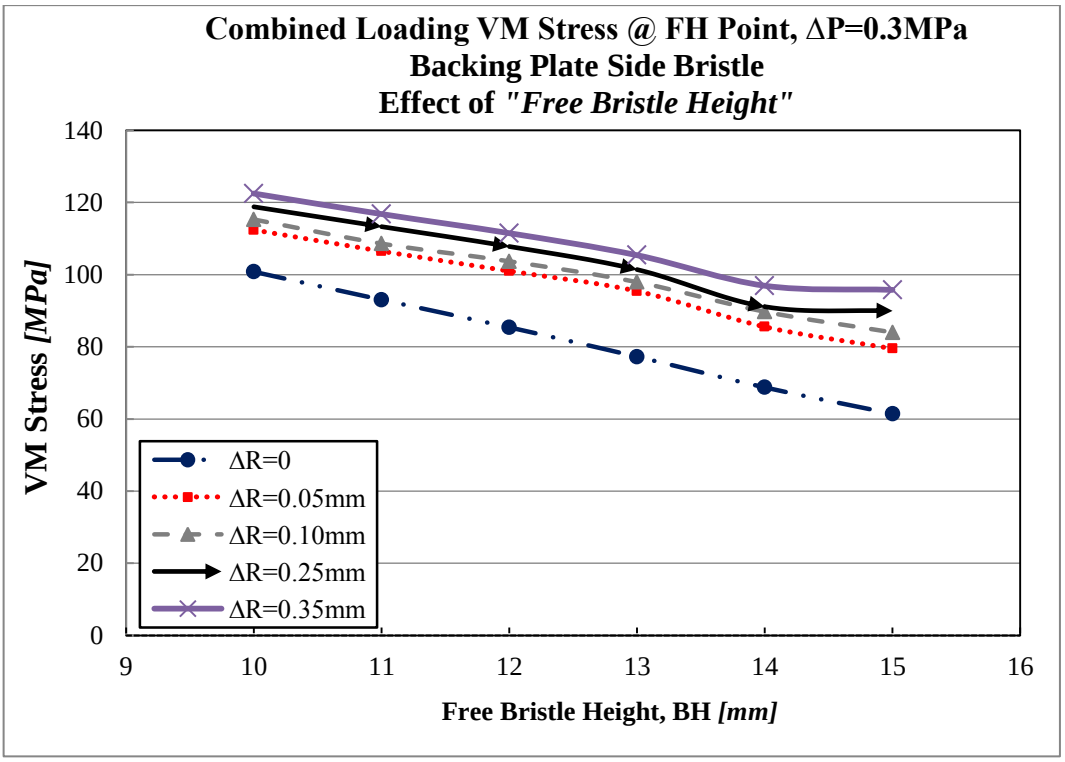

Figure 7.18: Change of backing plate side FH point-VM stress levels with free bristle height, Pressurized-nonrotating rotor interference-loading step, ΔP=0.3MPa, ΔR_{max}=0.35mm

7.5 Effect of Fence Height

Fence height, *"FH"*, is defined as the radial distance between backing plate inner radius and bristle tip, where full pressure load of ΔP is applied to overhung portion of bristles at that region. In terms of leakage, FH is critical since main leakage flow takes place at that region. Ideally, designing shorter FH means less leakage and high sealing performance, but risk of rotor contact to backing plate at excessive rotor rub conditions will yield serious failure states like rotor instability, seal failure and turbine functionality loss. Therefore, FH design must be higher than the maximum rotor interference that can be come up during turbine life. Considering that the aft bending-forward bending transition of backing plate side bristles takes place at FH, this parameter has crucial importance in determining stiffness levels and stress magnitudes at steady state and combined loading conditions. In this chapter, effect of FH on BTF and stress levels of seal pack has been detailed for steady state and combined loading conditions.

7.5.1 Effect of Fence Height at Steady State Conditions

Effect of *"FH"* on bristle stress levels at steady state conditions *(pressure load without rotor interference)* has been examined by running the cases detailed in Table 7.7.

Effect of Fence Height					
	Case 1	Case 2	Case 3	Case 4	Case 5
Fence height, *FH [mm]*	1.15	1.2	1.3	1.4	1.5
PS: Nominal values given in Table 7.2 has been used for remaining parameters.					

Table 7.7: Effect of fence height – Cases for unpressurized nonrotating rotor interference conditions

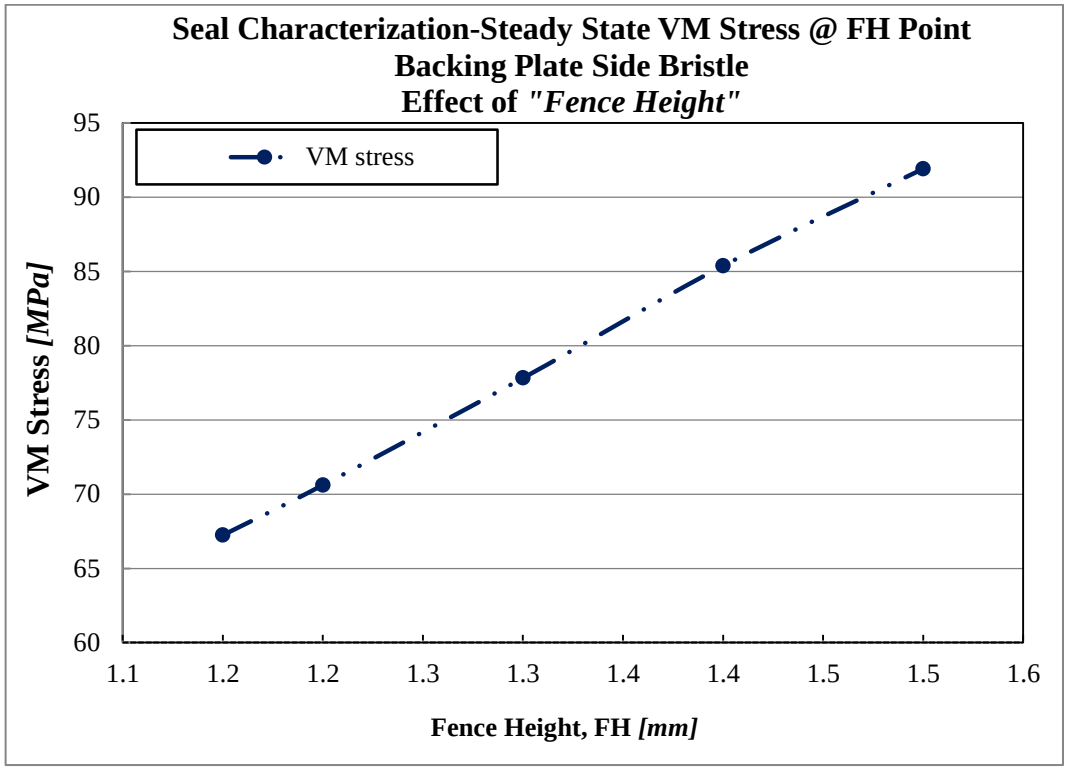

Figure 7.19: Change of backing plate side FH point-VM stress levels with fence height, steady state conditions at ΔP=0.3MPa

Bristle stress. FH point stress levels of downstream side bristles are examined, which has already been identified as critical section for loaded seal due to pressure induced localized contact at backing plate corner. VM stress levels at FH point of backing plate side bristles and their change with fence height is detailed in Figure 7.19 at steady state conditions *(ΔP=0.3MPa).* Larger FH dimensions result in extended region of fully loaded bristle portion and increased aft bending magnitudes, which in turn yields higher

VM stress levels under pressure load. As it can be seen from the figure, VM stress levels increase with FH.

7.5.2 Effect of Fence Height at Pressurized-Nonrotating Rotor Interference Conditions

Effect of fence height on BTF and bristle stress levels at pressurized-nonrotating rotor rub conditions *(combined loading)* has been examined by running the FH cases given in Table 7.7.

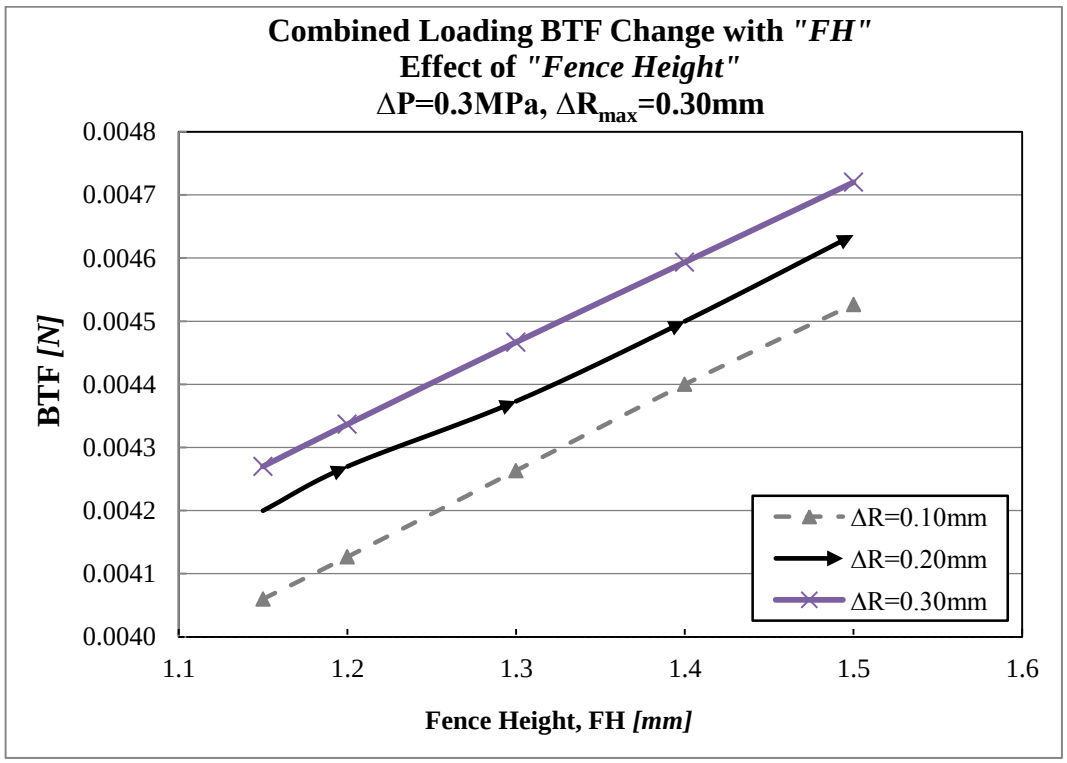

Figure 7.20: Change of BTF with fence height, Pressurized-nonrotating rotor interference-loading step, ΔP=0.3MPa, ΔR_{max}=0.30mm

Bristle tip force. Combined loading BTF change with fence height is given in Figure 7.20 for ΔP=0.3MPa and ΔR_{max}=0.30mm. As it can be seen from the figure, BTF values for pressurized seal increases with fence height, which is a direct result of extended region for full pressure load and increased aft bending of overhung portion of bristles.

Bristle stress. Downstream side bristles' cross-section at FH point is examined since this section is critical at combined loading conditions. VM stress levels at section and their change with fence height is detailed in Figure 7.21 for combined loading of

ΔP=0.3MPa and ΔR_{max}=0.30mm. Extended fully loaded region and increased aft bending in flow direction for larger FH values also result in higher VM stress magnitudes. VM stress levels at combined loading conditions increase with extended FH.

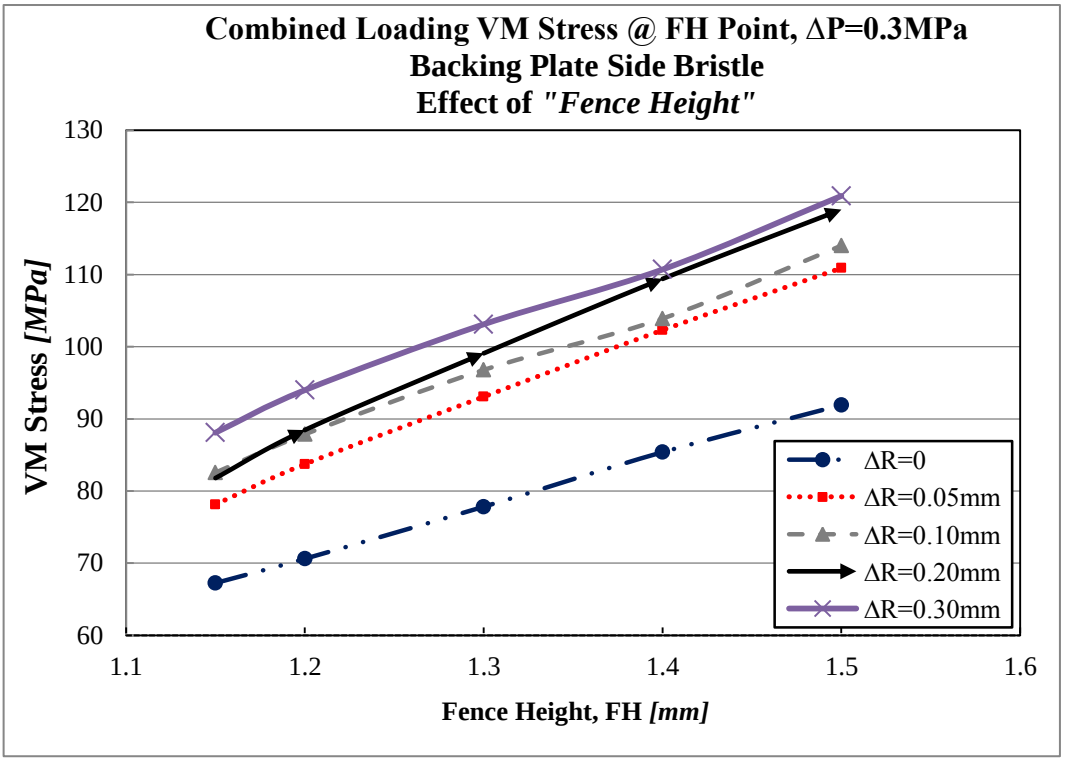

Figure 7.21: Change of backing plate side FH point-VM stress levels with fence height, Pressurized-nonrotating rotor interference-loading step, ΔP=0.3MPa, ΔR_{max}=0.30mm

7.6 Effect of Cant Angle

Cant angle, *"θ"*, is defined as the angle between bristle axis and normal of seal inner circle. As a result of angular contact with rotor, radial interference bends bristles rather than buckles them, which in turn enables seal to survive at long operating periods without bristle loss and performance degradations. However, excessive cant angle values result in increased free bristle length and extended frictional contact surfaces under pressure load. In this section, effect of cant angle on pressurized/unpressurized conditions has been carefully analyzed by using correlated CAE-models and detailed in the following sections. Since tangential spacing also depends on cant angle, number of bristle rows changes with cant angle. Therefore, contact force per rotor unit circumferential length, *"RF_{circ}"*, will also be examined in addition to BTF.

7.6.1 Effect of Cant Angle at Unpressurized-Nonrotating Rotor Interference Conditions

Effect of cant angle on seal response at unpressurized-nonrotating rotor interference conditions *(free-state rotor rub)* has been examined by running the cases detailed in Table 7.8.

Effect of Cant Angle				
	Case 1	Case 2	Case 3	Case 4
Cant angle, θ [degree]	35	40	45	50
Tangential spacing, S_T [mm]	0.131	0.140	0.152	0.167
Number of bristle rows, NR	11	11	12	13
Effective circumferential length, $l_{t\text{-}CAE}$ [mm]	0.362	0.381	0.404	0.435
PS: Nominal values given in Table 7.2 has been used for remaining parameters.				

Table 7.8: Effect of cant angle – Cases for unpressurized nonrotating rotor interference conditions

Bristle tip force. Free-state BTF change with cant angle is given in Figure 7.22 at different rotor interference levels. Free-state BTF decreases with increasing cant angle, and the effect of cant angle on BTF is more pronounced at small *"θ"* values. This inspection is consistent analytical methodologies developed in this study, where tip force is inversely proportions with sine and cosine of cant angle *(Chapter 5, Table 5.3)*. In Figure 7.23, free-state BTF change with rotor interference is detailed for different cant angle values. As it can be seen from the figure, reduction in free-state hysteresis is also observed with decreasing BTF magnitudes at larger cant angles.

Contact force per rotor unit circumferential length. Change of free-state RF_{circ} *(contact force per rotor unit circumferential length)* with cant angle is detailed in Figure 7.24 at different rotor interference levels. Although number of bristles rows increases with cant angle, contribution of BTF on contact force per rotor circumferential length is more dominant and free state-RF_{circ} change with cant angle show similar trend with free-state BTF.

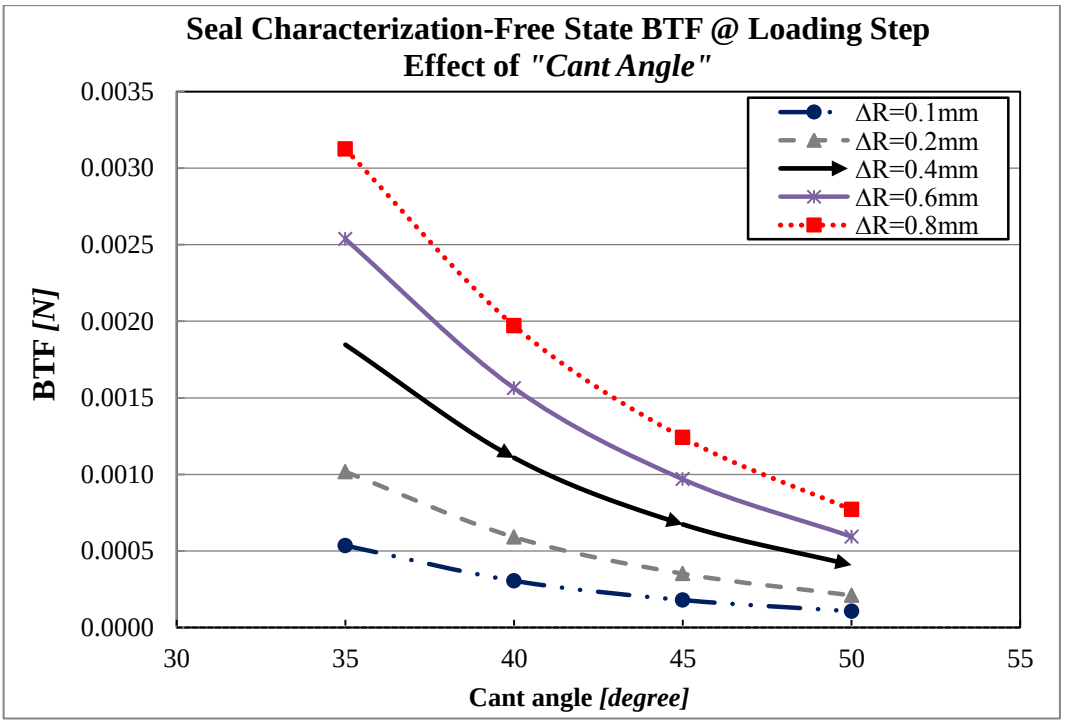

Figure 7.22: Change of BTF with cant angle, Unpressurized-nonrotating rotor interference-loading step

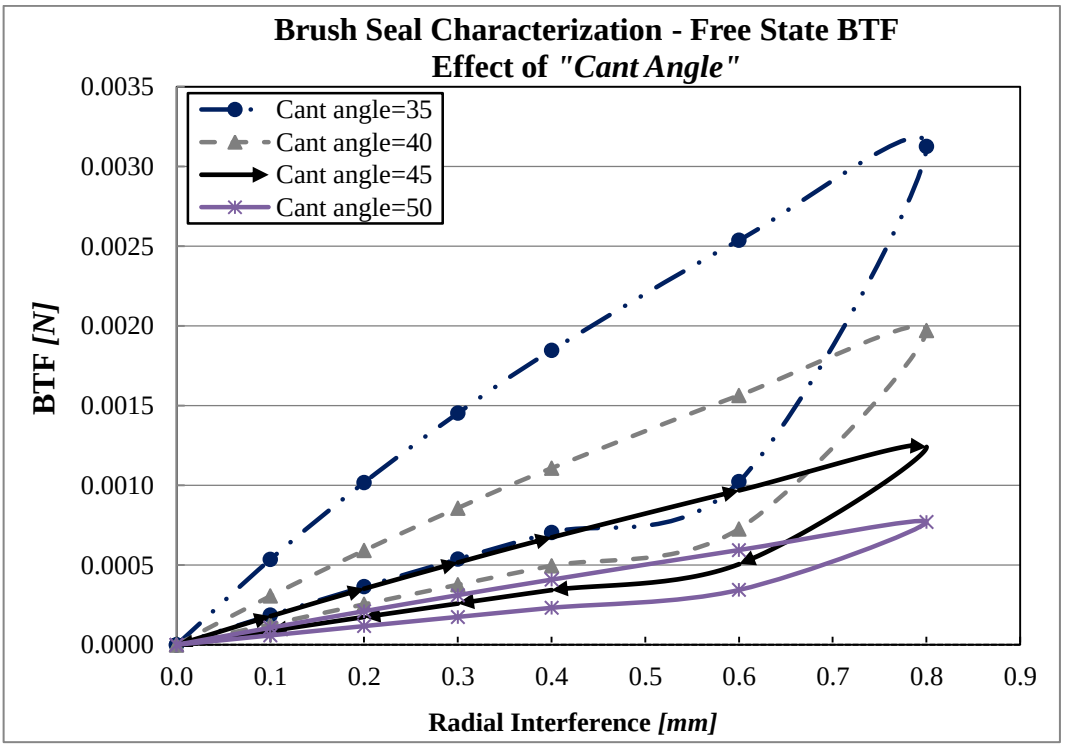

Figure 7.23: Effect of cant angle on BTF values at unpressurized-nonrotating rotor interference conditions

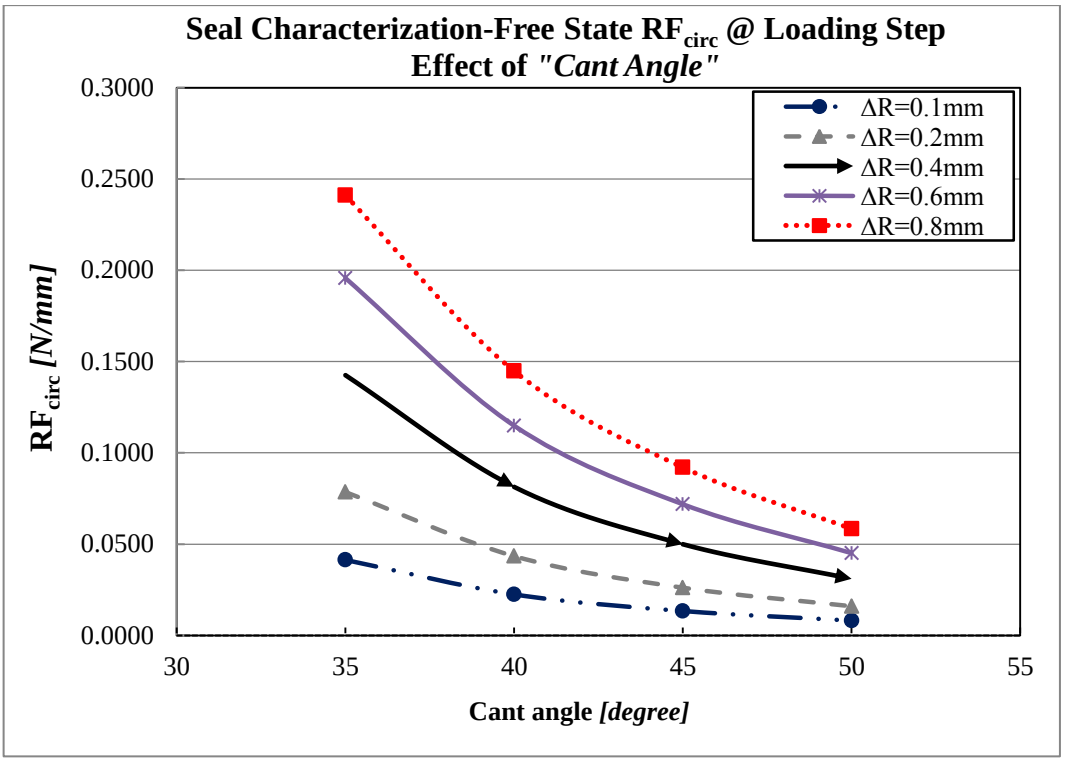

Figure 7.24: Change of RF$_{circ}$ *(Contact force per rotor unit circumferential length)* with cant angle, Unpressurized-nonrotating rotor interference-loading step

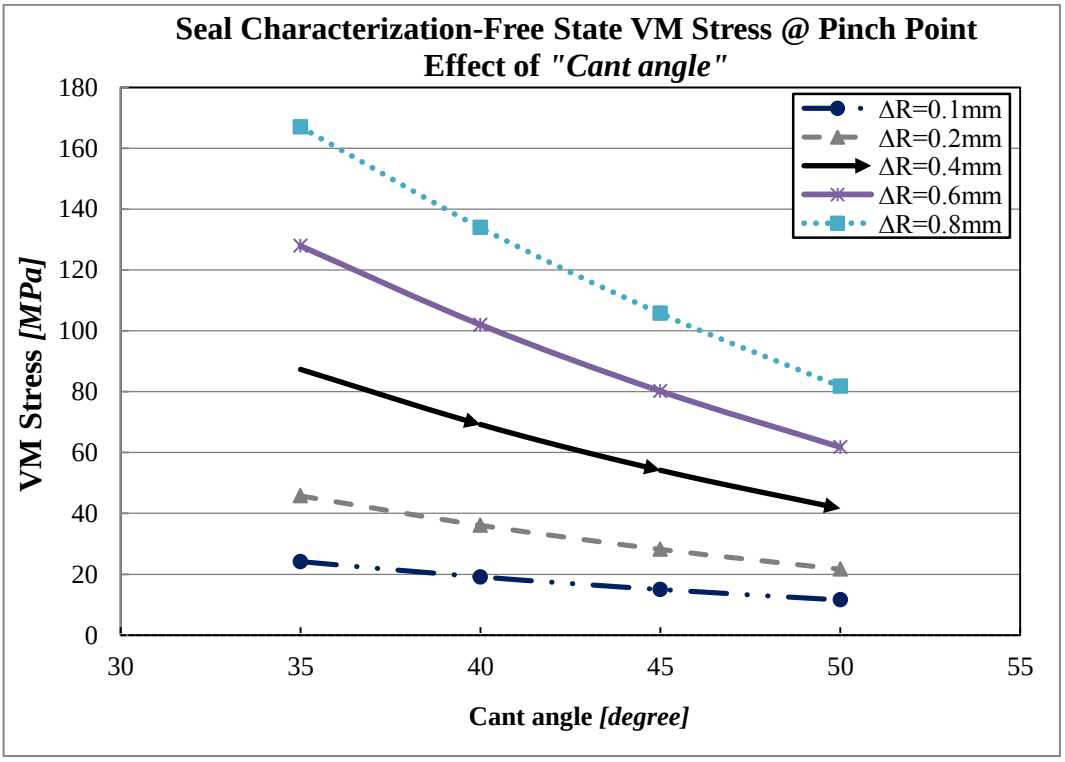

Figure 7.25: Change of pinch point VM stress levels with cant angle, unpressurized-nonrotating rotor interference conditions

Bristle stress. As detailed in the previous chapters, pinch point is critical for unpressurized rotor rub conditions since the BTF induces the maximum VM stress at that cross-section. Therefore, free-state characterization studies mainly focus on stress magnitudes at that critical bristle section. Pinch point VM stress change with *"θ"* at different interference levels of unpressurized seal is given in Figure 7.25. VM stress levels at unpressurized rotor interference conditions decrease with increasing cant angle, which is due to reduction in free-state tip force levels at larger cant angle values.

7.6.2 Effect of Cant Angle at Steady State Conditions

Effect of *"θ"* on bristle stress levels at steady state conditions *(pressure load without rotor interference)* has been examined by running the cases that has already been detailed in Table 7.7.

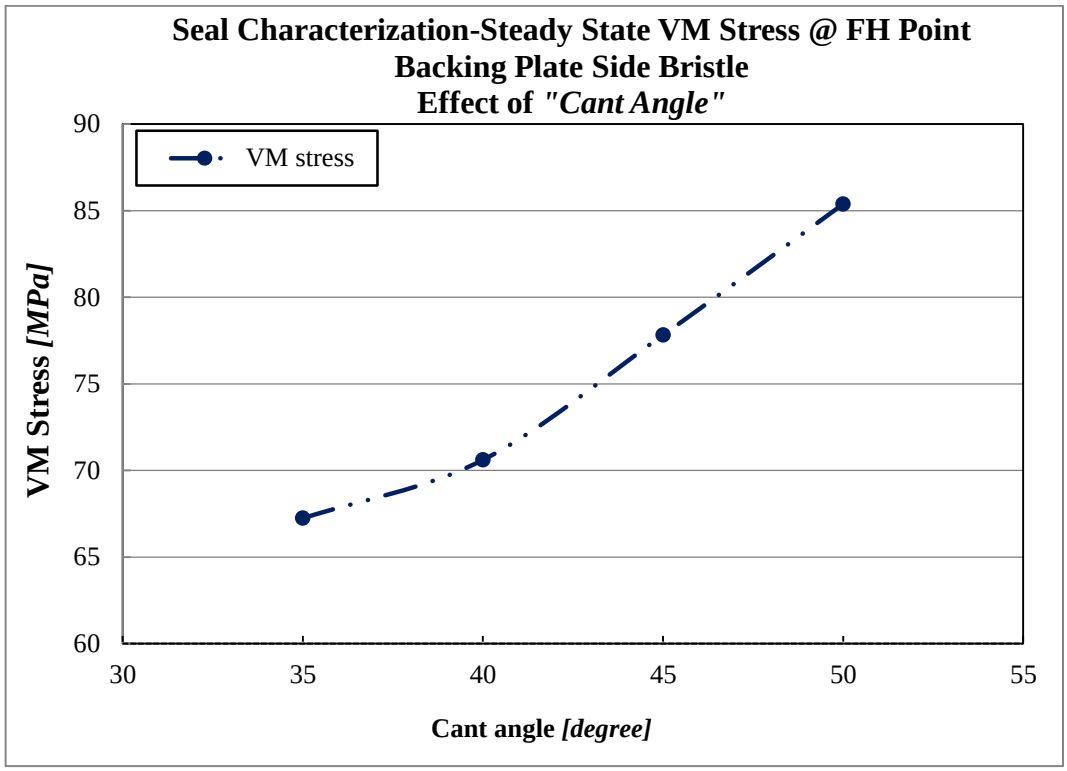

Figure 7.26: Change of backing plate side FH point-VM stress levels with cant angle, steady state conditions at ΔP=0.3MPa

Bristle stress. FH point stress levels of downstream side bristles are examined, which has already been identified as critical section for loaded seal due to pressure induced localized contact at backing plate corner. Maximum VM stress and its change with cant

angle is detailed in Figure 7.26 at steady state conditions *(ΔP=0.3MPa).* Although larger cant angle values result in stress levels to decreases at free-state rotor interference conditions, VM stress levels at FH point of loaded seal increases due to extended loaded length. The increase in steady state VM stress is more severe at larger cant angle values.

7.6.3 Effect of Cant Angle at Pressurized-Nonrotating Rotor Interference Conditions

Effect of cant angle on BTF and bristle stress levels at pressurized-nonrotating rotor rub conditions *(combined loading)* has been examined by running the cant angle cases given in Table 7.8.

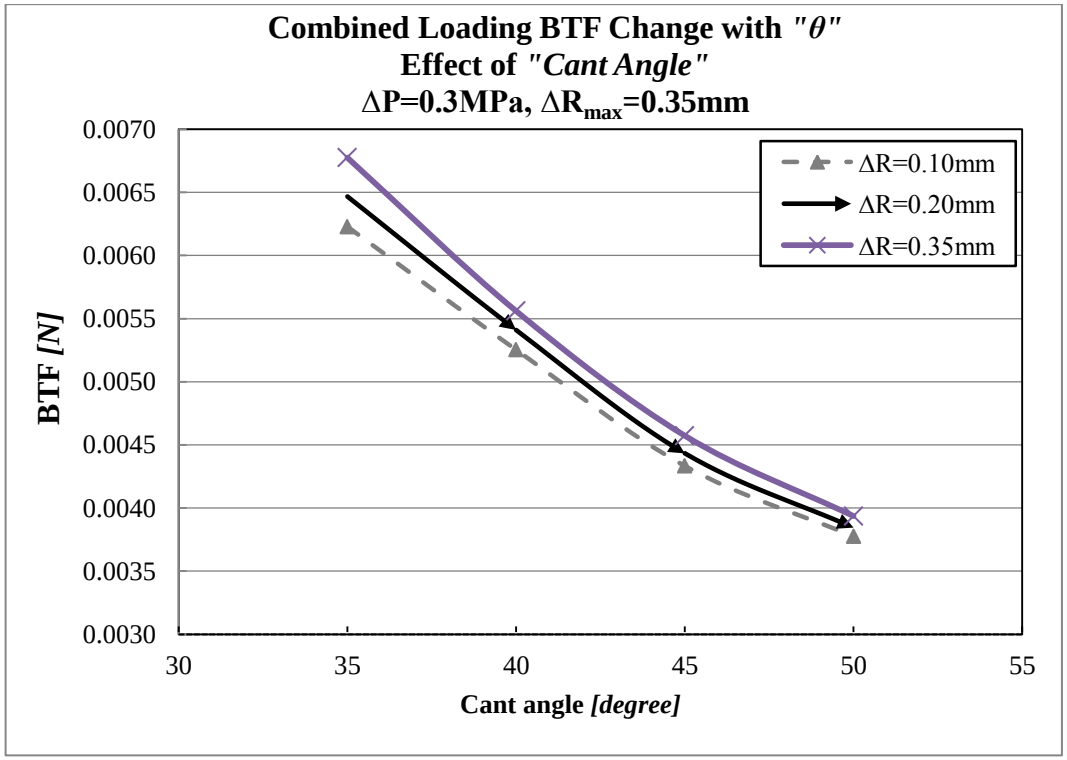

Figure 7.27: Change of BTF with cant angle, Pressurized-nonrotating rotor interference-loading step, ΔP=0.3MPa, ΔR_{max}=0.35mm

Bristle tip force. Combined loading BTF change with cant angle is detailed in Figure 7.27 for ΔP=0.3MPa and ΔR_{max}=0.35mm. As the cant angle is increased, the BTF for a loaded seal decreases, which is a direct result of having smoother contact with rotor at larger *"θ"* values.

Contact force per rotor unit circumferential length. Change of pressurized RF_{circ} *(contact force per rotor unit circumferential length)* with cant angle is detailed in Figure 7.28 at different rotor interference levels. Although number of bristles rows increases with cant angle, contribution of pressurized BTF on contact force per rotor circumferential length is more dominant and pressurized-RF_{circ} change with cant angle show similar trend with pressurized BTF.

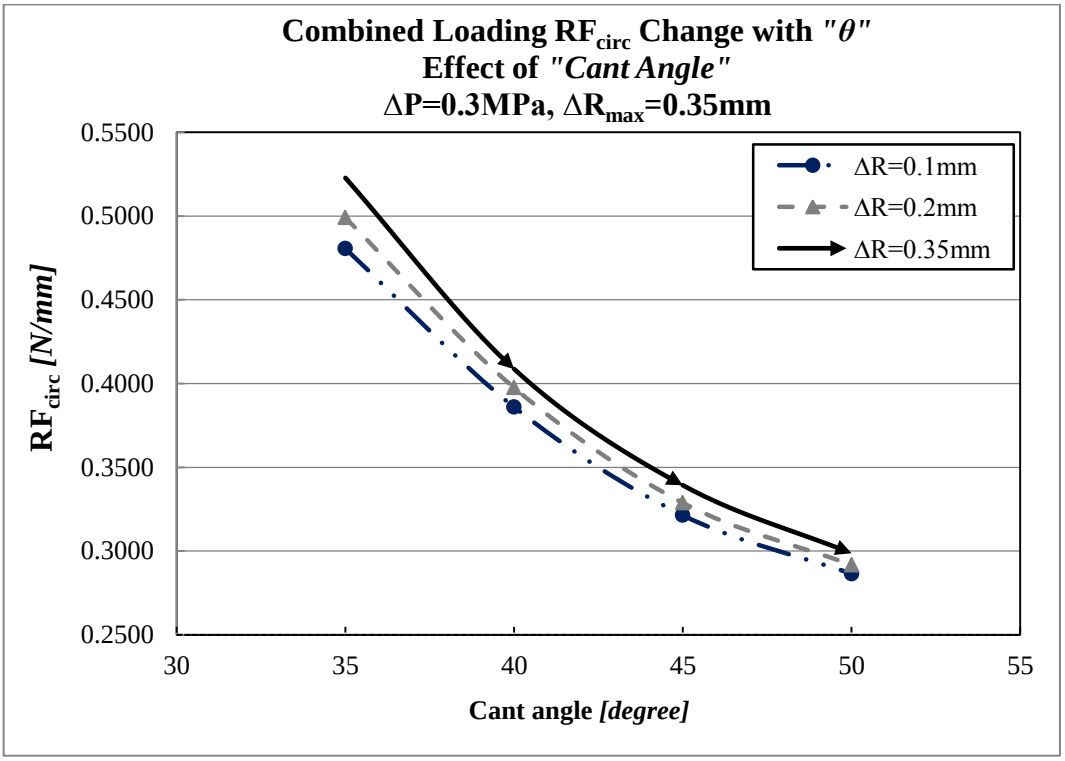

Figure 7.28: Change of RF_{circ} *(contact force per rotor unit circumferential length)* with bristle cant angle, Pressurized-nonrotating rotor interference-loading step, ΔP=0.3MPa, ΔR_{max}=0.35mm

Bristle stress. FH point stress levels of downstream side bristles are examined, which has already been identified as critical section for loaded seal. Maximum VM stress and its change with cant angle is detailed in Figure 7.26 at combined loading conditions *(ΔP=0.3MPa, ΔR_{max}=0.35mm).* VM stress levels at pressurized-rotor interference conditions increase with increasing cant angle, which is due to extended loaded length at higher cant angle values.

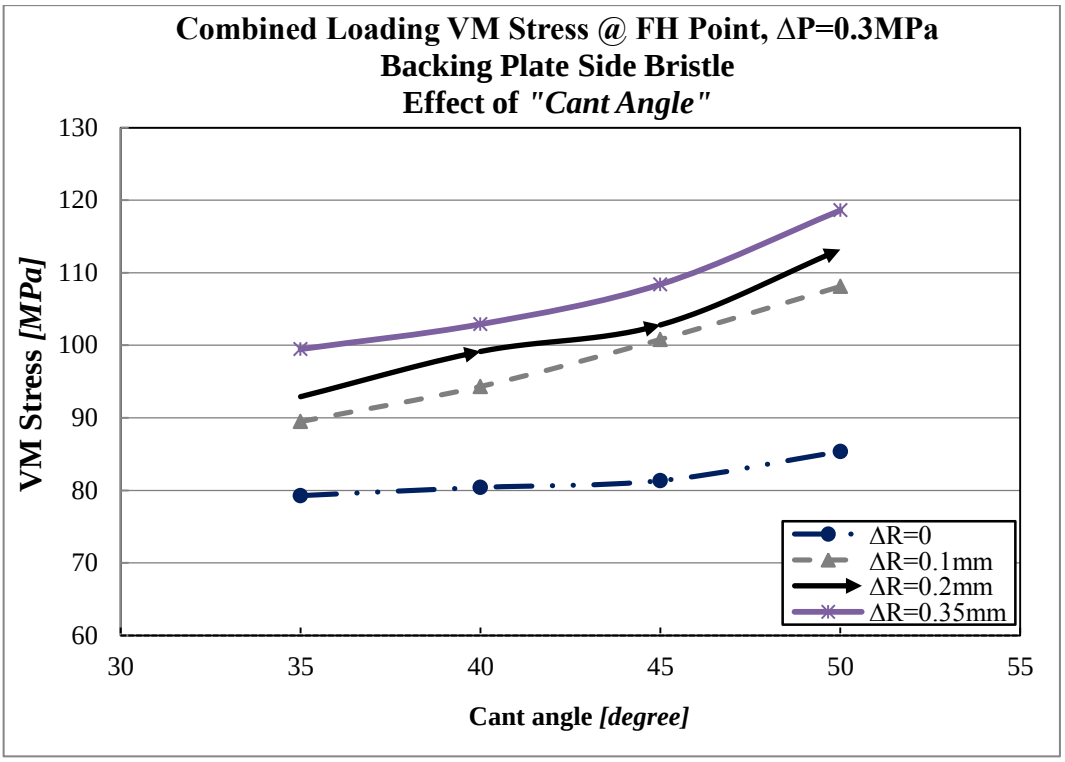

Figure 7.29: Change of backing plate side FH point-VM stress levels with cant angle, Pressurized-nonrotating rotor interference-loading step, ΔP=0.3MPa, ΔR_{max}=0.35mm

7.7 Effect of Bristle Density

Bristle density, *"η"*, is defined as the number of bristle rows per rotor unit circumferential length. The common exercise in industrial applications is to select higher bristle densities when the pressure load is high. Although bristle tip forces will be reduced since the same pressure load is carried by higher number of bristles rows, contact force per length and total heat generation may change in the reverse direction due to extended rotor contact areas and inter-bristle interactions. Brief literature survey reveals then lack of such data, and effect of bristle density on unpressurized/pressurized rotor rub conditions is inspected carefully through the correlated CAE models.

7.7.1 Effect of Bristle Density at Unpressurized-Nonrotating Rotor Interference Conditions

Effect of bristle density on seal response at unpressurized-nonrotating rotor interference conditions *(free-state rotor rub)* has been examined by running the cases detailed in Table 7.8.

Effect of Bristle Density					
	Case 1	Case 2	Case 3	Case 4	Case 5
Bristle density, η *[per mm]*	60	70	80	90	100
Number of bristle rows, NR	9	11	12	14	13
Effective circumferential length, $l_{t\text{-}CAE}$ *[mm]*	0.404	0.404	0.404	0.404	0.404
PS: Nominal values given in Table 7.2 has been used for remaining parameters.					

Table 7.9: Effect of bristle density – Cases for unpressurized nonrotating rotor interference conditions

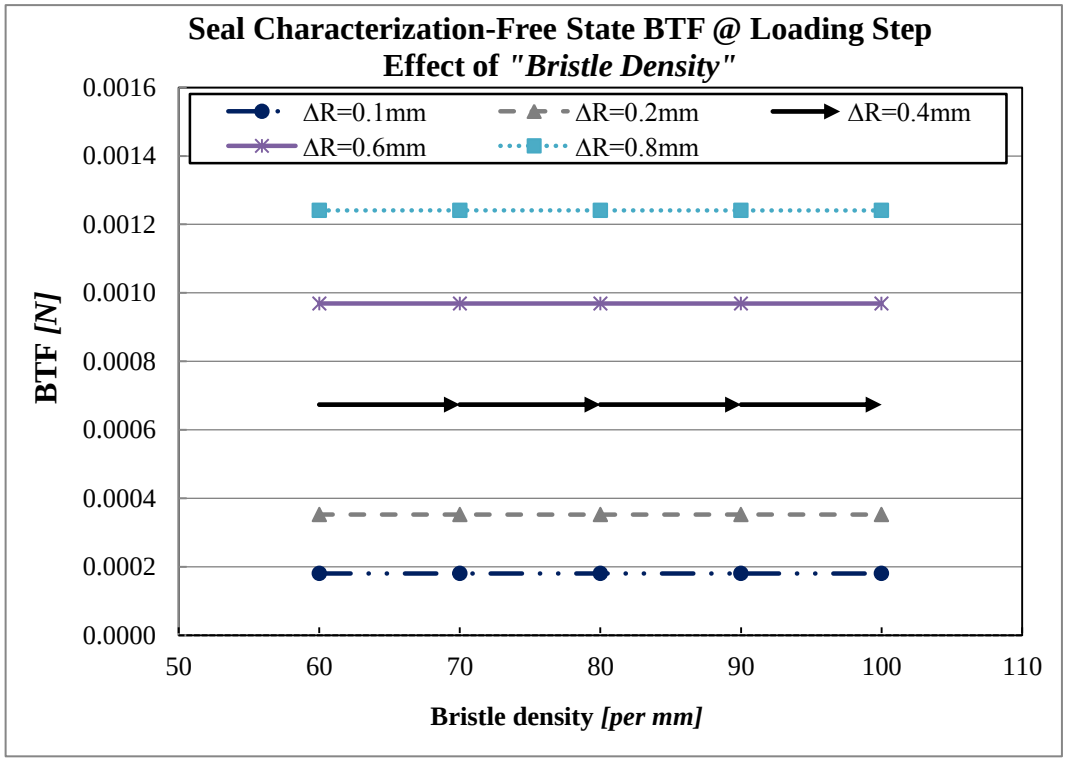

Figure 7.30: Change of BTF with bristle density, Unpressurized-nonrotating rotor interference-loading step

Bristle tip force. Free-state BTF change with bristle density is given in Figure 7.30 at different rotor interference levels. Changing the bristle density while keeping other design parameters same does not alter the free-state – BTF levels.

Contact force per rotor unit circumferential length. Change of free-state RF_{circ} *(contact force per rotor unit circumferential length)* with bristle density is detailed in Figure 7.31 at different rotor interference levels. Although changing *"η"* does not alter the free-state BTF, contact force per rotor unit circumferential length increases with bristle density due to the fact that higher values of *"η"* result in more number of bristle rows in rotor axial direction, which means extended rotor-bristle contact area.

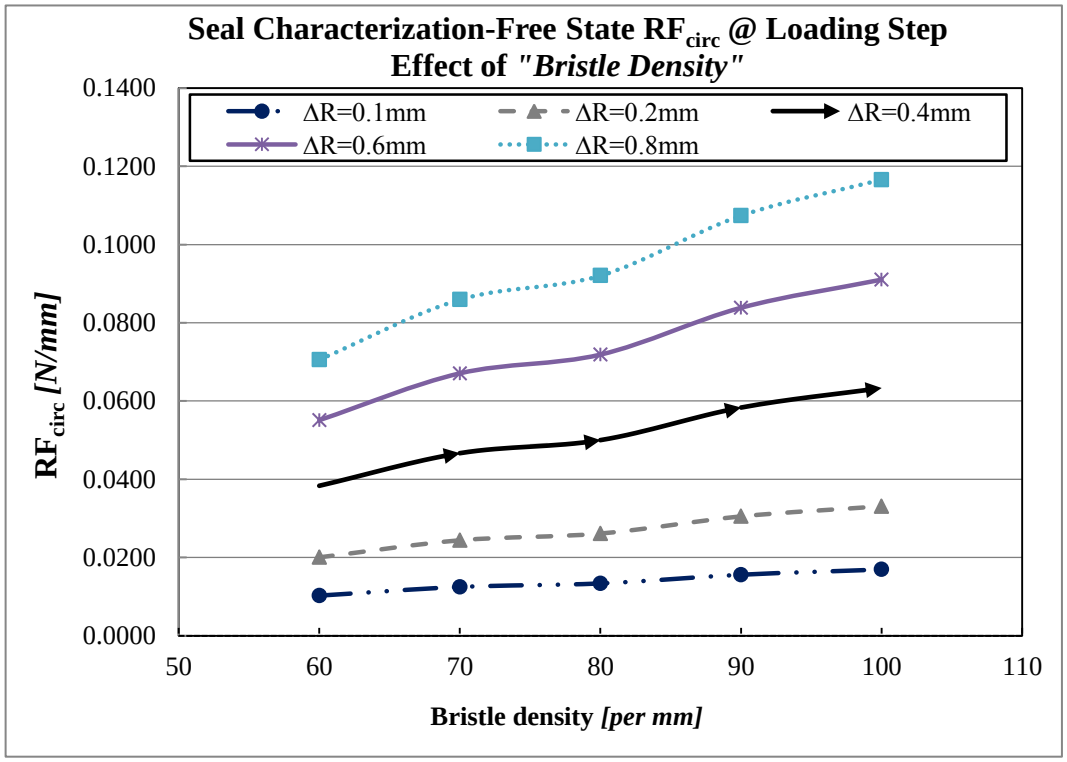

Figure 7.31: Change of RF_{circ} *(Contact force per rotor unit circumferential length)* with bristle density, Unpressurized-nonrotating rotor interference-loading step

7.7.2 Effect of Bristle Density at Pressurized-Nonrotating Rotor Interference Conditions

Effect of bristle density on BTF and bristle stress levels at pressurized-nonrotating rotor rub conditions *(combined loading)* has been examined by running the bristle density cases given in Table 7.9.

Effect of Bristle Density at Combined Loading Conditions, ΔP=0.3MPa, ΔR_{max}=0.30mm				
	Case 1	Case 2	Case 3	Case 5
Bristle density, η [per mm]	60	70	80	100
Number of bristle rows, NR	9	11	12	13
Effective circumferential length, $l_{t\text{-}CAE}$ [mm]	0.404	0.404	0.404	0.404
PS: Nominal values given in Table 7.2 has been used for remaining parameters.				

Table 7.10: Effect of bristle density – Cases for combined loading conditions, ΔP=0.3MPa, ΔR_{max}=0.30mm

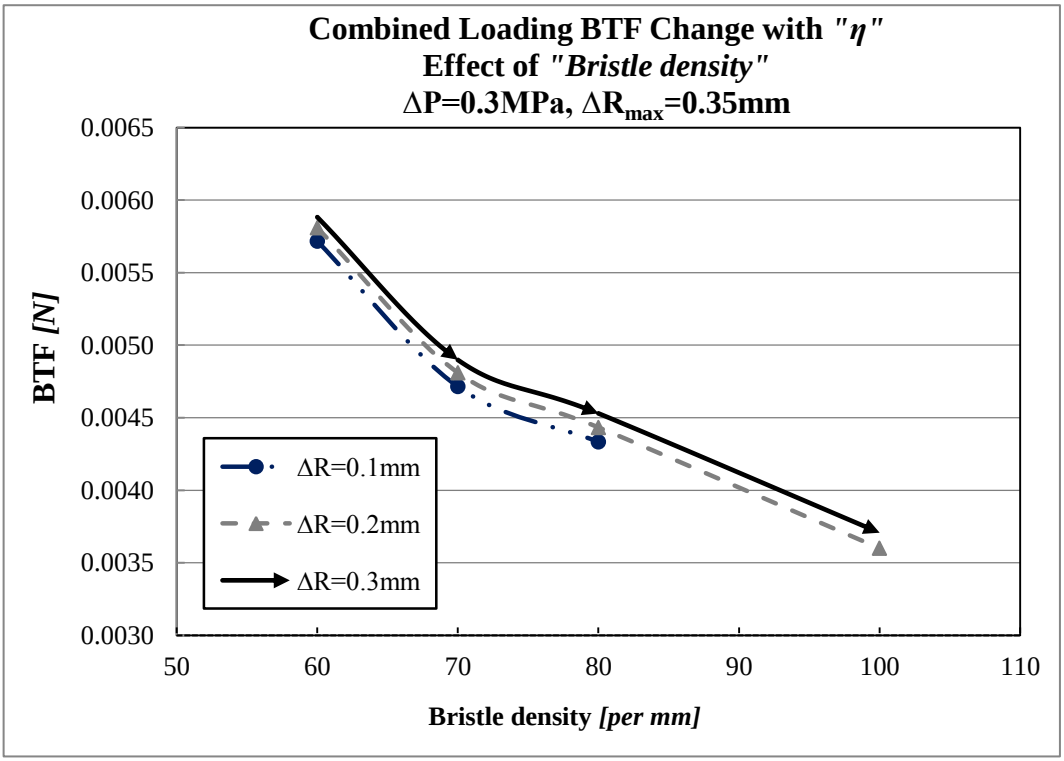

Figure 7.32: Change of BTF with bristle density, Pressurized-nonrotating rotor interference-loading step, ΔP=0.3MPa, ΔR_{max}=0.30mm

Bristle tip force. Combined loading BTF change with bristle density is detailed in Figure 7.32 for ΔP=0.3MPa and ΔR_{max}=0.30mm. As the bristle density is increased, the BTF for a loaded seal decreases since same pressure load is shared with more bristle rows at higher bristle densities, which reduces the pressure stiffening effect per bristle.

Contact force per rotor unit circumferential length. Change of pressurized RF_{circ} *(contact force per rotor unit circumferential length)* with bristle density is detailed in Figure 7.33 at different rotor interference levels. Although pressurized BTF decreases with increasing bristle density, same effect cannot be observed for RF_{circ} due to extended rotor-bristle contact surfaces as well as more complicated inter-bristle

interactions caused from increased number of bristles of higher bristle densities. As it can be seen from the figure, the contact force per rotor unit circumferential length has increasing trend with bristle density in overall response.

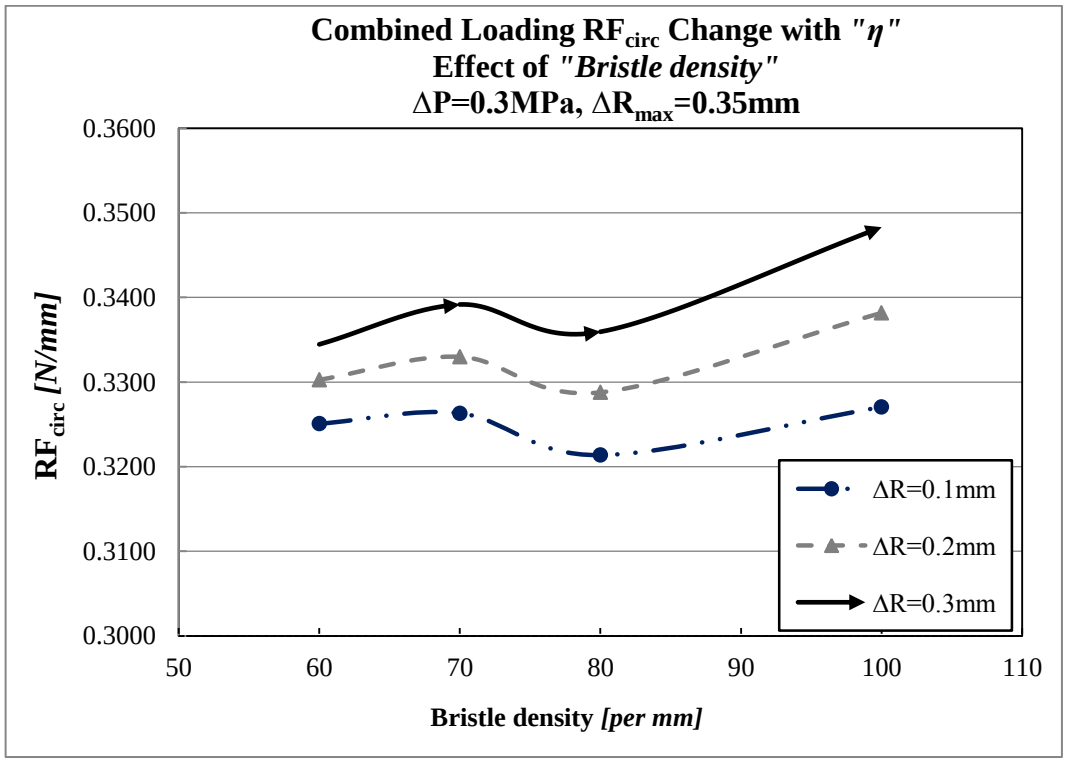

Figure 7.33: Change of RF$_{circ}$ *(Contact force per rotor unit circumferential length)* with bristle density, Pressurized-nonrotating rotor interference-loading step, ΔP=0.3MPa, ΔR$_{max}$=0.30mm

7.8 Effect of Rotor-Bristle Friction

Brush seals are known as their superior ability to compensate rotor transients at operating conditions. At turbine conditions, rotor-bristle contact takes place for numerous times and resulting generated heat is an important issue since the excessive heat generation may yield rotor instability and fatigue issues. At rotor rub conditions, friction coefficient between rotor and bristle surfaces becomes very important since it directly contributes to frictional heat generation. In this section, effect of *"μ_{rb}"* on seal stiffness and stress levels at pressurized/unpressurized rotor interference conditions will be inspected through correlated CAE models.

7.8.1 Effect of Rotor-Bristle Friction at Unpressurized-Nonrotating Rotor Interference Conditions

Effect of rotor-bristle friction coefficient on seal response at unpressurized-nonrotating rotor interference conditions *(free-state rotor rub)* has been examined by running the cases detailed in Table 7.11.

Effect of μ_{rb}					
	Case 1	Case 2	Case 3	Case 4	Case 5
Rotor-bristle friction coefficient, μ_{rb}	0.25	0.30	0.35	0.40	0.45
PS: Nominal values given in Table 7.2 has been used for remaining parameters.					

Table 7.11: Effect of bristle density – Cases for unpressurized nonrotating rotor interference conditions

Bristle tip force. Free-state BTF change with rotor-bristle friction coefficient is given in Figure 7.34 at different rotor interference levels. Bristle tip forces at unpressurized conditions take higher values as rotor-bristle friction coefficient, which acts in the reverse direction to bristle slid, increases. The change of BTF with μ_{rb} is consistent with tests as well as with modified beam theory developed and detailed In Chapter 5 *(Table 5.3)*. In Figure 7.34, free-state BTF vs. radial interference is presented where different friction coefficients are used for rotor-bristle contact. It is observed that free-state hysteresis also increases with μ_{rb} since larger friction coefficients increases BTF magnitudes in loading step while reducing the BTF during unloading.

Bristle stress. VM stress levels at pinch point, which is the critical section at rotor interference conditions, and its change with rotor-bristle friction coefficient is given in Figure 7.36. As it can be seen from the figure, the effect of rotor-bristle friction is almost negligible on bending dominated stress, which is function of interference level and independent of rotor-bristle friction at unpressurized conditions. Results are consistent with tests and modified beam theory developed in this study *(Chapter 5, Table 5.3)*.

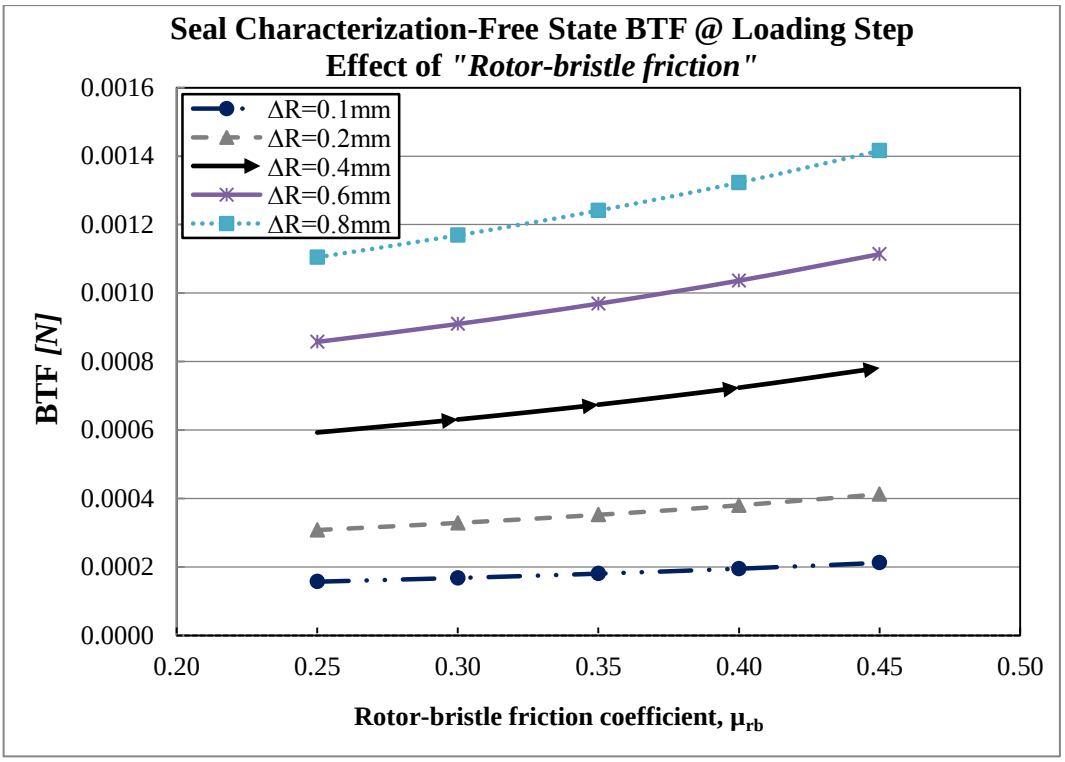

Figure 7.34: Change of BTF with rotor-bristle friction coefficient, Unpressurized-nonrotating rotor interference-loading step

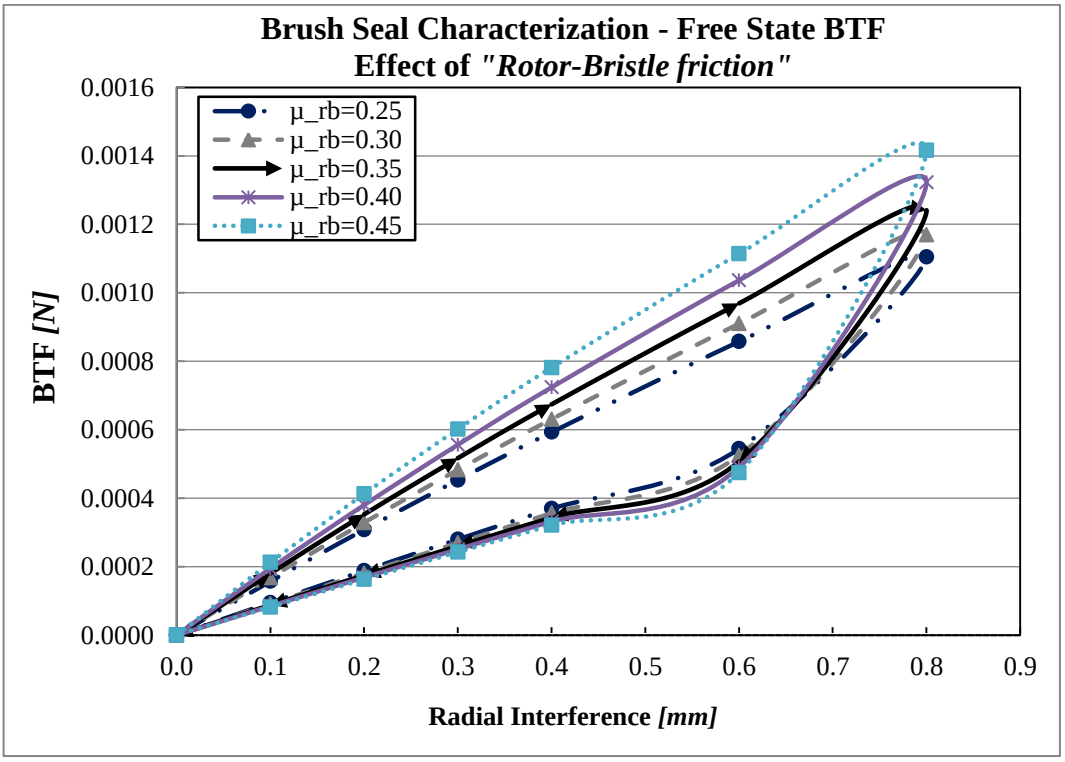

Figure 7.35: Effect of rotor-bristle friction coefficient on BTF values at unpressurized-nonrotating rotor interference conditions

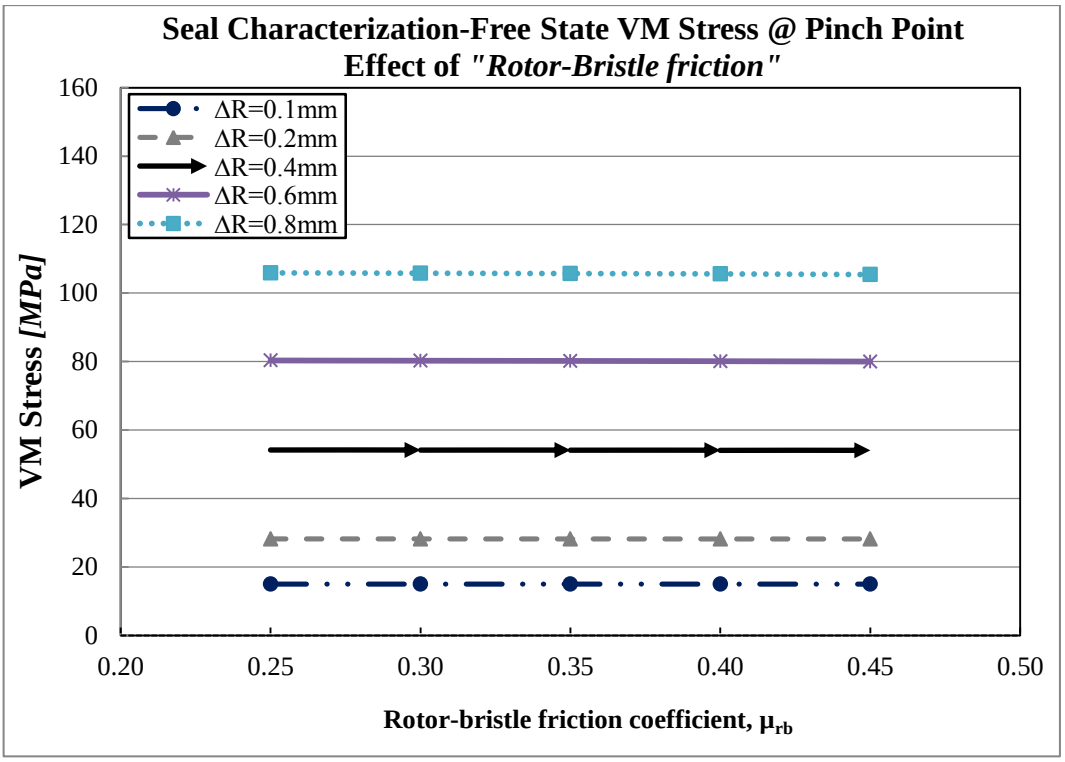

Figure 7.36: Change of pinch point VM stress levels with rotor-bristle friction coefficient, unpressurized-nonrotating rotor interference conditions

7.8.2 Effect of Rotor-Bristle Friction at Pressurized-Nonrotating Rotor Interference Conditions

Effect of *"μ_{rb}"* on BTF and bristle stress levels at pressurized-nonrotating rotor rub conditions *(combined loading)* has been examined by running the rotor-bristle friction coefficient cases given in Table 7.11.

Bristle tip force. Combined loading BTF change with rotor-bristle friction coefficient is detailed in Figure 7.37 for ΔP=0.3MPa and ΔR_{max}=0.35mm. As the rotor-bristle friction is increased, the BTF for a loaded seal also increase as in the case of free-state rotor interference.

Bristle stress. FH point stress levels of downstream side bristles are examined, which has already been identified as critical section for loaded seal. Maximum VM stress and its change with rotor-bristle friction is detailed in Figure 7.38 at combined loading conditions *(ΔP=0.3MPa, ΔR_{max}=0.35mm)*. Effect of rotor-bristle friction coefficient on FH point stress levels is almost negligible since they are mainly induced by aft bending and localized contact, both of which do not depend on μ_{rb}.

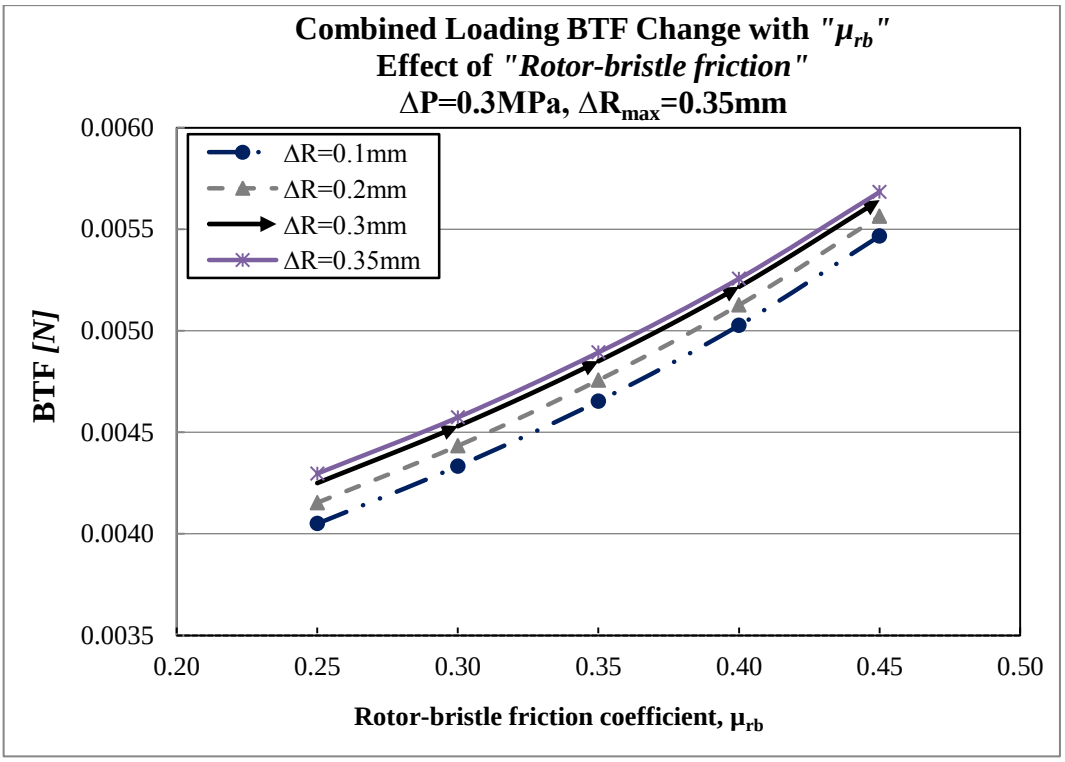

Figure 7.37: Change of BTF with rotor-bristle friction, Pressurized-nonrotating rotor interference-loading step, ΔP=0.3MPa, ΔR_{max}=0.35mm

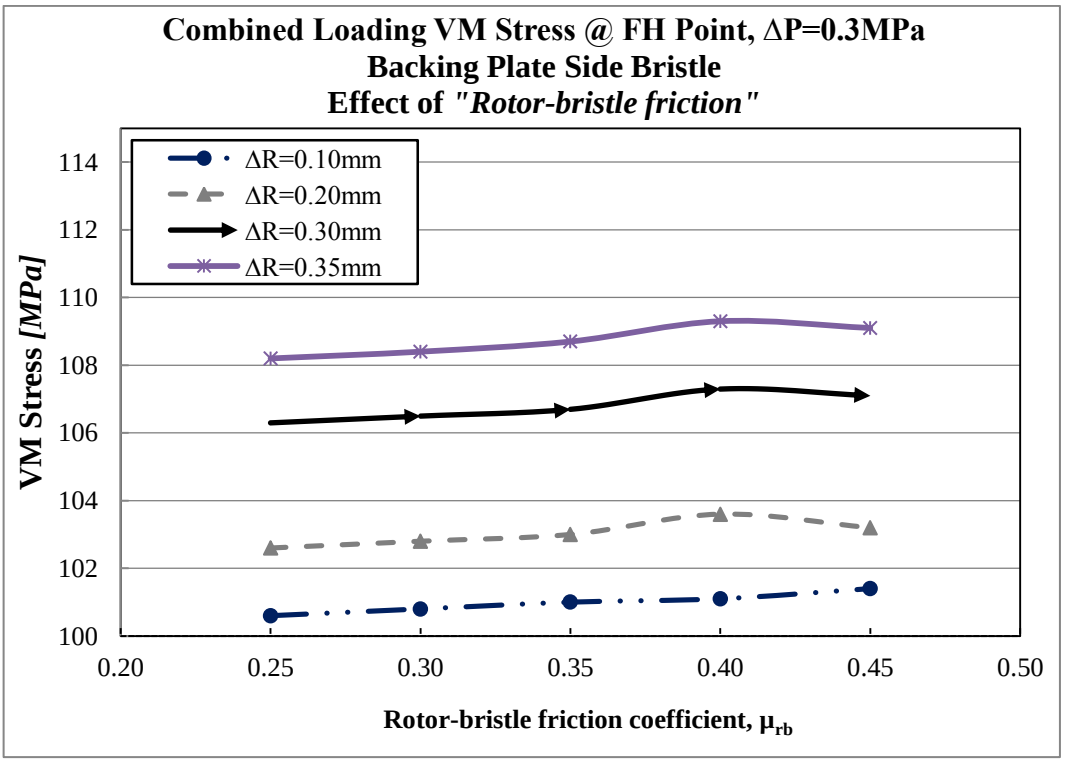

Figure 7.38: Change of backing plate side FH point-VM stress levels with rotor-bristle friction, Pressurized-nonrotating rotor interference-loading step, ΔP=0.3MPa, ΔR_{max}=0.35mm

7.9 Effect of Backing Plate-Bristle Pack and Inter-bristle Friction

At steady state turbine conditions, brush seals operate under pressure load without rotor interference. At rotor transients, rotor pushes the loaded seal outwards, which is named as pressurized-rotor interference. When a seal is loaded with pressure, the initial spacing between bristles as well as the space between backing-plate and bristle is closed, and interactions between those components become effective in determining seal stiffness and stress levels. Therefore, effect of inter-bristle and bristle-backing plate friction on stiffness and stress levels of loaded seal has been examined in this section. Considering the lack of such data in the literature, CAE-based friction characterization of brush seal will provide useful data for seal industry. Analyses have been run for the cases tabulated in Table 7.12.

Effect of μ_{ib} and μ_{bp} – Combined Loading at ΔP=0.3MPa, ΔR_{max}=0.35mm				
	Case 1	Case 2	Case 3	Case 4
Backing plate friction coefficient, μ_{bp}	0.25	0.27	0.30	0.45
Backing plate friction coefficient, μ_{bp}	0.25	0.27	0.30	0.45
PS: Nominal values given in Table 7.2 has been used for remaining parameters.				

Table 7.12: Effect of inter-bristle and bristle-backing plate friction coefficient – Cases for pressurized nonrotating rotor interference conditions

Bristle tip force. Combined loading BTF change with backing plate-bristle and inter-bristle friction coefficient is detailed in Figure 7.39 for ΔP=0.3MPa and ΔR_{max}=0.35mm. As *"$\mu_{bp}=\mu_{ib}$"* is increased, the BTF for a loaded seal also increase. This is expected behavior since higher frictional coefficients causes seal pack to behave much stiffer and result in more pressure stiffening. Results are also consistent with the CAE work performed for correlation with tests *(Chapter 6)* as well as with the analytical studies presented in Chapter 5.

Bristle stress. FH point stress levels of downstream side bristles are examined, which has already been identified as critical section for loaded seal. Maximum VM stress and its change with *"$\mu_{bp}=\mu_{ib}$"* is detailed in Figure 7.40 at combined loading conditions *(ΔP=0.3MPa, ΔR_{max}=0.35mm).* Effect of inter-bristle and backing plate-bristle frictions coefficient on FH point stress levels is very small since those stress levels are mainly related to contact normal forces instead of friction.

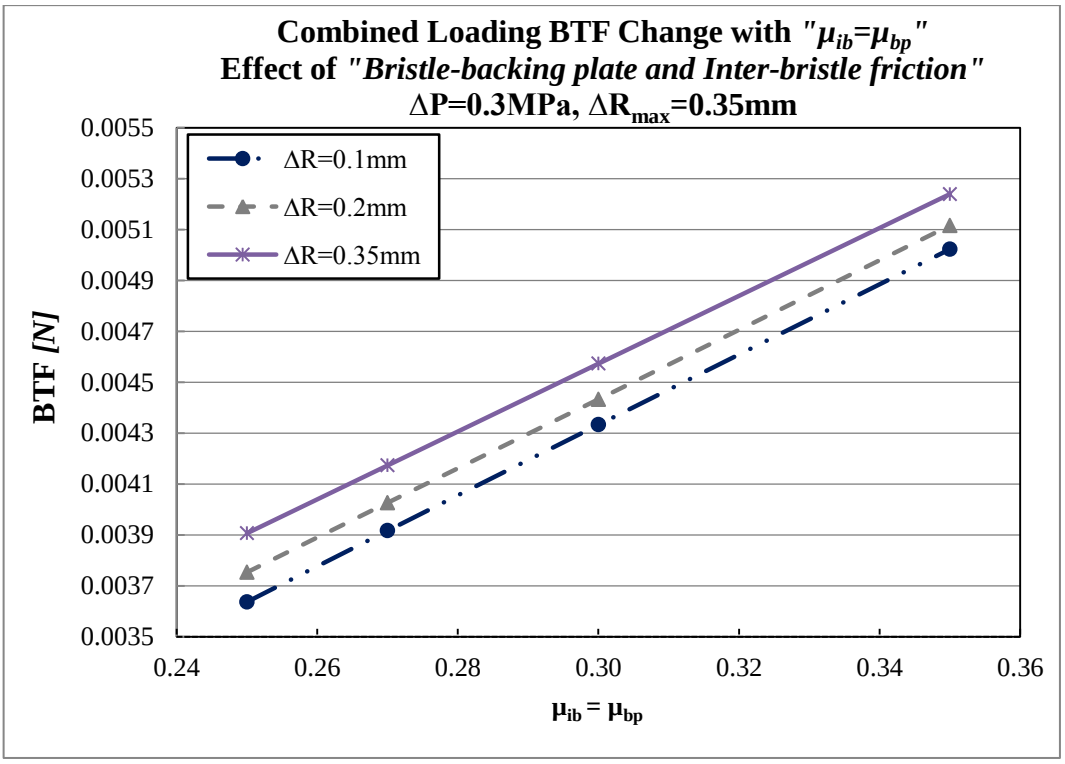

Figure 7.39: Change of BTF with $\mu_{ib}= \mu_{bp}$, Pressurized-nonrotating rotor interference-loading step, $\Delta P=0.3MPa$, $\Delta R_{max}=0.35mm$

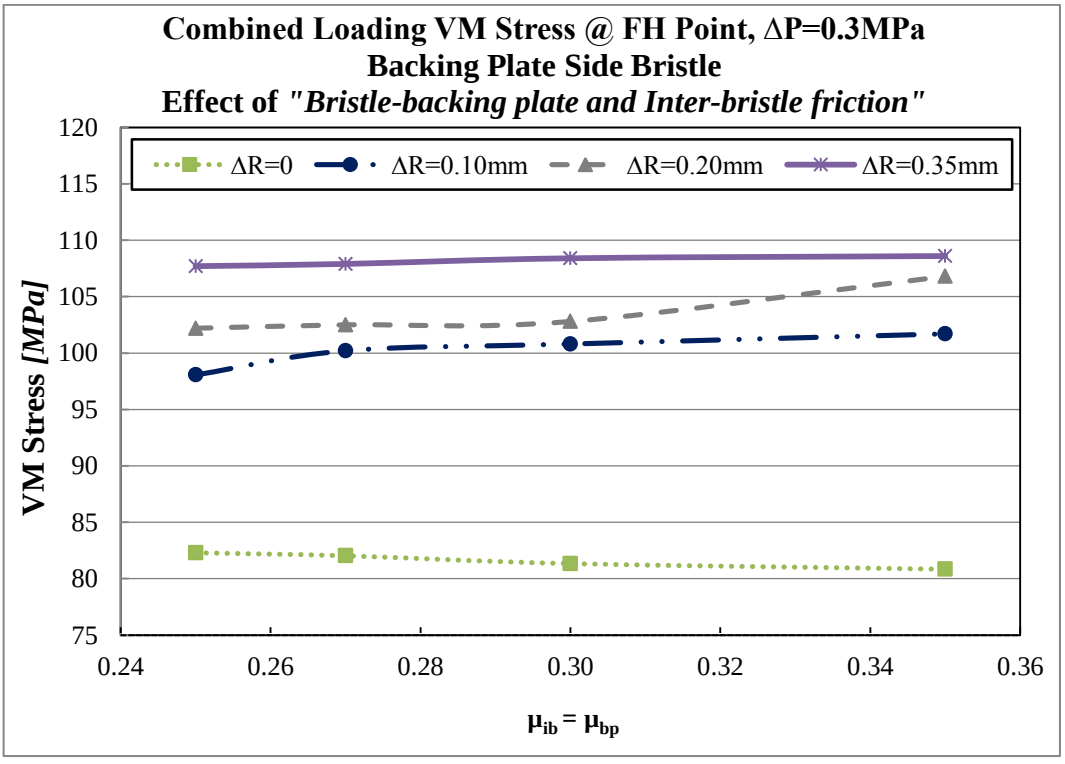

Figure 7.40: Change of backing plate side FH point-VM stress levels with $\mu_{ib}= \mu_{bp}$, Pressurized-nonrotating rotor interference-loading step, $\Delta P=0.3MPa$, $\Delta R_{max}=0.35mm$

8 CONCLUSION

Brush seals operate under pressure loads and rotor rub conditions, where wear and durability of seals are main factors affecting seal performance and stable leakage characteristics. Seal stiffness, hysteresis and pressure closure behaviors play important roles in determining the leakage performance and rotor stability due to the fact that they directly affect wear rates and pressure load capacity of a seal. Complicated nature of bristle-rotor-backing plate interactions at operating conditions makes it difficult to inspect stiffness and durability of brush seals. A brief literature survey reveals the lack of test data, analytical studies and correlated CAE analyses for simulating seal stiffness, friction and durability characterization. In this study, custom test rig design and methodology has been developed to perform stiffness tests at turbine operating conditions. Analytical studies and finite element simulations have been performed for test seals and results have been correlated with the test data of this study. Furthermore, stiffness and friction characterization of brush seals has been conducted through correlated FE models, and MATLAB based code has been developed for automatic brush seal FE model generation for ABAQUS simulations. Overall, work done in this study is as summarized below:

- **Brush Seal Inspection**
  - Test seal design has been selected.
  - Design parameters are calculated and geometric inspection of test seals has been performed.
  - Methodology has been developed for corrected design parameter and stiffness calculations.

- **Free-State Stiffness Test Rig Design and BTF Measurements**
  - Free-state stiffness test rig has been designed.
  - Free-state stiffness measurements have been performed for test seals. Hysteresis effects have been tested successfully.
  - Drawbacks of FSS-TR measurements and deviation from turbine conditions have been identified.

- **Rotary Test Rig Design and BTF Measurements**
  - Custom test rig has been designed to perform seal leakage and full rotor stiffness tests up to 45,000rpm.
  - Structural analyses have been performed by including assembly loads, gravity and rotational body forces in order to assure durability and functionality of the test rig
  - Rotor dynamic simulations have been conducted for identifying critical rotor speed
  - Impact analyses have been performed for seal housing in order to assure the system safety under the worst case scenario conditions of rotor sudden failure
  - Free-state full rotor stiffness tests have been conducted and post-process methodology has been developed for BTF examination
  - Free-state BTF measurements of RTR-Test rig has been compared with FSS-TR test data.
  - Pressurized-rotor interference BTF measurements have been performed by introducing rotor incursion to loaded seal. Pressure stiffening, BTF stabilization and pressurized hysteresis have been extracted properly.
  - Unpressurized-rotating rotor BTF measurements have been conducted in order to examine effects of inertial factors.
  - Pressurized-rotating rotor stiffness tests have been performed for simulating real turbine conditions. Test data shows good agreement with industrial applications.

- **Analytical Studies and Correlation with Tests**
  - Simple beam theory of Flower [17] has been run for test seals. BTF results have been compared with test data.
  - Rotor friction has been included and *"Modified Beam Theory"* has been developed for free-state rotor interference conditions. BTF results of developed methodology gives consistent results with test data and CAE.
  - Analytical methodologies have been developed in order to calculate bristle stress levels at steady state *(pressure load without rotor incursion)* and combined loading *(rotor interference to loaded seal)* conditions. *"Simple*

Approach" and *"Advanced Approach"* methodologies have been run for test seals and stress level have been calculated at test conditions.

- Analytical methodology including rotor-bristle and bristle-backing plate friction has been developed for simulating pressurized-rotor rub conditions. Developed methodology has been run for test seals, and BTF results of closed form function show good agreement with test as well as with CAE data.

- **Brush Seal Finite Element Analyses and Correlation with Tests**
  - Brush seal FE models have been constructed by including all interactions and frictions.
  - Two different FE models using C3D8I *(hexa)* and B31*(space beam)* elements have been prepared. All test conditions have been simulated and results have been compared with test data.
  - Unpressurized non-rotating rotor interference conditions have been simulated for test seals. CAE analyses results show good agreement with BTF measurements. Rotor-bristle friction coefficient has been correlated.
  - Pressurized-nonrotating rotor interference conditions have been simulated and BTF results have been compared with RTR-Pressurized nonrotating rotor interference tests. CAE results are well correlated with BTF measurements both in loading and unloading steps. Backing plate-bristle and inter-bristle friction coefficients have also been correlated.
  - Unpressurized-rotating rotor conditions have been simulated through transient analyses. Inertial affects, bristle loose and chattering phenomenon has been analyzed successfully. CAE results show good agreement with the dynamic test data.
  - Pressurized-rotating rotor conditions have been simulated through transient rotor interference analyses of a loaded seal. Comparison with test data reveals that analyses results are well correlated with the test data.
  - Stress and deformation profiles of brush seals have been inspected through correlated CAE models, which give better insight to understand seal pack behavior at turbine operating conditions.

- **CAE Based Brush Seal Characterization**
  - Stiffness, friction and durability characterization of brush seals have been conducted through correlated CAE models.
  - A MATLAB based code has been developed, which automatically generates the 3D brush seal model that is ready to be run in ABAQUS. The code shortens the pre-processing times from 3-4 days to 1-2 minutes.
  - Characterization studies examines effect of bristle diameter, free bristle height, fence height, bristle density, can angle, rotor-bristle friction and inter –bristle & bristle-backing plate friction on bristle tip force, stress magnitudes and stiffness of seals at unpressurized/pressurized rotor interference conditions. 70+ simulations have been conducted.
  - Characterization results are consistent with real life applications and give better understanding of nonlinear brush seal response.

9 REFERENCES

[1] Chupp, R.E. and Dowler, C.A., "Performance Characteristics of Brush Seals for Limited-Life Engines", ASME Trans. J. Eng. for Gas Turbines and Power, 115, pp 390-396, (1993).

[2] Pastrana, M.R., Wolfe, C.E., Turnquis, N.A. and Burnett, M.E., "Improved Steam Turbine Leakage Control with a Brush Seal Design", Proceedings of the 30th Turbomachinery Symposium, 33-38.

[3] Turnquist, N., Chupp, R., Baily, F., Burnett, M., Rivas, F., Bowsher, A. and Crudgington, P., "Brush Seals for Improved Steam Turbine Performance", NASA Seals Workshop, NASA/CP-2006-214383/VOL1, 107-127.

[4] Chupp, R.E., Hendricks, R.C., Lattime, S.B., Steinetz, B.M. and Aksit M.F., "Turbomachinery Clearance Control", NASA Technical Report ID: 20070005016, NASA Glenn Research Center, NASA Scientific and Technical Aerospace Reports (STAR), No.3, Vol.45, pp.114, February, 2007.

[5] Steinetz, B.M., "Mechanical Engineers' Handbook: Materials and Mechanical Design, Volume 1, Chapter 33 – Seal Technology", 3rd Edition, John Wiley & Sons, Inc., 2006.

[6] Burcham, R.E. and Keller, Jr., R.B., "Liquid Rocket Engine Turbopump Rotating-Shaft Seals", NASA SP-8212, 1979.

[7] Heidegger, N.J., Hall, E.J. and Delaney, R.A., "Parametrized Study of High-Speed Compressor Seal Cavity Flow", NASA CR-198504, 1996.

[8] Chupp, R.E., Ghasripoor, F., Moore, G.D, Kalv, L.S. and Johnston, J.R., "Applying Abradable Seals to Industrial Gas Turbines", AIAA Paper, 2002-3795, 2002.

[9] Ludwig, L.P. and Bill, R., "Gas Path Sealing in Turbine Engines", ASLE Trans., 23, pp 1-22, (1980).

[10] Chew, J.W. and Hogg, S.I., "Porosity Modeling of Brush Seals", Journal of Tribology (1997).

[11] Carlile, J.A., Hendricks, R.C. and Yoder, D.A., "Brush Seal Leakage Performance with Gaseous Working Fluids at Static and Low Rotor Speed Condition", Journal of Engineering for Gas Turbines and Power, 115, pp 397-403 (1993).

[12] Krawiecki, S., Mehta, J. and Holloway, G., "Rotating Intershaft Brush Seal Project", NASA/CP-2006-214383/VOL1, 239-262.

[13] Steinetz, B.M. and Hendricks, R.C., "Aircraft Engine Seals", Chapter 9 of Tribology for Aerospace Applications, STLE Special Publication, SP-37, 1997.

[14] Little, N.T., Sulda, E.M. and Terezakis, T.N., "Efficiency Improvements on Large Mechanical Drive Steam Turbines", Proceedings of the 30th Turbomachinery Symposium, 57-64.

[15] Aksit, M. F., "A Computational Study of Brush Seal Contact Loads with Friction", Thesis Project for Doctor of Philosophy, Rensselaer Polytechnic Institute, Troy, New York.

[16] "Ferranti Fluid Packing", Patent No. 885,032, 1908.

[17] Flower, R., "Brush Seal Development System", AIAA/ASME/SAE/ASEE 26th Joint Propulsion Conference, AIAA Paper 90-2143.

[18] Mahler, F. and Boyes, E., July 1995, "The Application of Brush Seals in Large Commercial Jet Engines", AIAA/ASME/SAE/ASEE, 31st Joint Propulsion Conference, San Diego, California.

[19] Gorelov, G.M., Reznik, V.E. and Tsibizov, V.I., "Experimental Study of Brush Seal Flow Characteristics and Comparison with a Labyrinth Seal", Izvestiya VUZ. Aviatsionnaya Takhnika, 31, pp 43-46, (1988).

[20] Ferguson, J.G., "Brushes as High Performance Gas Turbine Seals", ASME Gas Turbine and Aeroengine Congress Paper ASME 88-GT-182, (1988).

[21] Hendricks, R.C., Carlile, J.A., Liang, A.D., Steinetz, B.M., Easter, Onstott, J.W. and Howe, H., "Static Brush Seals for Propulsion System Interfaces", 5th Advanced Earth to Orbit Propulsion Technology Conference Paper NASA CP-3174-VOL-1, pp 243-439, (1992).

[22] Holle, G.F. and Khrishnan, M.R., "Gas Turbine Engine Brush Seal Applications", AIAA/SAE/ASME/ASEE 26th Joint Propulsion Conference Paper AIAA 90-2142, (1990).

[23] Mayhew, E.R., Bill, R.C., Voorhees, W.J. and O'Donnell, J., 'Military Engine Seal Development: Potential for Dual Use,' AIAA/SAE/ASME/ASEE 30th Joint Propulsion Conference Paper **AIAA 94-2699**, (1994).

[24] Dinc, S., Bagepalli, B., Cromer, R., Maynard, J., Calabrese, S. and Aksit, M.F., "High Temperature Vibratory Brush Seals for Gas Turbine Applications", AIAA/SAE/ASME/ASEE 30th Joint Propulsion Conference Paper AIAA 94-2704, (1994).

[25] Wolfe, C.E., Chiu, R.P., Cromer, R.H., Marks, P.T., Stuck, A.E., Turnquist, N.A., Reluzco, G. and Dinc, O.S., "Brush Seals in Industrial Gas Turbines", AIAA/ASME/SAE/ASEE 33rd Joint Propulsion Conference, AIAA Paper No. 97-2730, Seattle, Washington.

[26] Conner, K.J. and Childs, D.W., "Brush Seal Rotor-dynamic Damping Characteristics", AIAA/SAE/ASME/ASEE 26th Joint Propulsion Conference Paper AIAA 90-2139, (1990).

[27] Schlumberger, A.J., Margaret, P.P. and Hendricks, R.C., "Eccentricity Effects on Leakage of a Brush Seal at Low Speeds", NASA TM-105141, (1991).

[28] Hendricks, R.C., Proctor, M., Schlumberger, J., Braun, M. and Mullen, R., "Some Preliminary Results of Brush Seal/Rotor Interface Effects on Leakage at Zero and Low RPM using a Tapered-Plug Rotor", AIAA/SAE/ASME/ASEE 27th Joint Propulsion Conference Paper AIAA 91-3390, (1991).

[29] Basu, P., Datta, A., Johnson, R., Loewenthal, R. and Short, J., "Hysteresis and Bristle Stiffening Effects of Conventional Brush Seals", AIAA/SAE/ASME/ASEE 29th Joint Propulsion Conference Paper AIAA 93-1996, (1993).

[30] Short, J.F., Basu, P., Datta, A., Loewenthal, R.G. and Prior, R.J., "Advanced Brush Seal Development", AIAA/SAE/ASME/ASEE 32nd Joint Propulsion Conference Paper AIAA 96-2907, (1996).

[31] Hendricks, R.C., Wilson, J., Wu, T. and Flower, R., "Bidirectional Brush Seals", ASME Gas Turbine and Aeroengine Congress Paper ASME97-GT-256, (1997).

[32] Arora, G.K. and Proctor, M.P., "JTAGG II Brush Seal Test Results", AIAA/SAE/ASME/ASEE 33nd Joint Propulsion Conference Paper AIAA 97-2632, (1997).

[33] Chupp, R.E. and Loewenthal, R.G., "Brush Seals Can Improve Power Plant Efficiency by One-Fourth of a Percentage Point Yielding Huge Annual Savings", Lubr. Eng., **53**, pp 10-14, (1997).

[34] Chupp, R.E., Johnson, R.P. and Loewenthal, R.G., "Brush Seal Development for Large Industrial Gas Turbines", AIAA/SAE/ASME/ASEE 31st Joint Propulsion Conference Paper AIAA 95-3146, (1995).

[35] Chupp, R.E. and Prior, R.J., "Update on Brush Seal Development for Large Industrial Gas Turbines", AIAA/SAE/ASME/ASEE 32nd Joint Propulsion Conference Paper AIAA 96-3306, (1996).

[36] Chupp, R.E. and Prior, R.J., "Advanced Seal Development for Large Industrial Gas Turbines", AIAA/SAE/ASME/ASEE 33nd Joint Propulsion Conference Paper AIAA 97-2731, (1997).

[37] Owen, A. K., Jones, T. V., Guo, S. M., and Hogg, S., 2003, "An Experimental and Theoretical Study of Brush Seal and Shaft Thermal Interaction", ASME paper no. GT-2003-38276.

[38] Chew, J. W., and Guardino, C., 2004, "Simulation of Flow and Heat Transfer in the Tip Region of a Brush Seal", Int. J. Heat Fluid Flow, 25**,** No. 4, pp. 649-658.

[39] Demiroglu, M., 2004, "An Investigation of Tip Force and Heat Generation Characteristics of Brush Seals", Ph.D. Thesis, Rensselaer Polytechnic Institute, Troy, NY, USA.

[40] Dogu, Y., and Aksit, M., 2006, "Brush Seal Temperature Distribution Analysis", ASME J. Eng. For Gas Turbines and Power, 128, pp. 599-609.

[41] Wood, P.E. and Jones, T.V., "A Test Facility for the Measurement of Torques at the Shaft to Seal Interface in Brush Seals", ASME Gas Turbine and Aeroengine Congress Paper, ASME 97-GT-184, 1997.

[42] Long, C.A. and Marras, Y., "Contact Force Measurements Under a Brush Seal", ASME Gas Turbine and Aeroengine Congress Paper, ASME 95-GT-211, 1995.

[43] Bidkar, R.A, Zheng X., Demiroglu, M, Turnquist, N., 2011, "Stiffness Measurement for Pressure-Loaded Brush Seals", Proceedings of ASME Turbo Expo 2011, Vancouver, Canada, GT-2011-45399.

[44] Stango, R. J., Zhao, H., Shia, C. Y.,"Analysis of Contact Mechanics for Rotor-Bristle Interference of Brush Seals", Journal of Tribology, Vol. 125, 414-421, ASME Transactions, 2003.

[45] Zhao, H., Stango, R. J., "Effect of Flow-Induced Radial Load on Brush Seal/Roto Contact Mechanics", Journal of Tribology, Vol. 126, 208-215, ASME Transactions, 2004.

[46] Crudgington, P.F., Browsher, A., "Brush Seal Pack Hysteresis", American Institute of Aeronautics and Astronautics, AIAA-2002-3794, 2002.

[47] Crudgington, P.F., Browsher, A., "Brush Seal Blow Down", American Institute of Aeronautics and Astronautics, AIAA-2003-4697, 2003

[48] Guardino, C., Chew, J.W, "Numerical Simulation of 3D Bristle Bending in Brush Seals", ASME Turbo Expo, GT2004-53176, 2004.

[49] Lelli, D., Chew, J.W, Cooper, P., "Combined 3D Fluid Dynamics and Mechanical Modelling of Brush Seals", ASME Turbo Expo, GT2005-68973, 2005.

[50] Heinrich, M. S., McKeown, E., "Manufacturing Process and Arrangement for Manufacturing Brush-Type Seals", United States Patent, US006062463A, 2000.

[51] Bryant, D. P., Afzali S., "Method of Making Bristle Arrangement for Brush Seal", United States Patent, US007454822B2, 2008.

[52] http://www.haynesintl.com/literature.htm

[53] Norton, R. L., "Machine Design – An Integrated Approach", 2nd Edition, 2000

[54] http://hghouston.com/resources/material-property-data/stainless-steel-data/cold-working-properties.aspx

[55] GMN, "High Frequency Spindles for Manual Tool Change", 2508-0310.

[56] www.gmn.de

[57] Anonymous, MSC Software, “MSC.Nastran 2005 r2, Quick Reference Guide”, 2005.

[58] Hagg, A.C., Sankey, G.O., “The Containment of Disk Burst Fragments by Cylindrical Shells”, Journal of Engineering for Power, April 1974.

[59] Bayley, F. J. and Long, C.A., “A Combined Experimental and Theoretical Study of Flow and Pressure Distributions in a Brush Seal”, ASME Trans. J.Eng. for Gas Turbines and Power, 115, pp 404-410, 1993.

[60] Turner, M. T., Chew, J.W. and Long, C.A., “Experimental Investigation and Mathematical Modeling of Clearance Brush Seals”, ASME Gas Turbine and Aero-engine Congress Paper ASME 97-GT-282, 1997.

[61] Fellenstein, J. A., DellaCorte, C., “A New Tribological Test for Candidate Brush Seal Materials Evaluation”, NASA Technical Memorandum, NASA TM-106753, Chicago, Illinois, May15-20, 1995.

[62] Fellenstein, J. A., DellaCorte, C., Moore, K. D., Boyes, E., “High Temperature Brush Seal Tuft Testing of Metallic Bristles Versus Chrome Carbide”, AIAA/SAE/ASME/ASEE, 32nd Joint Propulsion Conference Paper, AIAA 96-2908, 1996.

[63] Fellenstein, J. A., DellaCorte, C., Moore, K. D., Boyes, E., “High Temperature Brush Seal Tuft Testing of Selected Nickel-Chrome and Cobalt-Chrome Superalloys”, AIAA/SAE/ASME/ASEE, 33rd Joint Propulsion Conference Paper, AIAA 97-2634, 1997.

[64] Fellenstein, J. A., DellaCorte, C., “Preliminary Tuft Testing of Metallic Bristles Versus PS212, PS300, and HVOF300”, NASA Technical Memorandum, 107522, Detroit, Michigan, May 17-21, 1998.

[65] Duran, E. T., “Analysis of Shear Heating and Effect of Temperature Dependent Viscosity on Hydrodynamic Lift of Oil Brush Seals”, MSc Thesis, Sabanci University, 2006.

[66] Bhate, N., Thermos, A. C., Aksit, M. F., Kizil, H., "Non-Metallic Brush Seals for Gas Turbine Bearings", Proceedings of ASME Turbo Expo 2004, GT2004-54296, 2004.

[67] Young, W.C., Budynas, R. G., "Roark's Formulas for Stress and Strain", 7th Edition, ISBN: 0-07-072542-X.

[68] Anonymous, Abaqus Analysis User's Manual, Abaqus 6.9.EF1.

[69] http://www.crossmanufacturing.com/brush_seals.html

[70] Patent No: US5192084A, "Brush Seal Arrangement"

[71] Kazuhiko, T., "Multi-Stage Brush Seal", Europen Patent Application, EP 2 305 956 A2, 2011.

[72] Zhebg, X., "Hybrid Multistage Brush Seal", WO 2010/076636 A1, 2008.

[73] Kazuhiko, T., "Sealing Apparatus with Multistage Brush Seal", US 2011/0072831, 2011.

[74] Patent No: US5201530A, "Multi-Layered Brush Seal"

[75] Patent No: CN201671661U, 2010.

[76] Dinc, S., Demiroglu, M., Turnquist, N., Mortzheim, J., Goetze, G., Maupin, J., Hopkins, J., Wolfe, C., Florin, M., "Fundemental Design Issues of Brush Seals for Industrial Applications", ASME Journal of Turbomachinery, April 2002, Vol.124/293.

[77] http://www.flickr.com/photos/wim_a-z_photo/6022805593/in/photostream/